DYKE PROPAGATION PATHS: THE MOVEMENT OF MAGMA FROM THE SOURCE TO THE SURFACE

A thesis submitted for the degree of Doctor of Philosophy at the University of London

Kyriaki Drymoni

Rock Fractures and Fluid Flow (RF^3) research group

Department of Earth Sciences

Royal Holloway, University of London

September 2019

Declaration of authorship

I, Kyriaki Drymoni, hereby declare that this thesis and the work presented is entirely my own, unless otherwise stated. The main body of the thesis, Chapters 4-7, is a collection either of co-authored papers that are submitted, or in preparation for publication. I am responsible for the data collection throughout the thesis and the first author of all four of the included papers. Statements of my contribution are included on the cover page of each paper as well.

Signed

Dated

Acknowledgements

When something <magical> is happening in your life, some call it just a coincidence, others great luck, or a lifetime opportunity. For me, this PhD was all the previous at the same time, and I would not be here today to write this if it were not for those people I met, and I kindly want to thank.

I owe so many to my Professor that picked the eccentric Mediterranean lady and gave her the most significant opportunity of her life, to grow up as a scientist and go down the rabbit hole like another Alice in Wonderland. I want to thank my supervisor, Prof. Agust Gudmundsson for giving me the scientific freedom to explore the world of science in the way I desired it, taught me new skills, instilled me into Volcanotectonics and became my scientific inspiration.

However, nothing would have been equally the same without Dr John Browning, who I sincerely thank. I massively appreciate his infinite passion and zeal to make me a better scientist every day. His mentorship, and foremost the ultimate help, support and the time he invested on me those four years to help me fulfil my academic desire, to learn more and question everything even better. Lastly, there is nothing more difficult than having to supervise a friend, and for that, I truly respect him.

I would like to thank Dr Alison Rust for allowing me to open my wings and fulfil my desire, to become a volcanologist (she pushed the button!). I thank her for being next to me, not only as a great supervisor but also as a person in the

most challenging times. The time she invested in the field and during the four years of this PhD, her on spot comments, her guidance and for believing in me whenever I lost hope. I would also like to thank Prof. Kathy Cashman for opening her door, <adopted> me and gave me the fantastic opportunity to be part of the volcanological team at the University of Bristol. There is nothing more valuable than this feeling after every Thursday meeting, the inspiration, the ideas, and the unforgettable emotions that I always had while returning home. For that reason, both Kathy and Alison will always be my precious <magma chamber>.

Beside my supervisors, my love and respect go to my partner Thomas who was next to me during those difficult four years (the scary PhD years as I used to call them) and was supporting me every day and every night, the good days and the bad days. I think he did a PhD in bravery and resilience too. Of course, I owe everything to my family, who allowed me to follow my heart and for always inspiring me to become a better person every day. I thank my dad, my mum and my brother. For what they are and for all their support through those four years.

I thank Prof. Margaret Collinson for her kind support during my PGR studies at RHUL. Dr Christina Manning for helping, mentoring, and supporting me professionally and personally throughout my studies, my first steps in academic teaching and beyond that, I thank her very much. I thank Dr Giulio Solferino for being such an excellent mentor and teaching me how to be a professional researcher and an inspiring teacher. Also, I would not be here without my Greek professors who will always be in my heart and were next to me, although far

away from me. I thank Dr Panagiotis Pomonis and Prof. Andreas Magganas for teaching me the academic ethos and the knowledge which I would love to transfer with the same passion in the future.

I kindly thank Prof. Tim Druitt for his unconditional precious guidance, help and feedback on Santorini geology throughout my studies, which was very important for me, and I very much appreciated. I thank Dr Thomas Mitchell for his kind help and for allowing me to learn and explore the Rock Physics world in the UCL Rock Physics Lab. I feel fortunate that I had this opportunity. A heartful thank you goes to Prof. Phil Meredith for his kind and invaluable advice and feedback during our team's presentation practice days. Massive thanks go to Dr Evi Nomikou for allowing me to enhance my transferable skills and participate in such valuable courses on Santorini island the last three years.

I want to thank those great and lovely friends that although I was away, it was like they were next to me every day. They know who they are. Massive thanks go to my new family at RHUL, the fantastic 3 (Rafika, Ania, Sibel), my office and team buddies for sharing their everyday life with me and honoured me with their friendship. A big thank you goes to my great colleagues (and friends) from around the world that make this volcanological community so great. I learned so many things from all of them and every meeting, conference, school, was unique! (If this coronavirus had struck earlier, I could have been a dangerous person - thanks that did not happen, and I could hug everyone without any guilt). Mr Frank and Mr Mark, for being so helpful and without them I don't know what I

could have done in this IT world, Kevin and Dan for the unconditional help every time I needed it. Alex for being this fantastic person, Nathaniel for being next to me like family, Basim for being my big brother, Fabio for being my field alter-ego and so many thanks to Julia my precious and lovely friend for being the sister I never had.

Abstract

Dyke propagation is the most efficient and common process of magmatransport from the source to the surface on earth. Dykes (magma-filled fractures) are initiated from deep-seated reservoirs and shallow magma chambers that form at various depths in volcanic areas. Triggering events increase the magmatic pressure inside chambers/reservoirs until the excess pressure reaches the tensile strength of the surrounding host rock resulting in dyke/sheet injection. The chambers/reservoirs together with injected dykes/sheets/sills define a volcanic plumbing system, a term which is used to describe the volcanotectonic framework and interconnections beneath a central volcano (polygenetic volcano). One of the fundamental unsolved problem in volcanology is how to make reliable forecasts of magma-chamber rupture and dyke propagation paths. Presently, we are generally unable to forecast the propagation paths. This thesis provides field data and numerical models with the view of understanding dyke-path formation and, eventually, being able to forecast dyke/sheet paths during volcano unrest periods. In particular, this study tries to assess the probability of an injected dyke to becoming a feeder by combining field studies (primary structural and petrological) with analytical and numerical modelling. Also, it defines novel methodologies for studying a magma plumbing system with application to the Santorini volcano in Greece. During this research, a detailed geological map of the Santorini dyke swarm was compiled in conjunction with the collection of primary field data. These were used as inputs in numerical

models (COMSOL Multiphysics) to forecast likely dyke paths, dyke arrest conditions, and dyke-fault interactions in heterogeneous and anisotropic crustal segments/volcanoes. A detailed study was also made of the Santorini dyke swarm itself, combining structural and petrogenetic analyses to understand better the formation and emplacement mechanics of the dykes. I also provide data on the dyke-fed products of the chambers. The results presented here have important scientific and sociological (hazard) implications, particularly in providing a new understanding of dyke-propagation paths and eruption forecasting.

List of Contents

Chapter 1: Evolution of the applied scientific ideas and research objectives

Chapter 2: Methodologies

2.1 Field methods

2.1.1 Fieldwork equipment

2.1.2 Geological mapping (field analysis)

2.1.2.1 Structural analysis

2.1.2.2 Petrological analysis

2.1.2.3 Host rock analysis

2.2 Laboratory research

2.2.1 Microscopic analysis

2.2.2 Thin section preparation laboratory-petrographic analysis

2.2.3 Modal analysis

2.2.3.1 Electromechanical point counting

2.2.3.2 Image J analysis

2.2.4 Carbon coating -scanning electron microscope (SEM)

2.2.5 X-Ray Fluorescence spectrometry (XRF)

2.2.6 CIPW Normative composition

2.2.7 Petrogenetic model

2.3 Numerical methods

2.3.1 COMSOL Multiphysics

2.3.1.1 Theoretical and numerical modelling background

2.3.1.2 Model design

2.3.1.3 Meshing

2.3.1.4 Model results & interpretations

2.3.1.5 FEM modelling versus other techniques

2.4 Analytical modelling

2.4.1 Conditions of dyke emplacement

Chapter 3: Multidisciplinary studies of the northern caldera wall dyke swarms

3.1 Introduction

3.2 Mechanics dyke emplacement

- 3.2.1 Northern caldera dyke swarm
- 3.2.2 Regional tectonics
- 3.2.3 Dyke thicknesses, overpressure and source depth
- 3.2.4 Probabilistic estimation of dyke fates

3.3 Host rock geology

- 3.3.1 Stratigraphy of the northern caldera wall
- 3.3.2 Reconstruction of the Peristeria stratovolcano

3.4 Petrography of the dyke swarm and host rock of the northern caldera wall

- 3.4.1 Dykes
- 3.4.2 Host rock
- 3.4.3 Modal Analysis
  - 3.4.3.1 Dyke samples
  - 3.4.3.2 Host rock samples
  - 3.4.3.3 Chilled margin or rims of the dykes' samples

3.5 Geochemistry of the dykes and their host rock

- 3.5.1 Host rock
- 3.5.2 Host rock spiderdiagrams
- 3.5.3 Dykes
- 3.5.4 Dyke spiderdiagrams
- 3.5.5 Geochemical correlations

3.6 Structural and Petrogenetic results

B4. Petrographic Data

Appendix C

C1: Supplementary data- Chapter 4

C2: Supplementary data- Chapter 5

C3: Supplementary data- Chapter 6

Appendix D

D1: CIPW results

D2: Image J results

List of figures

propagation with depth take place: 1) dyke injection triggering, 2) chamber rupture, 3) dyke propagation mechanisms, 4) caldera collapse.

Figure 1.6: Diagram from Gudmundsson and Lotveit (2012) showing the ratio of the strain energy release rate for fracture deflection Gd to that of fracture penetration Gp. Yellow part of the diagram encourages fracture/dyke deflection. Data from He and Hutchinson (1989) and Hutchinson (1996).

Figure 1.7: (A) Simplified map showing the main tectonic features of the Aegean Sea modified from Konstantinou et al. (2006).

Figure 1.8: A) Santorini bathymetric map (Hooft et al., 2017) with annotations of the locations of the Kameni islands (post-Minoan volcanism) and the Kolumbo submarine volcano. (B) Map from Hooft et al. (2017), and references therein, showing the major tectonic structures around Santorini island and the epicentre of the earthquake that hit near the island of Amorgos the 9th of July 1956.

Figure 1.9: Simplified geological map of Santorini Island from Druitt et al. (1999). The map shows the distribution of the lava flows, pyroclastic materials and metamorphic basement products. In addition, it includes the volcanotectonic lines that control magma ascent at Santorini (Druitt et al., 1999; Nomikou et al., 2013; Rizzo et al., 2016; Hooft et al., 2017). CSK: Christiana-Santorini-Kolumbo volcanic fields.

thickness as well as its studied parts core, rim, chilled margin studied here.

Figure 2.5: Flow chart showing the methodology followed during the petrogenetic analysis.

Figure 2.6: The microscope apparatus used during the microscopic analysis. (A) A polarised optical microscope. (B) A NIKON Microphot FX-35A optic polarised microscope supplied with the NIKON DS-5M camera system digital camera. (C) An electromechanical point counter attached to a polarising microscope used to obtain qualitatively the chemical composition of the studied specimens.

Figure 2.7: Backscattered SEM image edited by image J. (A) Original BSE image (WD 19.6mm, 20kV), (B) design of the different observed minerals with the use of vector graphic program, (C), Edited image showing the minerals and the vesicularity with a vector graphic program. (D) Calculation of the crystal and matrix area (white colour) and vesicularity (black colour), (E) Edited image showing the groundmass and vesicularity with a vector graphic program, (F) Calculation of the vesicularity (black colour) and crystal cracks, (G) the studied thin section scanned showing the position of the BSE image in the yellow circle. The Analysis gave the final measurements: Vesicularity (black) 12.95%, Opx (dark brown) 61.75%, Plag (pink) 19.04%, Groundmass (yellow) 6.26%

Figure 2.8: The carbon coating apparatus, property of the SEARG (RHUL).

Figure 2.9: Backscattered (BSE) image of Dyke_77 showing the complex

textures due to crustal assimilation during propagation. A super-heated melt that either belongs to the same dyke or a different lithology (e.g. pyroclastic) which assimilates the groundmass of the dyke while the dyke was propagating (parts of groundmass were captured inside the clot).

Figure 2.10: Geochem preparation lab. (A) Stage one, view of the Rock splitter & Jaw crusher, TEMA crusher, (B) tungsten TEMA crusher disks, (C) Stage two-sample weighting & LOI calculation.

Figure 2.11: Stage 3 - construction of pellet samples for trace element analysis.

Figure 2.12: The NORM excel spreadsheet used for the calculation of minerals originally derived by Hollocher Kurt (Union College, NY) after Johanssen (1931).

Figure 2.13: Flow chart of the numerical modelling procedure.

Figure 2.14: A screenshot of the Model Builder environment in COMSOL Multiphysics (COMSOL blog, 2017)

Figure 2.15: A rock parallelepiped subject to a triaxial stress field. The illustration shows the principal stresses $\sigma 1$, $\sigma 2$, $\sigma 3$ as well as the compressive strain $\varepsilon 1$ and tensile strains $-\varepsilon 2$ and $-\varepsilon 3$.

Figure 2.16: Benchmark model setup in 2D symmetric domain.

Figure 2.17: Triangular mesh setup in a 2D symmetric model. The setup is part

of a larger model showing the area of interest and the mesh elements.

Figure 2.18: A COMSOL benchmark model result output generated from a symmetric model setup (x-y axis in m). The only loading is magmatic overpressure of 5 MPa in the vertical dyke. The stress map is showing the distribution and magnitude of the minimum principal compressive (maximum tensile) stress (σ_3) as well as the orientation of the arrow surfaces (σ_1) (red arrows) and (σ_2) (white arrows).

Figure 2.19: Schematic illustration of the studied parameters. Pe denotes for the magmatic excess pressure of a magma chamber which can lead to dyke triggering and injection, Po is the magma overpressure away from the magma chamber and the driving parameter of dyke propagation, H is the depth of the magma source (here a magma chamber) (Not in scale).

Chapter 3: Multidisciplinary studies of the northern caldera wall dyke swarm and its host rock

Figure 3.1: Map showing the location of the dyke swarm in the northern caldera wall.

Figure 3.2: (A) Histogram showing the strike orientation in a 20˚ bin, (B) Rose diagram of the studied dyke swarm showing the orientation of the dykes.

Figure 3.3: (A) Dyke_24 and (B) Dyke_25 at the lower level of the caldera wall.

The observed vesicles are elongated parallel to the inferred direction of σ_1.

Figure 3.4: Map modified from Druitt et al. (1999), F1-F4 and fA normal faults mapped from Druitt et al. 1999. During this study F2, F3 and fA faults were also mapped, and faults fB-D were added.

Figure 3.5: (A) Graph showing the dip of the dykes to be mostly subvertical. Mode=84˚, Average=81˚, (B) Graph showing the thickness of the dykes in relation to their dip.

Figure 3.6: Graph showing the thickness of the dykes along the studied profile on the caldera wall.

Figure 3.7: Graph showing the source depths along profile for each dyke based on Eq. 2.10.

Figure 3.8: Statistical analysis of the qualitative measurements collected in the field. The distribution shows the percentages of the possible dyke paths; their qualitative analysis of arrest or propagation.

Figure 3.9: The location and distribution of lavas associated with the Peristeria volcano.

Figure 3.10: The location and distribution of the first explosive cycle at the northern caldera wall.

Figure 3.11: Illustrations showing the reconstruction of the first eruptive phase and distribution of the eruptive products from the pumice fall deposit isopaches

from Druitt et al. (1989, 1999) and mapped lava flows. (A) extrusions of Rhyodacites, remnants of the low shield (B): pink sillar facies of ignimbrite and red spatter agglomerate with abundant plutonic nodules dominates locally within the same area (C): yellowish pumiceous deposit of phreatomagmatic origin with a maximum thickness of 55 cm at the Northern caldera wall, (D) the caldera collapse event that accompanied the last eruption (Druitt and Francaviglia, 1992). The shields are not to scale and are extrapolated from the position of the deposits from Druitt et al. (1999).

Figure 3.12: The location and distribution of the second explosive cycle.

Figure 3.13: Illustrations showing the reconstruction of Peristeria edifice as suggested after this study. (A) A: av1 flow delineates a phreatomagmatic activity which is overlapped by an angular unconformity, (B): incremental caldera collapse, (C): av2 flow & angular unconformity, (D): av3 flow.

Figure 3.14: Spiderdiagram of Dyke_1 (green dotted line) with (a) Rt - rhyodacitic (milo Bay) sample and (b) Andesites of Oia.

Figure 3.15: Dyke 1 (core) under crossed (A,C,E) and parallel polars (B,D,F). The groundmass (Plag+pyrox+ol+glass) has an intergranular, porphyritic and trachytic texture and the main phenocrysts are Plag+opx+cpx+ol+op. Plagioclase populations have coarse sieve, fine rim sieve textures (C, E) and inclusions (C, E). Opx, Cpx and Ol phenocrysts are present in glomerocrysts or alone in the

groundmass. Opx and Cpx are usually twinned while Olivine has sometimes reaction rims.

Figure 3.16: Spiderdiagram of Akr lavas.

Figure 3.17: Dyke Akr 1(core) under crossed (A,C,E) and parallel polars (B,D,F). The groundmass (Plag+pyrox+ol+glass) is trachytic and intergranular (A,C,E) composed mainly by coarse lath plagioclase. The main phenocrysts are Ol+plag+cpx. Plagioclase crystals are either yellow or grey (E). They also form Glomerocrysts with opx. Olivine is present as the main phenocryst with reaction rims and altered rims replaced by iddingsite (C, E).

Figure 3.18: Bar diagrams showing the relative amounts of minerals in dyke samples (1, 4, 6, 21, 76, 77) that constitute the whole rock chemistry. Orange x axis denotes no calcite mineral present.

Figure 3.19: Bar diagrams of dyke samples (49, 6/s1, 81, 89) showing the amounts of the mineralogical assemblage that constitute the whole rock chemistry. Orange x axis denotes no calcite mineral present compared to green where it has been calculated to the total percentage.

Figure 3.20: Bar diagrams of host rock samples (As1, As2, Rp7, Ap4) showing the amounts of the mineralogical assemblage that constitute the whole rock chemistry.

Figure 3.21: Bar diagrams of dyke margin samples (21 rim (a), 81 rim (b), 76 rims 1 (c) and 2 (d), 77 rims 1 (e), 2 (f), 3 (g) and a xenolith found in dyke 77

(h), 89 rim 2 (i), 3 (j)) showing the amounts of the mineralogical assemblage that constitute the whole rock chemistry.

Figure 3.22: Bar diagrams of dyke margin samples (77 rims 1, 2, 3 and a xenolith found in dyke 77) showing the amounts of the mineralogical assemblage that constitute the whole rock chemistry.

Figure 3.23: Histograms of dyke margin samples (89 rim 2, 3) showing the amounts of the mineralogical assemblage that constitute the whole rock chemistry.

Figure 3.24: The northern caldera wall map showing the location of the sampling campaigns. The numbers 1-8 denote the scoria samples collected during the campaigns.

Figure 3.25: TAS classification diagram according to Le Bas et al. (1986) showing the host rock samples analysed in this study.

Figure 3.26: TAS classification diagram according to Le Bas et al. (1986) showing the host rock samples from Bailey et al. (2009).

Figure 3.27: CaO/MgO plot showing the fractionation trend of the host rock magmas. Data from Nicholls (1971); Mann (1983); Huijsmans (1985); Druitt et al. (1999); Zellmer (2000); Bailey et al. (2009); Fabbro et al. (2013, 2014) and this study. B denotes basaltic compositions, BA basaltic andesites, A andesites, B-TA basaltic trachyandesites and TA trachyandesites respectively.

Figure 3.28: Th/Yb versus Ta/Yb plot showing the difference between basalts in a subduction related setting and an oceanic setting derived from MORB depleted sources and OIB enriched sources. Vectors show the subduction enrichment, the within-plate enrichment, the crustal contamination and the fractional crystallisation while the lines separate the boundaries of tholeiitic, calc-alkaline and shoshonitic fields and the dashed lines the oceanic and continental arc origin (after Pearce 1983). Data from Nicholls (1971); Mann (1983); Huijsmans (1985); Druitt et al. (1999); Zellmer (2000); Bailey et al. (2009); Fabbro et al. (2013, 2014) and this study. B denotes basaltic compositions, BA basaltic andesites, A andesites, B-TA basaltic trachyandesites and TA trachyandesites respectively.

Figure 3.29: (A) Spiderdiagram of the REE basaltic compositions normalised by the primordial mantle. Data from Nicholls (1971); Mann (1983); Huijsmans (1985); Druitt et al. (1999); Zellmer (2000); Bailey et al. (2009); Fabbro et al. (2013, 2014) and this study. Localities: MPI, M.V., K.V., Ammoudi, Skaros, Therasia. (B) Spiderdiagram of the REE basaltic andesite compositions normalised by the primordial mantle of Peristeria stratocone. Data from Nicholls (1971); Mann (1983); Huijsmans (1985); Druitt et al. (1999); Zellmer (2000); Bailey et al. (2009); Fabbro et al. (2013, 2014) and this study. Localities: MPI, M.V., K.V., Finikia, Oia.

Figure 3.30: Spiderdiagram of the REE basaltic andesite compositions normalised by the primordial mantle for Simandiri, Cinder cone and TDC lavas.

Data from Nicholls (1971); Mann (1983); Huijsmans (1985); Druitt et al. (1999); Zellmer (2000); Bailey et al. (2009); Fabbro et al. (2013, 2014) and this study. Localities: M.V., K.V., Therasia.(B) Spiderdiagram of the REE basaltic andesite compositions normalised by the primordial mantle for Skaros lavas Data from Nicholls (1971); Mann (1983); Huijsmans (1985); Druitt et al. (1999); Zellmer (2000); Bailey et al. (2009); Fabbro et al. (2013, 2014) and this study. Localities: M.V., Ammoudi, Skaros, Therasia (Corfos Bay/Cape Tino).

Figure 3.31: (A) Spiderdiagram of the REE andesitic compositions normalised by the primordial mantle for Peristeria lavas. Data from Nicholls (1971); Mann (1983); Huijsmans (1985); Druitt et al. (1999); Zellmer (2000); Bailey et al. (2009); Fabbro et al. (2013, 2014) and this study. Localities: MPI., K.V., Finikia, (B) Spiderdiagrams found in andesitic compositions normalised by the primordial mantle for Simandiri, Cinder cones, Skaros and TDC lavas. Data from Nicholls (1971); Mann (1983); Huijsmans (1985); Druitt et al. (1999); Zellmer (2000); Bailey et al. (2009); Fabbro et al. (2013, 2014) and this study. Localities: K.V., Skaros, Therasia.

Figure 3.32: (A) trachyandesite normalised plots by the primordial mantle for Peristeria lavas. Data from Nicholls (1971); Mann (1983); Huijsmans (1985); Druitt et al. (1999); Zellmer (2000); Bailey et al. (2009); Fabbro et al. (2013, 2014) and this study. Localities: MPI., K.V., M.V., (B) trachyandesite normalised plots by the primordial mantle. Data from Nicholls (1971); Mann (1983); Huijsmans (1985); Druitt et al. (1999); Zellmer (2000); Bailey et al.

(2009); Fabbro et al. (2013, 2014) and this study. Locality: Therasia., (C) trachytic normalised plots by the primordial mantle for the Skaros and TDC lavas of Theresia. Data from Nicholls (1971); Mann (1983); Huijsmans (1985); Druitt et al. (1999); Zellmer (2000); Bailey et al. (2009); Fabbro et al. (2013, 2014) and this study. (D) trachydacitic normalised plots by the primordial mantle. Data from Nicholls (1971); Mann (1983); Huijsmans (1985); Druitt (1999); Zellmer (2000); Bailey et al. (2009); Fabbro et al. (2013, 2014) and this study. Localities: Therasia., (E) dacitic normalised plots to a primordial mantle for the TDC lavas of Therasia. Data from Nicholls (1971); Mann (1983); Huijsmans (1985); Druitt (1999); Zellmer (2000); Bailey et al. (2009); Fabbro et al. (2013, 2014) and this study.

Figure 3.33: TAS classification diagram from Le Bas et al. (1986) showing the host rock and dyke samples after this study and Bailey et al. (2009).

Figure 3.34: CaO/MgO plot showing the fractionation trend of the dyke swarm. Data from Nicholls (1971); Mann (1983); Huijsmans (1985); Druitt (1999); Zellmer (2000); Bailey et al. (2009); Fabbro et al. (2013, 2014) and this study. B denotes basaltic compositions, BA basaltic andesites, A andesites, B-TA basaltic trachyandesites and TA trachyandesites respectively. The figure shows that the samples analysed belong to the opx stability section, and hence they reflect contamination signatures and not primitive characteristics.

Figure 3.35: Spiderdiagrams of basaltic dykes normalised to a primordial mantle. Data from Bailey et al. (2009) and this study.

Figure 3.36: Spiderdiagram of the REE for basaltic andesite compositions normalised by the primordial mantle. Data from Nicholls (1971); Mann (1983); Huijsmans (1985); Druitt (1999); Zellmer (2000); Bailey et al. (2009); Fabbro et al. (2013, 2014) and this study.

Figure 3.37: Spider diagram of the REE for andesitic compositions normalised by the primordial mantle. Data from Nicholls (1971); Mann (1983); Huijsmans (1985); Druitt (1999); Zellmer (2000); Bailey et al. (2009); Fabbro et al. (2013, 2014) and this study.

Figure 3.38: Spiderdiagram of the REE trachyandesitic compositions normalised by the primordial mantle. Data from Nicholls (1971); Mann (1983); Huijsmans (1985); Druitt (1999); Zellmer (2000); Bailey et al. (2009); Fabbro et al. (2013, 2014) and this study.

Figure 3.39: Spiderdiagram of the REE trachytic compositions normalised by the primordial mantle. Data from Nicholls (1971); Mann (1983); Huijsmans (1985); Druitt (1999); Zellmer (2000); Bailey et al. (2009); Fabbro et al. (2013, 2014) and this study.

Figure 3.40: Spiderdiagram of the REE dacitic compositions normalised by the primordial mantle. Data from Nicholls (1971); Mann (1983); Huijsmans(1985);

Druitt (1999); Zellmer (2000); Bailey et al. (2009); Fabbro et al. (2013, 2014) and this study.

Figure 3.41: (A) Geological map of Santorini modified from Druitt et al. (1999) showing the Kameni and Kolumbo VT lines, and the location of the studied dykes and the lava samples, (B) TAS classification diagram from Le Bas et al. (1986) showing the dyke and lava samples from Nicholls (1971); Mann (1983); Huijsmans (1985) and Fabbro (2014), (C) Nb/Zr diagram, (D) La/Yb diagram, (E) rock/mantle spiderdiagrams of the aforementioned samples.

Figure 3.42: Strike Vs thickness diagrams for (A) Basaltic dykes, (B) Basaltic andesitic dykes, (C) Andesitic, Trachyandesitic and Trachytic dykes.

Figure 3.43: Schematic illustration showing the textural features as discussed before that could be observed on a two-magma chamber volcanic plumbing system such as the one hosted on Santorini volcano. Not to scale.

Figure 3.44: Illustration showing the evolution of the northern caldera wall plumbing system discerned from this multidisciplinary study. View of the plumbing system during the formation of (A) Peristeria stratovolcano, (B) Simandiri shield, (C) Cinder cones of the northern caldera wall, (D) Skaros shield, (E) TDC shield. Not to scale

Chapter 4: Dyke-arrest scenarios in extensional regimes: insights from field observations and numerical models, Santorini, Greece

Figure 4.1: Schematic illustration of the three primary mechanisms (Stress barriers, Elastic mismatch and Cook-Gordon debonding and delamination) that control fluid-driven fracture arrest. In part C the weak contact delaminates and opens ahead of the progressing fracture tip. The controlling factors of each mechanism are shown at the bottom.

Figure 4.2: (A) Geological map of the northern caldera wall modified from Druitt et al. (1999), showing the location of the dyke swarm. The key on the left shows the lithologies found on the northern caldera wall (Druitt et al., 1999). Av1: andesitic lavas, tuffs, scoria and breccia, av2: silicic andesitic lavas, av3: thinly bedded andesites and basalts with subordinate dacites, tuffs and scoria, ra: rhyodacites, ap2: pink sillar facies of a pyroclastic density current and red spatter agglomerate with abundant plutonic nodules, rp3: rhyodacitic pumice, ap4: middle tuffs thick scoria-fall deposits, as2:andesites and basalts of Cape Skaros, ap5: upper scoria 2- andesitic thick spatter agglomerate, ao: andesites of Oia, rp6: Cape Riva tuff, rp7: Minoan tuff. Cross sections along the caldera profile: (B) panorama of the northern caldera wall, the av3 horizon, annotations mark the horizons of andesitic lavas, tuffs and scoria, (C) a dyke that cuts through a heterogeneous segment which exhibits anastomosing textures at the base, annotations mark the horizons of andesitic lavas, tuff and scoria (D) panorama close to the NE corner of the caldera wall, the dykes were arrested or deflected

within different layers (and hence at different depths) in the heterogeneous host rock, which is comprised of tuffs, scoria and lavas.

Figure 4.3: Four model setups. (A) Homogeneous host rock with Young's modulus of 40 GPa and a 1 m thick cavity (dyke) with an internal pressure of 5 MPa (B) Example of a two layered or heterogeneous model with a Young's modulus of 40 GPa in E1 and a Young's modulus of 10 GPa in E2, again with a 1 m thick dyke (C) Homogeneous host rock with a Young's modulus of 40 GPa and a 1 m thick cavity (dyke) with an internal pressure of 5 MPa subjected to an extra horizontal extension of 0.5 MPa at the boundaries. D) Example of a two layered or heterogeneous model with a Young's modulus of 40 GPa in E1 and a Young's' modulus of 10 GPa in E2, again with a 1 m thick dyke and subjected to an extra extensional force of 0.5 MPa (denoted by the red arrows).

Figure 4.4: Studied dyke 1 and dyke 2 (annotated yellow) in the northern caldera wall. Older dyke populations (annotated pink) can also be observed in the cross-section.

Figure 4.5: Characteristics of the dykes exposed on the Santorini northern caldera wall. (A) Rose diagram of dyke strike directions, (B) Frequency of dykes along the profile, (C) Dyke thickness as a function of dyke dip, D) Thickness of dykes along the measured profile.

Figure 4.6: Observed dyke propagation paths on the northern caldera wall. (A) Segmented and branched propagated dykes, (B) a possibly multiple arrested

dyke which forms rounded tips as it propagates through a compliant host rock, (C) dyke-fault deflection; the inclined sheet on the left is being deflected into the shear fracture, the normal fault.

Figure 4.7: (A) Diagram showing the calculated dyke overpressures (P_o) with distance along the studied profile. (B) 90% of the measurements range between 0.1-6MPa.

Figure 4.8: Dyke 1 propagated through a heterogeneous segment of tuff, unconsolidated scoria and lava in the northern caldera wall of Santorini. (A): annotated field photograph, (B): corresponding FEM model setup. The stars correspond to the specific picked contacts from which 2D snapshots were produced in COMSOL Multiphysics as the dyke is propagating towards the surface.

Figure 4.9: FEM (finite element) models of dyke propagation (tensile stress σ_3) through a heterogeneous host rock based on Fig. 4.8B. (A1a-c): Overpressure (P_o=1MPa) is the only loading boundary condition, (B1a-c): Overpressure (P_o=1MPa) and an extensional stress field (F_{ext}=0.5MPa) are applied. The red arrow surface is σ_1 and the white arrow surface is σ_3, (a) scoria/ tuff contact, (b) scoria/ lava contact, (c) lava/scoria contact (y-axis in meters).

Figure 4.10: FEM (finite element) models of dyke propagation (tensile stress σ_3) in a heterogeneous host rock based on Fig. 4.8B. (A2a-c): Overpressure (P_o=5MPa) is the only loading boundary condition, (B2a-c): Overpressure

(P_o=5MPa) and an extensional stress field (F_{ext}=0.5MPa) are applied. The red arrow surface is σ_1 and the white arrow surface is σ_3, (a) scoria/ tuff contact, (b) scoria/ lava contact, (c) lava/scoria contact (y-axis in meters).

Figure 4.11: Dyke 2 has thinned out and became arrested within a lava unit in the northern caldera wall. (A): annotated field photograph, (B): FEM model setup. The stars correspond to the specific picked contacts from which 2D snapshots were produced in COMSOL Multiphysics as the dyke is propagating towards the surface.

Figure 4.12: FEM (finite element) models of dyke propagation (tensile stress σ_3) in a heterogeneous host rock based on Fig. 4.11B. (A3a-c): Overpressure (P_o=1MPa) is the only loading boundary condition, (B3a-c): Overpressure (P_o=1MPa) and an extensional stress field (F_{ext}=0.5MPa) are applied. The red arrow surface is σ1 and the white arrow surface is σ_3, (a) scoria/tuff contact, (b) scoria/lava contact, (c) lava/scoria contact (y-axis in meters).

Figure 4.13: FEM (finite element) models of dyke propagation (tensile stress σ_3) in a heterogeneous host rock based on Fig. 4.11B. (A4a-c): Overpressure (P_o=5MPa) is the only loading boundary condition, (B4a-c): Overpressure (P_o=5MPa) and an extensional stress field (F_{ext}=0.5MPa) are applied. The red arrow surface is σ1 and the white arrow surface is σ_3, (a) scoria/tuff contact, (b) scoria/lava contact, (c) lava/scoria contact (y-axis in meters).

Figure 4.14: Diagram showing the max stress concentration at the dyke tips for

both dykes at the studied loading conditions, in different type of contacts 1) very compliant - compliant (r=0.1), 2) very compliant - stiff (r=0.05), 3) stiff - very compliant (r=20). The figures on the right up corner of the graphs are showing the stress concentration on the dyke tips at the compliant - stiff contacts for dyke 1 and dyke 2.

Figure 4.15: Schematic illustrations showing the parameters studied in the sensitivity tests. (A): Connections between magmatic conditions (magmatic overpressure, P_o) and the stratigraphy-mechanical/material conditions of the host rock such as the sequence of the stratigraphy, the thickness of the layers (W_L), and the crustal thickness (W_C). (B): Conditions of magmatic overpressure (P_o) associated with different boundary conditions on the creation of stress rotations and stress barriers in an active volcanotectonic setting.

Figure 4.16: Results of the sensitivity tests as shown in Fig. 4.15 Part A. Different stiffness contrasts (E_U/E_L) (0.05, 0.5, 5, 50) subject to 1 and 5MPa overpressure control the observed stress rotations in three different rock type layers. Annotations: Red circle for possibly arrest, orange for unsure fate and green for propagation.

Figure 4.17: Figure showing the results of the second model suites of the sensitivity tests as shown in Fig. 4.15 Part B subject to different stiffness contrasts (E_U/E_L) (0.5, 5, 50). We observe the mutual connections between the magmatic conditions subjected to changes in the local stress field and producing

stress barriers. S1: application of horizontal extension (F_{ext}= 1MPa), S2: application of magmatic overpressure (P_o=1MPa), S3: application of magmatic overpressure (P_o=1MPa) and horizontal extension (F_{ext}= 3MPa), S4: application of magmatic overpressure (Po=1MPa) and horizontal extension (F_{ext}= 0.5MPa), S5: application of magmatic overpressure (P_o=1MPa) and horizontal compression (F_{cmp}= 3MPa), S6: application of magmatic overpressure (P_o=1MPa) and horizontal compression (F_{cmp}= 0.5MPa).

Chapter 5: Deflection of dikes and inclined sheets into faults at Santorini volcano, Greece

Figure 5.1: Illustration showing the progressive formation of a Mode I, extension, fracture. A) Microcracks are concentrated around the tip of a fracture in a linear elastic, brittle, material. Further crack nucleation and growth initiates (within the process zone) when the tensile stress at the tip of the fracture matches or exceeds the tensile strength of the host rock. B) Crack growth is encouraged if the strain energy release rate (GI) of the system rises. C) Crack propagation or fracture is controlled by the material properties of the host rock for any energy criteria used for the crack. D) Deflection mechanisms A. Stress barrier, B. Elastic mismatch and C. Debonding and delamination. W_S denotes for the work that enters the system to produce a fracture, K_I is the stress intensity factor of a Mode I fracture, K_{IC} is the critical stress intensity factor or fracture toughness, G_I is the

strain energy of a Mode I fracture, the energy release rate of the material that controls the growth of the fracture, G_{IC} is the critical elastic strain energy or material toughness, To is the tensile strength of the host rock, E is a materials Young's modulus (stiffness), σ_{max} is the maximum tensile stress at the tip of a semi-elliptical notch, α is the half length of a crack, σ_o is the remote tensile stress, σc is the critical tensile stress, σ1 is the maximum principal stress and σ_3 is the minimum principal stress or the tensile stress of the fracture, ρ_c is the radius of curvature.

Figure 5.2: (A) Map of the Aegean modified from Konstantinou et al. (2006) showing the main tectonic features and major faults. The direction of the rift zone is given from Nomikou et al. (2013) and the local direction of extension from Feuillet (2013). NAF: North Anatolian fault. (B) Simplified geological map of Santorini modified from Druitt et al. (1999).

Figure 5.3: Fault evolution from Late Pliocene to Holocene on the Santorini onshore and offshore region. The diagram shows the fault planes in time according to interpretations from seismic stratigraphic profiles (Perissoratis, 1995; Piper and Perissoratis, 2003; Pe-piper et al., 2005; Piper et al., 2007) and the dike swarm located at the northern caldera wall (Druitt et al., 1999; Chapter 4). As: Andesites and basalts of Cape Simandiri (172 ka), Ap4: Cinder cones of scoria-fall deposits from Megalo and Kokkino Vouno, and tuff ring (125-80 ka). As2: Skaros lavas (70-54 ka), Ap5: Upper scoria 2 (54 ka), Rt: Rhyodacites of

Therasia (224 ka), Rp6: Cape Riva tuff (21 ka), Rp7: Minoan tuff (3.6 ka) (Druitt et al., 1999).

Figure 5.4: Numerical model setups for a dike (D1, D2, D4), and an inclined sheet (D3, D5, D6). The cavities (D_T) are 1 m thick with an internal pressure of 5 MPa. The normal fault has a thickness (F_T) of 1m and dips (F_θ) at 65 degrees and it is composed of three layers where both the Young's modulus of the core or the rim could be between 0.001GPa to 10 GPa. The Young's modulus of the host rock (E_{hr}) is 40 GPa and the density of the fault (ρ_F) is 2000kg/m3. The minimum dip of the inclined sheet (D_φ) is 50 degrees. For the sensitivity tests we use a varied Young's modulus for the fault (5 orders of magnitude 0.001-10 GPa) and a magmatic overpressure (P_o) of 1MPa for the dike. We modelled the angle of the dike with the fault (D_θ) for 0˚ (D1), 25 (D2), 40˚ (D3), 50˚ (D4), 65˚ (D5) and 90˚ (D6), the thickness of the dike for i) 1m, ii) 3m, iii) 8m, the thickness of the fault for i) 1m, ii) 5m, iii) 25m, subject to an applied extensional stress field i) 0.5MPa, ii) 1MPa, iii) 3MPa, subject to an applied compressional stress field i) 0.5MPa, ii) 1MPa, iii) 3MPa, and a variant dip length of the fault zone i) 20m, ii)100m, iii) 200m. For all the corners at the bottom of the model are fixed to prevent motion whereas the top ones are free to simulate an area free of shear stresses.

Figure 5.5: (A1) Geological map of the area modified by Druitt et al. (1999) showing the location of the dike swarm from Chapter 4. (A2) Illustration showing the location and motion of F1-F4 faults modified from Druitt et al.

(1999), and the studied fault structures (F2, F3, F5, F6, F7, F8, F9, F10, F11, F12, F13) during this survey, (B) panorama of the northeast corner of the caldera wall showing the lithologies of the heterogeneous and anisotropic host rock from Druitt et al. (1999) as follows: Peristeria stratovolcano: (av1-3) basaltic to dacitic lavas, tuffs, scoria and breccia, First explosive cycle: (ra-ap2-rp3) rhyodacitic lavas to a pyroclastic density current atop by rhyodacitic pumice, Second explosive cycle: (ap4-as2) thick scoria-fall deposits under andesitic and basaltic lavas, the mapped fault structures and the emplaced dikes according to this study, (C) A closer look on the fault structures (F9, F10, F11) at the northern caldera wall formed in the av3 lavas of the old Peristeria edifice.

Figure 5.6: (A) Main structural elements in the northeast corner of the northern caldera wall. The tectonic structure implements a sequence of parallel normal faults dipping 60-70˚ to the northeast. Marker horizons: Av3: Peristeria stratovolcano, As2: Skaros shield. (B) View east towards the caldera wall showing the faults of varied scale observed on the studied area. The dashed area is showing the signs of possible strike slip motion of the F3 fault.

Figure 5.7: Interactions between dikes and fault F5, original photo (Part A) and annotated version (Part B). The numbers indicate two dikes of different ages. One of the dikes (1) is inside the fault and does not intrude into the fault although its path is highly anisotropic. Part C, heterogeneous structure of the fault zone. (D) Dike 2 deflected in the interpreted damage zone of fault F5.

Figure 5.8: FEM (finite element) models of tensile stress (σ_3) of the dike interacting with a low E fault (E fault=0.001 GPa). Their model setup of the dike and fault arrangements are at the top right corner of the snapshots. Overpressure in the dike is 1 MPa. D_θ is 50 degrees. The red arrow surface is σ_1 and black arrow surface is σ_3, (y-axis in meters).

Figure 5.9: FEM (finite element) models of tensile stress (σ_3) of the dike interacting with a high E fault (E fault=10 GPa). Their model setup of the dike and fault arrangements are at the top right corner of the snapshots. Overpressure in the dike is 1 MPa. Dθ is 50 degrees. The red arrow surface is σ_1 and black arrow surface is σ_3, (y-axis in meters).

Figure 5.10: FEM (finite element) models of tensile stress (σ_3) of the dike interacting with a low E fault core (Efault core=0.001 GPa) and a stiff (Efault core=10 GPa) damage zone. Their model setup of the dike and fault arrangements are at the top right corner of the snapshots. Overpressure in the dikes is 1 MPa. D_θ is 50 degrees. The red arrow surface is σ1 and black arrow surface is σ3, (y-axis in meters).

Figure 5.11: FEM (finite element) models of tensile stress (σ_3) of the dike interacting with a stiff E fault core (Efault core=0.001 GPa) and a soft (Efault core=10GPa) damage zone. Their model setup of the dike and fault arrangements are at the top right corner of the snapshots. Overpressure in the dikes is 1 MPa.

D_θ is 50 degrees. The red arrow surface is σ_1 and black arrow surface is σ_3, (y-axis in meters).

Figure 5.12: Illustration showing the results of the FEM models. We observed that regardless the range of the magmatic overpressure (P_o) for both the dike and the inclined sheet, deflection is acquired when the homogeneous fault is active (low Young's modulus) rather than inactive (high Young's modulus). In a heterogeneous fault zone both the vertical dike and the inclined sheet are deflected into the fault cores if the latter were soft and not stiff.

Figure 5.13: Conditions that encourage dike deflection (D) and dike propagation (P) in a series of dike and fault interactions associated with the angle of the dike to the fault (a), the dike thickness (b), the fault thickness (c), regional extension (d), regional compression (e), and the fault height (f) in relation to the mechanical properties of a homogeneous fault zone.

Figure 5.14: Schematic illustration showing the fault evolution at the northern caldera wall and the reconstruction of its geological history from this multidisciplinary study. (A) Peristeria stratovolcano, (B) 1st eruptive cycle, (C) Megalo and Kokkino Vouno cinder cones, (D) Skaros shield.

Chapter 6: Geological and volcanotectonic evolution of the Santorini dyke swarm, Greece

Figure 6.1: The structure of magmatic and volcanic plumbing systems and their dyke swarm architecture: (A) in monogenetic volcanoes and (B) in stratovolcanoes.

Figure 6.2: (A) Modified geological map from Druitt et al. (1999) showing the structure of the northern caldera wall dyke swarm and the stratigraphy of the host rock. (B) Modified geological map from Druitt et al. (1999) showing the volcanotectonic lineaments that partly control magma ascent in the island and the location of the dykes at the western and southern part of the island (1-5).

Figure 6.3: Schematic extrapolated distribution of the volcanic products that belong to the five shields-stratocones studied here. The distribution is according to the geological map of Santorini from Druitt et al. (1999). (A) Peristeria stratovolcano, (B) Simandiri shield, (C) Cinder cones of Megalo and Kokkino Vouno, (D) Skaros shield, (E) Therasia dome complex, (F) Present day.

Figure 6.4: Location of the dykes observed on the Santorini caldera walls. Localities: (A) Northern caldera wall, (B) Therasia caldera wall, (C) Akrotiri caldera wall

Figure 6.5: Map showing the geochemical composition of the studied dykes at the northern caldera wall and the Therasia island.

Figure 6.6: (A) xpl photo of Dyke_76, (B) xpl photo of Dyke_79, (C) Normalised spider diagrams to primordial mantle of Dykes_76 &_79.

Figure 6.7: (A) Location of Dykes_77, _84 &_85, (B) Normalised spider diagrams to primordial mantle of Dykes_77, _84 &_85. Geochemical data of Dykes_84 &_85 are Bailey et al. (2009).

Figure 6.8: (A) Location of dykes 18, 26 and 54, (B) Normalised spider diagrams to primordial mantle of Dykes_18, _26 &_54. Geochemical data of Dykes_18, _26 &_54 are from Bailey et al. (2009).

Figure 6.9: Map showing the location and geochemical composition of the Peristeria dyke subswarm. The dykes are from basaltic andesites (BA) to trachytes (T).

Figure 6.10: Schematic three-dimensional reconstruction of the Santorini plumbing system during the Peristeria stratovolcano activity (530-430 ka).

Figure 6.11: Map showing the location and composition of the Simandiri dyke subswarm. The dykes are mostly basalts and trachyandesites.

Figure 6.12: Schematic three-dimensional reconstruction of the Santorini plumbing system during the Simandiri shield activity (172 ka). (A) The geometry of the feeder dykes (Dyke_21 &_23). (B) The geometry and reconstruction of the Simandiri summit.

Figure 6.13: Map showing the location and composition of the possible Cinder

cones' dyke subswarm. The dykes are basalts to andesites.

Figure 6.14: Schematic three-dimensional reconstruction of the Santorini plumbing system during the activity that formed the Cinder cones at the northern caldera wall.

Figure 6.15: Map showing the location and composition of the Skaros dyke subswarm. The dykes are basalts to andesites.

Figure 6.16: Schematic three-dimensional reconstruction of the Santorini plumbing system during the activity that formed the Cinder Cones at the northern caldera wall.

Figure 6.17: Map showing the location and composition of the TDC dyke subswarm. The dykes are andesites to trachydacites.

Figure 6.18: Schematic three-dimensional reconstruction of the Santorini plumbing system during the activity that formed the Cinder Cones at the northern caldera wall. We observe the TDC edifice and the possible feeder dykes that intersect the caldera walls (Dykes_94, _95, _67, _70).

Figure 6.19: The Santorini caldera wall dyke swarm. The map shows the results of the multidisciplinary study, the location, the strike, the thickness and their triggered event.

Chapter 7: Dyke propagation in a heterogeneous and anisotropic crust, the reconstruction of a volcanic plumbing system.

Figure 7.1: (A) Classic, schematic view of a magmatic plumbing system in rift zones such as at mid-ocean ridges and ophiolites modified from Sinton and Detrick (1992), (B) Schematic illustration of a volcanic plumbing system in a stratovolcano. Not to scale.

Figure 7.2: Geological map of Santorini island with a focus on the studied areas and the observed dyke swarm along the northern caldera wall. The map shows also the two major volcanotectonic lines defined by Druitt et al. (1999) and rift zone by Nomikou et al. (2013).

Figure 7.3: (A) Dyke_6 as observed at Cape Eptapaides. The dyke turns into a sill and becomes arrested in the host rock which is highly heterogeneous and compliant (hyaloclastite), A1: PPL image of Dyke_6, the groundmass (Plag+pyroxene+ol+glass) includes angular or rounded xenoliths which are parts of possibly other magma batches. A2: SEM image of the anisotropic holohyaline groundmass (brown devitrified glass), (B) Dyke_4 as observed on the northern caldera wall (Cape Eptapaides). The dyke is found to intersect all the host rock stratigraphy. The host rock is composed by tuffs, scoria, lavas and hyaloclastites. Anastomosing textures on the latter horizon record macroscopically mixing processes. B1: PPL image of Dyke_4, the groundmass (Plag+pyroxene+ol+glass) has vesicles with crystallised Quartzite. We observe

in the middle a large plagioclase phenocryst (0.8 mm) with coarse sieve texture. B2: SEM image of the groundmass. A crystallised vesicle and a glassy groundmass rim surround a Cpx crystal.

Figure 7.4: Schematic vertical cross section of the transcrustal VPS of Santorini volcano. We propose the possible location of the observed components on the studied samples: 1) antecrysts, 2) phenocrysts (2a and b different populations), 3) xenoliths, 4) enclaves, (a and b are the ellipsoid geometrical terms with a>b).

Figure 7.5: XPL images of glomerocrysts in dykes and host rock samples from Santorini volcano. (A): A plag+ol+cpx glomerocrysts in Dyke_6, (B): plag+cpx aggregates in Dyke_1, (C): A plag+cpx+ol+opx glomerocryst in a scoria sample, (D): plag+cpx glomerocryst in a Minoan ignimbrite sample.

Figure 7.6: Data of recycled material in the transcrustal VPS of Santorini volcano. (A) Convection, (B) accumulates in the magma chamber(s), (a and b are the semi-axes of the ellipsoidal chambers, with a>b).

Figure 7.7: Macroscopic samples of dyke rock. (A) A dyke sample (rim) where we observe a chilled margin, a highly viscous core and scoria material attached on the rims, (B) Dyke_77 sample (core) which includes an enclave cumulate, (C) PPL image of a dyke which consists of xenoliths, scoria and two types of groundmass a black and brown one, (D) A cumulate in a dyke sample.

Figure 7.8: Schematic illustration of the crustal components in the transcrustal VPS of Santorini volcano. (I) Scoria, (II) Xenoliths (III) Cumulates (a and b are the ellipsoid geometrical terms with a>b).

Figure 7.9: Calculation of scoria entrainment into dyke_77. (A) We designed in situ a grid (30x30cm) and designed the number of the observed scoria xenoliths (red circular nodes) into the aphanitic groundmass. (B) Diagram reporting the frequency of the scoria xenoliths to the distance from the dyke rim (m).

Figure 7.10: Schematic illustration showing the flow of the different studied components into the VPS on Santorini volcano.

Figure 7.11: Schematic illustration showing the flow and location of the studied components in a dyke. The red arrows show the displacement of the host-rock entrainment (scoria) during emplacement. The blue arrow shows the flow of the cooling (from the rim to the core). The black arrows show the minimum principal compressive stress or tensile stress. Not to scale.

Chapter 8: Discussion, critical evaluation and future work

Figure 8.1: The stratigraphy of the northern caldera wall, where magma type. A means andesite, B – basalt, D – dacite or combinations of all three. Ages are taken from Druitt et al. (1999); stratigraphic symbolism from the BGS d at ab as e (http:// bgs.ac.uk), faults (172-3.6ka) from Druitt et al. (1999).

Figure 8.2: Illustration showing a two-magma chamber plumbing system (a double magma chamber with a cylindrical shallow one) which hosts a radial dyke swarm. The latter consists of dykes, which follow different paths often ending in (1) dyke arrest or (2) dyke deflection as studied in this thesis with finite element numerical modelling. The study shows that in addition to the stiffness of the layers and the regional tectonic setting other parameters can also control magma ascent in the crust such as the thickness of the layers (1a), the thickness of the crust (1b), the stratigraphic sequence (1c), the geometry of the dyke-fault interactions (2a), the thickness of the dyke and the fault (2b), the length of the fault (2c), the stiffness of the fault core (2d). Not to scale.

Figure 8.3: Schematic illustration showing a cross section of the dyke swarm and the volcanotectonic evolution of the northern caldera wall. The depth data of the magma chambers and their composition are derived from Andujar et al. (2015) and Cadoux et al. (2014). Not to scale.

Figure 8.4: Schematic illustration showing the evolution of a magma chamber through time. T_o stands for the initial magma chamber stages and T_1 for the evolved stage. The letters a and b denote the semi-axes of the ellipsoidal chambers. Not to scale.

Figure 8.5: Illustration showing different magmatic processes that can produce similar stratigraphic sequence in a volcanic edifice. Left: magma mixing. Right:

Magma chamber compartments due to a transverse impermeable fault. The letters a and b denote the semi-axes of the ellipsoidal chamber.

Figure 8.6: Schematic illustration showing a transcrustal system. The latter consists of a deep mafic reservoir and a felsic shallow magma chamber. Both generate dyke populations but of different compositions. The letters a and b denote the semi-axes of the ellipsoidal chamber.

List of Tables

Chapter 3: Multidisciplinary studies of the northern caldera wall dyke swarm and its host rock

Table 3.1: Petrographic analysis of Dyke 1 (core).

Table 3.2: Petrographic analysis of Akr 1 (core).

Table 3.3: Textural connections between the host rock phenocrysts from samples 1,4,6,21,76,77,79,80,81,89. Columns and rows denote the stages of a magmatic path at depth. The same colours represent the same observed probabilities. The last line on the left-hand colour (Unique textures) represents textures that were found individually in phenocrysts.

Table 3.4: Textural connections between the host rock phenocrysts from samples 21,76,77,81,89. Columns and rows denote the stages of a magmatic path at depth. The same colours represent the same observed probabilities. The last line on the left-hand colour (Unique textures) represents textures that were found individually in phenocrysts.

Table 3.5: Textural connections between the host rock phenocrysts from samples Scr, As2, Akr, Rp7. Columns and rows denote the stages of a magmatic path at depth. The same colours represent the same observed probabilities. The last line on the left-hand colour (Unique textures) represents textures that were found individually in phenocrysts.

Table 4.1: Modelling results for dyke 1 with an applied overpressure (P_o) of 1MPa and an additional horizontal extension loading of 0.5 MPa. The table also includes a qualitative interpretation of the dyke propagation path as defined through numerical modelling. Tensile stress is measured directly in ahead of the dyke tip (Low: 0.5- 1.5MPa, Moderate: 1.5-3MPa, High: 3-5MPa). The condition for propagation is met if the stress at the tip exceeds 0.5 MPa and if the trajectory

of σ_1 is close to 90˚. The dyke propagates in a σ_1 and σ_2 plane and their trajectories are shown in the models. The maximum tensile stress (σ_3) was assumed from the orientation of the other two principal stresses.

Table 4.2: Modelling results for dyke 1 with an applied overpressure (P_o) of 5MPa and an additional horizontal extension loading of 0.5 MPa. The table also includes a qualitative interpretation of the dyke propagation path as defined through numerical modelling. Tensile stress is measured directly in ahead of the dyke tip (Low: 0.5- 1.5MPa, Moderate: 1.5-3MPa, High: 3-5MPa). The condition for propagation is met if the stress at the tip exceeds 0.5 MPa and if the trajectory of σ_1 is close to 90˚. The dyke propagates in a σ_1 and σ_2 plane and their trajectories are shown in the models. The maximum tensile stress (σ_3) was assumed from the orientation of the other two principal stresses.

Table 4.3: Modelling results for dyke 2 with an applied overpressure (P_o) of

1MPa and an additional horizontal extension loading of 0.5 MPa. The table also includes a qualitative interpretation of the dyke propagation path as defined through numerical modelling. Tensile stress is measured directly in ahead of the dyke tip (Low: 0.5- 1.5MPa, Moderate: 1.5-3MPa, High: 3-5MPa). The condition for propagation is met if the stress at the tip exceeds 0.5 MPa and if the trajectory of σ_1 is close to 90˚. The dyke propagates in a σ_1 and σ_2 plane and their trajectories are shown in the models. The maximum tensile stress (σ_3) was assumed from the orientation of the other two principal stresses.

Table 4.4: Modelling results for dyke 2 with an applied overpressure (P_o) of 5MPa and an additional horizontal extension loading of 0.5 MPa. The table also includes a qualitative interpretation of the dyke propagation path as defined through numerical modelling. Tensile stress is measured directly in ahead of the dyke tip (Low: 0.5- 1.5MPa, Moderate: 1.5-3MPa, High: 3-5MPa). The condition for propagation is met if the stress at the tip exceeds 0.5 MPa and if the trajectory of σ_1 is close to 90˚. The dyke propagates in a σ_1 and σ_2 plane and their trajectories are shown in the models. The maximum tensile stress (σ_3) was assumed from the orientation of the other two principal stresses.

Ωδή στη Σαντορίνη - Οδυσσέας Ελύτης

<<Βγήκες από τα σωθικά της βροντής

Ανατριχιάζοντας μες στα μετανιωμένα σύννεφα

Πέτρα πικρή, δοκιμασμένη, αγέρωχη

Ζήτησες πρωτομάρτυρα τον ήλιο

Για ν' αντικρίσετε μαζί τη ριψοκίνδυνη αίγλη

Ν' ανοιχτείτε με μια σταυροφόρο ηχώ στο πέλαγος.>>

ODE TO SANTORINI - By Odysseus Elytis

<<You emerged from a thunderpeal's entrails

Shuddering amid repentant clouds

Bitter stone, proved, proud

You sought the sun for the first-martyred witness

To confront perilous splendor together

To head out to sea with a cross-bearing echo.>>

(Translation by Jeffrey Carson and Nikos Sarris – 1997, 2004, The translated poems of Odysseus Elytis, Johns Hopkins University press Baltimore and London)

Chapter 1: Evolution of the applied scientific ideas and research objectives

1.1 Introduction

Fantastic volcanoes (beasts) and how to study them.

<Since the days of the Greek philosophers', thousands of Memoirs have touched upon this complex problem of terrestrial dynamics, but geologists are still looking for a generally acceptable solution.>

The nature of volcanic action by Reginald A. Daly. 1911

Geology from the ancient Greek γη (earth) and λόγος (study) has been one of the most intriguing scientific fields since the era of the great Greek philosophers (Daly, 1911). During the evolution of life, over the last 15 million years, many important geological processes (e.g. related to global tectonics, ice periods, large volcanic eruptions, etc.) have occurred (Behrensmeyer, 1982). There were also many periods during this evolution when human migration was forced primarily by the chase after available commodities (Beaumont, 2010).

Volcanoes have always had both negative and positive effects on the human civilisation, and studies of volcanoes have therefore generally been of great importance. Volcanism on Earth is hence inseparable from human co-existence (Hutchison et al., 2016; Pyle, 2017) as has been shown from archaeological data

(Smith et al., 2018), legends and allegories (Galanopoulos and Bacon, 1969) and records of volcanic eruptions from human observations (Akilas, 1925) that have survived through time.

In the past few decades, volcanological studies have evolved from a primarily laboratory and field-oriented perspective (i.e., petrology/geochemistry and descriptions of eruptions) to a multidisciplinary modern scientific field by incorporating a variety of other applications (e.g., structural geology/tectonic aspects, geophysics, and analytical/numerical modelling). Technological development (new instrumentation and techniques) has played an essential role in assisting volcanologists to develop their ideas by allowing them to collect more data and to improve the accuracy and efficiency of their measurements. Volcanotectonics is a discipline that has united a wide range of expertise in order to understand and interpret processes and structures related to both volcanic and tectonic activity. In particular, it combines methods from structural geology/tectonics, field geology, physics, and analytical, analogue, and numerical modelling.

However, accurately forecasting the onset of a volcanic eruption is still a key challenge. Eruptions are still mostly unpredictable. Is this going to change soon? And as our ancestors would say: Is Ariadne going to help us find the exit from the labyrinth before we face the Minotaur? Time will tell.

1.2 Sectional plan

The thesis is written in an alternative structure to have both a thesis and a paper-style publication. For that reason, Chapter 1 is a general introduction to the topics of study which includes a literature review. Chapter 2 describes the methods that were used to tackle the questions posed in Chapter 1. The next chapters are papers that are either in preparation or under review. The last chapter is a discussion followed by appendices.

Specifically, Chapter 1 includes the evolution of ideas regarding dyke propagation, relevant solid mechanics, volcanic plumbing systems (VPS) and modelling. The chapter also gives the reader the main objectives and significance of this PhD as well as the scientific questions addressed by this study.

Chapter 2 describes the main methods that were used to collect as well as analyses and interpret the data from the field studies, the laboratory and the modelling applications. The chapter is divided into three main subsections: 1) the techniques that were used to collect data from the field (field analysis and sample collection), 2) the methods applied from the laboratory study, and 3) the numerical procedures used for data interpretation. I also report the methodology that designed the petrogenetic model of the northern caldera wall plumbing system.

Chapter 3 reports and describes all the data obtained from the northern caldera wall of Santorini in a paper format which will autonomously become future

publications. The latter includes the stratigraphic (volcanological) evolution of the northern caldera wall as well as a structural and petrogenetic study of the dyke swarm and the associated host rock (terrestrial deposits). In addition, I include a qualitative analysis of dyke propagation paths to investigate the likelihood of any future dykes becoming feeders for eruptions at Santorini, the detailed petrographic database of the dykes and the associated host rock and the reconstruction of the Santorini northern caldera wall plumbing system.

Chapter 4 presents part of the results of the field campaigns in a paper format. Structural field data was coupled with numerical models to investigate a series of dyke arrest scenarios related to arc volcanism under extensional stress regimes.

Specifically, the field data were used to generate geometries and boundary conditions for models using COMSOL Multiphysics which in turn allowed an examination of how host rock heterogeneity can rotate the stress field and encourage dyke arrest scenarios.

Chapter 5 presents a series of numerical models that study dyke-fault interactions observed on the caldera wall, in a paper format. The mechanisms that encourage dyke deflection were investigated as well as the parameters that control dyke- fault deflection in a mesoscale were studied through several sensitivity tests.

Chapter 6 contains the structural and petrogenetic analysis of the Santorini dyke swarm in a paper format. It combines the literature review with the new

quantitative and qualitative data and admits describing the volcanotectonic evolution of the studied area, the type of dyke swarm and the dyke-fed volcanism. A combined volcanotectonic and petrogenetic model of the crustal plumbing system at the northern caldera wall is the main objective.

Chapter 7 presents an investigation of the processes that encourage magma propagation in a plumbing system in a paper format. Field and petrological analysis are combined to investigate the host rock entrainment into the advancing dykes. Information in terms of the materials (components) that the dykes bring to the surface (erupt) while the plumbing system evolves is the primary goal.

Chapter 8 sums up the main topics studied in this Ph.D. and evaluates the results and the effectiveness of the applied methods associated with the questions stated in chapter 1. Ideas and concepts of future projects are also discussed.

Appendices consist of a large dataset which is divided into the following chapters:

Appendix A includes field photos which show the location of every mapped dyke segment during the field campaigns, the dyke/host rock annotations that let me interpret the dyke paths on the northern caldera wall, the laboratory protocols followed during the SEM and XRF analysis and the designed geochemical protocol that helped me to investigate dyke-fed volcanism at the caldera wall.

Appendix B was designed to introduce all the data collected for this multidisciplinary research. In detail I present the field observations, the

derivative overpressure and source (depth) calculations, the XRF results of six host rock samples and eleven dykes. I also provide the detailed petrographic database of twenty-two representative thin sections (dykes) and eight host rock thin sections.

Appendix C sums up the supplementary data of the paper manuscripts. In detail, firstly, it includes the designed sensitivity models of dyke arrest scenarios at the caldera wall (Chapter 4), then the sensitivity models of the dyke-fault interactions (Chapter 5) and lastly the geochemical data (spider diagrams) of the host rock analysis and a multidisciplinary dataset of the studied dykes (Chapter 6).

Appendix D finally shows the results of the CIPW and Image J methodologies which were not used directly in a chapter but were useful as comparative tools in the multidisciplinary study.

1.3 Aims and Objectives

As already discussed, forecasting volcanic eruptions is an important but so far difficult-to-reach goal in volcanology. This Ph.D. research is concerned with the study of the magma movement from the source to the surface, and it aims to:

1) Develop our understanding of the fundamental factors that control dyke paths in heterogeneous and anisotropic crustal segments using field observations

and analytical and numerical modelling.

2) Design a multidisciplinary methodology to study crustal volcanic plumbing systems that lie beneath stratovolcanoes.

3) Investigate the amount of magma assimilation and host rock entrainment associated with dyke propagation in heterogeneous and anisotropic volcano such as Santorini.

The main objectives of this research are (in general):

- To document the petrogenetic and structural characteristics of arrested (non- feeder), propagating, deflected dykes by collecting field data.

- To describe the local stresses at shallow depths in volcanic edifices, namely the stresses that control dyke propagation paths and potential dyke-fed eruptions.

- To provide numerical models to investigate dyke arrest and deflection paths in a heterogenous and anisotropic crust.

- To study how an anisotropic and heterogeneous successions affect dyke propagation/encourage dyke arrest and assess the degree of mechanical entrainment and chemical assimilation of wall rock materials.

In particular, as regards Santorini volcano the thesis addresses the following questions-topics:

Q1: Towards a reconstruction (geological history) of the early northern caldera wall. How were the structures in the northern part of the caldera formed?

Q2: Are Santorini dyke swarms locally or regionally controlled? And to what extent did the dykes interact with tectonic structures such as faults?

Q3: What is the probability that an injected dyke erupts at Santorini volcano?

Q4: What insights can multidisciplinary studies (i.e. petrography and structural geology) provide in the goal of understanding dyke arrest and deflection in the shallow crust?

Q5: Deciphering dyke fed volcanism in stratovolcanoes. Which methods are needed for reconstructing volcanic plumbing systems?

In addition, the origin of the dyke swarm is still not fully constrained. For example, it is not known whether the dyke swarm originated from the same magma chamber or from different magma chambers. To gain a more complete understanding of the dyke swarm I pose the following questions:

1) What is the petrography of the dykes and their chilled margins, and what do their textural heterogeneities tell us in terms of their path and magmatic source before their emplacement in the shallow crust?

2) What are the genetical correlations between the dyke and adjacent host-rock layers/units?

3) What does the comparison of the most primitive Akrotiri lavas with the northern caldera wall dykes tell us in terms of the evolution of the plumbing system?

4) Do the dykes that form clusters associated with the Megalo Vouno and Kokkino Vouno cinder cones (125-80 ka) differ from the dykes that appear to cluster near the edifice of the older Peristeria Volcano?

All those questions are being answered in the following Chapters (3-7).

1.4 Magmatic processes

Magma is the molten product of Earth's mantle and crust and is the result of the amalgamation of a melt phase, exsolved volatiles and crystals (Sparks et al., 2019). Magma accumulates beneath plate boundaries, and when the melting begins, it migrates towards regions of lower potential energy, that is, in the direction of the surface due, initially, to density changes (buoyancy) (Marsh, 1989). During propagation towards the Earth's surface, the magma either stalls at depth or contributes on building a volcano edifice in the form of intrusions or erupted products.

Understanding the mechanisms that govern the transport of magma in the crust are vital because they control: 1) the direction of magma movement, 2) the depth and rate of magma solidification, 3) the depth and rate of magmatic

differentiation, 4) the formation of volcanoes and 5) the production of oceanic and continental crust (Rubin, 1995). Also, the diversity of magmatic processes that occur at depth control the compositional range of the eruptive products found in the crust. There is significant compositional heterogeneity of magma found on Earth, and a wide chemical distribution can be observed in any volcano (Daly, 1911). Such observations allowed the creation of fundamental theories of magmatic differentiation which became the first pylons of modern petrology (Fig. 1.1) and are described below.

1.4.1 Magma generation and differentiation

The deep solid rocks of the upper mantle and lower crust are the result of melting that generate surface volcanism. Melting mainly occurs when the system rises above the solidus through three different possible changes: 1) temperature (T) increase, 2) reduction in pressure or decompression ($-\Delta P$) and 3) volatile influx (e.g. CO_2, H_2O). While magma advances from the source to the surface, it cools down and crystallises at different depths, and hence, at different pressures (P) and temperatures (T). As these P-T conditions change with depth, the magma undergoes a suite of processes that define the finite magmatic compositions that arise at the surface.

In 1897 the USGS chemist Becker described for the first time the term ‘magma chamber differentiation’ as being 1) differentiation; the result of material

diffusion from the centre to the rims of a defined melt storage region and 2) magma chamber; initially described as a homogeneous or stratified continuous system (Hildreth, 1979), later as the molten, semi-molten or rarely mush poroelastic system that allows chemical and textural transitions and, eventually, connect to lava products (Mc Kenzie, 1984; Marsh, 2000). However, more recently, a magma chamber has been described as the melt-dominated region of a magmatic system (Sparks et al., 2019). The magma chamber concept has remained as the central paradigm for understanding volcanic processes for many years (Cashman et al., 2017).

Magma chambers have been proposed as being formed through the accumulation of sills (i.e. Gudmundsson, 1990). In the case where the magma supply rate is high enough then a magma chamber or a magma reservoir can be formed from sills (Gudmundsson, 1990, 2012) as heat advection is higher than the heat loss derived from conduction. The same terms, however, from a petrological perspective are quite distinct. For example, if a constant amount of melt phase and volatiles grow above the Melt Connectivity Transition (MCT) of a magmatic system, then a continuous, interconnected domain 'reservoir' is formed. By contrast, when the melt fraction exceeds the Mush-Magma Transition (MMT) condition, then a 'chamber' is formed (Sparks et al., 2019).

The main driving processes that control magma differentiation in volcanic arcs are now recognised as partial melting, fractional crystallisation and assimilation, magma mixing, zone refining and liquid immiscibility (Bowen, 1920, Cox et al.,

1979; Best, 1982; Wilson, 1989). The terms are described below in detail, and their popularity is shown through time:

1) Partial melting is the melt production process that occurs in the absence of total melting (anatexis). The chemical composition of the residual magma differs from that of the parental magma. The equilibrium or batch partial melting produces a melt phase which is in equilibrium with the residual crystallised magma before their segregation. In contrast, fractional partial melting produces a melt phase that segregates without a reaction from the residual magma (Best, 2003) (Fig. 1.1A).

2) Fractional crystallisation is a process that describes the separation of the melt phase from the crystal phase (Bowen, 1928). Resulting melts migrate and become enriched with incompatible elements (LILs) of the parental magma and are hence depleted with the elements of the preferred crystal phases. The crystal-melt separation occurs due to gravitational sinking of the crystals from their density contrasts, a process known as gravitational crystal settling (Wright, 1971), or by convection due to different magma diffusivities and heat (convective fractionation) (Sparks et al., 1984) or through in-situ crystal growth (Irvine, 1960) (Fig. 1.1B).

3) Assimilation-Fractional crystallisation (AFC) is a process through which host rock is incorporated in an advancing magma as xenoliths. If the assimilation happens at the front of the propagating magma and crystallisation at the bottom,

then the process is described as zone refining (Harris, 1957). Other mechanisms can produce assimilated magmas such as through hydrous fluids due to wall rock dehydration (Huppert and Sparks, 1985) (Fig. 1.1C).

4) Magma mixing forms due to the periodical refluxing of new pulses of primitive magma that becomes mixed with residual fractionated magma (Walker et al., 1979) (Fig. 1.1D).

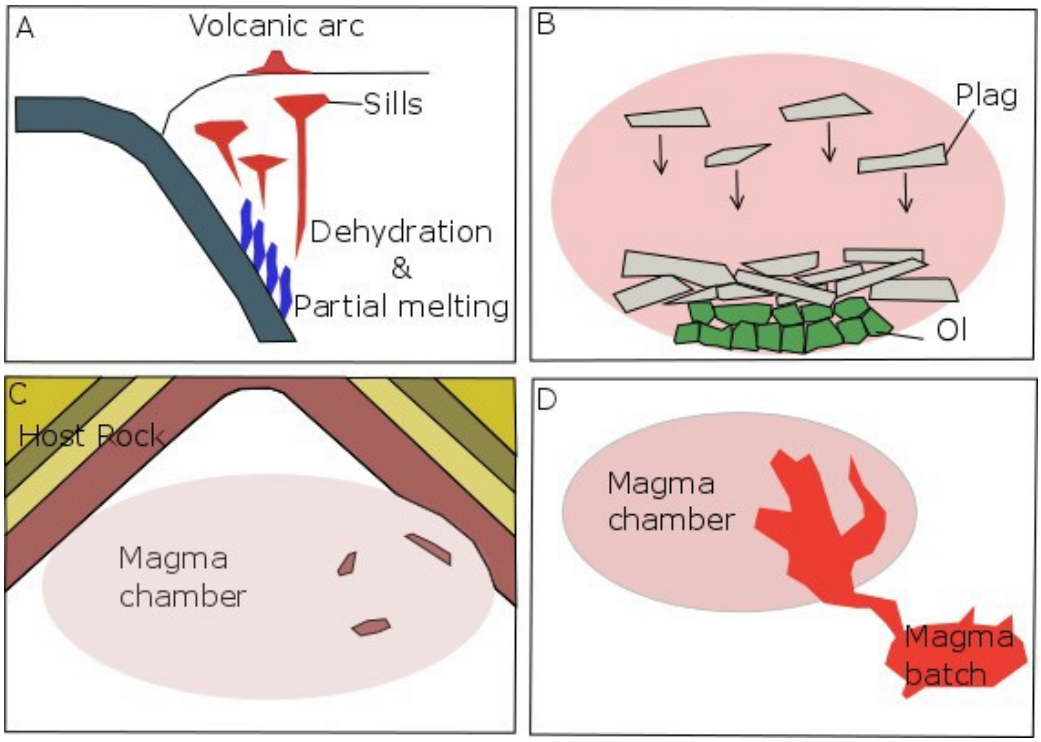

Fig. 1.1: The main processes of magmatic differentiation that define volcanic arcs formed in subduction zones. (A) Partial melting in the slab, (B) Fractional crystallisation (gravitational crystal settling), (C) wall-rock assimilation – fractional crystallisation, (D) Magma mixing in a magma chamber (Not to scale).

1.4.2 Volcanic plumbing systems

A volcanic plumbing system (VPS) is a modern way of defining the network that transports, stores and evolves magma in the crust. All these topics have been studied extensively and are essential in controlling volcanic eruptions.

Walker's pioneering observations of dyke swarms in Hawaii and Iceland became the fundamental concepts that allowed the creation of the modern volcanic plumbing system architecture (Kristjansson, 2005). Some of these pioneering observations (i.e. Walker, 1979, 1980, 1986) led Gudmundsson (1984, 1987) to create the concept of a mature stratovolcano hosting a deep magmatic reservoir linked with a shallow magma chamber through vertical dykes (Gudmundsson, 2003, 2006, 2012) (Fig. 1.2A). Shallower in the crust, the chamber channels magma within a system of inclined sheets or vertical dykes that could either stall in the crust, form sills, or ultimately feed volcanic eruptions. Magma injections can also periodically originate from deep-seated reservoirs and rejuvenate the crustal system during an active cycle.

The initial ideas deriving from petrology suggested that homogeneous magma chambers could produce stratified and monotonous single eruptive events (Smith, 1979; Hildreth, 1979). Sequences of identical eruptive products during individual eruptions were later described as being derived from zoned magma chambers with distinct melts of similar composition (Kennedy et al., 2018). Cashman and Giordano (2014) proposed a concept of multiple magma bodies

through the interpretation of volcanism in the Long Valley and Shikotsu calderas by Chamberlain (2014) and Smith (1979), respectively. Also, the lack of zonation patterns in some systems (e.g. the Lake City and Permain Ora calderas) generated the first ideas of distinct 'pockets' of magma which co-exist with a magma chamber before eruption (Kennedy et al., 2016, 2018).

Active volcanic systems such as the Taupo Volcanic Zone (TVZ) in New Zealand and the Southern Volcanic Zone (SVZ) in Chile seem to suggest strong interactions between magmatism and tectonics (Eggert and Walter, 2009; Sawi and Manga, 2018) similar to observations in the Icelandic volcanoes (Walker, 1964). It has been suggested that tectonism (e.g. graben or caldera collapse) can explain the release of large volumes of magma from a single magma chamber (i.e., Gudmundsson, 1988; Wilson, 2001). Other observations made at the TVZ allowed the creation of a hypothesis, which suggested that multiple magma bodies could co-exist in a volcanic plumbing system, and mixing events between these magma bodies could ultimately be the triggering mechanism that forces caldera collapse (Sparks et al., 1977; Woods and Pyle, 1997).

Tyrrell (1926) initially introduced the 'mesh' model (later mush), and further observations from Marsh (1996) introduced the idea of mush columns as the source and path of magma in volcanic systems. The concept was described as a 25-55 vol% crystallised magma (super-solidus rock) which remains in a thermodynamically controlled viscous state that cannot overcome the rigidity of the host rock to fracture. Later studies (Bachmann and Bergantz, 2004) supported

the mush model with experimental (Putirka, 1997) and geophysical models (Paterson et al., 2011). The most contemporary perspective considers a system of mush zones and dyke-sill interconnections (Annen et al., 2015) surrounded by a solid host rock.

Modern theories (Cashman et al., 2017) suggest that more permanent and eruptible magma chambers occupy only the upper parts of a larger Transcrustal Magmatic plumbing Systems (TCMS) which control magma accumulation in the shallow crust (Fig. 1.2B).

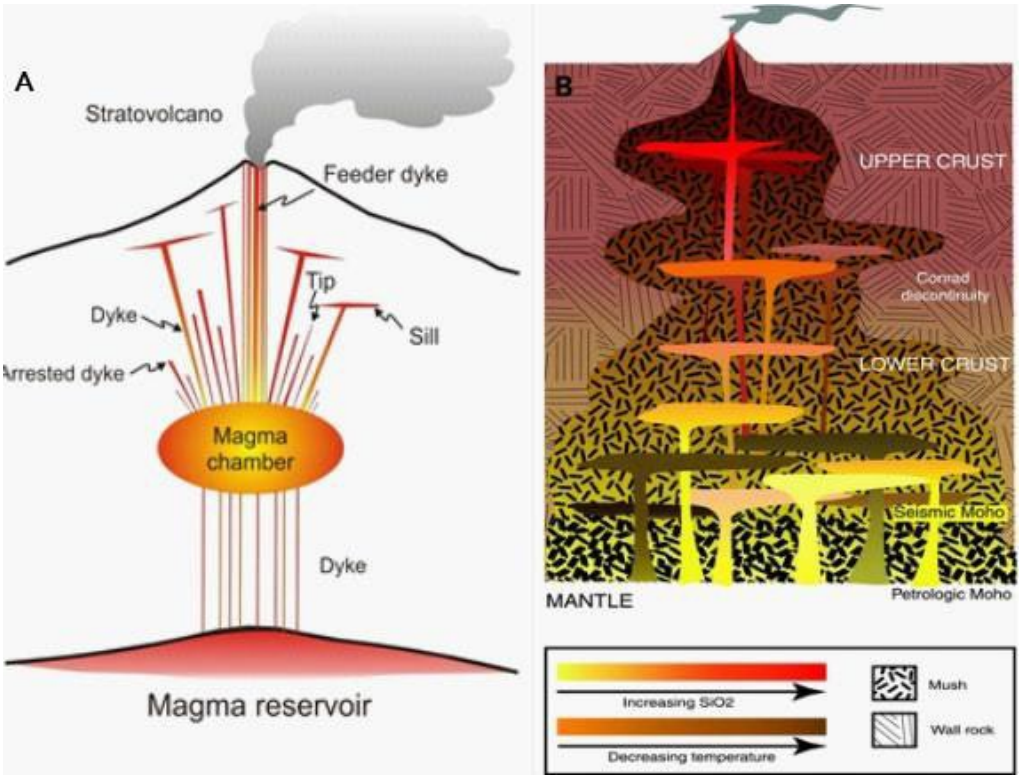

Fig. 1.2: (A) Schematic illustration from Gudmundsson (2006) of a volcanic edifice, here a stratovolcano, and its mature crustal plumbing system. (B) Schematic illustration from Sparks and Cashman (2017) showing a Transcrustal

magmatic system. Melt is produced in the deep mantle and is being transferred to the upper crust in both models.

TCM-systems can be characterised by three dominant processes: 1) magma transport, 2) formation of intrusions and 3) magma and mush processes. The first process is controlled by dyking in the brittle environment and diapirs in ductile environments. The second describes the presence of magma chambers and sills in the crust. They form mainly due to three processes 1) incremental intrusion, 2) remobilisation and 3) melt segregation (Sparks et al., 2019). The latter processes occur mainly in the lower crust, which subsequently feeds the upper crust and is defined by horizontal intrusions or downward magma migration due to density decreases caused by crystallisation. The third process characterises the remobilisation of magma and the formation of shallow crustal magma chambers that accommodate volcanic eruptions (Sparks and Cashman, 2017).

1.5 Solid Mechanics

Solid mechanics in geology focuses on the way that solid materials, primarily rocks, react under the action of a load such as a force, a displacement, and strain. Rigid displacement is defined either by translation or rotation and strain either by dilation or distortion. The stress application (force per unit area) on a solid material produces strain (extension/contraction) which is proportional to the initially applied stress and is described by the one-dimensional Hooke's law,

which relates stress and strain through Young's modulus (Fig. 1.3).

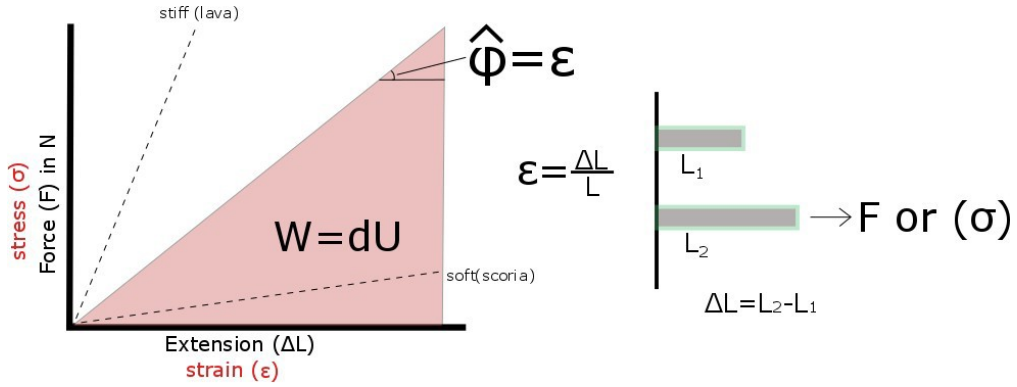

Fig. 1.3: (Left) stress-strain (force-extension) relationship of typical elastic materials in the crust. (Left) The slope of the dotted and solid (of the triangle) curve/line is a measure of Young's modulus. (Right) Illustration showing extension due to tensile force or stress.

Table 1.1: Commonly used elastic constants (Gudmundsson, 2011).

Elastic constants		
Term	Meaning	Equation
Young's Modulus (E)	Modulus of elasticity (measure of stiffness)	$E=\frac{\sigma}{\varepsilon}$ (GPa)
Poisson's ratio (v)	(the measure of relative contraction to relative	$V=\frac{-\varepsilon\ (diam)}{e\ (length)}$ (no unit)

	expansion)	
Shear modulus (G)	Modulus of rigidity (the measure of resistance to change shapes)	G=$\frac{\tau xy}{\Gamma xy}$ (stress unit)
Bulk modulus (K)	Incompressibility	$K = \frac{\sigma\ (mean)}{\Delta}$ (stress unit)
Lame's constant (λ)	(mathematical convenience)	$\lambda = \frac{2G\nu}{1-2\nu}$ (stress unit)

When subject to external forces, material stores energy (dU) through work (W). The strain energy per unit volume is equal to the shaded area (Fig. 1.3), and it is a measure of material toughness of the material. Young's modulus is the slope of the elastic (straight) portion of a stress-strain curve. Stress and strain relationships can be described using constants for elastic isotropic materials (Table 1.1).

1.5.1 Fluid flow during dyke propagation in dykes

Fluid transport depends predominantly on the permeability of the media (the ease with which the fluid can flow through rock, for example) and the hydromechanical properties of the fluid (e.g. the buoyancy, density, pressure and viscosity). The movement of magma requires changes in energy and chemical composition which occur via five main modes. Four of them take place in the deep mantle and are: 1) through diapirs, that take place in viscous materials (Marsh, 1982; Rubin, 1995), 2) fluid flow through porous media in partially molten source rocks as has been described experimentally through Darcy's law (Boone and Ingraffea, 1990), 3) through pervasive flow, where magma advances through channels formed by active deformation (e.g. migmatites) (Brown, 1994), 4) through fracturing on the microscale (Weinberg and Regenauer-Lieb, 2010; Cruden and Weinberg, 2018). The last mode takes place in the shallow crust and is 5) through dykes which are vertical to near-vertical magma-driven extension fractures observed as planar sheets with varying thickness, that propagate vertically and laterally through elastic/brittle rocks (Delaney, 1986).

1.5.2 Dyking from the source to the surface

Dyke (or any hydrofractures) propagation is a complex process which involves a combination of fluid mechanics, fracture mechanics, solid deformation and

thermodynamics (Lister and Kerr, 1991; Rubin, 1995; Gudmundsson, 2011). Magma overpressure, which includes excess pressure in the source due to accumulation of volume and buoyancy due to density difference between magma and host rock) are the driving forces during dyke propagation (Nakashima, 1993; Rubin, 1995; Gudmundsson, 2002; Pinel and Jaupart, 2004, Gudmundsson, 2011). During propagation, in principle, three factors control the fracture/dyke opening (aperture) depending on the depth of the source, and they are: 1) the controlling dimension of the fracture, which is commonly the strike dimension, 2) the Young's modulus (elastic moduli) of the host rock, and 3) the overpressure (Gudmundsson, 2011). However, observations of dyke swarms can be limited depending on how the measurement is taken. For example, there are essential differences between the dynamic and partially fluid state and the final, solid, state of the dyke. The latter depends on the cooling contraction of the magma. The amount of contraction or shrinkage has been estimated to be no more than 10%, as follows from the density difference between the magma and the solid dyke rock (Gudmundsson, 2011).

Three end-member types of dykes can be broadly described (as from Gonnermann and Taisne, 2015). 1) self-propagating dykes where propagation is driven by magma buoyancy, 2) reservoir/chamber driven dykes that propagate due to excess pressure gained from magma chamber inflation or deflation, 3) wall-rock dykes that propagate through molten rock genuinely supplied from the surrounding porous media (being confined to partially molten regions).

1.5.3 Fracture mechanics in dyke propagation

The basic equation that describes crack growth was established by Griffith (1921, 1925) based on stress field calculations made by Inglis (1913). The equations state that the elastic energy release rate G should be at least equal or exceed the critical energy release rate G_c described by the following equations (Eq. 1.1 and 1.2):

$$G = \frac{\pi \sigma_c^2 a}{E} \geq G_{Ic} \qquad (1.1)$$

Or

$$\sigma_c = \sqrt{\frac{E G_{Ic}}{\pi a}} \qquad (1.2)$$

where a is the crack length, E is Young's modulus, σc is the failure stress that describes the stress and strain at the tip of a crack in a critical stage when fracture toughness or the stress intensity factor (K_I) reaches a critical value. G is characterised as the driving force of a crack; however, it is essential to state that the energy criterion is necessary but not adequate for crack initiation as originally

the stresses and strains at the tips should exceed their critical values to initiate the crack. Accordingly, the growth of a crack can take place only if sufficient energy (G) is available to provide the essential work delivered by the system. The latter gets converted to kinetic energy which defines the movement of the material to make way for the crack path into the fracture surfaces, the walls of a dyke. The energy condition shall indicate only if crack growth can nucleate. Whether a crack growth increment will occur depends on the material properties (e.g. Young's modulus, Poisson's ratio), tensile stresses at the tip of the crack and the tensile strength of the host rock (Broek, 1982).

Dykes are typical Mode I extension fractures and hence propagate when the level of tensile stress in the rock is sufficiently high to break the rock (Anderson, 1951; Rubin, 1995; Gudmundsson, 2011). In circumstances where there is a misalignment with the principal stress axes, the rock may break in tension along with oblique features controlled by ambient stresses, commonly resulting in en echelon cracks (Rubin, 1995). Muller and Pollard (1977) described a qualitative agreement between ambient stress and dyke trend in curved cracks which they interpret to be the result of radial stress fields resulting from inflation of the magma source, called radial dykes. Later, Meriaux and Lister (2002) suggested that during dyke propagation, the dyke changes the stress field itself; therefore, the dyke trajectories differ from the theoretical trajectories.

An extension fracture can be mechanically separated into two types depending on the presence of fluid in the fracture: 1) tension fractures and 2) fluid-driven

fractures or hydrofractures (Gudmundsson, 2011). The first is formed in the shallow parts of the crust by absolute tension (e.g., large fractures and joints in rift zones) when the tensile stress (σ_3) is negative (absolute tension) and numerically equals or exceeds the in situ tensile strength of the host rock. It is not possible to generate absolute tension in the absence of fluid pressure at depths greater than about 1 km (Gudmundsson, 2011). In contrast, fluid-driven fractures occur at any depth under the condition that the total fluid pressure at the time of the initiation is larger than the total minimum principal compressive stress plus the in-situ tensile strength in that part of the crust (Gudmundsson, 2011).

A dyke (Fig. 1.4) propagates typically parallel to the maximum principal compressive stress ($\sigma 1$) and perpendicular to the minimum principal compressive stress ($\sigma 3$) (Anderson, 1951). Some dykes, however, use discontinuities (faults, contacts, joints) that are not parallel with $\sigma 1$ for parts of their paths when the discontinuities are otherwise favourably orientated in relation to the stress and/or have low tensile strength (cf. Gudmundsson, 1984; Delaney et al., 1986). The propagation path can also be modified in cases of significant variations in fracture toughness (due to stratification) (Maccaferri et al., 2010; Gudmundsson, 2011). Previous studies have suggested the theory that dykes use pre-existing paths (faults, cracks, openings) to propagate to the surface (Rivalta et al., 2015). Generally, however, it is known that state that dykes do not require pre-existing fractures to propagate upward in the crust or feed a volcanic eruption since the

tensile strength of rocks usually is very low, and they are easily ruptured by the magmatic pressure (Walker, 1986; Gudmundsson, 2011; Rivalta et al., 2015).

A propagating dyke produces a lateral opening, a fracture, through the host rock through which it intrudes (Le Corvec et al., 2013). In the case of uniaxial tension and the absence of a macroscopic fracture, a dyke propagates if only the tensile stress exceeds the material's tensile strength of the surrounding rocks. However, in the case that a macroscopic discontinuity/fracture (e.g. a fault) exists, increments of propagation can occur at lower levels of tensile stress or excess pressure because the tensile strength across an active fault may be close to zero (Gudmundsson, 1984; Rubin, 1995). This is especially important in the shallow crust (<1 km) where there are abundant crustal faults or partially open fractures. Still, at deeper crustal levels such fractures become closed due to the overburden pressure and commonly mineralised, so the effect generally becomes less with depth (Gudmundsson, 2011).

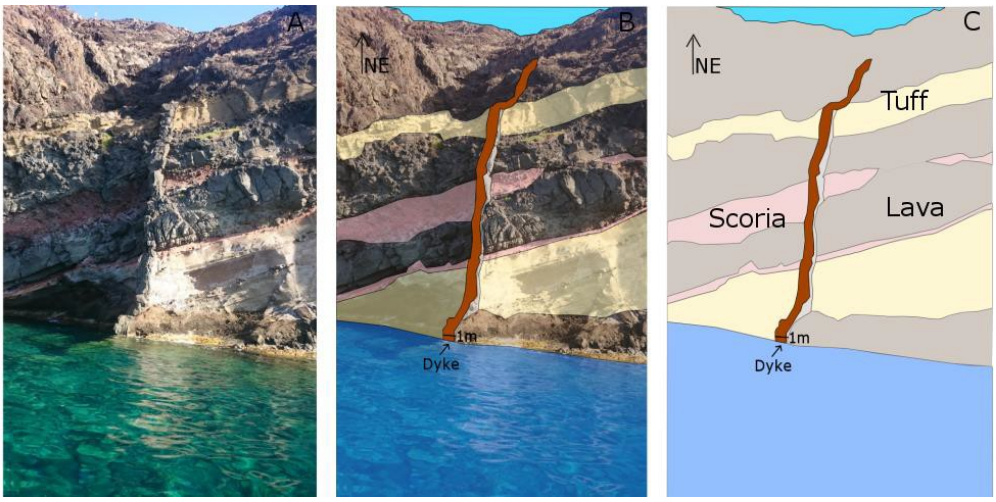

Fig 1.4: A dyke emplaced in a layered succession in the northern caldera wall of Santorini. (A) original photo, (B) annotated, (C) interpretation illustration.

1.5.4 Seismicity associated with dyke injection

Dyke injection is often associated with earthquake swarms or triggers in volcanic areas, and hence the study of seismicity related to dyke propagation is important (Rivalta et al., 2015). Measurements of the timing and location of seismic events as well as details of the seismic data, such as the focal mechanism and energy released, can provide valuable insights into dyking processes (Rubin and Gillard, 1998) and is one baseline for volcano monitoring (Benoit and McNutt, 1996).

Rubin (1998) examined the dyke-induced seismicity of the 1983 Kilauea event and found that the earthquake migration was associated with background seismicity (i.e. active pre-existing faults) an idea which supported the earthquake nucleation theory (Dieterich, 1994). Recent studies in Bardarbunga - Holuhraun 2014-15 rifting event revealed that most of the dyke seismicity was related to faulting ahead or adjacent to the dyke (White et al., 2006, White and McCausland, 2016).

1.6 Modelling of magma dynamics in dykes

1.6.1 Analogue modelling

Experimental studies of dyke propagation with analogue laboratory modelling were initiated in the 20th century. Such experiments allow scientists to study the kinematics and dynamics of dyke propagation by controlling parameters and scaling their observations. The goal is to gain insights into the fundamental processes operating and to evaluate the observations against dykes (Rivalta et al., 2015).

Crystal and bubble-free magmas were primarily treated as Newtonian viscous fluids initially studied in 2D (Lister and Kerr, 1991), and 3D (Kavanagh and Sparks, 2011) and later in 4D (Dobson et al., 2016). Many analogue models use gelatine as the brittle crust analogue due to its elastic behaviour and ability to accurately calculate material properties such as stiffness (Rivalta et al., 2005; Kavanagh et al., 2006).

Dyke propagation has been studied in both homogeneous and layered stratigraphic sequences in the laboratory (Kavanagh et al., 2006; Rivalta et al., 2015; Takada, 1990; Heimpel and Olson, 1994). Taisne and Jaupart (2009) created models suggesting that the dynamics of a propagating dyke are not highly influenced by variations in elastic moduli of the rocks. In addition, they indicated that fracture toughness affects the shape and width of the dyke near the tip but

not the length. Instead, they suggested that magma buoyancy is the crucial parameter that controls penetration through layering. Kavanagh et al. (2017, 2018) gave more insights on the role of fracture toughness with temperature, which is very poorly constraint. Fluid viscosity and heterogeneity in analogue experiments as layering and discontinuities modulate the geometry and type of intrusion (dyke, sill or hybrid forms) and the growth rate of sills.

1.6.2 Analytical modelling

In terms of modelling the processes driving magma flow in the dyke there are three main analytical theories: 1) the Weertman theory, 2) the lubrication theory and 3) fracture-mechanics theories which produce distinct mechanical models of dyke propagation and are described in the following section.

The Weertman theory of analytical modelling

The theory was initially introduced by Weertman (1971) and described vertical fluid flow driven only by buoyancy or tectonic forces (Rivalta et al., 2015; Townsend et al., 2017). The theory, which has been modified and extended (i.e. Taisne and Jaupart, 2009; Rivalta and Dahm, 2006; Dahm et al., 2010) to consider seismicity, studied fluid-filled fractures that advance from isolated

magma batches and preserve constant volume and finite height during propagation. The approach supports the assumption that the pressure gradient simplifies the role of fluid viscosity and instead focuses on fracture toughness (K_C) and elasticity. This theory importantly, does not consider the effects of fluid flow and/or heat transport as they were assumed to be negligible (Rivalta et al., 2015; Townsend et al., 2017). The Weertman fracture in its final phase elongates, and the fluid migrates to the trailing front while its lower tip closes due to low viscosity. The theory cannot explain any moderate to large dyke-fed eruptions because for those to occur; there must be a continuous feeder-dyke from the surface to the source.

The lubrication-theory of analytical modelling

The lubrication theory was proposed by Lister and Kerr (1991) and focuses on the dynamics of a purely vertical or horizontal dyke propagation controlled by magma flow (Rivalta et al., 2015). The theory neglects the heterogeneity and anisotropy of the host rock or any variations of fluid pressure (Rivalta et al., 2015) and downgrades the role of fracture toughness. Fluid fills the fracture in the lubrication theory with constant pressure that has a long neck (height) and migrates to an upper surface where it finally opens. Lister and Kerr (1991) made mechanical models of an ambient stress field in a state of lithostatic stress and showed that the injection point was always the tallest part of the lateral dyke

regardless of its leading edges. Pinel and Jaupart (2004), modified the scenario of a horizontal dyke injection to include the effects of a volcanic edifice and demonstrated the resultant change in stress fields generated by the volcanoes crustal load. Their dynamic model introduced the concept of a maximum overpressure level (MOL) which depends partly on magma buoyancy, the edifice size and the density stratification, such as the effect of the lithological boundaries above where the lateral propagation dominates.

Lateral dyke propagation from subvertical magma flow - a third theory

A third theory reviewed by Townsend et al. (2017) suggests that magma can change its flow direction from vertical to lateral but remain as a dyke during its propagation from the mantle to the shallow crust – a conclusion that has been well known in dyke studies for many decades (e.g. Gudmundsson, 1984, 1990). The theory assumes a primary gradient of driving pressure, associated with gravity. In a density stratified host rock, a fracture with a magma density value in between the upper and lower layer can propagate vertically for up to several kilometres. However, any density adjustments between the magma and the host rock can define the stability of the dyke and its flow direction (Roman and Jaupart, 2017). Also, the fracture toughness of the host rock plays a vital role in the magma overpressure. Lab-derived measurements of K_Ic, for example, give levels up to 0.5 MPa $m^{1/2}$ and hence a vertical propagation of a few tens of meters.

The main limitations of this approach are 1) it does not consider the heterogeneity and anisotropy of the crust which can alter the local stress field (Gudmundsson, 2011), 2) the models lack dynamic aspects (e.g. pressure changes, heat transfer),

2) the initial injection is always vertical, and 4) the model ignores the excess pressure in the source chamber, which is often the primary driving pressure, particularly for basaltic dykes injected from shallow chambers (where the buoyancy term is zero or even somewhat negative). The fracture in this mechanical model has a long blade shape with stable tips which limits its propagation and allows the fracture to flow also laterally.

Other authors have studied lateral dyke propagation (e.g., Gudmundsson, 1984, 1990; Rubin and Pollard, 1987; Ryan, 1993). Heimisson et al. (2015) studied the path (direction) of a laterally propagating dyke. Their probabilistic model combined the observations of real dyke paths (Bardarbunga eruptions 2014 and 1996) using the minimum potential energy principle (Reddy, 2013) which suggests that topography controls the potential energy change of both the magma and the crustal host rock. That conclusion, however, is unlikely to be generally valid since if true no large volcanic edifices, standing 1-2 km above their surroundings, could ever form.

1.6.3 Stochastic numerical modelling

Stochastic numerical modelling can be broadly categorised into three types according to their volcanological application (Jing, 2003), namely: 1) the boundary element method (BEM), 2) the finite element method (FEM), 3) the distinct (or discrete) element method (DEM).

Boundary element method (BEM)

BEM modelling is a numerical method that has been applied to hydraulic fracturing problems, including those of dykes and inclined sheets (Gudmundsson, 1998), since the 1980s (Rivalta et al., 2015). The method allows separate discretisations at the borders and the inner area of the model. In volcanology the technique has been used to couple the magma pressure and rock deformation using analytical solutions for elementary dislocations (Crouch and Starfield, 1983; Rivalta et al., 2015). The method also allows the re-meshing of new data in the dyke tip as well as quasi-static models and applications of external stress fields (Jing, 2003).

Finite element method (FEM)

In volcanology, the FEM has been used to study fundamental and efficient fluid-solid interactions. The technique has been successfully used in dyke growth simulations in complex geological settings (Gudmundsson, 2006). However, the nodes that make up a FEM model are unbreakable (continuum method) and so dislocations cannot be modelled (Jing, 2003) instead, fractures can be modelled as cavities.

Distinct element method (DEM)

Meshing in the DEM method is composed of spherical nodes that are represented by block assemblages. The nodes can break and move freely, which allows the technique to model dynamic fracturing processes (Holohan et al., 2015). However, their shape is not representative of the structural domains, i.e. there is a scale problem. In addition, the technique solves the relative motion inside a discrete fracture network domain as well as the case of block rotations, rigid movements and delamination (Jing, 2003).

1.7 Dyke propagation paths

1.7.1 Dyke swarms

A dyke swarm consists of multiple dyke injections fed by a magma chamber or magma chambers in the crust. Field studies have shown that the parameters that control dyke width, within a dyke swarm are mainly the dyke overpressure (driving magma pressure) that is generated within a magma chamber, elastic rock properties, dyke controlling dimension (length or height) (Gudmundsson, 2006, 2011, 2016) and rarely the magma rheology (Caricchi et al., 2016). An analysis of dykes in Hawaii; Walker (1987) reported marginally thinner dykes close to the rim of a caldera than further away from it. Other studies in the Spanish Peak, Colorado, suggest, instead, that dykes thin out further away from the edifice (Pollard and Muller, 1976) which could be due to the difference of the regional stress or the lack of composite dykes (secondary intrusions) near the rims. Geshi et al., (2010) reported an opposing observation from the caldera of Miyakejima volcano (Japan) which suggested that dyke thickness fluctuations depend highly on the regional stress field, the composition of the erupted magma and proximity to the Earth's surface, as well as the host-rock mechanical properties, regardless of the caldera proximity.

When a dyke is injected from a crustal magma chamber, it follows a path towards the surface. However, the potential propagation path of any dyke to the surface is still not fully constrained and hence cannot be forecasted. This section presents

fundamental information concerning the mechanics of dyke initiation and propagation (Fig. 1.5).

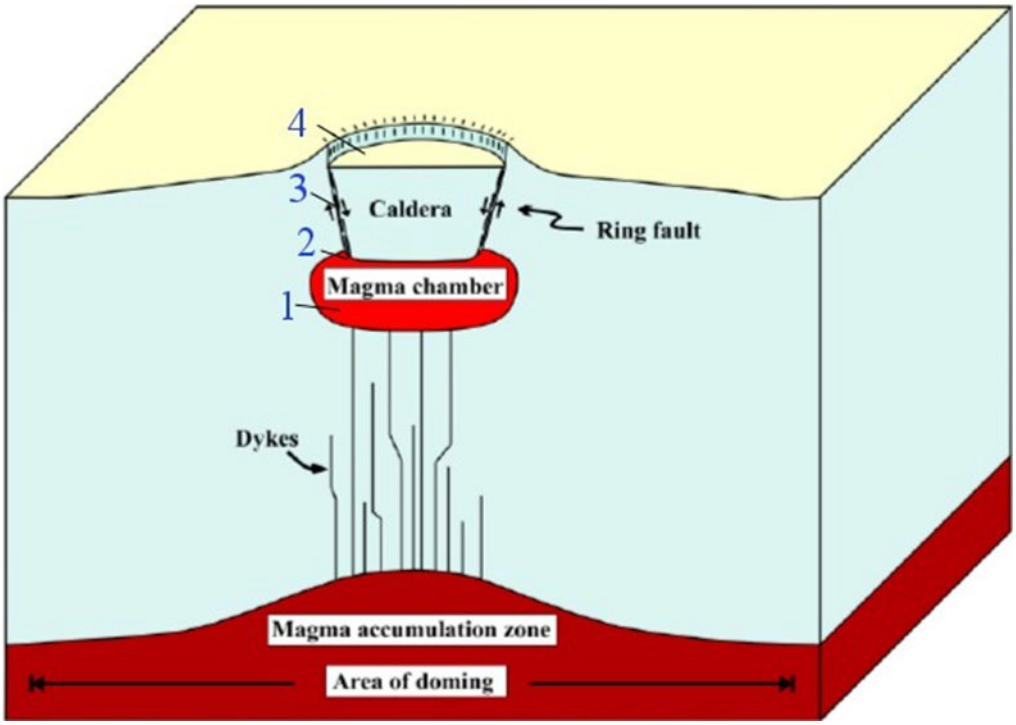

Fig. 1.5: Illustration showing caldera collapse in a cross-sectional plan geometry (Gudmundsson, 2008). The numbers indicate where the stages of dyke propagation with depth take place: 1) dyke injection triggering, 2) chamber rupture, 3) dyke propagation mechanisms, 4) caldera collapse.

1.7.2 Dyke injection triggering in a magma chamber

Magma chambers are open thermodynamic systems that for most of the time have an internal pressure (thermodynamic variable) which is equal to the

lithostatic pressure (environment) at the depth of the chamber. The chamber is thus most of the time in a lithostatic equilibrium with the surroundings. During the lifetime of a magma chamber, various events and processes, listed below, can change that equilibrium, giving rise to changes in pressure which can be followed by dyke injection.

1) Magma mixing: Sparks et al. (1977) and Morgavi et al. (2017) reported that magma mixing, the process where two different magmas unite in a magma chamber and form a hybrid magma with a composition between their two initial end members, can cause sufficient superheating and heat convection to change the volume of the chamber and increase the magmatic pressure.

2) Magma replenishment/recharge: the process that describes a new batch of hot primary magma which intrudes a cool evolved silicic storage region (Huppert et al., 1982). The intruding magma causes compression of the liquid phase in the chamber and expansion of the chamber walls which sometimes reach the tensile strength of the host rock (Machado, 1974; Blake, 1981; Gudmundsson, 1987; Tait, 1988).

3) Volatile triggering: After the intrusion of a mafic magma inside a magma chamber, the gradual cooling and crystallisation of the new magma saturates the melt phase forming gas bubbles which in turn increase the magma pressure through volume expansion (Burnham, 1979; Blake, 1984; Tait, 1988) or rejuvenate deep magma reservoirs (Armienti et al., 2013).

4) Gas exsolution: In magma chambers that reside at different depths and have different aspect ratios; pressure can drop during cooling and crystallisation and then rise again triggering a possible rupture (Woods and Pyle, 1997). Shallow chambers, hence, tend to increase their internal pressure during cooling, while deep reservoirs tend to decrease their pressure and contract. Also, high aspect ratio magma chambers can raise increase their pressure when the magma becomes saturated, producing crystal richer magmas. On the contrary, chambers with smaller aspect ratios which increase their pressure when they become vapour saturated provide unevolved crystal poor magmas.

5) Magma convection/advection: Heating can remobilise the residual magma due to convection and potentially increase the magmatic pressure of the chamber (Murphy et al., 2000; Couch et al., 2001)

6) Stress concentration due to external loading: When the tensile stress concentration around a magma chamber increases, for example, due to crustal spreading or doming of the crustal segment hosting the chamber, dyke injection, and sometime caldera collapse, may follow (Gudmundsson, 1988, 2007, 2014). Stress concentration can also contribute to long-term changes in the shape of the chamber, hence in the local stress field around it.

It is essential to clarify that although an increase in the excess pressure of a magma chamber could result in the magma-chamber rupture and dyke/sheet injection, many of the injected dykes/sheets will not become feeders to an

eruption. As such, crystal zoning, undercooling textures, glomerocrysts and Crystal Size Distribution (CSD) rates do not always describe an eruption event but often or more likely merely a stalled and fossilised dyke injection. Besides, it is essential to consider the 'bounce' effect of a magma chamber (Woods and Pyle, 1997). At the initial stages, while magma pressure increases, magma volume rises by a similar amount and can accommodate the extra stress. The amount of additional pressure that a chamber can absorb is calculated by Eq. 1.3 (Woods and Pyle, 1997):

$$\frac{dV}{dP} = \frac{V}{\beta w} \qquad (1.3)$$

where V is the volume of the magma chamber and βw compressibility of the country rock. In the case where new magma continues to fill the chamber the resulting tensile stress generated around the chamber causes the host rock to fracture and a dyke to become injected from the chamber (Tait, 1988).

1.7.3 Magma-chamber rupture

The triggering processes that increase the excess pressure inside a magma chamber change the stress field around the chamber, that is, result in local stress concentrations that induce dyke injection under the following condition Eq. 1.4 (Gudmundsson, 2011):

$$p_l + p_e = \sigma_3 + T_o \qquad (1.4)$$

where: p_l is the lithostatic stress or overburden pressure of the magma chamber, pe is the excess magmatic pressure, σ_3 is the minimum principal compressive stress or tensile stress of the magma, T_o is the tensile strength of the host rock. When Eq. 1.4 is satisfied, a dyke is injected from the source magma chamber. Its eventual fate, while dominated by the stress field of the magma chamber, is unknown. Most of the dykes/sheets stall, become arrested, close to their magmatic source (Gudmundsson, 2003). The reason for arrest is most commonly contacts between mechanically dissimilar rocks, resulting in delamination, elastic mismatch, or stress barriers (Gudmundsson, 1987, 1990, 2006).

1.7.4 Dyke arrest and deflection mechanisms

Studies on dyke propagation have shown that when a dyke meets a contact which acts like a discontinuity, it has three possible fates: 1) the fracture can become arrested and stall 2) it can penetrate the contact, 3) it can become deflected forming sills or offset dykes along the contact. Gudmundsson, (2011) suggests that the actual fate depends on three related parameters: 1) the tensile stress generated at the dyke tip, 2) rotation of the principal stresses at the contact, 3) the difference of the material toughness of the rocks above and below the contact and the contact itself. As a result, dykes easily become arrested in heterogeneous and anisotropic environments with weak contacts between layers where the local stress field or mechanical conditions are unfavourable to dyke propagation In detail, the principal mechanisms that control dyke paths are as follows:

Cook-Gordon debonding & delamination

Cook-Gordon debonding and delamination describes the opening mechanism of a weak contact when an extension fracture approaches the contact. This is thought to be a common mechanism of sill emplacement at shallow depths (Barnett and Gudmundsson, 2014). According to this mechanism, a dyke is deflected and can open the contact ahead of the dyke tip in cases where the tensile stress reaches as much as 20% of the initial perpendicular tensile stress of the dyke behind the delamination front (Freund and Suresh, 2003; Gudmundsson

and Lotveit, 2012). It is the tensile strength (T_o) of the contact that controls the opening of the dyke tip; if the strength is very low, the contact is likely to open.

Stress barriers-crustal layering

In heterogeneous and anisotropic volcanoes, the local stress field plays a vital role in dyke propagation. Vertical propagation occurs when the minimum principal compressive stress σ_3 is horizontal (Anderson, 1936). A stress barrier is either a stiff layer, e.g. a lava flow, or a compliant layer, e.g. a scoria layer that can flip the maximum principal compressive stress σ1 from vertical to horizontal and encourage dyke arrest (Gudmundsson and Phillip, 2006; Barnett and Gudmundsson, 2014).

A stiff layer can become a stress barrier when horizontal compressive stresses are applied to it. Such environments can be created either during normal faulting and especially during graben subsidence, or during multiple dyke injections where the magmatic overpressure can rise to tens of MPa (Geshi et al., 2010), alter the local stress field and affect the path of later dykes (Gudmundsson, 2011). Numerical studies in the Holocene rift zone in Iceland have shown that earlier dyke populations, normal faults and/or graben subsidence arrested dykes (Gudmundsson, 1995, 2003).

A compliant layer can become a stress barrier when extensional forces are applied to it. During an extension event, such as spreading in a rift zone with no earlier dyke propagation events, the stiff material takes on more of the load/force. It concentrates tensile stress so that the horizontal compression is reduced. On the contrary, compliant materials preserve the horizontal compression, which sometimes rises and makes them 'stress barriers' for vertical dykes (Gudmundsson and Brenner, 2001).

Material toughness and elastic mismatch

An elastic mismatch exists when the mechanical properties of the materials such as the material toughness and Young's modulus (E) substantially differ in the interface itself, or either side of the interface. In case the strain energy release rate (G_I), for Mode I fractures during dyke propagation, reaches the material toughness of the discontinuity the dyke is deflected into the interface and propagates in a mixed-mode way (II and III) (Hutchinson, 1996; Xu et al., 2003). The mechanical properties of the discontinuities depend on the Dundurs elastic mismatch parameters α, (Dundurs, 1969; He et al., 1994) that define the conditions for dyke penetration or deflection. Especially for a dyke to penetrate the following equations (Eq. 1.5 and 1.6) should be satisfied:

$$\frac{Gdeflection}{Gpropagation} < \frac{\Gamma deflection(\psi)}{\Gamma L^1} \qquad (1.5)$$

And for a dyke to become deflected the following equation should be satisfied:

$$\frac{Gdeflection}{Gpropagation} > \frac{\Gamma deflection(\psi)}{\Gamma L^1} \qquad (1.6)$$

where Gdeflection is the energy release rate for deflection, Gpropagation is the energy release rate for propagation, Γdeflection is the material toughness of the contact, Γ 1 is the material toughness of the layer on top of the discontinuity, and finally, Ψ is the relative rate of mode I and mode II during propagation (Fig. 1.6). Ψ denotes as tan-1(K_{II}/K_I) where K_{II} and K_I are the stress intensity factors of Mode II and Mode I respectively (He and Hutchinson, 1989; Sun and Jin, 2012). Finally, if the stress orientation does not encourage deflection, the dyke is arrested.

However, we must also consider some parameters that have been suggested as control on dyke arrest in crustal segments aside from the mechanisms mentioned above. Rubin (1995) proposed magma solidification (freezing) especially for dykes that carry little magma (low volume) and a possible cause of dyke arrest.

Heat transfer mechanisms that produce conduction on their walls or hydrothermal effects in the host rock can stop a vertical propagating dyke. It should be noted, however, the solidification of dykes is normally very slow in comparison with the rate of dyke propagation. And solidified dyke rock, say at the dyke tip, would generally have a similar tensile strength to that of the host rock and thus unlikely to arrest an otherwise fluid dyke. In case there is no constant supplied magma rate, the source gets exhausted, and after some time and depth, it will slow down, thin out and arrest (Thodarsson and Self, 1993). Chen et al. (2011) finally suggested that in some cases, dyke arrest is governed

by one factor or by multiple ones at the same time. For a dyke that propagates for a long time, the initial arrest mechanism is magma freezing (solidification). In contrast, for a propagating dyke that its volume is compared with the magma chamber volume, the initial arrest mechanism is the declining overpressure.

Another factor that may contribute to dyke arrest with depth is the growing edifice on top of the magma chamber (Pinel and Jaupart, 2004). The stresses which are generated at the top of the chamber can produce a compressive stress field which effects vertically propagating dykes and as a result tend to align with the regional stress field. The process is called tectonic forcing or loading by a tall volcanic edifice. However, this mechanism, if of general value, would imply that no dyke-fed large edifices could ever form – in direct contradiction with observations worldwide.

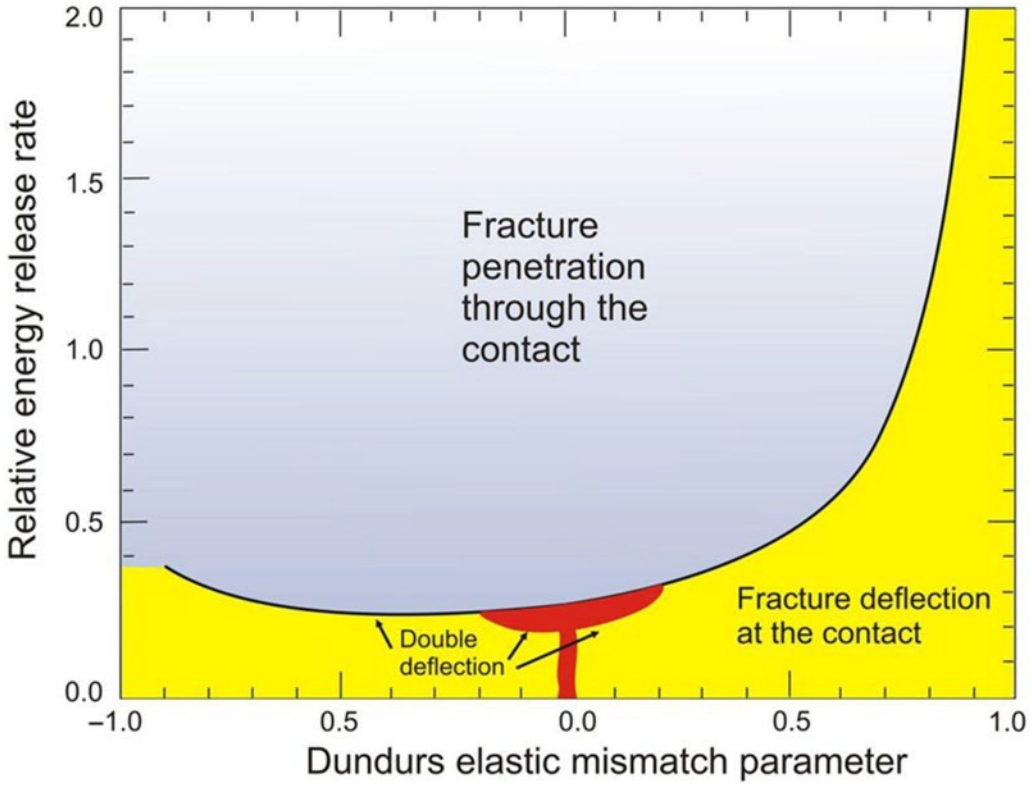

Fig. 1.6: Diagram from Gudmundsson and Lotveit (2012) showing the ratio of the strain energy release rate for fracture deflection Gd to that of fracture penetration Gp. Yellow part of the diagram encourages fracture/dyke deflection. Data from He and Hutchinson (1989) and Hutchinson (1996).

1.8 Caldera collapse

Caldera collapse and/or resurgence is the result of magma chamber inflation or deflation in an underlying magma chamber (Henry and Price, 1984; Lipman, 1997; Gudmundsson, 1998; Acocella et al., 2000). The formation of a caldera relies on the connection between normal or reverse ring-faults from the

underlying magma chamber to the surface (Gudmundsson, 1998; Holohan, 2008) or due to weight accumulation of the underlying intrusive segments (Walker, 1988). Piston-like caldera collapse calderas are associated with magma removal from a magma chamber (Lipman, 1997) bounded by circumferential faults, ring faults or outward dipping reverse ring faults which usually represent the structural boundaries of them (Walker, 1984).

1.9 Field case study

Santorini is an active volcanic centre, located between Ios and Crete island from the north to the south respectively, defining the southern volcanic facet of the South Aegean volcanic arc (Papazachos and Comninakis, 1971; Le Pichon and Angelier, 1979). The volcanism is mainly related to the subduction and rapid rollback of Eurasian plate beneath the African plate with a constant velocity rate of 35mm/yr. (Kalogeropoulos and Paritsis, 1990). The subduction vector has a NE-SW orientation (Nomikou et al., 2013) governed by two different tectonic stress fields, thrusting to the west (Ionian Basin) and strike-slip to the east (Le Pichon et al., 1982) (Fig. 1.7).

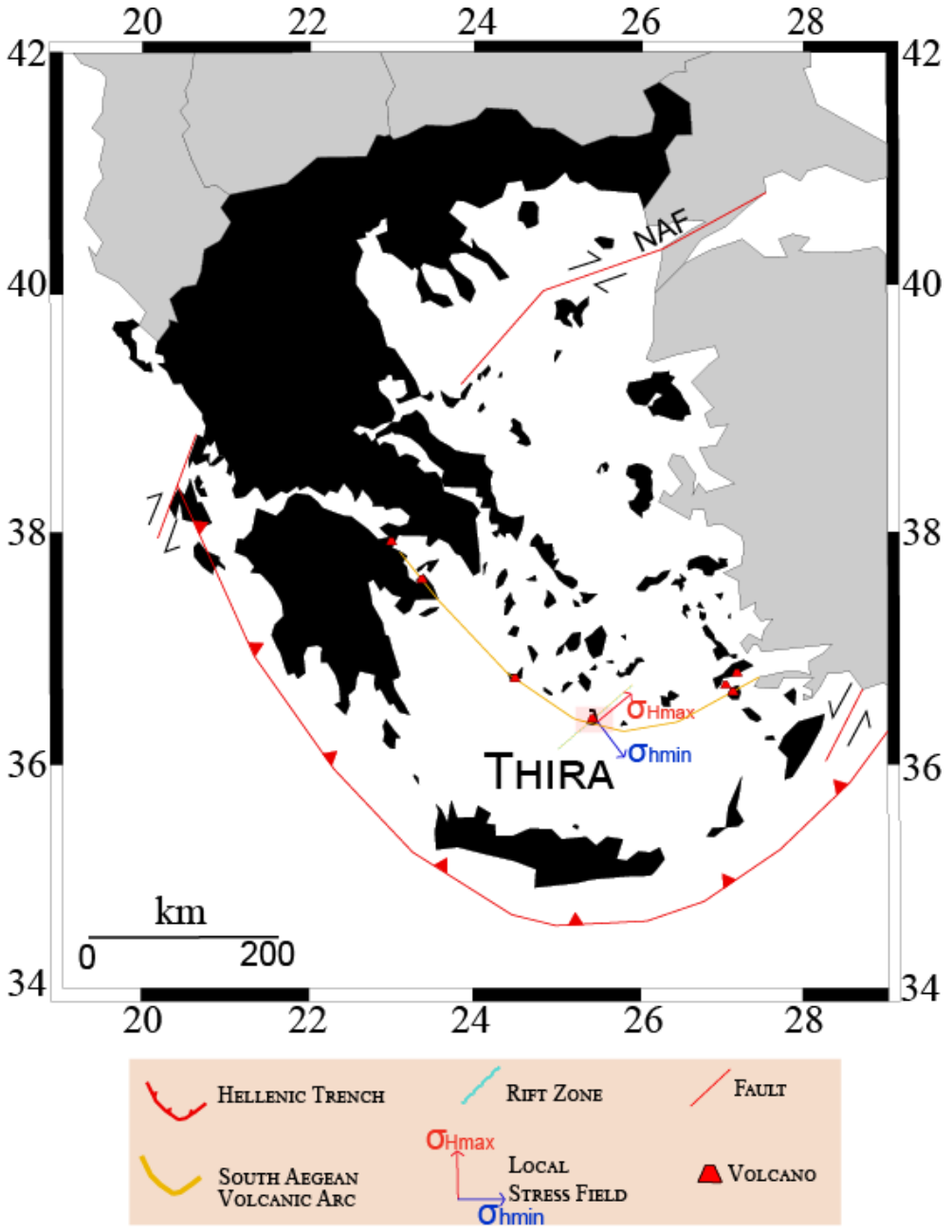

Fig. 1.7: (A) Simplified map showing the main tectonic features of the Aegean Sea modified from Konstantinou et al., 2006.

1.9.1 Santorini's volcanotectonic setting

The volcanic complex of Santorini (Thira) is comprised of five islands. Nea Kameni and Palea Kameni Islands (Kameni Islands) represent the latest products of the volcanic activity and were formed inside the flooded caldera surrounded by the islands of Thira, Therasia, and Aspronisi (Fig. 1.8A). The current caldera (11 × 7 km) is a circumferential ring fault that was formed after the catastrophic Minoan eruption (3.6 ka). A reconstruction of this eruption (Druitt, 2014; Johnston, 2015) advocates that its effects (ash fallout, tsunamis, climatic effects) possibly vanished the Mediterranean Bronze – Age civilisation (Marinatos, 1939) during its dominion (Druitt, 2014).

At the NE outer part of the Santorini complex lies the Kolumbo submarine volcano (Fig. 1.8A). The latter is formed atop an elongated strike-slip fault zone (Sakellariou et al., 2010) along with other 22 smaller volcanic cones (Hooft et al., 2017). The volcano erupted violently at 1650 AD posing a great threat to the nearby areas.

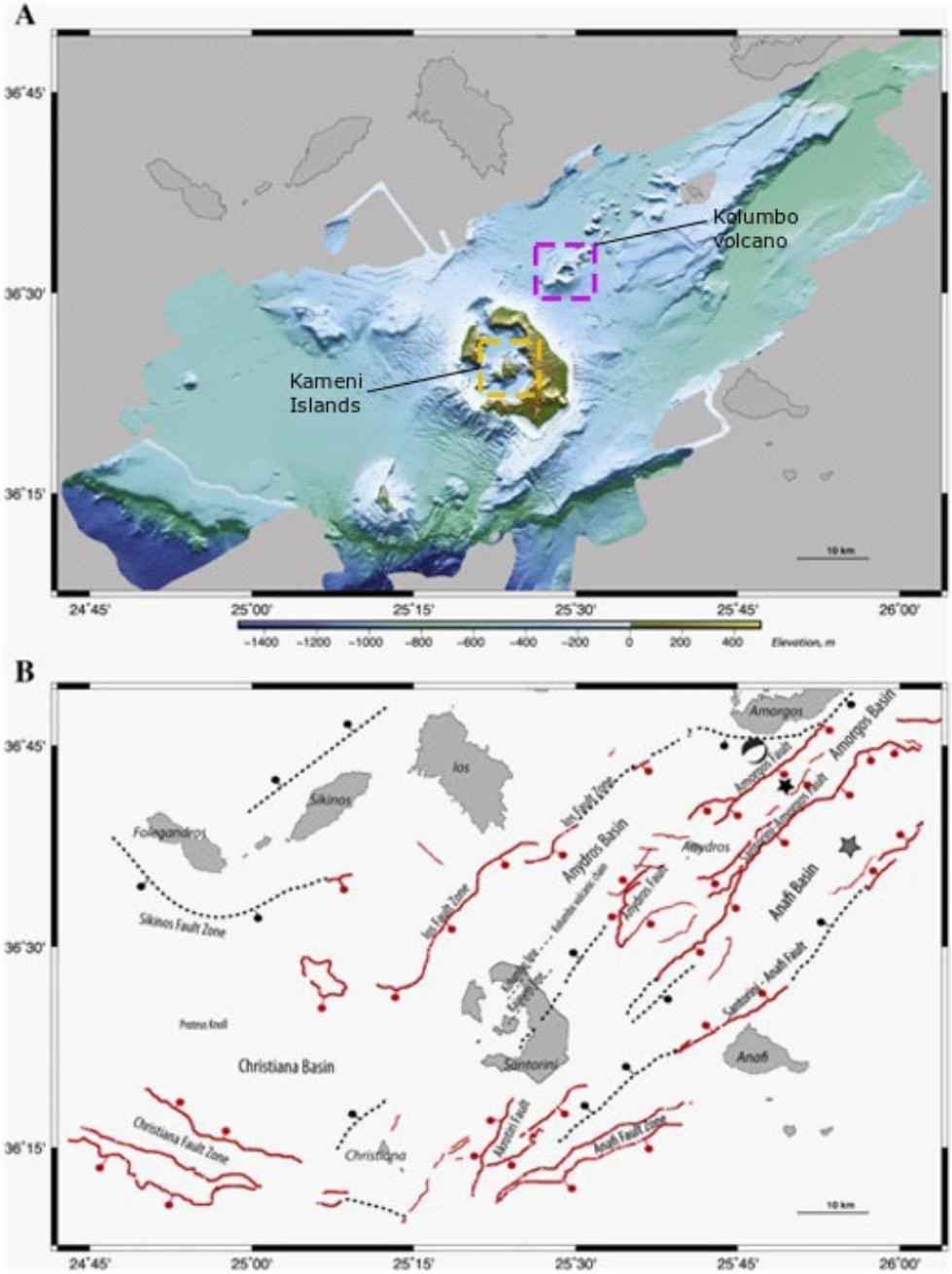

Fig. 1.8: A) Santorini bathymetric map (Hooft et al., 2017) with annotations of the locations of the Kameni islands (post-Minoan volcanism) and the Kolumbo submarine volcano. (B) Map from Hooft et al. (2017), and references therein,

showing the major tectonic structures around Santorini island and the epicentre of the earthquake at Amorgos island the 9th of July 1956.

The island is permeated by mainly three volcanotectonic lineaments. Two of them were described by previous authors (Druitt et al., 1999) as basement faults of unknown origin that controlled magma ascent in the shallow crust while the third one as a fault zone (Sakellariou et al., 2010). In detail (Fig.1.9):

1) Kameni VT line (NW-SE): It permeates the central part of the island (Fira town) and the post-caldera volcanic products (Nea and Palea Kameni volcano). According to Druitt et al. (1999), it could have been formed from the aligned migrated vents that have fed the 1st explosive cycle of Santorini's historical eruptions (360-172 ka). However, there were no signs of its actual existence since the 2011-2012 unrest episode when all the epicentres of the seismic activity were concentrated along this line showing a possible resurgence (Parks et al., 2012).

2) Kolumbo VT line (N50˚-60˚E): It dissects the northern part of the island and connects the cinder cones of Megalo and Kokkino Vouno in the north with the Kolumbo tuff ring in the north-east. The NW-SE line was suggested to have been a basement normal or strike-slip fault and have possibly controlled the volcanic activity at the northern part of the island (Druitt et al., 1999). However, actual signs of its existence are not found yet.

3) NE-SW fault zone / CSK rift zone (N30˚-50˚E): The last volcanotectonic line was introduced as a transtensional fault zone by Sakellariou et al. (2010) and studied later by Nomikou et al. (2012, 2013, 2016) after a focused bathymetric analysis of the seafloor at the northern, eastern part of the island. The PROTEUS expedition (Hooft et al., 2017) revealed with greater detail the rift zone that dissects the Christiana-Santorini-Kolumbo areas and probably controlled the magma ascent of Kolumbo submarine volcano and its crustal plumbing system (Rizzo et al., 2015,2016).

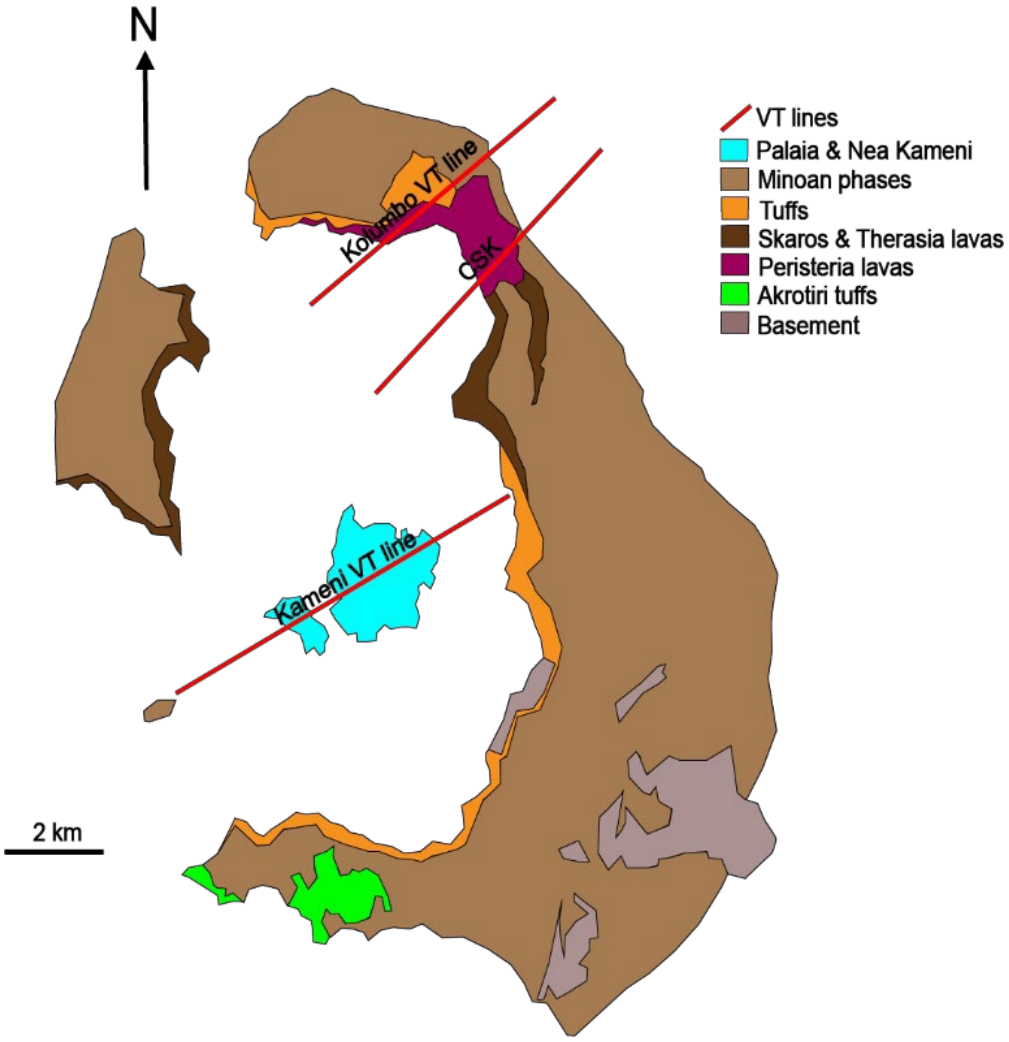

Fig. 1.9: Simplified geological map of Santorini Island from Druitt et al. (1999). The map shows the distribution of the lava flows, pyroclastic materials and metamorphic basement products. In addition, it includes the volcanotectonic lines that control magma ascent at Santorini (Druitt et al., 1999; Nomikou et al., 2013; Rizzo et al., 2016, Hooft et al., 2017). CSK: Christiana-Santorini-Kolumbo volcanic fields.

Four NE-SW trending normal faults are also situated between Megalo Vouno and Mikros Profitis Ilias. Faults F2 and F3 were suggested to have been triggered by the Cape Riva eruption (Rp6) and the collapse of the Therasia-Skaros complex at 22 ka (Druitt et al., 1999). This collapse forced the large block to slide into the collapsing depression forming a small graben. Earlier tectonic studies, however, (Mountrakis et al., 1996) suggested a dextral strike-slip fault zone (N 35-40˚ E) and a normal fault system (N 40-70˚E) in the same area.

1.9.2 Magmatic processes at Santorini volcano

The Santorini eruption products (lavas and pyroclastics) follow a continuous range from basaltic to rhyolitic compositions (Druitt et al., 1999; Francalanci et al., 2005). Basalts follow both the calc-alkaline and the tholeiitic series and have been found as lavas and magmatic enclaves and as basaltic scoria in one horizon (LP2) as a pyroclastic product. Basaltic andesites belong clearly to the calc-

alkaline series whereas andesites and dacites are mainly calk-alkaline and seldom HK-calk- alkaline.

From previous studies it is clear that the main processes that control magma generation at Santorini are:

1) Partial melting (deep source processes >20km)

The incomplete melting of up to 25% of the mantle parent rock (peridotite) generates liquids that are enriched with incompatible elements from less evolved elements. In subduction zones, partial melting occurs as the mantle wedge first undergoes metamorphism (especially the sediments that belong to the subducting plate) and then melts and releases aqueous fluids. The enriched melt phase starts to migrate to shallower depths into the overlying mantle; it re-melts and usually forms andesitic magmas (Rudnick, 1995; Pearce and Peate, 1995). In Santorini, this process is clear because the number of incompatible elements decrease with time (Huijsmans 1985) which is a trend that is clear both in the primary (mafic) and differentiated (felsic) products (Bailey et al., 2009). The depletion in incompatible elements and K are also observed in other volcanic centres in the Aegean (Francalanci et al., 2005).

2) Fractional crystallisation

Fractional crystallisation is the gradual separation of two or more phases induced by temperature and concentration changes. The magma is mixed with

the different phases, it melts and then slowly cools down so that each of the components crystallize at different temperatures and are hence removed from the solution (Wilson, 1989). The fractionation that produces primary, intermediate and felsic magmas on Santorini were derived experimentally using the parental basaltic magma located in Cape Balos (Nicholls, 1971; Mann, 1983; Druitt et al., 1999; Bailey et al., 2009; Andujar et al., 2015). Back-calculations by Nicholls 1978 estimated 9-12 wt.% MgO for the primary liquid (melt). The most primitive erupted basalt with 7 wt. % MgO was fractionated by 6-13 wt. % of Ol and lesser amounts of Cr-spinel and Cpx from the latter (Druitt, 2015).

The production of andesitic magma with 58 wt.% SiO2 was acquired experimentally from Andujar et al., (2015). It originated by 60-80 wt.% crystallisation of olivine, clinopyroxene, plagioclase, Ti-magnetite, orthopyroxene, pigeonite and ilmenite of the parental Balos magma with 3.5 wt.% water content. More felsic magmas needed higher rates of fractionation up to 75 % while cumulate phases from the residual magma were reported as nodules in various products and are still studied (Druitt, 2015).

3) Crustal assimilation

When hot mafic magma is transported from deeper reservoirs to the surface, it incorporates cool felsic components from the crust which mix with the melt and change its composition (Huppert et al., 1982). At Santorini, Druitt et al. (1999) and Bailey et al. (2009) showed that there is a positive correlation between the

$^{87}Sr/^{86}Sr$ and SiO_2 content which demonstrates that AFC (assimilation and fractional crystallisation) exists as the simple fractional crystallisation processes could not always reproduce the exact products.

4) Magma mingling and magma mixing

Primitive magmas propagate to the crust where they mix and differentiate to more intermediate and felsic compositions (Andujar et al., 2015; Cadoux et al., 2014). Magma mixing can be the result of a hot, primitive magma batch entering a cool and evolved magma chamber. Mafic enclaves on Santorini are found in many intermediate and silicic volcanic rocks (Bacon and Druitt., 1988; Coombs et al., 2002; Martin et al., 2006) and can be interpreted as the products of magma replenishment and mixing or signs from possible eruption triggering events (Sparks et al., 1977).

1.9.3 The crustal plumbing system of Santorini and Kolumbo volcanoes

The study of the crustal plumbing system of Santorini volcano has attracted broad scientific interest in the last two decades (e.g., Nicholls, 1971; Huijsmans, 1985; Druitt et al., 1999; Bailey et al., 2009; Gertisser et al., 2009; Michaud et al., 2000; Druitt et al., 2012, 2014, 2016; Fabbro et al., 2013; Kilias et al., 2013; Andujar et al., 2015; Martin et al., 2006; Klaver et al., 2016; Rizzo et al., 2016;

Flaherty et al., 2018) not only due to its inferred complex structure but also for its convoluted volcanological and geochemical characteristics. The studies have investigated both the Santorini and Kolumbo systems focusing on their eruptive products and suggest the occurrence of two separate plumbing systems for each volcano (Francalanci et al., 2005; Rizzo et al., 2006; Klaver et al., 2016).

The first system, the Santorini plumbing system, is fed by melt that originates from deeper sources but on its way to the surface becomes frequently stalled and stored in the crust. As a result, its products exhibit traces of primary magmas that underwent extensive magma mixing, fractionation, AFC and low-temperature hydrothermal activity (T<100˚C). However, the second system, the Kolumbo plumbing system is fed directly from magmas with pure mantle signatures without signs of other processes but, instead of high hydrothermal temperature activity (T=220˚C) (Fig. 1.9) (Rizzo et al., 2016).

Structurally, both systems lie on the same rift zone (CSK) and share the same geological structure, and tectonic history (Piper et al., 2007; Dimitriadis et al., 2010; Nomikou et al., 2013; Hubscher et al., 2015; Hooft et al., 2017) but have different morphological characteristics and are developed in different crustal segments with different stratigraphy.

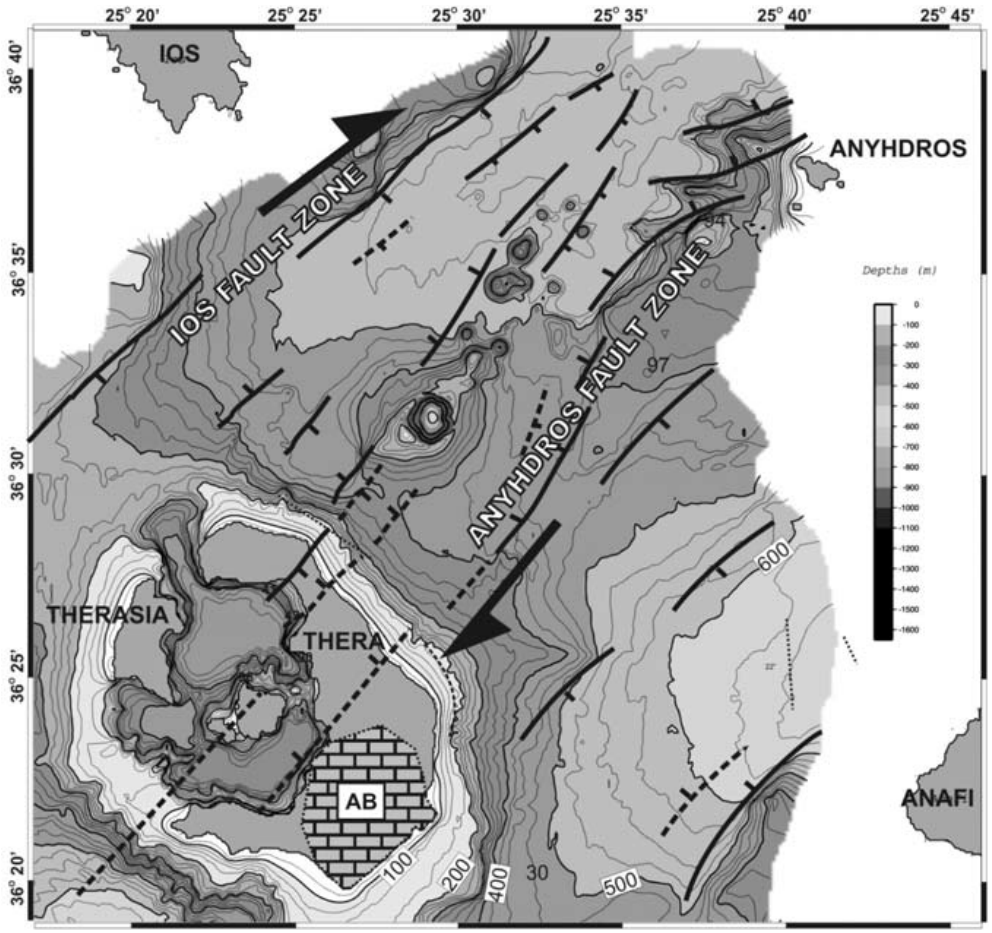

Fig. 1.10: Tectonic map of Santorini and the NE basin showing the fault systems around the two-active volcanic centres (Sakellariou et al., 2010).

Bathymetric and seismic studies (Fig. 1.8B and 1.10) revealed that the Kolumbo zone is surrounded by a denser system of normal and strike-slip faults than the Kameni island. This fact could imply that the crustal structure beneath the Kolumbo region could allow magma migration to the surface due to different loading conditions (e.g. fissure volcanism). Studies in Chilean stratovolcanoes (Cembrano and Lara, 2009; Sielfeld et al., 2019) that lie on a similar geodynamic setting (transtensional fault zone) propose that different morpho-structural

characteristics of the volcanic edifices such as elongated aligned-chains versus single central stratocones could be generated by different mechanisms, e.g. different tectonic fields (Lara et al., 2006; Mathieu et al., 2011), structural anisotropies (Tibaldi, 1995) or morphological effects such as the load and shape of the volcano (Van Wyk De Vries and Merle, 1998). Such comparisons in the Santorini volcanoes have not been made before. They should be considered in the future as they are essential for understanding the mechanism of magma propagation in both systems and the different paths that control their eruptive activity.

The Santorini plumbing system received considerable attention after the 2011 - 2012 unrest episode (Parks et al., 2012; Browning et al., 2015) as it reactivated not only the system itself but also the interest of the scientific community. Experimental studies from Andujar et al., (2015); Cadoux et al., (2014) and Andujar et al., (2016) have suggested that a large and long-lived magma chamber lies at 8-10km depth and 2 kb pressure which controls the shallow crustal system by feeding evolved silicic eruptions (Fig. 1.11A). The chamber is also related to a deeper magma chamber (deep reservoir) that lies at the upper-lower crust boundary at 15km depth. The pressure of the deeper reservoir would be 4kb and belong to a mafic system that fed the mafic eruptions (Fig. 1.11B).

The path of the mantle origin magma is defined as follows. First, it becomes stored at the deep reservoir where it fractionates to intermediate magma (andesitic) at a temperature of around 1000˚C, and pressure around 400 MPa

with around 4-6 wt.% H_2O and an oxygen fugacity fO_2 of FMQ-0.5. The magma crystallises with around 60-80wt% of a mineral assemblage that is composed by ol+cpx+plag+Ti-mag+opx±pig-ilm. The magma then ascends and becomes intruded into the shallow felsic magma chamber where it either differentiates before it feeds an eruption or fractionates producing more silicic magmas with dacitic to rhyodacitic compositions. The latter are stored at a lower temperature of 850-900°C and are accompanied by melts enriched with water and chlorine but depleted in fluorine and sulphur (Andujar et al., 2015; Fabbro et al., 2017).

Based on the previous experimental studies, the dykes of Santorini were generated mainly from a shallow source at 3-7 km and a deeper reservoir at 12-16 km. Experimental phase equilibria studies (Cottrell et al., 1999; Michaud et al., 2000; Gertisser et al., 2009; Cadoux et al., 2014; Fabbro et al., 2017; Flaherty et al., 2018) have assessed the storage conditions of volcanic products of Santorini prior to eruption. The Minoan eruption magma is estimated to have been initially stored at a pressure of >200MPa and ascended to ~50 MPa only months before the eruption (Cottrell et al., 1999).

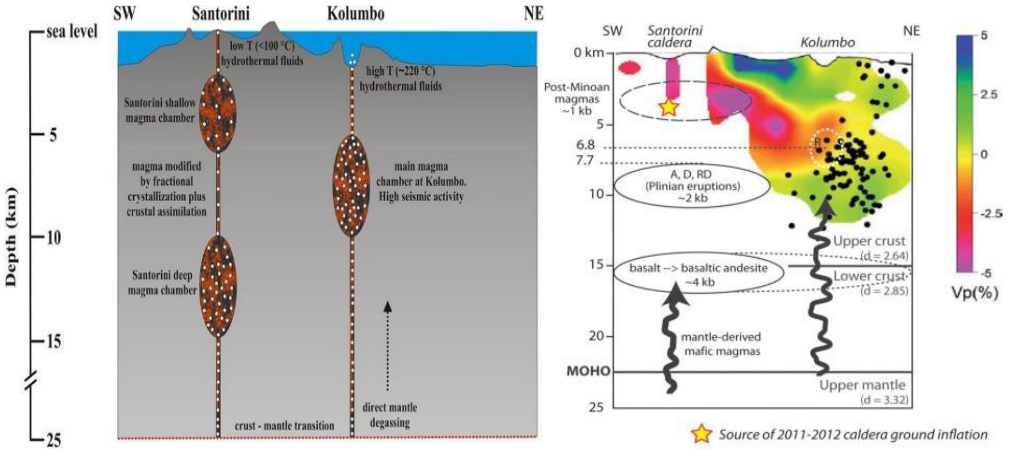

Fig. 1.11: (A) 40 km depth cross section along the CSK rift zone showing an illustration of the plumbing systems beneath the Nea Kameni (Santorini) and Kolumbo from Rizzo et al. (2016). (B) Cross-section of the Santorini-Kolumbo magma plumbing systems from Cadoux et al. (2014).

1.9.4 The petrography of the Northern caldera wall dyke swarm

The dykes, on the northern caldera wall, are fossilised injections of magma that represent both successful and unsuccessful eruptions. As a result, a petrological study of the Santorini dyke swarm can inform us about the mineral assemblage, the frequency of distinct geochemical compositions and, the conditions and types of residual magmatic phases or eruption triggers.

Petrological studies of the Santorini dyke swarm (Nicholls, 1971; Huijsmans,

1985; Puchelt, 1990; Eleftheriadis et al., 1998; Petersen, 2005; Bailey et al., 2009) have reported aphanitic macroscopic textures and cryptocrystalline to hypo crystalline sizes of groundmass and intergranular and intersertal groundmass textures. The petrographic analysis revealed a wide range of phenocryst percentages (2-39 %vol) and vesicularity (0-40%) and the presence of secondary minerals such as calcite. The chemical composition of the dykes' ranges from basalt to dacite (Nicholls, 1971; Mann, 1983; Huijsmans, 1985; Petersen 2005; Bailey et al., 2009). The dykes are generally abundant in glomerocrysts which are either monomineralic (plagioclase (Plag), clinopyroxenes (Cpx), orthopyroxenes (Opx)) or polymineralic (plag+ol±cpx, plag+cpx+op). The mineral textures were mostly described as seriate and trachytic while signs of olivine alterations along cracks seldom appeared. The phenocrysts have sizes from less than 0.5mm to 3.5mm, and the main minerals are described in Table 1.2.

The dykes were long studied with the assumption that they belonged to a continuously differentiated magma which followed a distinct crystallisation order from mafic (B (basalts): ol+cpx+plg) to more felsic products (TA (trachyandesites): cpx+plg+op±opx±ol) (Nicholls, 1971; Huijsmans, 1985; Hansen, 1997; Kann, 2000; Petersen, 2005). The first minerals which crystallized were olivine and clinopyroxene (simultaneously) followed by plagioclase. Orthopyroxene replaced olivine in evolved samples (A (andesites): cpx+plg±opx±op±ol to T: cpx+plg+op±opx), but both are found, although in a

limited amount, in the most mafic rock types especially in BA (basaltic andesites): ol+cpx+plg±opx±op. Opaque minerals were present as minute amounts either as phenocrysts and/or micro phenocrysts in all rock types except basalts.

Table 1.2: Compilation of characteristics of the phenocryst phases of the dykes from Petersen, (2005).

Mineral	**Textural Analysis**	**Chemical composition**
Plagioclase (Plag)	Abundant (2-28 vol%), euhedral or subhedral and angular crystals, twinning (polysynthetic or Carlsbad) and zoning (normal, reversed and oscillatory), inclusions of melt phases or other minerals are present	Anorthite, bytownite, labradorite, andesine
Orthopyroxene (Opx)	Abundant (1-12 vol%), euhedral or subhedral, twinning and zoning (colour, sector or concentrically)	Enstatite
Clinopyroxene (Cpx)	Not very common (<1 vol%) mostly found in evolved compositions and less in mafic	Diopside, augite
Olivine (Ol)	Quite common (1-11 vol%), often altered, embayments and resorption.	Mg-rich (>50%Fo)
Opaque (Op)	Abundant (1-4 vol%), subhedral and rarely euhedral along with Cpx and Plag	
Microxenoliths	Composed of different groundmass (larger or smaller grains, different minerals or glass), phenocrysts of other sizes, shapes and composition, microxenoliths of quartzite	

The observed groundmass textures most commonly found in the more evolved rocks were glomeroporphyritic and trachytic (Huijsmans, 1985). The observed mineral textures (Petersen, 2005) were: 1) jacketed orthopyroxenes; 2) resorption and embayments; 3) normally and reversely zoned plagioclase; 4) complex zoning; 5) spongy textures in plagioclase; 6) different textural populations of single minerals indicating disequilibrium, magma mixing, fractional crystallisation or other processes (e.g. pressure or temperature-dependent).

Chapter 2: Methodologies

In this chapter, I report the field, laboratory and numerical modelling methods used in this study. Specifically, I explain the standard geological techniques, conventions and limitations that were used to collect the field data during the campaigns. The result of the extensive geological mapping campaign was the compilation of a new geological map showing the location, strike and thickness of dykes found in the northern caldera wall. Laboratory methods are described in detail and these allowed the creation of a petrogenetic model of the studied dyke swarm, and a reconstruction of the volcanoes crustal plumbing system. I also present the software used to simulate the studied physical problems and observed dyke paths.

2.1 Field methods

The geological study of dyke swarms require mapping and collection of data regarding each dyke's attitude, aperture and length/height and other physical characteristics such as the chilled margins, shape, colour, vesicularity, petrology and cross-cutting relationships (Walker, 1992; Gudmundsson, 2003; Geshi et al., 2005; Tibaldi et al., 2011; Burchardt et al., 2011; Galindo and Gudmundsson, 2012). Acquisition of such data allows the construction of models to help understand the emplacement of dyke swarms.

During this study, I collected data regarding the structure of the dyke swarm, which was combined with petrological data (Fig. 2.1). The petrological analysis included collecting data associated with the dykes' magmatic history such as macroscopic mineral assemblage and textures, phenocrysts, vesicularity and the evolution in time such as weathering and signs of hydrothermal activity. For a completed petrogenetic model, I combined the petrological data with a detailed geochemical host rock analysis.

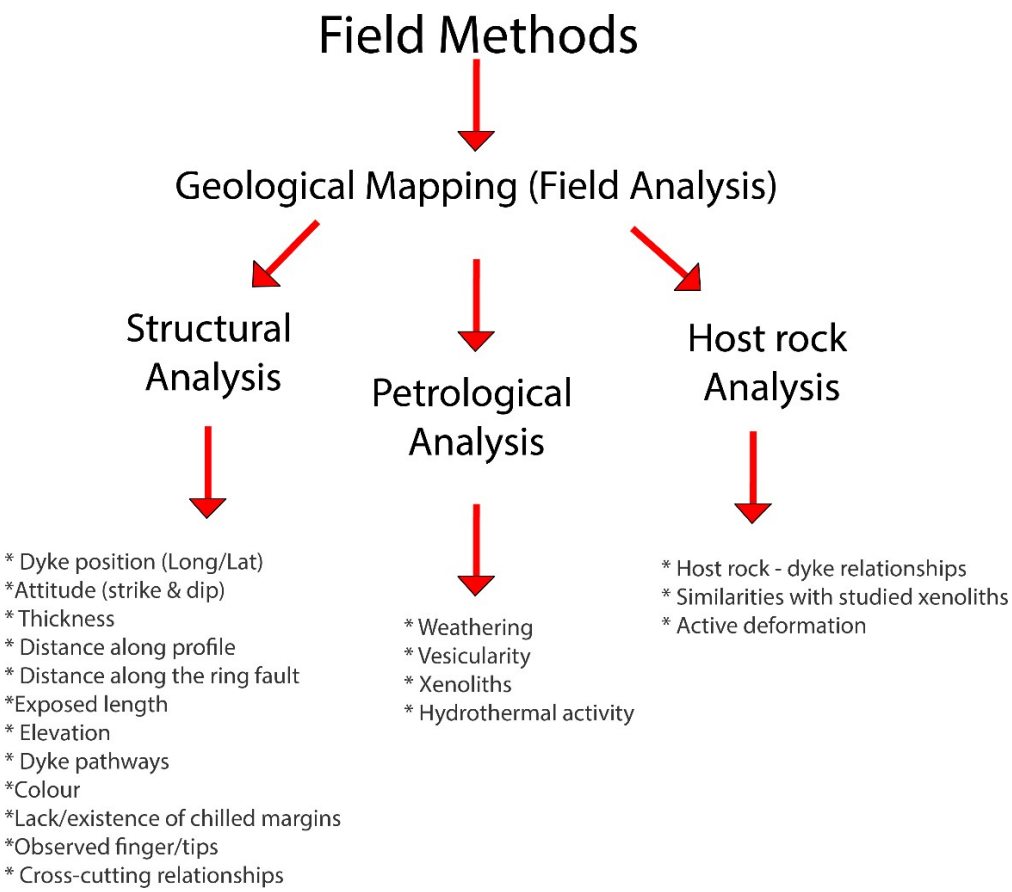

Fig. 2.1: Flow chart showing the methodology followed during the field analysis. The bullet pointed stars indicate common observations taken with respect to each analysis type.

2.1.1 Fieldwork equipment

During the field survey, I used the topographic-geological map from Druitt et al. (1999), originally published with Geological Society Memoir 19, at a scale of 1:20000 (Fig. 2.2). Samples were collected using an Estwing E30 (model), 22oz (length 330 mm) geological hammer with a pointed tip, which was also used as a scale in photographs.

A handheld GPS (Etrex Vista Cx in WGS 84 datum) was used for locating points of interest with an accuracy of less than 15 metres (33 feet). The thickness of dykes and units was measured with a tape measure, and attitude (strike & dip) measurements were made with a geological compass (69 Freiberger Praziskonmechanic DDR), a clinometer (Suunto MC-2), and the FieldMove Clino Android app (by Midland Valley Exploration Ltd). As some parts of the cliffs were dangerous to approach, in these cases geological measurements were taken from a distance.

2.1.2 Geological mapping (field analysis)

Four field campaigns were conducted at Santorini volcano. During the campaigns, sections of the northern caldera wall were mapped with a specific interest in the dyke swarm, the associated lavas and eruptive units (host rock) which are partially cut by a series of historic caldera collapse events (Druitt and Francaviglia, 1992) and faults (Druitt et al., 1999).

One of the first targets of this study was the production of a new geological map. The base map used for the study, was the northern section of the Santorini map by Druitt et al. (1999) and its fixed points for the correct calibration: Armenaki pier in Oia N 36 27 37.78, E 25 22 51.98 and Profitis Ilias church in Imerovigli N 36 27 12.81, E 25 25 23.98 (Fig. 2.2).

I studied the field area both by boat and on foot through the mountain footpaths. During the campaigns, the following specific conditions were considered as they added standard errors to the observations and data collected (Fig. 2.3):

- ✓ Weather conditions: Although the weather was generally good during the campaigns, the sea was rough close to the shore, because of strong currents, and sailing was dangerous. Unfortunately, a lot of samples were lost when I attempted to collect them during these conditions.

- ✓ Mountain environment: The vertical caldera wall was rough and steep with loose material and scree. Some dykes were impossible to sample as

they outcropped below the water level or too high in the cliff.

- ✓ Weathering: In many cases, it was challenging to collect fresh samples as the dykes were altered due to seawater and hydrothermal processes. For example, secondary minerals were often crystallised to calcite next to the sea level. This observation was more prominent on the dykes close to normal fault zones. A list of field photos is given in Appendix A.

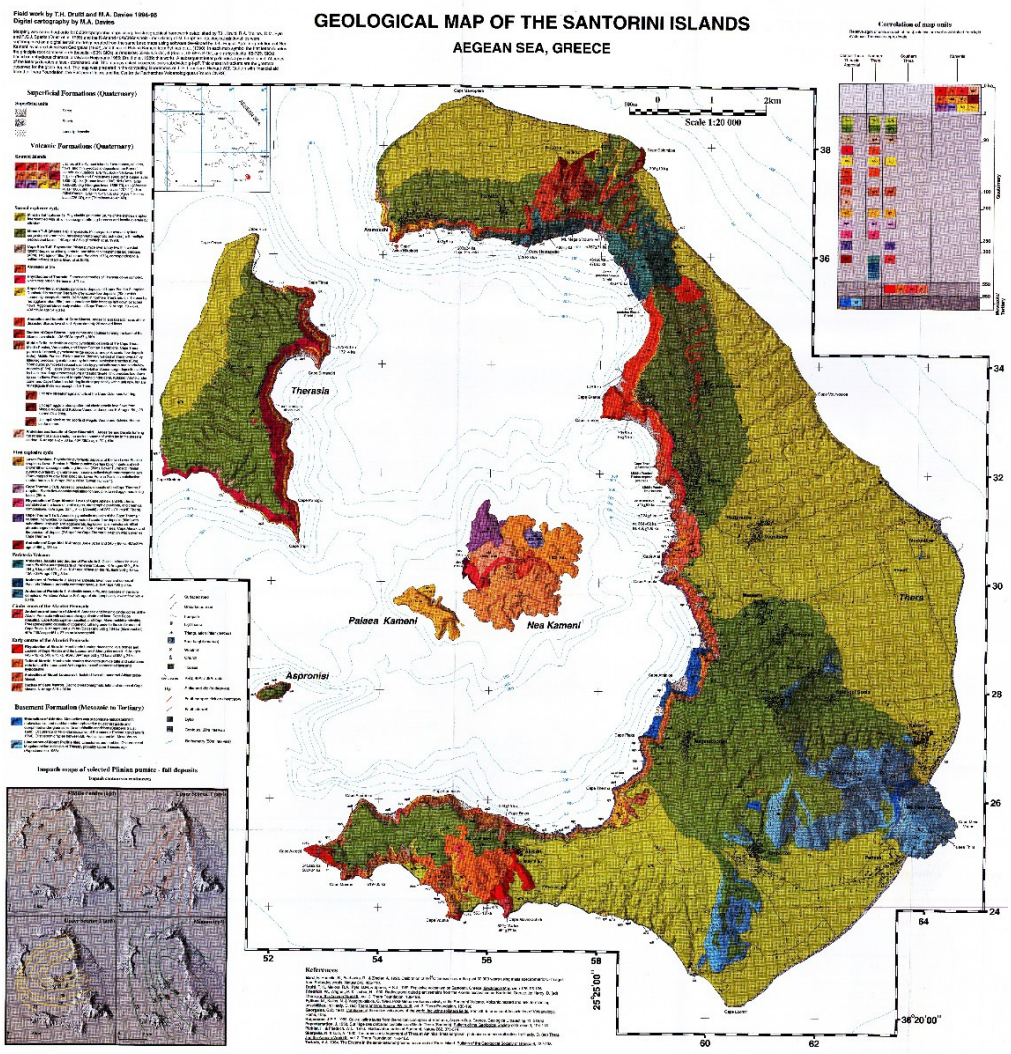

Fig. 2.2: Geological map of Santorini Islands from Druitt et al. (1999).

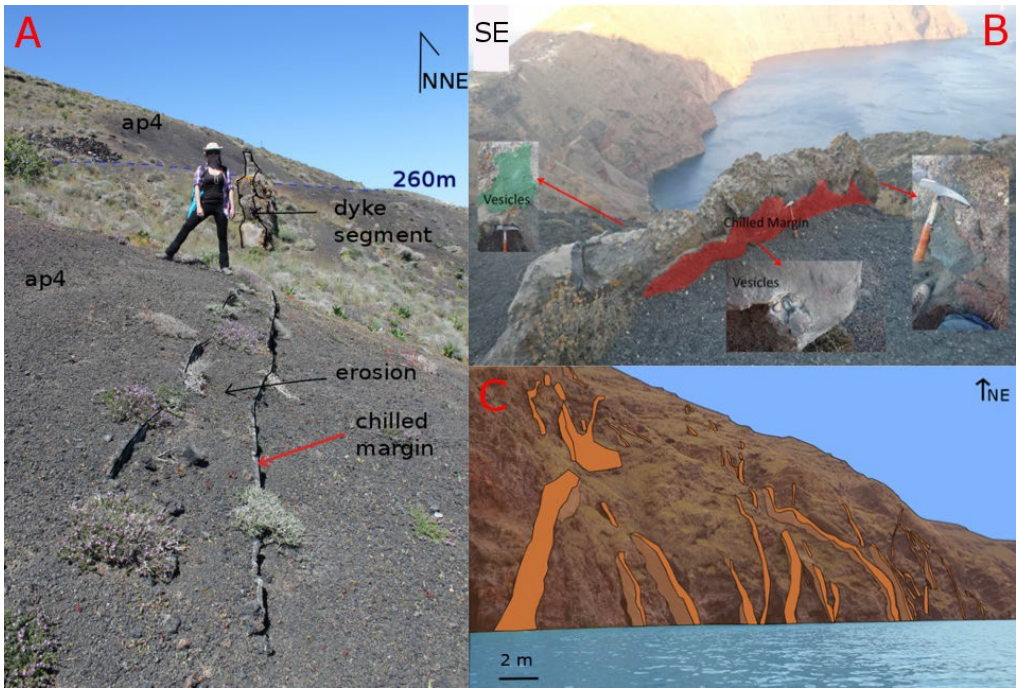

Fig. 2.3: Selection of photos of dykes at various scales from the northern caldera wall. (A): Segmented dyke on the Megalo Vouno that cuts the scoria ap4 layer. In the photo I observe the chilled margins and the eroded part of the dyke in front and the rest of the dyke in the back. (B): The same dyke as seen in A from a SE orientation. (C): An annotated photo of a section of the dyke swarm, where dykes are coloured orange.

2.1.2.1 Structural analysis

The structural analysis was completed over three of the campaigns. Initially, field observations were made to determine the exact dyke position, colour, and lack/existence of chilled margins, observed fingers/tips (if any) and cross-cutting relationships between the different dyke orientations (Appendix B1). Subsequently, structural data were collected on the longitude/latitude, attitude, thickness, and exposed length (where possible) of the dykes. Also, the distance along the profile, the dyke elevation, distance from the caldera ring-fault, the observed dyke paths (qualitatively) were reported using the length tool in Google Earth. I collected data from a total of 91 dyke segments at the northern caldera wall and made further observations at Therasia Island and Akrotiri (Balos).

For the final data compilation, previous measurements from other field campaigns by Fouque (1879); Petersen (2005); Bailey et al. (2009) and Browning et al. (2015) were compiled and compared. The GPS data collected from measurements made at sea were corrected using the Google Earth pro application (Imagery date: 7/2/2016) as they were made from a moving position (a boat). The data are listed in sections A1 and A2 (Appendix A) and B1 (Appendix B). In specific; I focused on mapping in different scales the signs of active deformation (faulting) as well as on their stratified lithologies (cross-sections). Thus, they could allow us to study the local stress field and how they affected the dyke paths.

2.1.2.2 Petrological analysis

Petrological sampling was conducted over two campaigns both by boat (sea-level access) and on foot (mountain level access). The sampling technique used was as described in common petrological books (e.g. Best, 2003). All the samples collected were representative hand samples, fresh and unweathered as possible to give comparable results through the geochemical analysis.

In detail, six dykes were chosen from the sea level and six dykes from the mountain level for petrographic analysis. The dykes represent the whole 5 km profile of the northern caldera wall, and for better statistical results they were sampled randomly along the caldera wall. Also, interest was given to their chilled margins. Not all the dykes had chilled margins which were more common in the mountain level dykes.

The methodology followed during the petrological sampling is as follows:

1) Each dyke was sampled on their rims and their cores if possible. Several similar samples were taken along the dyke if the dyke was exposed and could be followed upwards (e.g. bottom samples or top samples). The samples were not just petrologically representative but also oriented along the caldera fault and were cut in 3 different orientations such as (a) parallel to caldera strike, (b) normal to caldera strike, (c) parallel to caldera dip.

2) Scoria samples were found attached at the dyke rims on the mountain level, and thin sections of them were made to be compared with the scoria host rock samples.

3) Chilled margin samples were collected and studied along the dykes' exposed length on the Megalo Vouno edifice. A few thin sections of them were obtained. The sampling protocol is presented in Table. 2.2 (Appendix A) and the petrographic analysis in section B4-1 (Appendix B).

The petrological sampling included (if possible) core, and rim samples of the studied dykes as well as samples from their chilled margins (if any) (Fig. 2.4). The petrological analysis included observations of the dyke vesicularity, phenocrysts and entrainment as well as signs of active hydrothermal activity (calcite). The sampling protocol is shown in section A6 (Appendix A).

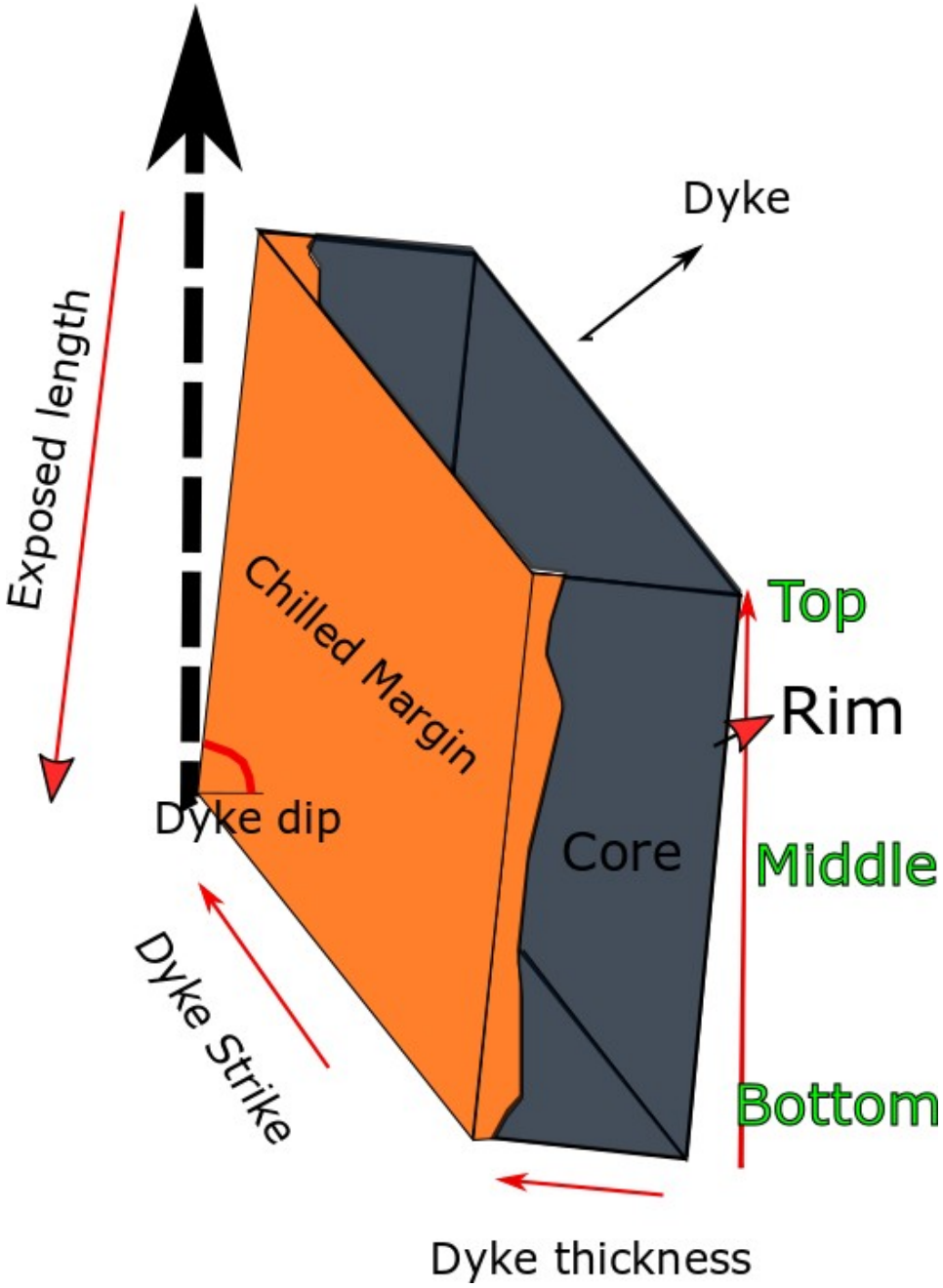

Fig. 2.4: A schematic illustration of a dyke showing the terms of strike, dip, thickness as well as its studied parts core, rim, chilled margin studied here.

2.1.2.3 Host rock analysis

Although the main focus of this study was the dykes observed on the northern caldera wall, I also sampled several host rock samples. These gave insights as to the propagated dyke paths, as the dykes contain evidence of host rock entrainment. I made thin sections of the host rock samples to compare them with the dyke samples. The analysis also allowed geochemical comparisons to be made between the stratigraphy and the dyke swarm. This technique was used to identify potential dyke fed relationships between the dykes and the flows/deposits and allowed qualitative analysis of age relationships. In addition, the amount of host rock deformation was studied (percentage of assimilated material) to record the volcanotectonic evolution of the plumbing system. Here dyke fault deflections, and faulting prior to dyking were also examined. The sampling protocol is shown in section A6 (Appendix A).

2.2 Laboratory research

Petrology tries to understand the nature and origin of rocks by making critical observations, asking questions and integrating all collected data into self-consistent interpretive petrogenetic models (Best, 2003). As a result, after the sample collection, laboratory analysis was performed on all samples using a range of analytical techniques, as shown in Figure 2.5.

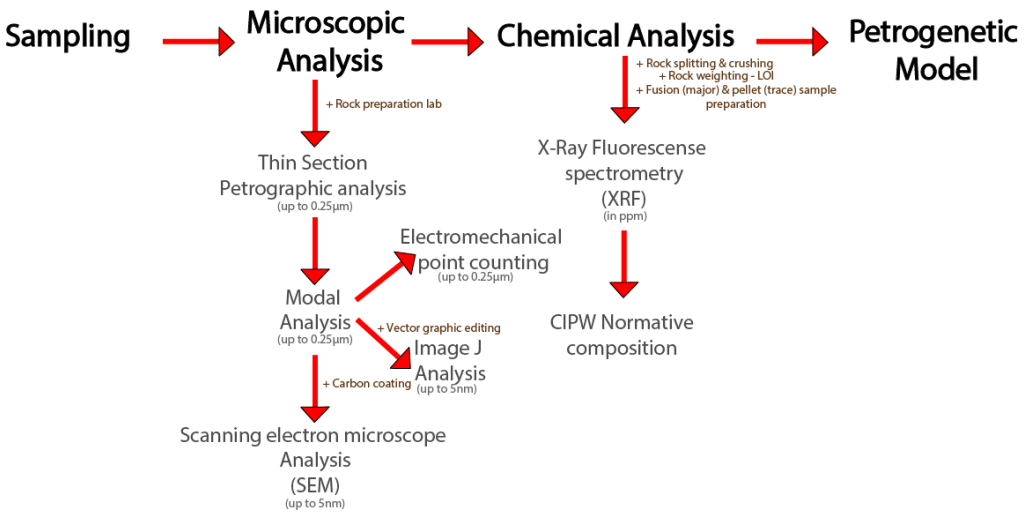

Fig. 2.5: Flow chart showing the methodology followed during the petrogenetic analysis.

2.2.1 Microscopic analysis

Petrography is a sub-discipline of petrology which studies mineral textures and rock fabrics in thin sections by means of an optical microscope and defines the systematic classification and description of rocks (Encyclopedia Britannica, 2018). It is mainly a qualitative method based on observations that depend on the experience and training of the petrographer (Robinson, 1991). The resolving power limit of the optical procedure is up to 0.25 µm.

2.2.2 Thin section preparation laboratory - petrographic analysis

The preparation of thin sections was conducted at the preparation laboratory at Royal Holloway University of London by the technician Mr Neil Holloway. Blocks of all samples were initially cut with a geological hammer into smaller hand pieces with intensive care avoiding any external contamination and handed into the thin section lab. Seventy thin sections were prepared in total.

The microscopic study of the samples was carried out in a diffused light polarising microscope to determine 1) the mineral assemblages, 2) any structural relationships of the participating minerals (textures and fabrics) and 3) their degree of fractionation. Petrographic analyses were conducted with a polarised optical microscope (Vickers Instruments) (Fig. 2.6A) and the thin sections were analysed with an optic polarised microscope supplied with a digital camera (NIKON Microphot FX-35A with a NIKON DS-5M camera system) (Fig. 2.6B).

2.2.3 Modal analysis

Modal analysis is a quantitative method first announced by Delesse (1848) and is used to determine the distribution and volume percent of the minerals (mode) in a thin section. The analysis can be acquired by a variety of techniques that

have different precision and accuracy (van der Plas and Tobi, 1965) such as (Best, 2003):

1) A visual estimate of a hand specimen
2) Gridding overlying polished slabs of rock
3) Electromechanical point counting on thin sections
4) Analyses of digital images on a computer

For the quantitative analysis of the mineral compositions in our rock specimens, I used the electromechanical point-counting method and the program Image J, which are described below.

2.2.3.1 Electromechanical point counting

Electromechanical point counting is a fast, economical and user-friendly technique used by petrographers to obtain an approximate composition of the studied rock. The method uses an automatic point counter attached to a polarising microscope (Fig. 2.6C). A systematic selection of 300 - 2000 points on a thin section is required to record the rock composition (Bailey and Stevens, 1960).

The main disadvantages (Livingood and Cordell, 2008) regarding the statistical analysis of the method are 1) the precision of the volumetric equivalence proportions with real measurements, 2) the ability to reproduce the estimates of the proportions successfully, 3) the efficiency of the thin section (failure to capture heterogeneity), and 4) the consistency and bias of the petrographer.

During this study, thirty-two samples were scanned with a hitting point frequency of 1500 the maximum. Inside the studied samples, multiple measurements were recorded to reduce the user-based uncertainty (random error). In addition, twelve samples that belonged to a different collection were scanned to calculate the uncertainty between different observers (systematic error of the technique).

Fig. 2.6: The microscope apparatus used during the microscopic analysis. (A) A polarised optical microscope. (B) A NIKON Microphot FX-35A optic polarised microscope supplied with the NIKON DS-5M camera system digital camera. (C) An electromechanical point counter attached to a polarising microscope used to obtain qualitatively the chemical composition of the studied specimens.

2.2.3.2 Image J analysis

Image J is a Java-based image-processing program initially developed at the US NIH (National Institute of Health) in 2010, offering image analysis processing in different disciplines (Schneider et al., 2012). The program calculates area and pixel value statistics using thresholds, distances and angles, density histograms and line profile plots, etc. During this study, the program was used to obtain area calculations (percentages) of xenoliths and clots inside the dykes. Initially, the thin sections were scanned and then the image processing was developed using backscattered (BSE) images produced from the SEM images. The following photos (Fig. 2.7) show the method steps and deliveries.

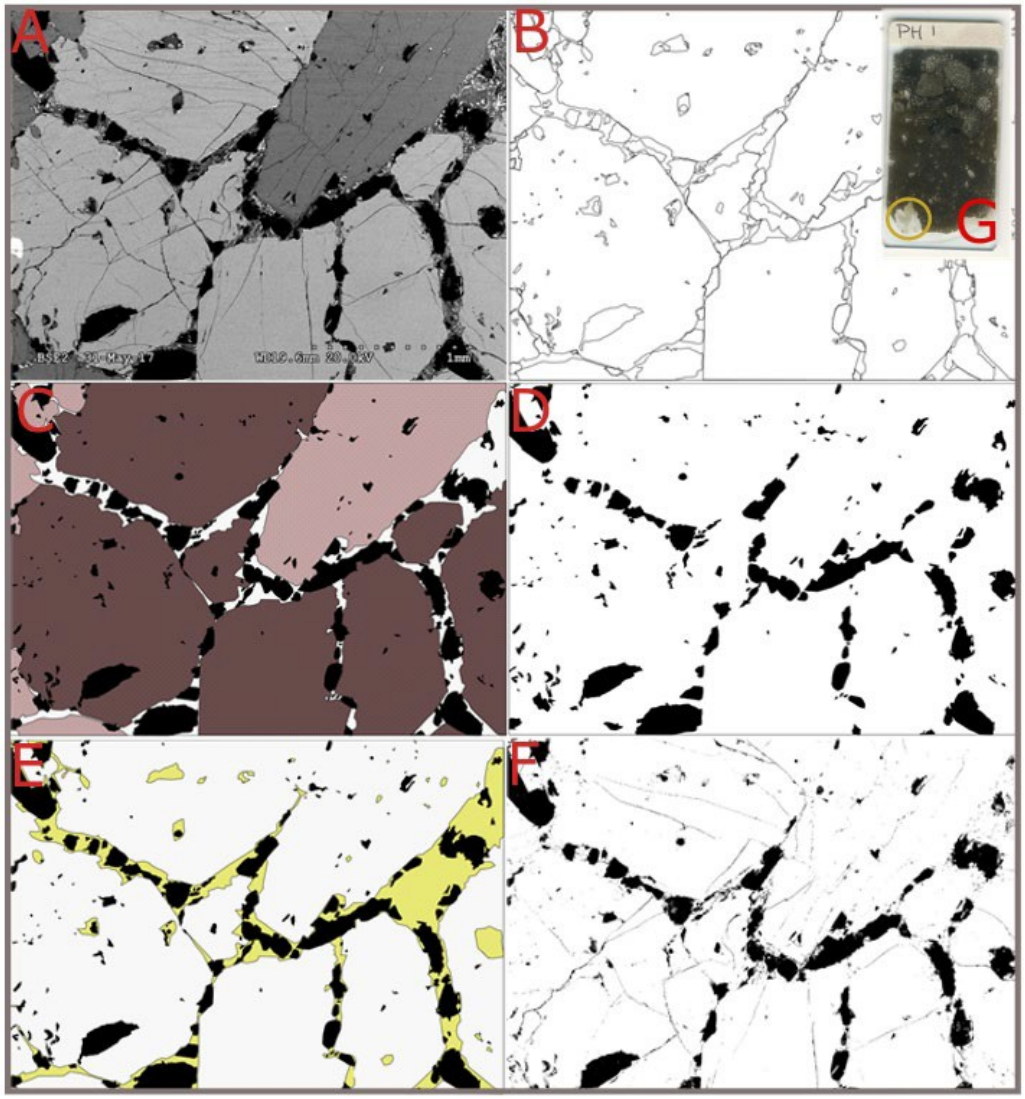

Fig. 2.7: Backscattered SEM image edited by image J. (A) Original BSE image (WD 19.6mm, 20kV), (B) design of the different observed minerals with the use of vector graphic program, (C), Edited image showing the minerals and the vesicularity with a vector graphic program. (D) Calculation of the crystal and matrix area (white colour) and vesicularity (black colour), (E) Edited image showing the groundmass and vesicularity with a vector graphic program, (F) Calculation of the vesicularity (black colour) and crystal cracks, (G) the studied

thin section scanned showing the position of the BSE image in the yellow circle. The Analysis gave the final measurements: Vesicularity (black) 12.95%, Opx (dark brown) 61.75%, Plag (pink) 19.04%, Groundmass (yellow) 6.26%

2.2.4 Carbon coating - scanning electron microscope (SEM) analysis

Part of the petrological study included scanning electron microscope (SEM) analyses which offered better accuracy and optical analysis over the μm to nm scale. The microscopy technique uses electrons instead of light which scan the surface of the thin section and collects information about the surface topography as well as the composition.

For a successful analysis with the scanning electron microscope, the studied thin sections had to be carbon-coated prior to the microscope use. This preparation stage is essential as it enables/improves the imaging of the thin sections. Eight thin sections for insulating purposes and high-resolution observation were carbon-coated ranging from 50 nm or 500 Angstroms depending on the application.

The carbon coating method for the studied samples was conducted at the EMU Lab in Royal Holloway University of London under the supervision of the

SEM lab technician Mrs Sharon Gibbons. The instrument was a Quorum Q 150R E and is a property of the SEARG (South East Asia Research Group) (Fig. 2.8). The thickness of the coating was calibrated to be around 7nm (±3nm) and was achieved through multiple pulses (2-3) of carbon infusion.

The protocol used belongs to the EMU lab is included in section A3 (Appendix A).

Fig. 2.8: The carbon coating apparatus, property of the SEARG (RHUL).

Based on the optical microscopic study, representative rock samples were selected for Scanning Electron Microscopy (SEM) analysis. SEM has been performed on a scanning electron microscope (Hitachi S-3500N of variable pressure) equipped with a Thermo Noran energy dispersive spectrometer (energy dispersive X-Ray detector (EDS)) which belongs to the electronic microscopy laboratory at the School of Earth Sciences, University of Bristol. In addition, the instrument was supplied with a backscatter electron detector (BSE) for imaging specimens with a mean atomic mass change of > 0.1. The stage could move in

x,y,z directions providing quantitative analysis and advanced x-ray mapping capabilities for heavy and light elements (carbonless or not). The detection limits of the instrument are in order of 0.5 wt.% (highly dependent on elements and operating conditions) and the analytical volumes around to 2-3 cubic microns.

During this study, the method focused on 1) analysing the textures observed in the studied thin sections, 2) possible reactions between the crystals and the melt phase, 3) measuring the size of the microlites and the glass in the groundmass. Particular focus was given to the dykes that included xenocrysts, signs of crustal assimilation due to propagation through a very heterogeneous host rock (Fig. 2.9).

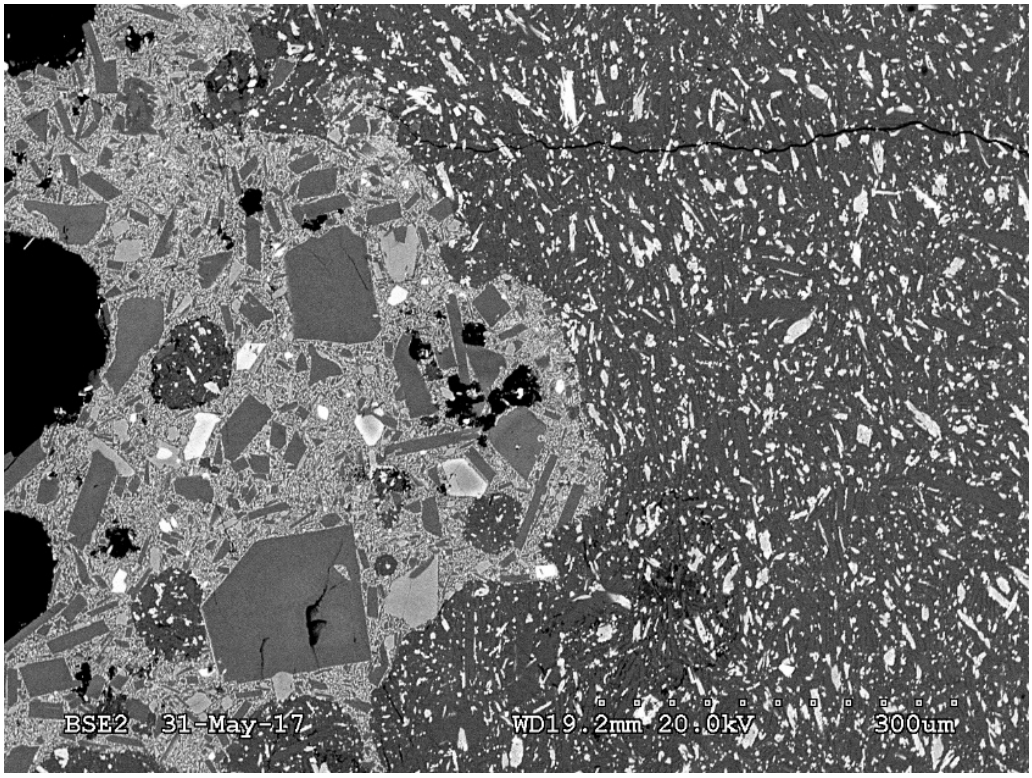

Fig. 2.9: Backscattered (BSE) image of Dyke_77 showing the complex textures due to crustal assimilation during propagation. A super-heated melt that either belongs to the same dyke or a different lithology (e.g. pyroclastic) which assimilates the groundmass of the dyke while the dyke was propagating (parts of groundmass were captured inside the clot).

2.2.5 X-Ray Fluorescence spectrometry (XRF)

Over the last sixty years, instrumental methods in geochemistry (atomic absorption spectrophotometry (AAS), flame photometry, coupled plasma spectrometry (ICP)) have brought a significant evolution into the techniques of chemical analysis of rocks and minerals. The new methodologies are based on the intensity comparisons of measured quantities in an unknown sample towards a given one (standard sample) (Best, 2003).

X-Ray fluorescence spectrometry (XRF) is a method that uses X-Ray energy to eject inner orbital electrons from the samples' atoms. When an outer electron replaces the vacated position, an intensely fluorescent X-Ray wavelength is developed which is characteristic of the specific atom (Ca, Na, K, etc.) with intensity proportional to the concentration of the element in the sample. The method also calculates the concentrations of some volatiles contained in the samples such as H_2O, CO_2, S, F, Cl as well as the Loss of Ignition (LOI) which

is a quantitative way for geochemists to estimate the percentage of weathering into the sample. Finally, the technique involves both human and instrumental errors which are depicted in their total percentages which deviate from the total 100 wt. % (Best, 2003).

A suite of geochemical and modal analysis was performed on the same samples and compared with data from previous literature. The geochemical analysis aimed to study the different compositions of the dykes by combining the structural data with the petrogenetic and geochemical data. It also designed to investigate the relationship between the dykes and the host rock on the northern caldera wall.

The preparation for the XRF analysis was conducted on a 2010 PANalytical Axios XRF spectrometer at the laboratories of Royal Holloway, the University of London under the supervision of Prof. Matthew Thirlwall and Dr Christina Manning. During this study, twenty-five samples were analysed following the preparation and laboratory protocols:

· Stage 1: Rock splitting and crushing

· Stage 2: Sample weighting – LOI measurements

· Stage 3: Preparation of fusion and pellets for the major and trace elements respectively

And are described below in detail:

Stage 1: Based on the microscopic study, representative rock samples were selected for geochemical analyses. The preparation stage included (Fig. 2.10A and 2.10B):

1) Step 1: cut in the rock splitter (bigger sizes, more representative samples and fresher surfaces were picked out)

2) Step 2: cut in the jaw crusher (the samples were crushed for better homogenisation in a sample size of 3-4 cm)

3) Step 3: cut in the TEMA disc tungsten crusher (sample size of a fine powder)

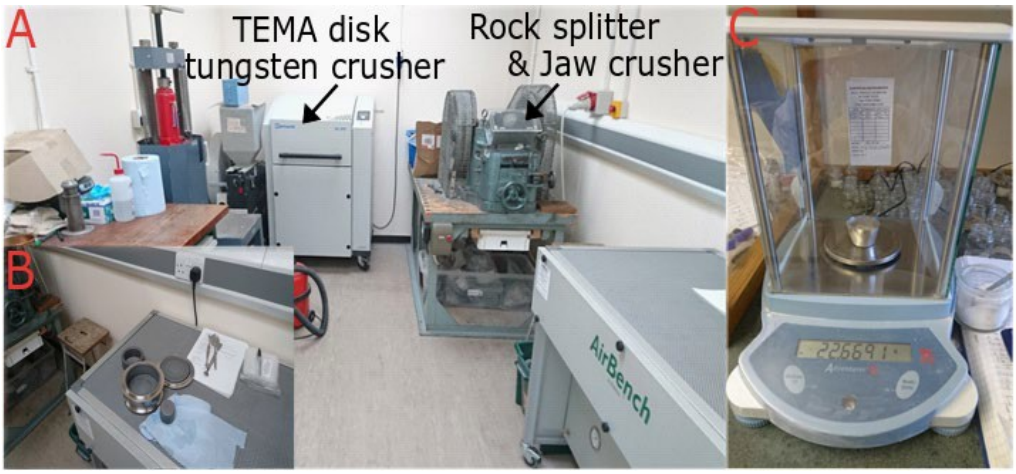

Fig. 2.10: Geochem preparation lab. (A) Stage one, view of the Rock splitter & Jaw crusher, TEMA crusher, (B) tungsten TEMA crusher disks, (C) Stage two-sample weighting & LOI calculation.

The powder samples were then prepared for Stage 2. The latter were first weighted and kept in an oven to dry for at least 48 hours. A complimentary weighting was conducted after their water loss (humidity) to calculate the LOI (Loss of ignition). Then they were measured again for the fusion beads' preparation (Fig. 2.10C).

Stage 3

Includes the production of the fusion beads for the concentrations of major elements (oxides) and powder pellets for the trace element concentrations (Fig. 2.11). The protocols belong to the XRF analysis lab and designed by Prof. Thirlwall, the lab director and are found on sections A4 and A5 (Appendix A).

Fig. 2.11: Stage 3 - construction of pellet samples for trace element analysis. (A): weighting, (B): pellets pressing.

2.2.6 CIPW normative composition

Normative or NORM analysis is a taxonomic method (artificial analysis) used by petrologists to define the calculation of the theoretical assemblage of water-free standard minerals for a rock relied on their chemical analysis (whole-rock composition) as determined by analytical techniques. Various types of NORMS exist nowadays (CIPW, Niggli, Barth), and each of them has specific advantages and disadvantages.

For this study, the CIPW NORM method was used (Fig. 2.12) as it can define any extensive solid solutions in the rock-forming minerals which the geochemical analysis may not detect but could change the mineralogical and modal composition of the samples (Best, 2003). It took its name from its authors (Cross, Iddings, Pirsson and Washington). It was proposed, initially, in 1919 to compare and classify all igneous rocks of which their chemical analysis was available. The method was based on the following simplifications:

1) The magma crystallises only under anhydrous conditions (only water-free minerals)

2) The ferromagnesium minerals are assumed to be free of Al2O3

3) The Fe/Mg ratio for all mafic minerals is supposed to be constant

4) The method considers the incompatible minerals (e.g., quartz-olivine)

5) The technique is beneficial in aphanitic or porphyritic igneous rock samples as well as understanding the degree of silica saturation of the melt that composed the rock in the absence of incompatible elements.

The main disadvantages of this method are possible estimations of some cumulative rocks, the miscalculations of the oxidation state, the calculation of the real thermodynamic conditions that produced the melt, the influence of CO2 in the samples and finally the difficulties with estimating mineral disequilibrium phases (like breccias and rocks including xenoliths) (Johanssen, 1931; Hess, 1989; Blatt and Tracy, 1996). The results are reported in section D1 (Appendix D).

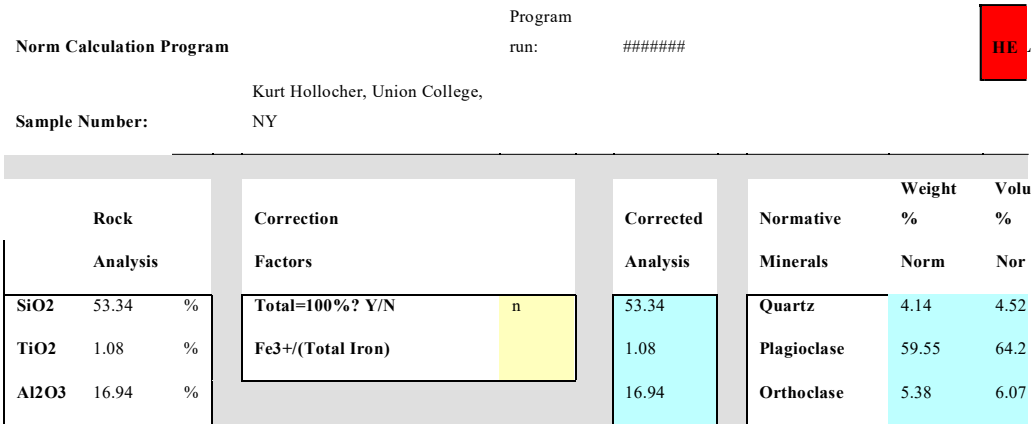

Norm Calculation Program			Program run:	#######			HE
Sample Number:	Kurt Hollocher, Union College, NY						
	Rock Analysis		Correction Factors		Corrected Analysis	Normative Minerals	Weight % Norm	Volu % Nor
SiO2	53.34	%	Total=100%? Y/N	n	53.34	Quartz	4.14	4.52
TiO2	1.08	%	Fe3+/(Total Iron)		1.08	Plagioclase	59.55	64.2
Al2O3	16.94	%			16.94	Orthoclase	5.38	6.07

Fig. 2.12: The NORM excel spreadsheet used for the calculation of minerals originally derived bv Hollocher Kurt (Union College, NY) after Johanssen (1931).

2.2.7 Petrogenetic model

In this study, I investigated the magmatic processes from the source to the surface by studying the dyke swarm on the northern caldera wall. In detail, a petrogenetic model was designed after the combination of the petrographic and geochemical analysis.

For the petrogenetic analysis, an updated form was designed to combine both the petrographic, structural and geochemical data collected or calculated from the field data. The dataset includes data from dykes, chilled margins, and host rock. The designed form is shown below (Table 2.1).

For a petrographer, the interpretation of the observed microscopic textures is the key to understand the processes that occurred during the evolution of the magma from the source to the surface. So far previous studies (Hildreth, 1981; Anderson, 1984; Tepley et al., 1990; Humphreys et al., 2006; Holness et al., 2007; Jerram and Martin, 2008; Viccaro et al., 2010; Renjith, 2013) have studied the deposits of lavas extruded from volcanic eruptions to reconstruct the active volcanic plumbing systems. The studies connected the observed textures with specific petrogenetic processes which allowed them to rebuild the open thermodynamic plumbing systems.

Here I designed new tables (Table 2.1 and 2.2) for reporting the petrological and geochemical data. A summary of these data is given in section 3.2.3 in Chapter

3. Considering these twelve dykes and seven host rock samples were analysed, the full dataset is provided at length in section B4 (Appendix B) of this thesis.

Table 2.1: A form designed to present data for individual dykes for the study of the northern caldera wall plumbing system.

	Dyke #	
Structural	Lat/Lon	
	Strike	
	Thickness (in m)	
	Calculated overpressure (in MPa)	
Petrography	Groundmass: (minerals-texture)	
	Minerals (phenocrysts)	
	Textures	Glomerocrysts:
		Xenoliths:
	Secondary minerals/alterations	
	Fabric	
	Vesicles	
	Chemical composition	

	Processes	
	Spiderdiagram	

Table 2.2: Review of commonly observed textures in volcanic products.

Texture	Process	Author
Sieve coarse texture	Undersaturated magma ascent	Humphreys et al 2006, Viccaro et al 2010; Renjith 2013
Synneusis	Collision of crystals (same or different origin) due to convection	Viccaro et al 2010; Renjith 2013
Zoning (a=normal, b=oscillatory)	Crystal growth, magma mixing or convection or ascent	Hildreth 1981, Humphreys et al 2006, Holness et al., 2007, Viccaro et al 2010; Renjith 2013
Resorbed rims	Magma mixing of a mafic volatile rich magma batch	Humphreys et al 2006, Viccaro et al 2010; Renjith 2013
Fine sieve or embayments	Crystal growth after magma mixing	Viccaro et al 2010; Renjith 2013
Resorbed cores	Magma mixing - Decompression of an explosive magma (recharge event)	Humphreys et al 2006, Viccaro et al 2010; Renjith 2013
Swallow tails-inclusions	Degassing-conduit processes	Hildreth 1981, Viccaro et al 2010; Renjith 2013

In this study, I was interested in reconstructing the path of dykes with depth. Then the interpretations from previous studies could be compared to build a model of the genetic processes of every sampled dyke from the source to the surface. A methodology was designed to study the dykes of the northern caldera wall based on the textures observed in each dyke. In detail, in a plumbing system

like Santorini's where two magma chambers exist, the textures can be categorised to represent four different stages that represent the location of the magma or more commonly the path of the dykes into the plumbing system prior to emplacement (Table 2.3).

Early stage: This stage represents the deeper part of the system, which can be fossilised through the observed textures in a dyke. The magma after the partial melting it enters a deep magma chamber or a reservoir where it stalls for a while. Coarse sieve textures were reported as forming in the conduits between the deep magmatic system and the magma chamber.

Near-Equilibrium: This stage is characterised mainly by an equilibrium state and can be in a deep magma chamber which crystalises by fractionation, and the phenocrysts can have normal zoning due to crystal growth. In a magma chamber; a mass transfer is continually occurring due to convection produced by heat, and it combines heat transfer by advection and conduction. Advection refers to the bulk fluid motion. Those processes can stick crystals with each other forming textures such as synneusis and glomerocrysts.

Mixing-Recharge stage: Dykes are triggered by the deep reservoirs/chambers and propagate towards the surface. However, on their path towards the surface, they can enter shallow crustal magma chambers triggering magma mixing if the magma is primary (mafic). In some case, mafic magma batches may intrude shallow magma chambers directly from the deeper parts of the system without

entering deeper reservoirs or chambers. Also, during that stage, the plumbing system can face a resurgent period where magma propagates to the surface and fills shallow reservoirs before eruptions due to increased excess pressure. The shallow magma chamber becomes evolved due to magma mixing, forming either more fractionated or hybrid magmas. This stage can be identified by resorbed rims, oscillatory zoning, fine sieve textures and embayments around the crystals.

Decompression stage: If the magmatic overpressure reaches critical levels due to magma mixing, then resorbed cores are formed, and a dyke can be triggered from the magma chamber.

Conduit stage (degassing): In the shallowest part of the system during magma ascent in the crust, if dyke propagation occurs rapidly then swallow tail structures can be formed in the phenocrysts or mineral inclusions can crystallise atop the existing minerals.

These stages can represent a magmatic plumbing system from the source to the surface, and so I reported the observed textures extensively in every studied dyke. The simple report of the textures in a dyke builds understanding of the number of processes and the possible depth origin of the dyke. It also allows an investigation of the differences between the processes and thermodynamic state of the different magma chambers as well their possible depth correlations. For that reason, the mutual connections between crystals and textures found to co-exist at the same time within the same phenocryst were reported. That could give

us insights on the longevity of the magma in the system, the structure of the magma, a qualitative frequency of the textures that formed in the same chamber and the relative age of the chamber. One could assume that the more textures observed then, the longer-lived the chamber. A table that reflects the methodology mentioned above is explained in Table 2.3:

Table 2.3: Mutual textural connections in phenocrysts in a plumbing system. Row and column headers indicate the stages of a magmatic path at depth as designed from this study. The same colours represent the same observed features which can co-exist. The last line (unique textures) represents textures that found to appear alone in a phenocryst.

		Early stages	**Near-equilibrium**	**Mixing/Recharge**	**Decompression**	**Degassing/ conduit**
		Coarse sieve	Synneusis Glomerocrysts Normal zoning	Resorbed rim Oscillatory zoning Fine sieve texture Embayment	Resorbed core	Swallow-tail Inclusions
Early stages	Coarse sieve					
Near-equilibrium	Synneusis Glomerocrysts Normal zoning					
Mixing/ Recharge	Resorbed rim Oscillatory zoning Fine sieve texture Embayment					
Decompression	Resorbed core					
Degassing/ conduit	Swallow-tail Inclusions					
	Unique textures					

2.3 Numerical methods

Numerical modelling is the method which simulates, reproduces and studies scientific problems such as physics or engineering experiments when other techniques (e.g. analogue, analytical) lack on processing due to mathematical complexity (Fig. 2.13).

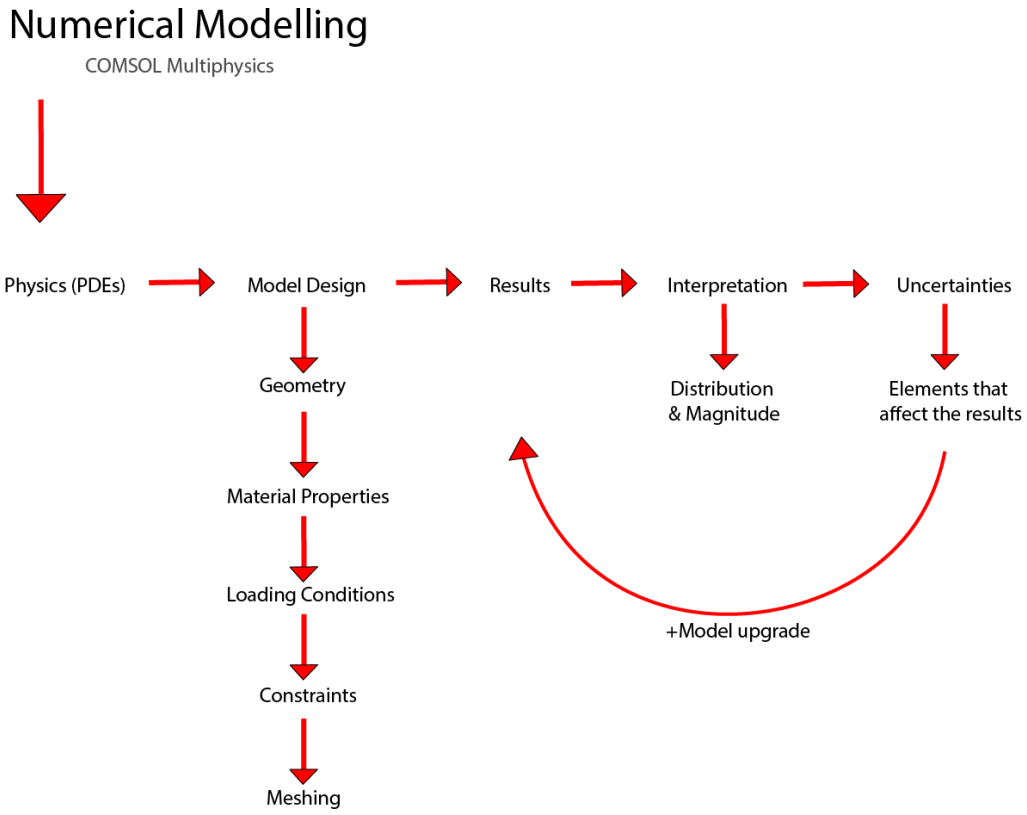

Fig. 2.13: Flow chart of the numerical modelling procedure.

2.3.1 COMSOL Multiphysics

'COMSOL' (formerly known as FEMLAB) is a high-tech FEM (Finite elements method) program which provides solutions for Multiphysics modelling (Fig. 2.13). The term finite refers to a continuum (discrete) approach where the studied systems require infinite subdivisions of their domains, the infinitesimal elements with infinite degrees of freedom, respectively (Jing, 2003).

The Structural Mechanics module is a tool which analyses a variety of mechanical features that are mainly based on static and dynamic loading. Dynamic loads are used in this study to simulate 2D deformation processes of fractures with geometrical complexity, mechanical contacts, as well as fluid-structure interactions (FSI). In addition, the modules allow the user to couple structural analysis with a wide range of Multiphysics phenomena, such as studying the interaction of mechanical structures with fluid flow (www.comsol.com) (Fig. 2.14).

The program is explicitly used in numerical modelling to simulate the stresses around materials subject to pressure or displacement or wide load variations. The program was used by earlier (Hickey and Gottsmann, 2014; Browning, 2016; Le Corvec et al., 2018; Forbes Inskip, 2019) to define processes related to heterogeneity and anisotropy both in volcanotectonics and hydraulic fracturing.

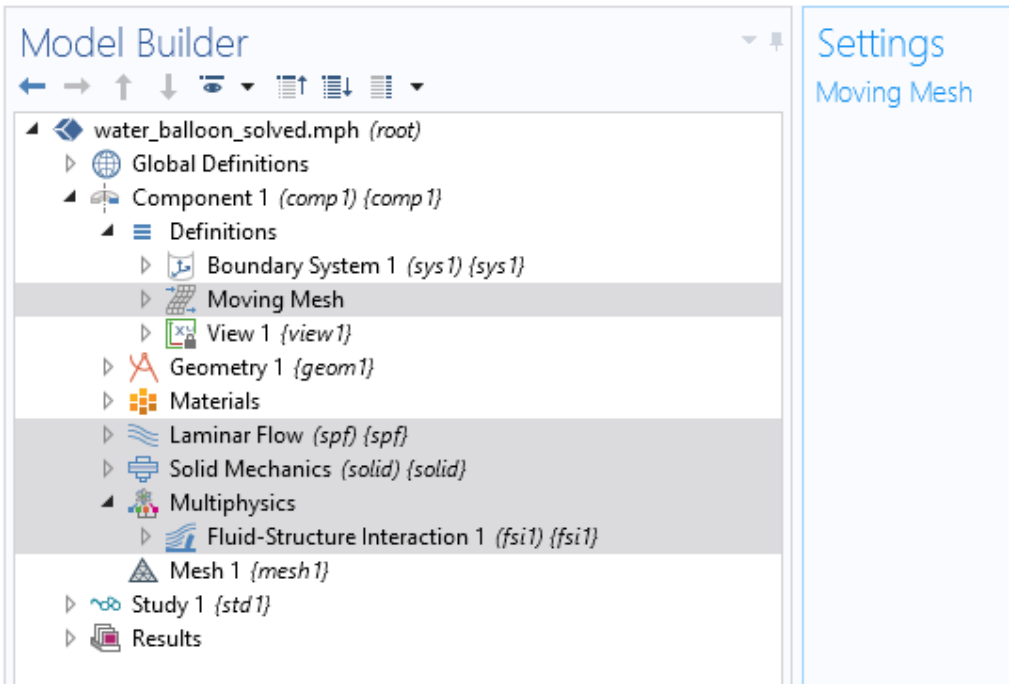

Fig. 2.14: A screenshot of the Model Builder environment in COMSOL Multiphysics (COMSOL blog, 2017)

2.3.1.1 Theoretical and numerical modelling background

A critical constitutive equation (Gudmundsson, 2011) for brittle deformation in rock materials is Hooke's law which supports that the strain in a body is directly proportional to the stress which produced the strain. The modulus of elasticity or the Young's modulus (E) is the ratio of stress σ to strain ε and is a material property (Eq 2.1).

$$E = \sigma/\varepsilon \quad (in\ N/m^2\ or\ Pa) \tag{2.1}$$

Eq. 2.1 describes the behaviour of a linear-elastic material which returns to its original shape and the strain tends to zero when the applied load is removed. Young's modulus is in other words the measure of the material's stiffness (resistance to strain).

In nature the state of stress at any given point is defined by the three principal stresses σ_1, σ_2, σ_3 which express the maximum the intermediate and the minimum compressive principal stresses, respectively, with $\sigma_1 \geq \sigma_2 \geq \sigma_3$ (Fig. 2.15) and:

$$\sigma_1 = \lambda\Delta + 2G\varepsilon_1 \tag{2.2}$$

$$\sigma_2 = \lambda\Delta + 2G\varepsilon_2 \tag{2.3}$$

$$\sigma_3 = \lambda\Delta + 2G\varepsilon_3 \tag{2.4}$$

where Δ is the dilation or volume strain

$$\Delta = \frac{Vd - Vu}{Vu} = \frac{\Delta V}{Vu} = \varepsilon_{\chi\chi} + \varepsilon_{yy} + \varepsilon_{zz} \tag{2.5}$$

and λ is Lame's constant, which is related to Young's modulus and Poisson's ratio (v) through the equation:

$$\lambda = \frac{vE}{(1+v)(1-2n)} \qquad (2.6)$$

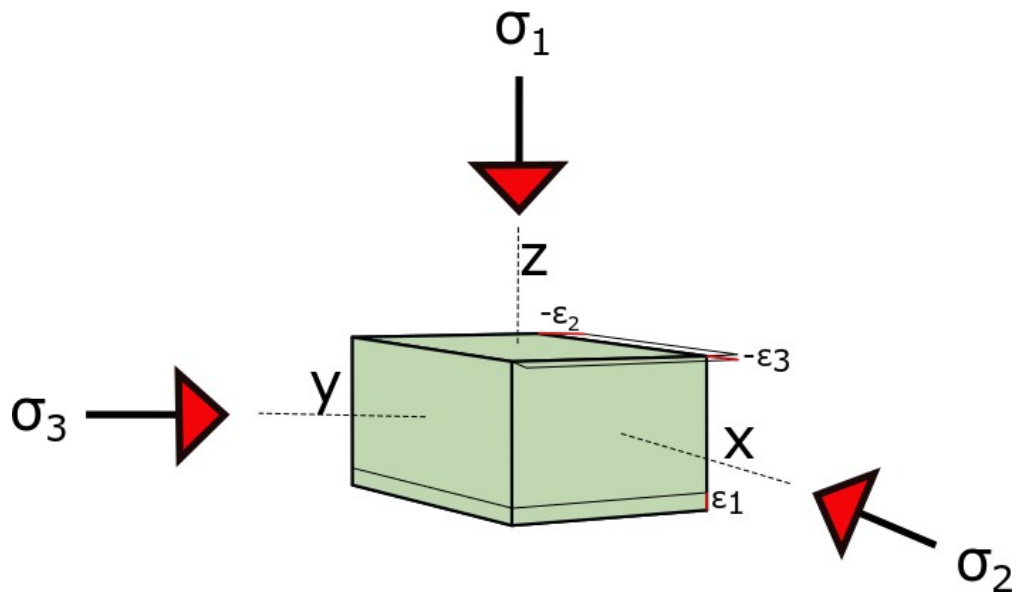

Fig. 2.15: A rock parallelepiped subject to a triaxial stress field. The illustration shows the principal stresses σ_1, σ_2, σ_3 as well as the compressive strain ε_1 and tensile strains $-\varepsilon_2$ and $-\varepsilon_3$.

Partial differential equations (PDEs) are useful for studying physical problems that cannot be studied with analytical methods, but alternatively, an approximation of them can be designed with specific discretisations. The latter are numerical model equations which are solved using the Finite Element Method (FEM) (COMSOL, 2017). COMSOL Multiphysics has a Lagrangian formulation for structural analysis. The material properties are inserted with tensor components that depend on the coordinate system of the material frame.

The solid in the program deforms freely without any repetitive change in its material configuration (COMSOL, 2012).

2.3.1.2 Model design

The computer-aided design (CAD) models were generated in the Solid Mechanics module and utilise two dimensional (2D) symmetric domains (plane stress and plane strain). All of the models are static or stationary and built over the m to km scale. Hence, they provide snapshots of the studied processes subject to different boundary conditions.

In this study, the models' geometries (size, shape, thickness, rotation, depth) and their details were defined and imported to the program from the field observations (Chapters 4 & 5), their mechanical and physical parameters (Young's modulus, Poisson's ratio, density) were taken from laboratory and field studies found in the literature (Gudmundsson, 2011). Model measurements were scaled from original sizes to avoid edge effects.

The regional stress field defined the loading boundary conditions of the models, which in other words are the stresses or fluid pressures applied and responsible for the deformation in the host rock (Gudmundsson, 2011). In these studies, the only loading boundary conditions were the excess pressure in the magma chamber(s), extension at the vertical boundaries (edges) of the models - defined

as force per unit area and given values between 1 MPa to 10 MPa – and the overpressure in the dyke, taken as 5 MPa (Fig. 2.16). The models are fixed on the bottom corners to avoid rotations and friction due to sliding while the upper edge is a free surface or a surface free from shear stress. None of the models considers the effect of topographic loading for the reason that that loading usually is already considered when considering the excess pressure in a magma chamber.

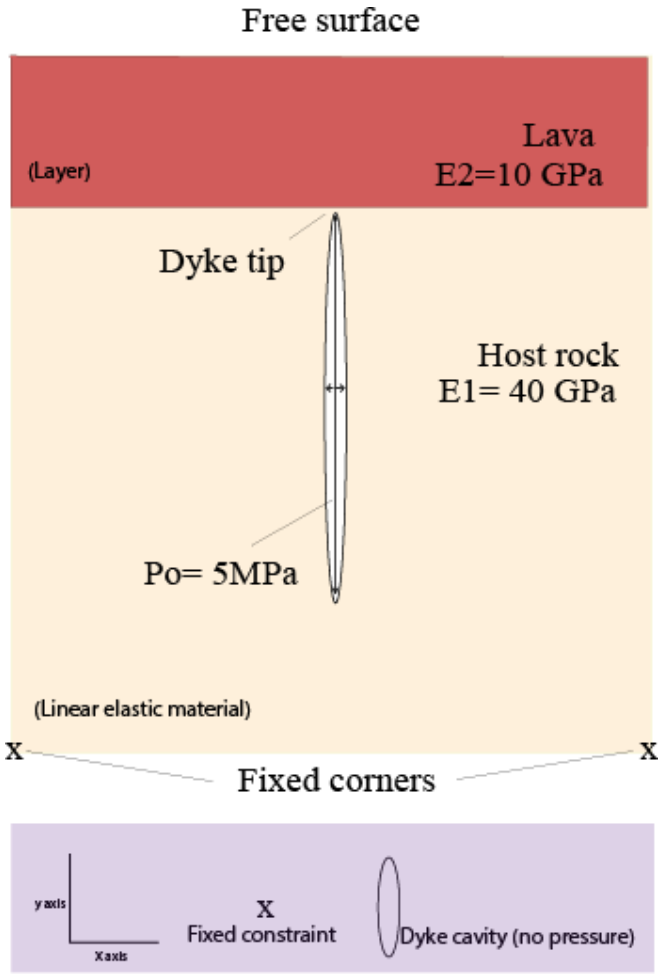

Fig. 2.16: Benchmark model setup in 2D symmetric domain.

2.3.1.3 Meshing

An advantage of the FEM is that it allows high accuracy through the generation of high-resolution meshing. The FEM mesh subdivides the CAD model into smaller elements over which the mathematical equations are solved and translated to a set of polynomial functions elucidated over each element. The finer the mesh, the more accurate the solution; however, there is a trade-off between element size and computational expenditure. The elements exploit their behaviour by algebraic solutions and are defined when the user adds the initial boundary conditions in the system (Jing, 2003). The geometries of the elements can vary such as triangular, square etc. as well as their size and their degrees of freedom (DOF). A triangular mesh of maximum nodal lengths <0.306 m was generated for all of the models during this study. The generated mesh was finer at areas of interest, for example at the dyke tips, and coarser further away offering high-resolution results in the area of interest (Fig. 2.17)

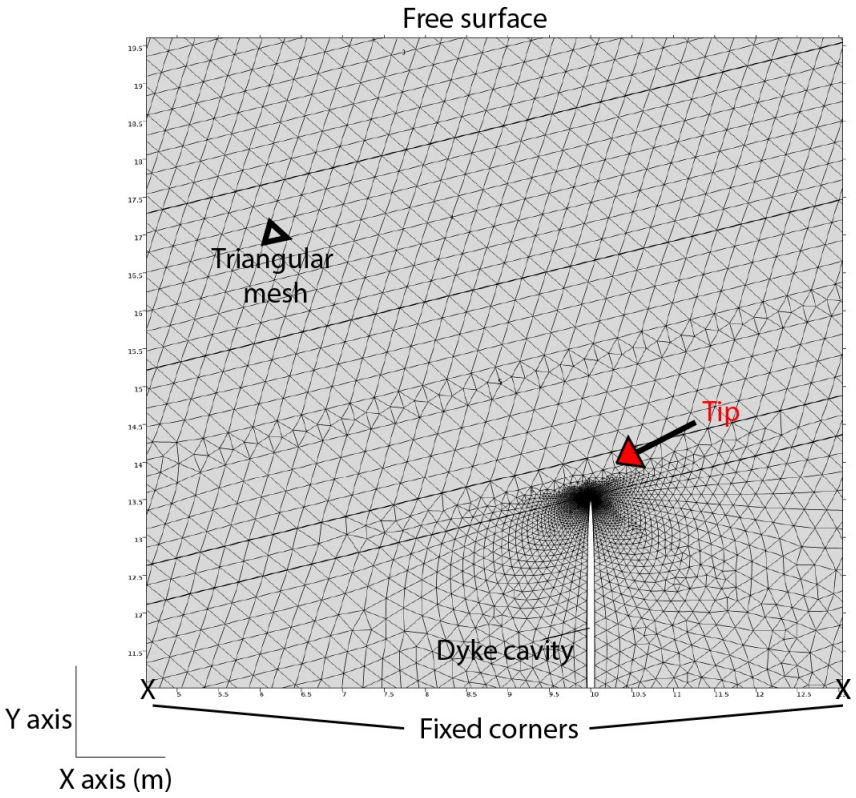

Fig. 2.17: Triangular mesh setup in a 2D symmetric model. The setup is part of a larger model showing the area of interest and the mesh elements.

2.3.1.4 Model results and interpretations

COMSOL solves PDEs to calculate a strain and stress distributions resulting from displacements in the rock body. Model results always display the stress field as contours of the minimum principal compressive stress (σ_3) which is the maximum tensile stress and the arrow surfaces expressed are the maximum principal compressive stress (σ_1) (red arrows) and the intermediate principal

stress (σ_2) (white arrows) respectively. Stress orientations are presented as arrows which are practically interpreted by their orientation and not by their actual direction. It is important to note that by convention, the maximum and minimum principal stress in engineering is often opposite from in geology. As COMSOL was developed as an engineering tool, the resulting orientations are reversed to apply to a geological application (Fig. 2.18).

After the interpretation of the outputs, I define the uncertainties of the modelling procedure and the elements that affect the results (e.g. density, constant overpressure, etc.) which are discussed below.

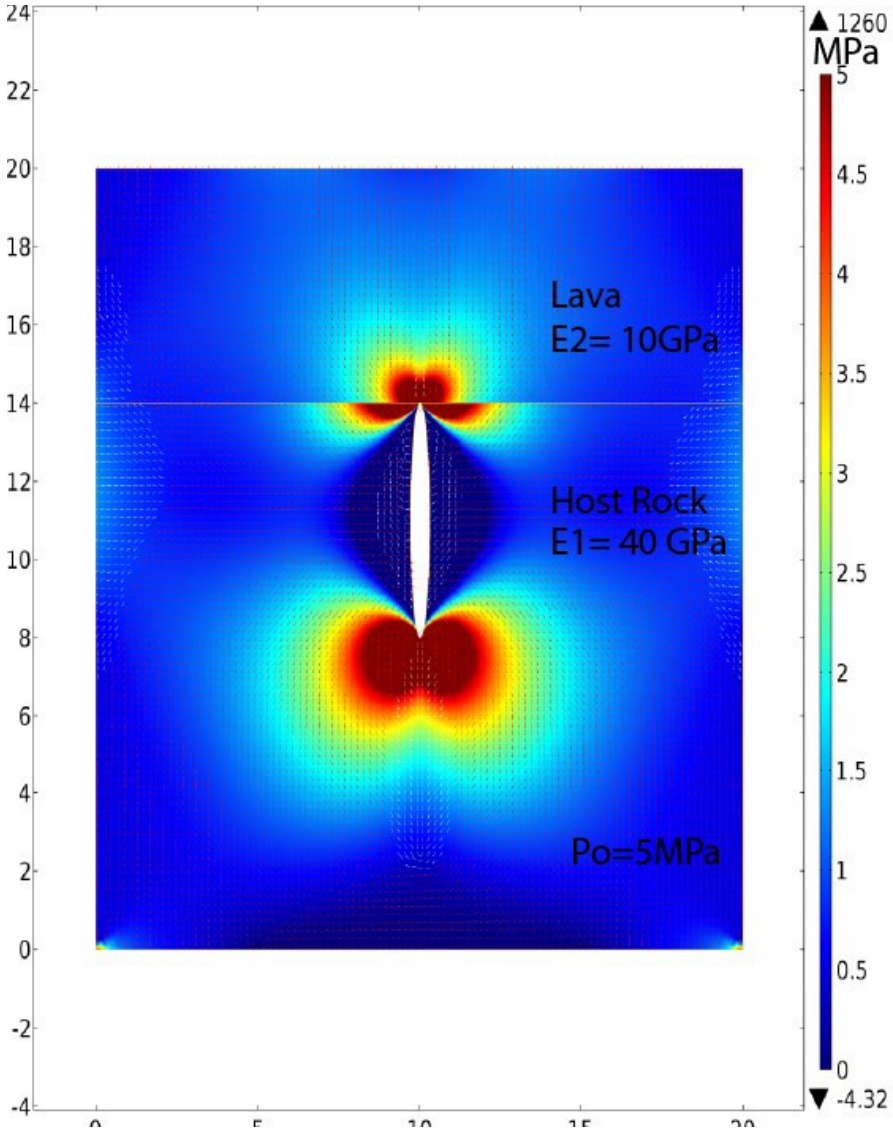

Fig. 2.18: A COMSOL benchmark model result output generated from a symmetric model setup (x-y axis in m). The only loading is magmatic overpressure of 5 MPa in the vertical dyke. The stress map is showing the distribution and magnitude of the minimum principal compressive (maximum tensile) stress (σ_3) as well as the orientation of the arrow surfaces (σ_1) (red arrows) and (σ_2) (white arrows).

2.3.1.5 FEM modelling versus other techniques

In Chapter 1 I discussed the different numerical methods that simulate dyke propagation in an elastic domain and the main differences between them. The advantages of the FEM method are briefly reported in Table 2.4 (Grosfils, 2007; COMSOL, 2012; Jing, 2003).

Table 2.4: Advantages and disadvantages of FEM versus other modelling techniques.

(+) FEM allows space and function element discretization and depending of the problem and the method can use a variety of equations and functions even in very complex materials.
(+) The method is well developed, and it gives solution in a computer environment that cannot be solved with a PDE formulation (user-friendly).
(+) The errors associated with solution in FEM modelling with respect to comparative analytical procedures are less than 1% .
(+) FEM has established commercial codes with large capacity (large computing power).
(-) The method loses its efficiency when higher degrees of freedom are set.
(-) FEM models cannot break the bonds between elements so they cannot model inelastic deformation (e.g. faulting).

2.4 Analytical modelling

Analytical modelling is a type of mathematical modelling where time-independent equations (mathematical concepts and language) are used to investigate a system and study how specific parameters affect a complex physical process. The primary outcome is to make predictions and define the behaviour of a mechanical system affected by very complex and multiparametric physical parameters. In our study we use analytical modelling to calculate i) the range of overpressure (P_o) of the Northern caldera wall dyke swarm and ii) the depth of the magma source (H) that the dykes mentioned above were injected from.

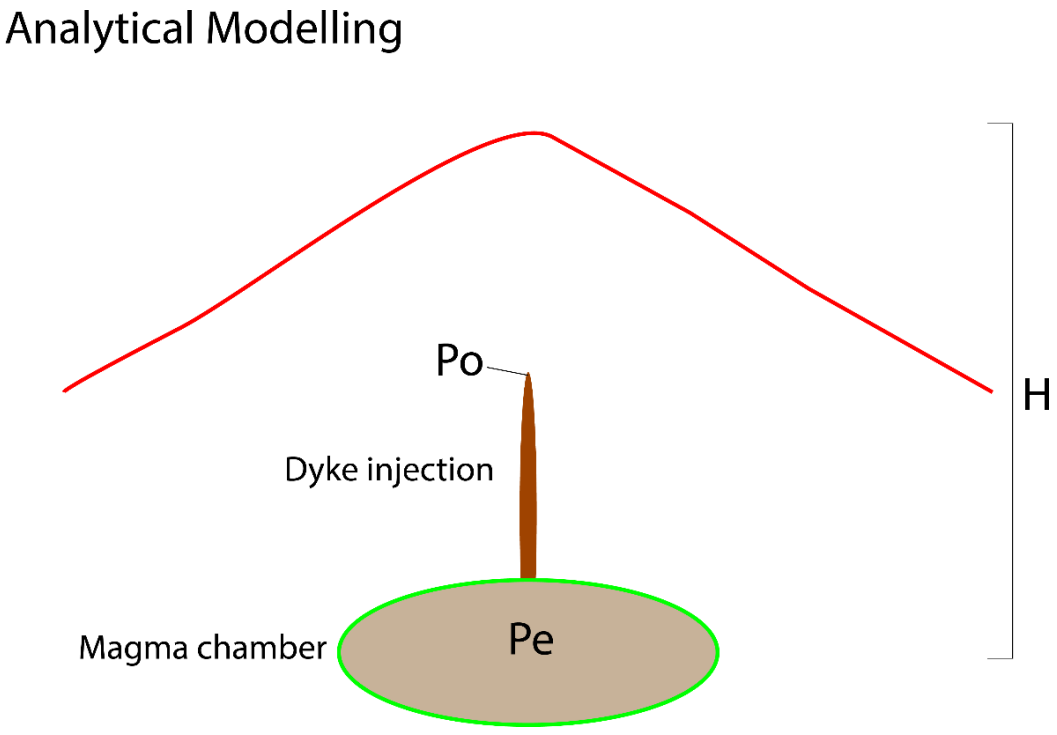

Fig. 2.19: Schematic illustration of the studied parameters. P_e denotes for the magmatic excess pressure of a magma chamber which can lead to dyke triggering

and injection, P_o is the magma overpressure away from the magma chamber and the driving parameter of dyke propagation, H is the depth of the magma source (here a magma chamber) (Not in scale).

2.4.1 Conditions of dyke emplacement

Dyke propagation and emplacement are controlled, in part, by the mechanical conditions of the magma chamber (Gudmundsson, 2006, 2011). Specifically, dyke thickness is dependent on the overpressure (driving pressure) and the difference between the magmatic excess pressure (P_e) and the theoretical crack-dyke tip stress (σ_3) the time of the emplacement as shown in the following equations:

$$Po = Pe + (\rho r - \rho f)\, g\, h + \sigma d \qquad (2.7)$$

and

$$\sigma_3 = -Po\,[2(a/r_c)^{1/2} - 1] \qquad (2.8)$$

where P_o is the magma overpressure, P_e is the excess pressure, ρ_r is the crustal density, ρ_f is the fluid density, g the acceleration due to gravity, h the dip dimension of the fracture, σ_d the differential stress (σ_1-σ_3), α is the semi-major axis of an elliptical hole, b is the semi-minor axis of an elliptical hole rc=b2/a is the radius curvature of the dyke tip (Gudmundsson, 2011).

In equations (2.7) and (2.8), the viscosity of the magma is neglected, and the dyke thickness increases with rising driving pressure. The latter can happen either through the increase of excess pressure (P_e) or decrease of the minimum horizontal compressive stress ($\sigma_{h\,min}$) or both.

When a dyke is injected from a magma chamber and propagates to the surface, it does so by fracturing the rock at its tip. The fracturing happens only if the tensile stress generated by the magmatic overpressure exceeds the tensile strength or the fracture toughness of the host rock, as described in Eq. 2.9 from the analytical solution from Gudmundsson (2011) after Sneddon (1946):

$$Po = \sigma_3 + T + (EW/2(1-v^2)\,L \qquad (2.9)$$

where E is the Young's modulus of the host rock, W is the thickness of the dyke, v is the Poisson's ratio, L the length of the dyke (assuming that the dykes height (depth dimension) is the controlling dimension).

There have been attempts to understand the change of dyke width (thickness) in different tectonic settings. For example, mafic dykes that are emplaced in rift zones (e.g. Iceland) have an average thickness of 4 m and generated with a P_o range of 1-4 MPa and low σ_3 (tensile stress). In contrast, tectonic settings with high σ_3 (e.g. Hawaii) have an average thickness of 1m (Walker, 1987). For that reason, Wada (1994) suggested that the driving pressure is likely affected more by σ_3 (minimum horizontal compressive stress).

When the dyke thickness, length and driving pressure are known, it is possible to estimate the depth of the magma source (H) (i.e. Becerril et al., 2013) as follows from Eq. 2.10:

$$H=\frac{\Delta u1E}{2L(1-v2)\,(\rho r-\rho m)\,g}-\frac{Pe+\sigma d}{(\rho r-\rho m)\,g} \qquad (2.10)$$

where Δ_{u1} is the initial displacement of an elastic mode I fracture subject to internal fluid pressure P_o, σ_d is the differential stress, ρ_m the average magma density, ρ_r the average host rock density, g is gravity acceleration and the other symbols as defined before.

Wada (1994) also investigated the relationship between dyke width and magma viscosity on dyke swarms in Japan and the Andes and suggested that viscosity could control dyke width while Ui et al. (1984) reported that dyke thickness

could also increase with higher K_2O/MgO ratios for similar reasons. Both studies suggest that dyke width rises proportionally with the viscosity of the magma. Assuming constant physical and chemical magma parameters, the viscosity of a 1m thick dyke was found to be 10^1-10^2 Pa s but 10^6-10^7 Pa s for dykes with thicknesses >100m (Wada, 1994).

According to the same author (Wada, 1994), viscosity can affect the fracturing at the tip of a dyke. In a hypothesised dyking process with a constant magmatic driving pressure and host rock stiffness, high viscosity felsic magmas cannot fit in a fracture due to internal friction. Hence, the viscous magma widens the fracture for accommodation. In contrast, a low viscosity mafic magma flows more readily into the fracture tip.

Other studies determine that the final thickness of a dyke is highly dependent on a combination of thermal and mechanical processes (Gudmundsson, 1995) which are derived by the cooling (solidification) of the dyke and the driving pressure of the magma. Most thick dykes are either ‘composite’ resulting from the injection of several columnar rows of variable magma types in a mechanically weak median plane of an earlier dyke or ‘multiple’ consisting of more than two dykes with the same compositions detached by their chilled margins where either their contact weaknesses or their still hot axial zones encouraged the dykes to be exploited (Bell, 1983; Duff, 1993). However, during the cooling process (solidification), the dyke thickness reduces by up to 10% (Gudmundsson, 1998). Most commonly in nature, thicker dykes with fine-grained margins called chilled

margins, act as insulators, allowing the core of the dyke to cool down more slowly and hence grow coarser crystals (Huppert and Sparks, 1989; Duff, 1993).

CHAPTER 3

Multidisciplinary studies of the northern caldera wall dyke swarm and its host rock

Statement of contribution:

Collection of primary field data and geological mapping done by KD

All field photographs and figures designed by KD

Complete 1st draft of manuscript and figures by KD

Revisions and subsequent drafts made with co-authors input

Interpretation of all data along with final model conducted by KD with support from co-authors

3.1 Introduction

In this chapter, I consolidate and integrate both structural and petrogenetic data from the host rocks, dykes and faults in the northern caldera wall of Santorini. The multi-disciplinary approach allows for a complete understanding of the volcanic plumbing system which could not be discerned from any one individual approach. Results are presented in four sections and concern, firstly, the mechanical emplacement of the shallow dyke swarm through analysis of the orientation and size of the dykes and faults; secondly, the volcanological study of the host rock; thirdly, the petrographic aspects of the dykes; and, fourthly, the geochemical analysis of the host rock and the associated dykes. The main aim is the design of a new geological map that shows the location and orientation of the northern caldera dyke swarm of Santorini. This chapter provides the basis for which the models and ideas of the following sections are built upon.

The results and interpretation of the collected data are considered to follow four sections:

1. Mechanical dyke emplacement
2. Host rock geology
3. Petrography of the dyke swarm and host rock
4. Geochemistry of the dyke swarm and host rock

3.2 Mechanics of dyke emplacement

This section provides insights on the emplacement and structure of the emplacement of the Santorini northern caldera wall dyke swarm.

3.2.1 Northern caldera dyke swarm

The dyke swarm at the Northern caldera wall consists of at least 91 dyke segments (Fig. 3.1) that were emplaced in a heterogeneous host rock succession. The lithologies of the host rock consist mainly of lava flows, pyroclastics, scoria layers, hyaloclastites and tuffs.

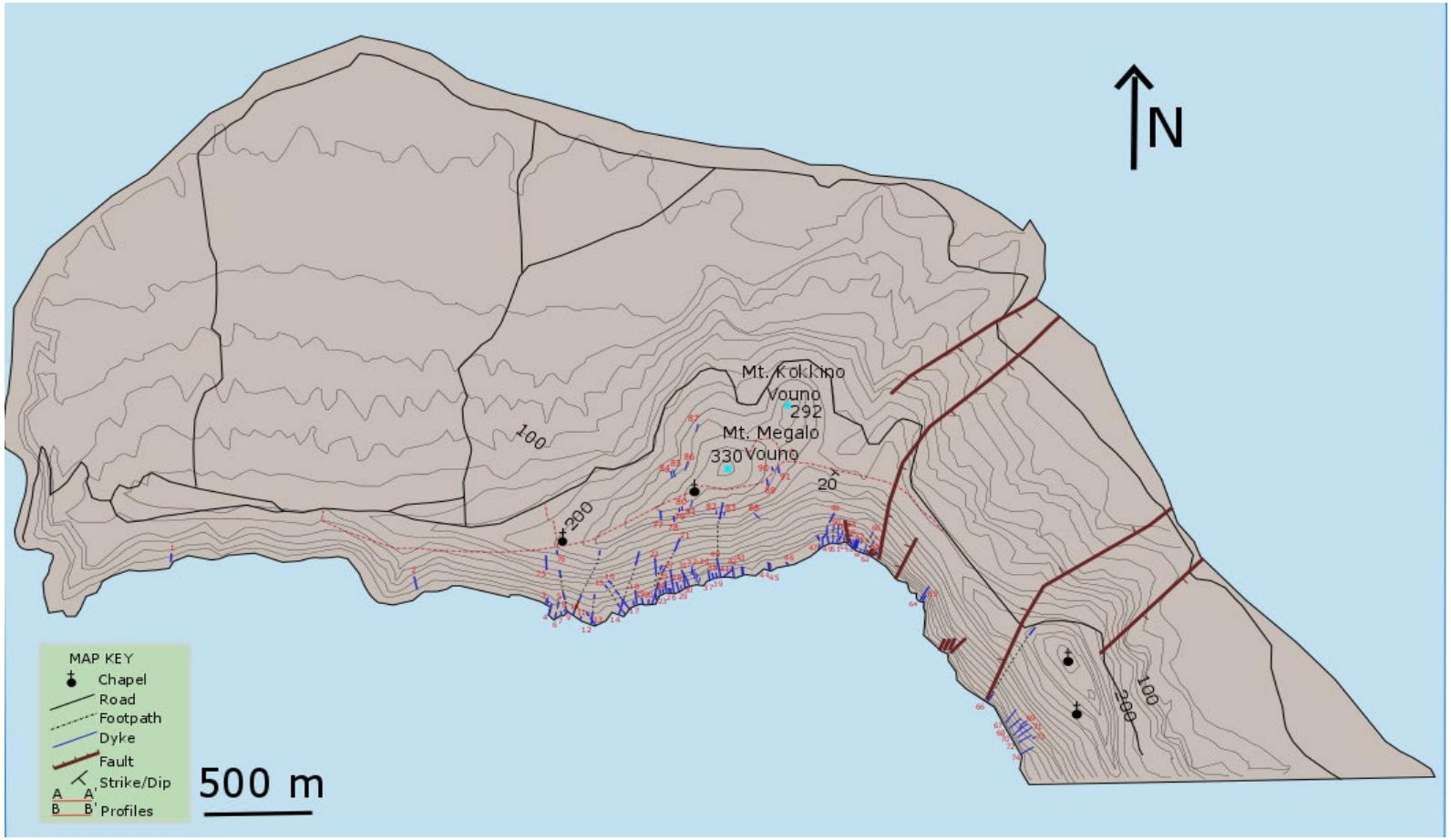

Fig. 3.1: Map showing the location of the dyke swarm in the northern caldera wall.

The orientation of the dykes can be divided into six different clusters (or dyke populations/subswarms):

- N 20-60˚W (300-340˚/ NW-SE) (Population 1)
- N 10˚W- N 5˚E (350- 005/ NNW-SSE, N-S, NNE-SSW) (Population 2)
- N 5-15˚ E (005-015/ NE-SW) (Population 3)
- N 16-35˚ E (015-035/ NE-SW) (Population 4)
- N 36-60˚ E (036-060/ NE-SW) (Population 5)
- N 61-75˚ E (061-075/NE-SW) (Population 6)

26 of the dykes' strike N21-40^{o}E which according to Druitt et al., (1999); Nomikou et al., (2013); Rizzo et al., (2016) coincides roughly with the Kolumbo VT line (Fig 3.2). The majority (31) of dyke's strike N1-20˚ E, 14 of the dykes' strike N41-60˚ E, 3 of the dykes' N 20-60˚W, 6 of the dykes' N 10˚W- N 5˚E and 10 of the dykes' N 61-75˚ E. The data are presented in section B1 (Appendix B).

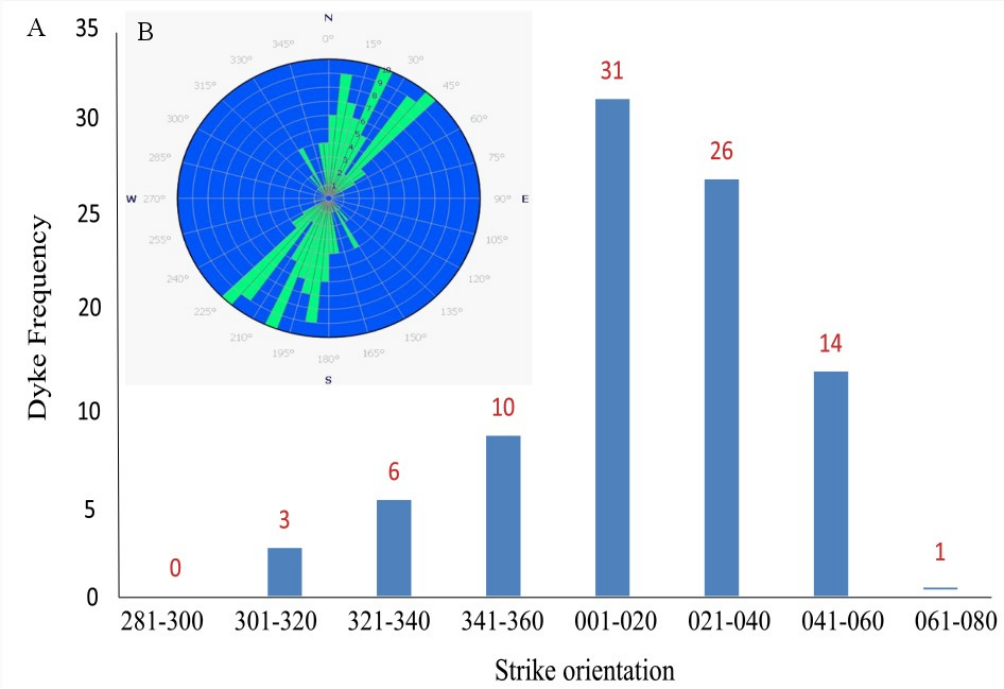

Fig. 3.2: (A) Histogram showing the strike orientation in a 20˚ bin, (B) Rose diagram of the studied dyke swarm showing the orientation of the dykes.

In Santorini, dyke propagation was encouraged through vertical propagation, and hence the height or depth is hypothesised to be the controlling dimension. The dykes are perpendicular to the regional direction of σ_3, which coincides with the direction of the spreading (or rifting) vector or defined by the elongation of the caldera collapse (Gudmundsson, 2006). Further observations consistent with this theory include the subvertical orientation of the dykes (91% have dips >75degrees); the few dykes (9%) that dip 45-60 degrees can be then categorised

as inclined sheets.

Field observations during this study reported signs of vertical flow, such as vesicles elongated parallel to the dip dimension (Fig. 3.3). Still, no elongated minerals were found as the dykes are either aphyric, or plagioclase crystals are the only phenocrysts present. Horizontal magma flow was in general out of the scope of this study.

We report that only three dykes in total were found to include vesicles; two of them found during the sea level campaigns, and only one at the mountain level, so the data are limited to allow us further spatial graphs to be produced. If the dykes are very shallow, it is highly possible to reflect the degassing process in the last phases of magma emplacement. As such that could be an indication of a possible feeder dyke.

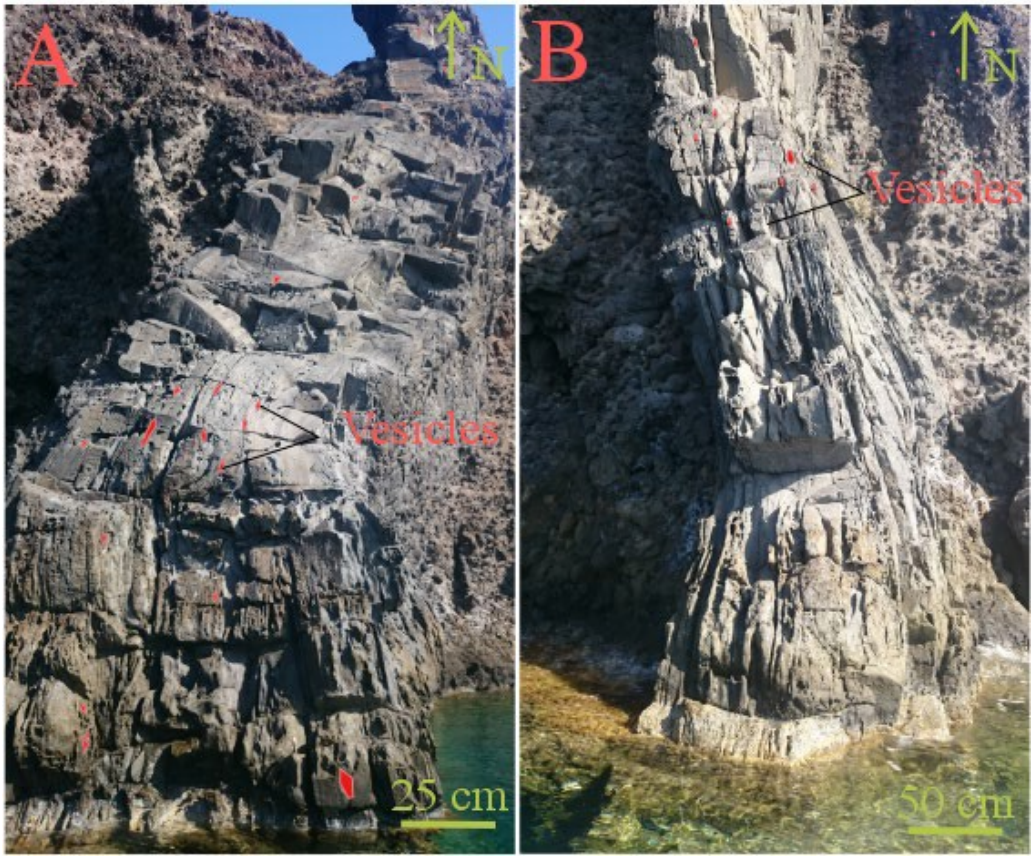

Fig. 3.3: (A) Dyke_24 and (B) Dyke_25 at the lower level of the caldera wall. The observed vesicles are elongated parallel to the inferred direction of σ_1.

3.2.2 Regional tectonics

The fieldwork campaign revealed two suites of both large (offsets >100 m) and short (offsets < 2m) normal faults. In Figure 3.4, I present the map of the faults studied by Druitt et al. (1999) and, the faults mapped during this study. Field observations and the structural study revealed a system of large metre scale

normal faults, with offsets greater than 100 m. These faults mark the boundaries of graben subsidence, defining a possible pull-apart graben. Their lateral extent was not studied, and slip indicators were not observed. A system of much smaller normal faults with flower structures, indicating strike-slip displacement, with much smaller offsets of less than 2m were observed. These faults were found at the NE corner of the island and below Megalo Vouno.

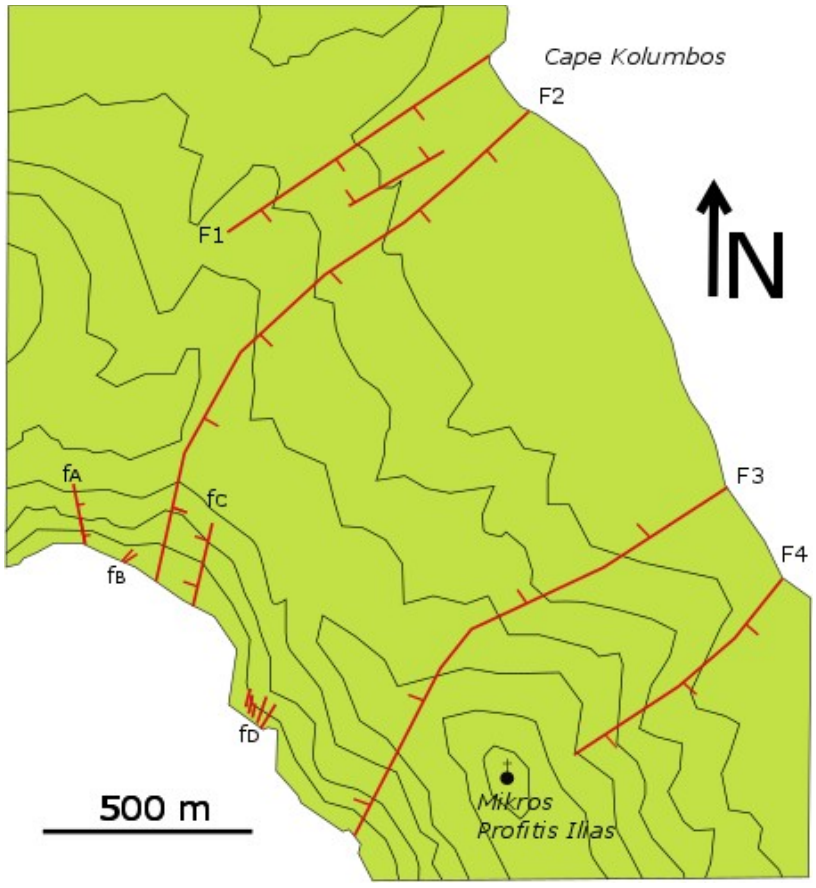

Fig. 3.4: Map modified from Druitt et al., (1999), F1-F4 and fA normal faults mapped from Druitt et al., 1999. During this study F2, F3 and fA faults were also mapped, and faults fB-D were added.

3.2.3 Dyke thicknesses, overpressure and source depth

The aspect ratio of dyke thickness to length can be used to calculate the range of the magmatic overpressure driving the dykes (Kusumoto et al., 2013). Multiple measurements from a single dyke from different positions allow an average thickness to obtained (Rickwood, 1990; Daniels et al., 2012; Delcamp et al., 2012). Determining dyke length is more challenging as it is often difficult to recognise a single dyke over a long distance (Gudmundsson, 1983; Wada, 1994).

The dyke measurements on Santorini have shown a range of sizes from a minimum of 0.1 m to a maximum of 8m (Figs. 3.5 and 3.6). Mafic dykes have a variety of thicknesses from 0.1m to 2m while the felsic dykes vary from 0.1m to 8m. The field measurements were combined with previous datasets (Petersen, 2005; Browning et al., 2015), and the averaged values were used to calculate the overpressure range of the dykes using the Eq. 2.9, as mentioned above. For that, I used a value of 5 GPa for the Young's modulus of the shallow crust, 0.25 for the Poisson's ratio and 1:1500 for the aspect ratio (thickness/length) of the dykes, a typical value in Iceland (Gudmundsson, 2011). The overpressure of the dykes has a large spread and ranges from between 0.01-244 MPa. The mean overpressure is 1MPa, the mode is 0.44 MPa, and the average is 5.04 MPa. The data are presented in Appendix B2 (Appendix B).

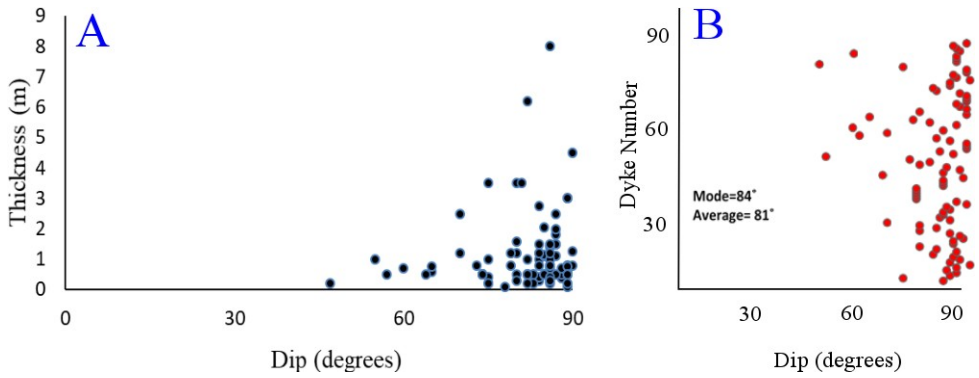

Fig. 3.5: (A) Graph showing the dip of the dyke segments to be mostly subvertical. Mode=84˚, Average=81˚, (B) Graph showing the thickness of the dykes in relation to their dip.

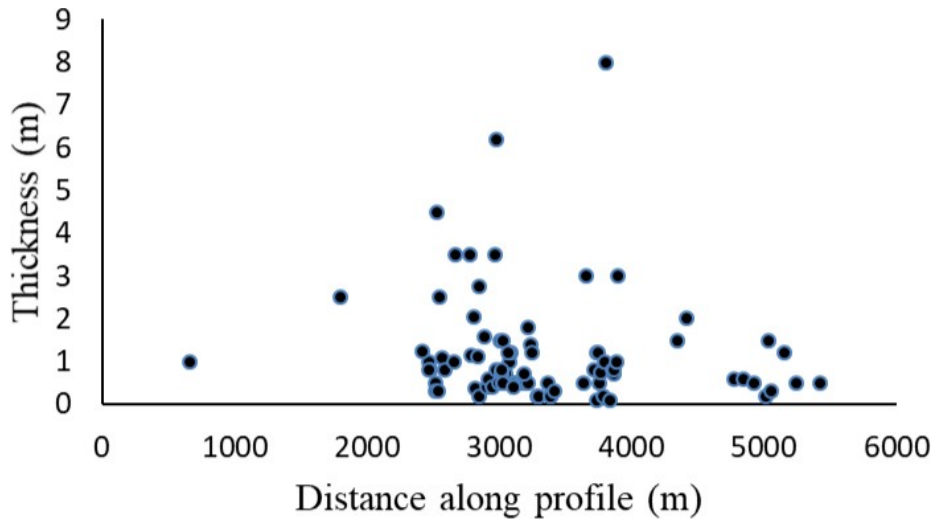

Fig. 3.6: Graph showing the thickness of the dyke segments along the studied profile on the caldera wall.

Using the derived dyke overpressures, it was possible to estimate the magmatic

source depths from equation 2.10 (Fig. 3.7). It is essential to report that the lack of length constraints highly affect the results presented which are calculated with an assumed typical ratio of length to thickness as defined by previous authors (Gudmundsson et al., 1999; Becerril et al., 2013). As such, the results are only representative of the thickness data collected in the field.

However, previous experimental studies have reported that the Santorini plumbing system is defined by a large and long-lived silicic magma system the lies at 8 km depth (Cadoux et al., 2014; Andujar et al., 2015) and a deeper mafic reservoir at 15 km depth (Andujar et al., 2015). Our statistical results show a wide range of depths from very near surface to 55 km below the surface.

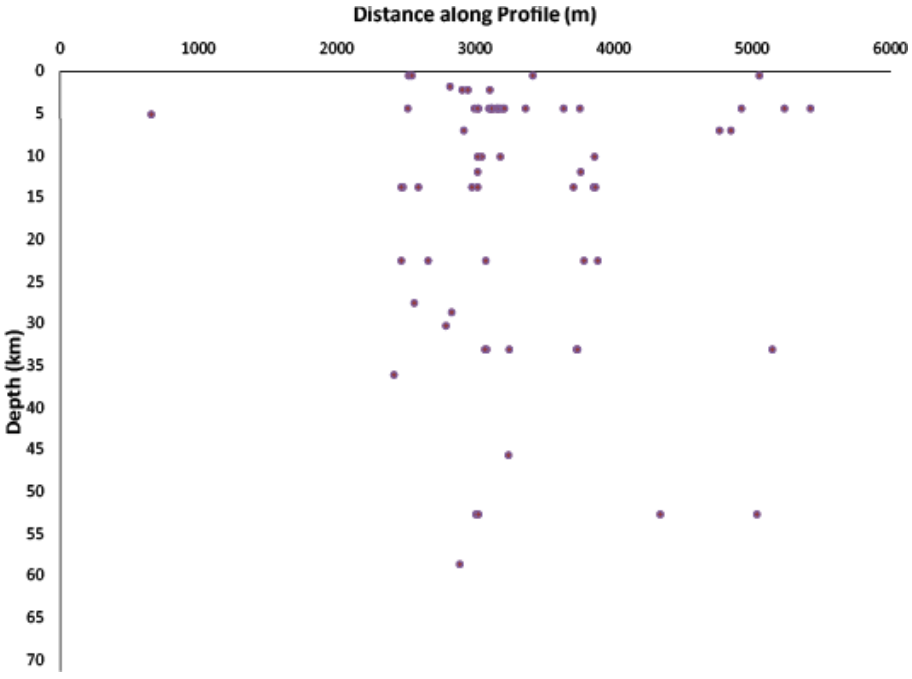

Fig. 3.7: Graph showing the source depths along profile for each dyke based on Eq.2.10.

3.2.4 Probabilistic estimation of dyke fates

Fluid dynamical systems, which often have great similarities with quantum mechanics (Vervoort, 2016), are probabilistic physics systems described by the relative frequency of the randomness or chance of an outcome and can be mathematically described by probability distributions. In this section, the probability of any one dyke becoming arrested, deflected propagated to the surface or with an unknown fate is estimated based on the following assumptions and observations from the field.

I assume that the probability (likelihood) of a dyke choosing a specific path is a random quantity (stochastic variable) of equal possibly and disjoint outcomes. For an event A of a discrete sample space Ω, the probability of A can be defined using the formula described by Von Mises (1928):

$$P(A) = \frac{N(A)}{N(\Omega)} \qquad (3.1)$$

Where N(A) is the number of elements of outcome A defined by the rule $0 \leq P(A) \leq 1$ and $N(\Omega)$ is the number of the sample space and equals with 1.

For events that overlap between the two outcomes then either one outcome or another outcome exists simultaneously (they are mutually exclusive events), their conditional probability is defined by the formula (Kolmogorov, 1956):

$$P(A \cup B) = P(A) + P(B) - P(A \cap B) \qquad (3.2)$$

Where P(A) is the probability of A and P(B) is the probability of B as defined already by Eq. 3.1 and $P(A \cap B)=0$ because $A \cap B = \emptyset$

The application of Eq. 3.1 calculates that the probability of a dyke feeds an eruption, or not, follows the aforementioned scenarios and their results are given:

If $\Omega=91$ ($\neq \emptyset$) then:

$$P(A)_{propagation} = \frac{N(A)}{N(\Omega)} = \frac{43}{91} = 0.47\ (47\%)$$

$$P(B)_{arrest} = \frac{N(B)}{N(\Omega)} = \frac{3}{91} = 0.03\ (3\%)$$

$P(C)_{\text{unsure fate}} = \frac{N(C)}{N(\Omega)} = \frac{39}{91} = 0.43\ (43\%)$

$P(D)_{\text{deflection}} = \frac{N(D)}{N(\Omega)} = \frac{6}{91} = 0.07\ (7\%)$

The probability of propagation is according to Eq. 3.2

$P(A \cup C) = P(A) + = \frac{P(C)}{2} = 0.47 + 0.215 = 0.685\ (69\%)$ whereas for arrest I use Eq. 3.2 as follows:

$P(B \cup C \cup D) = P(B) + \frac{P(C)}{2} + P(D) = 0.03 + 0.215 + 0.07 = 0.31\ (31\%)$

The statistical analysis reveals that dyke propagation is the most likely and represents 69% of the dykes that were observed to propagate through contacts and layers, the combination of arrest and deflection was responsible for the remaining 31% (Fig 3.8).

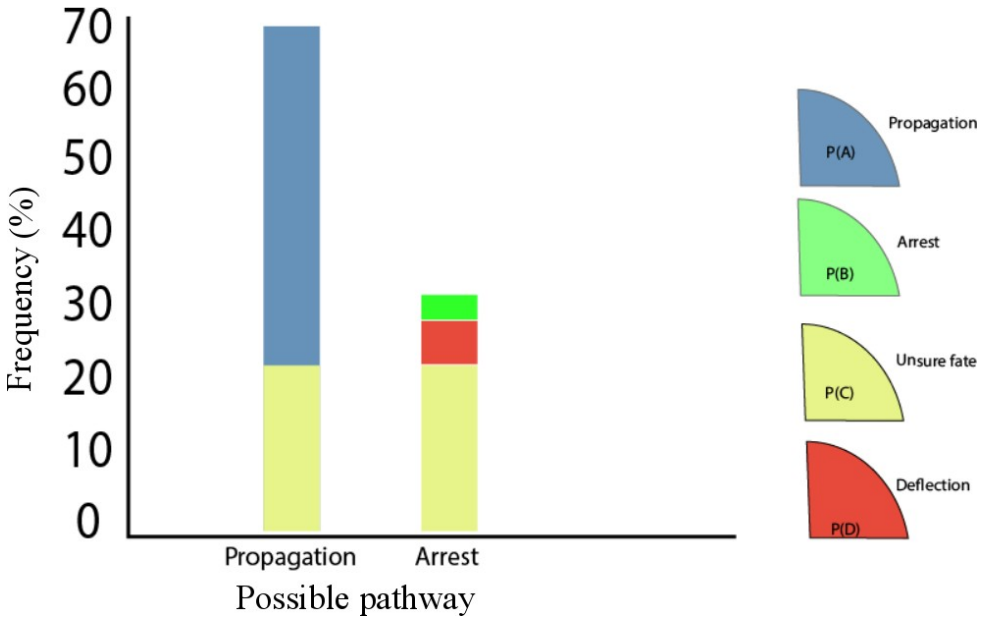

Fig 3.8: Statistical analysis of the qualitative measurements collected in the field. The distribution shows the percentages of the possible dyke paths; their qualitative analysis of arrest or propagation.

3.3 Host rock geology

In this section, I summarize the volcanological characteristics of the host rock. It is imperative to understand the distribution of the host rock as well as the physical and material properties to understand the processes that governed dyke emplacement in the research area. Below I present the results of the literature survey and my geological observations.

3.3.1 Stratigraphy of the northern caldera wall

The stratigraphy of the Northern caldera wall consists of twelve volcanic eruptions from basaltic to rhyolitic compositions that were interrupted by at least four caldera collapse events (Druitt and Francaviglia., 1992). The lithology of the host rock products, the age of the deposits and their physical characteristics were analysed by previous studies (Druitt et al., 1999; Vespa et al., 2006; Gertisser et al., 2009; Fabbro et al., 2013) and are summarised here in chronological order.

PERISTERIA VOLCANO

The Peristeria stratovolcano (530-430 ka) is the earliest known major subaerial volcanic edifice of Santorini island. Based on field observations Druitt et al. (1999) hypothesised that the edifice was exposed up to 350 m above sea level with a diameter of 4 km and a subaerial volume of at least 2 km^3. The subaerial portion consisted of three main units/phases (as shown in Figure 3.9):

- Av1: andesitic lavas, tuffs, breccias and hyaloclastites (528 ka)
- Av2: Silicic andesitic lavas (496 ka)
- Av3: Thinly bedded andesites and basalts with subordinate dacites, tuffs and scoria (464 ka)

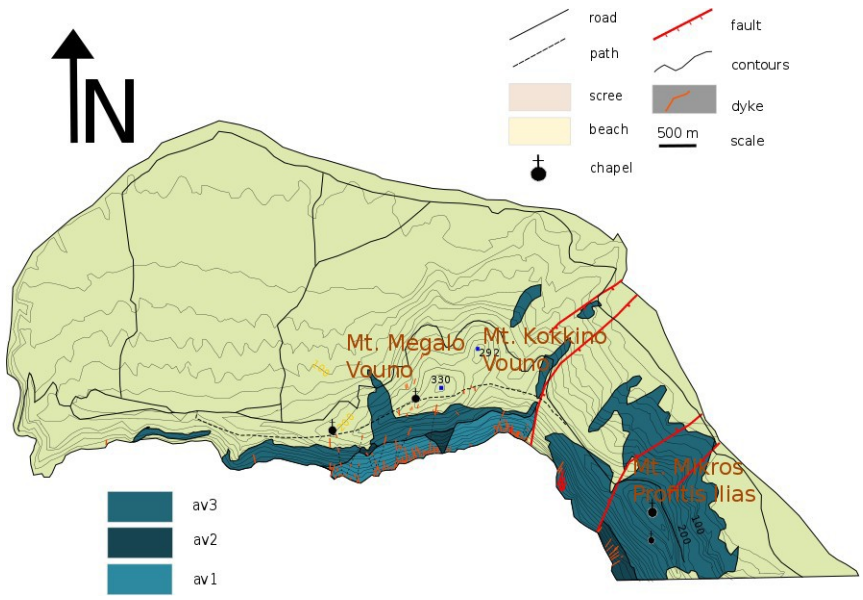

Fig. 3.9: The location and distribution of lavas associated with the Peristeria volcano.

FIRST EXPLOSIVE CYCLE

The first explosive cycle lasted from 360-172 ka; an activity that focused around the Kameni volcanotectonic line with lavas and pyroclastics products extruded from vents that belonged on the Kameni Line. The products were widely spread on the south and sporadically to the north. A caldera collapse episode marked the end of the eruptive cycle, remnants of it revealed close to the Fira caldera wall (Druitt and Francaviglia, 1992; Simmons et al., 2017).

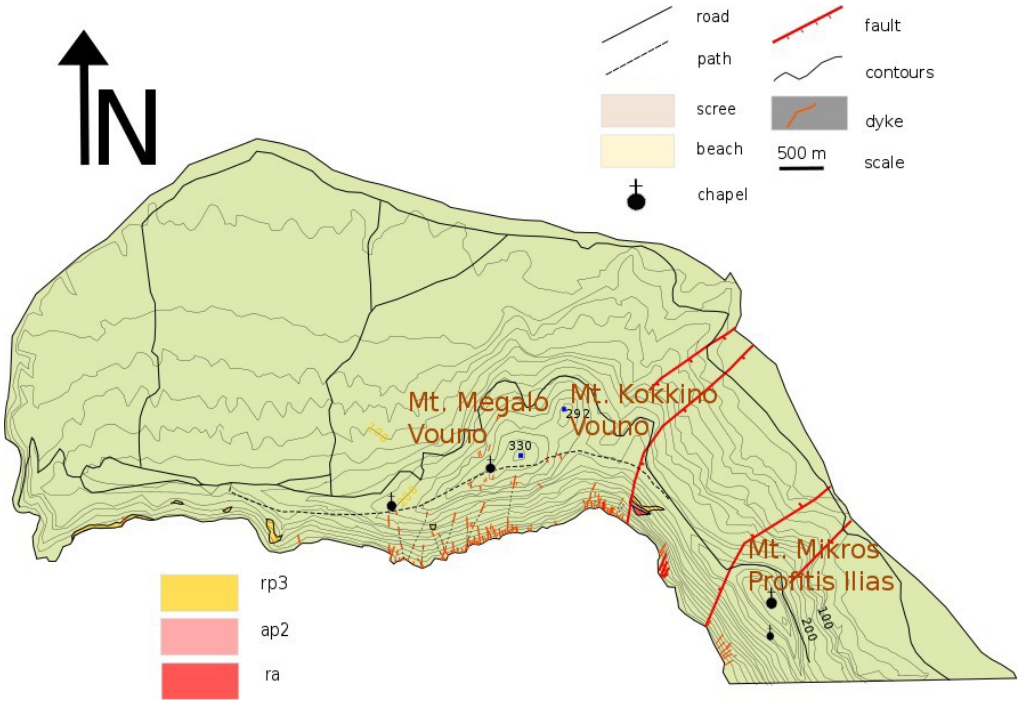

Fig. 3.10: The location and distribution of the first explosive cycle at the northern caldera wall.

In the northern caldera wall, there is a limited distribution of products that belonged to the first explosive cycle and their stratigraphic sequence involves (Fig. 3.10):

- Ra: Rhyodacitic extrusion (224 ka)
- Ap2: Cape Therma 3 - Pink sillar facies of ignimbrite and red spatter agglomerate with abundant plutonic nodules (196 ka)
- Rp3: Pumiceous phreatomagmatic deposits of yellow colour (172 ka)

The exposure of the oldest phase is a very thin silicic lava layer (K-Ar dating of 224 ka, Druitt et al., 1999), and is a remnant of the shield that existed at that time between Mt Kokkino Vouno and Mikros Profitis Ilias. The second lithology dominates locally in the same area. Its age (196 ka) was obtained from the Intra S7 deep see ash layer from Keller et al., (2000). The first explosive cycle terminated with the large rhyodacite Lower Pumice 2 eruption (Druitt et al., 1999), which is represented by a poorly sorted yellowish pumiceous phreatomagmatic deposit that is a critical marker horizon (Fig. 3.11).

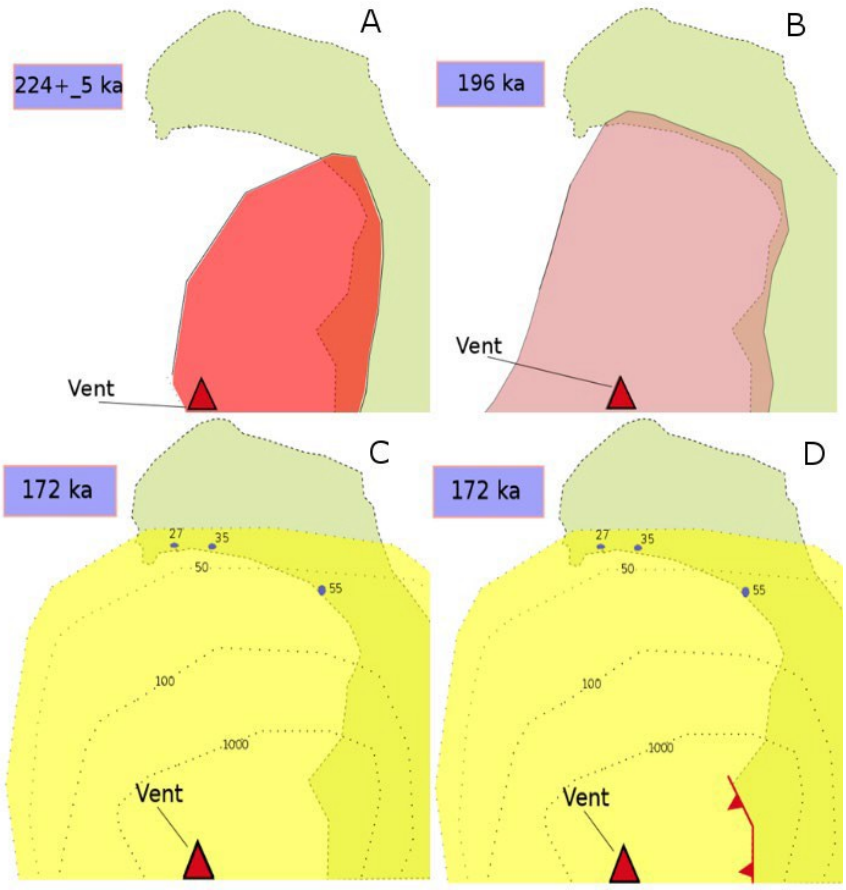

Fig. 3.11: Illustrations showing the reconstruction of the first eruptive phase and distribution of the eruptive products from the pumice fall deposit isopaches from Druitt et al. (1989, 1999) and mapped lava flows. (A) extrusions of Rhyodacites, remnants of the low shield (B): pink sillar facies of ignimbrite and red spatter agglomerate with abundant plutonic nodules dominates locally within the same area (C): yellowish pumiceous deposit of phreatomagmatic origin with a maximum thickness of 55 cm at the Northern caldera wall, (D) the caldera collapse event that accompanied the last eruption (Druitt and Francaviglia, 1992). The shields are not to scale and are extrapolated from the position of the deposits from Druitt et al. (1999).

SECOND EXPLOSIVE CYCLE

The second explosive cycle is defined by six distinct units which show a gradual evolution from intermediate to felsic compositions, and they are described below and in Figure 3.12):

- Ap4: Cinder cones of scoria-fall deposits of Megalo and Kokkino Vouno, and tuff ring (125-80 ka)
- As2: Skaros lavas (70-54 ka)
- Ap5: Upper scoria 2 (54 ka)
- Ao: Andesites of Oia
- Rp6: Cape Riva eruption (22 ka)
- Rp7: The Minoan eruption (3.6 ka)

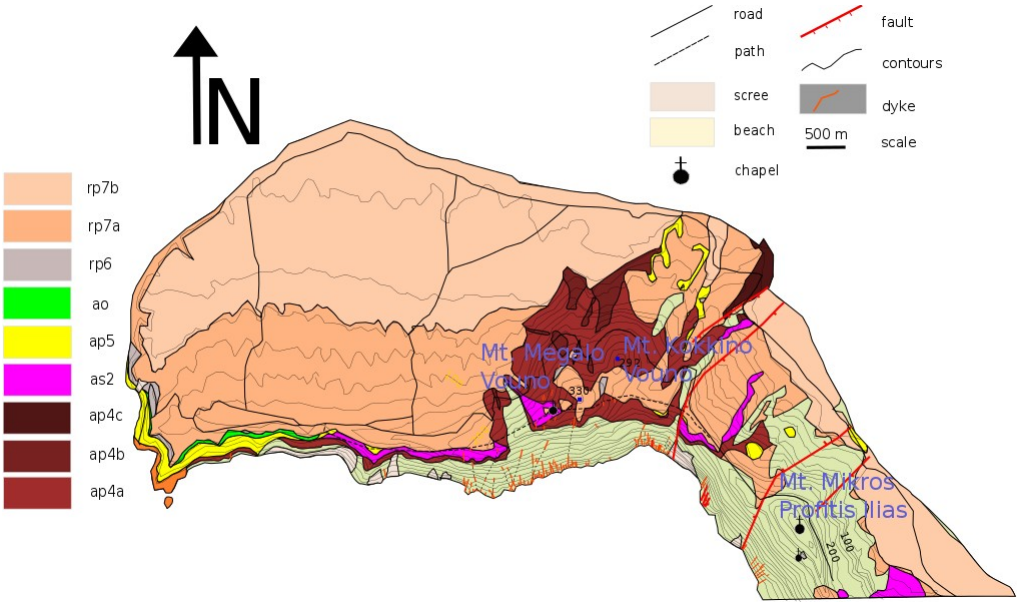

Fig. 3.12: The location and distribution of the second explosive cycle.

The beginning of the second eruptive phase at the northern caldera wall is characterised by scoria-fall deposits and especially two cinder cones and a tuff ring. Both the cinder cones that form the Megalo Vouno and Kokkino Vouno were generated by a scoria fall deposit of phenocryst poor andesite (Druitt et al., 1999) and atop the Peristeria products. Their morphology suggests that they formed simultaneously, although K-Ar dating gave ages of 76 and 54 ka (Druitt et al., 1999) respectively. The tuff ring was of a phreatomagmatic origin when sea level was approximately ≤25 m below the present-day level (Shackleton, 1987).

The next event in the area was the formation of the Skaros shield, which was by

followed the Middle tuff explosive eruptions. Andesitic, basaltic and dacitic lava flows covered the old caldera rim. These formed a shield volcano of 9 km diameter and a total volume of ~12 km^3. Its central summit was ~350 m above the present sea level and was in front of Cape Skaros (Druitt et al., 1999). The crescendo of this activity was an explosive andesitic eruption which produced the Upper Scoria 2 unit. Previous studies (Mellors and Sparks, 1991; Druitt et al., 1999) have shown that the vent originated next to the present-day Nea Kameni volcano and the scoria flows transported lithic blocks forming lag deposits 10-20m thick close to Oia village. However, scattered deposits appeared all around the northern part. A later Therasia shield of more silicic composition covered the Skaros shield and is well exposed on Therasia. Still, in the study area, its deposits cover only the village of Oia (A_o: andesites of Oia) and not any other part of the northern caldera wall.

The Skaros and Therasia shields both collapsed during the Cape Riva eruption that took place at 22 ka (Druitt et al., 1999). The eruption was accompanied by a rhyodacitic pumice fall, two ignimbrites and phreatomagmatic explosions which took place during the latter stages of the eruption.

The last eruptive event was the Minoan Plinian eruption that covered the entire island, with a thickness of up to 55 m (Druitt et al., 1999). The eruption discharged a dense-rock equivalent (DRE) volume of 39 km3 (Sigurdsson et al., 2006) dominated by the last fine-grained, non-welded ignimbrite (Phase Four) which likely formed coevally with the major caldera collapse.

3.3.2 Reconstruction of the Peristeria stratovolcano

Field studies (Druitt et al., 1999) on the northern caldera wall revealed that the Peristeria stratovolcano (530-430ka K-Ar dating) and deposits of two explosive cycles above are interrupted by a steep unconformity. At the contact there are signs of plastered lava flows interpreted as the wall of an ancient vent. During this study, specific interest was given to the origin and formation of this unconformity as several dykes were found to intersect it. It is classified as an angular unconformity and represents a 64-30 ka hiatus between silicic (av2) and an andesitic (av3) lava flows.

Lucchi et al. (2013) proposed a classification for unconformities that form in volcanic environments utilizing their genetic processes. Allogenic unconformities are global-large scale phenomena created by sea-level fluctuations while autogenic are middle scale (km range) processes arranged basically by internal modifications such as:

1) continued volcanic inactivities,

2) rapid changing of eruptive vents and/or

3) volcanotectonic events (caldera or lateral collapse).

Previous volcanological studies (Heiken and McCoy 1984; Druitt and Francaviglia 1992) have reported evidence of vent migration to the south at the Kameni volcanotectonic line during the Bronze Age while Druitt et al. (1999)

supported the theory that the Kolumbo volcanotectonic line, which permeates the northern caldera wall, is also associated with the evolution of a volcanic activity that was oriented in a NE-SW orientation.

Recent geophysical and bathymetrical studies (Hooft et al., 2019) revealed a shallow low-velocity and high-porosity vent correlated with the LBA eruption due to its phreatomagmatic origin on the western extension of the Kolumbo volcanotectonic line. The structure accommodates collapse structures, faulting and localized magma recharge that could make it a candidate of an old collapsed vent which formed even earlier than the second eruptive phase characterized by shifting activation period and migration. Such a scenario can accommodate the formation of the observed unconformity on the northern caldera wall, as proposed in Figure 3.13.

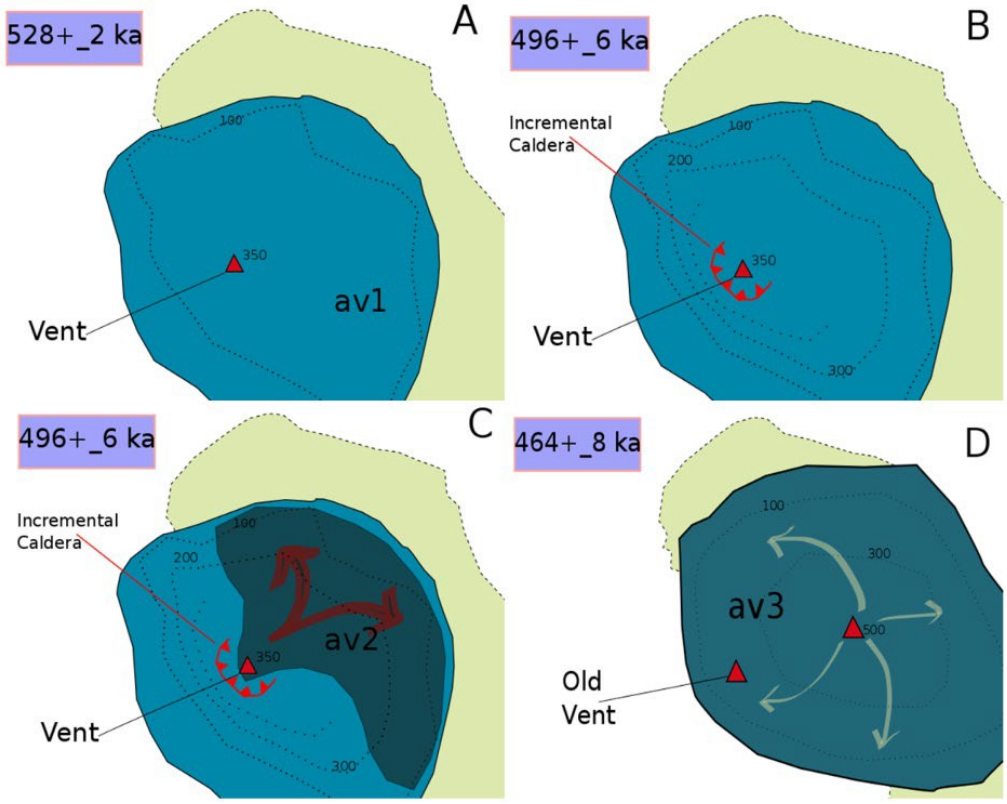

Fig. 3.13: Illustrations showing the reconstruction of Peristeria edifice as suggested after this study. (A) A: av1 flow delineates a phreatomagmatic activity which is overlapped by an angular unconformity, (B): incremental caldera collapse, (C): av2 flow & angular unconformity, (D): av3 flow.

3.4 Petrography of the dyke swarm and host rock of the northern caldera wall

In this section, a novel petrogenetic database of sampled thin sections was combined with volcanotectonic data collected from the field or derived from the observations mentioned above. This innovative methodology attempts to study the evolution of the crustal volcanic plumbing system and reconstruct the emplacement of the dyke swarm on the northern caldera wall. The structural and petrological observations are presented in Table (3.1). Key petrographic observations are also shown in representative thin section images in Figure 3.14 and section B4 (Appendix B).

3.4.1 Dykes

In this section I present the petrographic analysis of the sampled dykes.

Table 3.1: Petrographic analysis of Dyke 1 (core).

	Dyke 1 (core)		
Structural data	Lat/Lon	36 27.610 N/ 25 22.619 E	
	Strike (degrees)	010	
	Thickness (m)	1	
	Calculated overpressure (MPa)	0.7	
Petrography	Groundmass: (minerals-texture)	*Plag+pyrox+ol+glass* Intergranular texture, porphyritic, pilotassitic, seriate, slightly trachytic	
	Minerals (phenocrysts)	*Plag+opx+cpx+ol+op*	
	Textures 	Glomerocrysts: *Plag+opx+cpx+ol* (0.5-4mm)	
		Xenoliths: No	
		Plag: (0.3 - 3mm)	sieve textures, resorption, zoning (normal, oscillatory and patchy), twinning (Carlsbad- albite), nucleates, inclusions, sodic cores and calcic rims (yellow centres)
		Plag morphology	Synneusis, embayments, rounded zones
		Cpx: (0.5 – 1.5 mm)	2 generations (zoned (resorbed core rarely) or not), twinning (simple or polysynthetic), mutual connections with plag or alone
		Opx: (0.3 - 0.5 mm)	Zoning and twinning

		Ol: (0.3-0.6mm)	Zoning, reaction rims, mutual connections with Cpx or alone in the groundmass
	Secondary minerals/alteration	Inclusions of pyroxenes in plagioclase phenocrysts	
	Fabric	No cracks or any tectonic signs	
	Vesicles	Less than 10%	
Geochemistry	Chemical composition	Basaltic Andesite (BA)	
	Processes	Magma mixing, equilibrium, ascent (conduit processes), recharge, deep chamber	
	Spiderdiagram	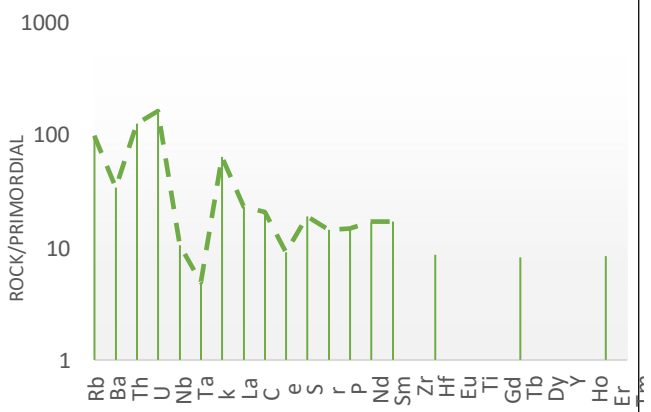	

Dyke_1 (Table 3.1) is basaltic andesite which represents the western margin of the studied dyke swarm. The dyke permeates a cross-section that belongs to the Cinder cones, Skaros and Therasia shield deposits and its exposed segment stalls in the Middle Tuffs deposit horizon (ap4-scoria of Megalo and Kokkino Vouno cinder cones) so the dyke should have fed later deposits. The structural data reveal that the dyke is 1m thick, so it belongs statistically to the same main populations that formed the regional dyke swarm, has an NNW-SSE orientation and a calculated overpressure of 0.7MPa.

The petrographic data show that the main mineral assemblage is Plag+opx+cpx+ol+op. The main textures described were seriate, porphyritic and slightly trachytic showing crystal growth in a near-equilibrium state, and molten magma flow. The plagioclase phenocrysts had both coarse and fine sieve textures, resorbed cores, embayments and zoning. The dyke's phenocrysts formed glomerocrysts of Plag+opx+cpx+ol (0.5-4 mm), but no xenoliths were found in all three studied thin sections that were analysed (Fig 3.15 A-F).

The geochemical data show this is a typical arc magmatic dyke (Nb-Ta negative anomaly) with positive anomalies of Rb, Th, K, P from crustal materials or due to the enriched metasomatized mantle wedge (Druitt et al., 1999; Rudnick and Gao, 2003; Zellmer 2000) and negative Ba and Sr anomalies respectively. The Zr-Hf elements were not curved but stable, so the dyke had no signs of crustal contamination which agreed with the lack of xenoliths observed in the thin sections. Comparisons of the REE in the dykes with the available host rock database showed a significant similarity of the dyke with the Andesites of Oia (samples from Huijsmans, 1985; Zellmer, 2000; Bailey et al., 2009; Fabbro et al., 2013) the RT deposit (sample TR0015 from Bailey et al., 2009) (Fig. 3.14).

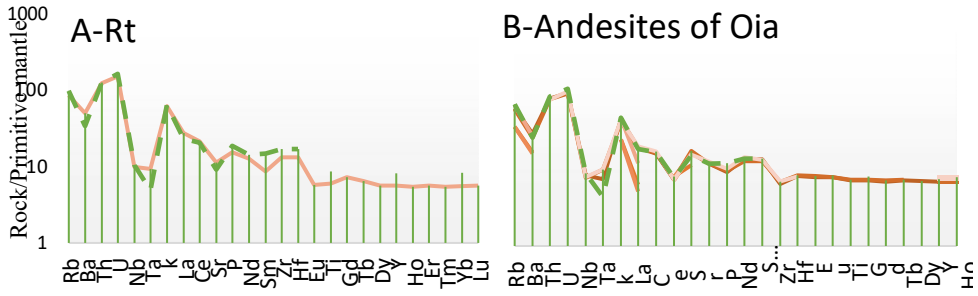

Fig 3.14: Spiderdiagram of Dyke_1 (green dotted line) with (a) Rt - rhyodacitic (milo Bay) sample and (b) Andesites of Oia.

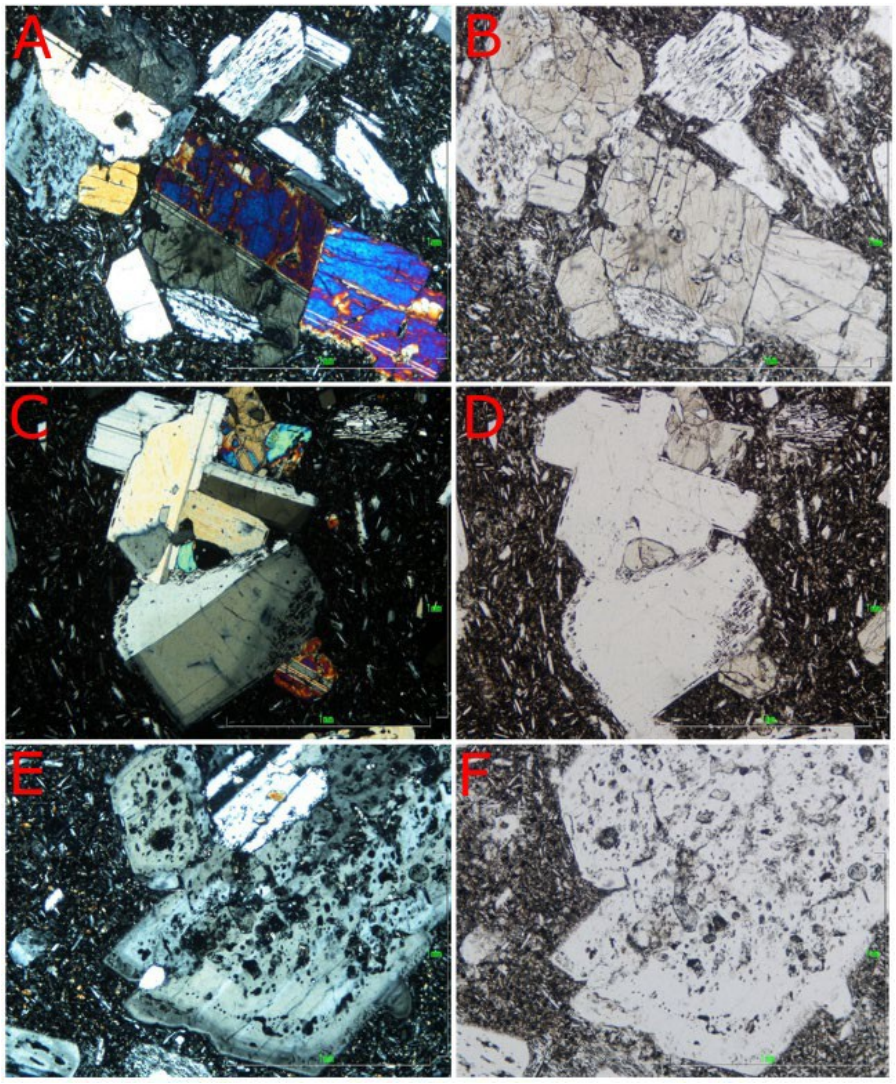

Fig 3.15: Dyke 1 (core) under crossed (A,C,E) and parallel polars (B,D,F). The groundmass (Plag+pyrox+ol+glass) has an intergranular, porphyritic and trachytic texture and the main phenocrysts are Plag+opx+cpx+ol+op. Plagioclase populations have coarse sieve, fine rim sieve textures (C, E) and inclusions (C, E). Opx, Cpx and Ol phenocrysts are present in glomerocrysts or alone in the groundmass. Opx and Cpx are usually twinned while Olivine has sometimes reaction rims.

3.4.2 Host rock

I collected six samples from the Cinder cones of Megalo Vouno and Kokkino Vouno, the Skaros lavas at Megalo Vouno, the Minoan ignimbrite to compare them with the dykes' petrography and geochemistry. For a background measurement, I also collected and analysed a sample from Cape Balos, which represents the most primary magma found on the island (Druitt et al., 1999).

The Akrotiri sample (Fig. 3.16, Table 3.2) showed distinct petrographic properties. The groundmass is trachytic, and the plagioclase crystals found in the groundmass were coarser and had a characteristic size and shape (laths). The dyke lacks xenoliths, and the glomerocrysts were very few (Fig. 3.17). The Balos lavas, according to the petrographic analysis, were probably fed from a deep-seated magma chamber due to the lack of sieve or resorbed textures in the

plagioclase phenocrysts. The geochemistry revealed very primary signatures such as low LILs, and Th, Nd and Nb negative anomalies, hence their possible great depth.

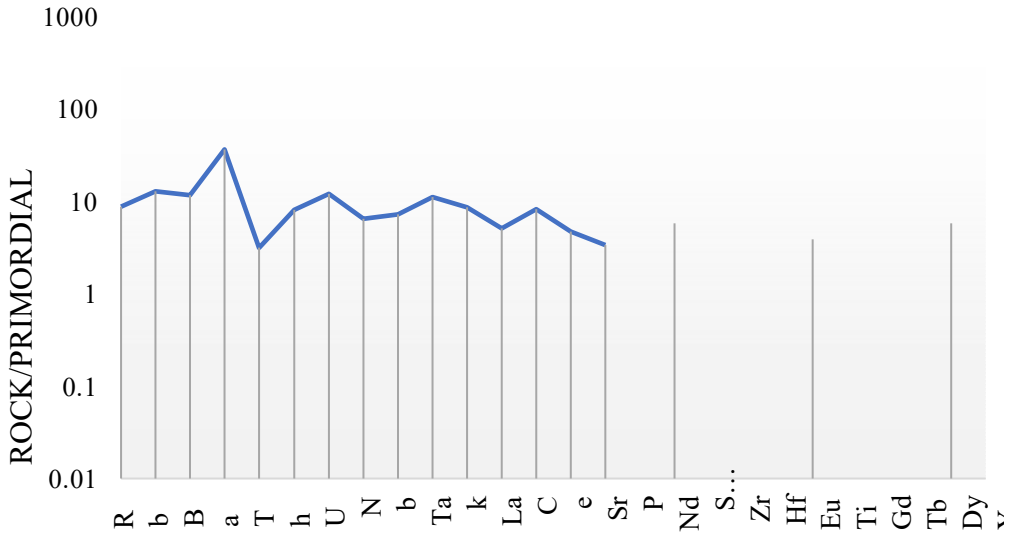

Fig 3.16: Spiderdiagram of Akr lavas.

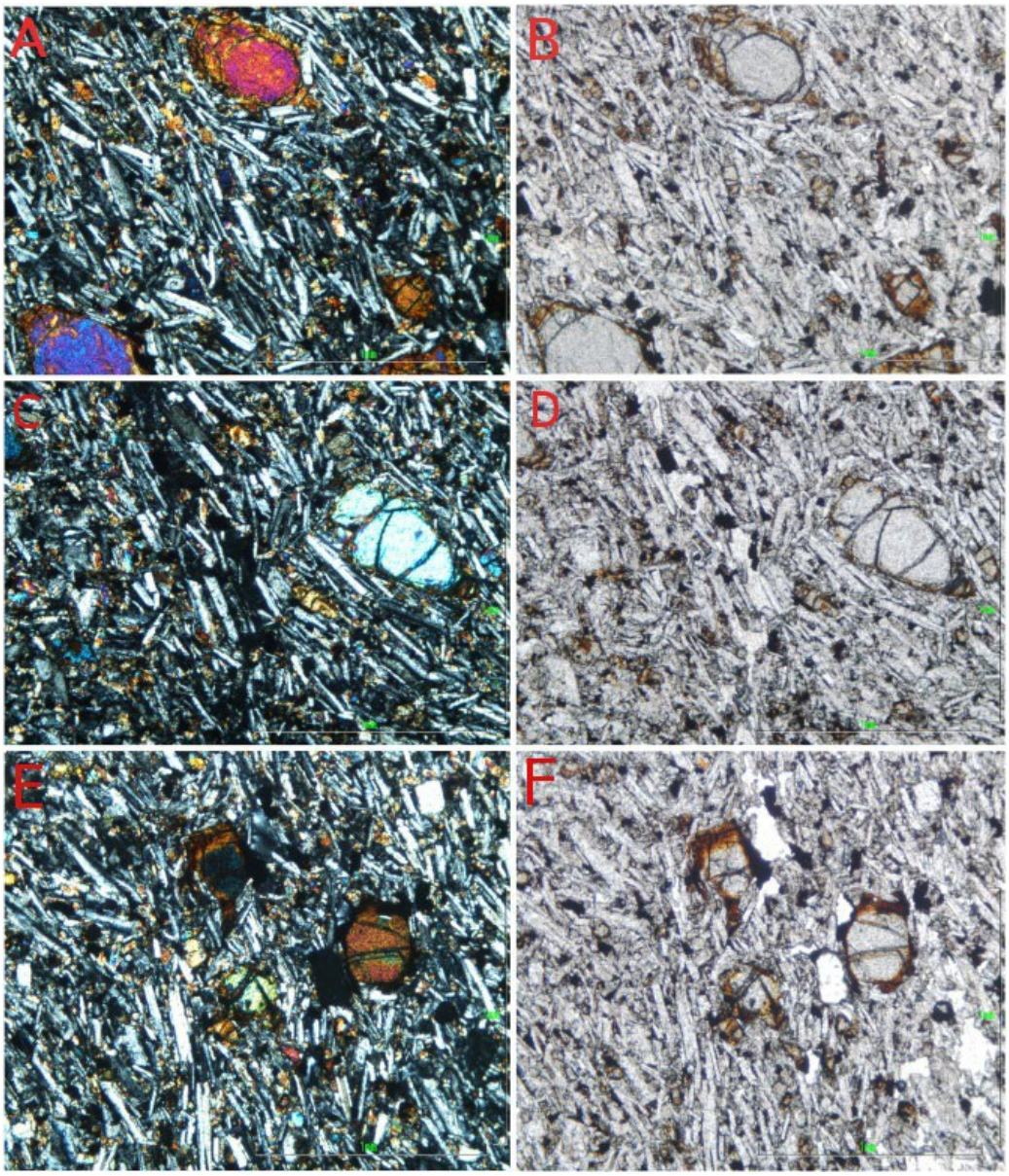

Fig. 3.17: Dyke Akr 1(core) under crossed (A,C,E) and parallel polars (B,D,F). The groundmass (Plag+pyrox+ol+glass) is trachytic and intergranular (A,C,E) composed mainly by coarse lath plagioclase. The main phenocrysts are Ol+plag+cpx. Plagioclase crystals are either yellow or grey (E). They also form Glomerocrysts with opx. Olivine is present as the main phenocryst with reaction rims and altered rims replaced by iddingsite (C, E).

Table 3.2: Petrographic analysis of Akr 1 (core).

Akr 1 (core)		
Groundmass: (minerals-texture)	*Plag+pyrox+ol+glass* Coarse lath plag size, hyalopilitic, pilotassitic, Intergranular, porphyritic, trachytic texture	
Minerals	*Plag +ol+opx+cpx*	
Textures  	Glomerocrysts: plag+opx (rare) (0.5-1mm)	
	Xenoliths: -	
	Plag: (0.3-1.5mm)	2 generations, Yellow plags rarely as phenocrysts & grey plags
	Plag morphology	laths
	Cpx: (0.3-1mm)	In Groundmass
	Opx: (0.3-1mm)	Blue I.C.
	Ol: (0.5-1mm)	The main phenocryst with altered rims (iddingsite)
Secondary minerals/alterations /inclusions	Iddingsite rims in Olivine	
Fabric	No cracks or any tectonic signs	
Vesicles	<1%	
Processes	Equilibrium	

3.4.3 Modal Analysis

I performed modal analysis measurements, using the point-counting method, in ten dyke samples (four of them were measured three times), four host rock samples (one of them was measured three times) and ten margins of dyke samples. As the method is both quantitative and qualitative, I also analysed ten samples from a separate collection to calculate the systematic error of the technique as well as the user induced error. The results are presented in the following graphs (Figs. 3.18-23).

3.4.3.1 Dyke samples

In Figures 3.18-3.19 I report the modal analysis results from selected dykes. The method allowed us to calculate the amount of groundmass, clinopyroxene, plagioclase, orthopyroxene, olivine, opaque minerals, vesicularity and calcite minerals (if any, reported with the green x axis) as part of the whole rock chemistry. The results are presented as bar diagrams.

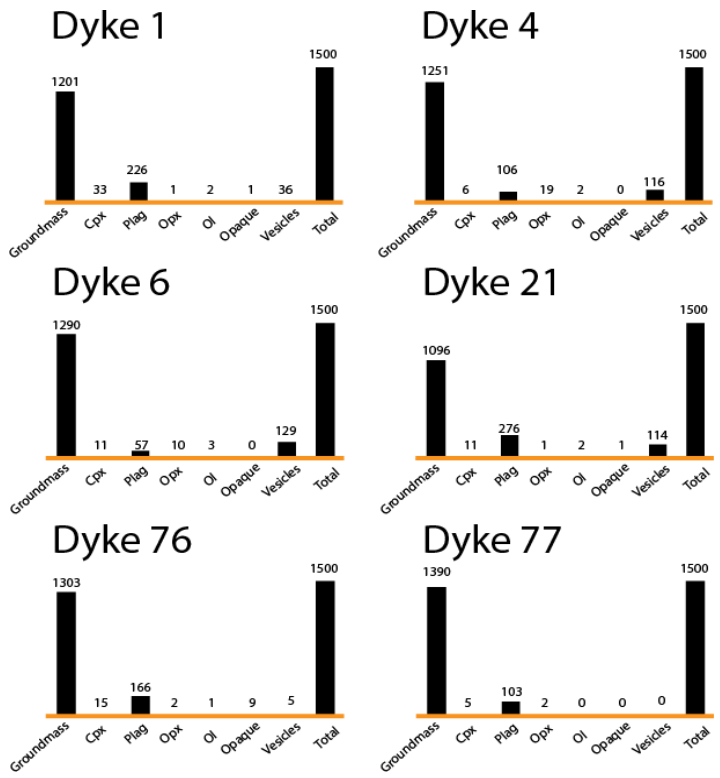

Fig. 3.18: Bar diagrams showing the relative amounts of minerals in dyke samples (1, 4, 6, 21, 76, 77) that constitute the whole rock chemistry. Orange x axis denotes no calcite mineral present.

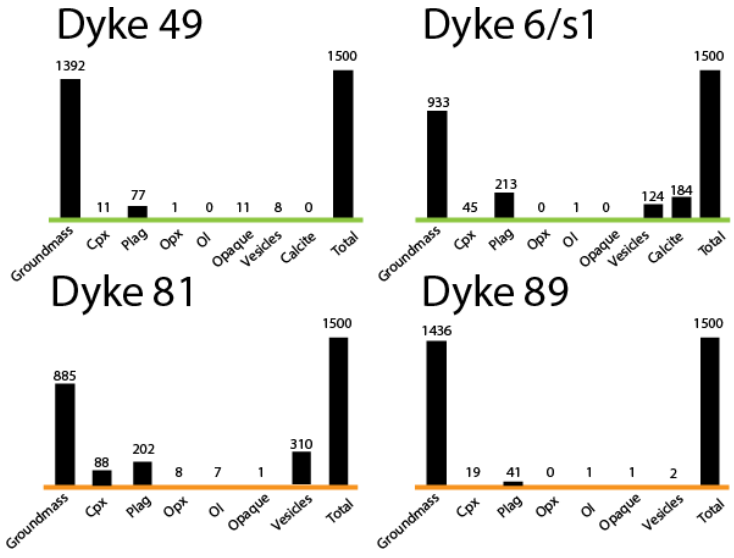

Fig. 3.19: Bar diagrams of dyke samples (49, 6/s1, 81, 89) showing the amounts of the mineralogical assemblage that constitute the whole rock chemistry. Orange x axis denotes no calcite mineral present compared to green where it has been calculated to the total percentage.

The bar diagrams reported that dykes 4, 6, 21 and 6/s1 are vesicular dykes and Dyke_ 21 has the highest amount of plagioclase crystals. Dyke_81 has the least groundmass (is the most vesicular).

3.4.3.2 Host rock samples

In Figure 3.20 I report the modal analysis results of the selected host rock samples. The method allowed us to calculate the amount of groundmass, clinopyroxene, plagioclase, orthopyroxene, olivine, opaque minerals, vesicularity and calcite minerals (if any, reported with the green x axis) as part of the whole rock chemistry. The results are presented as bar diagrams.

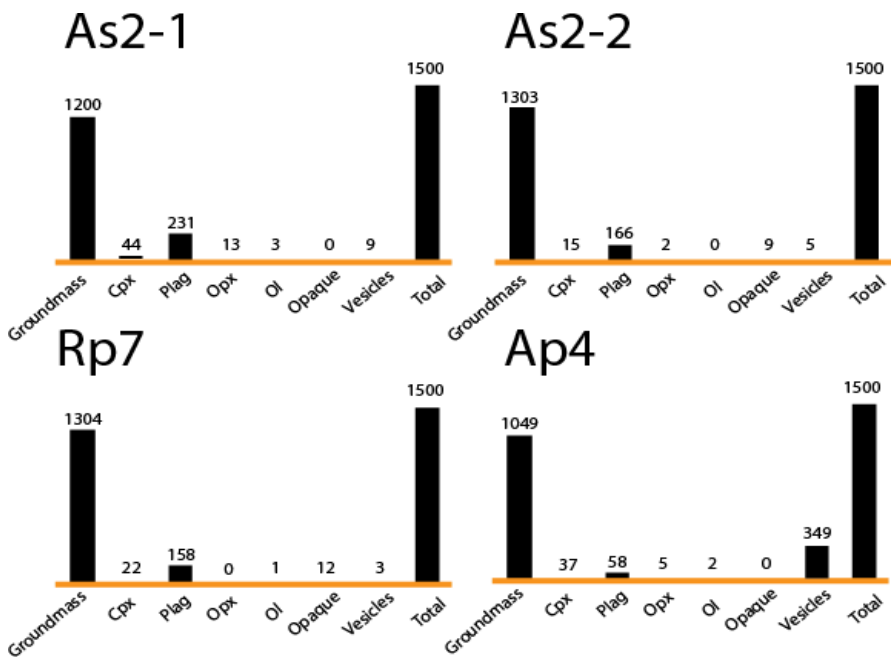

Fig. 3.20: Bar diagrams of host rock samples (As1, As2, Rp7, Ap4) showing the amounts of the mineralogical assemblage that constitute the whole rock chemistry.

The bar diagrams reported that the scoria sample is the most vesicular while the Skaros lavas and the ignimbrite are less vesicular (Fig. 3.20).

3.4.3.3 Chilled margin or rims of the dykes' samples

In Figures 3.21-3.23 I show the modal analysis results of the selected chilled margins or dyke rims. The method allowed us to calculate the amount of groundmass, clinopyroxene, plagioclase, orthopyroxene, olivine, opaque minerals, vesicularity and calcite minerals (if any, reported with the green x axis)

as part of the whole rock chemistry. The results are presented as bar diagrams.

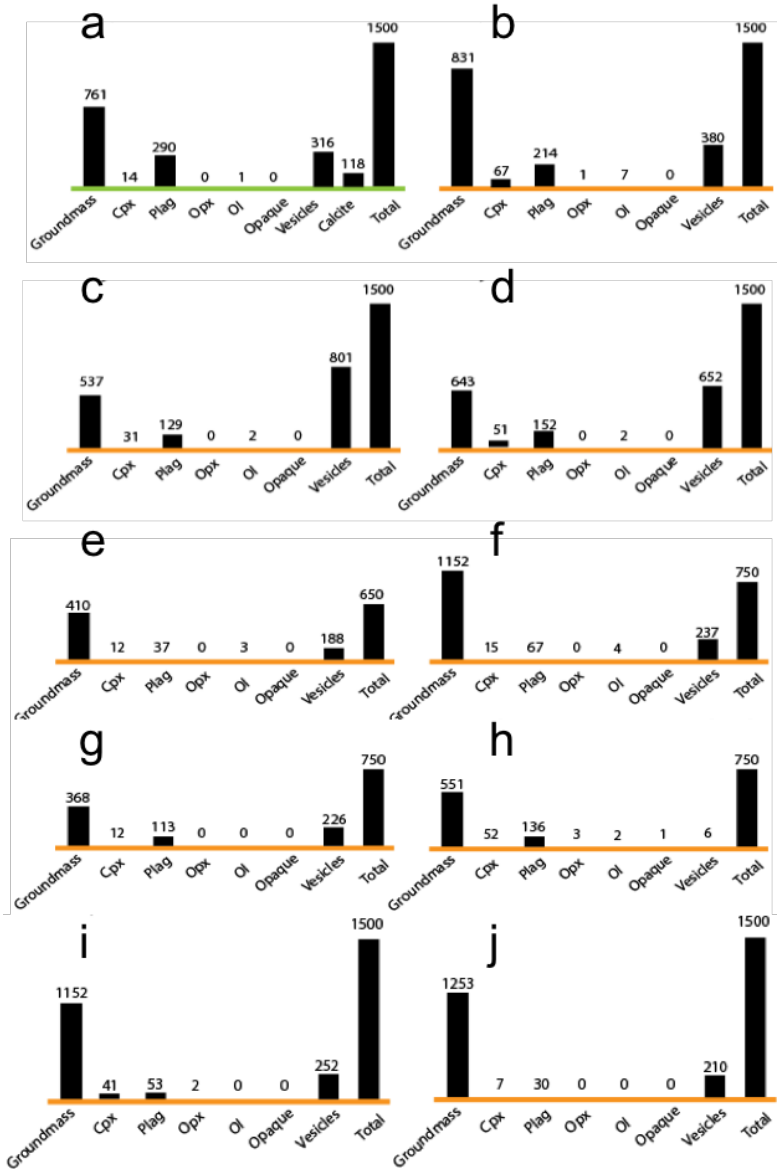

Fig. 3.21: Bar diagrams of dyke margin samples (21 rim (a), 81 rim (b), 76 rims 1 (c) and 2 (d), 77 rims 1 (e), 2 (f), 3 (g) and a xenolith found in dyke 77 (h), 89 rim 2 (i), 3 (j)) showing the amounts of the mineralogical assemblage that constitute the whole rock chemistry.

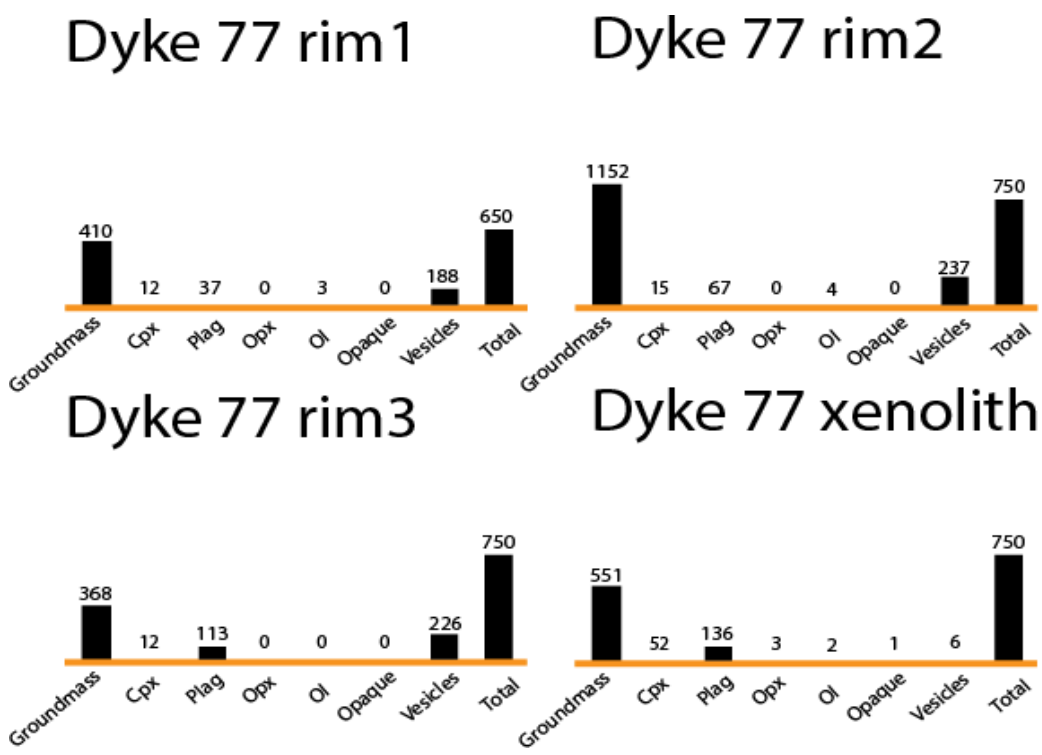

Fig. 3.22: Bar diagrams of dyke margin samples (77 rims 1, 2, 3 and a xenolith found in dyke 77) showing the amounts of the mineralogical assemblage that constitute the whole rock chemistry.

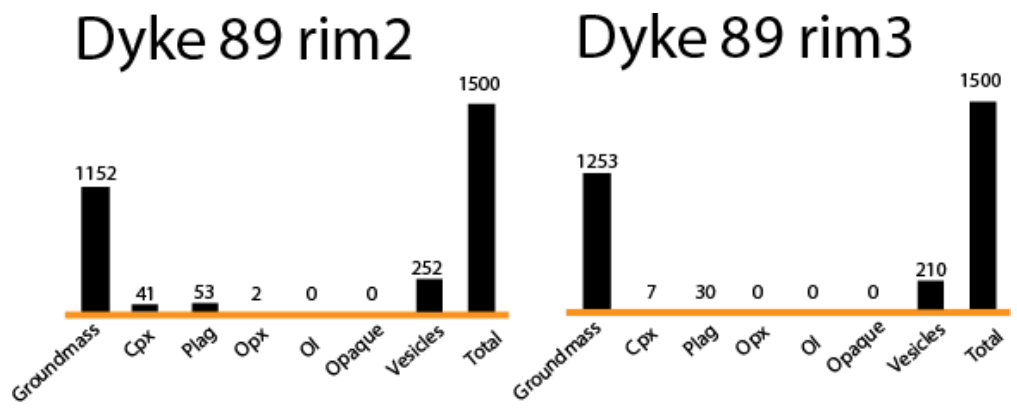

Fig. 3.23: Histograms of dyke margin samples (89 rim 2, 3) showing the amounts of the mineralogical assemblage that constitute the whole rock chemistry.

The bar diagrams reported that the scoria samples are vesicular, but the highest vesicularity belongs to the rim sample of Dyke_76. Dyke_21 crystallised calcite and has the highest amount of plagioclase phenocrysts. In terms of the methodology, the results have shown that the mean absolute error of the studied samples is ±0.093 for groundmass, ±0.28 for Cpx, ±0.51 for plagioclase, ±0.42 for the vesicularity. In terms of the technique, I calculated the errors of 3.84% for the olivine, 3.17% for plagioclase, 0.59% for Cpx, 0.31% for Oxides, 3,78% for vesicularity and 8,85% for groundmass measurements.

3.5 Geochemistry of the dykes and their host rock

Here I present, analyse and compare the geochemical data collected for each group of host rock lavas and dykes from both previous literature and the conducted field campaign. The aim is to trace the magmatic path from the source to their emplacement and eruption. The collected host rock database consists of 200 analyses that cover the compositional range of the five shields-stratocones that covered the studied area. The geochemical host rock protocol is presented at section A7 (Appendix A).

During this study, I conducted seventeen XRF analyses of dykes and hostrocks. In Figure 3.24, we observe the map that was produced after the sampling campaigns. These results were compared with the host rock database to investigate dyke fed relationships. The XRF dataset is presented at section B3 (Appendix B).

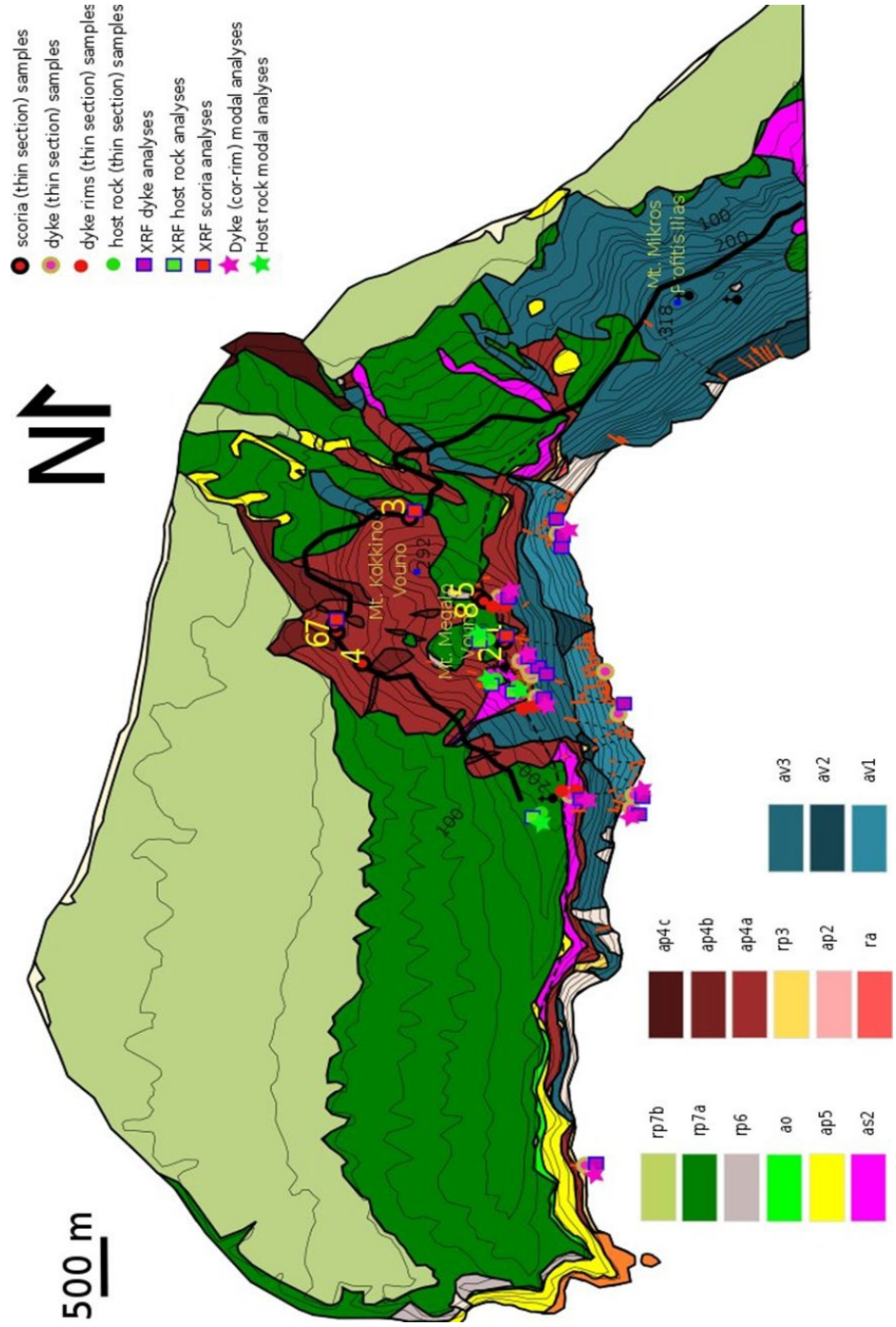

Fig. 3.24: The northern caldera wall map showing the location of the sampling campaigns. The numbers 1-8 denote the scoria samples collected during the campaigns.

3.5.1 Host rock

Figure 3.24 shows samples collected from the eruptive products of the northern caldera wall which were later analysed and compared with samples analysed by Bailey et al. (2009) (Geochemical sampling protocol is at section A7-Appendix A). The results highlight bimodal compositions and represent a low to high K series from mafic to felsic products. In the following figures, we observe their classification (Figs. 3.25 and 3.26). The classification highlights a transition from calc-alkaline to tholeiitic magmas.

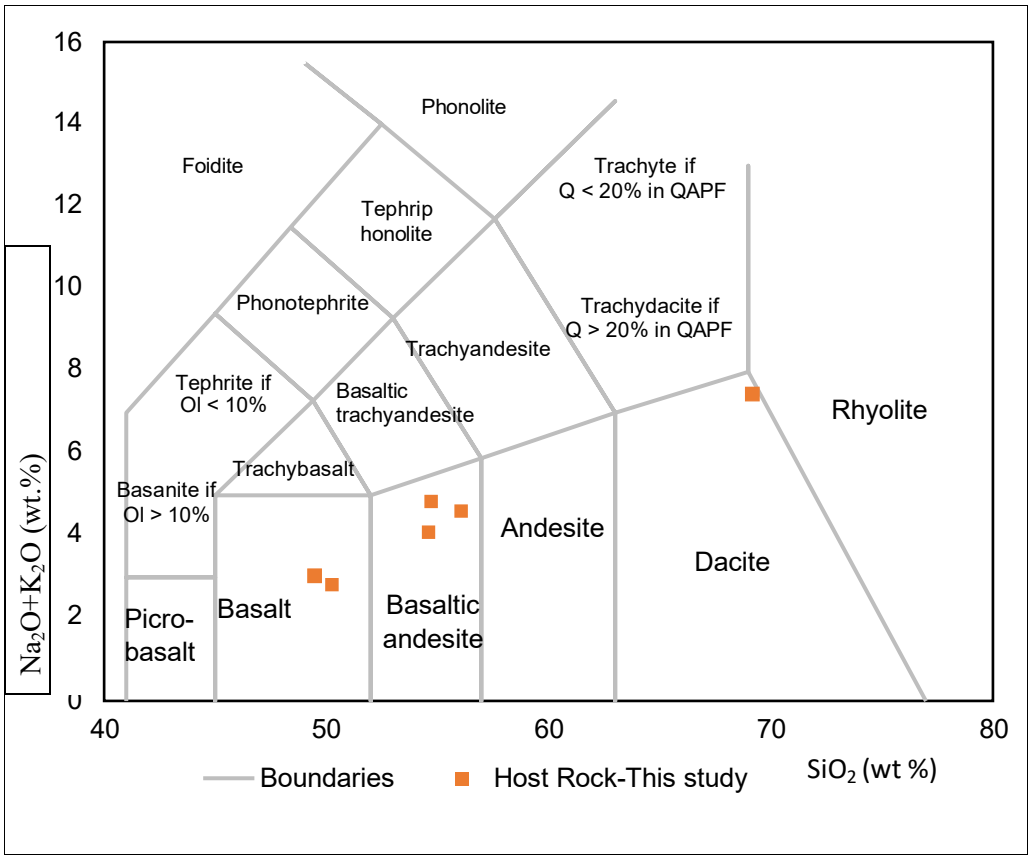

Fig. 3.25: TAS classification diagram according to Le Bas et al. (1986) showing the host rock samples analysed in this study.

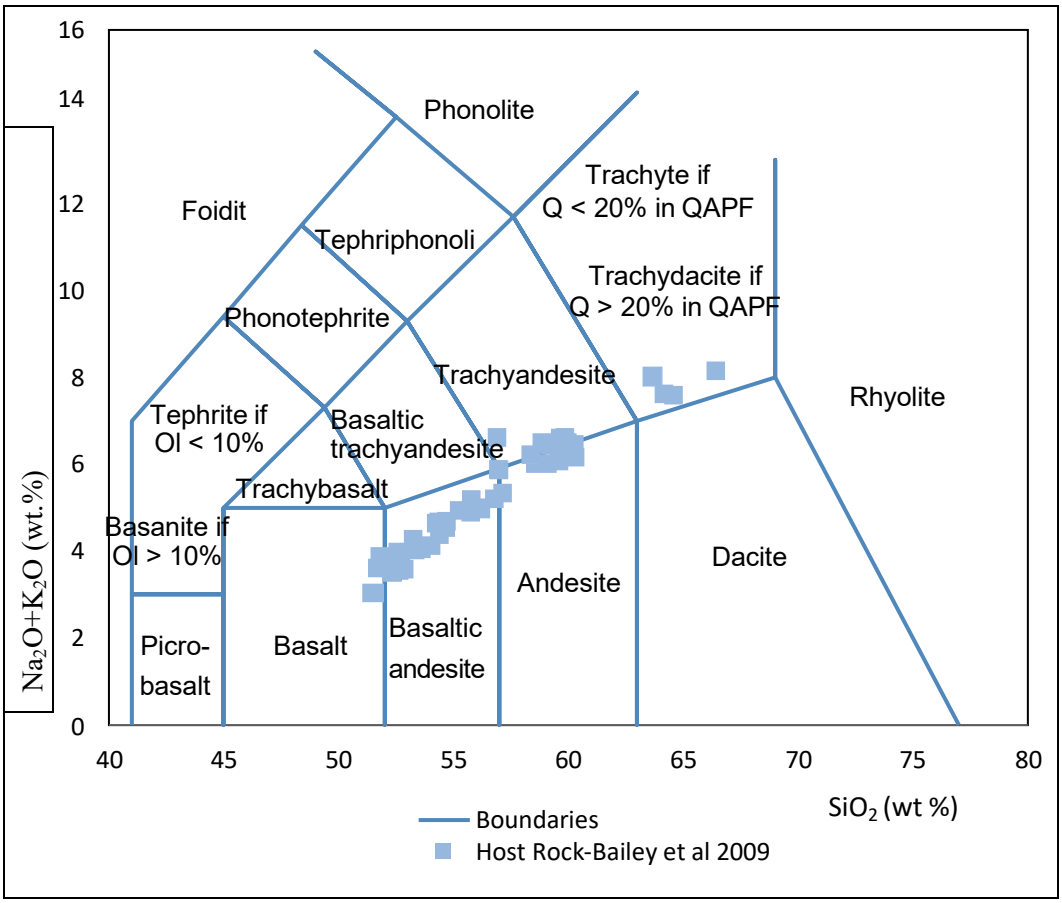

Fig. 3.26: TAS classification diagram according to Le Bas et al. (1986) showing the host rock samples from Bailey et al. (2009).

For our study I used the CaO/MgO ratios (Best, 2003) to investigate the amount of fractionation in the host rock samples (Fig. 3.27).

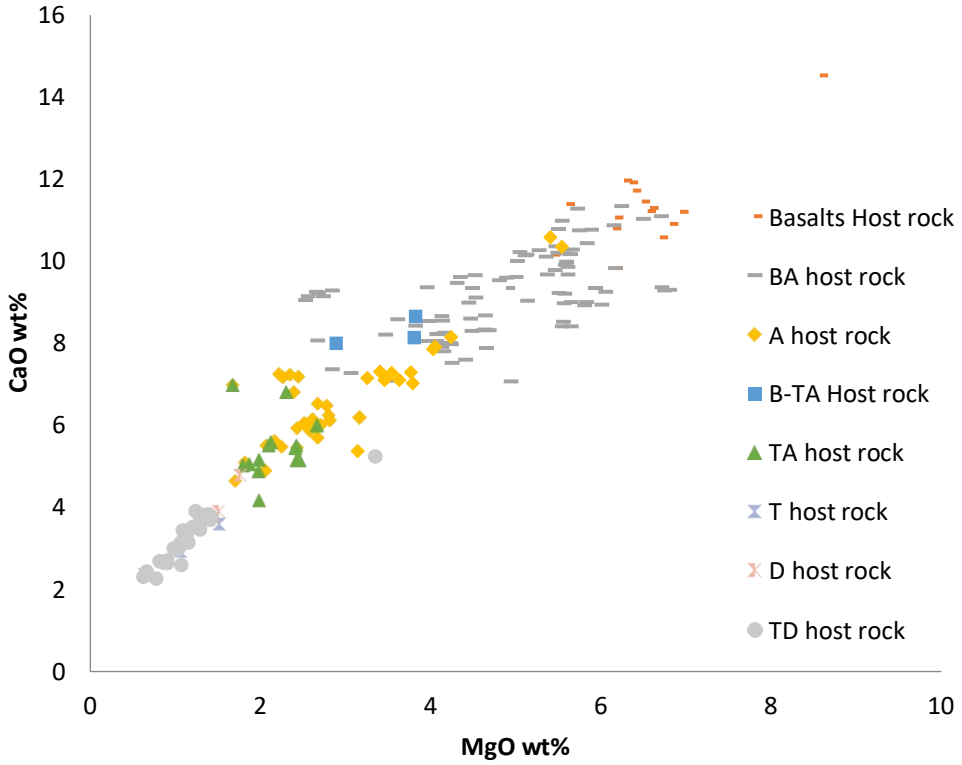

Fig. 3.27: CaO/MgO plot showing the fractionation trend of the host rock magmas. Data from Nicholls (1971); Mann (1983); Huijsmans (1985); Druitt et al. (1999); Zellmer (2000); Bailey et al. (2009); Fabbro et al. (2013, 2014) and this study. B denotes basaltic compositions, BA basaltic andesites, A andesites, B-TA basaltic trachyandesites and TA trachyandesites respectively.

The host rock samples showed a calc-alkaline to shoshonitic continental arc origin according to the Th/Yb Vs Ta/Yb plot (Fig. 3.28). The magmas that fed the volcanic eruptions were affected by both crustal assimilation and fractional crystallisation.

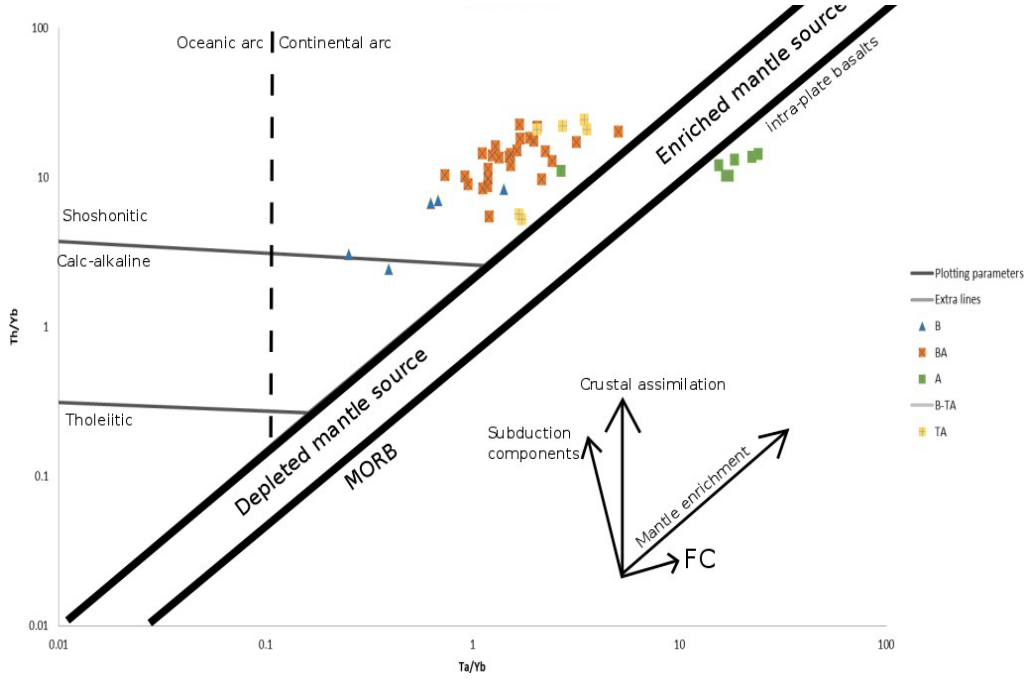

Fig. 3.28: Th/Yb versus Ta/Yb plot showing the difference between basalts in a subduction related setting and an oceanic setting derived from MORB depleted sources and OIB enriched sources. Vectors show the subduction enrichment, the within-plate enrichment, the crustal contamination and the fractional crystallisation while the lines separate the boundaries of tholeiitic, calc-alkaline and shoshonitic fields and the dashed lines the oceanic and continental arc origin (after Pearce 1983). Data from Nicholls (1971); Mann (1983); Huijsmans (1985); Druitt et al. (1999); Zellmer (2000); Bailey et al. (2009); Fabbro et al. (2013, 2014) and this study. B denotes basaltic compositions, BA basaltic andesites, A andesites, B-TA basaltic trachyandesites and TA trachyandesites respectively. Both axes are in ppm.

3.5.2 Host rock spiderdiagrams

I normalised the LIL, HSFS, and REE concentrations of the host rock samples with the primordial mantle from McDonough and Sun (1983) and the resultsare shown in Figures 3.29-3.32 The aim is to diagnose distinct geochemical fingerprints and correlate them with the studied dykes to unfold possible dyke-fed interactions.

The spider diagrams, shown in Figures 3.29-3.32., have similarities with typical island arc calc-alkaline basalts (Sun, 1980; Thompson et al., 1984). Arc magmas are typically enriched in Rb, Ba, K incompatible elements and depleted in Ta and Nb. In Santorini, trace element patterns from previous studies have shown variable metasomatism by terrigenous-rich bulk or partial melt sediments (Bailey et al., 2009) but not fluids (Vaggelli et al., 2009). Also, they show a variable Eu anomaly which corresponds to plagioclase fractionation (Druitt et al., 1999).

Basalts

Basaltic compositions are found in four (Peristeria, Simandiri, Cinder cones of the Northern caldera wall and Skaros) of the five volcanic shields-stratocones that formed the northern caldera wall (Druitt et al., 1999).

For the basaltic dataset, I used a sample from Peristeria stratovolcano (av2)

collected from the Mikros Profitis Ilias (MPI) locality by Huijsmans (1971), and a sample from Cape Simandiri from Bailey et al. (2009). Three samples represented the Cinder cones: one from the scoria cone of Kokkino Vouno sampled from this study and two samples from Huijsmans (1971) sampled at the Megalo Vouno locality. Two samples from the Skaros shield (Am 0004&0006) collected from Ammoudi bay, and two specimens from Therasia locality both by Bailey et al. (2009), three from Skaros shield (possibly from Imerovigli) by Huijsmans (1985) and a sample of the Skaros lava flow at the top of Megalo Vouno from this study. I also infer a Cape Balos basalt from Akrotiri lavas. The latter represents the most primary magmatic compositions. The spider diagrams of the basalts are shown in Figure 3.29.

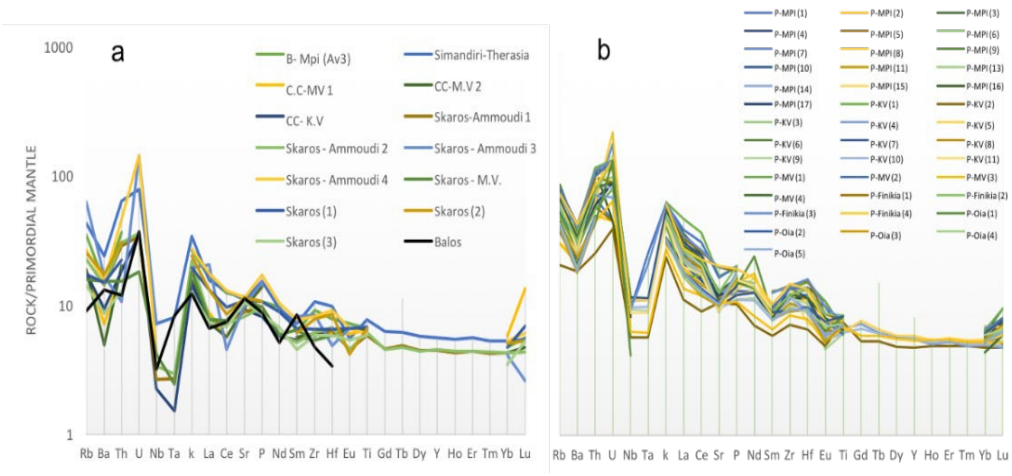

Fig. 3.29: (A) Spiderdiagram of the REE basaltic compositions normalised by the primordial mantle. Data from Nicholls (1971); Mann (1983); Huijsmans (1985); Druitt et al. (1999); Zellmer (2000); Bailey et al. (2009) and this study. Localities: MPI, M.V., K.V., Ammoudi, Skaros, Therasia. (B) Spiderdiagramof

the REE basaltic andesite compositions normalised by the primordial mantle of Peristeria stratocone. Data from Nicholls (1971); Mann (1983); Huijsmans (1985); Druitt et al. (1999); Zellmer (2000); Bailey et al. (2009); Fabbro et al. (2013, 2014) and this study. Localities: MPI, M.V., K.V., Finikia, Oia.

The data in the spider diagrams (Figure 3.29) do not totally overlap. The sample collected at the Megalo Vouno has lower light LILs (Rb, Ba, Th) which suggests a more primitive origin. Bailey's samples are similar between them, but the scoria sample from the cinder cones and the sample from the Skaros lavas (M.V) differ in their light LILs. The Cinder cones have their distinct fingerprint with a negative Ta anomaly and a positive Sr anomaly. The two cinder cones (Kokkino and Megalo Vouno) differ suggesting that they were sourced from distinct magma reservoirs, even though field evidence from their spatter lavas and their morphology (Druitt et al.,1999) indicated that their eruptive activities were partly simultaneous. Lastly, the whole suite of Skaros samples do not overlap with each other, but they show different localisation characters. The Peristeria basalts are distinctly showing a small negative Sm anomaly while the Simandiri basalts have similarities with the Skaros lavas (Ammoudi flow).

Basaltic andesites

Basaltic andesites are found in all the shields-stratocones except the last Minoan eruption. I included in our list three samples from av1 Peristeria horizon at the caldera wall opposite the Megalo Vouno, four samples from the Megalo Vouno area and fourteen samples from the MPI area all by Huijsmans 1985, twelve samples from Bailey et al., 2009 collected at the Megalo and Kokkino Vouno area. Cape Simandiri is represented by one sample collected at cape Riva (As) lava flow from Bailey et al. (2009) in Therasia island while the cinder cones, are represented by six samples in total by Huijsmans (1985), Bailey et al. (2009) and this study. The Therasia dome formation is represented only by one sample which sampled at Cape Tino in Therasia.

Due to their heterogeneity I plotted them subject to their locality from the east to the west: MPI, K.Vouno, M.Vouno, Finikia and Oia. In general, the lavas have the typical Nb-Ta anomaly and negative Sr anomaly. The Peristeria lavas localised at the MPI area have a Th-U positive anomaly and positive Nd anomaly. All sixteen samples are quite similar to each other except the high U anomalies on some av3 samples (Fig. 3.30B).

The basaltic andesites at K.Vouno and M.Vouno cinder cones are overlapped showing a negative Nb anomaly, a positive K anomaly and negative Sr, and Sm anomaly. However, the two samples at KV have a positive Sr anomaly and low LILs. That could imply a different magma origin. On the contrary, the Simandiri

sample is similar to the Skaros lavas and the TDC sample is similar to the Simandiri sample respectively. (Fig. 3.30) Finally the Skaros lavas have generally negative Sr and Nb anomalies and positive Th anomalies (Fig. 3.30).

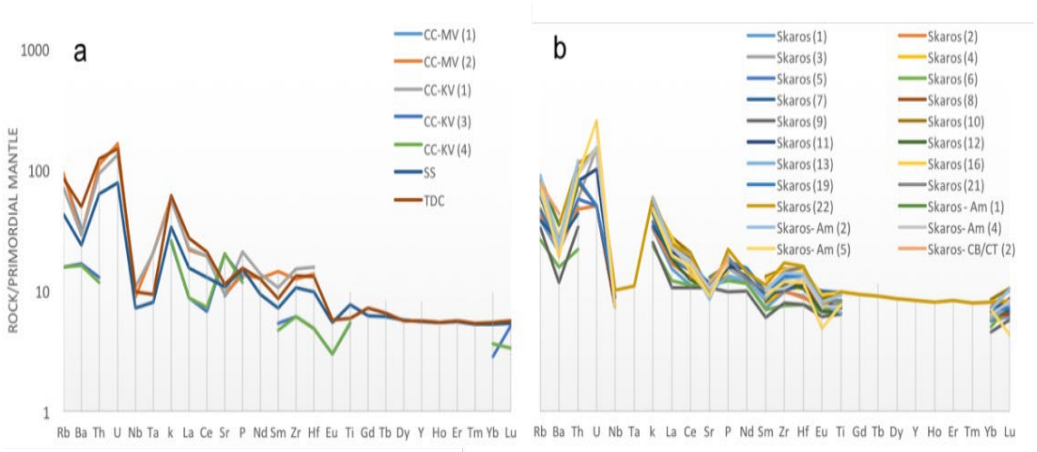

Fig. 3.30: Spiderdiagram of the REE basaltic andesite compositions normalised by the primordial mantle for Simandiri, Cinder cone and TDC lavas. Data from Nicholls (1971); Mann (1983); Huijsmans (1985); Druitt et al. (1999); Zellmer (2000); Bailey et al. (2009); Fabbro et al. (2013, 2014) and this study. Localities: M.V., K.V., Therasia. (B) Spiderdiagram of the REE basaltic andesite compositions normalised by the primordial mantle for Skaros lavas. Data from Nicholls (1971); Mann (1983); Huijsmans (1985); Druitt et al. (1999); Zellmer (2000); Bailey et al. (2009); Fabbro et al. (2013, 2014) and this study. Localities: M.V., Ammoudi, Skaros, Therasia (Corfos Bay/Cape Tino).

Andesites

Andesitic compositions were found in all five shields-stratocones. 20 andesitic lavas from Peristeria representative of the Megalo Vouno (M.V) and MPI localities were analysed. One sample from Simandiri represents the shield from Cape Simandiri. For the cinder cones, I retrieved only one sample from M.V; the Skaros lavas were represented by nine samples. Finally, for the Therasia dome complex (TDC), I used nine samples both from Ammoudi and Therasia island.

The Peristeria andesites (Megalo Vouno locality) have significant similarities, and their characteristic signature is defined by a positive U and K anomaly and a Sr, Sm negative anomaly (Fig. 3.31). However, two samples (K.V and Finikia) showed different Sr anomalies and no negative Ta anomalies, which could also imply different origins. Finally, the MPI Peristeria andesitic lavas are very similar to the MV Peristeria lavas and have the same geochemical fingerprint. For the rest of the shields-stratocones (Simandiri-Cinder cones-Skaros) have overlapped spider diagrams with a typical U, K positive anomaly and Nb-Ta, Sr negative anomaly (Fig. 3.31). The Therasia dome complex andesite is also similar to the previous andesitic compositions.

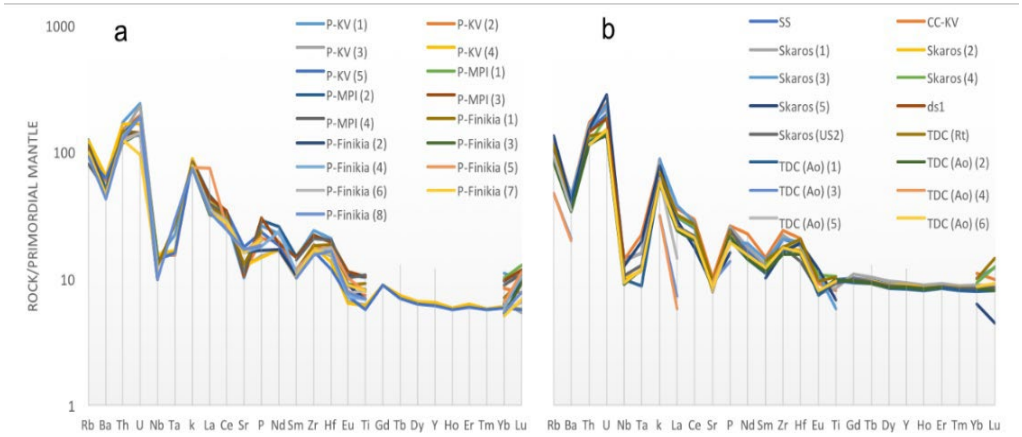

Fig. 3.31: (A) Spiderdiagram of the REE andesitic compositions normalised by the primordial mantle for Peristeria lavas. Data from Nicholls (1971); Mann (1983); Huijsmans (1985); Druitt et al. (1999); Zellmer (2000); Bailey et al. (2009); Fabbro et al. (2013, 2014) and this study. Localities: MPI., K.V., Finikia, (B) Spiderdiagrams found in andesitic compositions normalised by the primordial mantle for Simandiri, Cinder cones, Skaros and TDC lavas. Data from Nicholls (1971); Mann (1983); Huijsmans (1985); Druitt et al. (1999); Zellmer (2000); Bailey et al. (2009); Fabbro et al. (2013, 2014) and this study. Localities: K.V., Skaros, Therasia.

Trachyandesites

Trachyandesites are present predominantly in the Peristeria stratovolcano both in the MV and MPI area (seventeen samples) where three of them have initially been basaltic trachyandesitic and the rest of them trachyandesites. In addition, four representative lava samples were sampled from the Simandiri shield, one of which was representative of the Skaros shield.

The trachyandesites are separated into two teams showing different anomalies subject to different localities (M.V., K.V., and MPI). The Megalo Vouno samples are benmoreites and have a negative Ti anomaly while the MPI lavas have stronger negative Ti anomalies. The K.V samples showed similarities with the Skaros andesites (Fig. 3.32). On the contrary, the trachyandesitic samples are very similar within the Simandiri shield to the previous eruptive cycle (at Peristeria) with the same characteristic positive U and K anomalies and Sr and Sm anomalies. The TDC sample also has a negative Ti anomaly like the Peristeria lavas (Fig. 3.32).

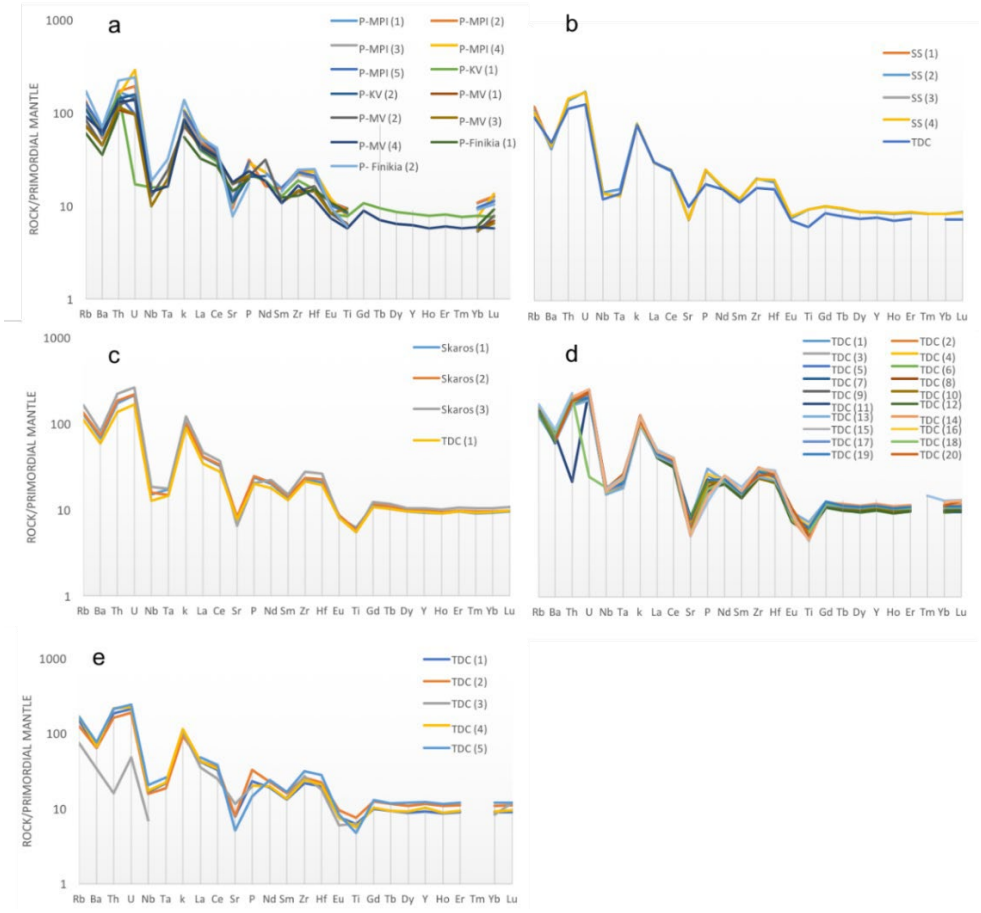

Fig. 3.32: (A) trachyandesite normalised plots by the primordial mantle for Peristeria lavas. Data from Nicholls (1971); Mann (1983); Huijsmans (1985); Druitt et al. (1999); Zellmer (2000); Bailey et al. (2009); Fabbro et al. (2013, 2014) and this study. Localities: MPI., K.V., M.V., (B) trachyandesite normalised plots by the primordial mantle. Data from Nicholls (1971); Mann (1983); Huijsmans (1985); Druitt et al. (1999); Zellmer (2000); Bailey et al. (2009); Fabbro et al. (2013, 2014) and this study. Locality: Therasia., (C) trachytic normalised plots by the primordial mantle for the Skaros and TDC lavas of Theresia. Data from Nicholls (1971); Mann (1983); Huijsmans (1985);Druitt

et al. (1999); Zellmer (2000); Bailey et al. (2009); Fabbro et al. (2013, 2014) and this study., (D) trachydacitic normalised plots by the primordial mantle. Data from Nicholls (1971); Mann (1983); Huijsmans (1985); Druitt et al. (1999); Zellmer (2000); Bailey et al. (2009); Fabbro et al. (2013, 2014) and this study. Localities: Therasia., (E) dacitic normalised plots to a primordial mantle for the TDC lavas of Therasia. Data from Nicholls (1971); Mann (1983); Huijsmans (1985); Druitt et al. (1999); Zellmer (2000); Bailey et al. (2009); Fabbro et al. (2013, 2014) and this study.

Trachytes-Trachydacites-Dacites

The most acidic magma compositions were found predominantly in the Therasia dome complex (thirty three samples) and the Skaros shield (three samples) (from the Cape Tino locality). The rare earth elements (REE) found in the Trachytes are similar to both Skaros and Therasia dome complex shields. Both complexes have typical Th-U and K positive anomalies and Nb-Ta, Sr, Ti anomalies (Fig. 3.32). Also, the REE found in trachydacites have great similarities to all of them and show typical negative Th and U anomalies (Fig. 3.32).

3.5.3 Dykes

The dyke swarm has a range of compositions from basaltic to dacitic, and their characteristics are shown in Figs. 3.33 and 3.34. The tholeiitic and calc-alkaline signatures that were observed in the host rock analysis are also reflected in the dykes too.

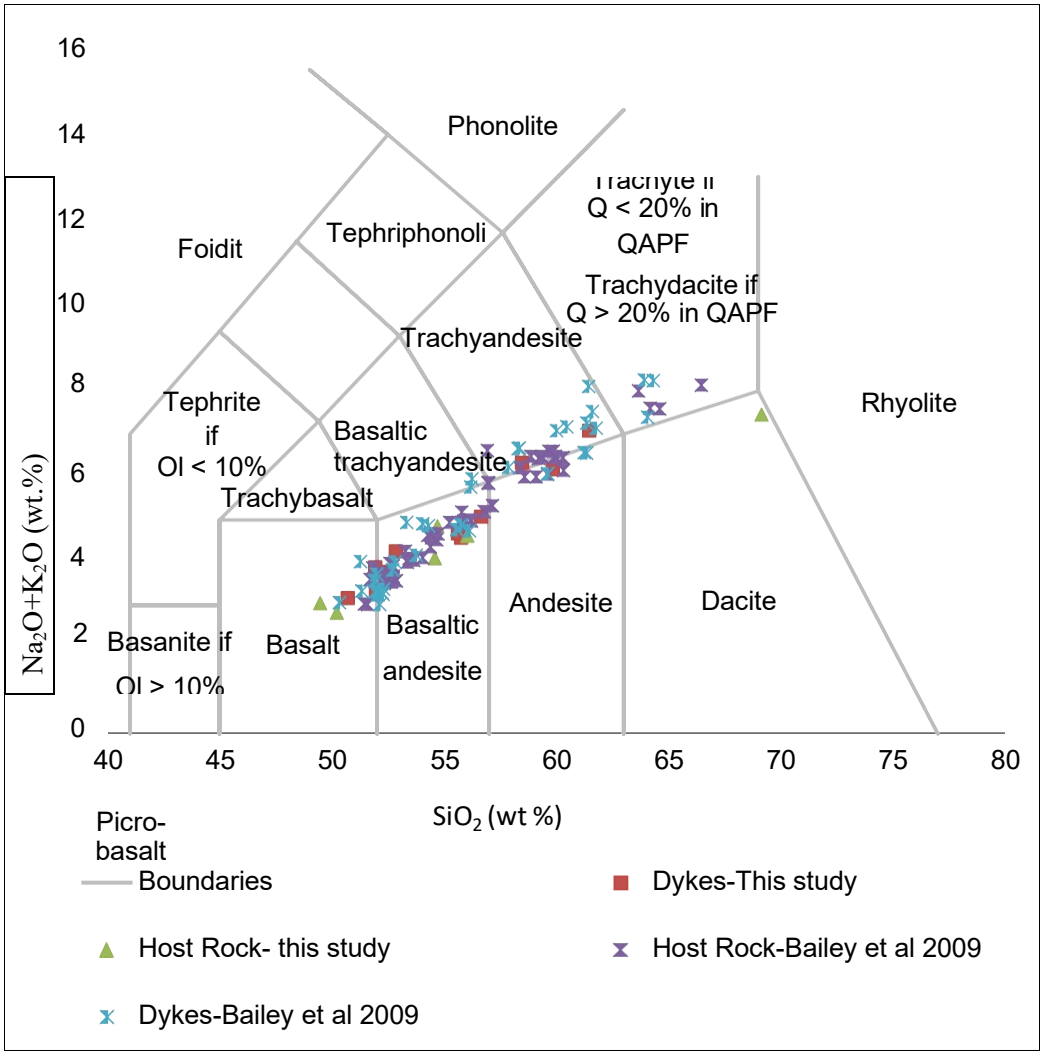

Fig. 3.33: TAS classification diagram from Le Bas et al. (1986) showing the host rock and dyke samples after this study and Bailey et al. (2009).

The CaO/MgO ratio (Fig. 3.34) as explained before is an indicator of the primitive components present in the magma and whether they have experienced magmatic differentiation (fractionation) during their path to the surface. Mg-rich samples represent more primitive magmas (Best, 2003). The transition is defined at around 12 wt.% and the system shifts from pure crystal fractionation that is being governed by ol±opx to a cpx±plag system.

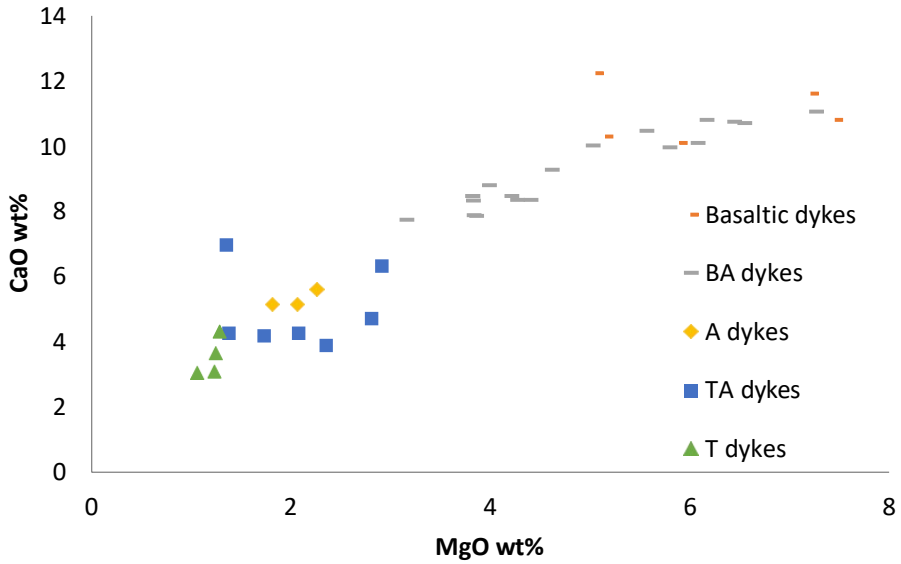

Fig. 3.34: CaO/MgO plot showing the fractionation trend of the dyke swarm. Data from Nicholls (1971); Mann (1983); Huijsmans (1985); Druitt et al. (1999); Zellmer (2000); Bailey et al. (2009); Fabbro et al. (2013, 2014) and this study. B denotes basaltic compositions, BA basaltic andesites, A andesites, B-TA basaltic trachyandesites and TA trachyandesites respectively. The figure shows that the samples analysed belong to the opx stability section, and hence they reflect contamination signatures and not primitive characteristics.

3.5.4 Dyke Spiderdiagrams

Basaltic dykes

Four dykes were categorised as basaltic dykes in our study. Dyke_6 was emplaced on the caldera wall while dykes_76 and_79 were sampled and located at the top of Mt. Megalo Vouno. In terms of their composition, they range between 49.54-51.33 wt. % SiO_2, they are all calc-alkaline (K_2O wt.% = 2.85-3.7 wt. %) and have a continental arc origin.

By correlating the dykes with the host rock analysis, it is possible to determine similarities between the origins of the dykes and the processes that formed the erupted magmas. The samples were normalised to a primitive mantle, and the results are shown in Figure 3.35. A typical arc signature is evident in all samples as Nb, Ta and Ti are normally depleted as they are less mobile than the other elements. Dyke_6 does not follow the absolute arc signature but forms negative anomalies at Ta and Nb only respectively. A comparison of the geochemical signatures of the dykes with the host rock samples reveals that the dykes are mostly overlapped with the Skaros lavas. They all begin with a flat and not a curvature line of LILs which is not common in an arc environment as the arc signature are also characterised by enrichment of the very incompatible light LILs. Typically, P follows the positive anomaly in such an environment which is evident here.

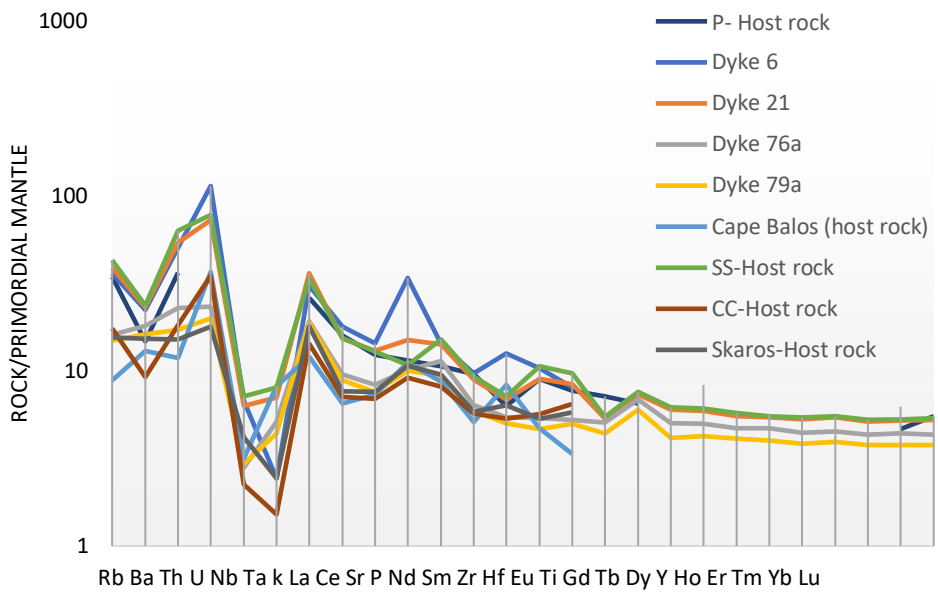

Fig. 3.35: Spiderdiagrams of basaltic dykes normalised to a primordial mantle. Data from Bailey et al. (2009) and this study.

Basaltic andesitic dykes

The basaltic andesite dykes on the caldera wall were normalised to the primordial mantle, and their plots are shown in Fig. 3.36. A typical arc signature is evident in all samples as Nb, Ta and Ti usually are depleted as they are less mobile (lower solubility in the migrating fluids) than the other elements. However, three distinct groups can be observed. Dykes_3,_4,_87 and _89 have overlapped spiderdiagrams with low LILs, typical arc signatures and positive Sr, P, Hf anomalies. The latter does not belong to any typical host rock signature so I hypothesise that the dykes_3,_4,_87 and _89 could have probably belonged to

the same arrested population of the Skaros shield. Dykes_1 and 76 (composite dyke) are similar and overlap with the Skaros shield. Lastly, dykes_19,_22,_28 and _81 are the third observed group which also shows similarities with the Skaros group.

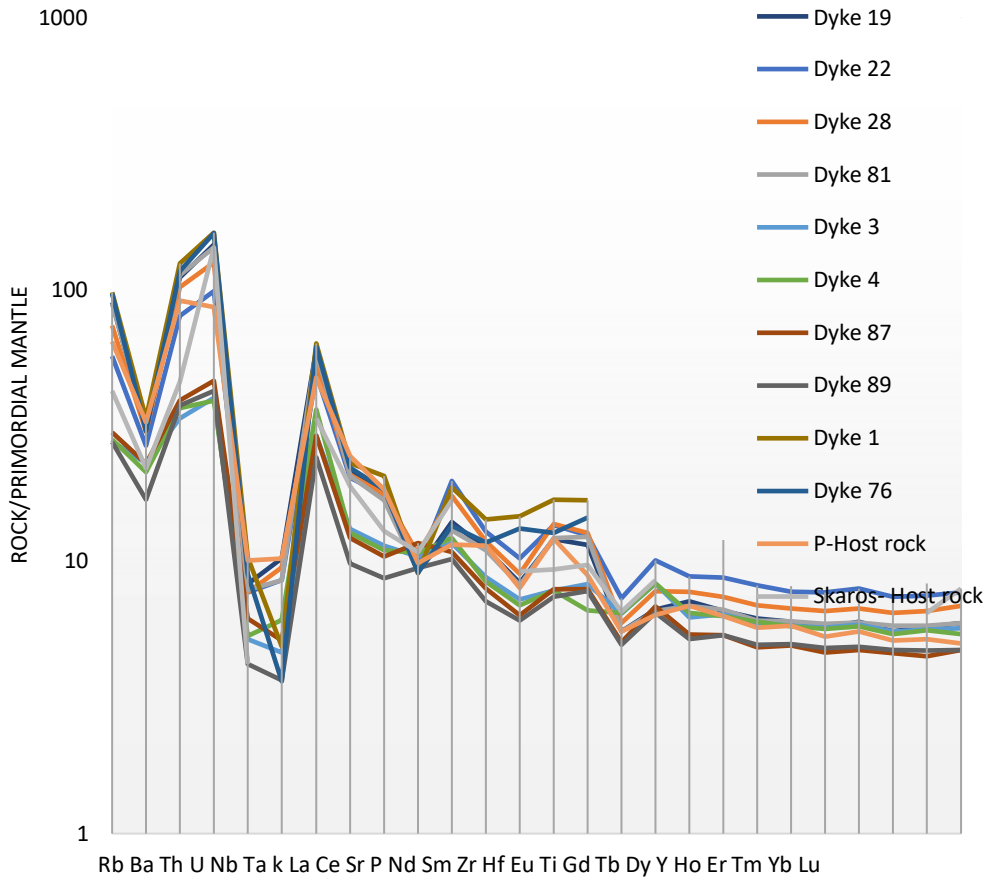

Fig. 3.36: Spiderdiagram of the REE for basaltic andesite compositions normalised by the primordial mantle. Data from Nicholls (1971); Mann (1983); Huijsmans (1985); Druitt et al. (1999); Zellmer (2000); Bailey et al. (2009); Fabbro et al. (2013, 2014) and this study.

Andesitic, Trachyandesitic, Trachytic and Dacitic dykes

I found four andesitic dykes on the northern caldera wall. All of them are overlapped with the andesitic lavas of the Skaros shield except dyke_16 which was found similar to the Simandiri lavas. Their plots are shown in Fig 3.37.

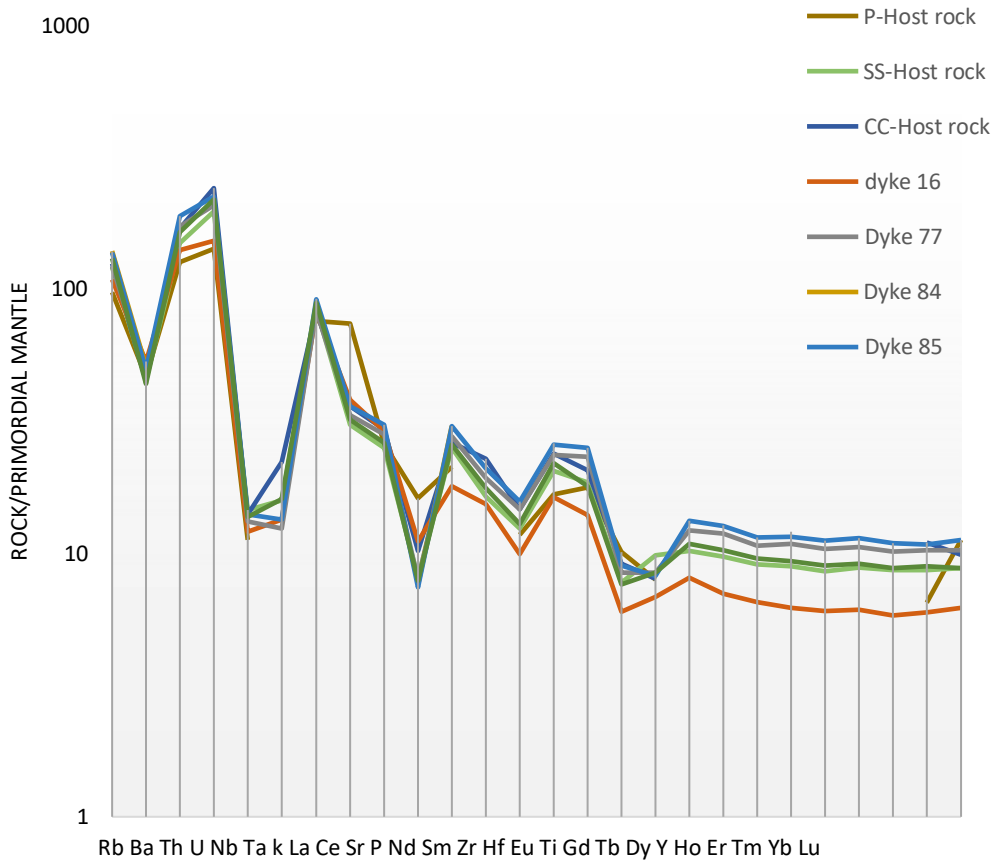

Fig. 3.37: Spider diagram of the REE for andesitic compositions normalised by the primordial mantle. Data from Nicholls (1971); Mann (1983); Huijsmans (1985); Druitt et al. (1999); Zellmer (2000); Bailey et al. (2009); Fabbro et al. (2013, 2014) and this study. The trachyandesitic dykes all show quite similar spiderdiagrams and they overlap with the TDC and Simandiri shields. The

Simandiri shield had latitic compositions while the Peristeria and TDC compositions were benmoreites (Fig. 3.38). The trachytes belonged to the Skaros or TDC shields that fed the Therasia lavas (Fig. 3.38) and the trachydacites belonged to the TDC shield (Fig. 3.39 and 3.40).

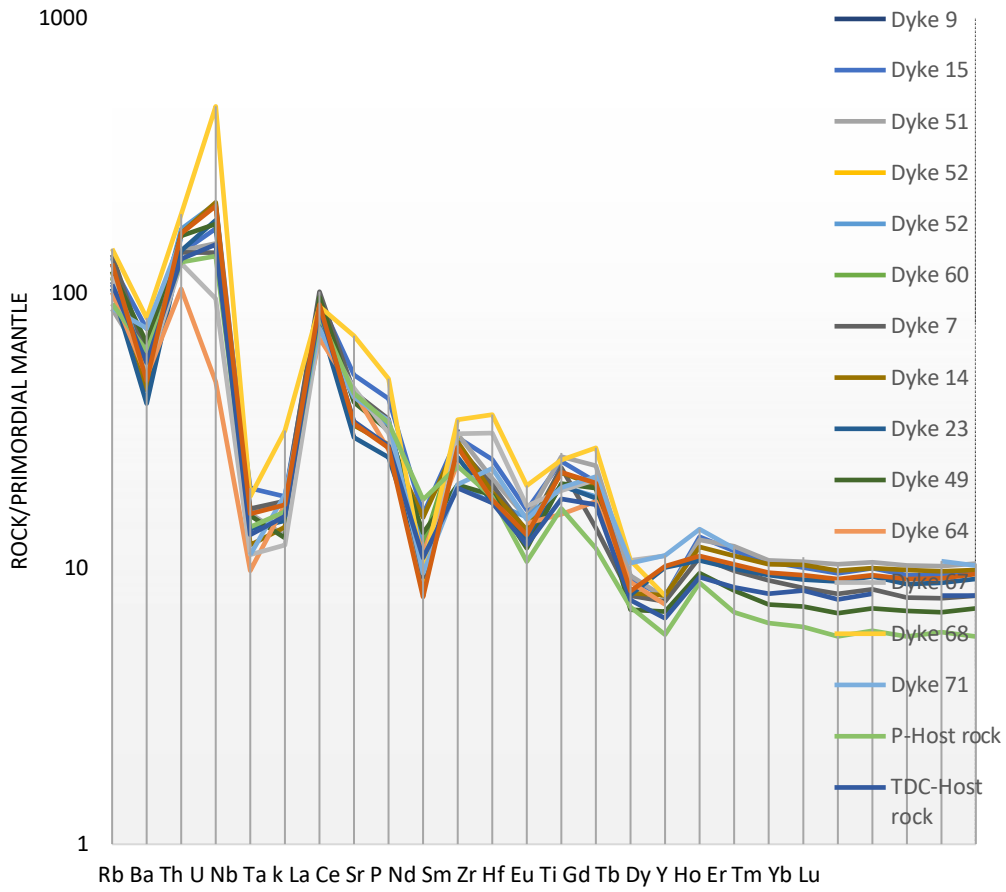

Fig. 3.38: Spiderdiagram of the REE trachyandesitic compositions normalised by the primordial mantle. Data from Nicholls (1971); Mann (1983); Huijsmans (1985); Druitt et al. (1999); Zellmer (2000); Bailey et al. (2009); Fabbro et al. (2013, 2014) and this study.

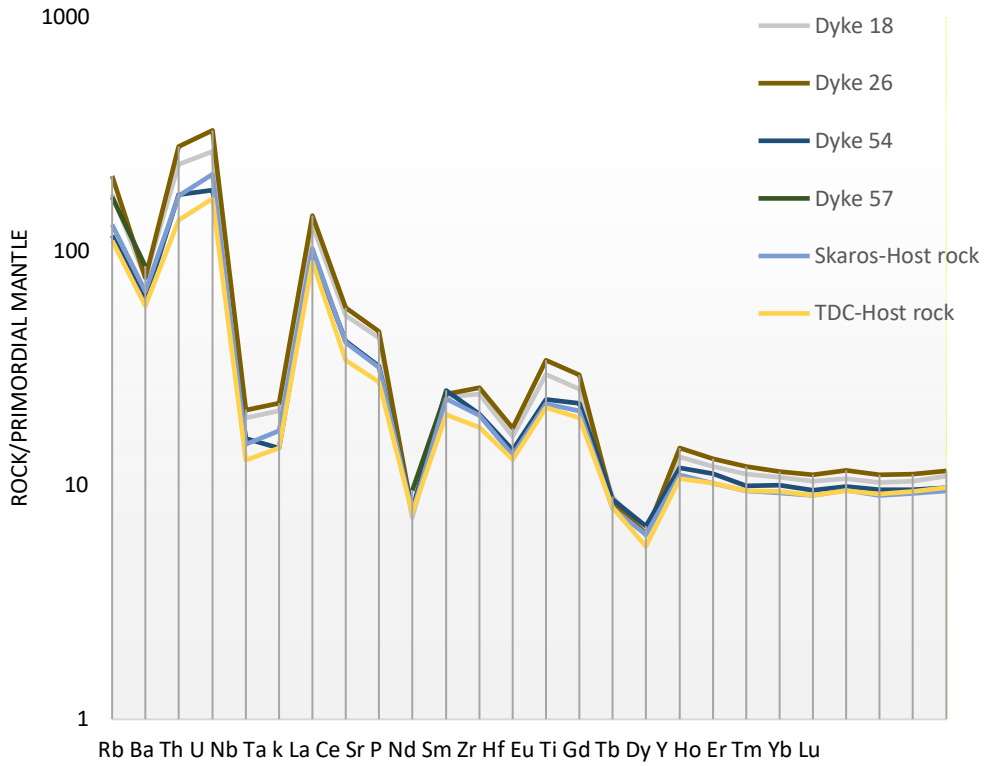

Fig. 3.39: Spiderdiagram of the REE trachytic compositions normalised by the primordial mantle. Data from Nicholls (1971); Mann (1983); Huijsmans(1985); Druitt et al. (1999); Zellmer (2000); Bailey et al. (2009); Fabbro et al. (2013, 2014) and this study.

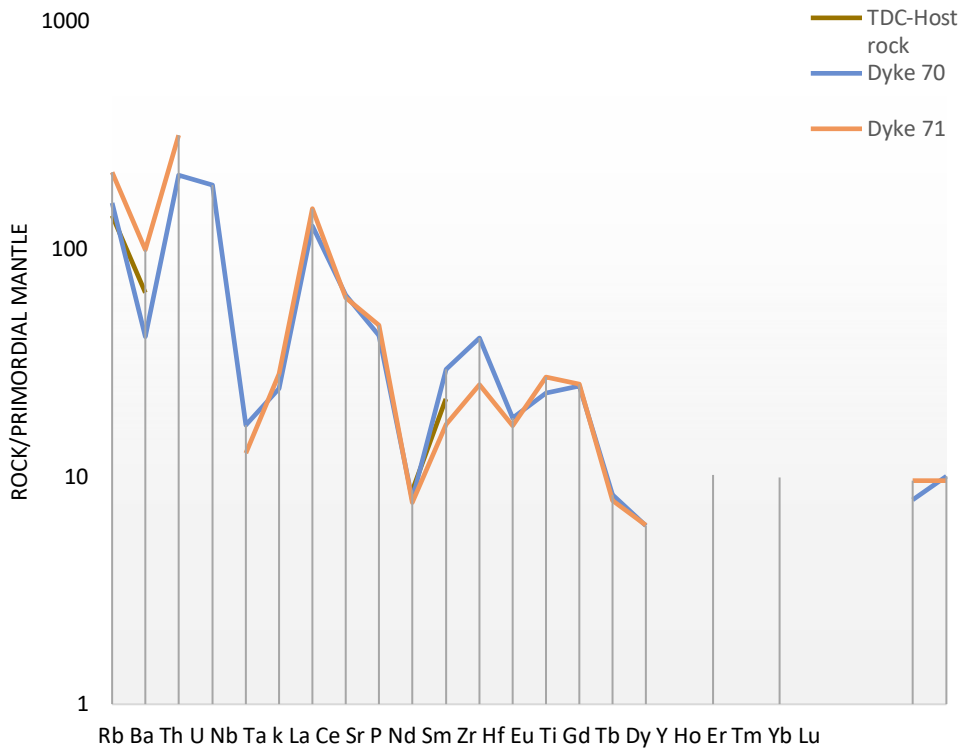

Fig. 3.40: Spiderdiagram of the REE dacitic compositions normalised by the primordial mantle. Data from Nicholls (1971); Mann (1983); Huijsmans (1985); Druitt et al. (1999); Zellmer (2000); Bailey et al. (2009); Fabbro et al. (2013, 2014) and this study.

3.5.5 Geochemical correlations

Previous studies have revealed the existence of two felsic dykes at the southern part of Therasia Island (Fig. 3.41). One of them is suggested to have fed a dacitic lava flow (Fabbro et al., 2013) which has been dated with Ar-Ar dating techniques at 33 ka years (Fabbro et al., 2014). The eruption belongs to the construction of the Therasia dome complex that was interrupted by the Caper Riva eruption and the third caldera collapse event at 21 ka (Druitt et al., 1999).

The whole-rock chemistry of the dacitic Therasia lava flow which was fed by the observed dyke (Fabbro et al., 2013) and assumed to have similar compositions has been compared with the three dacitic dykes emplaced on Mt Mikros Profitis Ilias (MPI) analysed by Nicholls (1971); Mann (1983); Huijsmans (1985). The Therasia dyke has a similar attitude to the MPI dacitic dykes and similar geochemistry as found from an analysed sample by Huijsmans (1985) and no other age constraints (such as cross-cutting relationships or dyke fed volcanism)

To determine the origin of the different magmatic melts, we used incompatible trace elements ratios such as Nb/Zr which are known to only change by source melting but not through fractional crystallisation (Green, 1980). Furthermore, diagrams with ratios of similarly incompatible elements such as Ba/Nb and K/Nb have been conducted to investigate the source conditions as LIL (large iron lithophile) elements should not be changed by melting or fractional crystallisation but instead only reflect changes in the source composition.

The results show both structural and geochemical overlap between the two dykes. This analysis provides us with the reasonable scenario that the Therasia feeder dyke is the south westernmost extent of an MPI dacitic dyke. This interpretation suggests that the dyke mentioned above, which fed the 33-ka lava flow could have had a minimum length of 7.5 km and striked parallel to the Kolumbo volcanotectonic line. The central part of the dyke would have subsequently been eroded by the Cape Riva caldera collapse around 21 ka.

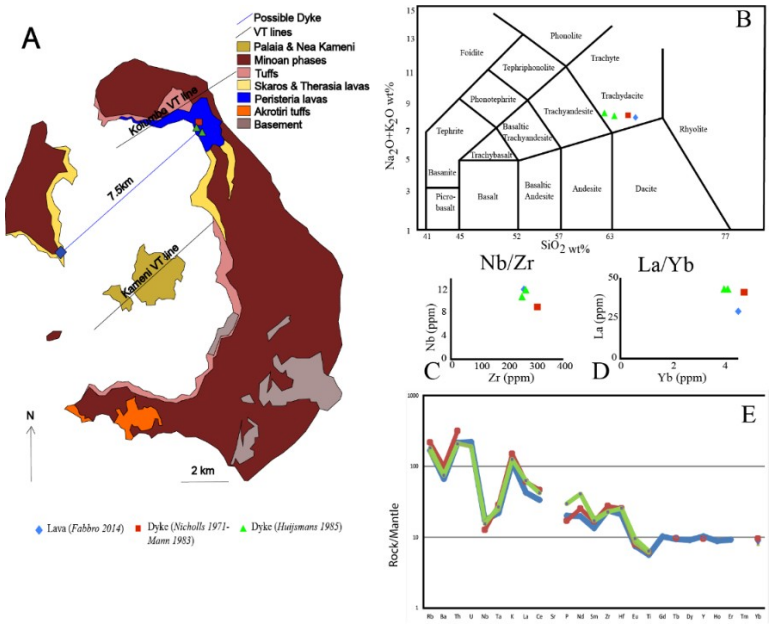

Fig. 3.41: (A) Geological map of Santorini modified from Druitt et al., (1999) showing the Kameni and Kolumbo VT lines, and the location of the studied dykes and the lava samples, (B) TAS classification diagram from Le Bas et al., (1986) showing the dyke and lava samples from Nicholls (1971); Mann (1983); Huijsmans (1985) and Fabbro (2014), (C) Nb/Zr diagram, (D) La/Yb diagram, (E) rock/mantle spiderdiagrams of the aforementioned samples.

3.6 Structural and Petrogenetic results

In this section results from the structural data are correlated with the petrogenetic analysis of the dykes to generate a complete model of the volcanic plumbing system of Santorini. I examined if the attitude of the dykes correlates with the compositions and the different populations.

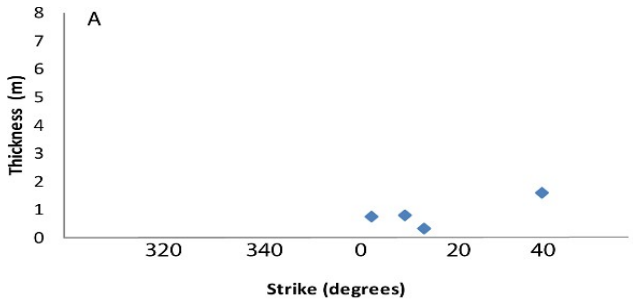

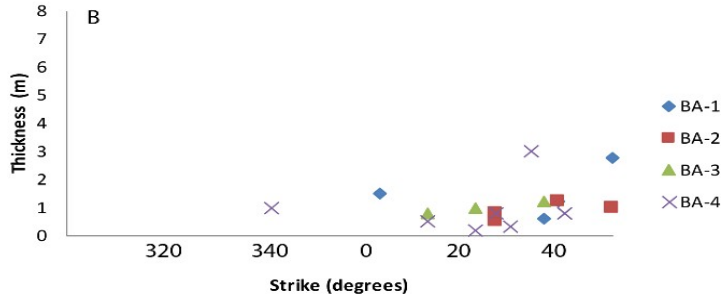

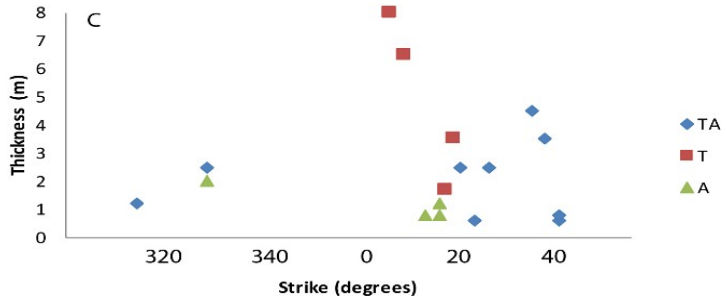

Fig. 3.42: Strike Vs thickness diagrams for (A) Basaltic dykes, (B) Basaltic andesitic dykes, (C) Andesitic, Trachyandesitic and Trachytic dykes.

The basaltic dykes (_6,_21,_76,_79) are found close to the Mt. Megalo Vouno area. These dykes have similar strikes of between 355 and 25 degrees, they all dip towards the east by varying amounts, and have a small range of thicknesses 0.3 m to 1 m) (Fig. 3.42).

The four basaltic andesites dykes (_19,_22,_28,_81,_3,_4,_87,_89,_1,_76b) strike between 340 and 50 degrees, they are usually vertical or dip towards the east by different amounts and their thickness range between 0.1-3m. The intermediate and felsic dykes (A, TA, T) do not show similarities.

The methodology described in section 2.2.7 was used to reconstruct the evolution of the magmatic plumbing system. To recap, the phenocryst textures found in samples from both dykes and the host rock were analysed under the microscope. To do this, the mutual connections between the dykes (Table 3.3), their rims (Table 3.4) and the host rock (Table 3.5) lithologies were considered to understand the individual propagation path of any one of the dykes.

The textural characteristics were separated into five different observations; 1) coarse sieve, 2) Synneusis glomerocrysts with normal zoning, 3) any crystals with resorbed rims and oscillatory zoning with fine sieve textures and

embayments, 4) any crystals with resorbed cores, and 5) Inclusions with shallow tails. Each textural observation is associated with a volcanic plumbing system process along with depth, as follows: 1) is related to early stage, 2) indicates processes occur at or near-equilibrium, 3) relates to mixing or recharging, 4) to decompression and 5) to degassing within the conduit. Many samples exhibited multiple textural characteristics and hence may have also undergone numerous processes in the volcanic plumbing system. To diagnose the multiplicity of those processes, a table was designed that allowed each sample to be listed along with each textural observation made, as shown in Tables 3.3, 3.4 and 3.5. Many samples contain textural characteristics that indicate two or more dominant processes (Fig. 3.43).

For example, Dyke_1 contains textures that reflect all five of the inferred processes. This indicates that the dyke underwent a very long propagation path from a deep-seated reservoir. The dyke passed from at least two magma chambers and recorded a mixing event which rapidly raised the excess pressure in a magma chamber and triggered a new dyke injection. Both the structural and petrogenetic data agree with the petrography because dyke_1 belongs to the TDC shield population of dykes. Dyke_21 probably also propagated through the whole transcrustal system. However, it does not contain any textural characteristics consistent with a decompression triggering event. The dyke may have been triggered by another mechanism rather than a mixing event and is associated with the Simandiri shield. Dykes_4,_76,_79,_80,_81 show

similarities in their textural characteristics and imply a propagation path from a deep-seated reservoir (like dykes_1 and_21) during the Skaros volcanism. Dyke_77 and a xenolith found within the dyke, exhibit the final stage of its propagation path. This implies that the dyke assimilated a lot of material during emplacement. Dyke_49 exhibits textures that suggest it propagated from a shallow chamber which was in near-equilibrium and intruded by a mixing episode. The dyke belongs either to the Peristeria or the Skaros shield. Dyke_6 brought to the surface many mush components; however, the dyke is completely devitrified and may have become arrested during fast cooling. The dyke belongs to the Skaros shield. Dyke_4 belongs to an arrested population that likely coincides with the evolution of the Peristeria stratovolcano (Fig. 3.43).

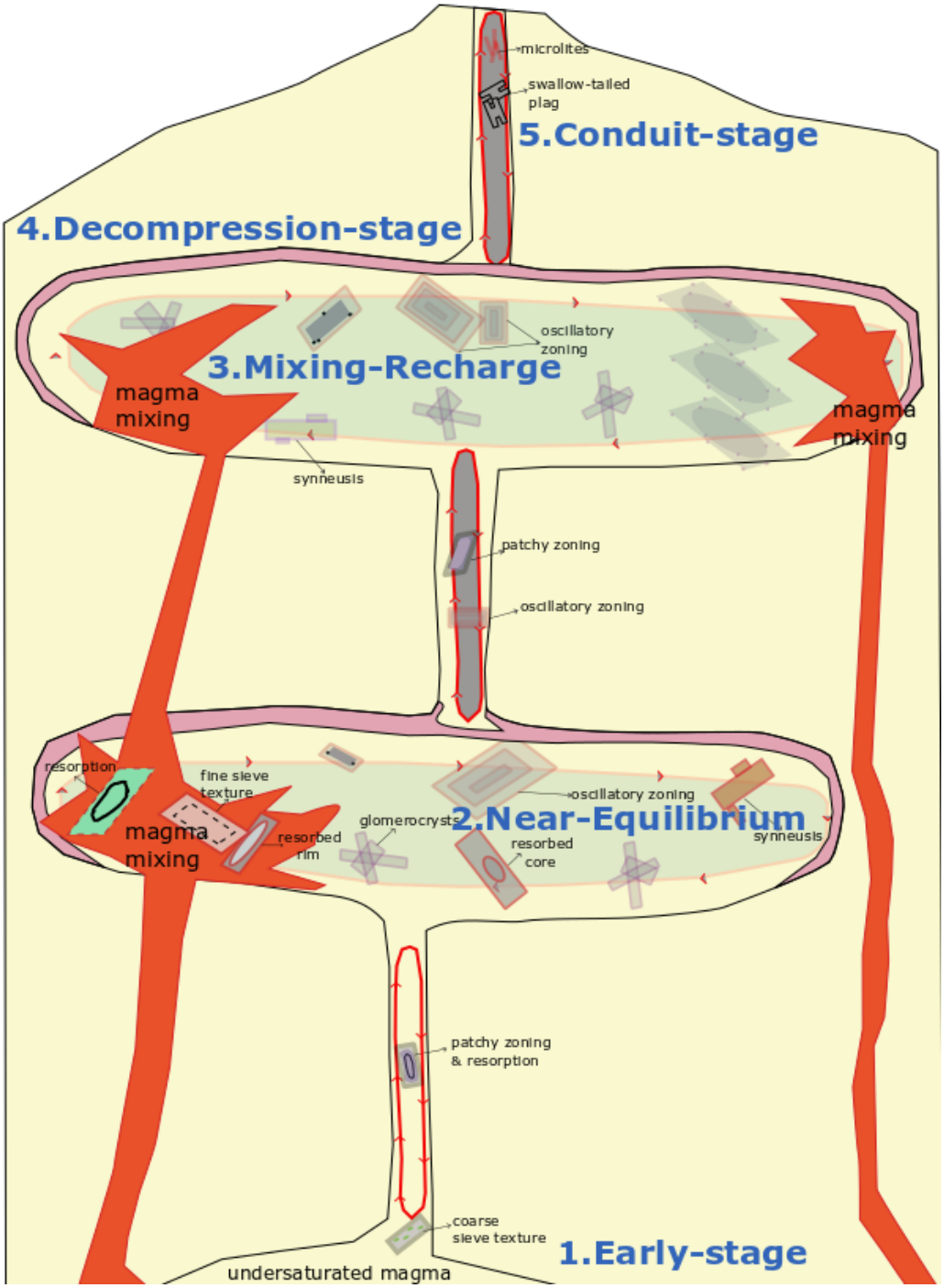

Fig. 3.43: Schematic illustration showing the textural features as discussed before that could be observed on a two-magma chamber volcanic plumbing

system from the source to the surface such as the one hosted on Santorini volcano. Not to scale.

Table 3.3: Textural connections between the host rock phenocrysts from samples 1,4,6,21,76,77,79,80,81,89. Columns and rows denote the stages of a magmatic path at depth. The same colours represent the same observed probabilities. The last line on the left hand colour (Unique textures) represents single textures that were found individually in phenocrysts.

		Early stages	**Near-equilibrium**	**Mixing/Recharge**	**Decompression**	**Degassing/ conduit**
		Coarse sieve	Synneusis Glomerocrysts Normal zoning	Resorbed rim Oscillatory zoning Fine sieve texture Embayment	Resorbed core	Swallow-tail Inclusions
Early stages	Coarse sieve		1, 21, 76b	1,4,6,21,76b,77	1,4,76a,76b	1,2177x, 81
Near-equilibrium	Synneusis Glomerocrysts Normal zoning	4,6,76a,77,77x		6		4,6,77,77x
Mixing/ Recharge	Resorbed rim Oscillatory zoning Fine sieve texture Embayment	21,76a	1,21,49,76a,77,77x,79,80,81,89		76a,76b,79,81	77x,79
Decompression	Resorbed core		80,81,89			
Degassing/ conduit	Swallow-tail Inclusions					
	Unique textures	1,21,79	4,6,49,76a,80,81,89	1,21,79,80,81		

Textural analysis of the dyke rims, which contain enclaves of scoria, show that the scoria in the rims is similar to the deposits found within the cinder cones of Megalo Vouno and Kokkino Vouno (Table 3.5). The host rock data suggests that the Akrotiri basalts were stored in a deep-seated magma chamber which was at near-equilibrium conditions. The Skaros deposits instead originated from a deep reservoir and passed through both magma chambers (Druitt et al., 1999). The Minoan ignimbrite was produced from a shallow chamber that indicates a mixing event (Table 3.5).

Table 3.4: Textural connections between the host rock phenocrysts from samples 21,76,77,81,89. Columns and rows denote the stages of a magmatic path at depth. The same colours represent the same observed probabilities. The last line on the left hand colour (Unique textures) represents textures that were found individually in phenocrysts.

		Early stages	**Near-equilibrium**	**Mixing/Recharge**	**Decompression**	**Degassing/ conduit**
		Coarse sieve	Synneusis Glomerocrysts Normal zoning	Resorbed rim Oscillatory zoning Fine sieve texture Embayment	Resorbed core	Swallow-tail Inclusions
Early stages	Coarse sieve		21,89	21,76a,76b,77	21,76a,76b	21,77,81
Near-equilibrium	Synneusis Glomerocrysts Normal zoning	76a,76b		77		77
Mixing/ Recharge	Resorbed rim Oscillatory zoning Fine sieve texture Embayment	77	21,76a,76b, 81		81	
Decompression	Resorbed core	77	81			
Degassing/ conduit	Swallow-tail Inclusions	21	76a,76b	21		
	Unique textures	21	77,81,89	21,76b, 81	76b	

Table 3.5: Textural connections between the host rock phenocrysts from samples Scr, As2, Akr, Rp7. Columns and rows denote the stages of a magmatic path at depth. The same colours represent the same observed probabilities. The last line on the left hand colour (Unique textures) represents textures that were found individually in phenocrysts.

		Early stages	**Near-equilibrium**	**Mixing/Recharge**	**Decompression**	**Degassing/ conduit**
		Coarse sieve	Synneusis Glomerocrysts Normal zoning	Resorbed rim Oscillatory zoning Fine sieve texture Embayment	Resorbed core	Swallow-tail Inclusions
Early stages	Coarse sieve		Akr, As2, Scr			
Near-equilibrium	Synneusis Glomerocrysts Normal zoning	As2, Rp7				As2
Mixing/ Recharge	Resorbed rim Oscillatory zoning Fine sieve texture Embayment	As2, Rp7	As2, Rp7, Scr			
Decompression	Resorbed core	As2, Rp7	As2, Rp7, Scr		As2, Rp7	
Degassing/ conduit	Swallow-tail Inclusions					
	Unique textures		Akr			

Figure 3.44 presents a reconstruction of the magmatic plumbing system. The results interpretation can be summarised as follows:

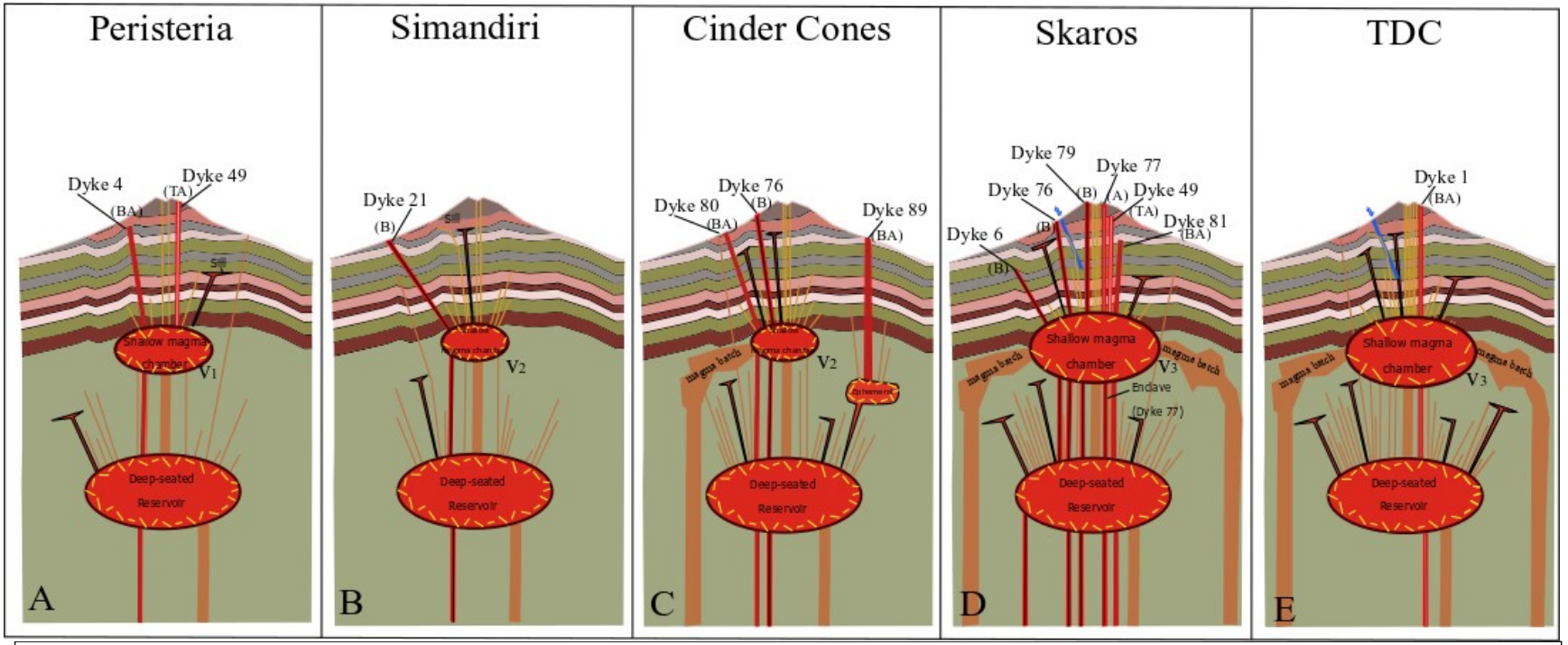

Fig. 3.44: Illustration showing the evolution of the northern caldera wall plumbing system discerned from this multidisciplinary study. View of the plumbing system during the formation of (A) Peristeria stratovolcano, (B) Simandiri shield, (C) Cinder cones of the northern caldera wall, (D) Skaros shield, (E) TDC shield. Not to scale

The northern caldera wall plumbing system was evolving through time, both horizontally and laterally as described in Figure 3.44. The volume of the shallow magma chamber was also changing throughout this time. This is evident from the number of dykes and deposits that belonged to the Peristeria, Skaros and TDC volcanic centres (Fig. 3.44 A, D, E). On the contrary, the Simandiri and Cinder cones (Fig. 44 B, C) likely reflect a smaller chamber volume as both the number of dykes and the number of subaerial deposits associated to these eruptions are limited (Druitt et al., 1999).

The plumbing system likely consisted of two magma chambers, as proposed by Druitt et al. 1999. The deep-seated reservoir injects mafic dykes (mantle material), and the upper chamber produces fractionated felsic dykes which feed the most evolved products of the island. However, evolved material has also produced hybrid magmas through mixing and mingling processes (Fabbro et al., 2014). The cinder cone plumbing system was likely somewhat different with eruptions sourced from a shallow residing mafic sill that injected dykes which were arrested during their emplacement. Dykes_87 and_89 derived from this sill and the reason for their arrest was likely an insufficient amount of overpressure and magma volume.

The Peristeria, Skaros and TDC shields have significant geochemical similarities. For that reason, the dyke populations associated with these eruptive centres could only be delimited by their relative location in the sequence.

Chapter 4

Manuscript in preparation for journal submission

Dyke-arrest scenarios in extensional regimes: insights from field observations and numerical models, Santorini, Greece

Statement of contribution:

Collection of primary field data and geological mapping done by KD

All field photographs and figures designed by KD

Complete 1st draft of manuscript and figures by KD

Revisions and subsequent drafts made with co-authors input

Interpretation of all data along with final model conducted by KD with support from co-authors

Dyke-arrest scenarios in extensional regimes: insights from field observations and numerical models, Santorini, Greece

Kyriaki Drymoni[a*], John Browning[b, c], Agust Gudmundsson[a]

[a]Department of Earth Sciences, Queen's Building, Royal Holloway University of London, Egham, Surrey TW20 0EX, UK

[b]Department of Mining Engineering and Department of Structural and Geotechnical Engineering, Pontificia Universidad Católica de Chile, Santiago, Chile

[C]Andean Geothermal Centre of Excellence (CEGA), Santiago, Chile

* Corresponding author

E-mail address: Kyriaki.Drymoni.2015@live.rhul.ac.uk

Abstract

During a volcanic unrest period with magma-chamber rupture, fluid-driven fractures (dykes) are injected either from deep reservoirs or shallow magma chambers. Subsequently, the dykes follow propagation paths towards the surface, some eventually reaching the surface to erupt while others become arrested. Here we study dyke paths resulting in eruption or arrest in an excellent 5-km wide exposure of the northern caldera wall of the Santorini volcano in Greece. Mapping of more than 90 dyke segments shows that they were emplaced in a host rock consisting of layers (of breccia, tuff, scoria, and lava) with a wide variety of mechanical properties. At the contacts, some dykes are arrested or deflected and hence change their propagation paths. Here we combine the field data with numerical models to explore dyke paths resulting in (1) arrest and (2) eruption. We

investigate the effect of different host-rock mechanical properties, magmatic overpressures, and tectonic loading on dyke paths. We find that layers with unfavorable local stresses for dyke propagation, namely stress barriers, result from layer stiffness (Young's modulus) contrast and thickness variations and are a common cause of dyke arrest. The study also shows how the details of the dyke path, and eventually dyke-fed eruptions, depend on the mechanical layering and local stresses in volcanoes. The results are of great importance for understanding dyke-propagation paths, and the likelihood of eruption, during unrest periods, particularly in stratovolcanoes fed by shallow chambers, such as Santorini.

KEYWORDS: dyke arrest, dyke propagation paths, Santorini Volcano, field studies, numerical modelling, mechanical layering

1. Introduction

Volcanic eruptions are typically fed by magma-filed fractures, dykes, many of which become arrested while others feed eruptions. Dykes have a variety of orientations or attitudes which relate to the local stresses controlling their formation (Anderson, 1951; Rubin and Pollard, 1987; Rubin, 1995; Dahm, 2000; Gudmundsson, 2002, 2006; Burchardt, 2008; Tibaldi, 2015). To feed the eruption in the upper or top part of a volcanic edifice that stands high above its surroundings the feeder dyke must propagate vertically for at least part of its path. Many flank eruptions, by contrast, may be partly or entirely fed by laterally propagating dykes as is often the case at Etna volcano (e.g. Acocella and Neri, 2003; Scudero et al., 2019). As vertically propagating dykes approach the surface they may become arrested, some being deflected into sills (Pollard and Johnson, 1973; Geshi et al. 2010; Gudmundsson, 2011a; Barnett and Gudmundsson, 2014). Some dykes eventually

reach the surface to erupt. There, is however, presently no way of predicting whether a dyke injected during an unrest period will reach the surface to feed an eruption or become arrested in the crust.

Part of the reason that this is a remaining problem in volcanology is due to the ascent path of the magma being commonly through highly anisotropic and heterogeneous crustal segments (Gudmundsson, 2011a). Field observations suggest that as little as 10-20% of dykes become feeders in stratovolcanoes (higher percentage in basaltic edifices) which are by nature highly heterogeneous (Gudmundsson et al., 1999; Gudmundsson and Brenner, 2005; Gudmundsson, 2011a). Previous studies (Lister and Kerr, 1991; Gudmundsson, 2002, 2011a; Rivalta, 2005; Kavanagh et al., 2006; Rivalta et al., 2015; Kavanagh et al., 2017; Townsend et al., 2017) have provided insights into the mechanisms that control dyke propagation and hence ultimately govern the likelihood of an eruption. Among suggested factors affecting dyke propagation are magma overpressure (Gudmundsson, 2011a,b), heat exchange between the magma and host rock (Rubin, 1995), the local stress field ahead of the dyke (Dahm, 2000), volatiles within the magma (Cashman, 2004), density and/or buoyancy (Taisne and Jaupart, 2009), the ambient deviatoric stress (Pinel and Jaupart, 2004), pre-existing crustal weaknesses (Le Corvec et al. 2013, 2018; Browning and Gudmundsson, 2015), and crustal heterogeneity and anisotropy, which, in turn, partly control local stresses (Gudmundsson, 2011a).

In this paper we address the mechanical conditions that affect dyke-propagation paths, in particular arrest, in stratovolcanoes, using the examples of dykes in the Santorini Volcano. The main focus is on the effect of crustal layering and discontinuities between dissimilar mechanical layers on dyke propagation. We use the Finite-Element Method (FEM) through the software COMSOL

Multiphysics together with data from field observations. We build model setups with realistic structural settings (attitude, thickness, host rock stratigraphy) and use calculated or literature-derived field mechanical properties (overpressure, stiffness) to gain insights into dyke propagation and arrest on Santorini volcano for the first time. The primary goal of the numerical models is to replicate the observed field structures and processes and define the likely mechanical conditions during the formation of the observed dyke path. To do this we made several model scenarios with varying magmatic overpressure for two dykes (Dyke 1 and Dyke 2) and loading conditions. In addition, we performed two suites of sensitivity tests. The first one investigated how the hostrock material properties (thickness and stiffness of the layers) and the stratigraphy (the sequence of layers) associated with variable magmatic overpressure promote stress rotations that affect dyke paths. The second suite studied explicitly the relationship between the regional stress field and the varying magmatic overpressure during the formation of the Santorini dyke swarm.

2. Mechanisms of dyke propagation and arrest – previous work

Before we describe the local geology of Santorini and the dykes themselves, we give a brief overview of the current understanding of the conditions for dyke propagation and arrest. This we do so as to put the geological information, provided in later sections, into the framework of mechanics of dyke propagation in layered rocks.

Dyke arrest is common in stratovolcanoes as the layers which make up a volcano are of widely different mechanical properties (particularly as regards Young's modulus/stiffness) which promote abrupt changes in the local stress field (Gudmundsson, 2003, 2011a,b). Analytical studies

(Hutchinson, 1996) and field observations (Gudmundsson, 2011a) show that when a vertical extension fracture such as a dyke meets a horizontal discontinuity such as a contact between dissimilar layers, the extension fracture/dyke may (1) penetrate the contact, and continue its vertical propagation, (2) become arrested at the contact, or (3) become deflected or offset, and so change its path or form a sill.

Analogue and numerical modelling indicate that when a dyke passes from a soft layer to a stiff layer, the dyke commonly becomes deflected into a sill, or it can become arrested (Kavanagh et al. 2006, 2018; Gudmundsson, 2011a,b). Conversely, if a dyke passes from a stiff layer to a soft layer, then it is more likely to continue its propagation towards the surface.

The basic criterion for extension (mode I) fracture propagation derives from the work of Griffith (1921, 1924), which is partly based on stress-field calculations made by Inglis (1913). In modern notation, the criterion states that for the fracture/dyke to propagate the elastic energy release rate G should be at least equal to (or exceed) the critical energy release rate, namely the material toughness, G_{IC}, which is the energy absorbed during the fracture propagation, primarily through the formation of the fracture surfaces (dyke walls). The criterion may be stated as (Broek, 1982; Gudmundsson, 2011b):

$$G = \frac{\pi \sigma_c^2 a}{E} \geq G_{Ic} \tag{4.1}$$

$$\sigma_c = \sqrt{\frac{EG_{Ic}}{\pi a}} \tag{4.2}$$

where a is half the crack length (total length for an edge crack), E is Young's modulus, and σ_c is the failure tensile stress at the tip. Accordingly, an extension fracture/dyke propagates when sufficient energy (G) is available (released or transformed) to rupture the rock and form the fracture surfaces/walls. For dyke propagation this energy is mostly elastic energy (strain energy) stored in the volcano during unrest-related inflation (Gudmundsson, 2012).

There are three primary mechanisms related to mechanical layering that control dyke propagation and arrest (Gudmundsson, 2011a,b). These mechanisms apply to extension fractures (mode I cracks) in general but are here applied to dykes. These mechanisms are stress barriers, elastic mismatch, and Cook-Gordon delamination (cf. Gudmundsson, 2011a,b) and are described below (Fig. 4.1).

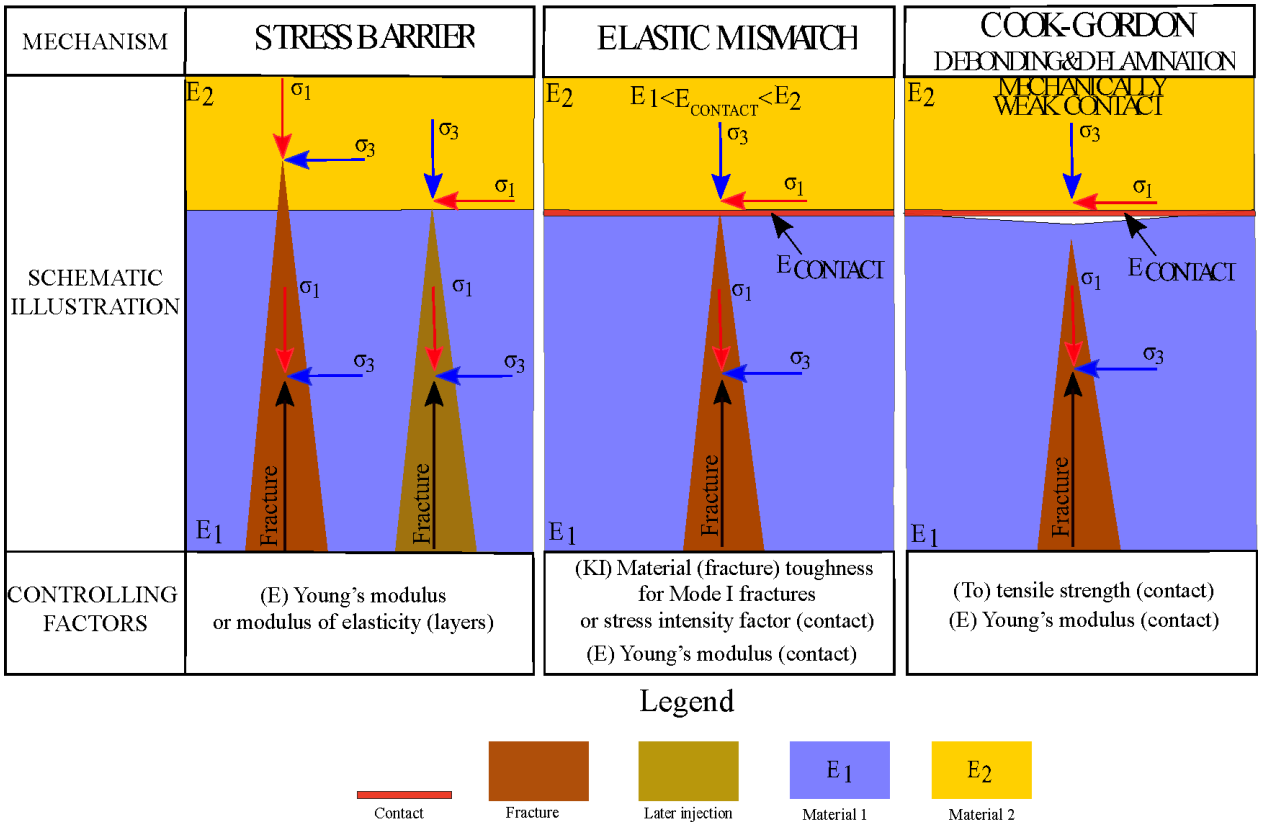

Fig. 4.1: Schematic illustration of the three primary mechanisms (Stress barriers, Elastic mismatch and Cook-Gordon debonding and delamination) that control fluid-driven fracture arrest. In part C the weak contact delaminates and opens ahead of the progressing fracture tip. The controlling factors of each mechanism are shown at the bottom.

2.1 Stress barriers

Rotation of the principal stresses is common at the contacts between rock layers of dissimilar stiffness. Dykes are predominantly extension fractures/mode I cracks and so normally propagate in the direction of/parallel with the maximum principal stress (σ_1). When the principal stress orientations rotate at a contact, then the dyke propagation path will change accordingly. Vertical

propagation can occur only if the maximum principal compressive stress σ_1 is vertical (and the minimum principal compressive stress σ_3 is horizontal), so that if σ_1 rotates to become horizontal at the contact (and σ_3 thus vertical), the vertical dyke propagation will stop. The dyke then either becomes arrested on meeting the contact or becomes deflected into a sill along the contact.

Both stiff and soft (high and low Young's modulus) layers can act as stress barriers (Gudmundsson and Phillip, 2006; Gudmundsson, 2011a). For example, a stiff layer can become a stress barrier subject to horizontal compression which may happened following normal faulting, particularly graben subsidence, or during multiple dyke injections where the magmatic overpressure of the previous injections (Geshi et al., 2010) may have generated horizontal compression in the adjacent stiff layers. Many studies show that earlier dyke intrusions or graben formation generate horizontal compression, thereby temporary stress barriers (Gudmundsson, 2008; Menand et al., 2010). Similarly, compliant layers can become temporary stress barriers for vertical dykes when the loading is horizontal tension (Gudmundsson and Brenner, 2001).

2.2 Elastic mismatch

In a heterogeneous and anisotropic material, the presence of interfaces with different mechanical properties may encourage-propagation along the interface in a mixed fracture mode (Garcia, 2014). In geology, interfaces are primarily contacts, fractures, and other discontinuities. When there is large contrast in stiffness across a contact/interface and the energy release rate (G_I) during extension fracture/dyke propagation reaches the material toughness of the interface/discontinuity then the dyke can become deflected into the discontinuity and propagate as a mixed-mode fracture (I and II) (Hutchinson, 1996; Xu et al., 2003). The mechanical properties of the discontinuities

depend on the Dundurs elastic mismatch parameters α (Dundurs, 1969; He et al., 1994) that partly define the conditions for dyke penetration of, or deflection into, the discontinuity. These findings are supported both by analogue (Kavanagh et al., 2017) and rock deformation experiments (Forbes-Inskip et al., 2018).

2.3 Cook-Gordon delamination

Observations from experiments and analytical calculations show that the contact between layers can both debond and delaminate in composite materials (Cook and Gordon, 1964; Wang and Xu, 2006). This process occurs when the tensile stress at the tip of a propagating extension fracture is sufficiently high so as to open the contact ahead. This mechanism applies also to layered rocks and is common during dyke-fed sill emplacement at shallow depths (Gudmundsson, 2011a; Barnett and Gudmundsson, 2014).

A dyke will open a contact ahead of its tip when the dyke-parallel tensile stress is large enough to overcome the tensile strength (T_o) of the contact. The dyke-parallel tensile stress is about 20% of the dyke-perpendicular tensile stress at the tip of the dyke (Freund and Suresh, 2003; Gudmundsson, 2011a). The tensile strength of a contact, particularly in an active volcano or volcanic zone, is often very low – close to zero – and thus easily opened, particularly at shallow depths. This mechanism has been studied in volcanic environments using numerical models (Gudmundsson, 2003) with a specific focus on shallow depths and stiff contacts (basaltic lavas) but is also well known as a major fracture-arrest mechanism in composite materials (Xu et al., 2003; Wang and Xu, 2006; Garcia, 2014).

3. Regional field setting

3.1 Geological setting

We now turn to the geology of the Santorini Volcano, within which the dykes discussed here are located. Santorini is a Quaternary central volcano, a volcanic complex, and part of the South Aegean Volcanic Arc in Greece. The volcanic complex formed in a trans-tensional regime and has been influenced by the oblique subduction and accelerated slab rollback (Brun et al., 2017) of the African tectonic plate underneath the Aegean tectonic plate (Le Pichon and Angelier, 1979). Sinistral and dextral strike-slip zones as well as other extensional structures (faults and grabens) (Sakellariou et al., 2013) have operated since the Miocene (Grasemann et al., 2012).

The orientation of the sub-horizontal minimum compressive stress (σ_3) is N135º E (N45°W), and the level of the deviatoric regional stress tensor (deviation from the mean stress, here the lithostatic state of stress) associated with an unrest period in 2011-12 has been estimated at around 3 MPa (Feuillet, 2013). The Coulomb stress in the region increased by up to 0.5 MPa during this period, as the magma chamber received new magma and inflated (Parks et al., 2012). Although there was an increase in magma chamber pressure, the shallow chamber did not rupture or form a dyke (Browning et al., 2015).

Santorini volcano has experienced many eruptive cycles, at least four caldera collapse events, and remains active (Druitt and Francaviglia, 1992; Druitt et al., 1999). The past Plinian and sub-Plinian volcanic activity formed a complex pile of stratigraphic horizons. There have been two explosive cycles with at least 12 pyroclastic eruptions and dyke fed eruptions that produced lava shields and lava domes (Druitt et al., 1999). The volcano hosts a magmatic plumbing system whose magmas are the result of many processes such as mantle wedge partial melting, fractional crystallisation,

magma mingling, mixing and crustal assimilation (Zellmer, 1999; Druitt et al., 1999; Andujar et al., 2015).

3.2 Santorini northern caldera wall

In this study, we focus on the eroded dyke swarm in the northern caldera wall of the central part of the island of Santorini between the villages of Oia (west) and Imerovigli (east) (Fouque, 1879; Nicholls, 1971; Puchelt, 1990; Browning et al., 2015). In Figure 4.2 we present a simplified geological map of the island showing the main units discussed here. The dykes are emplaced in a highly heterogeneous and anisotropic host rock that belongs mainly to the oldest composite stratocone, the remnants of the Peristeria volcano, which was constructed between 530 and 430 ka (Druitt et al., 1999). The Peristeria volcano is composed primarily of andesitic lava flows, but also of basaltic and silicic lava flows, tuffs, breccias (hyaloclastites) (av1-av3) (Druitt et al., 1999). Several dykes cut through middle tuffs (ap4, 125-80 ka) and thick scoria fall deposits (ap4a-c). The Cape Riva caldera collapse structure (~21ka) formed after the construction of the Skaros shield (54 ka) and the Therasia dome complex (25 ka). Both the latter erupted andesitic and basaltic lavas, as well as thick, spatter agglomerates (as2, ap5, and ao) (Druitt et al., 1999).

The dykes do not penetrate the eruptive materials of either the 1st explosive cycle (ra, ap2, rp3) which are mainly rhyodacites (224-72 ka), or the much later Minoan fall deposits (21-3.6 ka). The caldera collapse events, and other erosional processes have exposed the stratigraphic layers, contacts and dykes, allowing them to be examined in considerable detail.

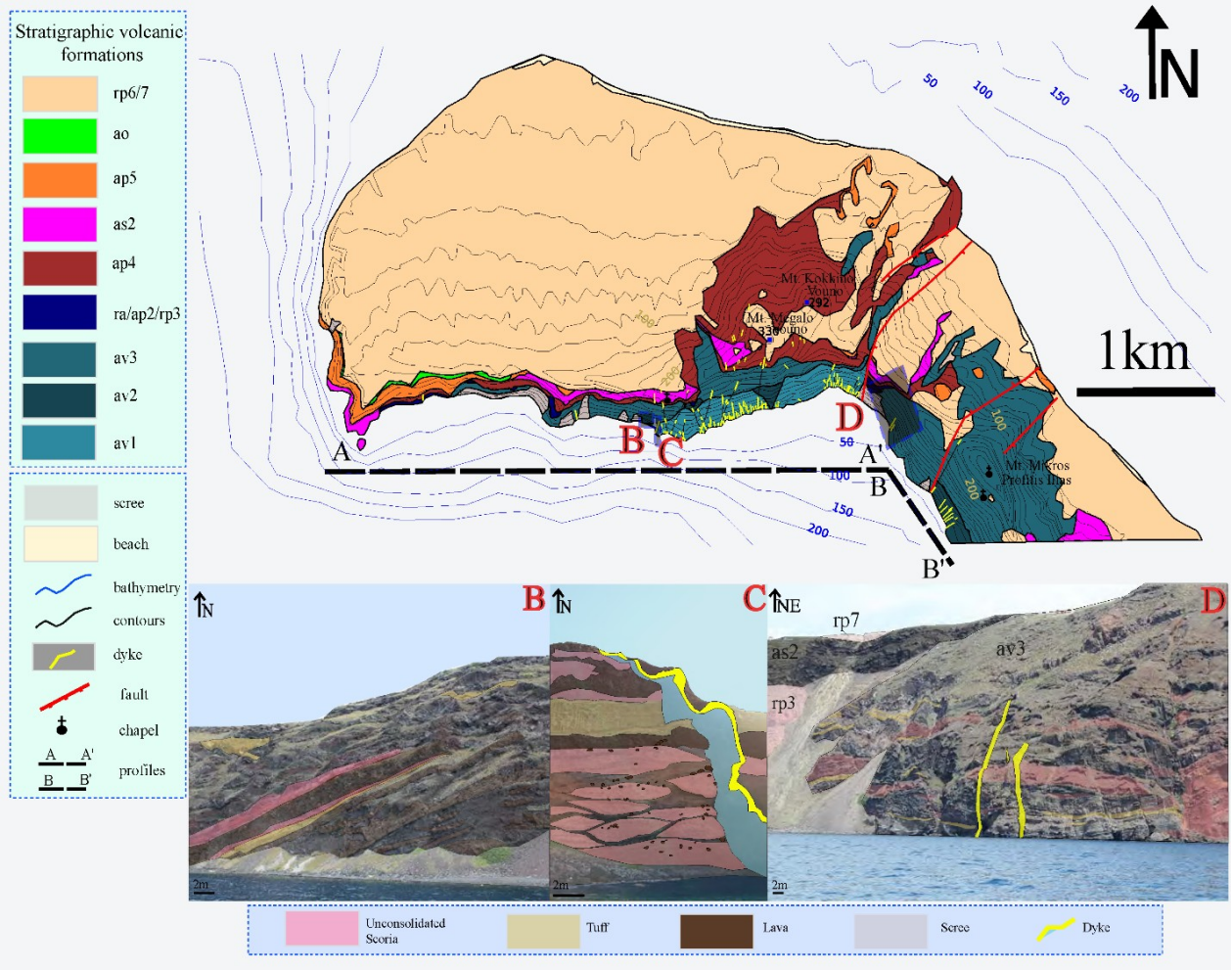

Fig. 4.2: (A) Geological map of the northern caldera wall modified from Druitt et al. (1999), showing the location of the dyke swarm. The key on the left shows the lithologies found on the northern caldera wall (Druitt et al., 1999). Av1: andesitic lavas, tuffs, scoria and breccia, av2: silicic andesitic lavas, av3: thinly bedded andesites and basalts with subordinate dacites, tuffs and scoria, ra: rhyodacites, ap2: pink sillar facies of a pyroclastic density current and red spatter agglomerate with abundant plutonic nodules, rp3: rhyodacitic pumice, ap4: middle tuffs thick scoria-fall deposits, as2:andesites and basalts of Cape Skaros, ap5: upper scoria 2- andesitic thick spatter agglomerate, ao: andesites of Oia, rp6: Cape Riva tuff, rp7: Minoan tuff. Cross sections along the caldera profile: (B) panorama of the northern caldera wall, the av3 horizon, annotations

mark the horizons of andesitic lavas, tuffs and scoria, (C) a dyke that cuts through a heterogeneous segment which exhibits anastomosing textures at the base, annotations mark the horizons of andesitic lavas, tuff and scoria (D) panorama close to the NE corner of the caldera wall, the dykes were arrested or deflected within different layers (and hence at different depths) in the heterogeneous host rock, which is comprised of tuffs, scoria and lavas.

4. Material properties and methods

4.1 Material properties

The observed dykes propagate through layers with different Young's moduli (E). Young's modulus generally increases with depth in the crust but decreases with increasing host rock porosity, temperature, weathering, and fracture damage (Ray et al., 2006). It is worth noting that E values that are derived from static laboratory measurements are often significantly higher than the ones measured in-situ (Gudmundsson, 1988; Bell, 2000) and the difference between the two measurements can be as much as 20-65% (Ray et al., 2006). E values generally range between 10-40 GPa for basement rocks (Gudmundsson, 2011b) and between 1-15 GPa for shallow crustal rocks (Ray et al., 2006; Becerril et al., 2013), although in active volcanic areas layers of pyroclastics and sediments may have E values as low as 0.1 GPa or, occasionally, 0.01 GPa (Heap et al., 2019).

For the modelling setups, we used realistic material properties (cf. (Gudmundsson, 2011a,b). For compliant materials such as tuffs, unconsolidated scoria and breccia (hyaloclastites) we used the values of 5 GPa, 0.08-0.5 GPa and 0.1 – 8 GPa. For stiff materials, such lava flows we used the

values of 10 GPa. We gave all the rocks a constant Poisson's ratio of 0.25 (Babiker and Gudmundsson, 2004) and density values of ρL=2600 kg/m^3 for the lava flows and ρT= 2000 kg/m^3 for the tuff and scoria layers. For all the models we used the stiffness ratio contrasts of the studied contacts which were defined as the dimensionless ratio (r) E_U/E_L where E_U is the Young's modulus of the upper layer and E_L is the Young's modulus of the lower layer.

4.2 Field methods

We carried out field campaigns at Santorini volcano and mapped sections of the northern caldera wall with a specific focus on the dyke swarm, as well as the associated lavas and eruptive units. The dyke swarm in the area extends through two profiles, profile 1) A-A' which is 4 km long and profile 2) B-B' which is 1.5 km long (Fig. 4.2). The profiles were studied both offshore (from a boat) and onshore. The location (longitude/latitude), attitude, thickness (width) of each dyke was recorded as well as host rock lithologies, observed dyke paths, cross-cutting relationships, and exposed length (where possible).

4.3 Numerical modelling methods

The numerical models were made using the finite element method (FEM) program COMSOL Multiphysics (v5.2). The Structural Mechanics module allows the analysis of static stresses and strains resulting from a set of imposed boundary conditions and solid-mechanical properties. Dynamic boundary loads can be simulated by altering both the magnitude and orientation of loads and hence simulate 2D deformation processes of fractures and rock units with geometrical complexity.

In our numerical models we assign different levels of Young's modulus (stiffness) to a series of mechanical units based on the field observations. The differences in Young's moduli between units generates elastic mismatch. We consider the assigned amount of mismatch and plot the resulting stress distribution (contour surface) and principal stress orientation (arrow surfaces) to assess how the level of mismatch alters the crustal stresses and influences fracture propagation. As we are interested in dyke propagation, we plot the concentration of tensile stresses at the dyke tips. It is now well known that the range of tensile stress should be between 0.5 to 9 MPa (Amadei and Stephansson, 1997; Gudmundsson, 2011b) for the fracture to grow or propagate. Hence, a criterion (Dundurs, 1969; He et al., 1994; Gudmundsson, 2011b) between the elastic mismatch between layers and the amount of stress can be generated and this is what is evaluated from the models which in turn reflect the field observations.

4.3.1 General model setup

The 2D models were designed to investigate how the orientation and magnitude of stresses change as a dyke propagates through mechanically dissimilar layers and also what effect a regional extension has at the distribution of stresses. The modelling procedure is as follows. Initially, we imported the geometries of the observed geological structures into the models. Each dyke was modelled as an elliptical cavity with internal overpressure. Each layer of the models was assigned material properties (Young's modulus, Poisson's ratio, and density) and boundary loading conditions on the horizontal edges to simulate extension. For all the models we kept the lower boundary fixed while the upper boundary is a free surface (i.e. a surface free from shear stress and constraints). We generated a triangular mesh of maximum nodal lengths <0.306 m and checked to

ensure that the modelled area of interest was sufficiently far from the model edges so as not to be contaminated by edge effects.

4.3.2 Baseline model setup

In Figure 4.3 we present the setup for a suite of baseline models used to test to later models that simulated more complex geometry. In the baseline model (Fig. 4.3A), we simulated a dyke with 5 MPa overpressure in a homogenous crustal segment. In Figure 4.3B the model geometry is identical but with an added extra layer atop with a Young's modulus of 10GPa. In Figures 4.3C and 4.3D we show the same baseline models as in Figs. 4.3A, B but add an additional horizontal loading extension of 0.5MPa to simulate an extensional stress field.

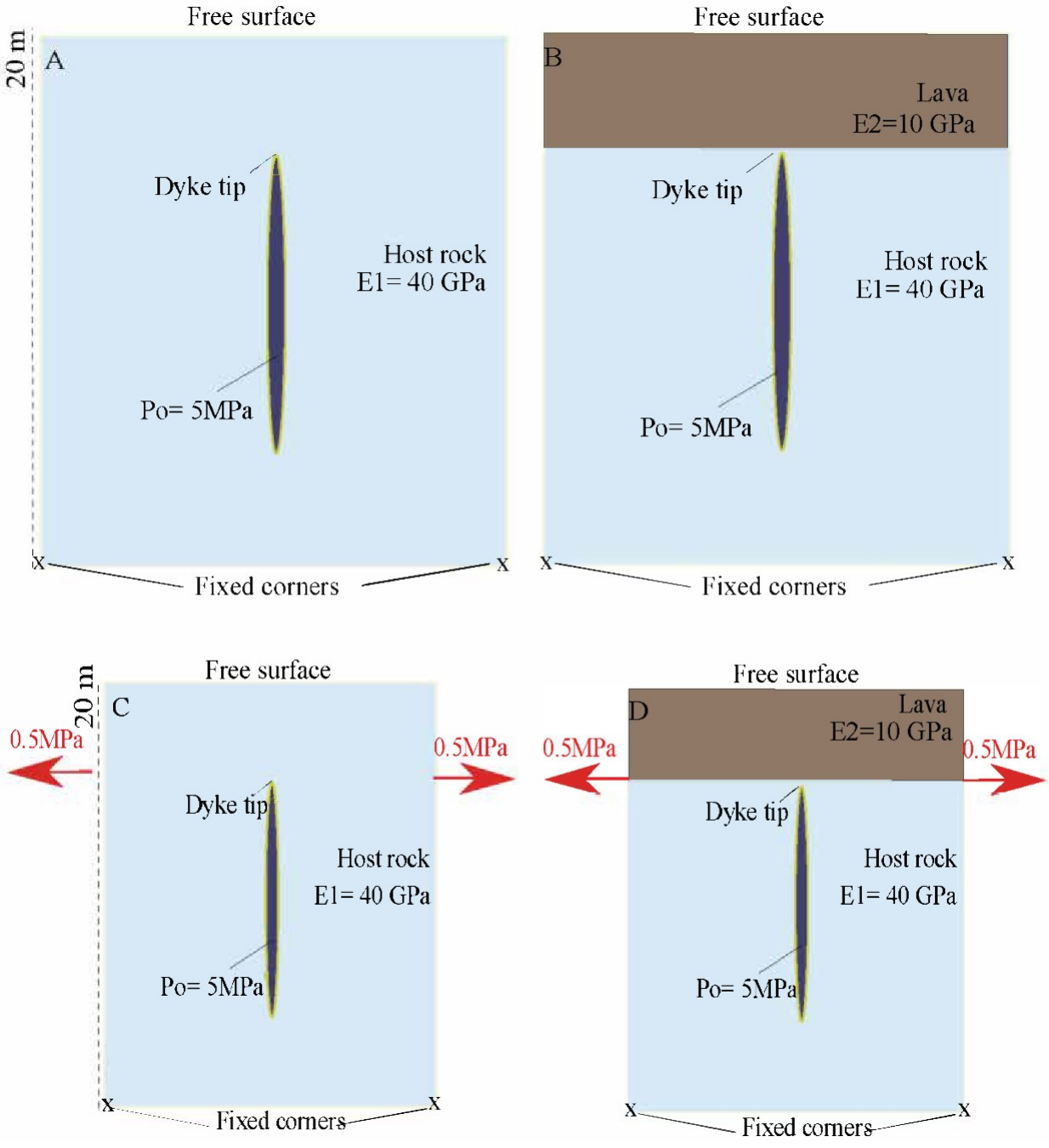

Fig. 4.3: Four model setups. (A) Homogeneous host rock with Young's modulus of 40 GPa and a 1 m thick cavity (dyke) with an internal pressure of 5 MPa (B) Example of a 2 layered or heterogeneous model with a Young's modulus of 40 GPa in E1 and a Young's modulus of 10 GPa in E2, again with a 1 m thick dyke (C) Homogeneous host rock with a Young's modulus of 40 GPa

and a 1 m thick cavity (dyke) with an internal pressure of 5 MPa subjected to an extra horizontal extension of 0.5 MPa at the boundaries. D) Example of a two layered or heterogeneous model with a Young's modulus of 40 GPa in E1 and a Young's' modulus of 10 GPa in E2, again with a 1 m thick dyke and subjected to an extra extensional force of 0.5 MPa (denoted by the red arrows).

4.3.3 Modelled field example model setup

We measured 91 dyke segments in this part of the caldera wall of Santorini. Of these we selected two that had exceptionally clear paths for modelling (Fig. 4.4). While we particularly model these two dykes, the results are general and apply to other dykes as well – these were simply selected because they are so well exposed.

The two dykes, hereafter referred to as dyke 1 and dyke 2, are compositionally identical, both being basaltic andesites (Bailey et al., 2009), have similar attitude and average thicknesses, and propagated through essentially the same host-rock stratigraphy. We identified five distinct dyke populations through analysis of petrological data and attitude on Santorini. The two dykes belong to the same dyke population and were likely injected from the same magma chamber. We assume that the dyke propagation paths follow the direction (or trajectory) of σ_1, as is normal (Gudmundsson, 2006, 2011a).

All the models reflect snapshot simulations of the magnitudes and directions of the stress field around the dykes and the host rock. For the interpretation of the results, we plot the magnitudes – the contours – of maximum tensile stress (σ_3), on a two-dimensional surface to examine stress concentration at the dyke tips. The contours show the location of the highest stress concentration

and their ranges in different type of contacts. We also plot the trajectories of the maximum principal compressive stress (σ_1) and the minimum principal compressive stress (σ_3) in all the models.

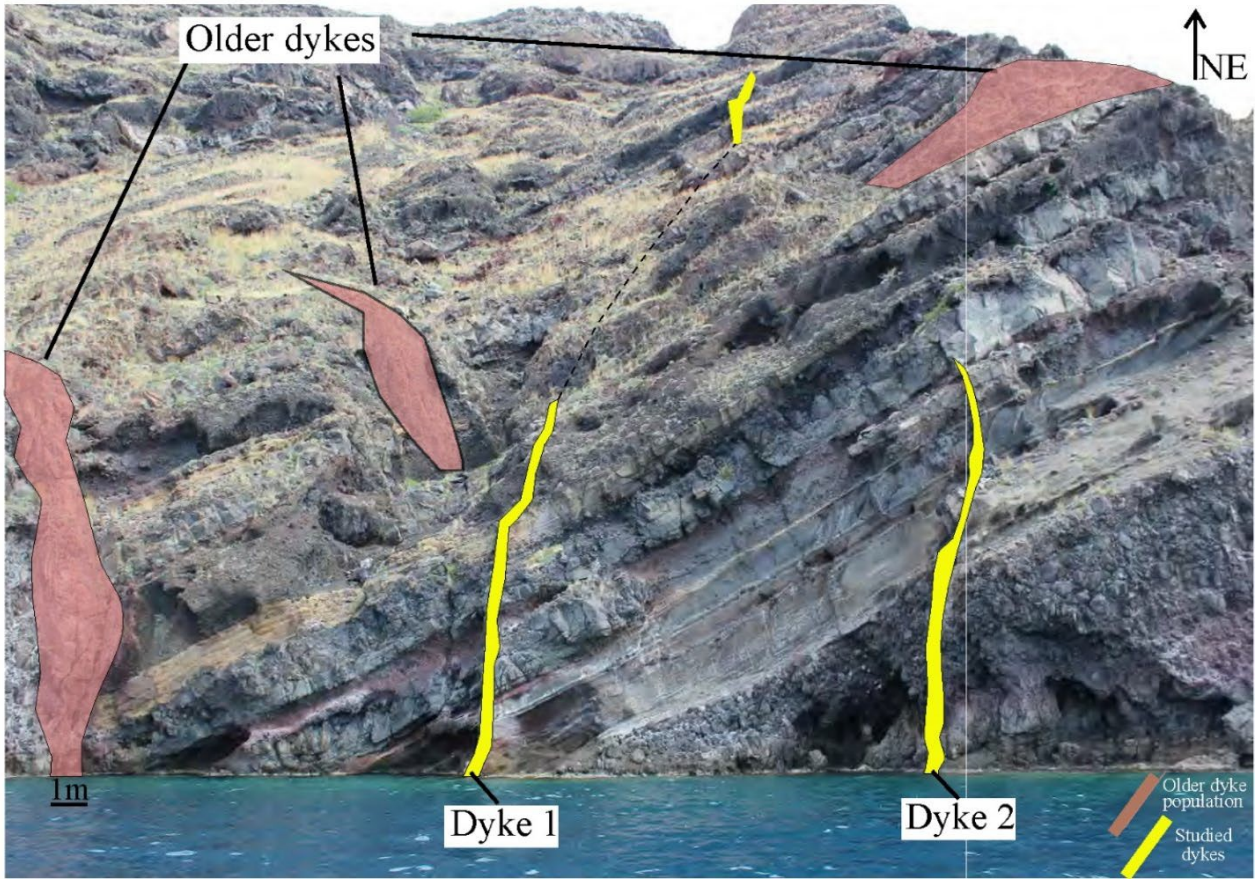

Fig. 4.4: Studied dyke 1 and dyke 2 (annotated yellow) in the northern caldera wall. Older dyke populations (annotated pink) can also be observed in the cross-section.

4.3.4 Sensitivity tests

The first round of sensitivity tests provides insights into the effects of stratigraphy and mechanical properties for different loading conditions on stress rotations (stress barriers). For dyke 2 we made the following tests to explore this effect:

1) Increasing the thickness of a lava flow by an order of magnitude (from 1 to 10m).

2) Increasing the thickness of a scoria layer by an order of magnitude (from 1 to 10m).

3) Alternating the layer sequence.

4) Increasing the thickness of the crustal segment above the dyke (more layers on the top of the observed stratigraphic sequence).

We made these sensitivity tests (1,2,4) for the same two overpressures in the dyke, namely alternatively 1 MPa and 5 MPa, testing the same contact (E2 (tuff) / E1 (breccia)) by keeping the tuff stiffness constant (E2=5GPa) and changing the stiffness of the breccia layer from very compliant (0.1 GPa), to compliant (1 GPa), and ,finally, to comparatively stiff (10 GPa). The performed ratios of stiffness were respectively: E_U/E_L= 5/0.1 =50, E_U/E_L= 5/1 =5 and E_U/E_L= 5/10 =0.5.

For the alternative layer sequence (sensitivity test 3) we tested for the same two overpressures in the dyke, namely alternatively 1 MPa and 5MPa, using the contacts (E2 (scoria) / E1 (breccia) and keeping the scoria stiffness constant (E2=0.5GPa) while changing the stiffness of the breccia layer from very compliant (0.01 GPa), to compliant (1 GPa), and finally to comparatively stiff (10 GPa). The performed stiffness ratios were respectively: E_U/E_L= 0.5/0.1=5, E_U/E_L= 0.5/1 =0.5 and E_U/E_L= 0.5/10 =0.05.

For the second round of sensitivity tests, the models focused on the relationship between the magma chamber loading conditions and the regional stress field subject to different material properties of the breccia layer (i.e., 0.1 GPa, 1 GPa, and 10 GPa), as above, and testing the same contact ((E2 (tuff) / E1 (breccia)). These models allow us to investigate whether the stress rotations relate to the regional extensional stress regime or to local stress effects, such as due to dyke-induced

compression. Six different loading conditions that reflect 6 tested distinct stress fields are presented below:

S1: Horizontal extension of 1MPa - benchmark model.

S2: Magmatic overpressure of 1 MPa – simulating dyke conditions close to a magma chamber.

S3: Magmatic overpressure of 1MPa and horizontal extension of 3MPa – simulating a dyke emplaced in a rift zone (or, as possible for Santorini, an accelerated slab retreat).

S4: Magmatic overpressure of 1MPa and horizontal extension of 0.5MPa – simulating a dyke emplaced in a rift zone.

S5: Magmatic overpressure of 1MPa and horizontal compression of 3MPa –simulating a dyke emplacement following recent previous dyke injections.

S6: Magmatic overpressure of 1MPa and horizontal compression of 0.5MPa – simulating a dyke emplacement that is subject to a tectonic event, here graben subsidence or formation.

For all the models, three arrow surfaces were used to express the principal stresses for better visualisation of the stress field. Here the maximum principal compressive stress (σ_1) is shown by red arrows, intermediate principal stress (σ_2) by white arrow and the maximum tensile stress (σ_3) by black arrows. The loading condition is again magmatic overpressure. The original models are included in the supplementary files (Supporting information files 1-6, Appendix C1).

5. Field results

We obtained structural data on 91 well exposed dyke segments observed in the northern caldera wall of Santorini island. These data were combined and compared with previous measurements by Fouque (1879), Petersen (2005), and Browning et al. (2015).

5.1 Dyke attitude and thickness

Regional dyke swarms usually show normal-curve strike and dip distributions, being mostly composed of sub-vertical and subparallel dykes that consequently, seldom cross-cut (Gudmundsson, 2002). In Santorini, dyke propagation is thought to have been primarily vertical from a shallow magma chamber (Browning et al., 2015). The present field observations provided indications of vertical flow such as elongated vesicles parallel to the dip dimension but no elongated minerals as the dykes are often aphyric or plagioclase crystals are the only phenocrysts. The dykes are primarily perpendicular to the regional direction of σ_3, which coincides with the direction of the spreading (or rifting) vector or defined by the elongation of the caldera collapse (Gudmundsson, 2006). The great majority of the dykes are subvertical. More specifically, 91% have dips >75degrees; the few dykes (9%) that dip 45-60 degrees can be then categorised as inclined sheets (Fig. 4.5C). Since the dykes are mostly derived from a shallow chamber, we assume the dip dimension (height) to be the controlling (smaller) dimension.

The predominant strike is in the range N20-45ºE, but there are also other minor sets of N-S, (between N0-20ºE) and NW-SE striking dykes (Fig. 4.5A). The variation in frequency of dykes along the profile shows that the dykes occupy four distinct localities. We infer that these localities

mark the boundary between at least two of the main historical eruptive centres (cinder cones) in the northern part of Santorini, namely Mt. Megalo Vouno (or Mavro Vouno), Mt. Kokkino Vouno as well as two other localities such as the Mt. Mikros (or Chamilos) Profitis Ilias and the village of Finikia (Fig. 4.5B).

Field measurements suggest that the length and thickness size distributions of dykes are normally power laws (Gudmundsson, 1995). Dyke thicknesses in Santorini range from 0.1m to 8 m with an arithmetic average thickness of 1.1m. Field observations have shown that in some cases the dyke thickness varies along both the strike and dip dimension of the same dyke (or segment). In Fig. 4.5D we show how dyke thickness varies along with each profile and in Fig. 4.5C we show the variation in dyke thickness with dyke dip.

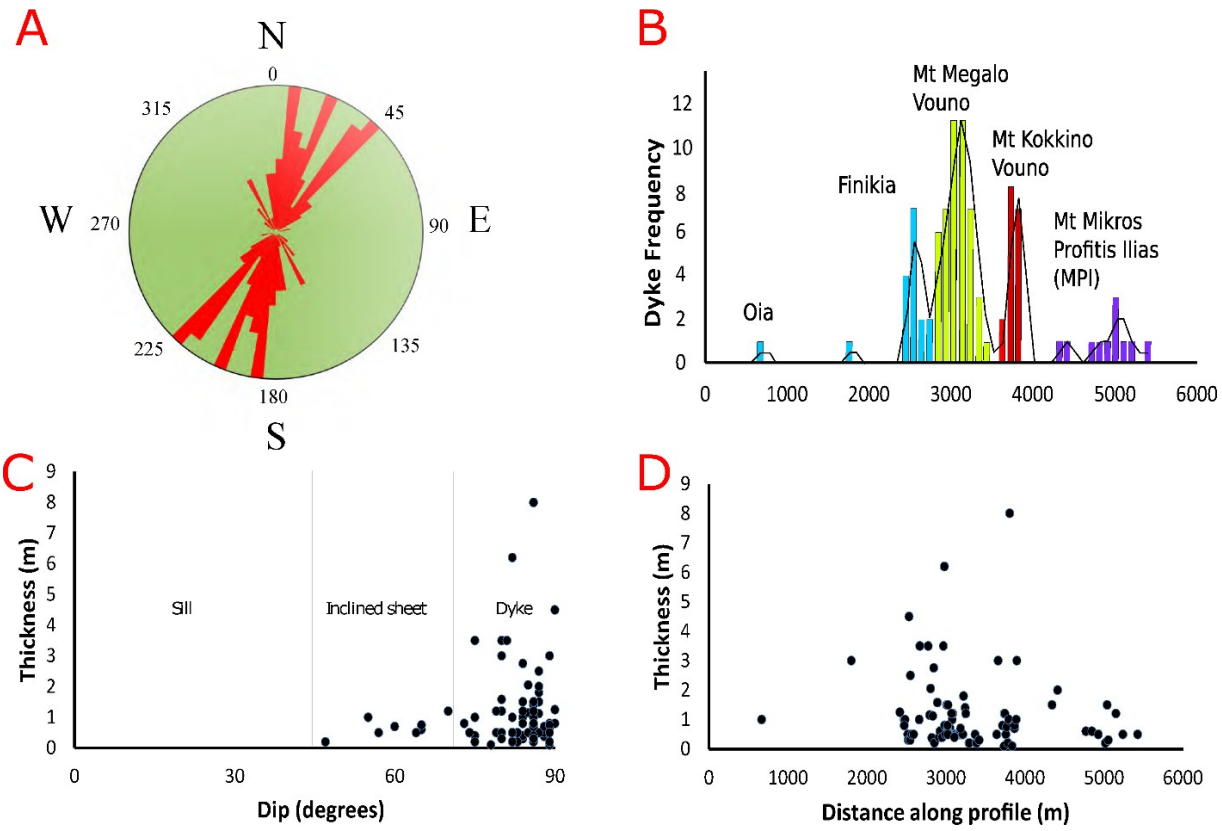

Fig. 4.5: Characteristics of the dykes exposed on the Santorini northern caldera wall. (A) Rose diagram of dyke strike directions, (B) Frequency of dykes along the profile, (C) Dyke thickness as a function of dyke dip, D) Thickness of dykes along the measured profile.

5.2 Dyke attitude, deflection and arrest

Dyke attitudes vary both along the length of the profile and also with depth in the caldera wall. During the field campaigns, we collected measurements of dyke attitudes from a distance along the profiles as we could not directly measure the along dip variations because the caldera wall was too steep and difficult to access in many sections. For that reason, we made many qualitative observations on how the dyke attitudes change along dip. The observed criteria were:

- Propagation/feeder: the dyke penetrates the host rock, and its segments were visible throughout the succession. Because the top parts of the dyke are then essentially at the surface (which is only slightly eroded), it is highly likely that the dyke fed a volcanic eruption. We do not see direct evidence for this except 2 dykes that could have been connected to crater cones.

- Uncertain fate: the dyke changes attitude with depth, and we do not observe any of the dyke segments at higher levels in the succession exposed in the caldera wall.

- Arrest: the dyke is clearly arrested, and the arrested dyke tips can be observed. In this case, the dyke did not feed an eruption in the observed section.

- Deflection: the dyke changes dip and deflects into pre-existing weaknesses (faults) and either becomes arrested in a pre-existing fault zone or propagates through the fault and then becomes arrested higher up in succession. In all of these cases, it is unclear if the dyke has fed an eruption.

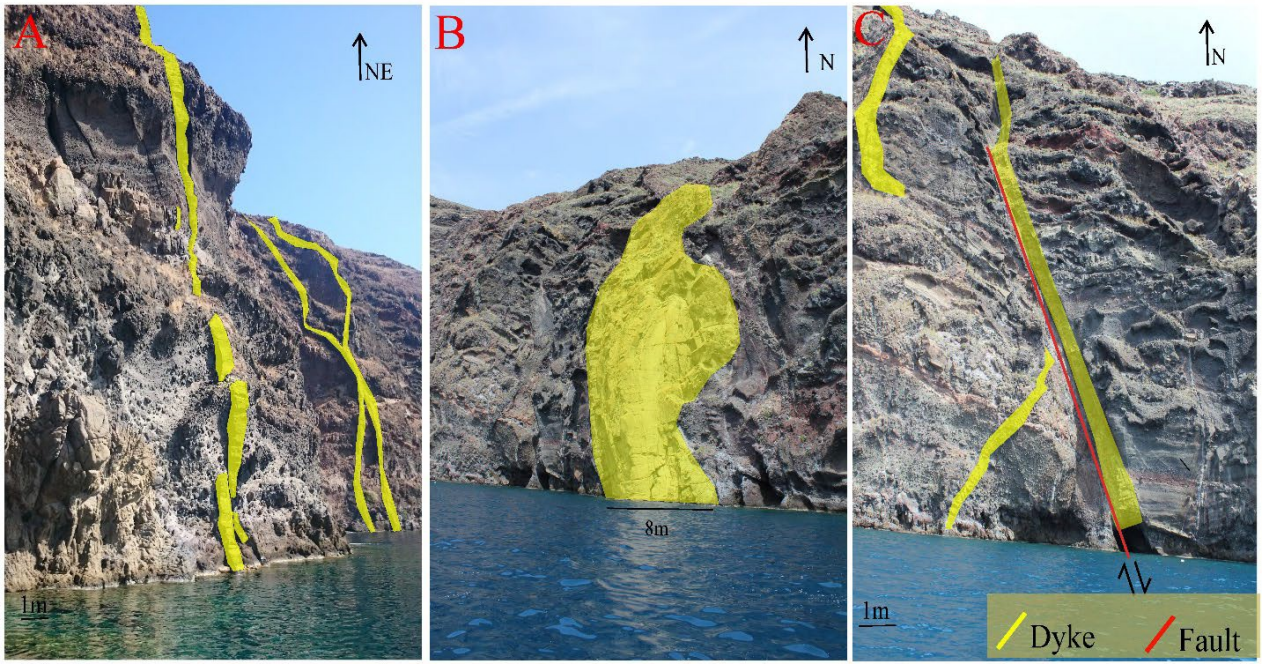

Fig. 4.6: Observed dyke propagation paths on the northern caldera wall. (A) Segmented and branched propagated dykes, (B) a possibly multiple arrested dyke which forms rounded tips as it propagates through a compliant host rock, (C) dyke-fault deflection; the inclined sheet on the left is being deflected into the shear fracture, the normal fault.

The studied dykes broadly follow three different propagation patterns, namely:

1) Propagation: the dyke penetrates the host rock layers and follows the direction of the stress field active during emplacement. Of the 91 dyke segments measured we observed 43 dykes that penetrate all the host-rock layers and were thus apparently neither arrested nor deflected along contacts (Fig. 4.6A). Due to the steep cliffs, erosion, and coverage by scree and vegetation the segmented dykes cannot be followed as continuous structures up their dip dimension to the top of the succession.

2) Arrest: we observed three clearly arrested dykes. The arrested tips occur at bedding planes in volcaniclastic rocks and at contacts between lava flows. The dykes that propagated into soft volcaniclastics developed rounded tips (Fig. 4.6B) or thinned out - tapered away - to a pointed tip or became arrested with a blunt-ended tip at the contact between layers of different stiffness. The geometry of the tips plays a vital role in the mechanism that controls their paths (Gudmundsson, 2003).

3) Deflection: we observed six dykes that became deflected along discontinuities, which they then followed as parts of their propagation paths. We regard a dyke as deflected when the dip changes more than 30°. All the deflected dykes occur close to normal (regional) faults (Fig. 4.6C).

5.3 Dyke lengths

Due to the multiple caldera collapse events and the dynamic changes in Santorini's morphology, absolute dyke lengths are difficult to measure or estimate. Additionally, the caldera floor is under the sea, and the vertical caldera cliffs are difficult to climb to study the details of the dyke segmentation. Due to these limitations, it was not possible to trace individual dykes continuously for any long distances along strike, and so exact measurement of dyke length (and dyke height as well) was not possible. Instead, we inferred the length of dykes from the available outcrops.

Many previous studies have attempted, with varying degrees of success, to estimate the lengths of dykes in the field, both those found in well-exposed swarms (Gautneb et al., 1989, Gudmundsson, 2003) as well as during emplacement (e.g. Jousset et al., 2003). The lengths (strike dimensions) of feeder dykes close to the surface can be inferred from the lengths of the volcanic fissure to which they supply magma (Gudmundsson, 1995). For the length of dykes at greater depths in the crust

(in eroded dyke swarms) Gudmundsson (1983) measured the minimum lengths of five dykes in the eastern part of Iceland and found that they ranged from 4 km to more than 22 km. The uncertainty in length was primarily because the lateral ends/tips of some of the dykes were not exposed. Other data from feeder dykes in El Hierro, Canary Islands, revealed near-surface lengths from 75 m to 535m (Becerril et al., 2013) while in continental flood basalt provinces estimated dyke lengths vary from around 1 km to 80 km (Ray et al., 2006).

5.4 Dyke overpressure calculations

In the simplest case, a magma-filled fracture (a dyke) is initiated once the excess pressure (P_e, pressure above σ_3) in a magma chamber and the lithostatic stress or pressure (P_l) reach the in-situ tensile strength (T_o) of the host rock surrounding the chamber plus the minimum principal compressive stress (σ_3) (Eq.4.3). The value of P_e for chamber rupture is roughly equal to the in-situ tensile strength T_o of the host rock (the chamber roof, normally) which is generally in the range from 0.5 MPa to 9 MPa (Amadei and Stephansson 1997) but is most commonly 2-3 MPa (Gudmundsson 2011a). Thus, magma-chamber rupture occurs when:

$$P_l + P_e = \sigma_3 + T_o \tag{4.3}$$

The overburden pressure or vertical stress σ_v (overlying host-rock pressure) as defined as:

$$\sigma_v = \int_0^z \rho_r(z)\, g\, dz \tag{4.4}$$

where z is the vertical coordinate axis (depth in the crust below the surface), g the gravity acceleration (9.81 m s^{-2}) and ρ_r (z) the density of the overlying material as a function of depth. When the state of stress is lithostatic, then the horizontal principal stresses are equal to the vertical stress given by Eq. (4.4), which is also a principal stress (cf. Jaeger and Cook, 1979; Gudmundsson, 2011a).

Analytical and numerical models (Gudmundsson, 2006; Gudmundsson and Phillip, 2006) show that the minimum principal compressive (maximum tensile) stress (σ_3) generally decreases substantially with distance from the magma chamber/reservoir. This situation dictates that dykes are may become arrested on their way to the surface, while actual arrest depends much on the mechanical layering. Combining Eq. (4.3) and Eq. (4.4), we can provide a formula to calculate the magmatic overpressure (P_o), which is the magmatic pressure or driving pressure in excess of the normal stress σ_n on the fracture plane. For a dyke that follows the trajectory of σ_1 and is therefore an extension fracture (mode I crack), σ_n must be σ_3. Once the dyke-fracture is initiated, it propagates away from the chamber and is driven by the magmatic overpressure (P_o), given by:

$$P_o = P_e + (\rho_r - \rho_m)\, gh + \sigma_d \qquad (4.5)$$

where h is the height of the dyke above the magma chamber (or reservoir), $\rho_r - \rho_m$ denotes the difference in density between the host rock and the magma and as such is a major contributor to buoyancy, and σ_d is the difference between the maximum (σ_1) and minimum (σ_3) principal compressive stresses in the host rock at the depth where the dyke tip is located at that moment (for

a propagating dyke) or the depth of exposure below the original surface (for a solidified dyke in an eroded area).

The overpressure can also be found from the maximum dyke thickness (aperture) W and its controlling dimension L through the equation (Gudmundsson, 2011b, Becerril et al., 2013) initially derived by Sneddon (1946):

$$\mathrm{Po} = \frac{\mathrm{W\,E}}{2(1-\mathrm{v}^2)\mathrm{L}} \tag{4.6}$$

where E is the Young's modulus of the host rock, v is the Poisson's ratio of the host rock, L is the strike dimension (length) of the dyke, and the other terms are as defined above. The aspect ratio W/L can be used to calculate the overpressure in the dyke (Gudmundsson, 1983; Delaney et al., 1986).

5.5 Magmatic overpressure results

We used Eq. 4.6 to determine the range of overpressures that propagated the studied dykes (Fig. 4.7) during emplacement. The results allow us to pick the most appropriate overpressure values for the numerical models. Furthermore, the results show that the overpressure responsible for dyke formation does not depend on location within the dyke swarm; the greatest variation or range in overpressure is simply where the dyke intensity (number) is highest (Fig. 4.7). For the calculations we used the value of 5 GPa for Young's modulus (E) of the shallow crust, an appropriate value of 0.25 for Poisson's ratio (ν), and the measured thickness of the dykes. For the length dimension, we

used the 1:1500 ratio for thickness/length, as is commonly measured in the field (Gudmundsson, 2011a). The resulting magmatic overpressures range from 0.1 to 113 MPa (Fig. 4.7), with an arithmetic mean overpressure of about 5 MPa. Of course, if the Young's modulus used were 10 GPa rather than 5 GPa, then the mean calculated overpressure would be about 10 MPa. But the dykes are measured at very shallow depths, so that 5 GPa may be more appropriate than 10 GPa. 90% of the dyke overpressures range between 0.1 and 6MPa which agrees well with previous field studies (Gudmundsson, 2011a) and the conditions for rupture (in-situ tensile strength). More specifically, the results indicate that the dykes generally had low overpressure at the very shallow depths where they are exposed, as expected from mostly mafic dykes injected from a shallow magma chamber, as is the case for Santorini.

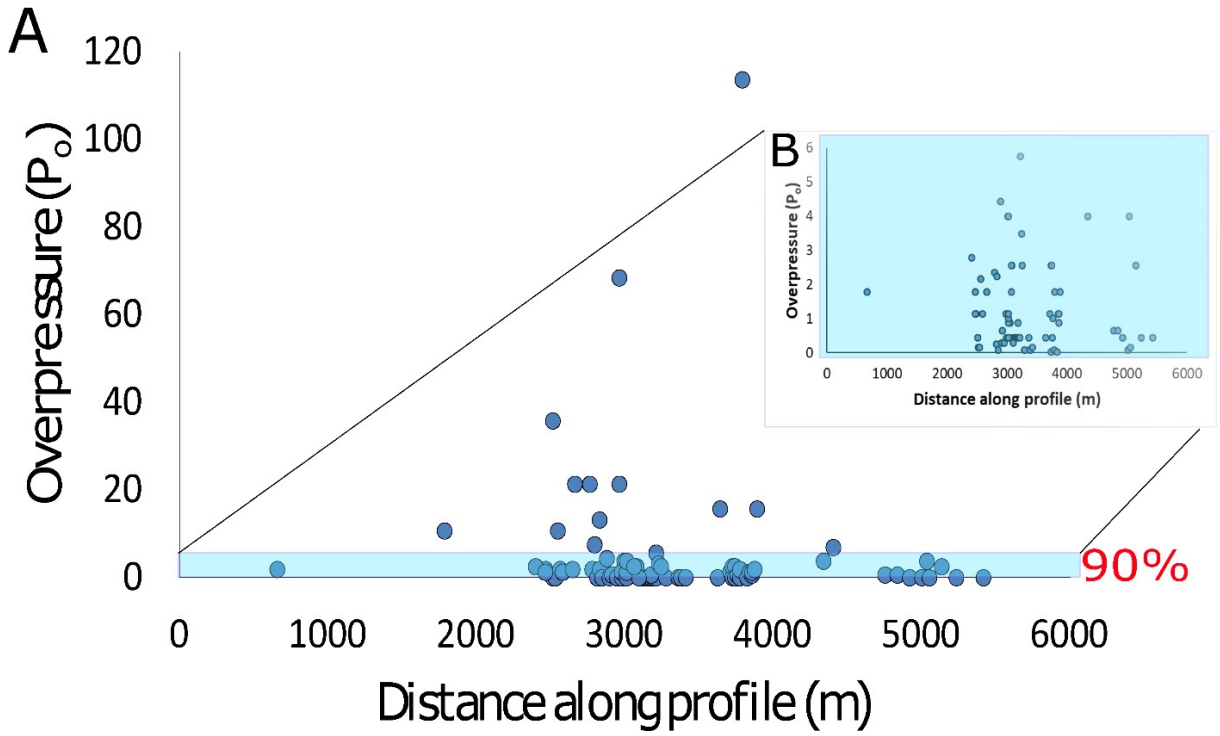

Fig. 4.7: (A) Diagram showing the calculated dyke overpressures (P_o) with distance along the studied profile. (B) 90% of the measurements range between 0.1-6MPa.

6. Numerical modelling results

We modelled two dykes observed in the field which were of similar compositions and located within 10 m of each other. The dykes are of similar thickness and strike (NW-SE) and emplaced in the same layered rock mass with no active faults that could alter the local stress field and encourage dyke deflection (Le Corvec et al., 2013, 2018; Browning and Gudmundsson, 2015). The geometry of the rock layers dissected by the two dykes is essentially identical, but the detailed sequence, material properties, microstructure (grain sizes) and layer thicknesses, are different.

The segmented dyke 1 penetrates vertically the caldera wall and exhibits no sign of arrest in the exposed vertical cross-section. Whilst dyke 2 is geometrically and compositionally similar it has clearly become arrested within a contact between soft scoria and a stiff lava layer. The primary goal of the numerical models was to investigate which parameters control these contrasting dyke paths.

We also studied the level of stress near the tip of each dyke and at the contact between layers ahead of each dyke. 1) very compliant - compliant (r=0.1), 2) very compliant-stiff (r=0.05), 3) stiff - very compliant (r=20) where r denotes for the stiffness contrast between two layers (E_U/E_L) (Kavanagh et al., 2006).

6.2 Dyke 1

In the results from the following models, we concentrate on the specific field example of dyke 1 and use the field measured geometries as input for a suite of numerical models. Dyke 1 is a mafic dyke with an attitude of 025/85E and an average thickness of 0.5 m (Fig. 4.8A). The host rock through which the dyke propagates in the exposure consists of 6 layers. Using the results from our in-situ study and those of Druitt et al. (1999) we identify them as basaltic or andesitic lavas (layers E4, E6, and E8), tuffs (layers E2 and E7), and unconsolidated scoria (layers E3 and E5). The breccia (E1) is not seen in the field but underlies all of the starting layers in the models.

We produce 2D snapshots of the dyke stresses very close to three mechanically different contacts which were selected according to the observed stratigraphy so as to favour contrasting stiffnesses and marked in Figure 4.8B as stars. We also simulated two loading boundary conditions. The three contacts were as follows:

Contact 1: scoria (E3 = 0.5 GPa) - tuff (E2 = 5 GPa) –/ very compliant-compliant, E=0.5/5, (r=0.1).

Contact 2: scoria (E5 = 0.5 GPa) - lava (E4 = 10 GPa) –/ very compliant-stiff, E=0.5/10, (r=0.05).

Contact 3: lava (E6 = 10 GPa) - scoria (E5 = 0.5 GPa) –/ stiff - very compliant, E=10/0.5, (r=20).

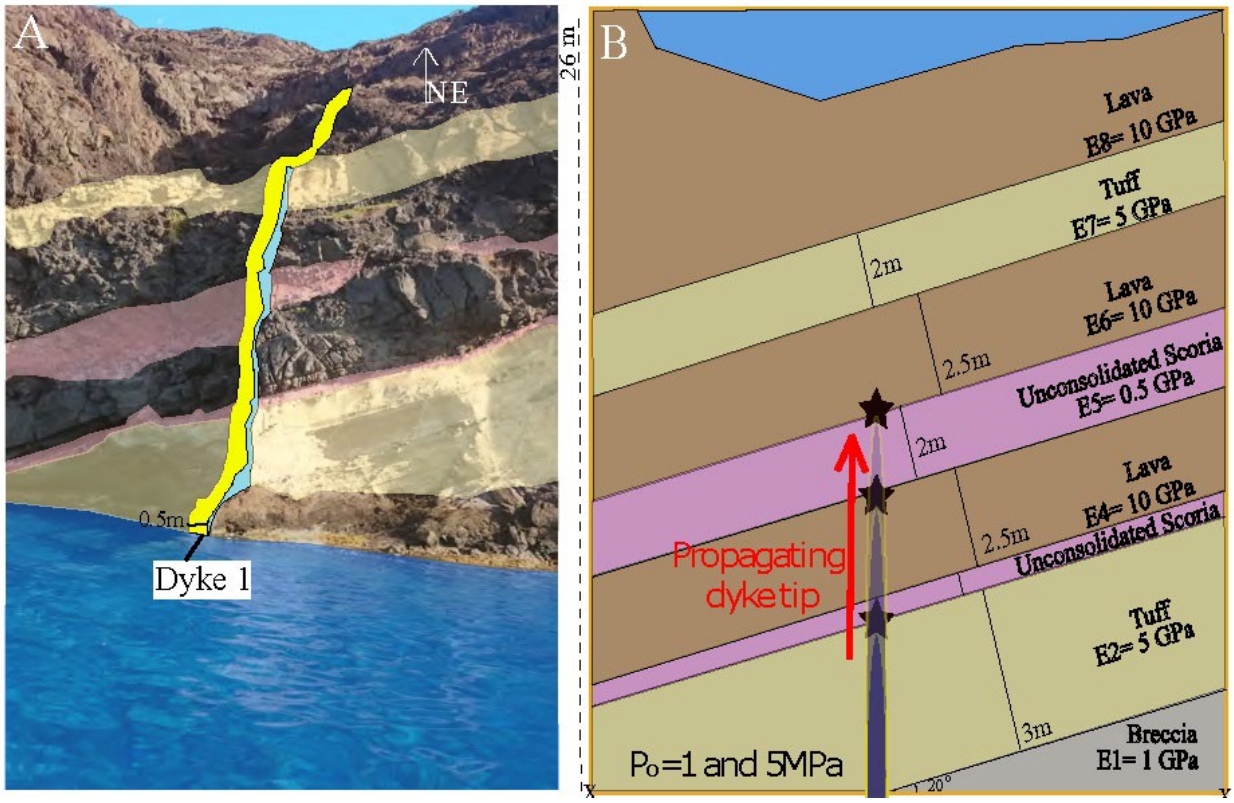

Fig. 4.8: Dyke 1 propagated through a heterogeneous segment of tuff, unconsolidated scoria and lava in the northern caldera wall of Santorini. (A): annotated field photograph, (B): corresponding FEM model setup. The stars correspond to the specific picked contacts from which 2D snapshots were produced in COMSOL Multiphysics as the dyke is propagating towards the surface.

6.2.1 Dyke 1 with a 1 MPa driving pressure

We modelled dyke 1 with 1 MPa driving (over) pressure (P_o) as the only loading and studied the stress concentration at the dyke tip on the contacts mentioned above (Fig. 4.9, A1a-c). We then performed the same model runs with added regional horizontal extension of 0.5 MPa (Fig. 4.9, B1a-c). The model runs are shown in Fig. 9 and the results in Table 4.1. In Fig. 4.9 the stress shown as contours is the minimum principal compressive stress (σ_3) which is the maximum tensile stress,

and the arrow surfaces express the maximum principal compressive stress (σ_1) (red arrows) and the minimum principal stress (σ_3) (white arrows) respectively.

In model A1-a (Fig. 4.9) the dyke tip tensional stresses are concentrated predominantly in the tuff (E2) and scoria (E3) units. The trajectories of the maximum principal compressive stress (σ_1) are oriented along the dyke dip dimension, i.e. vertically, indicating that the propagation path in this model would tend to be vertical. In model A1-b the tensional stress is concentrated within the lava flow (E4) and only slightly in the overlying scoria (E5) unit. The trajectories of σ_1 are oriented sub-vertical directly above the dyke tip and thus promoting further (sub-vertical) propagation. Near the tip, however, σ_1 dips between 0° and 45° within a few tens of cm up to the next contact between the scoria (E5) and lava (E6). This suggests that if the dyke could penetrate the contact between scoria (E5) and lava (E6) it would propagate vertically for some tens of centimetres and then likely become deflected (inclined). In the next set of unit contacts (A1-c) the tensional stresses are concentrated above the dyke tip in the stiff lava (E6) unit and the trajectories of σ_1 are mainly vertical.

In model B1-a and B1–b the dyke tip tensional stresses and the trajectories of σ_1 follow similar patterns with A1-a and A1-b, although in the latter, σ_1 stays almost vertical. However, in the next unit or layer contacts (B1-c), the tensile stresses again concentrate above the dyke tip in the stiff lava (E6), but σ_1 is vertical which indicates a high likelihood of propagation as in A1-c.

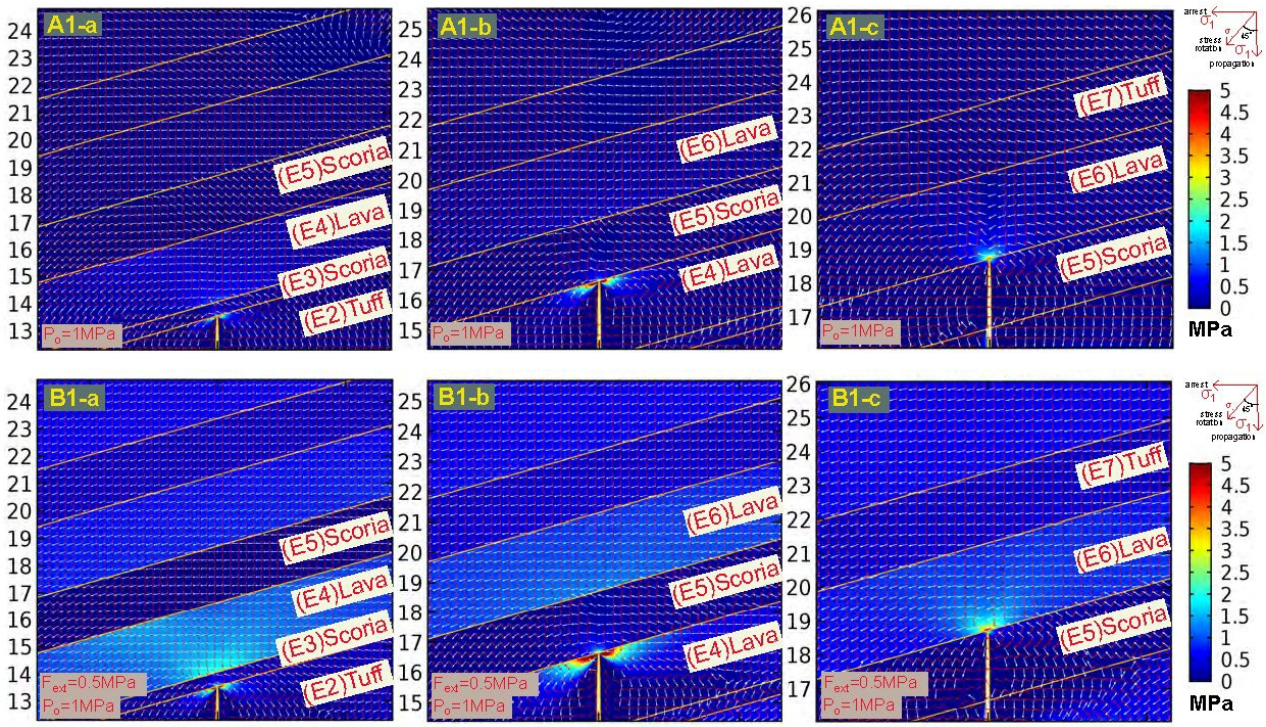

Fig. 4.9: FEM (finite element) models of dyke propagation (tensile stress σ_3) through a heterogeneous host rock based on Fig. 4.8B. (A1a-c): Overpressure (P_o=1MPa) is the only loading boundary condition, (B1a-c): Overpressure (P_o=1MPa) and an extensional stress field (F_{ext}=0.5MPa) are applied. The red arrow surface is σ_1 and the white arrow surface is σ_3, (a) scoria/ tuff contact, (b) scoria/ lava contact, (c) lava/scoria contact (y-axis in meters).

Table 4.1: Modelling results for dyke 1 with an applied overpressure (P_o) of 1MPa and an additional horizontal extension of 0.5 MPa. The table also includes a qualitative interpretation of the dyke propagation path as defined through numerical modelling. Tensile stress is measured directly ahead of the dyke tip (Low: 0.5- 1.5MPa, Moderate: 1.5-3MPa, High: 3-5MPa). The condition for propagation is met if the stress at the tip exceeds 0.5 MPa and if the trajectory of σ_1 is close to 90˚. The dyke propagates in a σ_1 and σ_3 plane and their trajectories are shown in the

models. The intermediate principal stress (σ_2) was calculated (if possible) from numerical models not shown here.

(A1) P_o= 1MPa	**Layer contacts (E_U/E_L)**	**Stress concentration at the tip**	**Stress rotation at the tip and its vicinity**	**Dyke path**	**(B1) P_o=1 MPa and 0.5 MPa extension**	**Stress concentration at the tip**	**Stress rotation at the tip and its vicinity**	**Dyke path**
(a)	Scoria/ Tuff	Low	(σ_1): 0˚- 45˚ (σ_2): N/A (σ_3): 0˚- 45˚ (A1-a)	Propagation	**(a)**	Low	(σ_1): 0˚- 45˚ (σ_2): 0˚- 45˚ (σ_3): 0˚- 45˚ (B1-a)	Propagation
(b)	Scoria/ Lava	Moderate	(σ_1): 0˚- 45˚ (σ_2): 0˚- 45˚ (σ_3): 0˚- 45˚ (A1-b)	Propagation	**(b)**	Moderate	(σ_1): 0˚- 45˚ (σ_2): 0˚- 45˚ (σ_3): 0˚- 45˚ (B1-b)	Propagation
(c)	Lava/ Scoria	Moderate	(σ_1): 0˚- 10˚ (σ_2): N/A (σ_3): 0˚- 10˚ (A1-c)	Propagation	**(c)**	Moderate	(σ_1): 0˚- 10˚ (σ_2): 0˚- 10˚ (σ_3): 0˚- 10˚ (B1-c)	Propagation

6.2.2 Dyke 1 with a 5 MPa driving pressure

Here we modelled dyke 1 by changing the overpressure (P_o) to 5MPa. The models are shown in Fig. 4.10 and the results in Table 4.2. We find that dyke tip tensional stresses concentrate both in the tuff layer (E2) and in the scoria (E3) layer, although we note that there is much greater concentration of tensile stress in the lava (E4) unit. The trajectories of σ_1 are generally vertical indicating that the propagation dyke path in this model would favour vertical propagation. In model A2-b the tensional stress concentrates within the lava flow (E4) and less in the overlying scoria

(E5) layer. However, the trajectories of σ_1 are oriented sub-vertically directly above the dyke tip which suggests a sub-vertical path if the dyke were to continue propagating. In the vicinity of the dyke tip, the trajectories of σ_1 and σ_3 dip from 0° to 45° within a few tens of cm up to the next contact between scoria (E5) and the lava (E6). In the following model (A2-c) the σ_1 - σ_3 plane rotates by 10°.

The application of a 0.5 MPa horizontal extension in this suite of models (B2a-c) creates similar results and stress rotations as in A2a-c although the σ_1 plane rotates by 10°. These stress conditions all encourage dyke propagation.

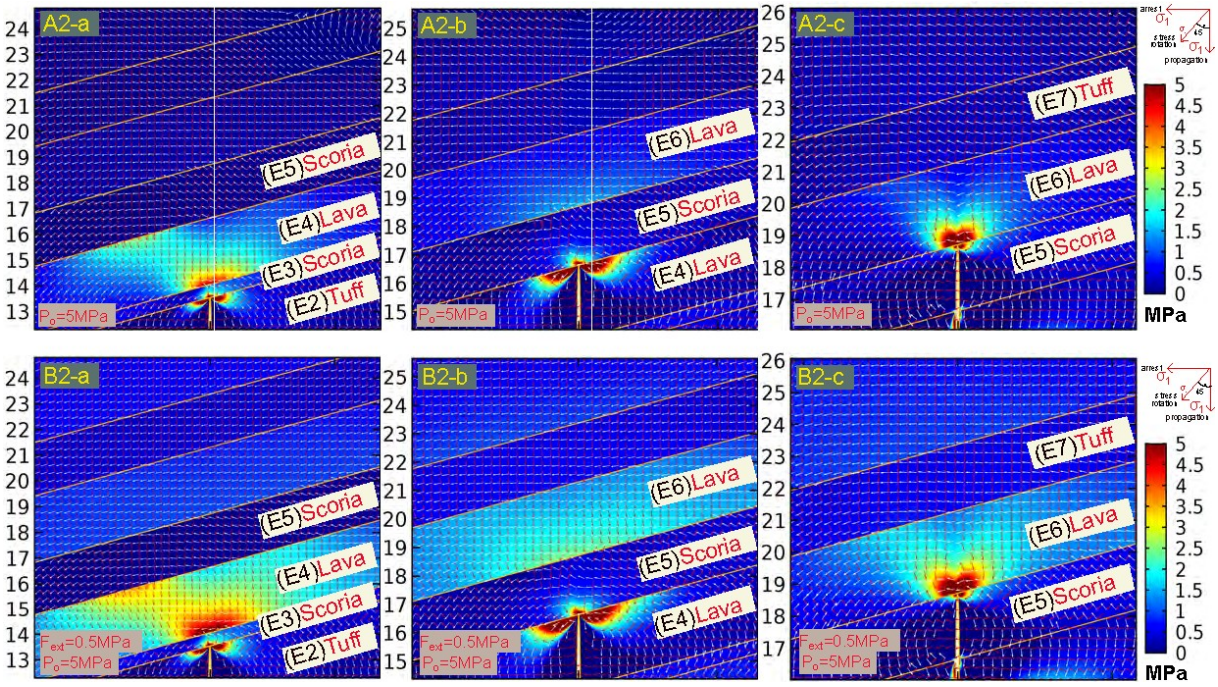

Fig. 4.10: FEM (finite element) models of dyke propagation (tensile stress σ_3) in a heterogeneous host rock based on Fig. 4.8B. (A2a-c): Overpressure (P_o=5MPa) is the only loading boundary condition, (B2a-c): Overpressure (P_o=5MPa) and an extensional stress field (F_{ext}=0.5MPa) are

applied. The red arrow surface is σ_1 and the white arrow surface is σ_3, (a) scoria/ tuff contact, (b) scoria/ lava contact, (c) lava/scoria contact (y-axis in meters).

Table 2: Modelling results for dyke 1 with an applied overpressure (Po) of 5MPa and an additional horizontal extension of 0.5 MPa. The table also includes a qualitative interpretation of the dyke propagation path as defined through numerical modelling. Tensile stress is measured directly in ahead of the dyke tip (Low: 0.5- 1.5MPa, Moderate: 1.5-3MPa, High: 3-5MPa). The condition for propagation is met if the stress at the tip exceeds 0.5 MPa and if the trajectory of σ1 is close to 90˚. The dyke propagates in a σ1 and σ3 plane and their trajectories are shown in the models. The intermediate principal stress (σ2) was calculated (if possible) from numerical models not shown here.

(A2) P_o=5 MPa	**Layer contacts (E_U/E_L)**	**Stress concentration at the tip**	**Stress rotation at the tip and its vicinity**	**Dyke path**	**(B2) P_o=5MPa and 0.5 MPa extension**	**Stress concentration at the tip**	**Stress rotation at the tip and its vicinity**	**Dyke path**
(a)	Scoria/ Tuff	High	(σ_1): 0˚- 10˚ (σ_2): N/A (σ_3): 0˚- 10˚ (A2-a)	Propagation	**(a)**	Low	(σ_1): 0˚- 10˚ (σ_2): 0˚- 45˚ (σ_3): 0˚- 10˚ (B2-a)	Propagation
(b)	Scoria/ Lava	High	(σ_1): 0˚- 45˚ (σ_2): 0˚- 45˚ (σ_3): 0˚- 45˚ (A2-b)	Propagation	**(b)**	High	(σ_1): 0˚- 45˚ (σ_2): 0˚- 45˚ (σ_3): 0˚- 45˚ (B2-b)	Propagation
(c)	Lava/ Scoria	High	(σ_1): 0˚- 10˚ (σ_2): 0˚- 45˚ (σ_3): 0˚- 10˚ (A2-c)	Propagation	**(c)**	High	(σ_1): 0˚- 10˚ (σ_2): 0˚- 10˚ (σ_3): 0˚- 10˚ (B2-c)	Propagation

6.3 Dyke 2

Dyke 2 is an arrested mafic dyke but otherwise very similar to dyke 1 (Fig. 4.11A). The host rock again is composed of six layers of dissimilar mechanical materials while their thicknesses and sequence differ from those in the previous models. We again produce 2D snapshots of the dyke stresses very close to the same three mechanically different contacts (which are those seen in the field at different depths) and for the two loading boundary conditions. The three contacts denoted with a star are as follows (Fig. 4.11B):

Contact 1: scoria (E3 = 0.5 GPa) - tuff (E2 = 5 GPa) –/ very compliant-compliant, E=0.5/5, (r=0.1)

Contact 2: scoria (E5 = 0.5 GPa) - lava (E4 = 10 GPa) –/ very compliant-stiff, E=0.5/10, (r=0.05)

Contact 3: lava (E6 = 10 GPa) - scoria (E5 = 0.5 GPa) –/ stiff- very compliant, E=10/0.5, (r=20)

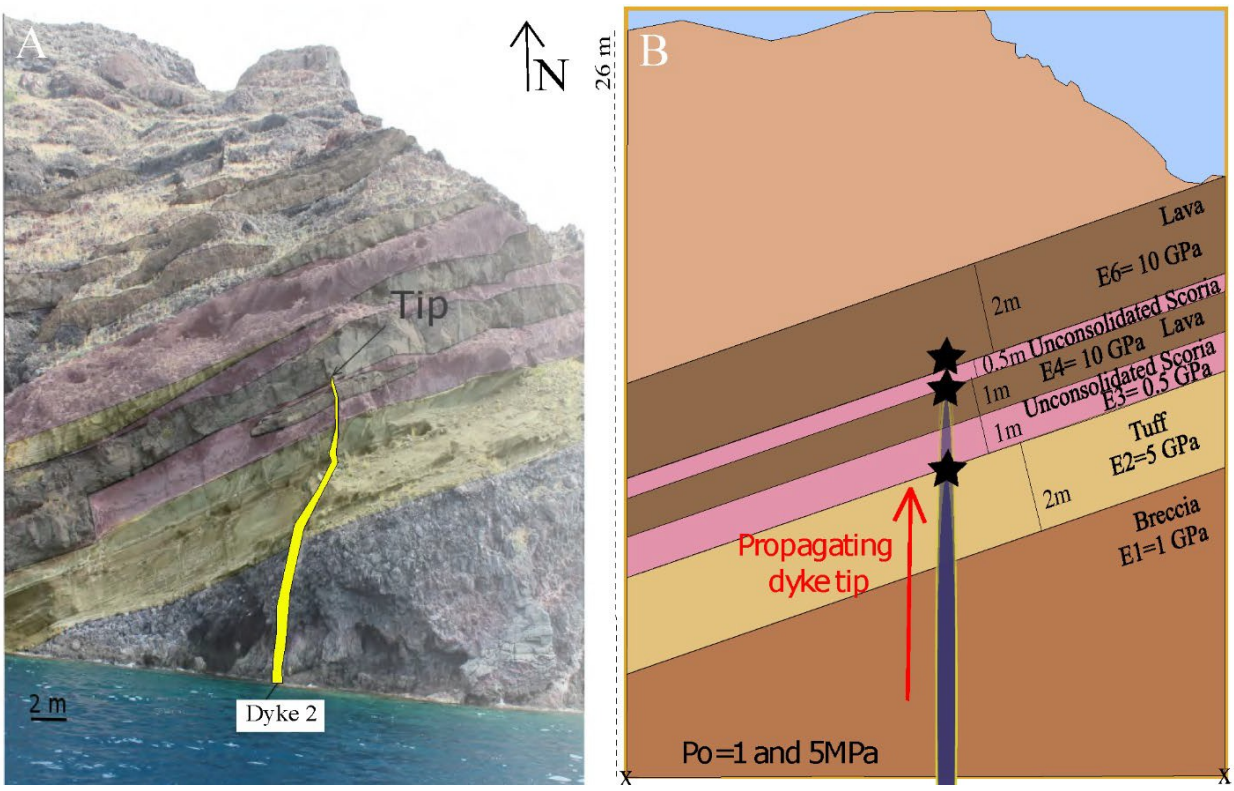

Fig. 4.11: Dyke 2 has thinned out and became arrested within a lava unit in the northern caldera wall. (A): annotated field photograph, (B): FEM model setup. The stars correspond to the specific picked contacts from which 2D snapshots were produced in COMSOL Multiphysics as the dyke is propagating towards the surface.

6.3.1 Dyke 2 with a 1 MPa overpressure

We initially modelled dyke 2 with a 1 MPa driving pressure (P_o) (A3a-c) and then added an additional regional extension of 0.5 MPa (B3a-c). The models are shown in Fig. 4.12 and the results in Table 4.3. In model A3-a the dyke tip tensional stresses are concentrated predominantly in the tuff (E2) and lava (E4) and less so in the scoria (E3) layer. The trajectories of the maximum principal compressive stress (σ_1) in front of the tip are oriented along the dyke flow. There is also

stress concentrations at the scoria (E5) and lava (E6) contact in conjunction with σ_1 stress rotation of almost 90°. In model A3-b the tensional stress is concentrated within the lava layer (E4) and only slightly in the overlying scoria (E5) unit. However, the trajectories of σ_1 rotated by approximately 45° directly above the dyke tip and close to 90° in the overlying scoria (E5) and lava (E6) contact which would likely favour arrest. In the next set of unit contacts (A3-c) the tensional stresses are concentrated above the dyke tip in the stiff lava (E6) unit, and the stress trajectories are both nearly vertical.

Accordingly, in model B3-a and B3-b,the dyke tip tensional stresses and the trajectories of σ_1 follow similar patterns with A3-a and A3-b. Also, in the next set of unit contacts (B3-c), the tensile stresses are concentrated above the dyke tip in the stiff lava (E6), and σ_1 is vertical which indicates a high likelihood of propagation like A3-c.

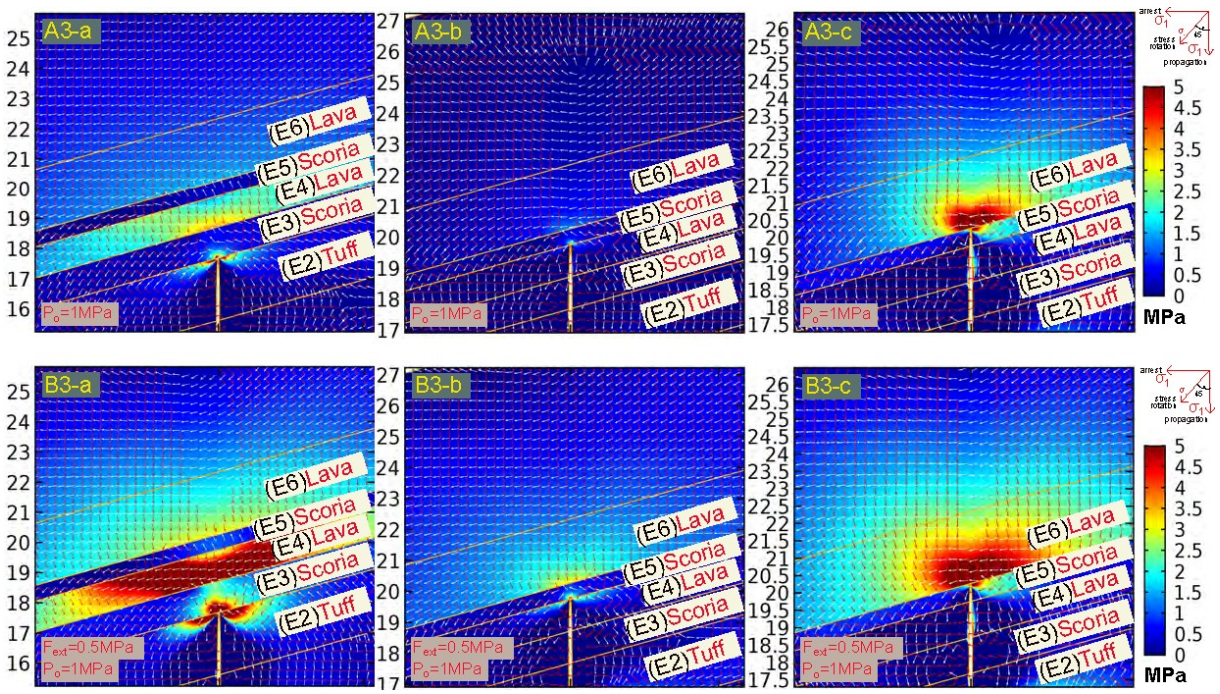

Fig. 4.12: FEM (finite element) models of dyke propagation (tensile stress σ_3) in a heterogeneous host rock based on Fig. 4.11B. (A3a-c): Overpressure (P_o=1MPa) is the only loading boundary condition, (B3a-c): Overpressure (P_o=1MPa) and an extensional stress field (F_{ext}=0.5MPa) are applied. The red arrow surface is σ_1 and the white arrow surface is σ_3, (a) scoria/tuff contact, (b) scoria/lava contact, (c) lava/scoria contact (y-axis in meters).

Table 4.3: Modelling results for dyke 2 with an applied overpressure (P_o) of 1MPa and an additional horizontal extension of 0.5 MPa. The table also includes a qualitative interpretation of the dyke propagation path as defined through numerical modelling. Tensile stress is measured directly in ahead of the dyke tip (Low: 0.5- 1.5MPa, Moderate: 1.5-3MPa, High: 3-5MPa). The condition for propagation is met if the stress at the tip exceeds 0.5 MPa and if the trajectory of σ_1

is close to 90˚. The dyke propagates in a σ_1 and σ_3 plane and their trajectories are shown in the models. The intermediate principal stress (σ_2) was calculated (if possible) from numerical models not shown here.

(A3) P_o=1 MPa	**Layer contacts (E_U/E_L)**	**Stress concentration at the tip**	**Stress rotation at the tip and its vicinity**	**Dyke path**	**(B3) P_o=1MPa and 0.5 MPa extension**	**Stress concentration at the tip**	**Stress rotation at the tip and its vicinity**	**Dyke path**
(a)	Scoria/Tuff	Moderate	(σ_1): 0˚- 90˚ (σ_2): 0˚- 90˚ (σ_3): 0˚- 90˚ (A3-a)	Likely Arrest	**(a)**	High	(σ_1): 0˚- 90˚ (σ_2): 0˚- 90˚ (σ_3): 0˚- 90˚ (B3-a)	Likely Arrest
(b)	Scoria/Lava	Moderate	(σ_1): 0˚- 90˚ (σ_2): 0˚- 90˚ (σ_3): 0˚- 90˚ (A3-b)	Likely Arrest	**(b)**	Moderate	(σ_1): 0˚- 90˚ (σ_2): 0˚- 90˚ (σ_3): 0˚- 90˚ (B3-b)	Likely Arrest
(c)	Lava/Scoria	Low	(σ_1): 0˚- 10˚ (σ_2): 0˚- 10˚ (σ_3): 0˚- 10˚ (A3-c)	Propagation	**(c)**	High	(σ_1): 0˚- 10˚ (σ_2): 0˚- 10˚ (σ_3): 0˚- 10˚ (B3-c)	Propagation

6.3.2 Dyke 2 with a 5 MPa driving pressure

We modelled dyke 2 by modifying only the overpressure (P_o) to 5MPa. The models are shown in Fig. 4.13 and the results in Table 4.4.

The results from models A4-a and A4-b are similar to models A3-a and A3-b and show a higher concentration of stresses at the same locations and within the same rock units. The trajectories of σ_1 rotate by approximately at 45° directly above the dyke tip and up to 90° at the overlying scoria (E5) and lava (E6) contact promoting possible arrest - although the scoria (E5) and lava (E6) contact (A4-c) indicates no stress rotations. Models B4-a-c were developed similarly and also suggest the likelihood of dyke arrest at the scoria (E5) and lava (E6) contact.

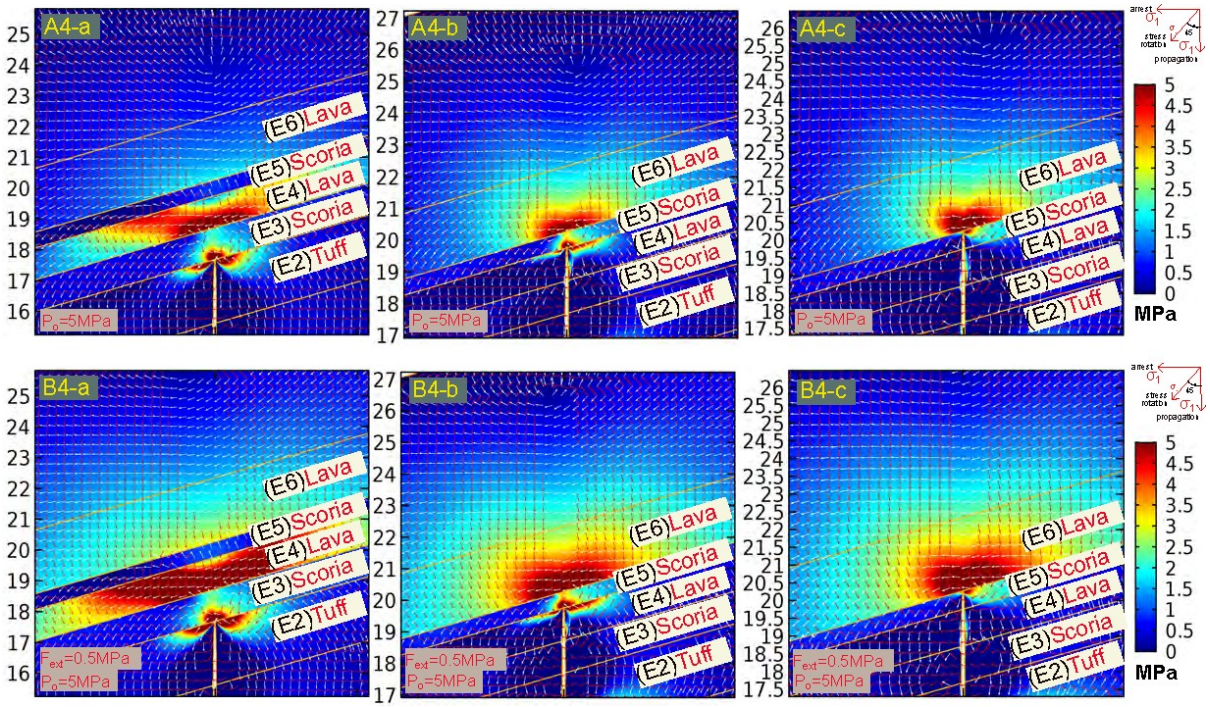

Fig. 4.13: FEM (finite element) models of dyke propagation (tensile stress σ_3) in a heterogeneous host rock based on Fig. 4.11B. (A4a-c): Overpressure (P_o=5MPa) is the only loading boundary condition, (B4a-c): Overpressure (P_o=5MPa) and an extensional stress field (F_{ext}=0.5MPa) are

applied. The red arrow surface is σ_1 and the white arrow surface is σ_3, (a) scoria/tuff contact, (b) scoria/lava contact, (c) lava/scoria contact (y-axis in meters).

Table 4.4: Modelling results for dyke 2 with an applied overpressure (P_o) of 5MPa and an additional horizontal extension of 0.5 MPa. The table also includes a qualitative interpretation of the dyke propagation path as defined through numerical modelling. Tensile stress is measured directly in ahead of the dyke tip (Low: 0.5- 1.5MPa, Moderate: 1.5-3MPa, High: 3-5MPa). The condition for propagation is met if the stress at the tip exceeds 0.5 MPa and if the trajectory of σ_1 is close to 90˚. The dyke propagates in a σ_1 and σ_3 plane and their trajectories are shown in the models. The intermediate principal stress (σ_2) was calculated (if possible) from numerical models not shown here.

(A4) P_o=5 MPa	**Layer contacts (E_U/E_L)**	**Stress concentration at the tip**	**Stress rotation at the tip and its vicinity**	**Dyke path**	**(B4) P_o=5MPa and 0.5 MPa extension**	**Stress concentration at the tip**	**Stress rotation at the tip and its vicinity**	**Dyke path**
(a)	Scoria/Tuff	High	(σ_1): 0˚- 90˚ (σ_2): 0˚- 90˚ (σ_3): 0˚- 90˚ (A4-a)	Likely Arrest	**(a)**	High	(σ_1): 0˚- 90˚ (σ_2): 0˚- 90˚ (σ_3): 0˚- 90˚ (B4-a)	Likely Arrest
(b)	Scoria/Lava	High	(σ_1): 0˚- 90˚ (σ_2): 0˚- 90˚ (σ_3): 0˚- 90˚ (A4-b)	Likely Arrest	**(b)**	High	(σ_1): 0˚- 90˚ (σ_2): 0˚- 90˚ (σ_3): 0˚- 90˚ (B4-b)	Likely Arrest
(c)	Lava/Scoria	High	(σ_1): 0˚- 10˚ (σ_2): 0˚- 10˚ (σ_3): 0˚- 10˚ (A4-c)	Propagation	**(c)**	High	(σ_1): 0˚- 10˚ (σ_2): 0˚- 10˚ (σ_3): 0˚- 10˚ (B4-c)	Propagation

6.4 Theoretical stress concentration at the dyke tips

For dyke 1 we report a range of theoretical stresses at the dyke tips. For 1MPa magmatic overpressure the maximum theoretical stress concentrating at the tip of the dyke at a 1) very compliant-compliant contact is 0.23 GPa, 2) very compliant-stiff contact is 2.28 GPa, 3) stiff-very compliant contact is 0.13 GPa. For an extra horizontal extension, the stress at the tips rises in the first contact by 40%, in the second by 78% and in the third by 62% generating maximum stresses of 0.32 GPa, 4.05 GPa and 0.2 GPa respectively. For 5 MPa overpressure, the calculated maximum stress is 1.1 GPa for the first contact (r=0.1), 11.4 GPa for the second contact (r=0.05) and 0.67 GPa for the third (r=20) and by adding the extra horizontal extension the stresses increase to 1.43 GPa (30%), 13.2 GPa (16%) and 0.75 GPa (12%).

We used the same methodology for dyke 2 and calculated the maximum stress concentration for 1 MPa magmatic overpressure in the same three contacts which showed 0.22 GPa, 0.67 GPa and 0.10 GPa. For an extra horizontal extension, the stress at the tips rises in the first contact by 68%, in the second by 70% and in the third one by 80% presenting maximum stresses of 0.37 GPa, 1.14 GPa and 0.18 GPa respectively. For 5 MPa the calculated maximum stress is 1.13 GPa for the first contact (r=0.1), 3.82 GPa for the second contact (r=0.05) and 0.61 GPa for the third one (r=20) and they rise to 1.43 GPa (13%), 13.2 GPa (14%) and 0.75 GPa (16%). The results are shown in Fig. 4.14.

All these tip stresses are entirely theoretical and follow primarily from the mechanical properties of the layers hosting the tips and, in particular, from the geometric constraints (tips are commonly very narrow), and the applied load (overpressure). The stress magnitudes are similar to those obtained for dyke tips in other numerical models (Gudmundsson, 2003). For comparison,

analytical mathematical mode I crack models yield infinite stresses (a singularity) at the tip (Sneddon, 1946). No rocks are known to tolerate in-situ tensile stresses in excess of about 9 MPa (Gudmundsson, 2011b).

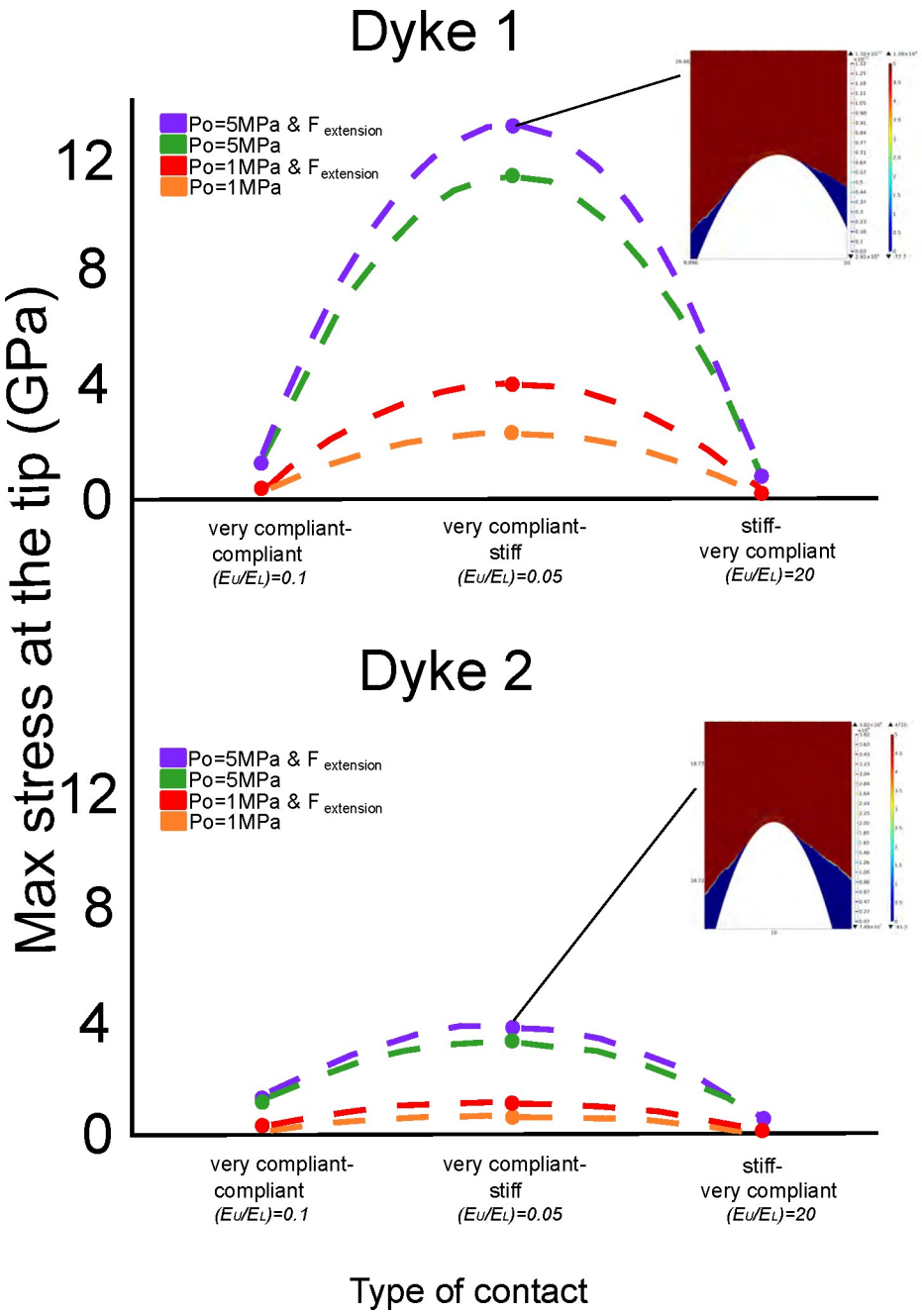

Fig. 4.14: Diagram showing the max stress concentration at the dyke tips for both dykes at the studied loading conditions, in different type of contacts 1) very compliant - compliant (r=0.1), 2) very compliant - stiff (r=0.05), 3) stiff - very compliant (r=20). The figures on the right up corner of the graphs are showing the stress concentration on the dyke tips at the compliant - stiff contacts for dyke 1 and dyke 2.

6.5 Sensitivity tests

Although the numerical models agree with the field observations indicating that stress rotations contributed to the arrest of dyke 2, the questions as to which factors encourage stress rotations and subsequently the formation of stress barriers, are only partially answered. For that reason, we conducted multiple runs (sensitivity tests) to explore the possible cause(s) that could promote stress rotations at the tip of dyke 2.

We investigated the contribution of combinations of parameters in our numerical model setups. Two suites of sensitivity tests were designed to reflect the possible arrest conditions. Initially, the study focused on the combination of the material and magmatic properties (Fig. 4.15A), and in a second stage, we studied the external stress field with the material properties of the host rock (Fig. 4.15B). The sensitivity test models are shown in the supplementary files (Supporting information files 1-6, Appendix C1).

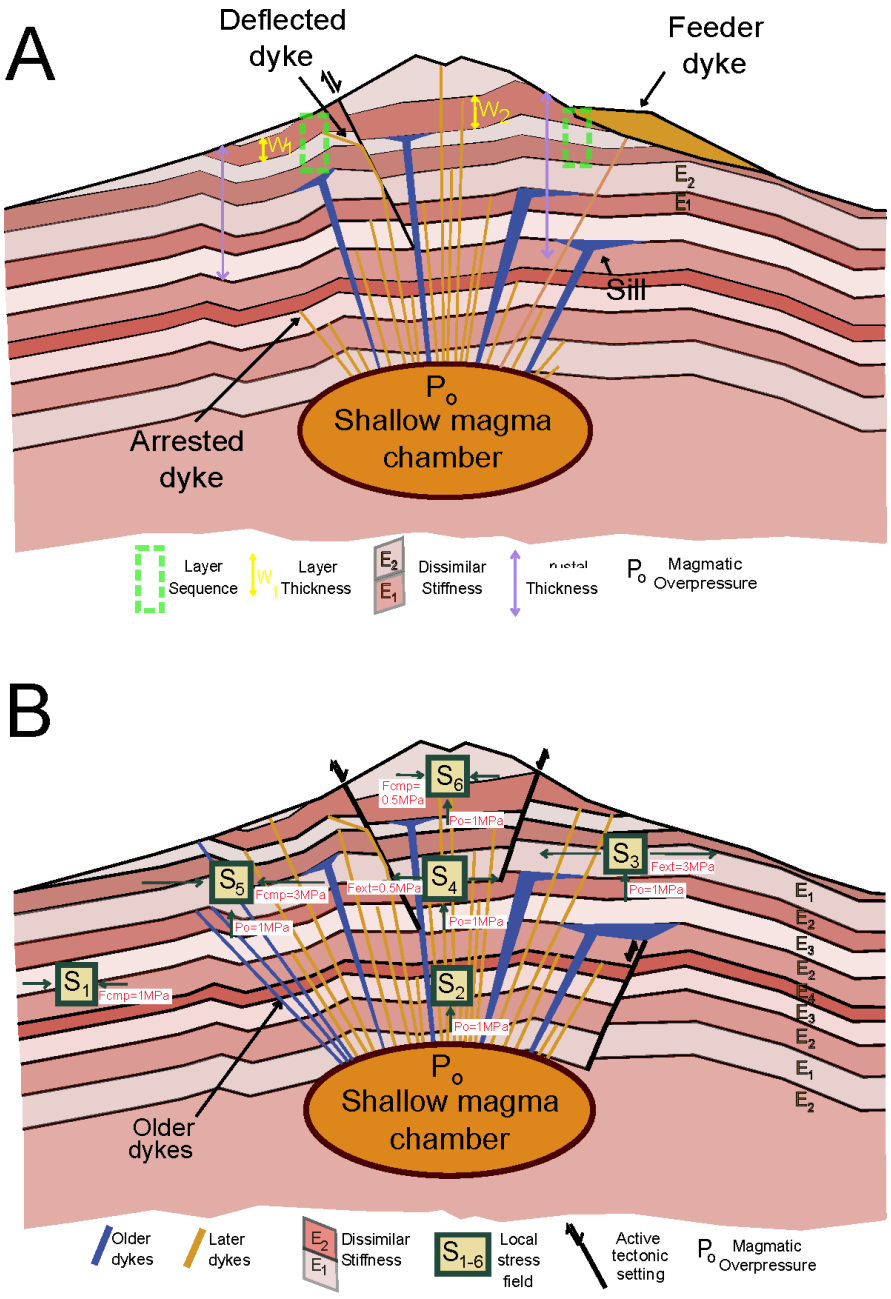

Fig. 4.15: Schematic illustrations showing the parameters studied in the sensitivity tests. (A): Connections between magmatic conditions (magmatic overpressure, P_o) and the stratigraphy-mechanical/material conditions of the host rock such as the sequence of the stratigraphy, the thickness of the layers (W_L), and the crustal thickness (W_C). (B): Conditions of magmatic

overpressure (P_o) associated with different boundary conditions on the creation of stress rotations and stress barriers in an active volcanotectonic setting.

Layer thickness (W_L):

We modelled the effects of layer thickness on the local stress and found that principal-stress rotations were mostly controlled by the stiffness contrast of the layers. However, when the thickness of a stiff layer (e.g. a lava flow) is increased by a factor of ten we observe stress rotations in the lava layer and in the vicinity of the dyke tip regardless the stiffness values (Fig. 4.16-1). In addition, when the thickness of a soft layer (e.g. scoria) is increased by a factor of ten, stress rotations in both the scoria and lava layers were observed in the vicinity of the dyke tip at a low stiffness contrast (Fig. 4.16-2). Thus, a thick stiff layer can become a stress barrier whereas a thick soft layer can generate stress rotations if the dyke propagates through soft layers with low stiffness contrasts (r=0.5)

Stratigraphic sequence

The sensitivity models reflect how effectively the stratigraphy of the host rock together with the stiffness of the layers can control stress rotations. Stress rotations were observed only when the stiffness contrast was low (r=0.5 or 5). Apparently, this parameter can make soft layers to stress barriers as shown in Figure 4.16-3.

Crustal thickness (Wc)

We tested how the variable thickness of the crust can promote stress rotations. In our models as shown in Figure 4.16-4 we designed thicker domains by adding an extra thick layer atop the sequence. We observed that a thick sequence can generate stress rotations especially in compliant layers such as scoria if the dyke propagates again through layers of high stiffness contrast (r=50).

Overpressure (P_o):

We made many models to test the effect of overpressure on dyke arrest. The magmatic overpressure is important parameter as it provides to the dyke the essential pressure to propagate subject to a satisfactory energy criterion. However, other parameters are also important in that they control principal stress rotation and other effects that lead to dyke arrest. We did not test the relation between the overpressure and dyke thickness because both studied dykes are of the same average thickness. We know, however, that the aperture or thickness of the dyke is positively correlated with its overpressure (Eq. 4.6).

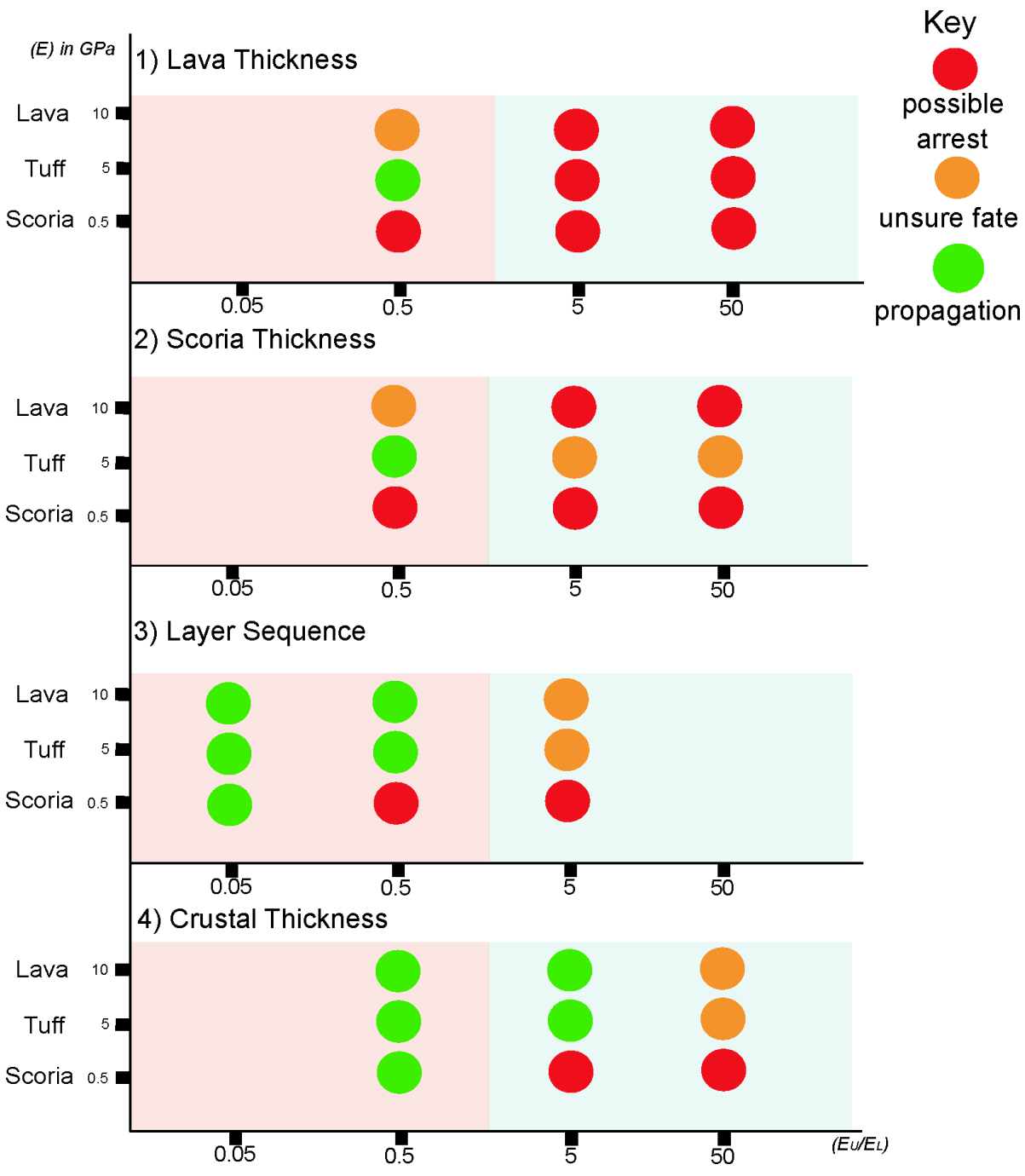

Fig. 4.16: Results of the sensitivity tests as shown in Fig. 4.15 Part A. Different stiffness contrasts (E_U/E_L) (0.05, 0.5, 5, 50) subject to 1 and 5MPa overpressure control the observed stress rotations

in three different rock type layers. Annotations: Red circle for possibly arrest, orange for unsure fate and green for propagation.

Regional and local stress field

We examined stress rotations under different loading boundary conditions and with layers of contrasting stiffness (Fig. 4.17). The S1 scenario was used as a benchmark model while S2 mainly describes the conditions close to a magma chamber where the overpressure should be sufficient as a principal control on the propagation of the dyke. The scenarios S3&4 simulate an extensional regime such as a rift zone, or the regional extension due to the extension and the rapid roll-back that the Aegean Sea experiences. The models clearly show that if a dyke propagates in an extensional stress regime (Fig. 4.17-S3&4) stress rotation can occur in all layers for every studied stiffness contrast except in compliant layers (e.g. scoria) when a dyke propagates from a soft/compliant to a stiff layer (r=50). However, under a horizontal compression (Fig. 4.17-S5&6) stress rotations can occur again regardless of the stiffness contrasts in all type of layers except in a soft layer (e.g. scoria) where propagation can be encouraged in high stiffness contrasts (r=50). Compressional stress fields describe regional stress conditions due to previous dyke injections, faulting, or graben subsidence.

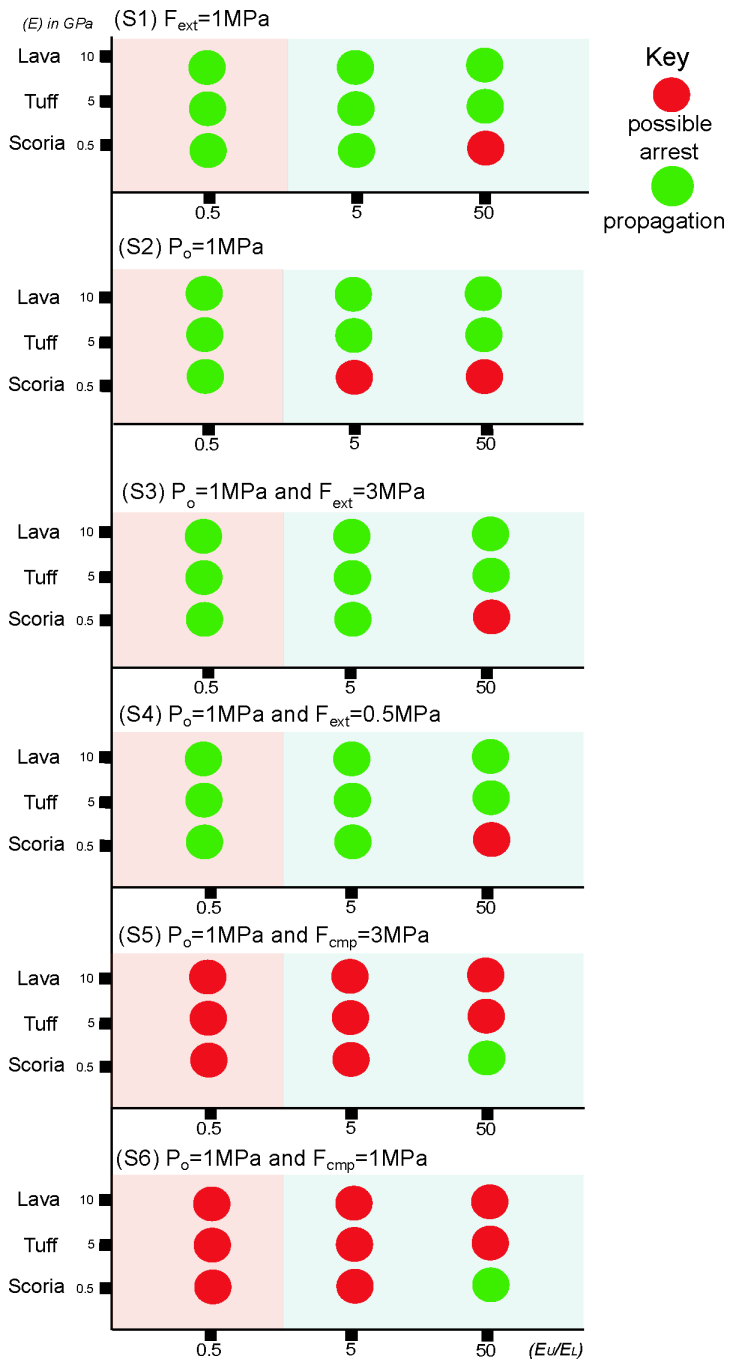

Fig. 4.17: Figure showing the results of the second model suites of the sensitivity tests as shown in Fig. 4.15 Part B subject to different stiffness contrasts (E_U/E_L) (0.5, 5, 50). We observe the

mutual connections between the magmatic conditions subjected to changes in the local stress field and producing stress barriers. S1: application of horizontal extension (F_{ext}= 1MPa), S2: application of magmatic overpressure (P_o=1MPa), S3: application of magmatic overpressure (P_o=1MPa) and horizontal extension (F_{ext}= 3MPa), S4: application of magmatic overpressure (P_o=1MPa) and horizontal extension (F_{ext}= 0.5MPa), S5: application of magmatic overpressure (P_o=1MPa) and horizontal compression (F_{cmp}= 3MPa), S6: application of magmatic overpressure (P_o=1MPa) and horizontal compression (F_{cmp}= 0.5MPa).

7. Discussion

The results of the numerical models have various theoretical and applied implications. For example, we calculated the theoretical tensile stresses ahead of a dyke snapshot in both homogeneous and heterogeneous crustal segments. We found that the tensile stress increases with increasing overpressure as well as with horizontal extension at the model boundary (Figs. 4.9-4.10 and 4.12-4.13). In addition, higher stresses concentrate in the stiff lava layers while the soft scoria and tuff layers suppress the stresses.

We also investigated the theoretical stresses close to and at the tips in all the studied types of contacts (Fig. 4.14). The results show that the tensile stresses at the tip can theoretically become 3 to 4 orders of magnitude higher than the overpressure. In detail, the study revealed the following for both the dykes:

1) Stress concentration is positively correlated with the stiffness of the host rock layers. More specifically, the stiffer they are, the higher the theoretical tensile stress.

2) Stress concentration is also positively correlated with magmatic overpressure and with the application of the external horizontal extension. More specifically, when either of these increases, then so does the theoretical tensile stress.

The numerical models also show that crustal anisotropy (layering) has a substantial effect on the alignment and rotation of principal stresses. This is of great importance for dyke paths and the potential for eruption. For example, rotation of σ_1 from being vertical to horizontal will almost always result in the arrest - or deflection into a sill - of a vertically propagating dyke, the layer with the rotated stresses acting as a stress barrier.

However, a stress barrier was not generated in any of the models for dyke 1. As a result, the numerical modelling supports the field-based indication of a continuous and non-arrested path, albeit with slight variations in path dip. In the models for dyke 2, we observed minor stress rotations at the contact between the tuff and unconsolidated scoria (as shown in part A3a-c of Fig. 4.12). By contrast, stress rotations of up to 90° were observed at the contact between very stiff lava flows and soft layers such as unconsolidated scoria (as shown in part B3-a of Fig. 4.12), generating stress barriers. The dyke in this instance, however, may also have become arrested by the elastic mismatch process as the soft unconsolidated scoria and the stiff lava flows have very different elastic properties (Young's modulus). This is very much in agreement with the field observations which clearly show that the dyke tip thinned out gradually until it stopped at the E6 (lava) - E5 (scoria) contact.

We also made comparisons of the present results with laboratory experiments. Analogue models (Kavanagh et al., 2006) suggest that a dyke may become arrested when the driving pressure is almost equal to the excess pressure needed for a dyke to penetrate the stiffer layer atop. We

compared the proposed dyke paths (with possible stress rotations) of our tested stiffness ratios with the proposed experimental dimensionless stiffness ratios (two-layered system with high stiffness ratios) from Kavanagh et al. (2006). The results showed that experimentally arrested dykes form when the ratio of E_U/E_L is 14.95. In our models with a six-layer sequence, Eq. 4.6 indicates that dyke 2 would promote stress rotations and become arrested when the ratio of E_U/E_L was as high as 20 (E_U/E_L=10/0.5=20) and so in agreement with the analogue experiments.

2D BEM numerical models and laboratory experiments (Maccaferri et al., 2010) suggest that the elastic energy release rate (G) during crack propagation through a boundary from a soft to a stiff layered elastic body with high stiffness contrast diminishes steeply promoting dyke deflection to inclined sheets. These results are in agreement with analytical results on the effects of elastic mismatch on mode I fracture deflection (He and Hutchinson, 1989; Gudmundsson, 2011a,b). Our models show that vertical dykes with the same stiffness contrast (r=5 or 20) can produce stress rotations and probably dyke arrest in heterogeneous domains. Future studies on how the energy criteria affect the dyke propagation paths in terms of their dip should be encouraged.

The numerical models indicate that dyke arrest can occur due to variations in mechanical properties of layers, particularly in stiffness (Young's modulus). Layer stiffness, however, changes during time and depends on the age of and depth below the surface at the time of dyke emplacement. Generally, rock layers become stiffer with time, particularly pyroclastic and sedimentary layers, primarily due to secondary mineralisation and compaction. Thus, generally, the tendency to dyke arrest is greatest in a comparatively young stratovolcano while the mechanical contrast between layers that constitute the roof of the source chamber is great. Gradually, due to compaction and mineralisation, the mechanical properties of the crustal segments or sequences become more

similar, that is, homogenized, and normally easier to penetrate by dykes. Thus, contacts that early in the history of the volcano arrest dykes, may allow dykes to penetrate later in the history of the volcano.

This brings us to the age of the layers and thus to a brief overview of the relevant geological history of the sections dissected by dykes 1 and 2. The deposition of av1 (Fig. 4.4) took place between 530-430 ka followed by av2 and av3 horizons which formed the Peristeria stratovolcano. Later eruptions formed the cinder cones and then the Skaros and Therasia shields on top of the stratigraphy of Peristeria. The oldest dyke population in Figure 4.4, which strikes NW-SE was possibly emplaced during the formation of the Peristeria volcano as it was found to dissect only the av1 horizon. The dykes are extensively weathered and of a characteristic red (or light) colour possibly due to oxidation and are likely of felsic composition. A second, younger dyke population was emplaced in the same section, cross-cutting the stratigraphy and the earlier dykes. These dykes strike NE-SW and have an average thickness of 0.5 m and are generally of mafic composition. Dyke 1 propagated to the higher stratigraphic horizons while dyke 2 became arrested at the contact between a scoria and a lava layer in av1.

The host rock is formed by a seemingly random sequence of andesitic lavas, tuffs, scoria and breccia (hyaloclastites). The layers are dipping 20° to the east and have variable thicknesses. The base layer is formed by a sequence of lava and breccia with variable thickness and grain size.

Given the structural study of the area, the possible scenarios of the observed dyke path are:

1) Dyke 1 and dyke 2 were emplaced after the formation of the Peristeria volcano. The emplacement of dyke 1 (or dyke 2) and the paths were then primarily determined by the variation in mechanical properties and local stresses of the layers.

2) Dyke 1 is propagating through the stratigraphy subject to a local compressional stress field imposed by the previous dyke injections and a regional extensional stress field imposed by the rift zone. Dyke 1 may have propagated partly due to the extensional stress field that do not mainly promote stress rotations in combination with low stiffness contrasts (r=0.5 or 5). Subsequently injected dyke 2 interacts with the local stress field imposed by dyke 1.

In detail, dyke paths in the shallow crust are much affected by the local material properties of the rock layers and by associated local stresses. Local stresses commonly generate stress barriers encouraging dyke arrest. Also, while the overpressure is primarily the driving force of dyke propagation from and near the magma chamber (Gudmundsson, 2003), it is not constant and, particularly for mafic dykes injected from shallow chambers, the overpressure tends to decrease towards the surface – because of negative buoyancy (Eq. 4.5). Other factors that may contribute to dyke arrest, discussed here, include layer thickness and layer stiffness. Stiffness, particularly rather stiffness contrast across contacts, is the most fundamental parameter as regards dyke arrest. This is not only because stiffness largely controls principal stress rotations and the formation of stress barriers, but also because variation in stiffness between layers is the main contribution to elastic mismatch, which is the major contribution to dyke arrest, particularly in stratovolcanoes such as Santorini.

8. Conclusions

Our combined field and numerical modelling study allow the following conclusions to be drawn on the structure and emplacement of dykes within arc volcanic settings such as at Santorini volcano.

1) Host-rock layering and anisotropy largely controls dyke propagation path and arrest in the shallow crust of Santorini volcano. The arrangement of layers with different stiffnesses determines the local stress fields within a volcano and hence the attitude and fate of the propagating dykes.
2) The dyke swarm at Santorini was formed over several episodes. Analysis of the attitude and location of dykes indicates that the swarm fed four distinct localities atop.
3) Most dykes injected from a crustal magma chamber do not make it to the surface to feed an eruption; instead, they become arrested, commonly at contacts between mechanically dissimilar layers.
4) Analytical results suggest that the dykes at Santorini formed and propagated under an overpressure (driving pressure) between 0.1 MPa to 6 MPa (90% of the measurements).
5) We suggest that most arrested dykes were either arrested on meeting stress barriers (where σ_1 has rotated to become horizontal instead of vertical) or on meeting contacts between layers of contrasting stiffness, an elastic mismatch. In agreement with stress barriers and elastic mismatch mechanisms, our FEM models show that soft-stiff contrasts (stiff layer hosting dyke tip below the contact with a soft layer above the contact) may encourage dyke penetrating the contact whereas stiff-soft ones can produce stress barriers and elastic mismatch that encourage dyke arrest.

6) The results suggest that thicker lava or scoria layers are more likely to promote stress rotations and dyke arrest than thin layers with the same mechanical properties. By contrast, magmatic overpressure, although partly controlling stress concentrations at dyke tips, cannot as such induce stress rotations.
7) Soft scoria layers can encourage stress rotations/barriers, even when a dyke propagates from a stiff to a soft layer, unless the stiffness contrast stiff-soft-(E_U/E_L) is low.

Acknowledgements

We thank the editor D. Roman and two anonymous reviewers for comments which helped improve this manuscript. Furthermore, we thank A. Rust and K. Cashman for helpful comments and suggestions which significantly improved an earlier version of the manuscript. We also thank N. Forbes Inskip for discussions about the numerical modelling aspects. KD is grateful for a Kirsty Brown memorial fund which enabled fieldwork in the Aegean. JB gratefully acknowledges support from the projects Fondecyt 11190143 and Fondap-Conicyt 15090013.

Declarations of interest: None

REFERENCES

Acocella, V., Neri, M., 2003. What makes flank eruptions? The 2001 Etna eruption and its possible triggering mechanisms. Bull Volcanol. 65, 517-529.

Amadei, B., Stephansson, O., 1997. Rock stress and its measurement. Chapman and Hall, London

Anderson, E.M., 1951. Dynamics of faulting and dyke formation, 2nd edn. Olivier and Boyd, Edinburgh.

Andújar, J., Scaillet, B., Pichavant, M., Druitt, T. H., 2015. Differentiation conditions of a basaltic magma from Santorini, and its bearing on the production of andesite in arc settings, J. Petrol. 56, 765–794.

Babiker, M., Gudmundsson A., 2004. The effects on dykes and faults on groundwater flow in an arid land: the Red Sea Hills, Sudan. J. Hydrol. 297, 256-273

Bailey, J. C., Jensen, E., Hansen, A., Kann, A., Kann, K., 2009. Formation of heterogeneous magmatic series beneath North Santorini, South Aegean island arc, Lithos, 110, 20–36.

Barnett, Z.A., Gudmundsson, A., 2014. Numerical modelling of dykes deflected into sills to form a magma chamber. J. Volcanol. Geother. Res. 281, 1-11.

Becerril, L., Galindo, I., Gudmundsson, A., Morales, J. M., 2013. Depth of origin of magma in eruptions. Sci. Rep., 3, 2762; doi:10.1038/srep02762.

Bell, F.G., 2000. Engineering properties of Soils and Rocks, 4th edn. Blackwell, London.

Brun, J.P., Faccenna, C., Gueydan, F., Sokoutis, D., Philippon, M., Kydonakis, K., Gorini, C., 2017. Effects of slab rollback acceleration on Aegean extension. Bulletin of the Geological Society of Greece. 50, 5-23.

Burchardt, S., 2008. New insights in the mechanics of sill emplacement provided by field observations of the Njardvik Sill, Northeast Iceland. J. Volcanol. Geother. Res. 173, 280-288

Broek, D., 1982. Elementary engineering fracture mechanics, The Hague, The Netherlands Martinus Nijhoff.

Browning, J., Gudmundsson, A., 2015. Caldera faults capture and deflect inclined sheets: an alternative mechanism of ring dike formation. Bull. Volcanol. 77, 1-13

Browning, J., Drymoni K., Gudmundsson A., 2015. Forecasting magma-chamber rupture at Santorini volcano, Greece. Sci. Rep.. 5, 15785; doi: 10.1038/srep15785

Cashman, K.V., 2004. Volatile controls on magma ascent and eruption, in Sparks R.S.J. Hawkesworth C.J. (eds.), The State of the Planet: Frontiers and Challenges in Geophysics: Geophysical Monograph 150: Washington, D.C., American Geophysical Union, p.109–124, doi: 10.1029/150GM10.

Cook, J., Gordon, J.E., 1964. A mechanism for the control of crack propagation in all-brittle systems. Proceedings of the Royal Society, Vol 282, 1364-5021, doi.org/10.1098/rspa.1964.0248.

Dahm, T., 2000. On the shape and velocity of fluid-filled fractures in the Earth. Geophys. J. Int. 142, 181-192

Delaney, P., Pollard, D., Ziony, J., McKee E., 1986. Field relations between dikes and joints: emplacement processes and paleostress analysis J. Geophys. Res., 91, 4920-4938

Druitt, T. H., Francaviglia, V., 1992. Caldera formation on Santorini and the physiography of the islands in the late Bronze Age. Bull. Volcanol. 54, 484–493

Druitt, T.H., Edwards, L., Mellors, R.M., Pyle, D.M., Sparks, R.S.J., Lanphere, M., Davis, M., Barriero, B., 1999. Santorini Volcano. Geological Society Memoir No. 19, 165

Dundurs, J., 1969. Edge-bonded dissimilar orthogonal wedges. Journal of Applied Mechanics, 36, 650-652.

Feuillet, N., 2013. The 2011–2012 unrest at Santorini rift: Stress interaction between active faulting and volcanism, Geophys. Res. Lett., 40, 3532–3537, doi:10.1002/grl.50516.

Forbes Inskip, N.D., Meredith, P.G., Chandler, M.R., Gudmundsson, A., 2018. Fracture properties of Nash Point shale as a function of orientation to bedding, J. Geophys. Res. Vol 123, 10, 8428-8444, doi:10.1029/2018JB015943

Fouqué, F.A., 1879. Santorin et ses éruptions. Masson, Paris, 440 pp.

Freund, L.B, and Suresh, S., 2003. Thin film materials: Stress, defect formation and surface evolution. Cambridge University Press, Cambridge.

Garcia, I.G., 2014. Crack initiation in composites at micro and meso scales: Development and applications of finite fracture mechanics. Ph.D. thesis, Universidad de Sevilla, Spain

Gautneb, H., Gudmundsson, A., Oskarsson, N., 1989. Structure, petrochemistry and evolution of a sheet swarm in an Icelandic central volcano. Geol .Mag. 126, 659–673

Geshi, N., Kusumoto, S., Gudmundsson, A., 2010. Geometric difference between non-feeder and feeder dikes. Geology 38, 195-198

Grasemann, B., Schneider, D.A., Stöckli, D. F., Iglseder, C., 2012. Miocene bivergent crustal extension in the Aegean: Evidence from the western Cyclades (Greece). Lithosphere. 4, 23–39, doi.org/10.1130/L164.1

Griffith, A.A., 1921. The phenomena of rupture and flow in solids. Phil.Trans. Roy. Soc. A., 221, 163-198

Griffith, A.A., 1924. The theory of rupture. First international congress of Applied Mathematics, Delft, pp. 55-63

Gudmundsson, A., 1983. Form and dimensions of dykes in eastern Iceland Tectonophysics, 95, 295-307

Gudmundsson, A., 1988. Formation of collapse calderas. Geology, 16, 808-810.

Gudmundsson, A., 1995. The geometry and growth of dykes. In: Baer, G., Heimann, A. (eds), Physics and Chemistry of Dykes. Balkema, Rotterdam, pp.23-34.

Gudmundsson, A., 2002. A. Emplacement and arrest of sheets and dykes in central volcanoes J. Volcanol. Geotherm. Res., 116, 279-298

Gudmundsson, A., 2003. Surface stresses associated with arrested dykes in rift zones Bull. Volcanol. 65, 606-619, 10.1007/s00445-003-0289-7

Gudmundsson A., 2006. How local stresses control magma-chamber ruptures, dyke injections, and eruptions in composite volcanoes Earth Sci. Rev., 79, 1-31.

Gudmundsson, A., 2008. Magma-chamber geometry, fluid transport, local stresses, and rock behaviour during collapse-caldera formation. In: Gottsmann, J., Marti, J. (eds.), Caldera Volcanism: Analysis, Modelling and Response. Developments in Volcanology 10. Elsevier, Amsterdam, pp. 313-349

Gudmundsson, A., 2011a. Deflection of dykes into sills at discontinuities and magma-chamber formation. Tectonophysics, 500, 50–64.

Gudmundsson, A., 2011b. Rock fractures in geological processes. Cambridge University Press, Cambridge.

Gudmundsson, A., 2012. Magma chambers: formation, local stresses, excess pressures, and compartments. J. Volcanol. Geotherm. Res., 237-238, 19–41

Gudmundsson, A., Brenner, S.L., 2001. How hydrofractures become arrested. Terra Nova, 13, 456–462.

Gudmundsson, A., Brenner, S., 2005. On the conditions of sheet injections and eruptions in stratovolcanoes. Bull. Volcanol., 67, 768–782

Gudmundsson, A., Marinoni L.B., Marti J., 1999. Injection and arrest of dykes: implications for volcanic hazards. J. Volcanol. Geotherm. Res. 88, 1-13.

Gudmundsson, A., Philipp, S. L., 2006. How local stress fields prevent volcanic eruptions. J. Volcanol. Geotherm. Res. 158, 257–268.

He, M.Y., Evans A.G, Hutchinson J.W., 1994. Crack deflection at an interface between dissimilar elastic materials. Int. J. Solids Struct. 25,1053-1067.

He, M.Y., Hutchinson, J.W., 1989. Crack deflection at an interface between dissimilar elastic materials. Int J Solids Struct 31, 3443–3455

Heap, M.J., Villeneuve, M., Albino, F., Farquharson, J.I., Brothelande, E., Amelung, F., Got, J-Luc., Baud, P., 2019. Towards more realistic values of elastic moduli for volcano modelling, J. Volcanol. Geotherm. Res. doi: https://doi.org/10.1016/j.jvolgeores.2019.106684

Hutchinson, J.W., 1996. Stresses and failure modes in thin films and multilayers. Technical University of Denmark-Notes for a DCAMM course.

Inglis, C.E., 1913. Stresses in a plate due to the presence of cracks and sharp corners. SPIE Milestone Series, 137, 3-17.

Jaeger, J.C. and Cook N.G.W., 1979. Fundamentals of rock mechanics. Chapman and Hall, London

Jousset, P., H. Mori and H. Okada., 2003. Elastic models for the magma intrusion associated with the 2000 eruption of Usu Volcano, Hokkaido, Japan, J. Volcanol. Geotherm. Res., 125, 81-106.

Kavanagh, J., Menand, T. and Sparks, R., 2006. An experimental investigation of sill formation and propagation in layered elastic media, Earth planet. Sci. Lett., 245, 799–813

Kavanagh, J.L, Rogers, B.D., Boutelier, D., Cruden, A.R., 2017. Controls on sill and dyke-sill hybrid geometry and propagation in the crust: The role of fracture toughness. Tectonophysics, 698, 109-120.

Kavanagh, J.L, Burns, A.J., Hazim, S.H., Wood, E.P., Martin, S.A., Hignett, S., Dennis, D.J.C., 2018. Challenging dyke ascent models using novel laboratory experiments: Implications for reinterpreting evidence of magma ascent and volcanism, J. Volcanol. Geotherm. Res., 354, 87-101.

Lister, J. R., and Kerr, R. C., 1991. Fluid-mechanical models of crack propagation and their application to magma transport in dykes. J. Geophys. Res. 96, 10049–10077. doi: 10.1029/91JB00600

Le Corvec, N., Menand, T., Lindsay, J., 2013. Interaction of ascending magma with pre-existing crustal fractures in monogenetic basaltic volcanism: an experimental approach. J. Geophys. Res. Solid Earth 118, 968–984.

Le Corvec, N., Muirhead, J.D. & White, J.D.L., 2018. Shallow magma diversions during explosive diatreme-forming eruptions. Nature Communications, 9, 1459, 105 https://doi.org/10.1038/s41467-018-03865-x.

Le Pichon, X., and Angelier, J., 1979. The Hellenic arc and trench system: A key to the neotectonic evolution of the eastern Mediterranean area. Tectonophysics, 60, 1-42

Maccaferri, F., Bonafede, M., Rivalta, E., 2010. A numerical model of dyke propagation in layered elastic media Geophys. J. Int.,180 ,1107-1123

Menand, T., Daniels, K. A., Benghiat, P. 2010. Dyke propagation and sill formation in a compressive tectonic environment, J. Geophys. Res., 115, B08201

Nicholls, I.A., 1971. Petrology of Santorini Volcano, Cyclades, Greece, J. Petrol, 12, 67–119

Parks, M.M., Biggs, J., England, P., Mather, T.A, Nomikou, P., Palamartchouk, K., Papanikolaou, X., Paradissis, D., Parsons, B., Pyle, D.M., Raptakis, C. and Zacharis, V., 2012. 'Evolution of Santorini Volcano dominated by episodic and rapid fluxes of melt from depth. Nature Geoscience, 5, 749-754. doi: 10.1038/NGEO1562

Petersen, A.D.J., 2005. A geological and petrological study of the dikes in the Megalo Vouno volcano complex, Santorini. M.Sc. thesis, Copenhagen University, Denmark

Pollard, D. D. Johnson, A. M., 1973. Mechanics of growth of some laccolithic intrusions in the Henry mountains, Utah, II. Bending and failure of overburden layers and sill formation. Tectonophysics, 18, 311-354

Pinel, V., and Jaupart, C., 2004. Magma storage and horizontal dyke injection beneath a volcanic edifice, Earth Planet. Sci. Lett., 221, 245–262.

Puchelt, H., Hubberton, H. W., Stellrecht, R., 1990. The geochemistry of the radial dykes of the Santorini Caldera and its implications, Thera and the Aegean World III Pro. 3rd Int. Cong., Santorini, Greece, 1989 (D. A. Hardy et al., eds) 229–236 (Thera Found, London 1990)

Ray, R., Sheth, H.C., Mallik, J., 2006. Structure and emplacement of the Nandurbar–Dhule mafic dyke swarm, Deccan Traps, and the tectonomagmatic evolution of flood basalts, Bull. Volcanol. 69, 537-551, doi:10.1007/s00445-006-0089-y

Rivalta, E., Bottinger, M. and Dahm, T., 2005. Gelatine experiments on dike ascent in layered media, J. Volc. Geotherm. Res., 144, 273–285.

Rivalta, E., B. Taisne, A. P. Bunger, R. F. Katz., 2015. A review of mechanical models of dike propagation: Schools of thought, results and future directions, Tectonophysics, 638, 1–42, doi:10.1016/j.tecto.2014.10.003.

Rubin, A.M., Pollard, D.D., 1987. Origins of blade-like dikes in volcanic rift zones R.W. Decker, T.L. Wight, P.H. Stuffer (eds.), Volcanism in Hawaii, US Geological Survey Professional Papers, 1350,1449-1470

Rubin, A. M., 1995. Propagation of magma-filled cracks. Annu. Rev. Earth Planet. Sci. 23,287–336. doi: 10.1146/annurev.ea.23.050195.001443

Sakellariou, D., Mascle, J., and Lykousis, V., 2013. Strike slip tectonics and transtensional deformation in the Aegean region and the Hellenic arc: Preliminary results. Bulletin of the Geological Society of Greece, 47, 647-656

Scudero, S., De Guidi, G., Gudmundsson, A., 2019. Size distributions of fractures, dykes, and eruptions on Etna, Italy: Implications for magma-chamber volume and eruption potential, Sci. Re, 9, 4139

Sneddon, I.N., 1946. The distribution of stress in the neighbourhood of a crack in an elastic solid. Proceedings of the Royal society doi: 10.1098/rspa.1946.0077

Taisne, B., and Jaupart, C., 2009. Dike propagation through layered rocks, J. Geophys. Res., 114, B09203, doi: 10.1029/2008JB006228.

Tibaldi, A., 2015. Structure of volcano plumbing systems: A review of multi-parametric effects. J. Volcanol. Geotherm. Res. 298, 85-135

Townsend, M.R., Pollard, D.D., Smith, R.P., 2017. Mechanical models for dikes: A third school of thought Tectonophysics, 703-704, 98-118.

Wang L.P and Xu, R., 2006. Dynamic interfacial debonding initiation induced by an incident crack International Journal of Solids and Structures, 43,6535-6550

Xu, R., Huang Y.Y., Rosakis A.J., 2003. Dynamic crack deflection and penetration at interfaces in homogeneous materials: experimental studies and model predictions, Journal of the Mechanics and Physics of Solids, 51, 461-486

Zellmer, G., Blake, S., Vance, D., Hawkesworth, C., Turner, S., 1999. Plagioclase residence times at two island arc volcanoes (Kameni Islands, Santorini, and Soufrière, St. Vincent) determined by Sr diffusion systematics. Contrib. Mineral. Petrol. 136, 345–357

Chapter 5

Manuscript in preparation for journal submission

Deflection of dikes and inclined sheets into faults at Santorini volcano, Greece

Statement of contribution:

Collection of primary field data and geological mapping done by KD

All field photographs and figures designed by KD

Complete 1st draft of manuscript and figures by KD

Revisions and subsequent drafts made with co-authors input

Interpretation of all data along with final model conducted by KD with support from co-authors

Deflection of dikes and inclined sheets into faults at Santorini volcano, Greece

Kyriaki Drymoni[a*], John Browning[b, c], Agust Gudmundsson[a]

a Department of Earth Sciences, Queen's Building, Royal Holloway University of London Egham, Surrey TW20 0EX, UK

b Department of Mining Engineering and Department of Structural and Geotechnical Engineering, Pontificia Universidad Católica de Chile, Santiago, Chile

c Centro de Excelencia en Geotermia de los Andes (CEGA), Chile

* Corresponding author

E-mail address: Kyriaki.Drymoni.2015@live.rhul.ac.uk

Abstract

Crustal discontinuities such as faults have long been considered important in controlling and facilitating the emplacement of magma. However, mechanisms by which dikes, and inclined sheets deflect into and exploit faults are poorly understood. To address this, we have made observations of dike-fault interactions at a well-exposed dike swarm at Santorini volcano, Greece. We observe multiple interactions between the dikes and faults, such as vertical dikes propagating along pre-existing fractures or inclined sheets that deflect into faults. Here we combine these field observations with FEM numerical models using COMSOL Multiphysics. The deflected dikes belong to a local swarm (of 91 dike segments) that were emplaced in a highly heterogeneous and anisotropic host rock and partially cut by a series of historic caldera collapse events and faults,

hence their exposure. Our models simulated a normal-fault damage zone, dipping 65°E, as composed of parallel layers or zones of progressively more compliant rocks with increasing distance from the fault rupture plane and the core. We simulate two sheet intrusions approaching the fault: an inclined sheet and a vertical dike, using overpressure of, alternatively, 1 MPa and 5 MPa. We wanted to test the angle of the dike-fault interaction so we modelled both intrusions on a range of rising angles from 0˚-90˚.We further tested the effects of changing the thickness of the dikes and sheets, the thickness of the fault zone, the dip-dimension (height) of the fault, and additional boundary loading to simulate both regional compression and regional extension. We find that the stiffness of the fault core, a measure of the activity of the fault (recently active faults having a compliant core) has great effect on the orientation and magnitudes of the local stresses, hence the likelihood of the fault capturing the sheet intrusion. Thus, the fault-zone thickness, mechanical properties and attitude with respect to the attitude of the sheet intrusion largely control the fault-sheet interaction. Lastly, we combine the previous volcanological and geophysical studies with our structural analysis and modelling to report the geological history of the northern caldera wall.

KEYWORDS: dike deflection, faults, inclined sheet, numerical modelling, Santorini

1. Introduction

Dike propagation is the most efficient form of magma transfer from the mantle or lower-crustal reservoirs to shallow magma chambers to eventually feed superficial volcanic eruptions

(Gudmundsson, 2011). Most dikes form their paths through the Earth's crust by rupturing the host rock and forming extensional fractures (Gudmundsson 1987; Tibaldi, 1992). However, there are cases where dikes and geo-fluids appear to follow pre-existing fractures such as faults or joints for at least a part of their propagation path (Cembrano and Lara, 2009; Spacapan et al., 2016; Sielfeld et al., 2019). One model to explain the propagation path of fluid-filled fractures into pre-existing fractures uses the concept of energy potential and hence suggests that self-propelled fracture propagates in orientations that favour a minimum energy use (Gudmundsson, 1984). As a result, a propagating dike will at any time pick the most economical path, either wholly or partly, and hence use normal, reverse or strike-slip faults, when they are favourably oriented (Delaney et al., 1986). However, precise field observations of the interactions between dikes and faults are limited. Rossetti et al., (2000) and Spacapan et al., (2016) have noted intrusion of dikes within strike-slip zones; and Browning and Gudmundsson (2015) also emphasised the deflection of magma sheets into a section of a normal fault bounding a caldera. Also, Magee and Jackson (2020) reported the structure and kinematics in 3D of dike-induced normal faults through reflection seismology. As field observations are limited, so is our understanding of the mechanisms and conditions under which fluid-driven fractures utilise pre-existing fractures.

Hence, this paper aims to address the mechanisms and parameters under which dikes, and inclined sheets interact with faults using data obtained from field observations and finite element numerical modelling methods. Specifically, we are interested in understanding how magma intrudes into a fault and hence help to address the long-standing issue of the relationship between crustal faults and magmatism. We propose a series of models, which when combined with real-time observations during unrest periods, will help forecast the likely path of a propagating dike and, specifically, whether a dike will favour the use of a fault in its path to reach the surface and form an eruption,

or not. Finally, we use for the first time the numerical modelling outcomes as a geological tool. We combine results from previous volcanological c and geophysical studies with our field observations, structural analysis and numerical models. We aim to reconstruct the geological history of the interactions between magmatic dikes and faults exposed in the northern caldera wall of Santorini volcano and unravel the volcanotectonics history of the northern caldera wall.

1.1 Mechanisms of fracture initiation, growth and propagation

Understanding dike propagation in the crust is essential for magma dynamics and eruption forecasting. Those concepts apply on Earth in different scales such as the microscale and the meso or macroscale where fracture mechanics and volcanotectonics are trying to encompass them respectively. A precise study of the fracture mechanics and material science advancements in the microscale allow us to focus on the parameters that control the initiation, growth and propagation of a crack/fracture. Subsequently, the combination of structural geology and numerical modelling in conjunction with the previously published knowledge give us valuable insights into the scale studied in this paper. In this stage, we would like to mention that although in the literature, the terms crack and fracture are often interchangeable, here, we follow the terminology of Broek (1982) and denote a fracture as an extended crack.

he mechanics that govern dike propagation in the shallow crust were essentially theorized by Griffith (1921, 1924) with an essential part of theory concerning the development of many fine ‘Griffith cracks’ generated at the tip (or process zone) of a propagating fracture (Atkinson, 1987; Atkinson and Meredith, 1987). These cracks are elliptical, thin, and atomically sharp (Fig. 5.1A).

If a sufficient level of tensile stress is concentrated at the tip of already formed flaws to become equal or greater than the tensile strength (T_o) of the rock, cracks nucleate and grow and eventually coalesce to form a fracture which propagates along the damaged process zone.

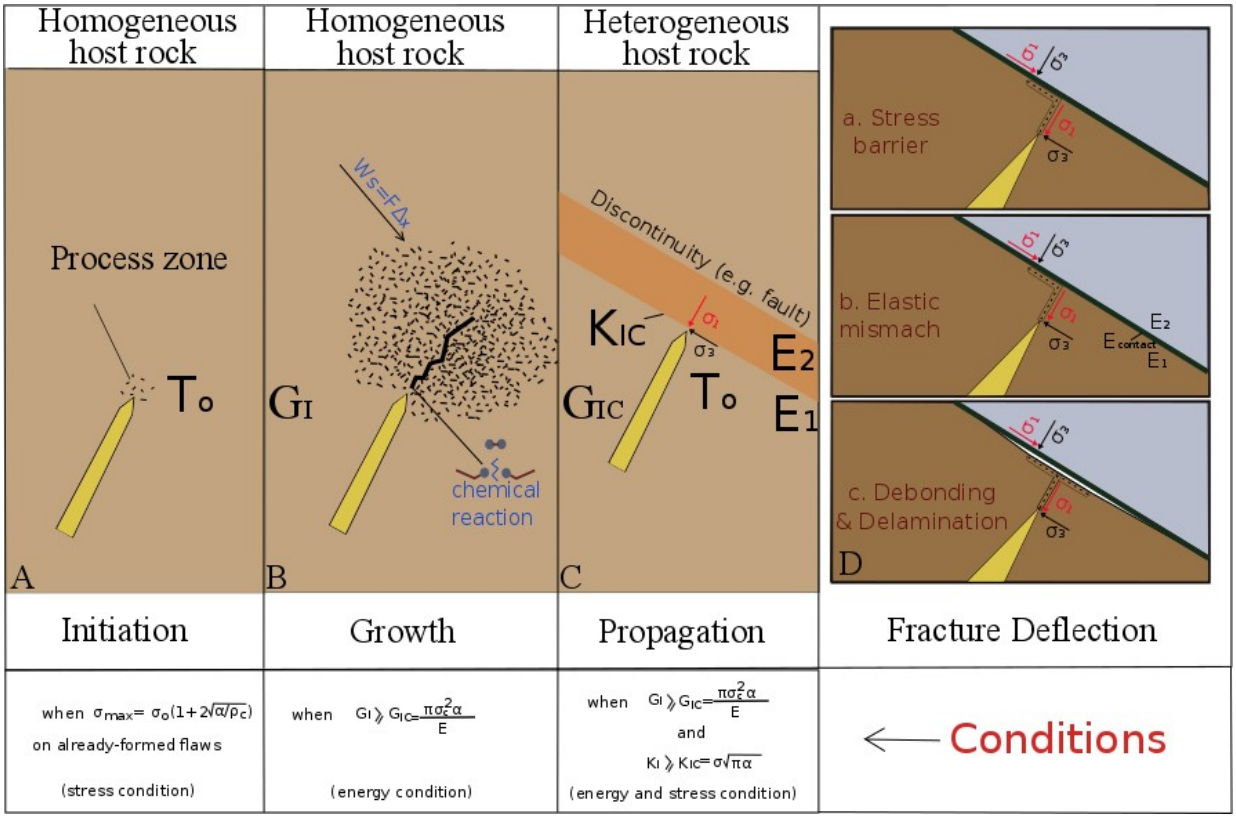

Fig. 5.1: Illustration showing the progressive formation of a Mode I, extension, fracture. A) Microcracks are concentrated around the tip of a fracture in a linear elastic, brittle, material. Further crack nucleation and growth initiates (within the process zone) when the tensile stress at the tip of the fracture matches or exceeds the tensile strength of the host rock. B) Crack growth is encouraged if the strain energy release rate (G_I) of the system rises. C) Crack propagation or fracture is controlled by the material properties of the host rock for any energy criteria used for the crack. D) Deflection mechanisms A. Stress barrier, B. Elastic mismatch and C. Debonding and delamination. W_S denotes for the work that enters the system to produce a fracture, K_I is the stress intensity factor

of a Mode I fracture, K_{IC} is the critical stress intensity factor or fracture toughness, G_I is the strain energy of a Mode I fracture, the energy release rate of the material that controls the growth of the fracture, G_{IC} is the critical elastic strain energy or material toughness, T_o is the tensile strength of the host rock, E is a materials Young's modulus (stiffness), σ_{max} is the maximum tensile stress at the tip of a semi-elliptical notch, α is the half length of a crack, σ_o is the remote tensile stress, σc is the critical tensile stress, σ_1 is the maximum principal stress and σ_3 is the minimum principal stress or the tensile stress of the fracture, ρ_c is the radius of curvature.

Fracture initiation and growth requires brittle rocks to overcome the resistance to failure. The energy and stress conditions are essential as they control the growth of cracks that coalesce to form a propagating fracture. The measure of rock resistance for Mode I fractures is controlled by the energy released rate G_I of the system and the stress intensity factor K_I. The first is the energy per unit area of crack extension and the second, the intensity of the stress field at the tip of the crack (Gudmundsson, 2011).

A sufficient amount of strain energy is required for a fracture to nucleate or grow (Fig. 5.1A&B). This elastic strain energy is stored in the body when the latter deforms elastically and is being released when the new fracture surfaces are generated. The amount of energy needed for crack growth is being transferred into the system in the following ways:

1) Elastic strain energy (U_O) that it is stored in the host rock and is produced by the separation of the material due to bond rupture at the atomic scale (Lawn, 1983).

2) The energy that enters the system as work from external loads such as stress generated by far-field strain accumulation or magmatic overpressure before fracture (W_L) (Gudmundsson, 2011).

3) The energy that is released simultaneously into the system during crack growth (W_S). The crack while it grows it increases its length and aperture, so the resulted amount of energy from the displacement at the crack walls is being transferred into the system (Gudmundsson, 2011).

The total energy U_{tot} needed for the generation of new crack surfaces is the stored elastic strain energy (U_O) minor the work that is being suppressed from the system by external displacements of the crack boundaries (subject to load control) (W_L), and the surface energy or work (W_S) which enters the system (if available) and is defined in Eq.5.1 (Gudmundsson 2011):

$$U_{tot}=(U_o-WL)+Ws \quad (5.1)$$

The strain energy release rate denoted as G_I (for Mode I fractures) is a mathematical condition and determines the growth of a fracture described below in Eq. 5.2:

$$G_I = \frac{\partial U_0}{\partial \alpha} = \frac{\partial}{\partial_{02}}\left(\frac{\sigma^2}{2E}\pi a^2\right) = \frac{\sigma^2 \pi \alpha}{E} \quad (5.2)$$

Where σ is the tensile stress, π=3,14, α is the half length of a crack and E the Young's modulus.

However, again the energy condition on its own does not govern fracture propagation, which is instead related to the material properties, the stress condition of the host rock. Specifically, at the propagation stage of fracture development, the driving forces of a fracture are the G_{IC} (material toughness) and K_{IC} (fracture toughness) for Mode I fractures which are connected through Eq. 5.3:

$$G_{IC} = \frac{{K_{IC}}^2}{E} \quad (5.3)$$

The material toughness (G_{IC}) is a material constant which has the units of J and hence depends on the energy required during the rupture of atomic bonds. K_{IC} is the stress intensity factor or the fracture toughness of a material which has the units of MPa. If both G_{IC} and K_{IC} reach their minimum critical level, then a fracture can propagate (Fig. 5.1C). Laboratory measurements of material and fracture toughness for solid rocks is 20-400 J and 0.5-3 MPa, respectively (Fourney, 1983; Atkinson and Meredith 1987; Gudmundsson 2011 and references therein).

Dike growth and hence propagation is in orientations parallel to the direction (or trajectory) of σ_1, or perpendicular to σ_3 (Anderson 1951; Gudmundsson, 2011). Fracture propagation on the other way, in heterogeneous crustal segments, is primarily controlled by the difference in material

properties between layers or by discontinuities by the layers such as contacts or faults (Fig. 5.1C) (Gudmundsson 2011). The main mechanisms that control this process are 1) stress barriers, 2) elastic mismatch and, 3) debonding and delamination (He and Hutchinson, 1989; Hutchinson, 1996; Xu et al., 2003; Wang and Hu, 2006; Gudmundsson and Lotveit, 2012). These mechanisms control whether a fracture will propagate, deflect or become arrested within the crustal segment (Fig. 5.1D). In this paper, we focus on dike-fault deflection paths and the mechanism that encourages them are analysed below.

1.2 Dike-Deflection mechanisms

Joints, inclined sheets and dikes are all tabular, planar extension fractures which form discordant to the host rock and dip from approximately 30˚ to 90˚. Inclined sheets and dikes are injected either from deep-seated reservoirs, which generally form sub-vertical dikes or from shallow magma chambers which can instead create sheets over a range of angles (cone sheets) as well as sub-vertical dikes (Gudmundsson, 1999).

A dike deflects when the orientation of the principal stresses rotates at its tip (Anderson, 1936, 1951) and the dike subsequently changes its direction. Stress rotation can happen either due to mechanical anisotropy in homogeneous segments or host rock heterogeneity (layering) at a heterogeneous interface. Dike deflection, as already reported, is a possible outcome from a change between the three mechanisms mentioned below. In more detail, the mechanisms are as follows.

1. Stress barrier: A stress barrier can be either a soft or a stiff layer that rotates the principal stress orientations and hence either stops or alters the propagation path of an extension fracture such as a dike.
2. Elastic mismatch: Mismatch relates the Dundurs mismatch criteria or the difference in elastic properties across a discontinuity or contact with the elastic properties of the contact itself. Great difference promotes deflection into the contact.
3. Cook-Gordon debonding and delamination: Due in part to the tensile stress ahead of a propagating fracture tip, a contact with abrupt stiffness contrasts on either side can debond and delaminate or pull apart (opens). In such circumstances, the fracture cannot propagate into the space formed by the debonding and so becomes arrested or deflects to form a sub-horizontal fracture or a sill.

1.3 Deflection of dikes into faults

Fault zones are mode II or III (shear) fractures that both encourage and inhibit fluid flow in the crust. They form mechanical and displacement discontinuities called process zones which can gradually grow and unite forming flip surfaces (Caine, 1996).

Two main hydromechanical units define the architecture of a fault:

1) a central fault core (commonly a few tens of meters thick), which accommodates the bulk of fault displacement, and

2) a brittle damage zone (several hundred meters thick) which is associated with the growth and evolution of fractures, veins, small faults or even folds, in the host rock (Chester and Logan1986; Caine et al., 1996, Faulkner et al., 2010, 2011). Intrinsic mechanical properties, such as strength and stiffness, of a fault zone, differ between the core and the damage zone. The fault core is mostly composed of narrow slip surfaces (Caine et al., 1991) soft breccia and geochemical alteration (Sibson, 1977), gouge and unconsolidated rocks (Anderson et al., 1983; Hoek 2000) which have a very low Young's moduli (typically less than 1GPa) (Gudmundsson, 2011). Similarly, the damage zone can become more densely fractured with time and hence the stiffness of rocks in this zone can grade from relatively soft near the core to relatively stiff nearer the protolith. As such, when the fault zone is active, the fault core accommodates most of the displacement along relatively weak fault planes. However, during periods of inactivity, the fault core can become locked and very stiff (with Young's moduli of higher than 10GPa (Gudmundsson 2011).

In this study, we test the mechanical conditions under which fault zones become barriers to dike propagation. We investigate those conditions under which dikes become deflected and document the interactions between dikes and faults in an active fault zone dominated by a series of normal

and reverse faults exposed in the caldera wall of Santorini volcano. Such observations are essential because it has long been thought that faults facilitate the movement of magma and hence control the location and timing of surface eruptions.

2. Geodynamic setting and extensional related triggering of the Aegean microplate

Active deformation in the Aegean is predominantly associated with two primary processes: 1) the relative motion of the Anatolian strike-slip fault zones and, 2) the northward subduction and roll-back of the African plate underneath the Eurasian plate (Mc Kenzie 1972; Le Pichon and Angelier, 1979; Taymaz et al., 2007). In detail, the two Anatolian fault zones represent two intracontinental transform fault systems with 1) a dextral (North Anatolian fault system-NAFS) and a 2) sinistral (East Anatolian fault zone) motion respectively (Taymaz et al., 2007). The dextral motion of the NAFS has played an especially important role in controlling Aegean geodynamics. Following the classical view (Barka 1992) the NAFS originates in the mid-Miocene as a structure that propagated gradually from the east (at 13 Ma) to the west (at 5 Ma). Nuriel et al., (2019) instead proposed that the NAFS started as the evolution of a pre-existing extensional normal fault system (42 Ma) that was reactivated and transferred to a dextral strike-slip fault zone (at around 11 Ma).

Both the dextral strike-slip faulting of the NAFS and regional subduction processes generated the crustal deformation that accommodated the formation of strike-slip, normal, reverse fault systems (Taymaz et al., 1991; Benetatos et al., 2004; Taymaz et al., 2007; Nocquet 2012) and volcanism in

the Aegean region. The main structures can be summarized from the northern to the southern part of the Aegean as follows (Royden 1993; Kokkalas and Audin 2013):

1. Right lateral strike-slip displacement due to the relative motion of the Anatolian block from the NE to the SW at a rate of 20-25 mm/year.
2. N-S extension due to slab roll-back, 6-10 mm/year, in the back-arc (central Aegean continental crust) which accommodated crustal thinning, by as much as 20mm/year, since the Miocene. The thinning accelerated to 40-50mm/year in the Quaternary, and so in the present day, the region experiences both a fast slab retreat (Brun et al., 2017).
3. E-W active crustal shortening due to gravitational collapse of the thickened crust into the mantle prior to the Miocene (Gautier et al., 1999; Jolivet et al., 2008). SW-SSW differential slab retreat due to rapid migration of the subduction hinge of the Crete trench rather than towards Cyprus - Anatolia (Doglioni et al., 2002, 2007; Agostini et al., 2010).
4. The differential velocity of the Aegean microplate over the African plate. The Aegean microplate overrides the African plate faster than their convergence, causing a prototype of subduction (Doglioni et al., 2007). Localized lateral extension, at a rate of 2-4 mm/year near to the subduction trench, which was due, in part, to the curved shape of the trench.

Active extension in the Southern Aegean region occurred in pulses since the Miocene (Le Pichon and Angelier, 1979; Jolivet et al., 2013) and was recorded by the following structural events: the fast exhumation of high-pressure metamorphic rocks channelled through detachment faults between 24 to 15 Ma (Jolivet et al., 1996; van Hinsbergen and Meulenkamp, 2006). Graben

formation along Plio-Quaternary high-angle faults due to crust stretching (Taymaz et al., 2007 and references therein) (Fig. 5.2).

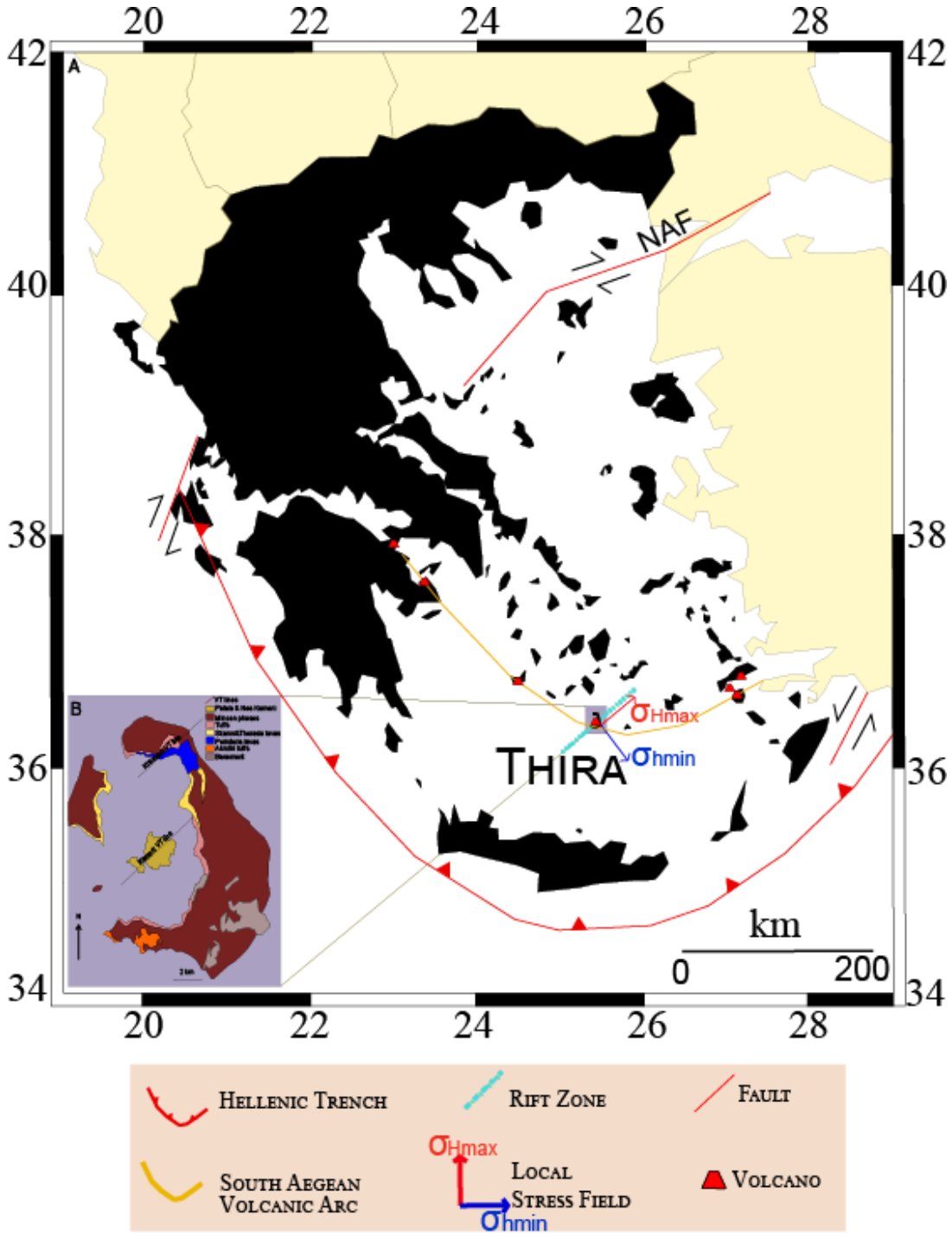

Fig. 5.2: (A) Map of the Aegean modified from Konstantinou et al. (2006) showing the main tectonic features and major faults. The direction of the rift zone is given from Nomikou et al. (2013) and the local direction of extension from Feuillet, (2013). NAF: North Anatolian fault. (B) Simplified geological map of Santorini modified from Druitt et al. (1999).

Those extension pulses also controlled the location of volcanism in the Aegean Sea (Fytikas et al.,1984; Papazachos and Panagiotopoulos, 1993). Christiana Islands, Santorini and the Kolumbo submarine volcano are developed on the faulted southern margin of Anhydros Basin along a NW-SE high angle rift zone, surrounded by neotectonic graben and horst formations (Papazachos and Panagiotopoulos 1993; Nomikou et al., 2016; Hooft et al., 2017).

2.1 Geological setting

As a typical stratovolcano, Santorini has experienced many eruptive cycles, at least four caldera collapse events and remains active (Druitt & Francaviglia 1992). The past Plinian or subplinian imminent volcanic activity has formed a complex pile of stratigraphic horizons, in particular, 1) two explosive cycles with at least 12 pyroclastic eruptions, 2) dike-fed eruptions that produced lava shields (at least three lava shield formations) and domes, 3) a significantly complex volcanic plumbing system (Zellmer 1998; Druitt et al., 1999; Bailey et al., 2009; Andujar et al. 2015).

The study area exhibits several dike segments that are emplaced in a highly heterogeneous host rock, the lithology of which belongs mainly to the oldest composite stratocone, the remnants of Peristeria Volcano (530-430 ka). The following events are the first eruptive cycle (360-172 ka),

the cinder cones of the Megalo and Kokkino Vouno (125-80 ka) and the Skaros shield (70-54ka). The Minoan eruption (3.6 ka) marked the last Plinian eruption, and the coeval caldera collapse has exposed the contacts, the stratigraphic layers, the dikes and the regional faults, allowing them to be examined.

The geology of the Northern caldera wall and the age of the deposits were described in detail by Druitt et al., 1999 and a summary is explained below in stratigraphic order. Most of the deposits of the northern caldera wall were formed as part of the Peristeria stratovolcano (530 – 430 ka) which consists of three units 1) av1: andesitic lavas, tuffs, breccias and hyaloclastites (528±23 ka), 2) av2: silicic andesitic lavas (496 ±16 ka), 3) av3: thinly bedded andesites and basalts with subordinate dacites and tuffs (464±8 ka).

The first explosive cycle in the studied area is represented by 1) ra: extrusions of rhyodacites at the contact between Megalo Vouno and Mikros Profitis Ilias in NE Thera (~224±5 ka), 2) ap2 (Cape Therma 3): pink sillar facies of ignimbrite and red spatter agglomerate with abundant plutonic nodules (196 ka, Keller et al., 2000), 3) rp3 (Lower Pumice 2): rhyodacitic pumice (172 ka, Keller et al., 2000).

The second explosive cycle is represented by 1) ap4 (Middle tuffs- Megalo Vouno and Kokkino Vouno cinder cones and Kolumbo tuff ring): thick scoria-fall deposits of phenocryst poor andesite (54±3 ka). 2) as2 (Skaros lava shield): andesites and basalts of Cape Skaros (70-54 ka), 3) ap5 (Upper scoria 2): andesitic thick spatter agglomerate, (54±3 ka), 4) ao (Andesites of Oia): andesitic lavas, 5) rp6 (Cape Riva eruption): rhyodacitic pumice fall phase overlain by two ignimbrites (welded and non-welded) topped by a lithic-rich lag breccia (21.8±0.4 ka, Fabbro et al., 2013), 6) rp7 (Minoan eruption): rhyodacitic pumice fall, overlain by surge deposits, phreatomagmatic ash

topped by an ignimbrite interstratified with a lithic co-ignimbrite and lag breccias, (3.6 ka, Eriksen et al., 1990).

2.2 Volcanotectonic faulting at Santorini

The island of Santorini has experienced at least four caldera collapse events (Druitt et al., 1999), and it is still active. The recent morphology of the caldera wall was formed by a circumferential ring fault that activated during the last collapse episode. The ring fault forms an ellipsoid (11x7km) closed loop at the periphery of the caldera rim, dips vertical and its displacement is of several hundreds of meters (around 300m). Those mechanical and geometrical characteristics of ring faults allow us to distinguish them from the earthquake faults which are usually straight, segmented, dip between 45-75˚ and rarely vertical, their slip is of a 20m maximum, and they form during different local stress fields (Gudmundsson 2008).

Two sub-vertical volcanotectonic lineaments strike roughly NE-SW, namely the Kolumbo line and the Nea Kameni line and intersect the island of Santorini. Both fault zones were characterised as surface expressions of either basement strike-slip or basement normal faults (Druitt et al., 1999). The Kolumbo volcanotectonic line (N 50˚E) is situated in the northern part of Thera and cuts the cinder cones of Megalo Vouno and Kokkino Vouno as well as the Cape Kolumbos tuff ring (Heiken and McCoy, 1984; Druitt et al., 1999). The 2011– 2012 unrest episode indicated a significant volume of magma accumulated and moved beneath this regime (Newman et al., 2012; Parks et al., 2012).

An angular unconformity of approximately 4 km in length interrupts the Peristeria lava horizons and forms a 30-ka hiatus in between a silicic (av2) and andesitic (av3) lava flow; an observation

also reported in previous studies (Druitt et al., 1999). Such processes in middle scales (km range) as at the northern caldera wall can be associated with volcanotectonic processes such as caldera collapse events originated by other internal modifications such as rapid migration of eruptive vents (Lucchi et al., 2013). Previous volcanological studies (Heiken and McCoy 1984; Druitt and Francaviglia 1992) have reported evidence of vent migration to the south along the Kameni volcanotectonic line during the Bronze Age, while Druitt et al., (1999) proposed that the Kolumbo volcanotectonic line, which cuts the northern caldera wall, is also associated with the evolution of NE-SW oriented volcanic activity.

Recent geophysical and bathymetric studies (Hooft et al., 2019) revealed a shallow low-velocity and high-porosity vent correlated with the phreatomagmatic LBA eruption on the western extension of the Kolumbo volcanotectonic line. The structure accommodates collapse structures, faulting and localized magma recharge that could make it a candidate of an older collapsed vent. This could support the hypothesis that the Kolumbo volcanotectonic line was also delineated by vent migration processes similar to the Kameni line and probably the angular unconformity on the northern caldera wall could be associated with another, possibly incremental, caldera collapse event after the formation of av2 (around 496ka) during the formation of Peristeria volcano. Heath et al. (2019) proposed an extrapolation of the VT Kolumbo fault zone into the SW up to a NE-SW striking dike at the southern part of Therasia Island. In terms of dike emplacement, a dike does not always mark the pre-existence of a fault zone as dikes are extensional fractures and make their paths into the crust (Gudmundsson 2011).

There are also four NE-SW trending normal faults (Druitt et al., 1999). reported to run between Megalo Vouno and Mikros Profitis Ilias along sections of the northern caldera wall. Two of these faults (marked F2 and F3) were suggested to have been triggered by the Cape Riva eruption (Rp6)

and the collapse of the Therasia-Skaros complex around 22 ka. The collapse accommodated the movement of a large section of the edifice to slide laterally into the collapsing depression forming a small NE-SW striking graben in a section of the caldera wall (Druitt et al., 1999) which was argued recently by geophysical studies (Tzanis et al., 2020). The latter proposed a different kinematic classification for the F2-F3 faults.

Earlier studies (Mountrakis, 1998), however, suggested that the Mt. Mikros Profitis Ilias faults were simply part of a primarily dextral (N 35-40˚ E striking) strike-slip fault zone and a normal (N 40-70˚E striking) fault system with subsidiary N-S trending displays. Those results were derived from measurements of the strike orientation of dikes collected along the caldera wall and based on the hypothesis that the dikes were exclusively emplaced through faults. The same hypothesis was used to define a regional NNW-SSE extensional regime. However, recent field observations and analysis of the dike paths at Santorini (Chapter 4) have shown that the dikes can either generate their own paths regardless of the distribution of crustal faults, so the dike segments observed on the northern caldera wall do not conditionally develop through faults. This interpretation is, of course, also supported by observations of dikes in many other places (Gudmundsson 1984, 2003, 2006, 2011; Tibaldi 2015) and supported by analogue models (Kavanagh 2006, 2018).

Regardless of the origin of the faults, some of them are spatially ubiquitous with a series of dikes, and hence there needs to be an explanation of why some dikes used the faults and others not. And so, what is still unclear is how, if at all, the faults facilitated or inhibited the transport of magma in the shallow part of the crust at Santorini. So here we investigate the interaction of dikes with the observed northern caldera wall faults to determine their role in the emplacement of magma.

2.2 The distribution of active faults and their evolution

The oldest fault system in the area of Santorini is described by the presence of an E-W listric normal fault trend (Papanikolaou et al., 1988) located in the Christiana and Folegandros basins (S and SW respectively) which was rotated gradually through time to more WNW – ESE trends (Perissoratis, 1995) and was followed by an N-S trend interpreted as a series of transfer faults (Piper and Perissoratis, 2003) forming the Santorini-Ios ridge at the northernmost part of the island. The latter trends primarily affected the metamorphic basement, (Atticocycladic massif) and the lower parts of the terrigenous sediments that were deposited in Late Pliocene as reported by seismic tomographic analyses (Perissoratis, 1995). However, a later study (Piper and Perissoratis, 2003) suggested a strike-slip motion for the same trends.

The initiation of Santorini's volcanic activity since the late Pliocene-early Pleistocene is represented by the early centres of Akrotiri, (650 ka) and could be associated with the transition of an E-W trending to NE-SW strike-slip faults (Perissoratis, 1995). This transition was developed between the late Pliocene and early Quaternary (Piper et al., 2007) which delineated the formation of a volcanotectonic line, the Kameni line.

In the mid-Quaternary, the previous E-W trend was replaced by NE-SW strike-slip faults indicating the collision of the African plate in the region or the buoyancy effects of the thicker continental crust (Bohnhoff et al., 2001; Piper and Perissoratis, 2003). The continuous collision activated ENE-WSW trending faults (Pe-piper et al., 2005) and rotated the N-S active transfer faults to NNW-SSE (Piper and Perissoratis, 2003). The firsts were dextral strike-slip (Bohnhoff et al., 2006) and initiated at about 200ka (Piper and Perissoratis, 2003). Subsidence of at least 600 m was reported to have begun during the first explosive cycle and especially in Late Pleistocene (in the last 200ka)

(Piper and Perissoratis, 2003). The latter could have been associated with the caldera collapse event that occurred at the end of the first cycle (172ka) and refereed to the activation of a circumferential ring (normal) faults. Previous studies (Druitt et al., 1999) reported at least four caldera collapse events that occurred at the beginning and towards the end of the second explosive cycle.

N65˚E strike-slip sinistral faults were initiated between 0.2-0.6 Ma at the Amorgos region forming a basin at the Santorini-Anafi region during late Pliocene and a positive (horst) region during the early Pleistocene (Piper et al., 2007). The latter could be associated with the sinistral strike-slip motion of the Anatolian block from the East (ten Veen and Meijer, 1998).

The upper parts of the offshore deposits around Santorini according to tomographic studies belong to Quaternary volcaniclastic sediments characterised by two sets of normal fault trends 1) NE-SW (Bohnhoff et al., 2006) and, 2) N65-75˚ E (Piper and Perissoratis, 2003) respectively. They have initiated as regional sinistral strike-slip faults showing crustal scales and continued their activity during early Quaternary providing probably the magma paths for the recorded volcanic eruptions. The latest NE-SW direction is parallel to the Kameni VT line fracture zone that showed signs of deep seismic activity in the past (Fytikas et al., 1990). The evolution of the faults, as described above, is shown in Figure 5.3.

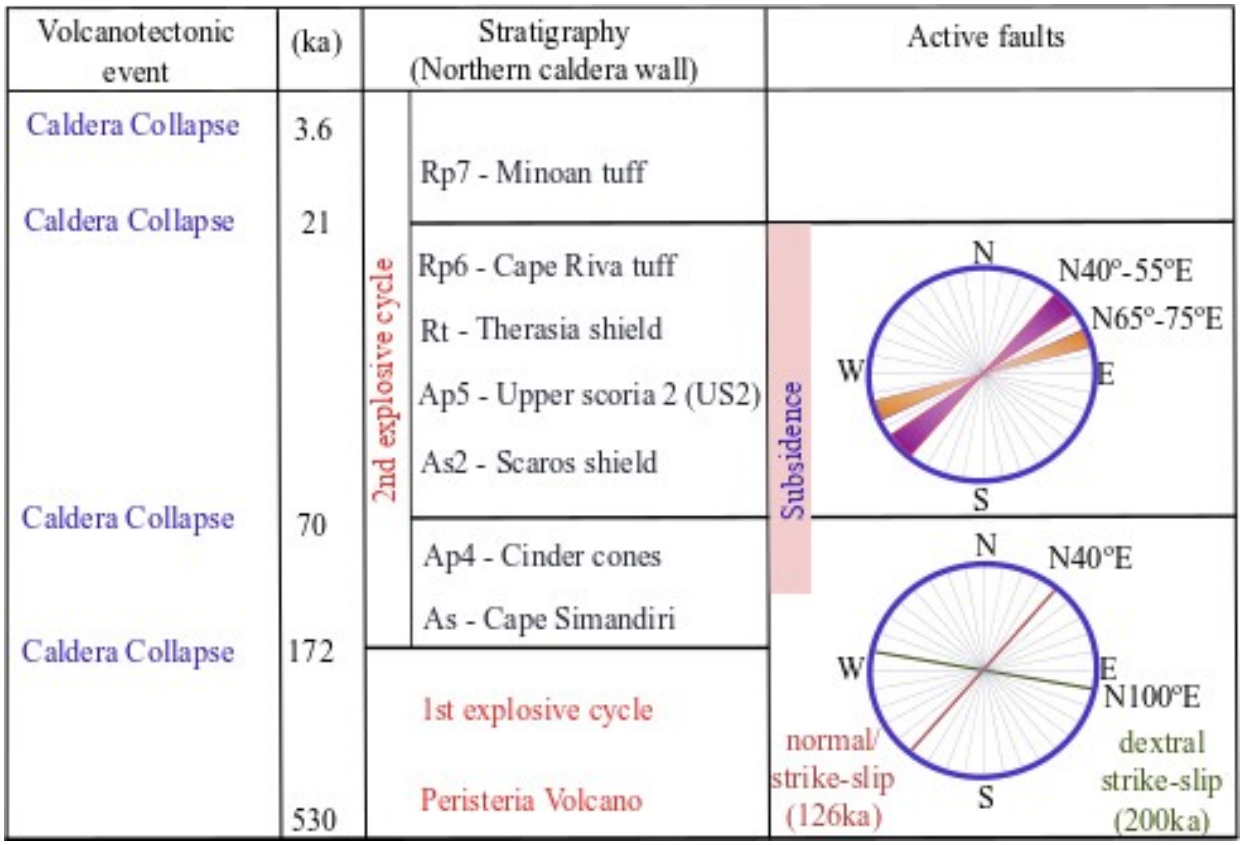

Fig. 5.3: Fault evolution from Late Pliocene to Holocene on the Santorini onshore and offshore region. The diagram shows the fault planes in time according to interpretations from seismic stratigraphic profiles (Perissoratis, 1995; Piper and Perissoratis, 2003; Pe-piper et al., 2005; Piper et al., 2007) and the dike swarm located at the northern caldera wall (Druitt et al., 1999; Chapter 4). As: Andesites and basalts of Cape Simandiri (172 ka), Ap4: Cinder cones of scoria-fall deposits from Megalo and Kokkino Vouno, and tuff ring (125-80 ka). As2: Skaros lavas (70-54 ka), Ap5: Upper scoria 2 (54 ka), Rt: Rhyodacites of Therasia, Rp6: Cape Riva tuff (21 ka), Rp7: Minoan tuff (3.6ka) (Druitt et al., 1999).

3. Methods

3.1 Field Geology

We performed field campaigns on the northern caldera wall and mapped the dike swarm, the associated host rock and the fault structures. We studied the fault segments by collecting information on their orientations and sense of slip. Also, as almost all the observed faults dip more than 60˚, we used the following criteria to define the kinematics (if possible, to observe) of the studied faults. The studied criteria were 1) striated surfaces (slickensides lineation) or bedding surfaces, 2) conjugate faults which indicate slip parallel to the fault-dip line, 3) drag folds, 4) syntectonic listric normal faults or filled fractures, 5) other fracture geometries that accommodate secondary crystallisation (hydrothermal veins, joints).

Several dikes were found to be deflected into the fault zones and were studied to investigate the mechanisms that controlled the deflection. The deflection was reported when the change of the dip angle exceeded 30 degrees. The field data was used as the geometrical and material parameters for a suite of FEM numerical models using COMSOL Multiphysics.

3.2 Numerical model setups

We used the Finite Element Method (FEM) software COMSOL Multiphysics (v5.2) to simulate the observed interactions between dikes and faults in the northern caldera wall of Santorini. The basic geometry of the models was derived from the field observations, and a variety of boundary conditions were investigated to interpret the mechanisms that encouraged the observed behaviours. In all the numerical models, the dikes were modelled as elliptical cavities driven by overpressure (Po) of 5MPa representative of the Santorini boundary conditions during dike emplacement

(Chapter 4) (Fig. 5.4). The resulted thickness of the dike and that of the fault at first point were always the same equal to 1m.

We modified the stiffness or Young's modulus of both the host rocks and the fault zone. This happened as the energy concept, and most importantly, the material properties (stress concept) of the host rock control the propagation of a fracture as reported from engineering fracture mechanics (Broek, 1982). Each fault zone was comprised of three layers that were symmetrically stratified in order to simulate a fault damage zone with progressively increasing or decreasing fracture damage and Young's moduli (Gudmundsson, 2011). If the core of the fault consists of gouge or breccia and is highly fractured or pulverized, we assume this zone to possess a very low Young's modulus of 0.01 GPa (Heap et al., 2019), especially when the fault is still active. However, we assume that inactive faults are much stiffer and hence assign Young's modulus of >10GPa. As such, the fault zone was assigned Young's modulus of E=0.01GPa for the core, simulating an active fault and E=10GPa thus of an inactive fault. The Poisson's ratio for the fault is 0.25 in all models (Babiker and Gudmundsson 2004; Heap et al., 2019). The fault zone was with an angle of 65° degrees from vertical, as was observed in the field. It is important to note also that the fault zone in these models is simply an area of stiffer or softer rocks and cannot deform or move (creep). In our first case study, we modelled the dike-fault interaction in a homogeneous (A) and a heterogeneous (B) fault zone of firstly a vertical dike (1) and secondly an inclined sheet (2).

We generated a triangular mesh before the model runs. We fixed the modelled area of interest to be in the middle of the assigned geometry to avoid edge effects. For the interpretation of the results, we plot the magnitudes of maximum tensile stress (σ_3) on a two-dimensional surface. We also plot both the trajectories of the maximum principal compressive stress (σ_1) and the minimum principal compressive (maximum tensile) stress (σ_3) in all the models.

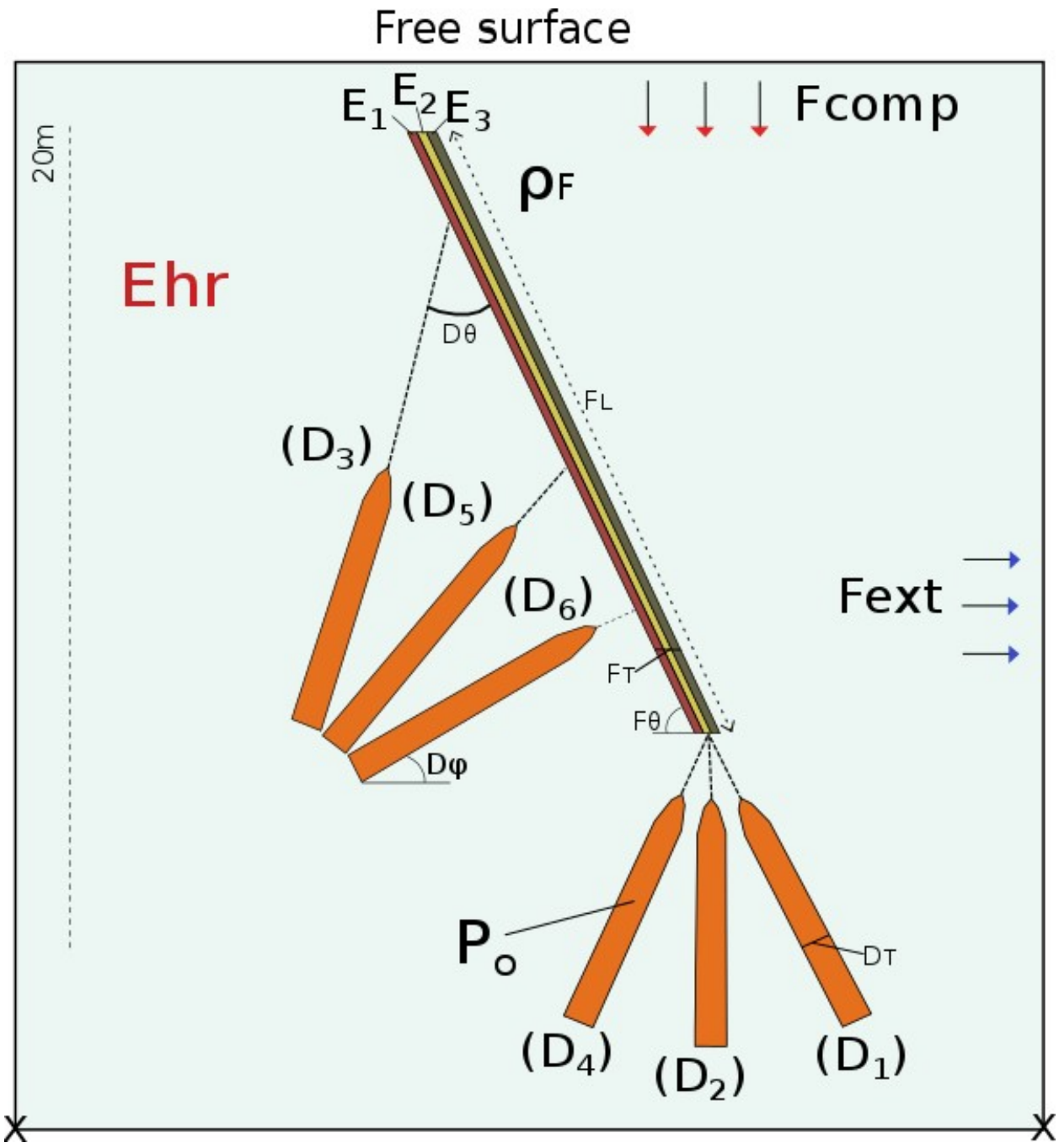

Fig. 5.4: Numerical model setups for a dike (D1, D2, D4), and an inclined sheet (D3, D5, D6). The cavities (D_T) are 1 m thick with an internal pressure of 5 MPa. The normal fault has a thickness (F_T) of 1m and dips (F_θ) at 65 degrees and it is composed of three layers where both the Young's modulus of the core or the rim could be between 0.001GPa to 10 GPa. The Young's modulus of

the host rock (E_{hr}) is 40 GPa and the density of the fault (ρ_F) is 2000kg/m^3. The minimum dip of the inclined sheet (Dφ) is 50 degrees. For the sensitivity tests we use a varied Young's modulus for the fault (5 orders of magnitude 0.001-10 GPa) and a magmatic overpressure (P_o) of 1MPa for the dike. We modelled the angle of the dike with the fault (Dθ) for 0˚ (D1), 25 (D2), 40˚ (D3), 50˚ (D4), 65˚ (D5) and 90˚ (D6), the thickness of the dike for i) 1m, ii) 3m, iii) 8m, the thickness of the fault for i) 1m, ii) 5m, iii) 25m, subject to an applied extensional stress field i) 0.5MPa, ii) 1MPa, iii) 3MPa, subject to an applied compressional stress field i) 0.5MPa, ii) 1MPa, iii) 3MPa, and a variant dip length of the fault zone i) 20m, ii)100m, iii) 200m. For all the corners at the bottom of the model are fixed to prevent motion whereas the top ones are free to simulate an area free of shear stresses.

3.3 Sensitivity tests model setups

We further investigated other parameters that could affect the dike-fault interactions at the specific studied area and scale. The in-situ study revealed that the fault zones had variable thickness, dip length, strike and were active possibly during different regional stress fields (regional extension or local compression). At the same time, the deflected dikes varied in dipping angles and thickness values. The designed realistic sensitivity tests depicted snapshots of their measured estimations. The first case study models the influence of changing the angle of the dike concerning the angle of the fault. Here the dip of the dike (A1) and the inclined sheet (A2) was modified from 0-90° degrees in steps, and the model re-ran every time (Fig. 5.4). Then, we investigated the effect of changing the thickness of the dike (B1) for 1, 3 and 8 m and the thickness of the fault (B2) for 1, 2 and 25 m

respectively. In the next stage, we modelled the dike fault interaction subject to an applied extensional (C1) and compressional stress field (C2). For both scenarios, we assigned to the stress fields a variable σ_3 equal to 0.5,1 and 3MPa, values that could simulate the active stress field (Chapter 4). We lastly modelled the dip-length of a variable fault zone for 20, 100 and 200 m respectively. In all models, the two-dimensional area was bounded by a box z × y. The corners of the model were fixed, but the upper surface was a free surface, hence simulating the Earth's surface. The fault was modelled subject to a wider range of Young's modulus values which are in specific five different orders of magnitude E1=0.001GPa, E2= 0.01GPa, E3=0.1GPa. E4=1GPa, E5=10GPa is showing a transition of a very active to an inactive fault core. Finally, weassigned a constant loading condition of Po=1MPa as numerous models that designed but not presented here revealed that changes of loading conditions in that scale do not alter the stress field and hence the path of the dike but only the magnitude of their stress concentration. The realistic sensitivity model setups are shown in Figure 5.4.

4. Field results

4.1 Faults

The fieldwork campaign revealed two suites of normal or transtensional faults which we broadly classify initially depending on the amount of displacement accommodated by each fault. Those faults in suite 1 accommodated displacements of over 100 m, as discerned from stratigraphic relationships but could not be directly measured from marker horizons. The faults in suite 2 accommodated displacements of less than 100 m and could be measured from marker horizons. In

Figure 5 we present the location of the faults mapped by Druitt et al. (1999) (F1, F2, F3, F4) and those mapped during this study (F5-F13).

The field observations revealed that the suite 1 faults were normal or reactivated strike-slip faults that marked the boundary of a graben according to the stratigraphy of the area (Druitt et al., 1999). Offset in units on either side of the graben indicate more than 100m of displacement. The lateral extent of the faults was not measured, and slip indicators were not easily observed except a west flow indicator close to F3 showing senses of horizontal shear (W-E) towards the interior of the caldera. These findings support those reported by Druitt et al. (1999), others who also noted normal or strike-slip neotectonic faults are cutting Mt. Mikros Profitis Ilias (Mountrakis et al., 1998) or block tilting (Tzanis et al., 2020). The profiles and analyses of these faults are now considered and presented in Figures 5.5 and 5.6:

F2 has an attitude of 60˚/050˚and cuts the complete stratigraphy of the northern caldera wall. The uppermost layer of the sequence (Skaros lavas – as2) was deposited between 70-54 ka. The offset is at least 200m and at least two dikes of different colours, and hence likely of varying composition and population, were deflected into the fault. Remnants of the first explosive cycle (ra-ap2-rp3) are found only at the NE corner of the caldera wall and are also cut by F2. All horizons are horizontal except the bottom layer (ra) which dips to the NW by 20 degrees (Fig. 5A). This implies that the unit ra was either deposited normally inclined at the slopes of the pre-existing summit or that F2 was at some point a listric normal fault that was activated after the deposition of ra (around 224ka). Later reactivations could have been with a normal sense again or with a strike-slip motion hence for all of this reasons we classify this as a transtensional fault (Fig. 5.5A).

F3 has an attitude of 70˚/060˚ and although it cuts the whole length of the stratigraphy restricted to old lavas (Peristeria stratovolcano, 530-430 ka) at the Mikros Profitis Ilias locality classified as a normal according to the stratigraphic horizons with an offset of at least 70 m. However, on the bottom of the fault zone, we observed signs of sliding (like bedding) and displacement to the SW which could infer to a strike-slip motion an observation which is in agreement with recent geophysical studies (Tzanis et al., 2019). Several dike segments (three were clearly observed) were deflected into the fault zone, and one of them found at the top of the Mikros Profitis Ilias mountain. The dikes were of similar colour and thickness, did not crosscut and hence it was difficult to discern relative ages. The fault showed signs of strike-slip and normal motion, and therefore we also classify it as a transtensional fault (Fig. 5.5B).

F7 is also a normal fault according to the marker horizons, has an attitude of 60˚/050˚ and strikes parallel to F2, but it does not cut any of the Skaros lavas (70-54ka) and hence was not active as long as F2 and so is older than 70 ka. The offset is 50 m, and there were no dike segments observed cutting or deflect into the fault zone (Fig. 5.5A).

F8 has a similar attitude to both F2 and F7. The stratigraphic horizons, through which the fault cuts, show a normal sense of displacement and its activity is restricted to the Peristeria stratovolcano. No dike segments cut or deflect into F8 (Fig. 5.5A).

F10 is also a transtensional fault according to our classification which may have originated as a strike-slip fault and later reactivated as a normal fault or the opposite. Strike-slip displacement is evidenced through fossilised negative flower structures in the uppermost part of the fault and markers of normal displacement were observed from the surrounding stratigraphic horizons. No dikes cut or deflect into the fault (Fig. 5.5B).

F11 is restricted in the Peristeria stratovolcano and our field analysis classified it as a transpressional fault showing positive flower structures and drag folds. No dikes were found to cut or deflect into the fault (Fig. 5.5B).

F12-13 are likely strike-slip faults. They were active during the construction of the av3 Peristeria unit. No dikes cut or deflect into the fault (Fig. 5.5B).

F1 and F4 faults are reported as normal faults (Druitt et al., 1999) but were not studied during this study as they were further away from the research area and no dike segments were emplaced near to these faults.

Some of those faults with offsets smaller than 100 m, i.e. suite 2 faults, were previously reported (Mountrakis et al., 1998; Druitt et al., 1999) but further analysis revealed some interesting features, as shown in Figure 5.6 and summarized below as follows:

F5 has an attitude of 65˚/010˚ and cuts only the av1 layer of Peristeria stratovolcano (530-430ka) which is composed of lavas, scoria, tuff and hyaloclastites. It has a vertical length of at least 20 m and an offset of 4-5 m which is recorded by a clear marker horizon in a scoria unit. We observed multiple dike injections that deflected into the fault zone (Fig. 5.6A) which according to their structural and petrogenetic classification (Chapter 6) were emplaced during the Peristeria and/or Skaros subswarms.

F6 has an attitude of 45-55˚/070˚. We observed two 10 m faults (a normal and a reverse fault) with convoluted crosscut geometries and a minimum offset of 3 m. Two dikes were deflected into both faults (Fig. 5.6A).

F9 has a series of fracture sets and conjugate joints which have an attitude of 60-70˚/060˚. No dikes were found to become deflected into this structure (Fig. 5.6B).

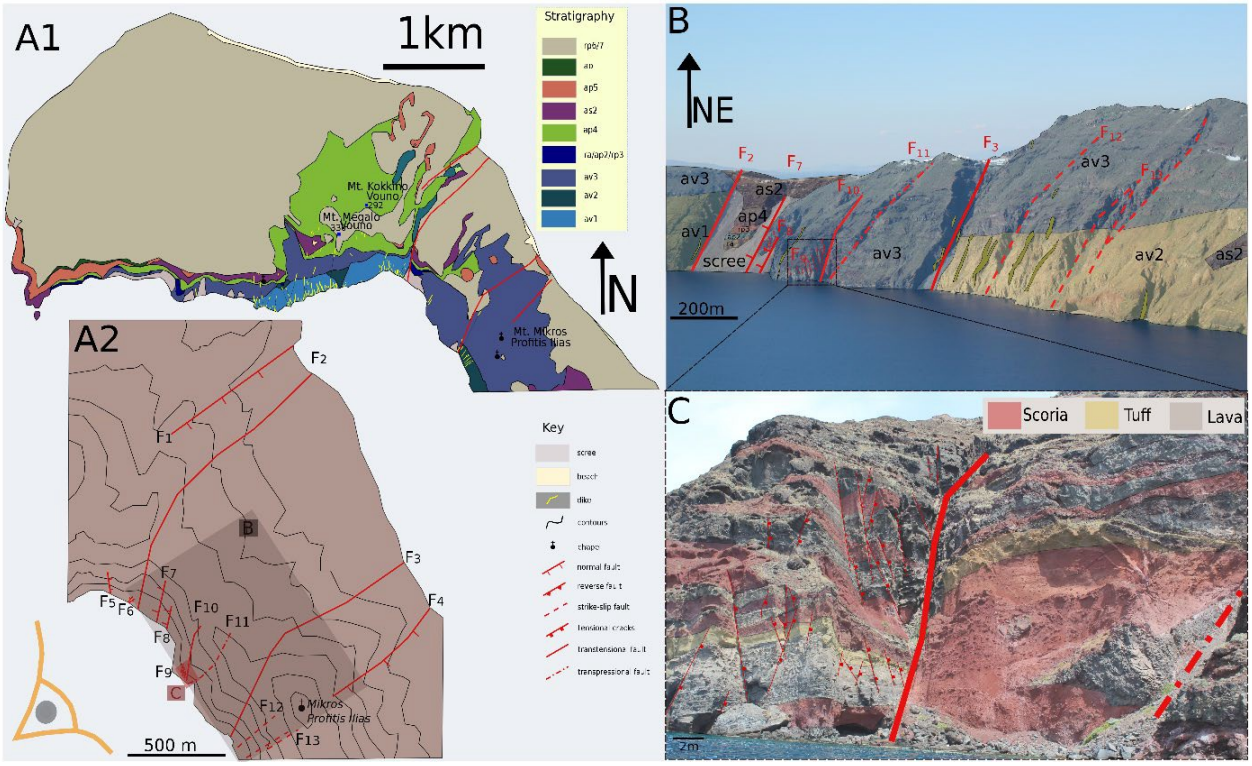

Fig. 5.5: (A1) Geological map of the area modified by Druitt et al., 1999 showing the location of the dike swarm from Chapter 4. (A2) Illustration showing the location and motion of F1-F4 faults modified from Druitt et al. (1999), and the studied fault structures (F2, F3, F5, F6, F7, F8, F9, F10, F11, F12, F13) during this survey, (B) panorama of the northeast corner of the caldera wall showing the lithologies of the heterogeneous and anisotropic host rock from Druitt et al. (1999) as follows: Peristeria stratovolcano: (av1-3) basaltic to dacitic lavas, tuffs, scoria and breccia, First explosive cycle: (ra-ap2-rp3) rhyodacitic lavas to a pyroclastic density current atop by rhyodacitic pumice, Second explosive cycle: (ap4-as2) thick scoria-fall deposits under andesitic and basaltic lavas, the mapped fault structures and the emplaced dikes according to this study, (C) A closer look on the fault structures (F9, F10, F11) at the northern caldera wall formed in the av3 lavas of the old Peristeria edifice.

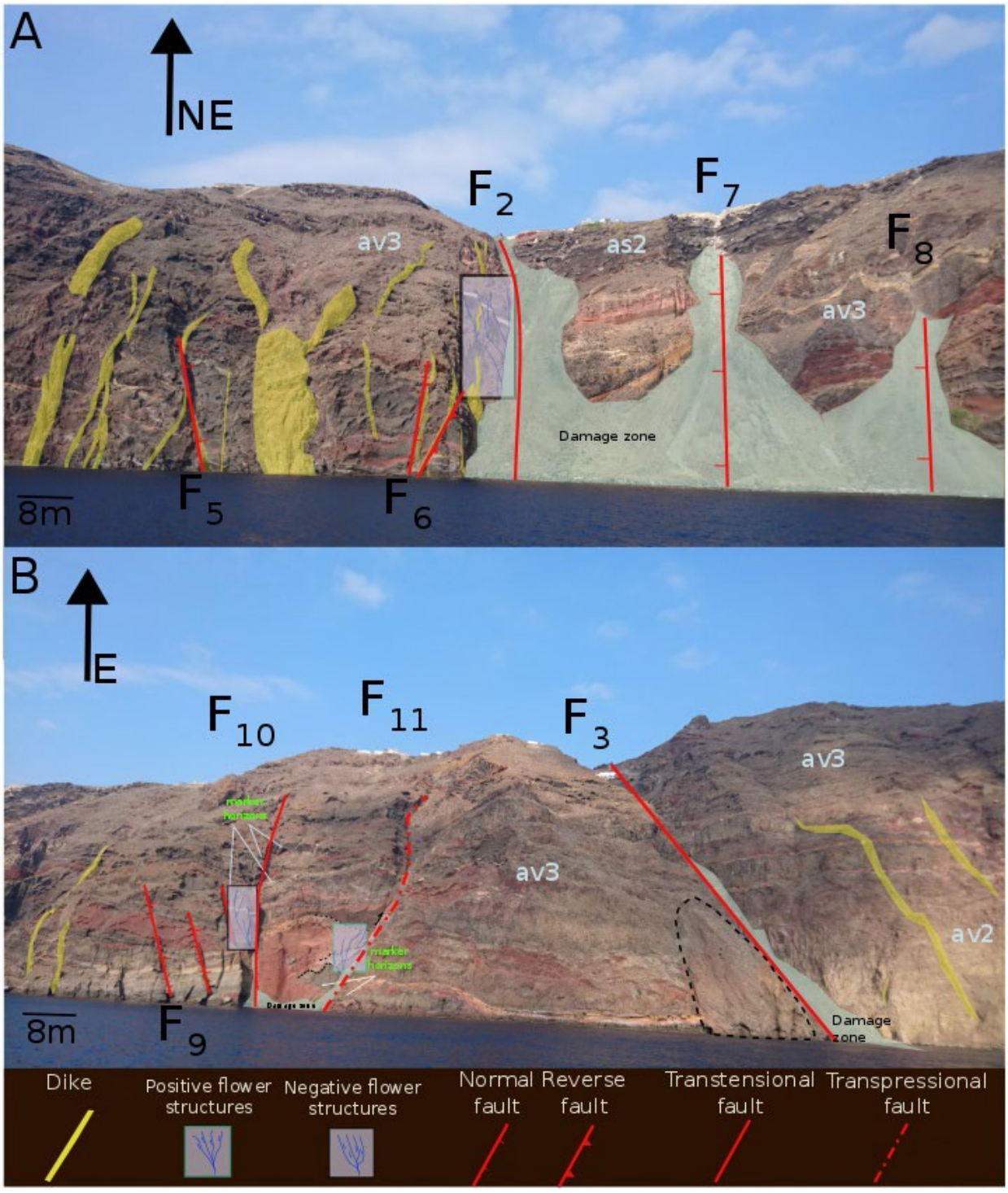

Fig. 5.6: (A) Main structural elements in the northeast corner of the northern caldera wall. The tectonic structure implements a sequence of parallel normal faults dipping 60-70˚ to the northeast.

Marker horizons: Av3: Peristeria stratovolcano, As2: Skaros shield. (B) View east towards the caldera wall showing the faults of varied scale observed on the studied area. The dashed area is showing the signs of possible strike slip motion of the F3 fault.

5. Numerical model results

We modelled one dike (dike 1) and one inclined sheet (dike 2) which were observed to be deflected into a normal fault zone (Fig. 5.7) which is firstly homogeneous and secondly heterogeneous. Both dikes are about 1 m thick but strike in different directions (N-S in the case of dike 1 and NE-SW in the case of dike 2). Both dikes were emplaced into the same heterogeneous and anisotropic host rock, which consists of lavas, breccias, tuffs and scoria units. The dip length of the fault was 20 m, and the observed offset along with the dip of the fault, as calculated from a scoria marker horizon, was approximately 6 m.

The field observations show that dike 1 became deflected into the fault. At the same time, the inclined sheet became also deflected into the fault but higher up in the succession (Fig. 5.7) Because it either belong to the same population but emplaced later (if belong both to Peristeria stratovolcano), or to different subswarms (Peristeria and Skaros subswarm) (Chapter 6). The primary goal was to replicate the field observations with numerical models and hence explore the conditions that encouraged the deflection of the dikes and recount their relative order of sequence.

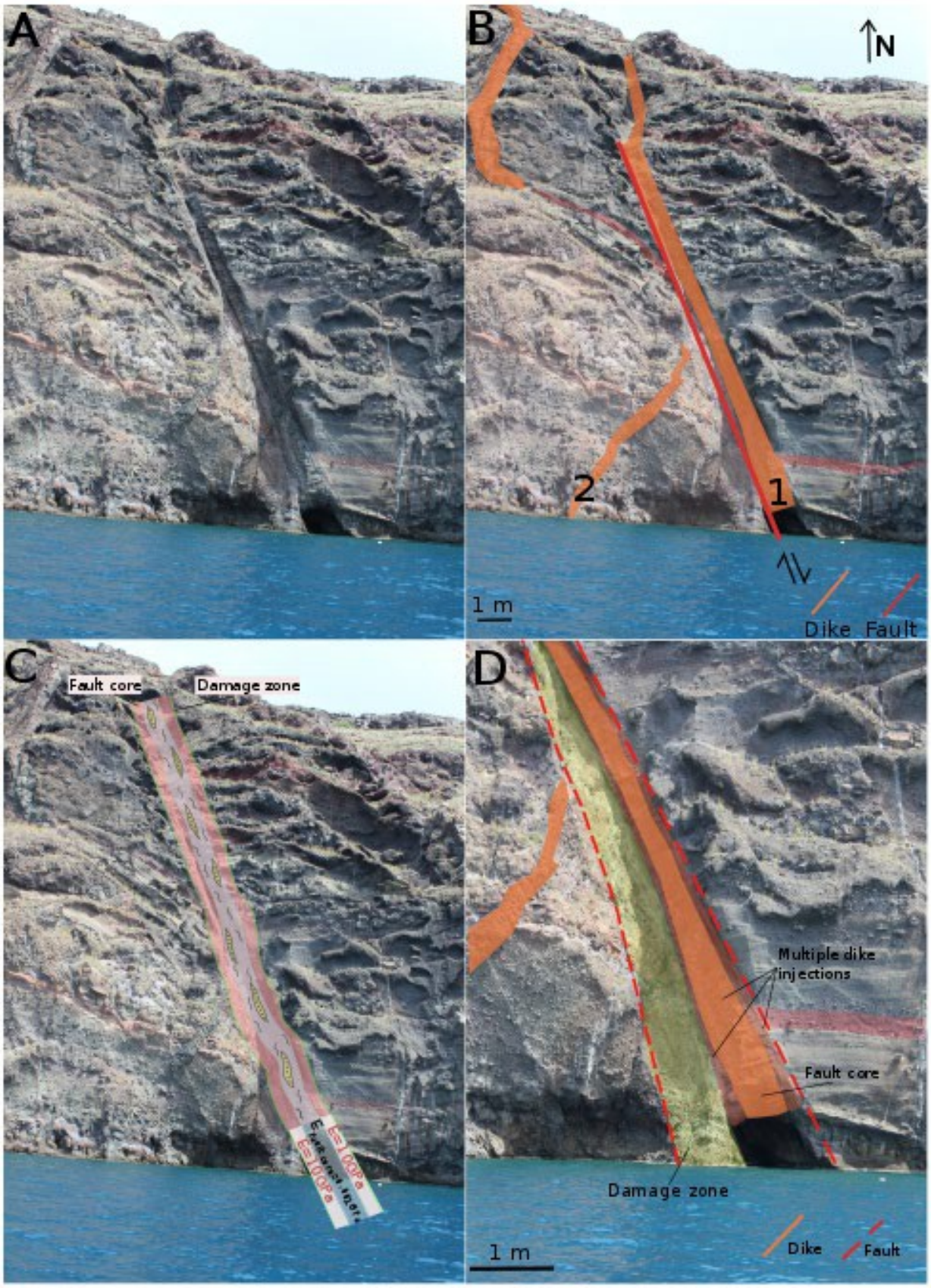
A
B
N
2
1
1 m
Dike
Fault
C
Fault core
Damage zone
D
Multiple dike injections
Fault core
Damage zone
1 m
Dike
Fault

Fig. 5.7: Interactions between dikes and fault F5, original photo (Part A) and annotated version (Part B). The numbers indicate two dikes of different ages. One of the dikes (1) is inside the fault and does not intrude into the fault although its path is highly anisotropic. Part C, heterogeneous structure of the fault zone. (D) Dike 2 deflected in the interpreted damage zone of fault F5.

5.1 Homogeneous fault zone

In Figure 5.8, we see the results from a suite of models which simulated a homogeneous fault zone, i.e. one which had the same level of Young's modulus (1GPa) throughout the fault. The vertical dike (dike 1) and the inclined sheet (dike 2) were modelled in separate models, and both were assigned magmatic overpressures of 1 MPa. The host rock in both models had Young's modulus of 40 GPa. We first modelled a homogeneous soft fault core (0.001GPa) and then a stiff core (10GPa). The models are shown below:

E_{fault} = 0.001GPa (soft)

We assigned to the normal fault a low Young's modulus value to examine the case study of dike-fault interaction in an active fault setting. We model first the interaction between the dike and the fault (Fig. 5.8A1.1) and secondly that of the inclined sheet (Fig. 5.8A2.1). The stress shown as contours is the minimum principal compressive stress (σ_3) which is the maximum tensile stress, and the arrow surfaces express the maximum principal compressive stress (σ_1) (red arrows) and the minimum principal stress (σ_3) (white arrows) respectively. We observe that higher stresses are

concentrated in the inclined sheet run. Both principal stresses (σ_1 and σ_3) in A1.1 shows a 90 degrees rotation at the front of the tip promoting dike deflection into the fault. However, the principal stresses at the front of the inclined sheet in A2.1 show no rotation; hence the inclined sheet run promotes propagation parallel to σ_1. In that case, the inclined sheet cuts the fault and pass through it, a scenario that is not depicting the in-situ observations.

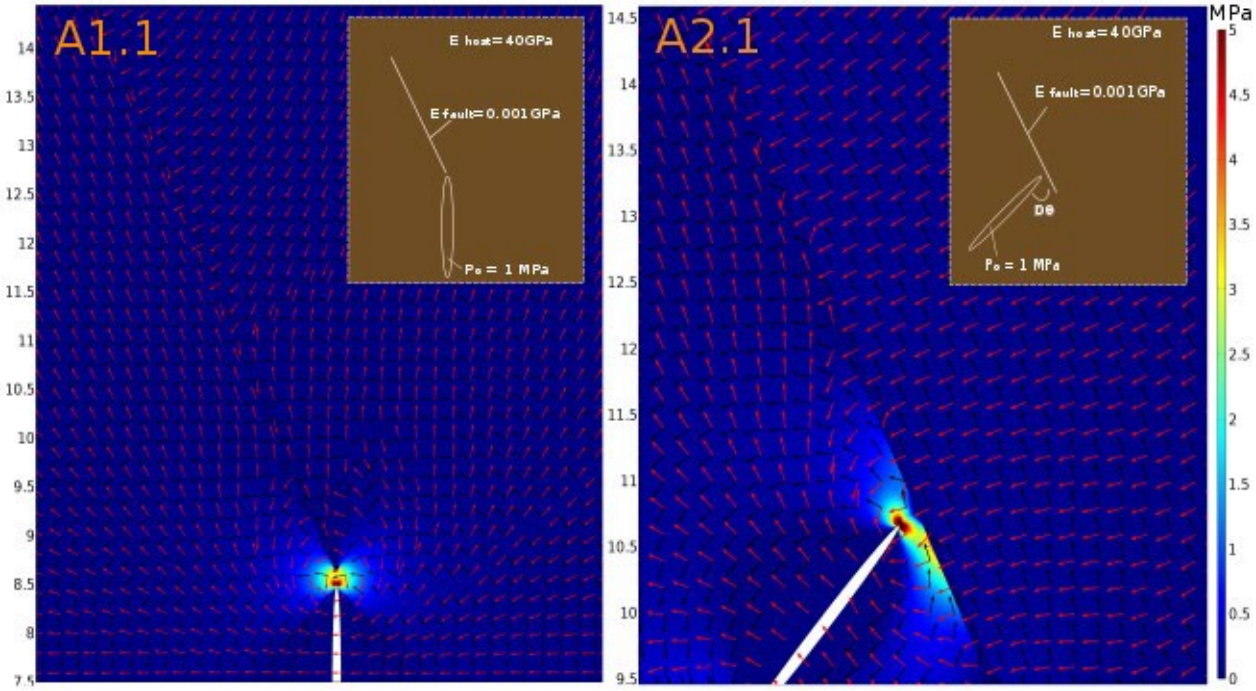

Fig. 5.8: FEM (finite element) models of tensile stress (σ_3) of the dike interacting with a low E fault (E fault=0.001 GPa). Their model setup of the dike and fault arrangements are at the top right corner of the snapshots. Overpressure in the dike is 1 MPa. D_θ is 50 degrees. The red arrow surface is σ_1 and black arrow surface is σ_3, (y-axis in meters).

E_{fault} =10GPa (stiff)

In the next stage (Fig. 5.9), we modelled both fractures again under 1 MPa of magmatic overpressure. The observed stress concentrations are shown in Figure 5.9. We assigned to the homogeneous normal fault a high Young's modulus value to investigate the dike-fault deflection scenarios if the fault core was stiff and subsequently inactive. We observe that higher stresses are concentrated again in the inclined sheet run. Both principal stresses (σ_1 and σ_3) at the tips were not rotated so dike deflection could not be a possible scenario. Instead dike propagation is clearly encouraged.

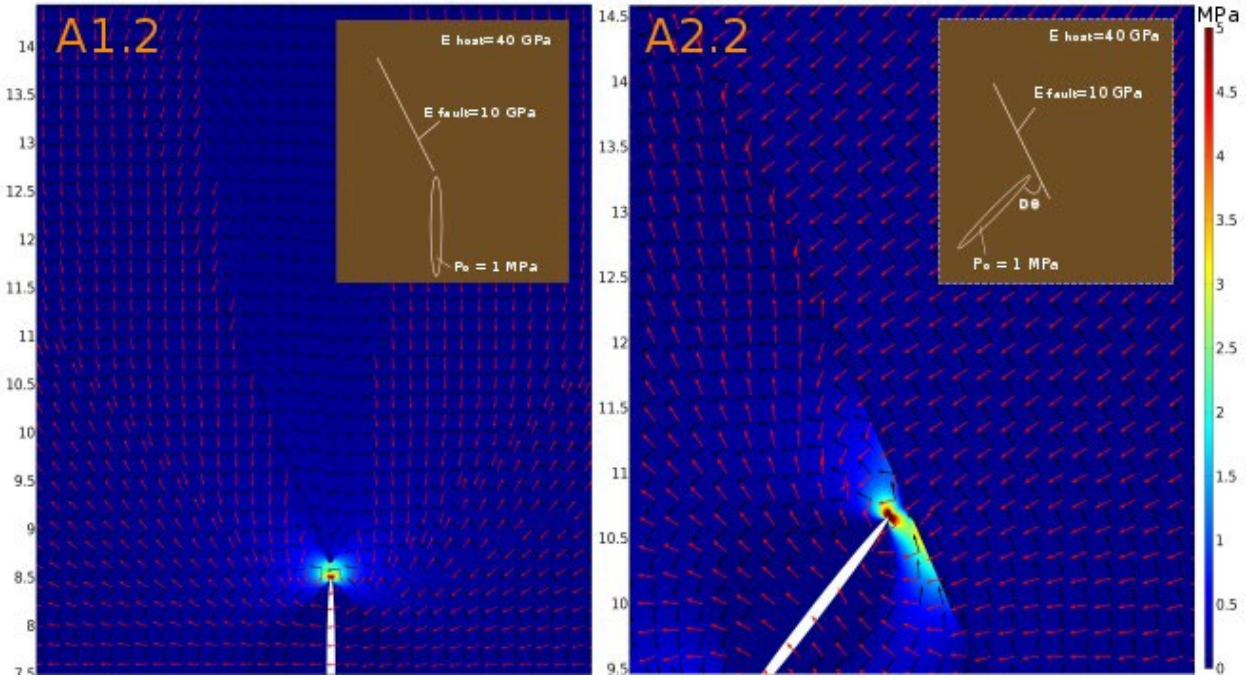

Fig. 5.9: FEM (finite element) models of tensile stress (σ_3) of the dike interacting with a high E fault (E fault=10 GPa). Their model setup of the dike and fault arrangements are at the top right corner of the snapshots. Overpressure in the dike is 1 MPa. D_θ is 50 degrees. The red arrow surface is σ_1 and black arrow surface is σ_3, (y-axis in meters).

The model runs show that the tensile stresses generated around the tip do not pass through the fault and the hanging wall part of the fault has a relatively lower amount of stress than the footwall. We observed that in the first scenario, the orientation of both σ_1 and σ_3 became rotated along and towards the dip of the fault zone but not in the second one. Our observations suggest that dike 1 may became deflected into the fault under these conditions due to stress rotations between the fault and the host rock. This result matches the field observation of Dike 1 but not of the inclined sheet, but another model setup is needed to explain that interaction, i.e. the heterogeneous fault zone.

5.2 Heterogeneous fault zone

On the next session the models are alike the previous ones, and their results are found in Figs. 5.10 and 5.11. Our models simulated a normal-fault damage zone, dipping 65°E, as composed of parallel layers or zones of progressively more compliant rocks with increasing distance from the fault rupture plane and the core or the opposite.

$E_{fault\ core}$= 0.001GPa (soft fault core and stiff damage zone)

In Figure 5.10 we observe the case study where the fault zone is heterogeneous, i.e. where different levels of Young's modulus exist throughout the fault. For the model snapshots we assigned to the fault high Young's modulus values (E_{rim}=10GPa) at the rims and a soft fault core (E_{core}=0.001GPa) We tested the dike-fault interaction of the dike (B1.1) and the inclined sheet (B2.1).

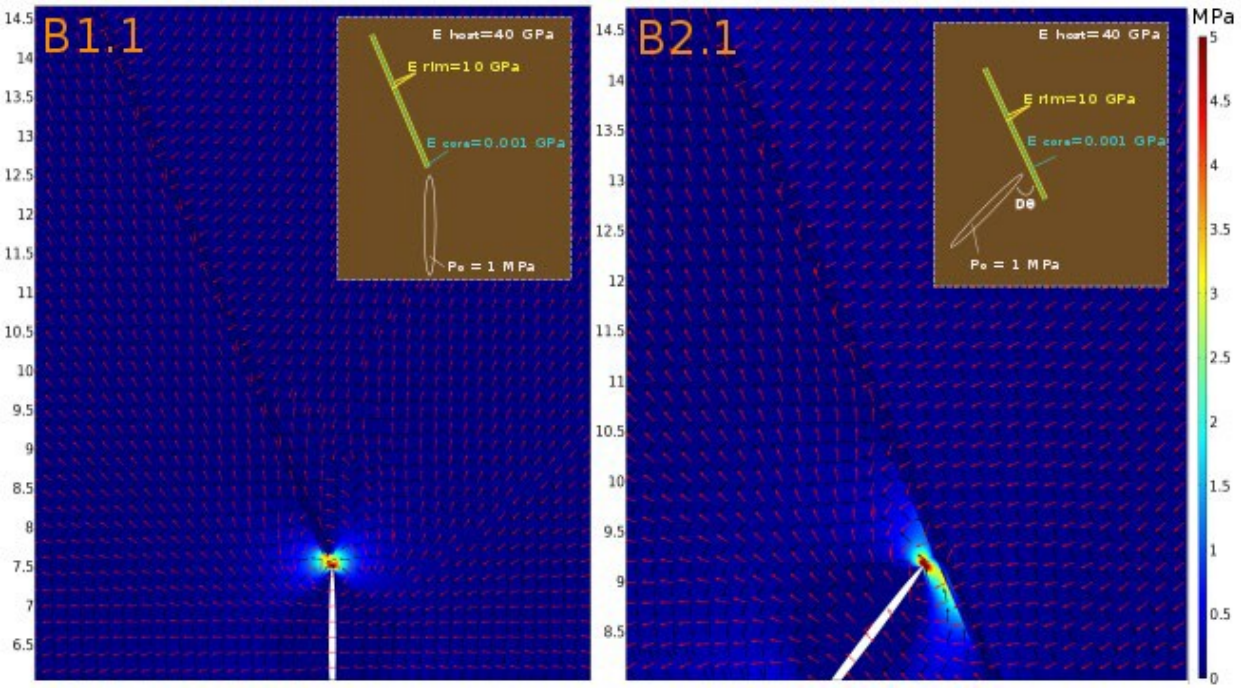

Fig. 5.10 : FEM (finite element) models of tensile stress (σ_3) of the dike interacting with a low E fault core ($E_{fault\ core}$=0.001 GPa) and a stiff ($E_{fault\ core}$=10 GPa) damage zone. Their model setup of the dike and fault arrangements are at the top right corner of the snapshots. Overpressure in the dikes is 1 MPa. D_θ is 50 degrees. The red arrow surface is σ_1 and black arrow surface is σ_3, (y-axis in meters).

We observe that higher stresses are concentrated once more in the inclined sheet run. Both principal stresses (σ_1 and σ_3) in B1.1 show a 90 degrees rotation at the front of the tip promoting dike deflection into the fault. In the inclined sheet model run, the principal stresses at the front of the inclined sheet (B2.1) show an almost 90-degree maximum rotation hence the inclined sheet run promotes possibly deflection. In that case, the dike will propagate through the stiff damage zone and deflect parallel to the soft fault core.

$E_{fault\ core}$= 10GPa (stiff fault core and soft damage zone)

In Figure 5.11 we observe the results of a new suite of model runs. The fault core had now a very high Young's modulus core (stiff) E=10GPa and a very low (stiff) damage zone.

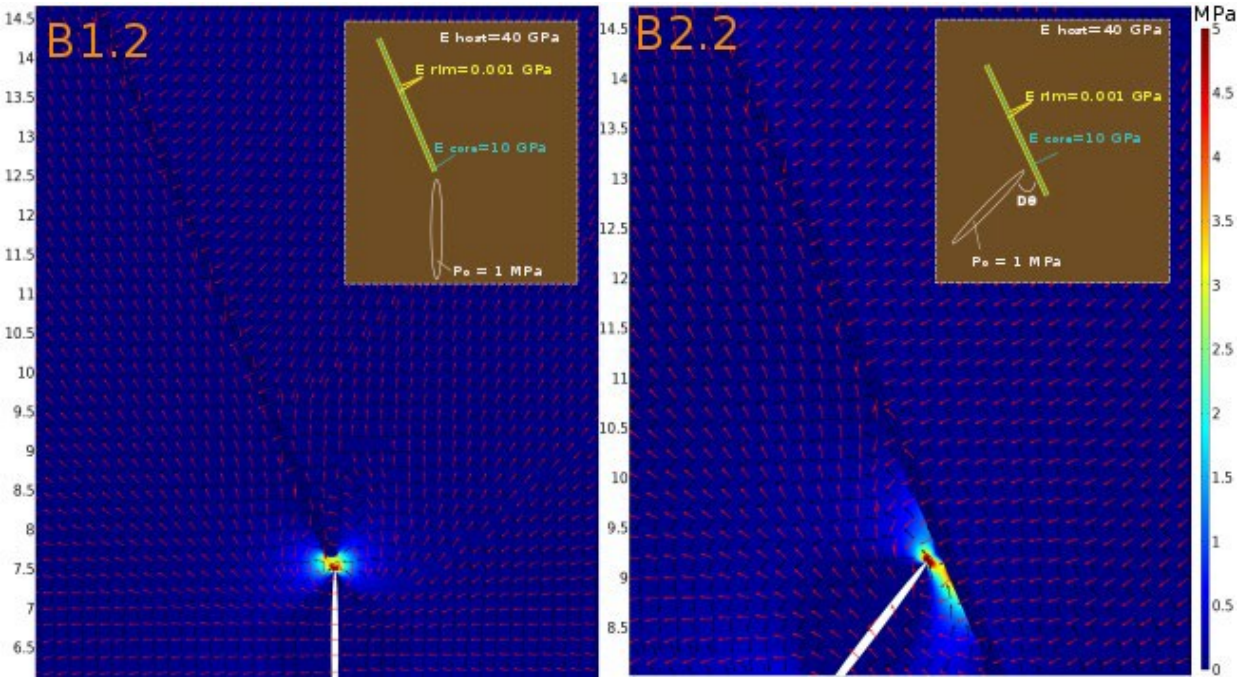

Fig. 5.11: FEM (finite element) models of tensile stress (σ_3) of the dike interacting with a stiff E fault core ($E_{fault\ core}$=0.001 GPa) and a soft ($E_{fault\ core}$= 10GPa) damage zone. Their model setup of the dike and fault arrangements are at the top right corner of the snapshots. Overpressure in the dikes is 1 MPa. D_θ is 50 degrees. The red arrow surface is σ_1 and black arrow surface is σ_3, (y-axis in meters).

The stress shown again as contours is the minimum principal compressive stress (σ_3) which is the maximum tensile stress, and the arrow surfaces express the maximum principal compressive stress (σ_1) (red arrows) and the minimum principal stress (σ_3) (white arrows) respectively. We observe that higher stresses are concentrated once more in the inclined sheet run. Both principal stresses (σ_1 and σ_3) in B1.1 shows a 90 degrees rotation at the front of the tip promoting dike deflection into the fault. In the inclined sheet model run, the principal stresses at the front of the inclined sheet (B2.1) show a 45-degree maximum rotation hence the inclined sheet run promotes likely deflection in the fault.

The numerical models were realistic representations of the dike-fault field interactions observed on the caldera wall. Our results showed that the tensile stress (σ_3) rise with higher amounts of applied magmatic overpressure (P_o). The stresses at the dikes are concentrated at the dike tips while in the fault zone, the stresses are concentrated at the tips and the bottom part of the fault. In addition, higher stresses are observed when the fault is stiffer rather than soft. We observed that in a homogeneous fault zone the stress rotations where subject to the mechanical properties of the fault (Young's modulus) and the stresses could rotate when the fault is active (soft).

In a heterogeneous fault zone, the stress rotations were subject to the mechanical properties of the fault core and the fault rims. When the fault core was soft a stress barrier condition was observed and both the vertical dike or the inclined sheet are seen to become deflected and propagate parallel to the soft core. That reflect a condition of an active fault. However, when the fault core is stiff, and inactive, we observe no stress rotations at the dike tip and the dike cannot become deflected into the fault (Fig. 5.12).

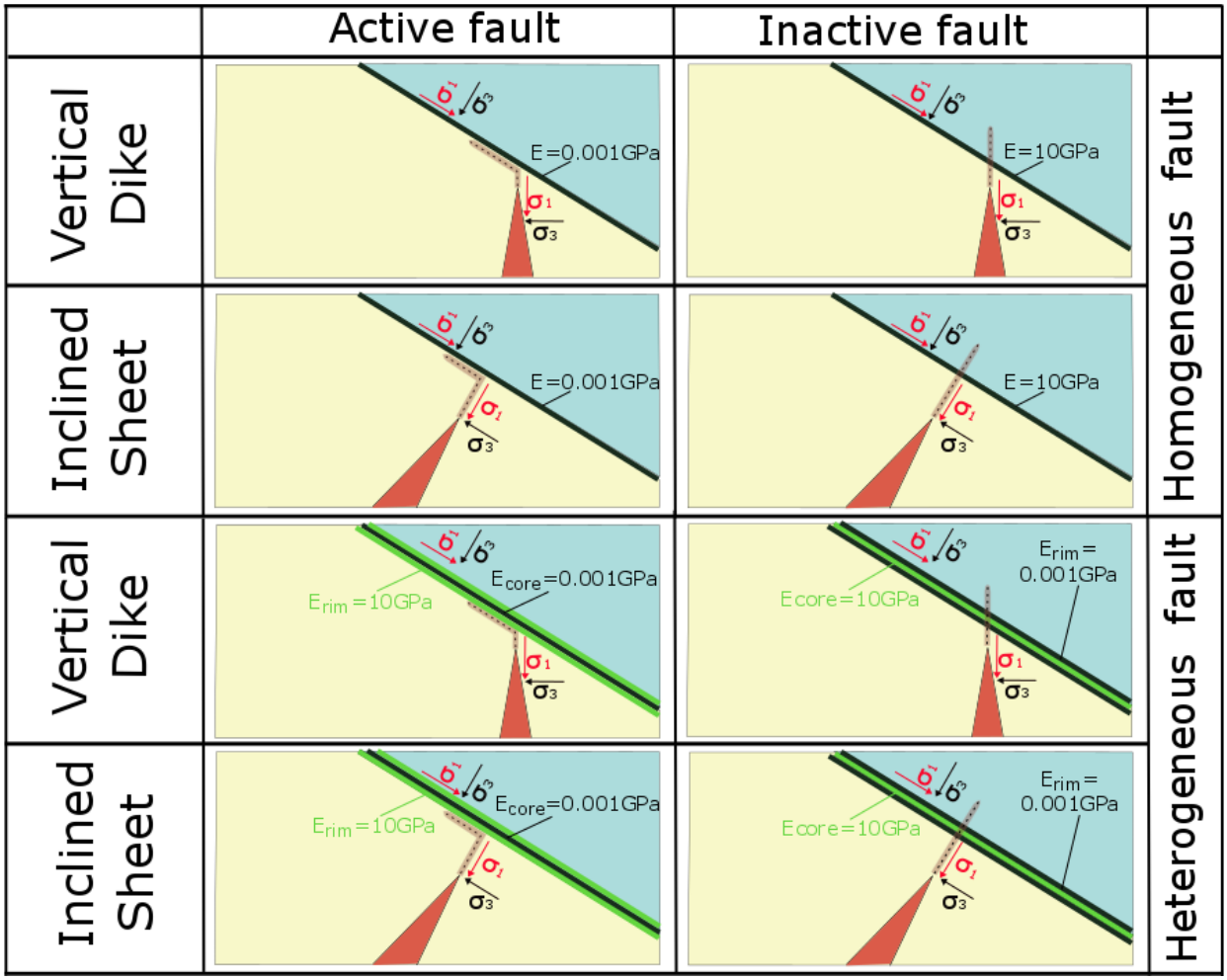

Fig. 5.12: Illustration showing the results of the FEM models. We observed that regardless the range of the magmatic overpressure (P_o) for both the dike and the inclined sheet, deflection is acquired when the homogeneous fault is active (low Young's modulus) rather than inactive (high Young's modulus). In a heterogeneous fault zone both the vertical dike and the inclined sheet are deflected into the fault cores if the latter were soft and not stiff.

5.3 Sensitivity test results

We conducted a variety of sensitivity tests to investigate how specific parameters could affect dike-fault deflection in the shallow crust. We gave specific interest in the following parameters: a) dike-fault angle (models A-F), b) dike thickness (models G-I), c) fault thickness (models J-L), d) extensional stress field (models M-O), e) compressional stress field (models P-R), and f) fault (dip) height (models S-U). It is evident that the dike-fault angle and the fault thickness are the parameters that could control the deflection mechanism subject to the stiffness of the fault. The results are observed in Figure 5.13 and the original models at the supplementary material (Appendix C2).

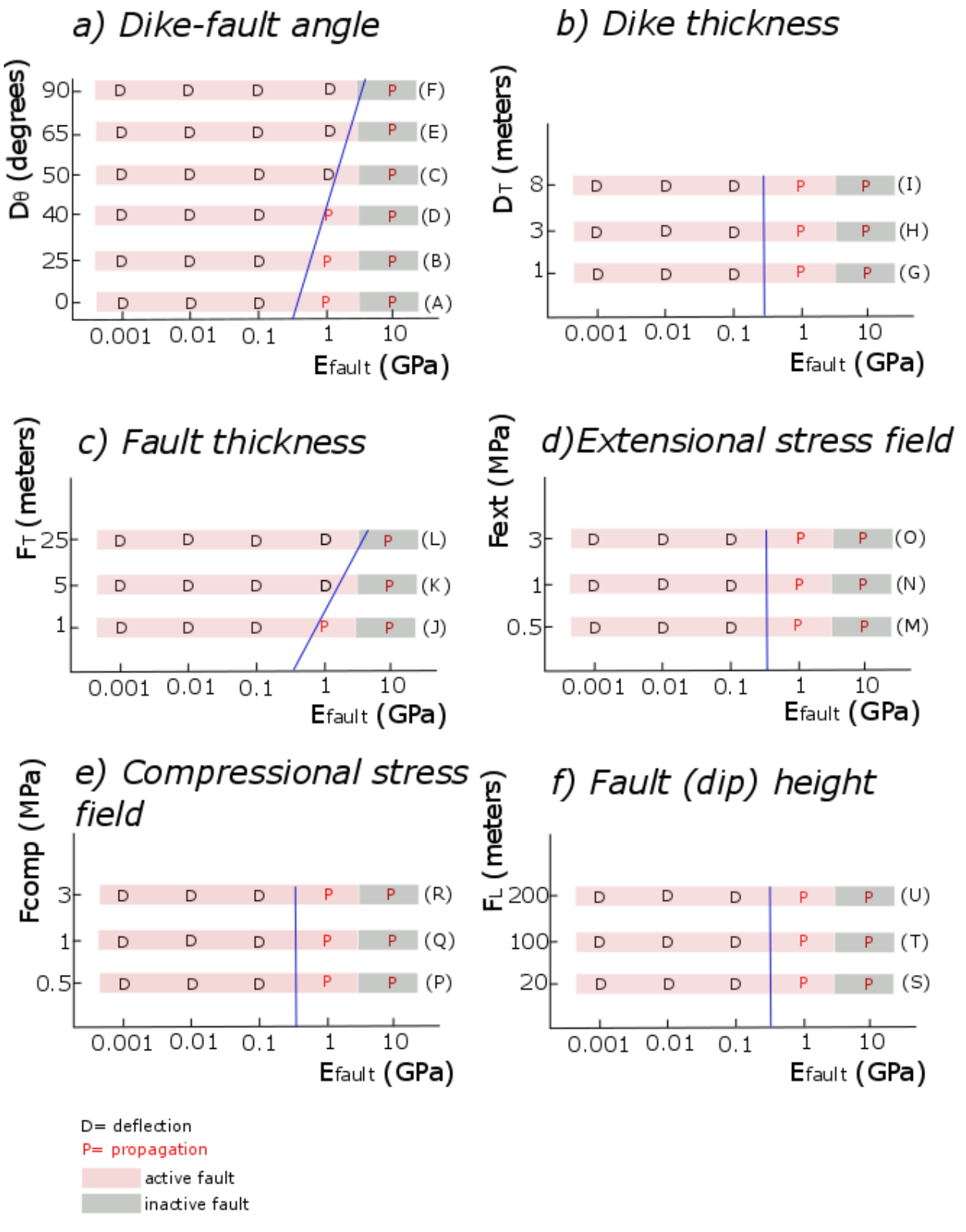
a) Dike-fault angle
Dθ (degrees)
90
65
50
40
25
0
D D D D P (F)
D D D D P (E)
D D D D P (C)
D D D P P (D)
D D D P P (B)
D D D P P (A)
0.001 0.01 0.1 1 10
Efault (GPa)
b) Dike thickness
DT (meters)
8
3
1
D D D P P (I)
D D D P P (H)
D D D P P (G)
0.001 0.01 0.1 1 10
Efault (GPa)
c) Fault thickness
FT (meters)
25
5
1
D D D D P (L)
D D D D P (K)
D D D P P (J)
0.001 0.01 0.1 1 10
Efault (GPa)
d)Extensional stress field
Fext (MPa)
3
1
0.5
D D D P P (O)
D D D P P (N)
D D D P P (M)
0.001 0.01 0.1 1 10
Efault (GPa)
e) Compressional stress field
Fcomp (MPa)
3
1
0.5
D D D P P (R)
D D D P P (Q)
D D D P P (P)
0.001 0.01 0.1 1 10
Efault (GPa)
f) Fault (dip) height
FL (meters)
200
100
20
D D D P P (U)
D D D P P (T)
D D D P P (S)
0.001 0.01 0.1 1 10
Efault (GPa)
D= deflection
P= propagation
active fault
inactive fault

Fig. 5.13: Conditions that encourage dike deflection (D) and dike propagation (P) in a series of dike and fault interactions associated with the angle of the dike to the fault (a), the dike thickness (b), the fault thickness (c), regional extension (d), regional compression (e), and the fault height (f) in relation to the mechanical properties of a homogeneous fault zone.

6. Discussion

6.1 Effect of the dike and sheet-fault angle (D_θ)

The dikes on the caldera wall are mostly subvertical. However, there are also three inclined sheets with angles between 50˚ and vertical. As a result, the angle between the dikes, sheets and faults (D_θ) could be as much as 25°. Here we investigate the influence of changing the angle with which the dike or sheet approaches the fault. We modelled the angles 25˚, 40˚, 50˚, 65˚ and 90˚ (Fig. 5.4) according to the more often observed field structures (Fig. 5.7). The studied angle can be changed by changing either the fault angle or the sheet angle. However, we keep the fault angle constant and change the fracture dips as we want to simulate the realistic conditions of the studied processes. The models are presented in the supplementary material (Appendix C2) supportive files 1-6.

We performed several models with variable stiffness values (five different orders of magnitude) and observed that deflection is always encouraged when the stiffness of the fault is soft (<0.1GPa), regardless of the angle at which the dike is to the fault. However, when the fault core is stiffer and the angle between the dike and the fault is 0˚- 50˚, i.e. shallow, the dike does not become deflected into the fault but instead propagates through the fault. When D_θ is more than 50˚ and closer to vertical, the dikes show a tendency to deflect when the fault core is (E=1GPa) but not when it is very stiff (E=10GPa) (Fig. 5.13a).

6.2 Effect of dike and fault thickness (D_T, F_T)

We modelled dike thicknesses (D_T) of the end members of the observed values (1 and 8m) as well as the average value (3m). In addition, a further comparison of dike thickness with composition showed that mafic dikes have a variable thickness of up 3m while felsic ones can be as thick as 8m. These thicknesses allow an examination of the mechanical effect of different magma compositions on fault interactions.

The results showed that dike deflection is encouraged in soft fault zones regardless of the dike thickness. In specific no correlation was found between the dike thickness and the stiffness of the fault in the sensitivity tests. Similarly, the previous results can give us insights on whether the composition of the magma could be a parameter that could affect the mechanisms of dike propagation. Our models so far reveal that dike thickness does not substantially affect dike-fault interactions and so the possibility of a mafic or a felsic dike being deflected into a fault is equal and depends exclusively on the mechanical properties of the fault and the host rock (Fig. 5.13b). The models that present the variable thickness of the dike are shown in supplementary material (Appendix C2) supportive files 7-9.

The faults on the Santorini northern caldera wall are from some meters to hundred-scales, and their variable thickness (F_T) was the next studied parameter. As explained in the methodology, we modelled the dike-fault interaction by assigning a range of fault thickness values (1, 5 and 25m) to rely on the field observations. Results showed that soft fault zones, regardless of their thickness, are always more likely to deflect dikes in contrast to stiff fault zones. When the thickness of a fault zone is larger than 5m, dike deflection is encouraged if the fault is suitably stiff ($E \geq 1$GPa). This result agrees with the field observations as we often observe a higher number of dike segments to

be deflected into thicker fault zones than thinner ones. Interestingly, in case studies where the thickness of the fault is less than 5m and the fault core is moderately stiff (E=1GPa) then deflection cannot occur (Fig. 13c). The models with the variable thickness of the fault are shown in the supplementary material (Appendix C2) supportive files 10-12.

6.3 Local extensional (F_{ext}) or compressional (F_{comp}) regime and fault zone length (F_L)

The local or regional stress field contributes to dike arrest (Chapter 4) and so we also investigated how a regional extensional or compressional stress field alters dike and fault interactions. The results show that both under an extensional or compressional stress fields the dikes can be deflected if the fault cores are soft (≤0.1GPa), but the deflection is not encouraged no matter what the stress field is if the stiffness of the core is larger than 1GPa (Fig. 5.13 d and e) in the supplementary material (Appendix C2), supportive files 13-18.

The results of the models are summarized in the supplementary material in the supplementary material (Appendix C2). Finally, the different values of dike length (20, 100 and 200m) are also aiming to simulate the real length scales on Santorini volcano.

We studied how the length of the fault can be a parameter on dike deflection. Our results have shown that the stiffness of the fault core controls the propagation mechanism. If the stiffness of the fault is less than 0.1GPa then regardless of the dike length, the dikes are deflected into the fault while the stiff fault cores cannot encourage dike deflection irrespective of the fault length (Fig. 13f). The results are shown in the supplementary material (Appendix C2) supportive files 19-21.

6.4 Timing of faulting and diking

Here we present a reconstruction of the dynamic evolution of faulting and diking at Santorini by considering the following factors: The stratigraphy of the host rock and geodynamic setting as reported by previous studies (Druitt et al., 1999; Mc Kenzie 1972; Le Pichon and Angelier, 1979; Taymaz et al., 1991, 2007; Royden 1993; Jolivet et al., 1996, 2013; Mountrakis et al., 1998; Gautier et al., 1999; Benetatos et al., 2004; van Hinsbergen and Meulenkamp, 2006; Doglioni et al.,2007; Agostini et al., 2010; Nocquet 2012; Kokkalas and Audin et al., 2013; Brun et al., 2017)) and from our field observations. The dynamic evolution of the faults at the northern caldera wall as a consequence of the extensional local regime imposed by the geodynamic setting as reported from seismic and geological studies (Papanikolaou et al., 1988; Perissoratis, 1995; Piper and Perissoratis, 2003; Pe-piper et al., 2005; Piper et al., 2007). Generalized fault zone and dike propagation mechanics (Chester and Logan 1986; Caine et al., 1996, Faulkner et al., 2010, 2011; He and Hutchinson, 1989; Hutchinson, 1996; Xu et al., 2003; Wang and Hu, 2006; Gudmundsson et al., 2011; Tibaldi, 2015), as well as the new dike-fault field interactions reported from our field and numerical observations.

Peristeria volcano edifice was formed in an extensional regime at between 530-430 ka. It was followed possibly by incremental caldera collapse dated, from an angular unconformity, in between the av2/av3 lava at around 496 ka. The extensional regime contributed to the formation of the meter scale F5 and F6 normal faults which are restricted to the av1 unit within the volcano. Both of these faults exhibit interactions with dikes which also likely emplaced during the formation of Peristeria volcano. Dike 2 (of this study) interacted with fault F5 by changing its propagation path to deflect into the fault for a few meters but eventually did not use the fault to continue the

propagation to shallower levels. We infer that this interaction occurred as a result of the properties of the damage zone surrounding the fault. Dike 1, instead, propagated only within the fault core and hence we interpret that the dike was captured in the fault in a deeper segment due to the compliance of the fault core. Dikes cut none of the F9 meter scale normal faults, and hence they must have formed later.

During the formation of Peristeria volcano, the first major eruptive cycle geophysical studies report the triggering of an N65˚ E sinistral strike-slip system (0.2-0.6 ka) which was associated with the motion of the Anatolian block from the East (Piper et al., 2007). Fault F3 was likely formed as an expression of the movement of the Anatolian fault following the recorded strike and location. We hypothesize that originated as a sinistral strike-slip fault according to the slip motion proposed by the field observations such as the observed signs of sliding of its northern part towards the SW. Later geodynamic events that restricted during the first major eruptive cycle of the current Santorini volcano commenced and lasted almost 200 thousand years between 360-172 ka. The eruptive activity during this cycle migrated to the central part of Santorini over time Druitt et al., (1999). Active stress filed operating during this time in the Aegean geodynamic setting was delineated by an ENE-WSW dextral strike-slip system (from 200ka) triggered either by the collision of the African plate or the buoyancy effects of the thicker continental crust (Pe-piper et al., 2005). We propose that faults F10-F13, that strike E-W and constrained to the Peristeria units and the location of MPI, were triggered due to the collision of the African plate as they are strike-slip faults with E-W strikes. They could have formed as subsidiary faults to the ENE-WSW system; during a period that could fit the stratigraphy of the host rock that was created. However, as already explained, during this period, diking was restricted to the central parts of the caldera. Hence, observations of emplaced dike segments at the northern caldera wall should be limited. Although

we observed dike segments to have been deflected into F3, we propose that either belong to the Peristeria or Skaros dike swarm and argue that could have fed the eruptions of the1st eruptive cycle. The reason is that the distribution of those stratigraphic horizons is restricted only at the NE corner of the wall next to F2 (Fig. 5.5) hence the possibility one of them to have fed one of those eruptions is not viable.

A caldera collapse at around 172ka followed the first explosive cycle (360-172 ka) of Santorini volcano and later eruptive activity migrated west to form the Simandiri edifice (Druitt et al., 1999). During the middle Pleistocene, around 126ka, the first NE-SW normal and strike-slip faults were triggered in the area and coincide with the formation of cinder cones at Megalo and Kokkino Vouno and the Kolumbo tuff ring (125-80 ka). Faults F2, F7, F8, F9 and F10, represent a system of normal faults that nucleated or reactivated due to local extension during this time. All motion on these faults ceased before the deposition of the scoria layer ap4. None of the mapped dikes deflects into faults F7, F8, F9 or F10 but some (at least three)were captured by fault F2.

The field observations show that F2 is the only fault that cuts the whole stratigraphic horizon of the caldera wall, a sign of a later reactivation as explained before. There was no synchronicity between the activity of the faults and dikes during the first explosive cycle so the dikes that deflected into F2 could not have been coeval with those events. More detailed field observations revealed a light coloured deflected multiple dike in the F2 fault zone which propose dike emplacement of silicic magma when the fault was active according to the numerical modelling results. As such the dike segments found deflected in the F2 fault zone, belong either to the Peristeria stratovolcano or the Skaros shield because both are characterised by silicic activity. An important implication is that F2 should have been active during the emplacement of the two dike swarms.

The Simandiri sub-dike swarm that followed the first explosive cycle and migrated the volcanism in the western part of Santorini did not interact with any of the Northern caldera wall fault zones as the Simandiri edifice is distal to the observed fault segments. Additionally, there were no Simandiri lavas found at the eastern part of the island.

The Megalo and Kokkino Vouno cinder cones (125-80 ka) were formed after the formation of the Simandiri shield. The scoria cones are composed by tephra developed from explosive eruptions of mafic and intermediate magmas (ap4) (Chapter 3). They are located at the northern part of the caldera wall and faults F5, F6 and F2 are the most proximal faults. However, no scoria dikes were found to become deflected into any fractures; hence we assume that the dark-coloured mafic dikes observed deflected into F2 fault zone belong to a later subswarm. The activity that formed unit ap4 terminated with the formation of a collapse caldera at around 70ka (Druitt et al., 1999).

During the second eruptive cycle, the formation of the Skaros and Therasia shields, two sets of normal faults striking N40-55˚ E and N65-75˚ E were triggered (Piper and Perissoratis, 2003; (Bohnhoff et al., 2006). Previous volcanological studies reported that the graben subsidence is coeval with the 21 ka Cape Riva caldera collapse event, which inslided the large block towards the Skaros shield summit (Druitt et al., 1999). However, later studies (Piper and Perissoratis, 2003) reported the initiation of subsidence of minimum 600 m in Late Pleistocene which tectonically could have met a crescendo at the caldera collapse event that occurred at the end of the first cycle (172ka). Although very rapid subsidence and fast flank uplift is possible in narrow grabens (less than 20km width), the primary mechanism requires an event that can cause horizontal extension, crustal thinning and mantle upwelling associated often with dike emplacement in an area where tensile faulting is already active (Jarvis, 1984). If active extension in the Southern Aegean region occurred in pulses since the Miocene (Le Pichon and Angelier, 1979; Jolivet et al., 2013), then we

propose that faults F2 and F3 were formed earlier than before the formation of caldera three reactivated during the latter. Strong evidence of this suggestion is that several dikes were foundto have been deflected into both sections of the graben faults. The numerical study proposed that such a mechanism could be possible only when the faults are active. Geochemical correlations between the host rock and those dikes have shown similarities with the Peristeria or Skaros sub swarms (Chapter 6). According to this hypothesis, the graben was still active during the most recent dike emplacement event, i.e. during the formation of the Skaros shield (70-54ka) and hence more recently than proposed by Druitt et al., (1999). F9 conjugate faults may have formed after the graben subsidence consequently no dikes are deflected into them. Possibly F12 and F13 faults could have faults expressions of F4 fault. The latter is located at the eastern part of the island and was reported as an accommodation structure of the graben (Druitt et al., 1999). The reconstruction is showing in Figure 5.14.

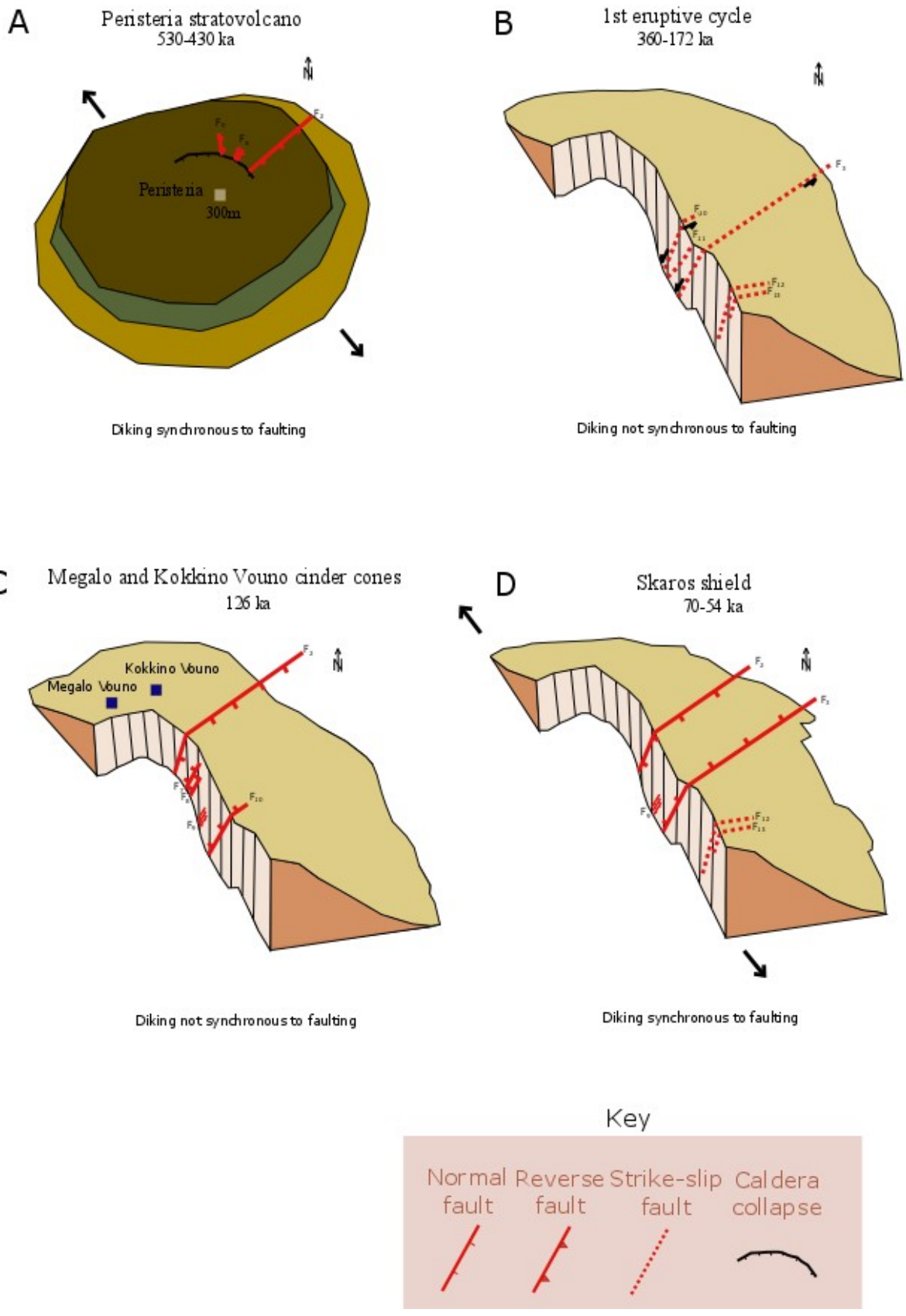
A
Peristeria stratovolcano
530-430 ka
Peristeria
300m
Diking synchronous to faulting
B
1st eruptive cycle
360-172 ka
Diking not synchronous to faulting
C
Megalo and Kokkino Vouno cinder cones
126 ka
Kokkino Vouno
Megalo Vouno
Diking not synchronous to faulting
D
Skaros shield
70-54 ka
Diking synchronous to faulting
Key
Normal fault
Reverse fault
Strike-slip fault
Caldera collapse

.

Fig. 14: Schematic illustration showing the fault evolution at the northern caldera wall and the reconstruction of its geological history from this multidisciplinary study. (A) Peristeria stratovolcano, (B) 1st eruptive cycle, (C) Megalo and Kokkino Vouno cinder cones, (D) Skaros shield.

7. Conclusions

When approaching a fault, the likelihood that a magmatic dike becomes deflected into the fault depends on the angle at which it meets the fault. In the case of Santorini, where most of the faults are high angle (> 65 degrees) normal or strike-slip faults, it is much more likely that vertical dikes will become captured or deflected into the faults than shallower dipping inclined sheets. However, the most critical factor controlling dike and fault interactions is the mechanical structure of the fault. Young or active faults that contain a defined fault core of brecciated or low Young's moduli material will preferentially deflect or capture dikes when compared to older or inactive faults that host stiffer fault cores. As a secondary factor, the thickness of the fault will promote stress rotations and encourage deflection if the active fault zones are thicker than 5m. However, in a less important factor, the thickness of the dike, the length of the fault zone and the regional setting will encourage dike-fault deflection only when the fault core is soft (<0.01GPa). In stiffer conditions (>1GPa) the dikes prefer to follow their paths into the crust and advance parallel to σ1 posed by their stress field.

Mapping of the northern caldera wall allowed us to record two suites of faults which we classified subject to their scale (meter or hundred-meter scale), type (normal, strike-slip) and active stress

field (e.g. transtension). For the first time, we used a coupled field and numerical study as a reconstruction tool of the geological history in an active volcanotectonic setting.

The volcanotectonic study revealed that the graben subsidence had occurred earlier than reported by previous studies. At the same time, the evolution of the regional tectonic stress field is highly associated with the Aegean active geodynamic setting, and the dikes did not always facilitate or inhibit the transport of magma in the shallow parts of the crust at Santorini.

Acknowledgements

We thank A. Rust & K. Cashman for helpful comments and suggestions which significantly improved the manuscript. KD is grateful for a Kirsty Brown memorial fund which enabled fieldwork in the Aegean. JB acknowledges support from Fondecyt 11190143 and Fondap-Conicyt 15090013

References

Anderson, E.M., (1951). Dynamics of faulting and dyke formation, 2nd edn. Olivier and Boyd, Edinburgh.

Anderson. L J., Osborne. R. H ., Palmer. D. F ., (1983). Cataclastic rocks of the San Gabriel fault- An expression of deformation at deeper crustal levels in the San Andreas fault, Tectonophysics v. 98, 209-251

Agostini, S., Doglioni, C., Innocenti, F., Manetti, P., Tonarini, S. (2010).On the geodynamics of the Aegean rift, Tectonophysics, 488, 7-21

Atkinson, B K., (1987). Introduction to fracture mechanics and its geophysical applications. In: Fracture Mechanics of Rock, Ed. B. K. Atkinson. Academic Press, London. 1–26.

Atkinson, B. K., Meredith, P.G., (1987). Experimental fracture mechanics data for rocks and mineral. In: Atkinson, B.K. (ed.), Fracture Mechanics of Rock. London: Academic Press, 477-525

Babiker, M., Gudmundsson A., (2004). The effects on dykes and faults on groundwater flow in an arid land: The Red Sea Hills, Sudan. Journal of Hydrology, 297, 256-273

Barka, A.A., (1992). The North Anatolian Fault Zone: Annals Tectonicae, 6, 164–195

Barnett, Z.A., Gudmundsson, A., (2014). Numerical modelling of dykes deflected into sills to form a magma chamber. J. Volcanol. Geotherm. Res. 281, 1-11.

Bailey, J.C., Jensen, E., Hansen, A., Kann, A., Kann, K., (2009). Formation of heterogeneous magmatic series beneath North Santorini, South Aegean island arc, Lithos, 110, 20-36.

Benetatos, C., Kiratzi, A., Papazachos, C., Karakaisis, G., (2004). Focal mechanisms of shallow and intermediate depth earthquakes along the Hellenic Arc, J. Geodyn., 37, 253-296

Bohnhoff M., Makris J., Stavrakakis G., Papanokolaou D., (2001). Crustal investigation of the Hellenic subduction zone using wide aperture seismic data. Tectonophysics 343, 239-262

Bohnhoff M., Rische M., Meier T., Becker D., Stavrakakis G., Harjes H.P. (2006). Microseismic activity in the Hellenic Volcanic Arc, Greece, with emphasis on the seismotectonic setting of the Santorini–Amorgos zone, Tectonophysics, 423, 17–33

Broek, D., (1982). Elementary engineering fracture mechanics. Martinus Nijhoff publishers,

Browning J., Gudmundsson A., (2015). Caldera faults capture and deflect inclined sheets: an alternative mechanism of ring dyke formation Bull. Volcanol., 77, 1-13

Brun, J.P., Faccenna, C., Gueydan, F., Sokoutis, D., Philippon, M., Kydonakis, K., Gorini, C., (2017). Effects of slab rollback acceleration on Aegean extension. Bulletin of the Geological Society of Greece, 50, 5-23

Cadoux, A., Scaillet, B., Druitt, T.H., Deloule, E., (2014). Magma storage conditions of large Plinian eruptions of Santorini. Journal of Petrology, 55, 1129–1171

Caine, J.S., Coates, D.R., Timofeef. N.P., and Davis, W.D., (1991). Hydrogeology of the Northern Shawangunk Mountains: New York State Geological Survey Open-File Report, 72 and maps

Caine, J.S., Evans, J.P., Forster C.B., (1996). Fault zone architecture and permeability structure Geology. 24, 1025-1028

Cembrano, J. and Lara, L., (2009). The link between volcanism and tectonics in the southern volcanic zone of the Chilean Andes: a review. Tectonophysics, 471, 96-113.

Chester, F.M., Logan, J.M. (1986). Implications for mechanical-properties of brittle faults from observations of the Punchbowl Fault ,one, California, Pure Appl. Geophys., 124, 79–106

Delaney, P., Pollard, D., Ziony, J., McKee E., 1986. Field relations between dikes and joints: emplacement processes and paleostress analysis J. Geophys. Res., 91, 4920-4938

Doglioni, C., Agostini, S., Crespi, M., Innocenti, F., Manetti, P., Riguzzi, F., Savascin, Y., (2002). On the extension in western Anatolia and the Aegean Sea. J. Virt. Expl. 7, 117–131.

Doglioni C., Carminati, E., Cuffaro, M., Scrocca, D., (2007). Subduction kinematics and dynamic constraints, Earth-Sci. Rev. 83, 125-175

Druitt, T.H., Edwards, L., Mellors, R.M., Pyle, D.M., Sparks, R.S.J., Lanphere, M., Davis, M., Barriero, B., (1999). Santorini Volcano. Geological Society Memoir No. 19, 165 p

Fourney, W.L., (1983). Fracture control blasting. In: Rossmanith, H.P. (ed.), Rock fracture Mechanics. New York: Springer-Verlag, 301-309

Fytikas, M., Karydakis, G., Kavourdis, T., Kolios, T., Vougioukalakis, N.G., (1990). Geothermal research on Santorini, D.A. Hardy (ed.), Thera and the Aegean World III: Volume 2 Earth Sciences, The Thera Foundation, London, pp. 241-249

Fytikas, M., Innocenti, F., Manetti, P., Peccerillo, A., Mazzuoli, R. & Villari, L., (1984). Tertiary to Quaternary evolution of volcanism in the Aegean region. In the Geological Evolution of the Eastern Mediterranean (eds J. E. Dixon & A. H. F. Robertson), 687–99. Geological Society of London, Special Publication no. 17

Faulkner, D.R., Jackson, C.A.L., Lunn, R.J., Schlische, R.W., Shipton, Z.K., Wibberley, C.A.J., Withjack, M.O., (2010), A review of recent developments concerning the structure, mechanics and fluid flow properties of fault zones, J. Struct. Geol., 32(11), 1557–1575,

Faulkner, D.R., Mitchell, T.M., Jensen, E., Cembrano, J., (2011). Scaling of fault damage zones with displacement and the implications for fault growth processes, J. Geophys. Res.-Solid Earth 116

Gautier, P., Brun, J.P., Moriceau, R., Sokoutis, D., Martinod, J., Jolivet, L., (1999). Timing, kinematics and cause of Aegean extension: A scenario based on a comparison with simple analogue experiments. Tectonophysics, 315, 31– 72.

Galland, O., Hallot, E. Cobbold, P. R. Ruffet, G., de Bremod d' Ars, J., (2007). Volcanism in a compressional Andean setting: A structural and geochronological study of Tromen volcano (Neuque´n province, Argentina), Tectonics, doi:10.1029/2006TC002011

Geshi, N., Kusumoto, S., Gudmundsson, A., (2010). Geometric difference between non-feeder and feeder dykes. Geology 38, 195-198

Griffith, A.A., (1921). The phenomena of rupture and flow in solids. Philosophical transaction of the royal society of London, Sierres A., Containing papers of a mathematical or physical character 221, 163-198

Griffith, A.A., (1924). The theory of rupture. In First international congress of Applied Mathematics, 55-63

Gudmundsson, A., (1984). Formation of dykes, feeder dykes, and the intrusion of dykes from magma chambers, Bulletin of Volcanology. 47, 537-550

Gudmundsson, A., (1995). The geometry and growth of dykes. In: Baer, G., Heimann, A. (eds), Physics and Chemistry of Dykes. Balkema, Rotterdam 23-34.

Gudmundsson, A. (1999). Fluid overpressure and stress drop in fault zones. Geophys. Res. Lett. 26, 115-118

Gudmundsson, A., Simmenes, T. H., Larsen, B., and Philipp, S. L. (2010). Effects of internal structure and local stresses on fracture propagation, deflection, and arrest in fault zones. J. Struct. Geol. 32, 1643–1655

Gudmundsson, A., (2011). Rock fractures in geological processes. Cambridge University Press, Cambridge.

Gudmundsson, A., Lotveit, I.F., (2012). Sills as fractured hydrocarbon reservoirs: examples and models. Geological society, London, Special publications, 374, 251-271

He, M.Y., Hutchinson, J.W., (1989). Crack deflection at an interface between dissimilar elastic materials. Int J Solids Struct 31, 3443–3455

Heap, M.J., Villeneuve, M., Albino, F., Farquharson, J.I., Brothelande, E., Amelung, F, Got J-Luc, Baud, P., (2019). Towards more realistic values of elastic moduli for volcano modelling, Journal of Volcanology and Geothermal Research

Heath, B.A., Hooft, E.E.E., Toomey, D.R., Papazachos, C.B., Nomikou, P., Paulatto, M., Morgan, J.V., and Warner, M.R., (2019). Tectonism and its relation to magmatism around Santorini volcano from upper crustal P-wave velocity: Journal of Geophysical Research: Solid Earth , https://doi.org/10.1029/2019JB017699.

Heiken, G., McCoy, F., (1984). Caldera Development During the Minoan Eruption, Thira, Cyclades, Greece. Journal of Geophysical Research, 89, 8441-8462.

Hoek, H., (2000). Practical rock engineering , www.rockscience.com

Holohan, E.P., van Wyk de Vries, B., Troll, V.R., (2007). Analogue models of caldera collapse in strike-slip tectonic regimes. Bull. Volcanol. doi.10.1007/s00445-007-0166-x

Hooft, E.E., Nomikou, P., Toomey, D.R., Lampridou, D., Getz, C., Christopoulou, M., O'Hara, D., Arnoux, G.M., Bodmer, M., Gray, M., Heath, B.A., Vander Beek, B.P., (2017). Backarc tectonism, volcanism, and mass wasting shape seafloor morphology in the Santorini-Christiana-Amorgos region of the Hellenic Volcanic Arc, Tectonophysics, 712-713, 396-414

Hubbert, M., Willis, D., (1957). Mechanics of hydraulic fracturing, J. Petrol. Technol., 9, 153-168

Hutchinson, J.W., (1996). Stresses and failure modes in thin films and multilayers. Technical University of Denmark-Notes for a DCAMM course.

Jarvis, G.T., (1984). An extensional model of graben subsidence - the first stage of basin evolution, Basin Analysis: Principles and Applications (eds) Jansa, L.F., Burollet, P.F., Grant, A.C. Sedimentary Geology, 40, 13-3

Jolivet, L., Goffé, B., Monié, P., Truffert-Luxey, C., Patriat, M. & Bonneau, M., (1996). Miocene detachment on Crete and exhumation P–T–t paths of high-pressure metamorphic rocks. Tectonics, 15, 1129-1153.

Jolivet, L., Augier, R., Faccenna, C., Negro, F., Rimmele, G., Agard, P., Robin, C., Rossetti, F., Crespo-Blanc, A., (2008). Subduction, convergence and the mode of backarc extension in the Mediterranean region, Bull. Soc. Geol. Fr., 179, 525–550

Jolivet L., Faccenna C., Huet B., Labrousse L., Le Pourhiet L., Lacombe O., Lecomte E., Burov E., Denèle Y., Brun J.-P., Philippon M., Paul A., Salaün G., Karabulut H., Piromallo C., Monié P., Gueydan F., Okay A. I., Oberhänsli R., Pourteau A., Augier R., Gadenne L., Driussi O., (2013). Aegean tectonics: strain localisation, slab tearing and trench retreat. Tectonophysics 597–598, 1–33.

Karlstrom, L., Dufek, J., Manga, M., (2010). Magma chamber stability in arc and continental crust, J. Volcanol. Geotherm. Res., 190, 249– 270.

Kavanagh, J.L., Menand, T., Sparks, R.S.J., (2006). An experimental investigation of sill formation and propagation in layered elastic media. Earth 2995 and Planetary Science Letters 245, 799–813.

Kavanagh, J.L., Burns, A.J., Hazim, S.H., Wood, E.P., Martin, S.A., Hignett, S., Dennis, D.JC., (2018). Challenging dyke ascent models using novel laboratory experiments: Implications for reinterpreting evidence of magma ascent and volcanism, J. Volcanol. Geotherm. Res., 354, 87-101.

Kokkalas, S., Aydin, A., (2013). Is there a link between faulting and magmatism in the south-central Aegean Sea? Cambridge University Press, Geol. Mag. 150, 193–224.

Konstantinou, K.I., Kalogeras, I.S., Melis, N.S., Kourouzidis, M.C., Stavrakakis, G.N., (2006). The 8 January 2006 Earthquake (Mw 6.7) Offshore Kythira Island, Southern Greece: Seismological, Strong-motion, and Macroseismic Observations of an Intermediate-depth Event Seismological Research Letters 77, 544-553

Lawn, B.R., (1983). J. Am. Ceram. Soc. 66, 83-91

Le Corvec, N., Menand, T., Lindsay, J., (2013). Interaction of ascending magma with pre-existing crustal fractures in monogenetic basaltic volcanism: an experimental approach. J. Geophys. Res.-Solid Earth 118, 3041 968–984.

Le Pichon, X., Angelier, J., (1979). The Hellenic arc and trench system: A key to the neotectonic evolution of the eastern Mediterranean area. Tectonophysics, 60, 1-42

Lucchi, F., Santo, A.P., Tranne, C.A., Peccerillo, A., Keller, J., (2013). Volcanism, magmatism, volcano-tectonics and sea-level fluctuations in the geological history of Filicudi (western Aeolian archipelago). In: Lucchi, F., Peccerillo, A., Keller, J., Tranne, C. A. & Rossi, P. L. (eds)., The Aeolian Islands Volcanoes. Geological Society, London, Memoirs, 37, 113-153.

Maccaferri, F., Bonafede, M., Rivalta, E., (2010). A numerical model of dyke propagation in layered elastic media. Geophys. J. Int. 180, 1107–1123

Maccaferri, F., Bonafede, M., Rivalta, E., (2011). A quantitative study of the mechanisms governing dyke propagation, dyke arrest and sill formation. J. Volcanol. Geotherm. Res. 208, 39–50

McKenzie D.P., (1972). Active tectonics of the Mediterranean Region Geophys. J.R. astr. Soc. , 30, 109.

Menand, T., Daniels, K. A., Benghiat, P. (2010). Dyke propagation and sill formation in a compressive tectonic environment, J. Geophys. Res., 115, B08201

Mountrakis, D., Pavlides, S., Chatzipetros, A., Meletlidis, S., Tranos, M., Vougioukalakis, G., & Kilias, A., (1998). Active deformation of Santorini. In: Proceedings of the 2nd Workshop on European Laboratory Volcanoes, Santorini (Casale, R., Fytikas, M., Sigvaldasson, G., Vougioukalakis, G., Eds), 13-22.

Newman A. V., Stiros S., Feng L., Psimoulis P., Moschas F., Saltogianni V., Jiang Y., Papazachos C., Panagiotopoulos D., and Karagianni E. (2012), Recent geodetic unrest at Santorini Caldera, Greece, Geophys. Res. Lett., 39

Nocquet, J.-M., (2012). Present-Day Kinematics of the Mediterranean a Comprehensive Overview of GPS Results. Tectonophysics, 579, 220-24

Nomikou, P., Hübscher, C., Ruhnau, M., and Bejelou, K. (2016). Tectonophysics Tectono-stratigraphic evolution through successive extensional events of the Anydros Basin, hosting Kolumbo volcanic field at the Aegean. Tectonophysics 671, 202–217

Papanikolaou, D., Lykousis, V., Chrinis, G., Pavlakis, P., (1988). A comparative study of neotectonic basins across the Hellenic arc: the Messiniakos, Argolikos, Saronikos and southern Evoikos gulfs, Basin Res., 1, 167-176

Papazachos, B.C., Panagiotopoulos, D.G., (1993). Normal faults associated with volcanic activity and deep rupture zones in the southern Aegean volcanic arc. Tectonophysics 220, 301–308.

Parks, M.M., Biggs, J., England, P., Mather, T.A., Nomikou, P., Palamartchouk, K., Papanikolaou, X., Paradissis, D., Parsons, B., Pyle D.M., (2012). Evolution of Santorini Volcano dominated by episodic and rapid fluxes of melt from depth, Nat. Geosci., 5, 749– 754.

Pe-Piper, G., Piper, D.J.W., Perissoratis, C., (2005). Neotectonics and the Kos Plateau Tuff eruption of 161 ka, South Aegean arc Mar. Geol., 139, 315-338

Perissoratis, C., (1995). The Santorini volcanic complex and its relation to the stratigraphy and structure of the Aegean arc, Greece Mar. Geol., 128, 37-58

Piper, D.J.W., Perissoratis, C., (2003). Quaternary neotectonics of the South Aegean arc Mar. Geol., 198, 259-288

Piper, D.J.W., Pe-Piper, G., Perissoratis, C., Anastasakis, G., (2007). Distribution and chronology of submarine volcanic rocks around Santorini and their relationship to faulting, 291, Geological Society, London, 99-111

Rivalta, E., Bottinger, M. and Dahm, T., (2005). Gelatine experiments on dyke ascent in layered media, J. Volc. Geotherm. Res., 144, 273–285.

Roberts, S. & Jackson, J.A., (1991). Active normal faulting in Central Greece: an overview. In: Roberts, A.M., Yielding, G. & Freeman, B. (eds) The Geometry of Normal Faults. Geological Society, London, Special Publications, 56, 125–142

Rossetti, F., Storti, F. and Salvini, F., (2000). Cenozoic noncoaxial transtension along the western shoulder of the Ross Sea, Antarctica, and the emplacement of Mc Murdo dyke arrays. Terra Nova, 12, 60–66

Royden, L. (1993). The tectonic expression of slab pull at continental convergent boundaries. Tectonics 12, 303–25.

Sibson, R.H ., (1977). Fault rocks and fault mechanisms. Geological Society of London Journal, 133 p. 191-231.

Sielfeld, G., Ruz, J., Brogi, A., Cembrano, J., Stanton-Yonge, A., Pérez-Flores, P. and Iturrieta, P., (2019). Oblique-slip tectonics in an active volcanic chain: A case study from the Southern Andes. Tectonophysics, 770, 228221.

Spacapan, J.B., Galland, O., Leanza, H.A., Planke, S., (2016). Control of strike-slip fault on dyke emplacement and morphology. Journal of the Geological Society, 173, 573–576

Spakman, W., Wortel, M.J.R., Vlaar, N.J., (1988). The Hellenic subduction zone: a tomographic image and its geodynamic implications Geophys. Res. Lett. 15, 60-63

Taymaz, T., Jackson, J., McKenzie, D., (1991). Active tectonics of the north and central Aegean Sea, Geophysical Journal International, 106, 433-490

Taymaz, T., Yilmaz, Y. & Dilek, Y., (2007). The Geodynamics of the Aegean and Anatolia. Geological Society, London, Special Publications, 291, 1–16.

Ten Veen, J.H., Meijer, P.Th., (1998). Late Miocene to Recent tectonic evolution of Crete (Greece): geological observations and model analysis. Tectonophysics 298, 191–208

Tibaldi, A., (1992). The role of transcurrent intra-arc tectonics in the configuration of a volcanic arc. Terra Nova, 4, 567–577

Tibaldi, A., (2008). Contractional tectonics and magma paths in volcanoes. Journal of Volcanology and Geothermal Research, 176, 291-301.

Tibaldi, A. (2015). Structure of volcano plumbing systems: a review of multi-parametric effects. J. Volcanol. Geotherm. Res. 298, 85–135

Tzanis , A., Chailas, S., Sakkas, V., Lagios, E., (2020). Tectonic deformation in the Santorini volcanic complex (Greece) as inferred by joint analysis of gravity, magnetotelluric and DGPS observations, Geophys. J. Int. 220, 461–489

van Hinsbergen D.J.J., Meulenkamp J.E., (2006). Neogene supradetachment basin development on Crete (Greece) during exhumation of the South Aegean core complex, Basin Research, 18, 103-124

van Wyk de Vries, B., Merle, O., (1998). Extension induced by volcanic loading in regional strike-slip zones, Geology, 26, 983

Vitale, S., Isaia, R., (2014). Int J Earth Sci (Geol Rundsch) 103, 801

Wang L.P and Xu R., (2006). Dynamic interfacial debonding initiation induced by an incident crack International Journal of Solids and Structures, 43, 6535-6550

Xu.R., Huang Y.Y., Rosakis A.J., (2003). Dynamic Crack Deflection and Penetration at Interfaces in Homogeneous Materials: Experimental Studies and Model Predictions Journal of the Mechanics and Physics of Solids 51, 461-486

Chapter 6

Manuscript in preparation for journal submission

Geological and volcanotectonic evolution of the Santorini dyke swarm, Greece

Statement of contribution:

Collection of primary field data and geological mapping done by KD with help from AR

All field photographs and figures designed by KD

Complete 1st draft of manuscript and figures by KD

Revisions and subsequent drafts made with all co-authors input

Interpretation of field and laboratory data along with final model conducted by KD with support from all co-authors

Geological and Volcanotectonic evolution of the Santorini dyke swarm, Greece

Kyriaki Drymoni[*a], Alison Rust[b], Katharine Cashman[b], John Browning[c] ,Agust Gudmundsson[a]

[a] Department of Earth Sciences, Royal Holloway University of London, Egham, TW20 0EX, UK

[b] School of Earth Sciences, University of Bristol, Wills Memorial Building, Queens Road, Bristol BS8 1RJ, UK

[c] Department of Mining Engineering and Department of Structural and Geotechnical Engineering, Pontificia Universidad Católica de Chile, Santiago, Chile

* Corresponding author

E-mail address: Kyriaki.Drymoni.2015@live.rhul.ac.uk

Abstract

Field studies of eroded dyke swarms can give insights into the volcanotectonic history of a volcano's activity through time. They unravel the conditions of magma dynamics, the structure of the plumbing system, the emplacement and can potentially help us understand why magma either stalls in the crust or feeds a volcanic eruption. We perform multidisciplinary studies on a dyke swarm at Santorini volcano. In detail, we combined structural, petrological and geochemical

analysis both on the dykes and the host rock. Multiple caldera collapse events exposed the regional dyke swarm of approximately 99 dyke segments that lie along the circumferential caldera fault. We produced maps of the exposed dyke swarm, showing their structural correlations (location, strike, thickness), petrogenesis (composition). We grouped them into populations that fed the deposits that formed the stratigraphy of the northern caldera wall: the Peristeria stratovolcano (530-430 ka), the Simandiri shield (172 ka), the Cinder cones (125-80 ka), the Skaros shield (70-54 ka) and the Therasia dome complex (48-24 ka). We present a reconstruction of the dyke subswarms emplacement through time. Our study unravels that the Santorini dyke swarm is composed of smaller radial dyke swarms that emplaced on the caldera wall and exposed after the multiple caldera collapses

1. Introduction

Magma generation, storage and propagation through the Earth's crust are some of the most enigmatic natural processes. Numerous studies since the 20th century have tried to unravel the mysteries of magmatic fractionation, the way that magma advances to feed volcanic eruptions and the parameters that affect their behaviour and frequency (Daly, 1911; Anderson, 1984; Yoder and Tilley, 1962; Williams and Mc Birney, 1979). From the pillars of modern petrology such as the paradigms of the magma chamber and magma mush (Sinton and Detrick, 1992; Yoder, 1976; Marsh, 1996; Lipman and Bachmann, 2015; Putirka, 2017; Sparks et al., 2019) to ideas on transcrustal volcanic plumbing systems (Sinton and Detrick, 1992; Cashman et al., 2018), scientists

have focused their research on active volcanic plumbing systems which eventually became their physical laboratories.

From a volcanotectonic framework, not all triggering events that take place result in a successful volcanic eruption. Historical data on volcanic unrest (Newhall and Dzurisin, 1988; Sturkell, 2006), as well as qualitative studies on dyke propagation paths (Chapter 4), indicate that more than the 50% of dyking events feed volcanic eruptions a result that can be reported only retrospectively. However, much as 30% of dykes are arrested before reaching the surface. So, by studying only the eruptive volcanic products, we are decoding a portion of the processes that took place in a plumbing system and restricted to the successful triggering episodes but not any unrest episodes (e.g. 2011-12 unrest episode on Santorini volcano).

Here we focus on the Santorini stratovolcano, Greece, which hosts a complex volcanic plumbing system. It produced a lot of volcanic eruptions with the famous crescendo of the Minoan eruption followed by a caldera collapse event that almost vanished the island from the map and destroyed the Cycladic civilization during its dominion (Druitt et al., 1999). Previous studies have described the timescales, the pre-eruptive This paper emphasises the importance of multidisciplinary dyke swarm studies in unravelling the volcanotectonic evolution of a dynamic plumbing system. We study the dykes by combining their structural data (strike, thickness) or derived data (overpressure) with their petrogenesis (composition, amount of fractionation, origin) to investigate the dyke-fed magmatism on the northern caldera wall and reconstruct the evolution of it. This research allows us to identify the active stress field, during dyke emplacement at Santorini and other volcanoes, which control their structure as well as record the parameters that prevent dykes to feed volcanic eruptions.

1.1 The architecture of a dyke swarm

A dyke swarm consists of a set of dykes (magma-driven extension (mode I) fractures) that originate from a magma chamber, propagate up into the crust and often feed volcanic eruptions (Gudmundsson, 1987, 2006, 2012; Tibaldi, 2015). The size and structure of a dyke swarm are highly dependent on the geotectonic environment and the active stress field (regional tectonics) during emplacement. In monogenetic volcanoes, rifts and MORB environments, the volcanic plumbing system consists of a single deep mantle reservoir from which dykes are originating and propagate to the surface (Gudmundsson et al., 1999, 2006, 2012). The dykes mostly propagate parallel to σ1 hence vertical in a rift zone (Fig. 6.1A).

In composite (or central) volcanoes, the structure of the volcanic plumbing systems and hence the architecture of their interconnections with the storage regions differ drastically. This is due to the presence of several magma chambers (or reservoirs) and the tendency for a broader range of compositions of magmas and a broader range of eruption styles. For example, the presence of a magma chamber atop a reservoir can generate locally compressional forces which produce a radial dyke swarm fan. Although the dykes still propagate parallel to σ1, the chamber rotates the stress field, and as a result, the dyke swarm consists of inclined sheets at the margins and sub-vertical dykes in the centre (Gudmundsson, 2011; Tibaldi, 2015) (Fig. 6.1B). For that reason, it is essential when studying such a volcanic plumbing system to consider not only the petrological and geochemical evolution of the system but also the mechanical and tectonic framework.

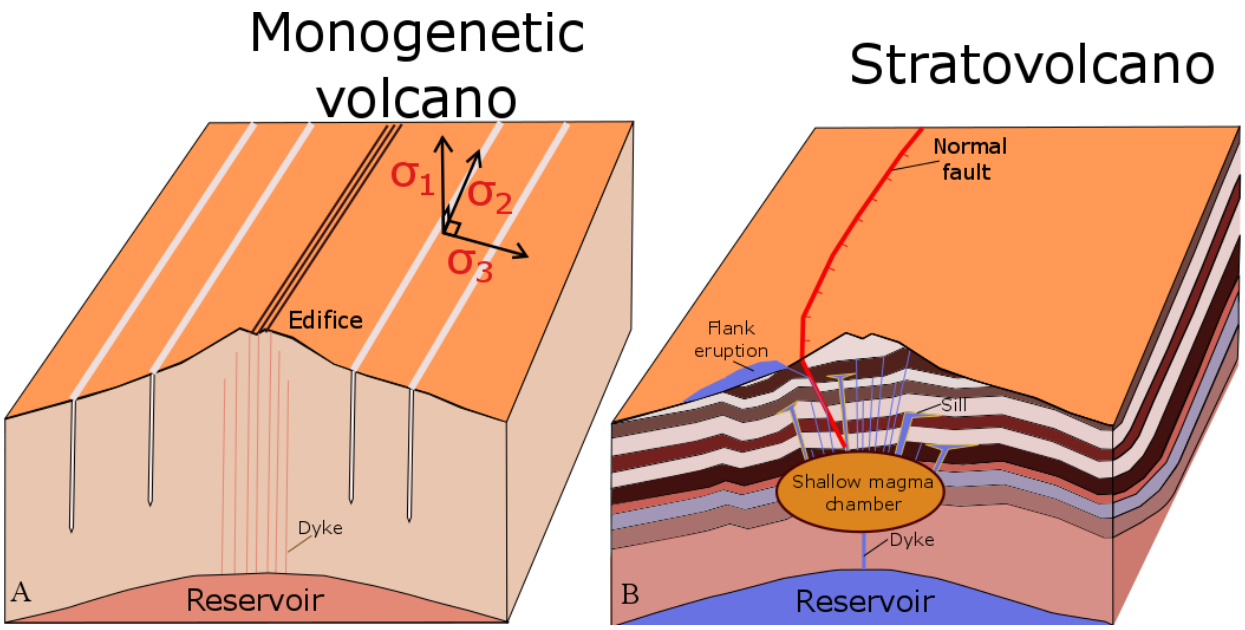

Fig. 6.1: The structure of magmatic and volcanic plumbing systems and their dyke swarm architecture: (A) in monogenetic volcanoes and (B) in stratovolcanoes.

2. Geological setting

The northern caldera wall dyke swarm comprises a group of magma fractures that were emplaced on a very heterogeneous host rock (lava flows, pyroclastic deposits and scoria) on Santorini island, Greece. The latter expresses the southernmost extent of the South Aegean volcanic arc (Jolivet et al., 2013). Its magmatic activity is associated with the subduction and rollback of the African plate beneath the Eurasian one (Le Pichon and Angelier, 1979). The dyke fed volcanism initiated in late Pleistocene, continued during Quaternary and remains active (Piper and Perissoratis, 2003; Pe-Piper and Piper 2005). Santorini's plumbing system is described as an open volcanic system which evolved through time by forming twelve Plinian eruptions. The latter were interrupted by

Interplinian effusive and explosive activities, domes (Therasia dome complex 39-25 ka), shields (Simandiri 172 ka, Skaros 67-54 ka), lava edifices (Peristeria stratocone, 530-430 ka), and atleast four caldera collapse events (Druitt and Francaviglia, 1992; Druitt et al., 1999) which shaped the current morphology of the island.

The eruptive vents of the aforementioned volcanic activities outline two volcanotectonic lines the Kameni line and the Kolumbo line. They both permeate the central and northern part of the island, respectively and control magma ascent according to previous authors (Druitt et al., 1999; Rizzo et al., 2016). Offshore oceanographic studies (Nomikou et al., 2013; Hooft et al., 2017) have also revealed an active rift zone that strikes approximately N30˚-50˚E, associated with the Kolumbo submarine volcanic activity (1650 BC). Its extrapolation permeates the northern part of the island, and it is also proposed to control the actual magmatic activity of the area (Fig. 6.2B).

Detailed geological mapping (Chapters 3, 4) have exposed at least 91 dykes on the northern part of the caldera wall and has established a comprehensive structural study indicating the strike populations, their structural characteristics (attitude, thickness) as well as their propagation paths (Fig.6.2A). The dyke swarm is emplaced on the remnants of Peristeria volcano (530-430ka), the Simandiri shield, the Kokkino and Megalo Vouno (andesitic and basaltic) cinder cones (76-54ka) covered by the Skaros shield (67-54 ka) at the northern caldera wall and by the Skaros lavas and Therasia dome complex deposits (39-25ka) at its western border (Fig. 6.2 B,2-5). The dyke swarm was thought to be limited to the northern and western part of the island. However, complementary field studies at the southern caldera wall next to cape Balos revealed a dyke segment as well (Fig. 6.2B, 1).

Geochemical studies (Nicholls et al., 1971; Mann, 1983; Huijsmans, 1985; Bailey et al., 2009) determined the composition of some of the studied dykes, which range from basaltic to trachydacitic. Their trace and REE element analysis (Bailey et al., 2009) showed that the dykes are separated into three series in terms of their Nb and K_2O concentrations which define fractional crystallisation and island arc basalt signatures distributed into the three groups.

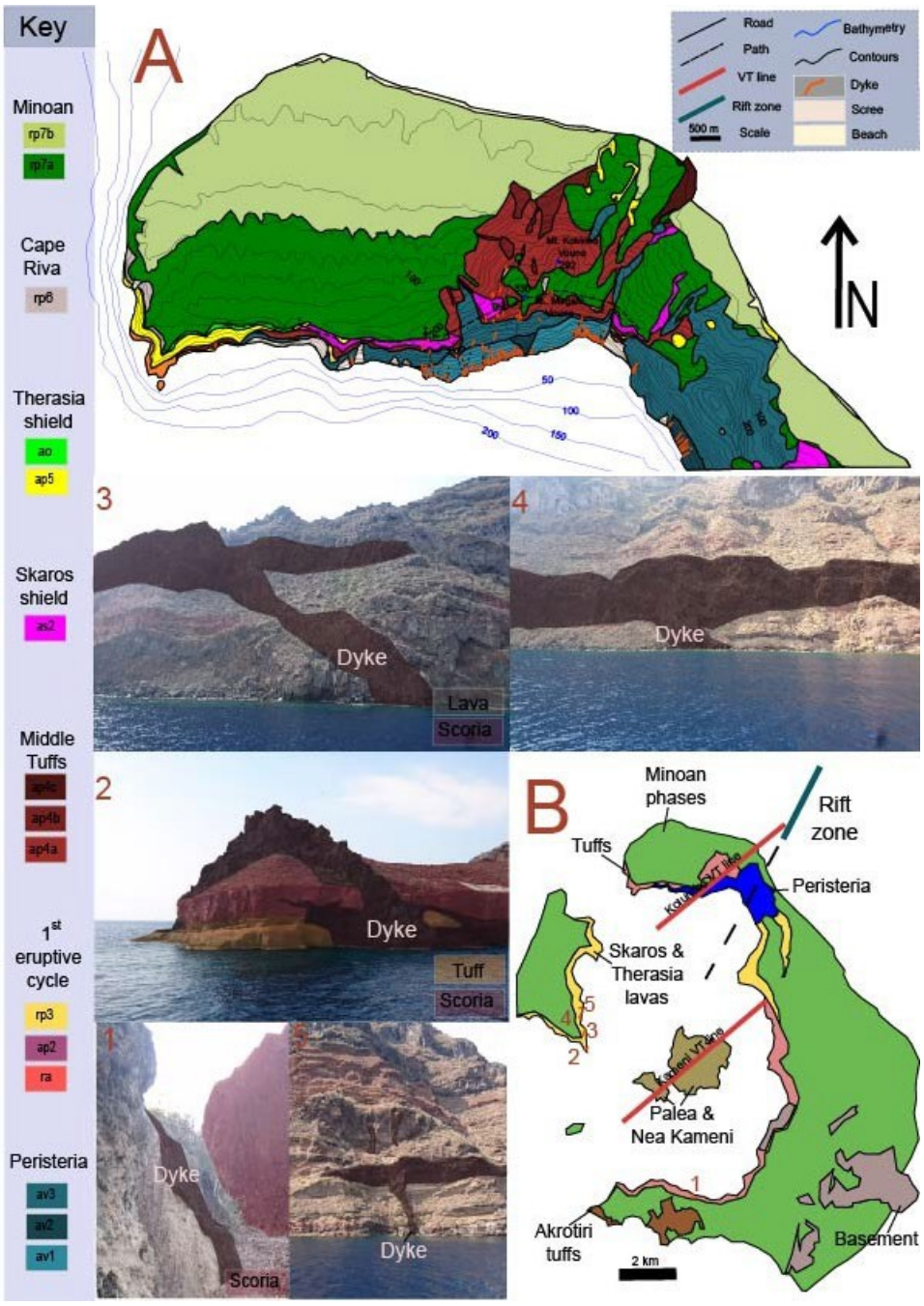

Fig. 6.2: (A) Modified geological map from Druitt et al. (1999) showing the structure of the northern caldera wall dyke swarm and the stratigraphy of the host rock. (B) Modified geological map from Druitt et al. (1999) showing the volcanotectonic lineaments that partly control magma

ascent in the island and the location of the dykes at the western and southern part of the island (1-5).

2.1 Host rock geology

Santorini is almost totally formed of volcanic products which atop 1) a sedimentary massif at the central and eastern part of the island (Profitis Ilias and Mesa Vouno) and 2) a metamorphic basement composed of schists and phyllites which crops out in the south-eastern part of Thera and on the caldera wall near Athinios port (Davis and Bastas, 1978). The latter is displayed as a Cycladic metamorphism trace (Skarpelis and Liati, 1990).

The island of Therasia and the northern part of the Santorini island are composed principally of pyroclastic products of Simandiri, Skaros and Therasia shields and an old composite stratocone (Peristeria volcano) (Druitt et al., 1999). For this study, as the dyke swarm is mainly exposed on the Northern caldera wall and the Therasia cliffs, we focused on sequence of lavas that formed the present-day stratigraphy in the northern and western part of the island. The latter are described below. (Fig. 6.3):

1) Peristeria volcano (av1-av3) (530-430 ka): The summit of this volcano is hypothesised to have been located somewhere on what is now a collapsed basin at the northern caldera wall, next to the Mikros Profitis Ilias mountain and reached a peak of 350 m above sea level (Druitt et

al., 1999). The lava compositions are from basaltic to dacitic (Nicholls, 1971, Mann, 1983; Huijsmans, 1985, Druitt et al., 1999; Bailey et al., 2009) (Fig. 6.3A).

2) Cape Simandiri (as) (172 ka): The lava shield covered the pre-existing flows and especially the Lower Pumice 2 eruption on the northern part of Santorini. Due to the composite collapse events, we observe only part of this shield at the base of Therasia Island. The compositions of the lavas are mainly andesitic (Druitt et al.,1999; Fabbro et al., 2013, 2014) (Fig. 6.3B).

3) Cinder cones of the northern caldera wall (ap4) (125-80 ka): The next event is the construction of the Megalo and Kokkino Vouno that occurred during an eruptive period focused in the southern part of the island and is called the Middle Tuff eruptions (Druitt et al., 1999). The eruption on the northern caldera wall formed a thick scoria deposit and a tuff ring (phreatomagmatic eruption) on the NE. Previous studies suggest that the cones formed simultaneously, and their compositions are andesitic (Druitt et al., 1999). The lavas are from basaltic to andesitic (Druitt et al., 1999 and this study) (Fig. 6.3C).

4) Skaros shield (ds1, as2, ap5) (70-54 ka) The Skaros shield was one of the gigantic shields as it had a basal diameter of 9 km which covered the island. The vent was estimated to have been approximately 1-2 km to the west of Skaros rock close to Imerovigli village. The culmination of this eruptive phase was the Upper scoria two (US2) deposit that covered the shield, and remnants

of which are found on both Skaros and Ammoudi in northern Thera. The composition of the Skaros shield is from basaltic to dacitic, and the upper scoria two (US2) deposit is purely andesitic (Druitt 1999; Fabbro et al., 2013, 2014) (Fig. 6.3D).

5) Therasia dome complex (rt, ao) (48-24ka). The Skaros shield was followed by the extrusion of a silicic magma that covered the western flank of the Skaros shield. The remnants of this eruptive phase were found on the cliffs of Therasia. The lavas are primarily silicic (dacitic) while intercalations of hybrid andesite (Fabbro et al., 2013) are also observed. Atop there are the Cape Riva lavas that extruded during the third caldera collapse episode and destroyed the Skaros-Therasia shields (Druitt et al., 1999; Fabbro et al., 2013, 2014) (Fig. 6.3E).

The Minoan phases covered all the previous activity on the island, and the composition of the lavas are sialic (rhyolitic). The dykes analysed so far (Bailey et al., 2009 and this study) were not found to have similarities with the Minoan lavas and they were not found to permeate Minoan phases in the field, so they are unlikely to have fed the Minoan eruptions. Finally, although the southern part is not studied here, a sample from the primitive Balos magma was analysed for magmatic comparisons with the rest of the data.

In the first part, we analyse the structure, petrology and geochemistry of the dykes and explain the methodology that was followed to reconstruct the evolution of the dyke swarm during the formation of each of the five shields-stratocones. In the second part, we combine all five phases and reconstruct the exposed dyke swarm that is emplaced in the study area (Fig. 6.3F).

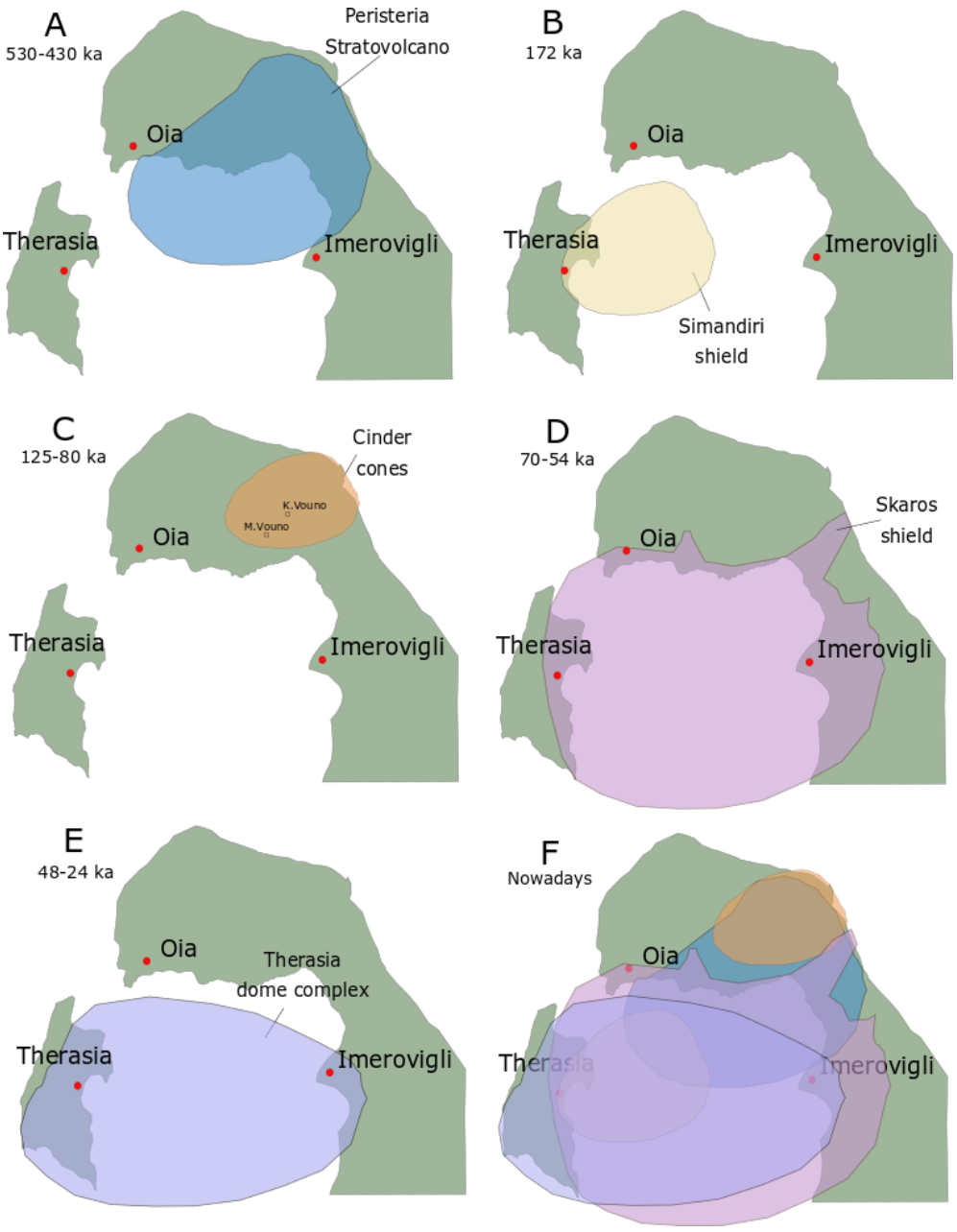

Fig. 6.3: Schematic extrapolated distribution of the volcanic products that belong to the five shields-stratocones studied here. The distribution is according to the geological map of Santorini from Druitt et al., (1999). (A) Peristeria stratovolcano, (B) Simandiri shield, (C) Cinder cones of Megalo and Kokkino Vouno, (D) Skaros shield, (E) Therasia dome complex, (F) Present day.

2.2 The Santorini dyke swarm(s)

We mapped out three localities around the caldera wall where part of the dyke swarm is exposed (Fig. 6.4). The main area belongs to the northern caldera wall from Oia village (west) to Mikros Profitis Ilias mountain (east) (Fig. 6.4A). We combined geochemical data from previous authors (Nicholls, 1971, Mann, 1983; Huijsmans, 1985, Druitt et al., 1999; Zellmer, 2000, Petersen, 2004; Bailey et al., 2009; Fabbro et al., 2013, 2014) and new data, covering a dataset with forty-five (45) of the ninety-one (91) mapped dyke segments (Fig. 6.5) The segmented dykes are from basalts to trachydacites. No physical connection between dykes and associated volcanic deposits was observed in the northern caldera wall area.

We also mapped out seven dykes at the Therasia caldera wall, of which four were observed to have fed lava flows (Fig. 6.4B) and thus allowed us to collect data on their geochemical composition which is from basaltic andesites to trachydacites (Figs. 6.2, B2-5 and 5). One of them was already suggested to have fed a dacitic lava flow (Fabbro et al. 2013) which has been dated with Ar-Ar dating techniques at 33 ka years (Fabbro et al. 2014). The eruption belongs to the construction of the Therasia dome complex that was interrupted by the Cape Riva eruption and the third caldera collapse event at 21 ka (Druitt et al., 1999). The other three feeder dykes have also fed lavas from the Skaros shield (ds1) and the Therasia dome complex (Rt).

Field studies at the third locality (Fig. 6.4C) revealed an approximately N-S to NNE-SSW dyke emplaced near Cape Balos. We obtained structural data, but it was not possible to retrieve a sample. More dykes were observed on the caldera cliffs but were not found in situ as the area was locally collapsed.

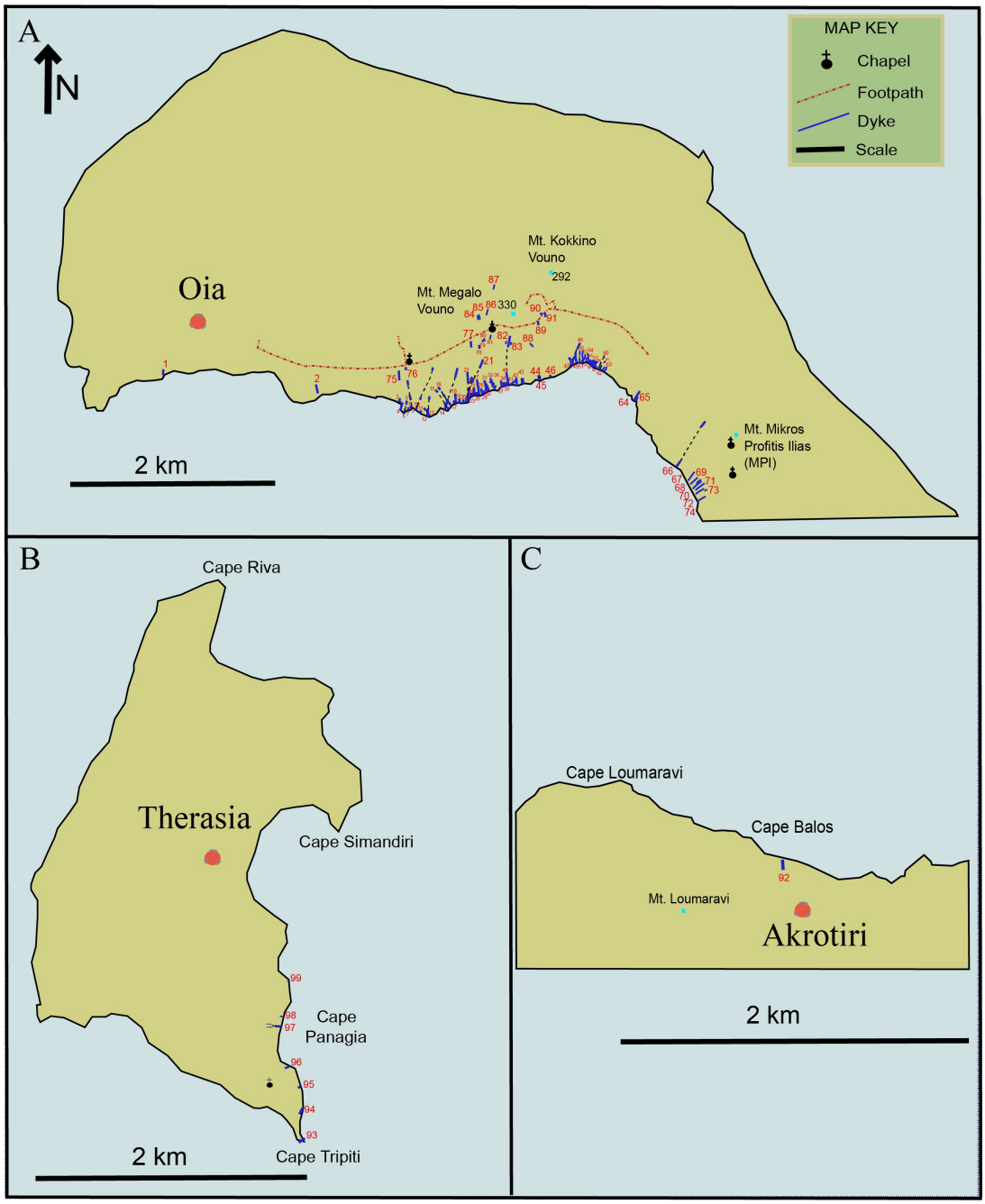

Fig. 6.4: Location of the dykes observed on the Santorini caldera walls. Localities: (A) Northern caldera wall, (B) Therasia caldera wall, (C) Akrotiri caldera wall.

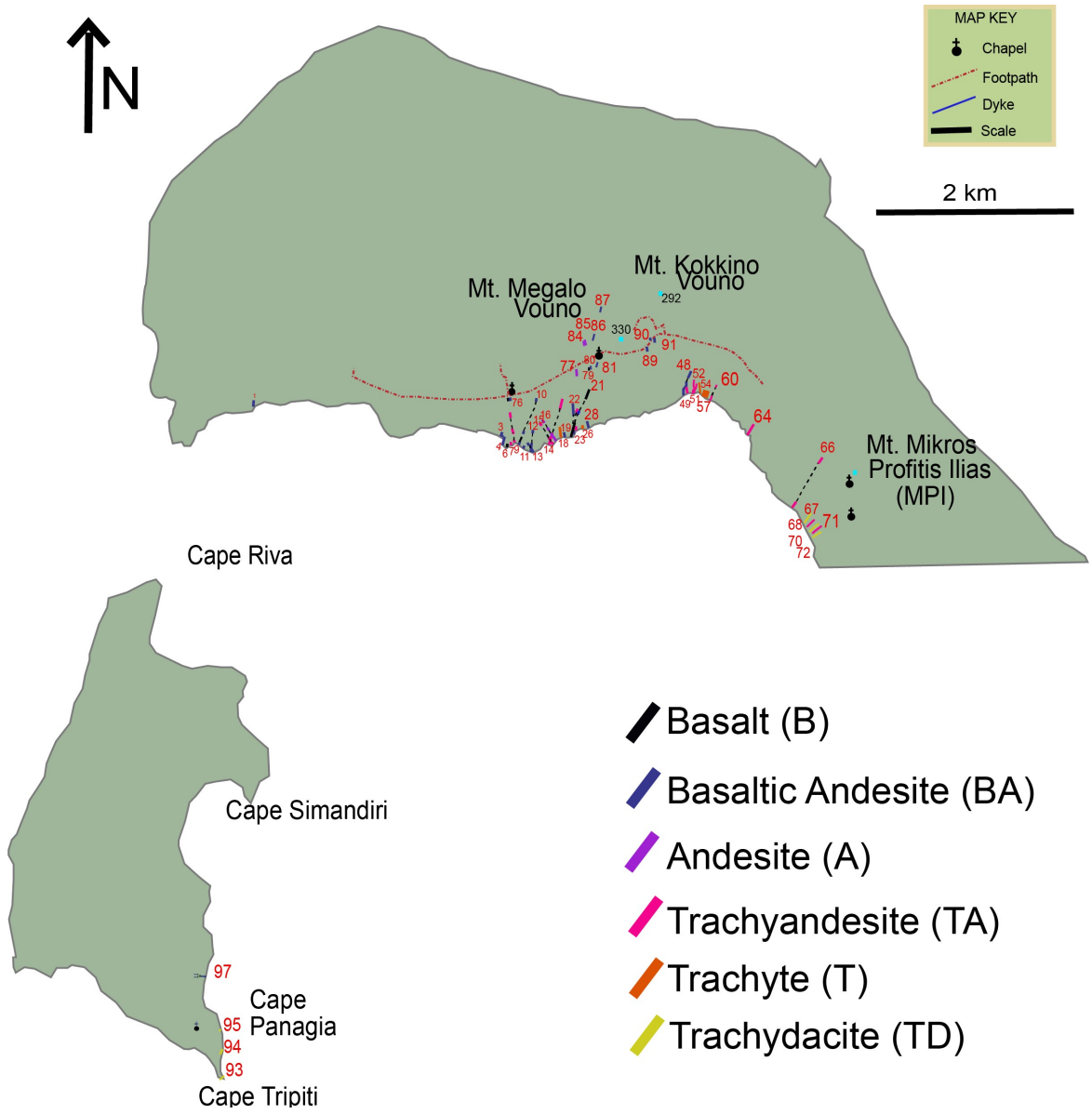

Fig. 6.5: Map showing the geochemical composition of the studied dykes at the northern caldera wall and the Therasia island.

3. Methods and materials

We completed a multidisciplinary study combining field geology (geological mapping, structural analysis) with laboratory methods (petrography, point-counting and XRF geochemical analysis) which are described in detail as follows.

Initially, we completed several campaigns and mapped out the dykes observed on the Northern caldera wall, the Therasia wall, the Akrotiri area (Cape Balos) and their host rock lithologies (Fig. 6.4). We designed a detailed dataset of the total 99 dyke segments found on the circumferential caldera cliff with specific information on their location (long/lat), attitude, thickness as well as their physical characteristics (chilled margins, scoria rims, flow indicators, vesicularity, xenoliths). That allowed us to identify different dyke populations which share similar paths or emplacement mechanisms (e.g. propagated, arrested, deflected dykes) and geometries (e.g. thinned-out, blunt, fingers) and can record different triggering events. Their thickness allowed us also to calculate the overpressure range that characterised every diverse population.

We collected seventy (70) samples of dyke cores and rims, chilled margins, host rock specimens and scoria samples through different geological campaigns. We performed a detailed petrographic analysis on all collected samples with a specific interest, including their mineralogical assemblage, textures and the type and number of xenoliths. The petrographic studies were conducted with a polarised optical microscope with a digital camera (NIKON Microphot FX-35A with a NIKON DS-5M camera system) at Royal Holloway University of London Optics Lab. We performed analyses using an electromechanical point-counting technique to establish the approximate composition of thirty-two (32) samples. The similar petrological characteristics between dykes and

subaerial deposits or scoria samples of the northern caldera wall complemented the structural dataset. They gave us more insights into the Santorini dyke fed volcanism.

We collected twenty-five dyke and host rock samples specifically for X-Ray fluorescence geochemical analysis (XRF). The latter was conducted on a 2010 PANalytical Axios XRF spectrometer at the laboratories of Royal Holloway, University of London. The data were combined with a large deposit and dyke dataset collected from previous studies (Nicholls, 1971, Mann, 1983; Huijsmans, 1985, Druitt et al., 1999; Zellmer, 2000, Petersen, 2004; Bailey et al., 2009; Fabbro et al., 2013, 2014). The following data were divided firstly into the five studied phases, and then we designed locality subsets to record the location of the possible dyke-fed correlations. In detail:

A. Peristeria volcano (530-430 ka): seventy-two (72) samples from the volcanic deposits from previous studies (Huijsmans, 1985, Bailey et al., 2009) were collected to study the geochemical signatures of this stratovolcano. The locality subsets included from the east to the west Mikros Profitis Ilias (MPI) (26 samples), K.Vouno (18 samples), M.Vouno (9 samples), Finikia (14 samples), Oia (5 samples).

B. Simandiri shield (172ka): Six (6) samples from previous studies (Bailey et al., 2009) were collected for this shield all of them located at Cape Simandiri.

C. Cinder cones of Northern caldera wall (125-80 ka): Seven (7) samples from a previous study (Bailey et al., 2009) and three (3) samples from this study. The locality subsets are M. Vouno (4 samples) and K.Vouno (6 samples).

D. Skaros shield (70-54 ka): Sixty-five (65) samples from the Skaros shield, from previous studies (Huijsmans, 1985, Bailey et al., 2009) and two (2) samples from this study will be used for the geochemical analysis of this shield. The locality subsets from the east to the west are Skaros (35 samples), M.Vouno (2 samples), Ammoudi (16 samples), Corfos Bay-Cape Tino (5 samples).

E. Therasia Dome Complex TDC (48-24 ka): Forty (40) samples of rhyodacites (Rt) from previous studies (Nicholls, 1971, Mann, 1983; Huijsmans, 1985, Druitt et al., 1999; Zellmer, 2000, Bailey et al., 2009; Fabbro et al., 2013, 2014, 2015) were collected. The locality subsets from the east to the west are Fira (1 sample), Ammoudi (1 sample), Milo Bay (1 sample), Therasia (32 samples). Also, six (6) samples from previous studies (Huijsmans, 1985, Zellmer, 2000, Bailey et al., 2009; Fabbro et al., 2013, 2014) were collected from the andesites of Oia.

Also, a sample from the Minoan ignimbrite was collected and analysed during this study along with a sample from Balos lavas to be both compared with the dataset.

Previous numerical models (Gudmundsson, 2006; Gudmundsson and Philipp, 2006) have shown that the minimum principal compressive stress (σ_3) decreases substantially with distance from the magma source. This situation dictates that dykes are likely to become arrested on their way to the surface. Eq. 1 calculates the magmatic overpressure (P_o) which is the driving pressure in excess of the normal stress on the fracture plane. The overpressure can be defined by the maximum dyke thickness (aperture) W of the dyke and its controlling dimension L through the equation (Gudmundsson, 2011) initially defined by Sneddon, (1946):

$$Po = \frac{W\,E}{2(1-v^2)L} \quad (6.1)$$

where P_o is the overpressure at the time of the dyke emplacement, E is the Young's modulus of the host rock and v is the Poisson's ratio of the host rock. A geometric feature, i.e. W/L (thickness/length), can define the static overpressure in the dyke, the ratio being typically between 10^{-2} to 10^{-5} (Delaney et al., 1986).

4. Dyke-fed parameters and correlations

Magma movement and solidification depends on many parameters including the overpressure, the temperature of the magma and its host rock, the mechanical properties of the host rock, its active stress field during emplacement, and the effusion rate of the magma (Rubin, 1995). Although dyke propagation is a polyparametric open system, through our study, we attempt to identify dyke-fed volcanism on the caldera wall by combining the studied dykes with available geochemical analysis of the caldera wall deposits. The actual challenge for our dyke-deposits correlations was to target and use for our reconstruction those parameters that are less or most sensitive to change during emplacement and can make themselves ideal for recording similarities between the emplaced dykes and the volcanic deposits that formed the heterogeneous caldera wall.

From a structural framework, the strike of a dyke in homogeneous crustal segments is a parameter that defines dyke emplacement which happened during the same event and can characterise a single

dyke swarm (Gudmundsson, 2003, 2011). Thus, it occurs as the stress field is always promoting propagation perpendicular to σ_3 (Anderson, 1951). In heterogeneous segments magma chambers alter the stress field around them, and as a result, the strike of the dykes cannot remain constant. Instead, one triggering event can form several inclined sheets with variable strikes which belong to the same population. However, in the case of an active volcanotectonic lineament present during the triggering event, the lineament can impose the same strike to the emplaced dykes as the pre-existing fractures only if it is energetically economical for them (Delaney, 1986; Gudmundsson, 2011). As a result, the strikes of the dykes that belong to the same population can reveal the conditions of the active stress field during emplacement. The thickness of a dyke is correlated with the magma overpressure and the mechanical properties of the host rock. Even if in a dyke population, we expect the dykes to have similar magmatic overpressures the same does not exist for their propagation paths. Hence, dyke thickness is not a parameter that could correlate dyke segments or dyke-deposits similarities with high certainty.

During dyke emplacement, magma solidifies in variable rates (slowly or rapidly) depending on the velocity of the advancing magma, the temperatures of the magma and its host rock, and the thickness of the dyke. If the magma is water-saturated, then there may also be decompression-induced crystallisation because as the melt loses water, the liquidus temperature increases. The rate of crystallisation is reflected in the textures (size, number and shape of crystals) in the crystallised magma; for example, if the margin of a dyke cooled much more quickly than its core it will be finer-grained. Dyke segments or dyke-deposit correlation should reflect a similar cooling rate and the studied thin sections should fossilise similar groundmass textures and crystal sizes.

From a geochemical perspective, the spider diagrams allow us to examine the melt variation between two solidified magmas and the amount of REE depletion or enrichment compared to normative rocks (e.g. N-MORB, chondrite, primitive mantle). Similar magmas like in dyke-fed volcanism shall have overlapped spider diagrams while synchronised events such as the triggering of a dyke population should reflect the same normalised anomalies. Those parameters were used to correlate dyke segments and dykes with the sampled deposits on the caldera wall.

4.1 Dyke path scenarios

We identified several dykes that belonged to the same dyke populations or are segments of the same dyke based on their location, thickness, attitude, petrographic and geochemical analysis. The results are reported below:

- Dyke_76 and Dyke_79

Both basaltic dykes were sampled close to the Megalo Vouno cinder cone at a similar altitude, strike approximately N-S and are 0.8-1m thick. The groundmass is brown with plag+cpx+opx+glass the mineral assemblage is Plag+cpx+opx+ol+op of similar sizes and their textures are both porphyritic and seriate. They both form glomerocrysts of plag+cpx+opx+ol and xenoliths of plag+opx+ol+cpx (Fig. 6.6A&B). Their spider diagrams overlap showing low large ion lithophile elements LILs (Rb, Ba, Cs, K), a negative Nb anomaly and positive P and Ti anomalies (Fig. 6.6C).

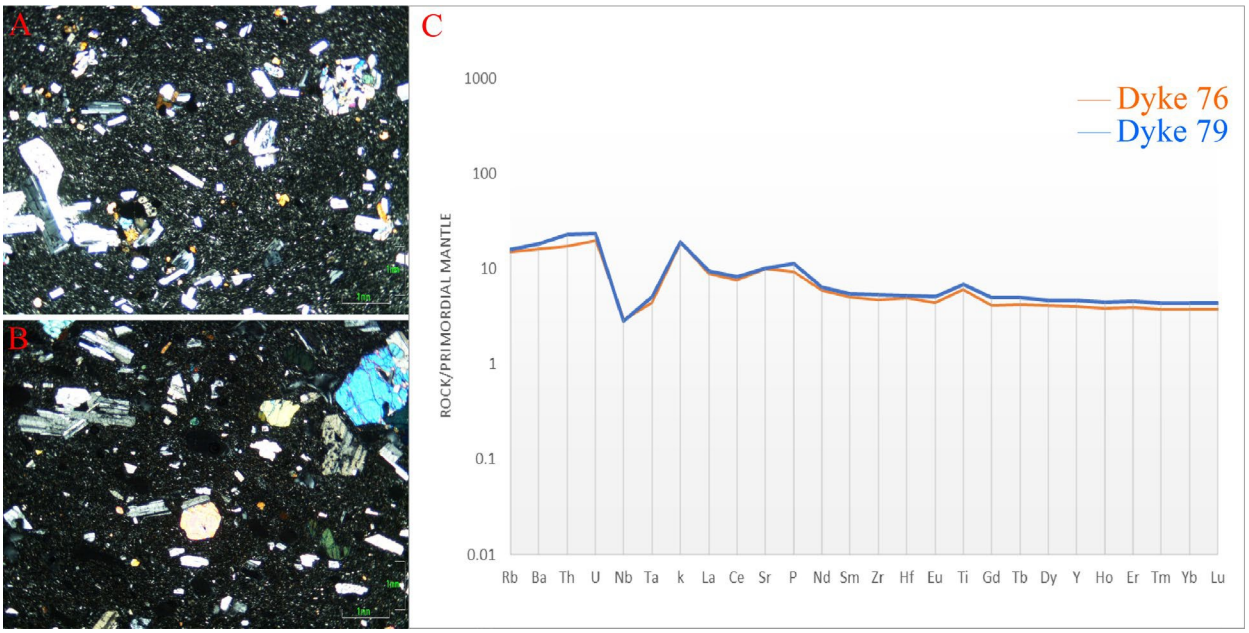

Fig. 6.6: (A) xpl photo of Dyke_76, (B) xpl photo of Dyke_79, (C) Normalised spider diagrams to primordial mantle of Dykes_76 & 79.

- Dyke_77, Dyke_84 and Dyke_85

All three dykes are andesites, and they are found on the Megalo Vouno cinder cone, they strike approximately N-S to NNE-SSW, and their thickness is 0.8-1.5m. We studied multiple thin sections from Dyke_77, but none from dykes 84 and 85 (Fig. 6.7). Their spider diagrams showed a complete overlap and the three dyke outcrops could be segments of the same dyke. The dykes chemically overlap with the Skaros lavas.

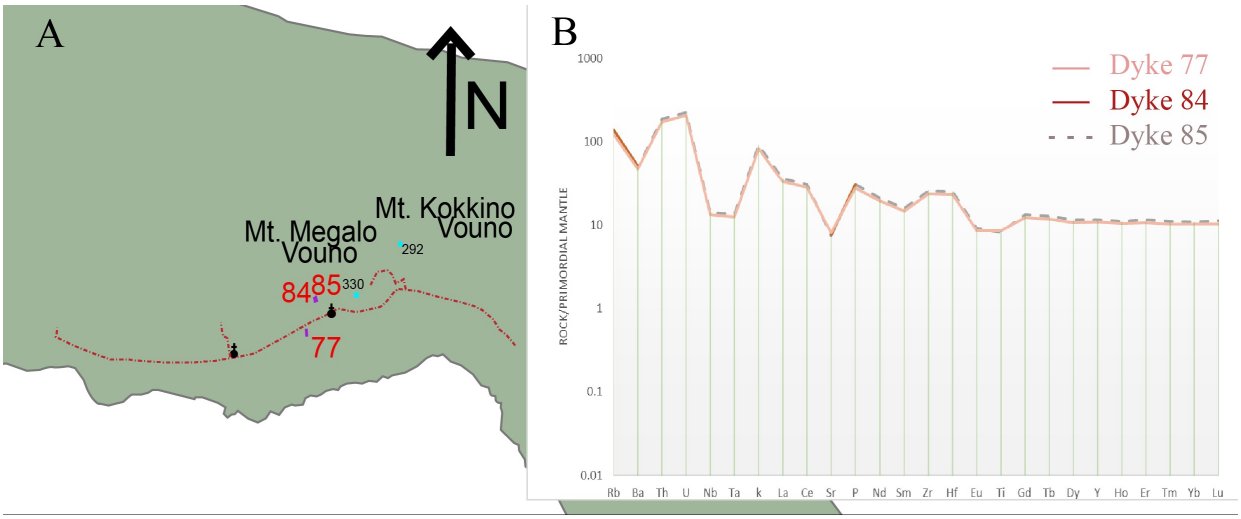

Fig. 6.7: (A) Location of dykes _77, _84 and _85, (B) Normalised spider diagrams to primordial mantle of Dykes_77, _84 & _85. Geochemical data of dykes_84 &_85 are from Bailey et al. 2009.

- Dyke_18, Dyke_26, and Dyke_54

Dykes_18, _26 and _54 are emplaced at the sea level of the Megalo and Kokkino Vouno. They strike NNE-SSW, and their thickness ranges from 1.2-6m. We correlated their spider diagrams, which showed a complete overlap between dykes_18 and _26, whereas dyke_54 is a bit more depleted (Fig. 6.8). Thin sections were not available to be studied; however, their structural and geochemical data indicate that dykes_18 and 26 belonged to the same population, which is localized at Megalo Vouno. Dyke_54 either belongs to the same event, but the dyke initiated from a different area of the magma chamber which was less depleted to LILs or belong to an earlier or later population that fed a deposit exposed on the Kokkino Vouno and brought to the surface similar magmas due to recycling. All dykes were found to have fed either the Peristeria lavas located at the MPI mountain or the Skaros lavas.

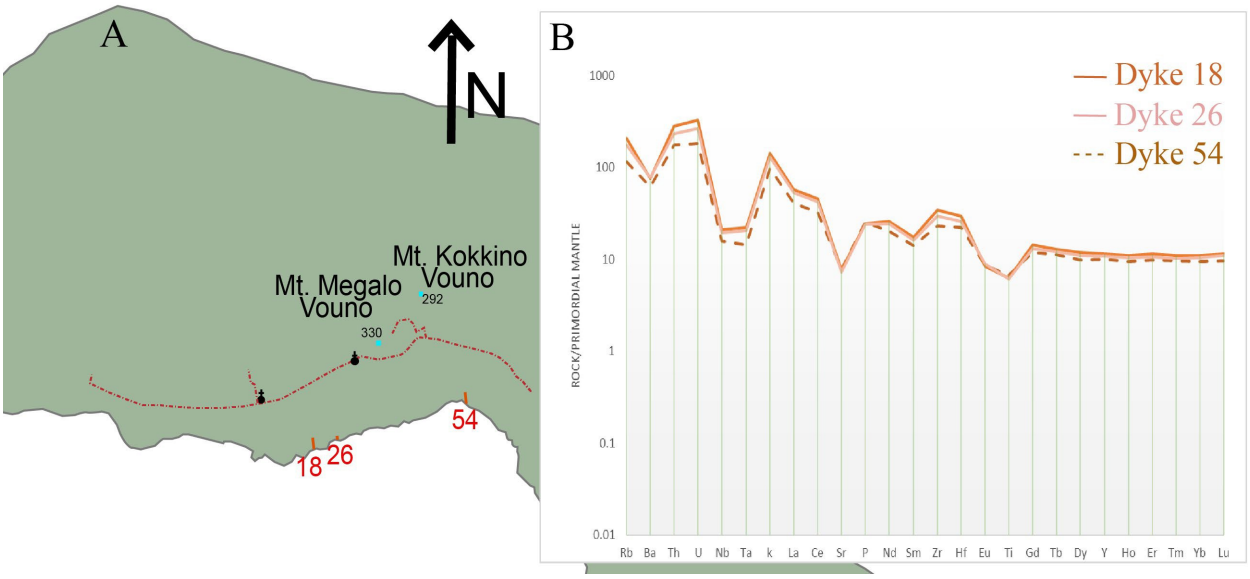

Fig. 6.8: (A) Location of dykes _18, _26 and _54, (B) Normalised spider diagrams to primordial mantle of Dykes _18, _26 and _54. Geochemical data of dykes_18, _26 & _54 are from Bailey et al. 2009.

4.2 Dyke-fed eruptions

We compared the thin sections of the dykes with those of the host rock wherever possible and the spider diagrams of both dykes and the host rock datasets. That allowed us to find possible correlations between the deposits and the emplaced dykes mapped on the caldera wall. The structural data in a later stage gave us the locality correlations and further insights on the active stress field during the dykes' emplacement.

The final reconstruction of the plumbing system is based on the two-magma chamber model that was introduced by Nicholls (1971) and was more recently suggested through experimental studies

(Druitt et al., 1999; Fabbro et al., 2013; Cadoux et al., 2014; Andujar et al., 2015, 2016). From a mechanical framework, a caldera collapse mechanism requires a shallow magma chamber and the simultaneous existence of a deep reservoir to feed magma from the depth and squeeze it to the surface (Gudmundsson, 2006, 2011). The results of the multidisciplinary study are reported in Table 1 at Appendix C3 along with the locality spider diagrams of the five shields-stratocones.

4.3 Arrested dykes

Indeed approximately 7% (6 from 91) of the dykes observed in this study appeared exclusively from field constraints to be arrested, and so never fed an eruption. As expected, the geochemical fingerprints of these dykes did not overlap with the geochemical fingerprint of any stratigraphic horizon analysed. Dykes_87 and 89 which were emplaced into the scoria layers produced by the cinder cones were compared with 205 spider diagrams. Still, no correlations were found with any other dykes or the scoria samples.

We also studied several thin sections from dyke_89, but no similarities were found with the other dyke petrographic analysis. In specific, the petrographic analysis revealed a very fine groundmass, < 10% phenocrysts and no vesicularity. The plagioclase crystals were monotonous without signs of magma mixing (resorbed cores) or zoning and sieve textures. That could be due to the magma following a fast cooling path initiated by a very shallow magma chamber (probably a sill) which was relatively young (hot) and hence there had not been time for many phenocrysts were crystallised and glomerocrysts to form. The shallow magma chamber could have formed due to the heterogeneous crust, which can easily produce stress barriers and generate short-lived sills if

the magma flux (volume or pressure) is not enough to maintain high magma temperatures. As such, this dyke could reflect an arrested event that resulted purely from magma chamber conditions and not due to mechanical heterogeneity where the dyke was emplaced. Alternatively, it could have been recharged quickly from a great depth and subsequently solidified fast on the surface. This scenario was rejected as its spiderdiagram showed enrichment to crustal elements.

The multidisciplinary study can also identify a few dykes that although belonged to a population (geochemical similarities with some localities) they never fed a volcanic eruption as found by their structural or petrographic study. From a structural framework, an arrested dyke is rarely observed. Still, it mostly thins out at contacts of layers of dissimilar mechanical layers and primarily when a dyke propagates from a soft (e.g. pyroclastic) to a stiff (e.g. lava) layer. Such an observation was made on dyke_11, where the tip was gradually thinning out at the contact between pyroclastic and a lava layer (Chapter 4). So, although the dyke geochemically belonged to the Peristeria or Skaros shield, it never made it to the surface and became an arrested dyke.

In other case studies, although the structural data cannot confirm a visual arrest, the geochemical and petrographic study can target it. As such dyke_4 & dyke_6 were both emplaced on the northern caldera wall, and their segments did not structurally reflect an arrest. Dyke_4 was observed to penetrate the Peristeria stratigraphy as seen from the sea level, while Dyke_6 deflects into a sill (Chapter 7). Dyke_4 belongs to the Peristeria dyke swarm while Dyke_6 has similarities with the Skaros dyke swarm. However, both their spider diagrams and petrography reflect unique magmatic signatures and they probably both were dykes that although triggered simultaneously with other dykes they finally got arrested to the surface. That could have happened either due to mechanical heterogeneity because we could not observe their continuation on the caldera wall or probably due

to changes that occurred in the magma chamber (e.g. lower overpressure or magma supply). Finally, other parameters that could not be identified but could cause insufficient correlations could be eroded eruption products that have not been analysed or deposits that have not been sampled and studied so far.

5. Reconstruction of the dyke swarm

The previous methodology allowed us to categorise the dykes into populations or triggering events and interpret their fossilised information. In the next stage, we combined the collected data and reconstructed the dyke swarm through time.

5.1 The Peristeria dyke subswarm

Twenty-five (25) dykes were found to correlate geochemically with the Peristeria stratigraphy. From the five (5) localities tested only three (M.Vouno, K.Vouno and MPI) were found to have similarities with the Peristeria activity. Eight (8) dykes overlapped with the M.Vouno lavas, seven (7) dykes with the K.Vouno lavas and ten (10) with the MPI lavas. Their details are reported in Table 6.1, and an extrapolation of the Peristeria dyke swarm, including their location and chemical composition, is shown in Figure 6.9.

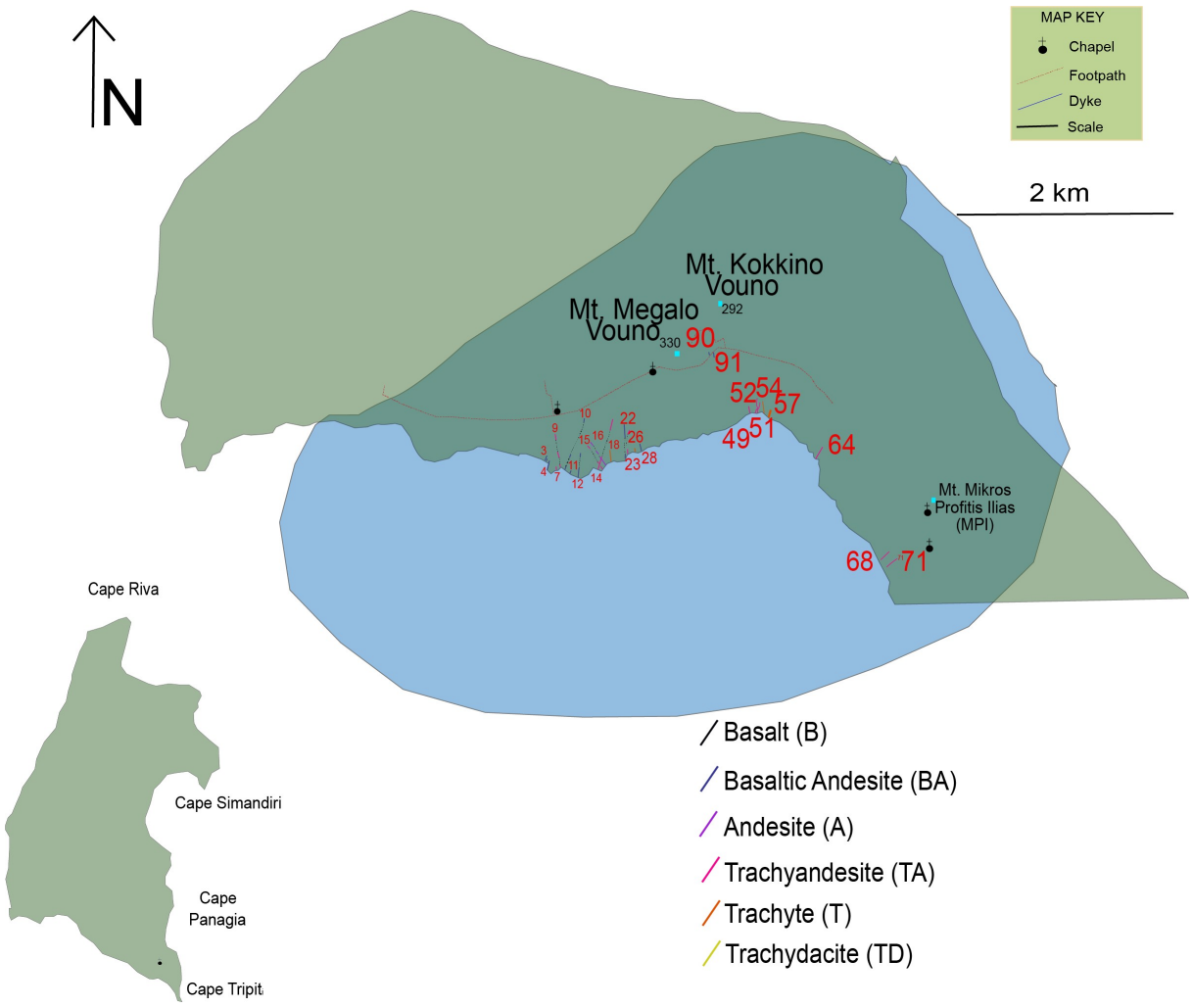

Fig. 6.9: Map showing the location and geochemical composition of the Peristeria dyke subswarm. The dykes are from basaltic andesites (BA) to trachytes (T).

The reconstruction of the plumbing system during the Peristeria formation could be illustrated in Fig. 6.10. The plumbing system hosts at least two magma chambers that probably produced a caldera collapse event during its formation, hence the existence of an angular unconformity between av2-av3 units. Both the dykes' spider diagrams and the host rocks' (Supporting files 1

and 2 Appendix C3) show that there are two possible origins. A deep one where Nb and Sr are low but Th high and one with the opposite characteristics which should reflect the shallow magma chamber. Dykes _10, _90 and _91 according to their analysis shall be fed directly from the deep-seated reservoir. The summit of the Peristeria volcano had a height of at least 350 m (Druitt et al., 1999) and it was located atop the dyke swarm.

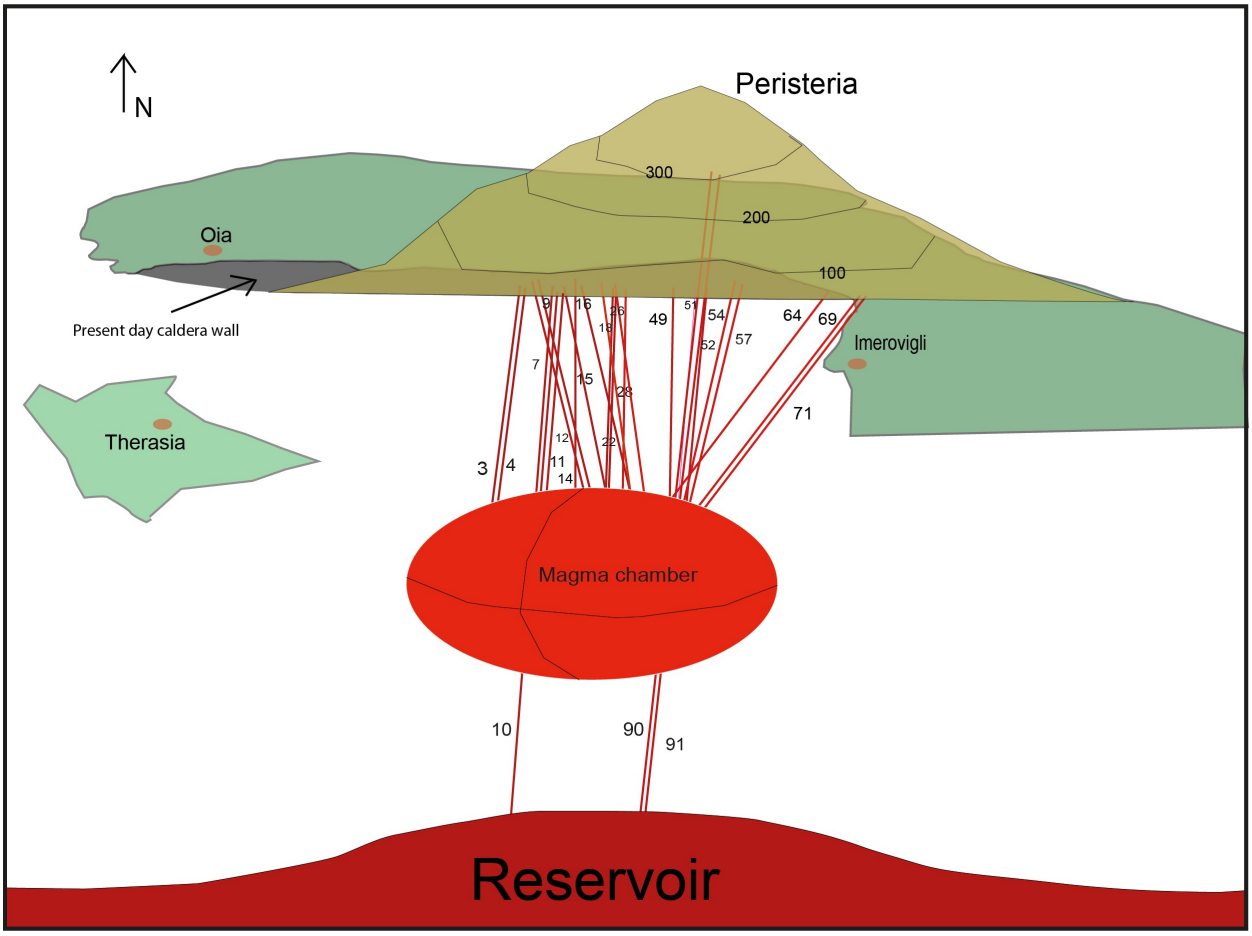

Fig. 6.10: Schematic three-dimensional reconstruction of the Santorini plumbing system during the Peristeria stratovolcano activity (530-430 ka).

5.2 Simandiri shield (172 ka)

Four (4) dykes were found to correlate geochemically with the Simandiri stratigraphy. The localities that were tested were limited to Cape Simandiri (Bailey et al., 2009). Dyke_21 overlaps with a host rock sample (TS0101, Bailey et al. 2009) showing just a slightly higher amount of Sr, which can indicate a slight evolution from the host rock sample. Dyke_23 also has significant similarities and could have fed the trachytes at Cape Simandiri however the Sr is slightly lower than the rest of the host rock. The same applies to Dyke_49. Dyke_52 is a latite that could have belonged to this shield. The details of the dykes are reported in Table 1 at Appendix C3, and an extrapolation of a part of the Simandiri dyke subswarm, including their location and chemical composition, is shown in Figure 6.11.

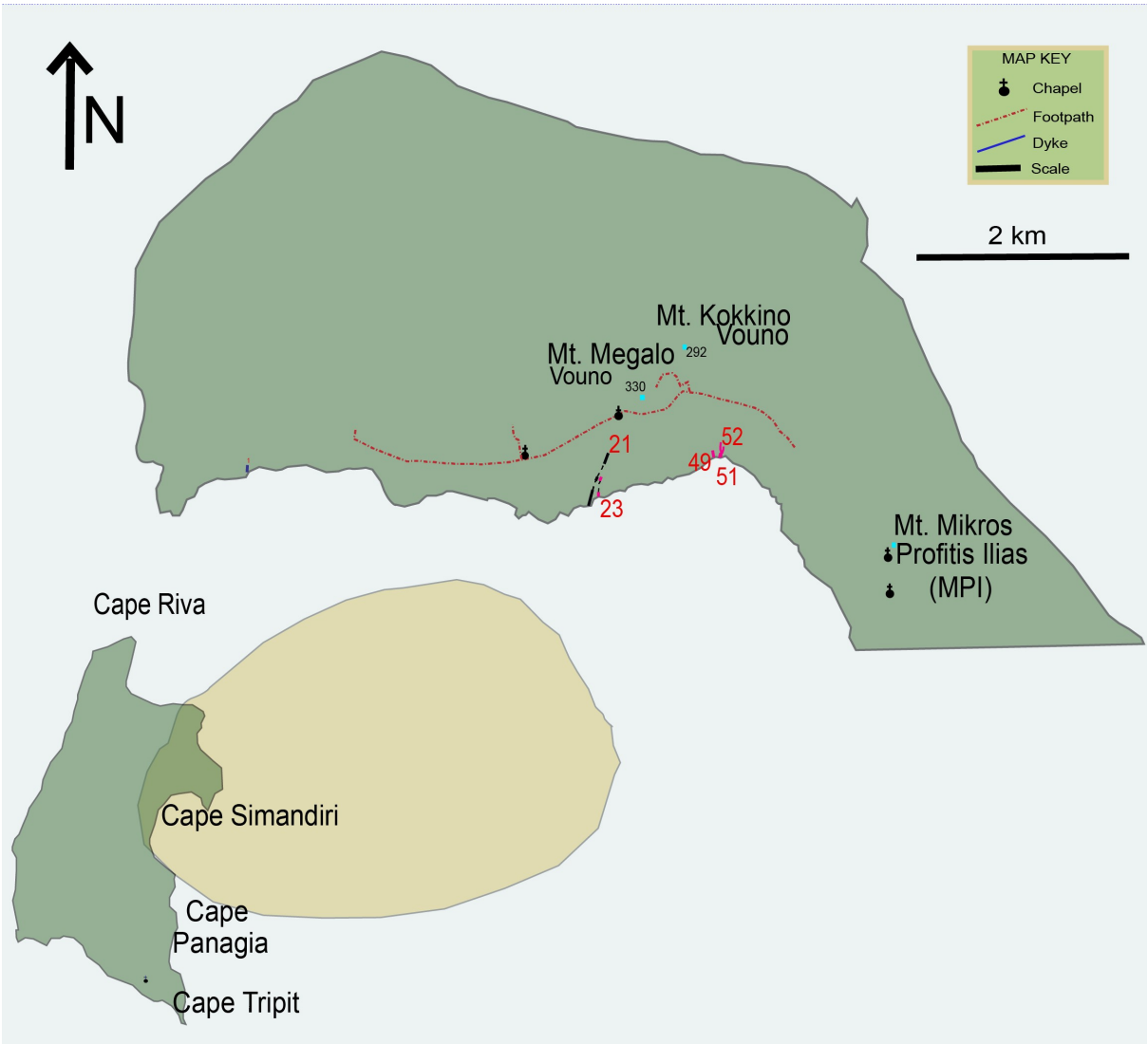

Fig. 6.11: Map showing the location and composition of the Simandiri dyke subswarm. The dykes are mostly basalts and trachyandesites.

A reconstruction of the plumbing system is shown in Figure 6.12. The geochemical analysis has been demonstrated that the dykes originated from the shallow chamber. Such a scenario could be highly possible as shields are usually fed by flank eruptions (Acocella et al., 2004). Subsequently, dykes_21 & _23 could have been lateral dykes that ejected from the shallow magma chamber and

triggered possible eruptions. However, the Riva caldera collapse (21 ka) had destroyed the summit of the shield, and hence the dykes cannot be seen at the western part. Dykes_21 and _23 formed fingers on their tips a sign of a pressure decrease as they flowed further away from the summit and got emplaced on the northern caldera wall (Fig. 6.12).

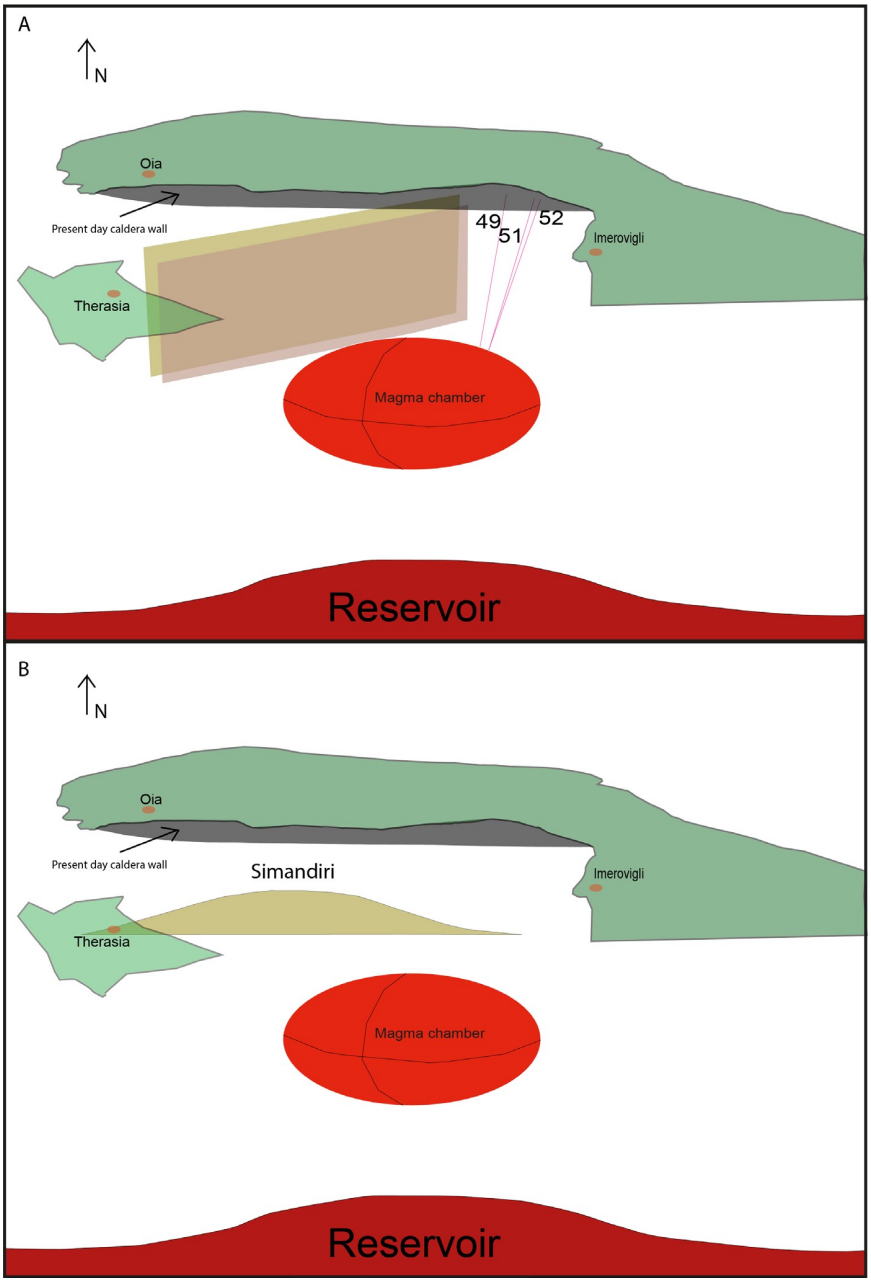

Fig. 6.12: Schematic three-dimensional reconstruction of the Santorini plumbing system during the Simandiri shield activity (172 ka). (A) The geometry of the feeder dykes (Dyke_21 & _23). (B) The geometry and reconstruction of the Simandiri summit.

5.3 Megalo Vouno and Kokkino Vouno cinder cones

Three (3) dykes were found to correlate geochemically with the Cinder cones of the northern caldera wall lavas and scoria units. The localities that were tested were limited to Megalo Vouno (M. Vouno) and Kokkino Vouno (K.Vouno). Dyke_80 has an absolute overlap both in petrography and geochemistry with a scoria sample that was analysed during this study at M.Vouno. Also, a sample that was collected from the bottom part of dyke_76 was similar to basaltic andesite M.Vouno lavas sampled by Nicholls (1971). Dyke_48 has similarities with the K.Vouno lavas. The details of the dykes are reported in Table 1 at Appendix C3 and an extrapolation of a part of the Cinder cones' dyke subswarm, including their location and chemical composition, is shown in Figure 6.13.

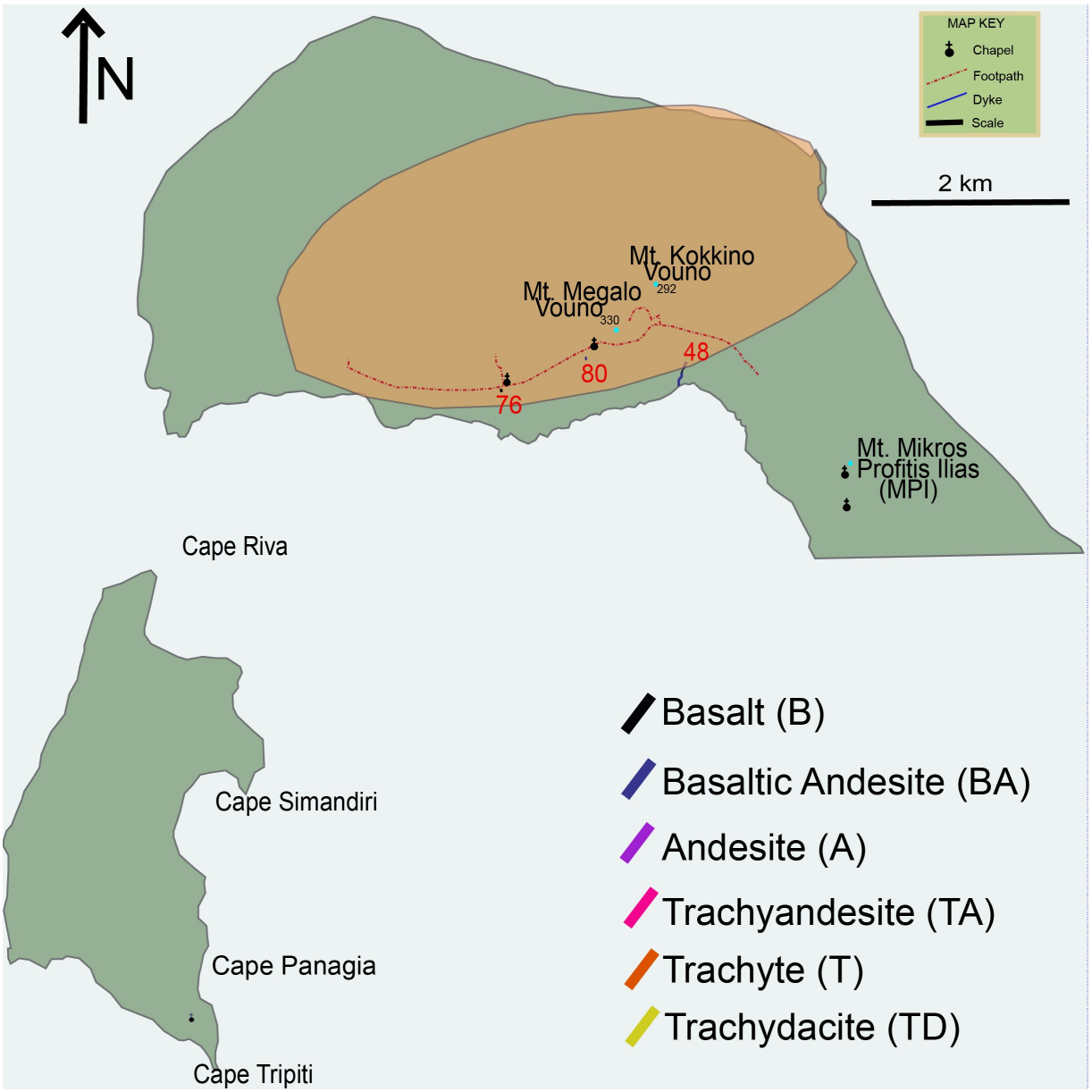

Fig. 6.13: Map showing the location and composition of the Cinder cones' dyke subswarm. The dykes are basalts to andesites.

The reconstruction of the plumbing system during the phreatomagmatic activity (Druitt et al., 1999) during this eruptive activity is shown in Figure 6.14. Dykes_48 & _80 have not got a negative Ta anomaly and has lower concentrations of Sr and Nb which probably records a different magmatic origin. Dyke_76 is a composite dyke that was initially emplaced during this population. In a later stage (Skaros shield), the path was reactivated.

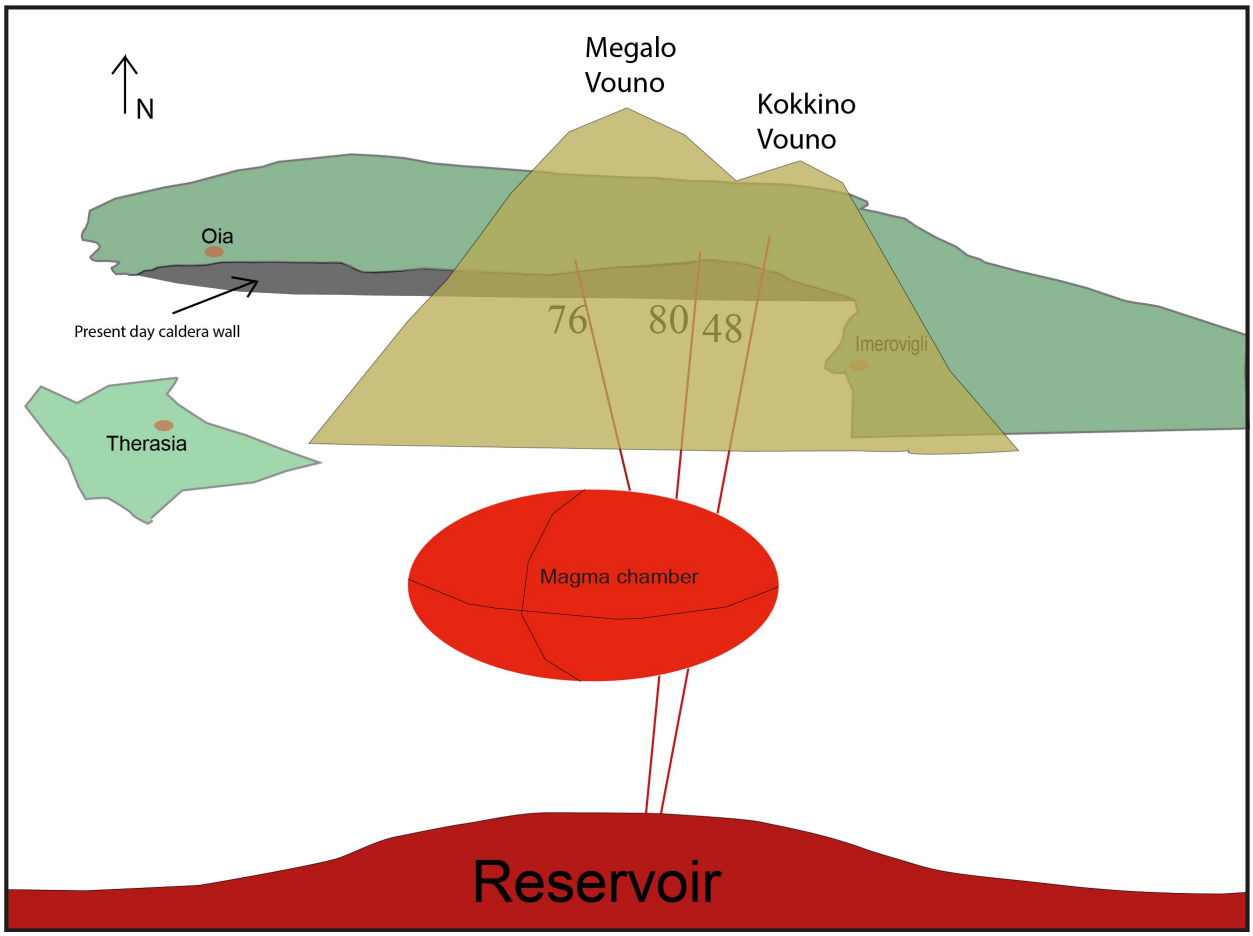

Fig. 6.14: Schematic three-dimensional reconstruction of the Santorini plumbing system during the activity that formed the Cinder Cones at the northern caldera wall.

5.4 Skaros shield

The shield that formed during the volcanic activity that formed the Skaros summit has significant similarities with the Peristeria stratovolcano, but the activity is slightly shifted southwesterly. For those reasons, the dykes are shown as parts of both plumbing systems. The host rock geochemical signatures have significant similarities with the Peristeria lavas and seemed to be recycled material from the same plumbing system. The lavas also could have been emplaced by two different magma chambers. Their compositional range is from basaltic to trachydacitic. Twenty-nine (29) dykes were possibly part of the dyke subswarm located both on the northern caldera wall but also at the Therasia caldera wall. Observations of dyke_97 show that the dyke fed a lava flow that, according to Druitt et al. 1999 belongs to the Skaros lavas (ds1 unit). Thus, characterised the composition of the dyke (basaltic andesite). The details of the dykes are reported in Table 1 at Appendix C3, and an extrapolation of a part of the Cinder cones' dyke subswarm, including their location and chemical composition, is shown in Figure 6.15.

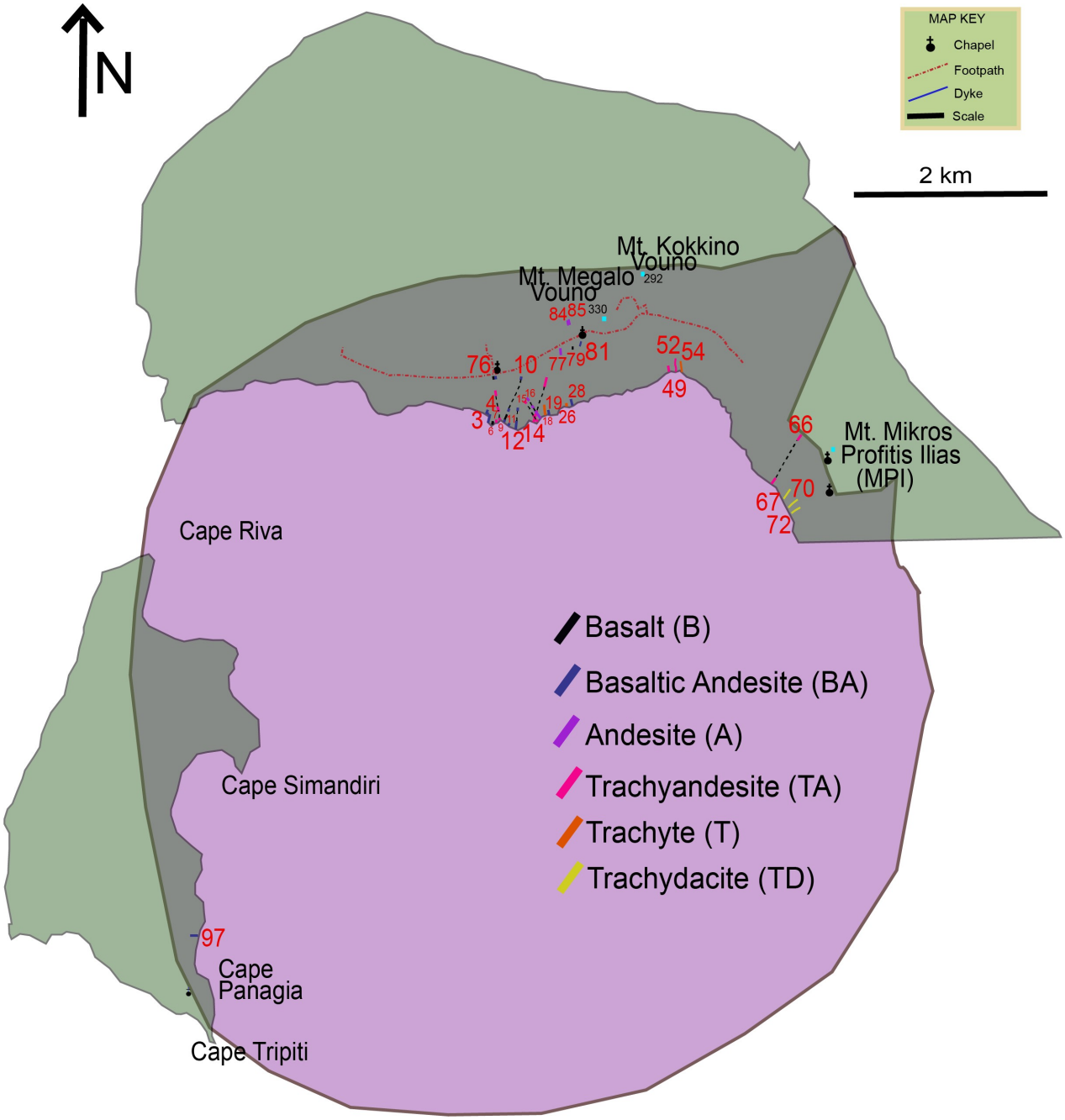

Fig. 6.15: Map showing the location and composition of the Skaros' dyke subswarm. The dykes are basalts to andesites.

The reconstruction of the plumbing system during the formation of the Skaros shield is as shown in Figure 6.16.

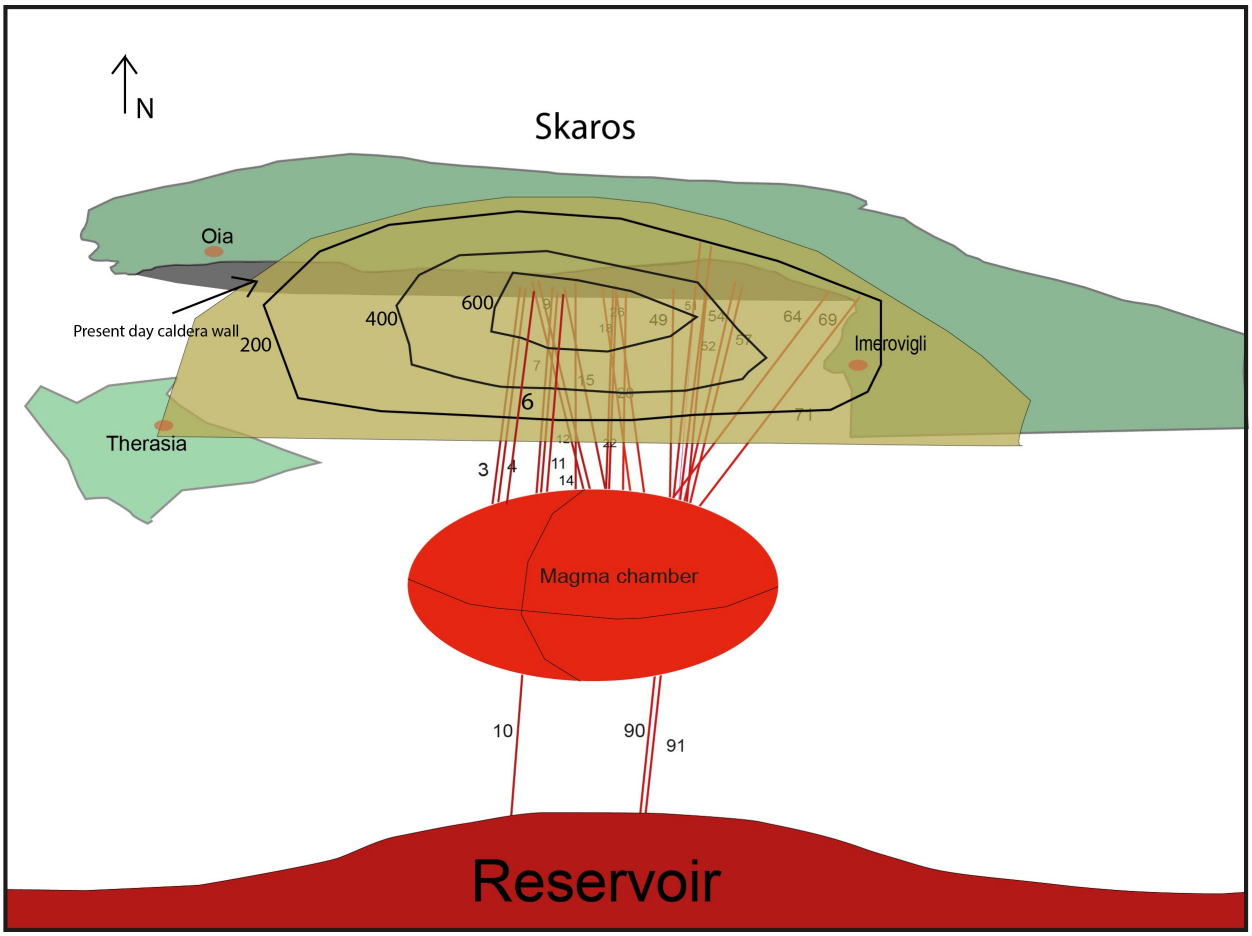

Fig 6.16: Schematic three-dimensional reconstruction of the Santorini plumbing system during the activity that formed the Skaros shield at the northern caldera wall.

5.5 Therasia dome complex

The formation of the Therasia Dome Complex (TDC) is the culmination of the Skaros activity. Although the deposits covered a great part of the main island, the majority formed Therasia hence the term (Druitt et al., 1999). The structural and geochemical data have shown that the feeder dykes that were observed to have fed the rhyodacites at the southern part of the Therasia wall have the same attitude and form similar spider diagrams with the trachydacitic dykes sampled by Nicholls, (1971), Mann, (1983) (Fig, 6.17). Only two (2) dykes except this part were found to be correlated with the TDC phase.

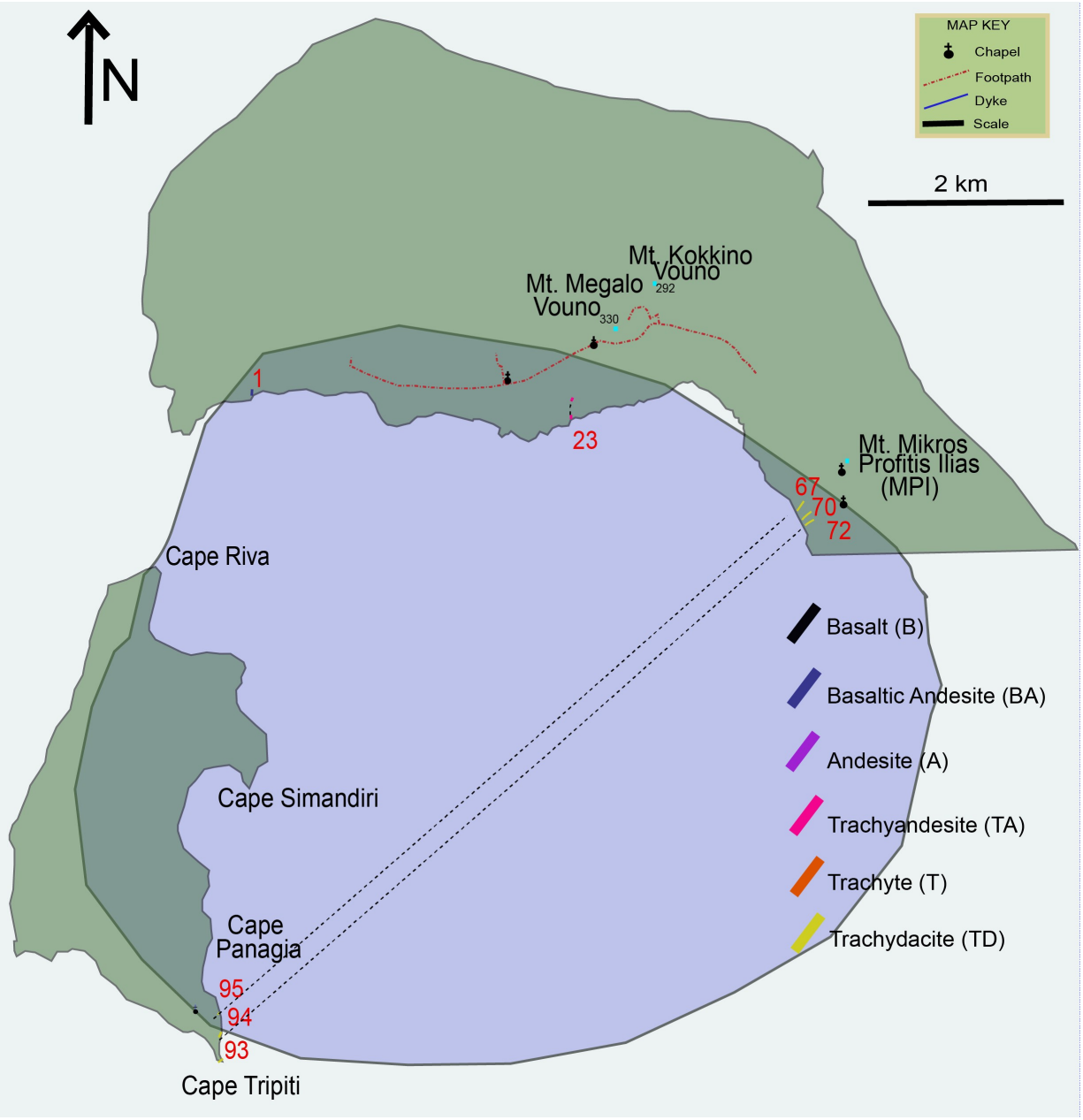

Fig. 6.17: Map showing the location and composition of the TDC dyke subswarm. The dykes are andesites to trachydacites.

The reconstruction of the plumbing system during the formation of the TDC shield is as shown in Figure 6.18.

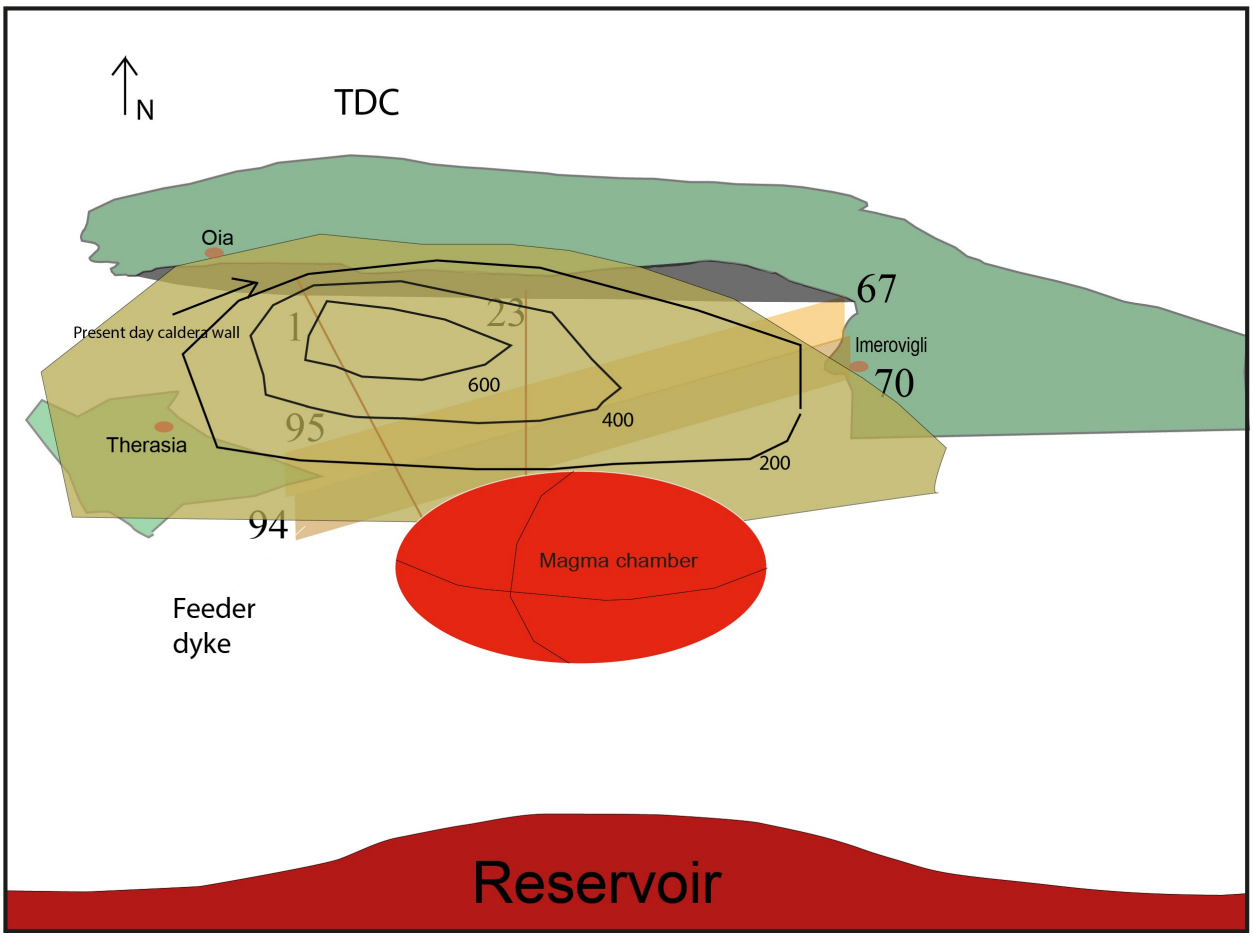

Fig. 6.18: Schematic three-dimensional reconstruction of the Santorini plumbing system during the activity that formed the Cinder Cones at the northern caldera wall. We observe the TDC edifice and the possible feeder dykes that intersect the caldera walls (Dykes_94,95,67,70).

6. Discussion and conclusions

The study revealed the location, structure, frequency and petrogenetic characteristics of the dyke swarms that formed during the five main phases as follows:

1. Peristeria dyke subswarm: It was a radial dyke swarm (N0˚-50˚E) that extended from M.Vouno to MPI, and its centre is now part of the flooded basin at the northeastern part of the caldera wall. We found eight dykes that belonged only in this stratovolcano and found both at the sea level and the M.Vouno. The petrogenesis promotes a two-magma chamber model, a deep and a shallow chamber that fed the lavas tuffs scoria and hyaloclastites (Druitt et al., 1999; Fabbro et al., 2013; Cadoux et al., 2014; Andujar et al., 2015, 2016). The composition of the dykes also revealed at least three main populations (events) which are 1) BA, 2) TA, 3) T. The more mafic products originated from the deep-seated reservoir and could propagate directly from it to the surface (e.g. dykes_10, _90 & _91). Finally, the mean overpressure of each population as determined by Eq. 6.1 was 0.55MPa, 1.05MPa and 3.44MPa, respectively.

2. Simandiri dyke subswarm: Only four dykes were observed to have similarities with the Simandiri host rock dataset and only one of them to be a possible feeder of a lava flow at cape Simandiri. They all strike NE-SW, and that is due to the type of the eruptions (flank eruptions); however, as the whole summit is collapsed that is only a current observation-based to the available data. The dykes record two populations-events which are: 1) B and 2) TA. The calculated overpressures are 1.12MPa and 0.72MPa, respectively.

3. Cinder cones dyke subswarm: Three (3) dykes were found to belong to the Cinder cones of the northern caldera wall. The structure of the dyke swarm is not possible to be reconstructed however

the petrogenesis reveal that the dykes mostly fed the two scoria cones and probably could have been fed from different sources Supportive file 3. The dykes are all basalts to basaltic andesites, and the mean overpressure is 1.01MPa.

4. Skaros shield: Twenty-eight (28) dykes were found to belong to this dyke swarm possibly and only eight (8) dykes correlated with the Skaros lavas. The dyke swarm is also radial as it was found both on the northern caldera wall and the Therasia wall. However, after the scoria cinder cones, it took place the formation of the graben in the north caldera wall and hence the normal faults (Chapter 5). A lot of dykes were found to propagate through these pre-existing fractures and as previous studies have shown that can exist only in the case that dyke emplacement is happening when the latter is active. The petrogenesis revealed a wide variety of compositions hence different dyke populations 1) B, 2) BA, 3) A, 4) TA, 5) T with overpressures of 0.57 MPa, 0.85 MPa, 0.80 MPa, 1.24 MPa and 1.91 MPa respectively.

5. TDC dyke swarm: The TDC dyke swarm also had a radial structure, although the limited number of dykes do not allow us to collect more data and compare it with the Skaros shield. The composition of the dykes was andesitic to trachyandesitic with a mean overpressure of 0.56 MPa. The dykes that fed the trachydacites of Therasia seem to follow the same strike (NE-SW) which coincides with the corresponding normal faults that partly controlled the emplacement of the dykes during the Skaros shield and the volcanotectonic line that was proposed by Druitt et al., (1999). That could be a piece of evidence that during the emplacement of the TDC dyke swarm this volcanotectonic lineament was probably active.

In Figure 6.19 we report the dyke swarm as shown from this multidisciplinary study.

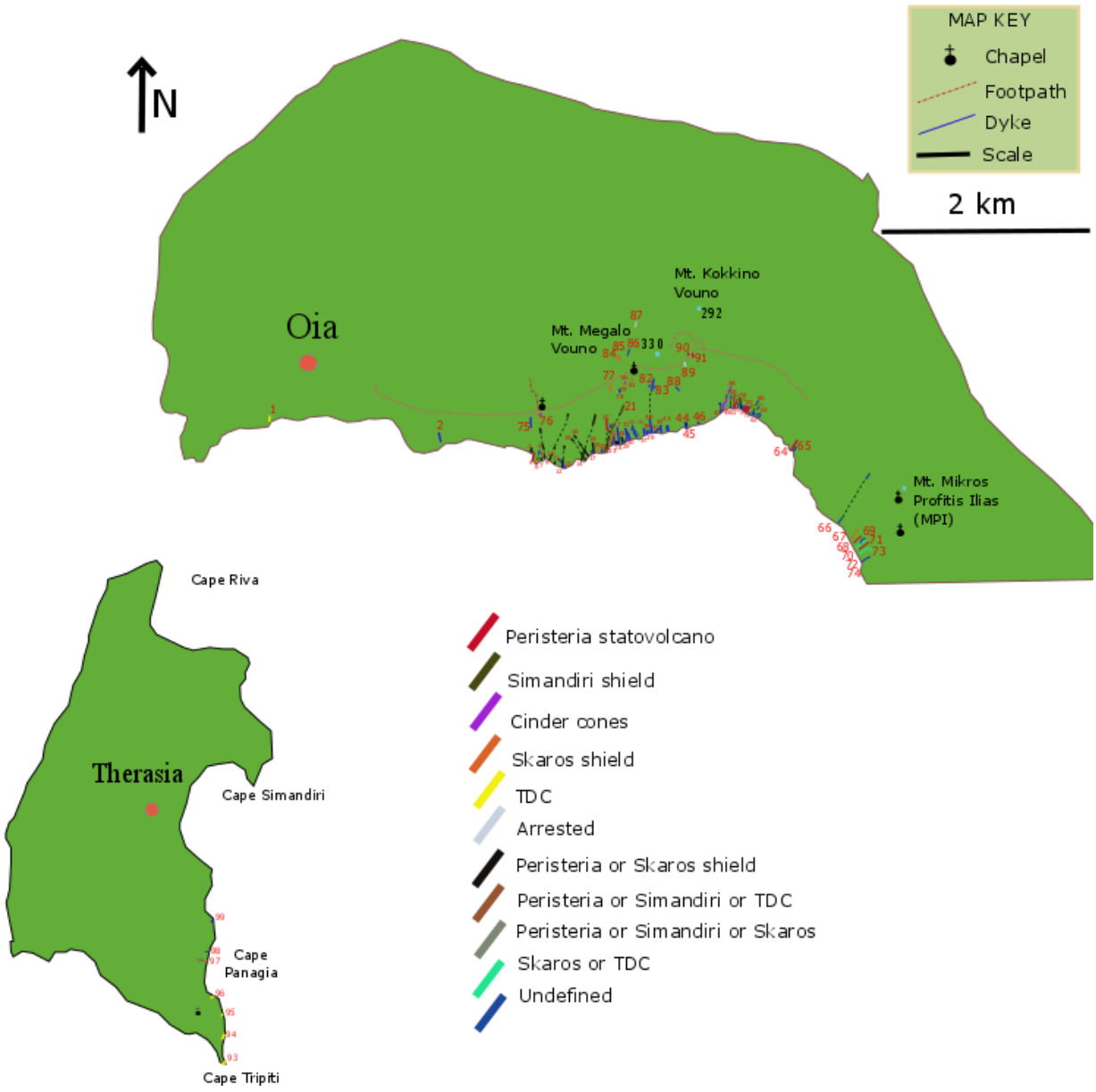

Fig. 6.19: The Santorini caldera wall dyke swarm. The map shows the results of the multidisciplinary study, the location, the strike, the thickness and their triggered event.

The following results were concluded after this study:

1. The Santorini northern caldera wall dyke swarm is not only restricted to the north but also found on the south and western parts of the volcanic activity. Radial dyke swarms formed during the formation of the last five shields-stratocones that shaped the area. However, during some periods volcanotectonic lineaments or basement faults were active and dykes a small number of dykes were sufficiently affected by the pre-existing fractures hence followed a path with an NW-SE strike. However, this should not coincide with the stress field due to extension (Feuillet, 2013) which promoted the preferential strike of the majority of the NE-SW dykes. Great parts of the dyke swarm are now lost on the flooded caldera.

2. The multidisciplinary study is in agreement with the previous studies in terms of the structure of the plumbing system (two magma chambers' model). This study has shown that the dykes should not only come from the shallow magma chamber but instead the deep-seatedreservoir too.

3. Peristeria and Skaros volcanic activities seem to have emplaced recycled materials as they have geochemically similar spider diagrams. However, all the spider diagrams suggest that the plumbing system is composed of two magma chambers and dykes could have been fed directly from the deep reservoir.

4. The calculated overpressures recorded during the different phases and populations reflect higher rates for the felsic materials and lower amounts for the mafic products.

5. A multidisciplinary study can record different dyke arrest reasons such as mechanical arrest due to the heterogeneity and anisotropy of the crustal segments and arrest that reflected changes of the magmatic conditions that took place in the magma chamber. In our study, we define a 7% of the dykes that were mechanically arrested, and 4% were magmatically arrested respectively.

6. The study of eroded dyke swarms can give us more insights into the magmatic processes and eruption dynamics. It unravels not only the successful eruptions but also the unsuccessful triggering events which so far are enigmatic for the volcanotectonic evolution of a volcano.

REFERENCES

Acocella, V., Funiciello, R., Marotta, E., Orsi, G., de Vita, S., (2004). The role of extensional structures on experimental calderas and resurgence. Journal of Volcanology and Geothermal Research 129, 199–217

Anderson, E.M., (1951). Dynamics of faulting and dyke formation, 2nd edn. Olivier and Boyd, Edinburgh.

Anderson, A.T., Swihart, G.H., Artioli, G., Geiger, C.A., (1984). Segregation vesicles, gas filter-pressing, and igneous differentiation, J. Geol., 92, 55– 72.

Andújar, J., Scaillet, B., Pichavant, M., Druitt, T. H., (2015). Differentiation conditions of a basaltic magma from Santorini and its bearing on basalt–andesite to andesite magma production in arc settings. Journal of Petrology 56, 765–794.

Andújar, J., Scaillet, B., Pichavant, M., Druitt, T. H., (2016). Generation conditions of dacite and rhyodacite via the crystallization of an andesitic magma. Implications for the plumbing system at Santorini (Greece) and the origin of tholeiitic or calc-alkaline differentiation trends in arc magmas. Journal of Petrology 57, 1887–1920.

Bailey, J.C., Jensen, E., Hansen, A., Kann, A., Kann, K., (2009). Formation of heterogeneous magmatic series beneath North Santorini, South Aegean island arc, Lithos, 110, 20–36.

Cadoux, A., Scaillet, B., Druitt, T. H., Deloule, E., (2014). Magma storage conditions of large Plinian eruptions of Santorini Volcano (Greece). Journal of Petrology 55, 1129–1171.

Daly, R. A., (1911). The nature of volcanic action. Proc. Am. Acad. Arts Sci. 47, 48–119.

Delaney, D.D., Pollard, J.I., Ziony, E.H., (1986). Mckee Field relations between dikes and joints: emplacement processes and paleostress analyses J. Geophys. Res., 91, 4920-4983

Druitt, T. H., Francaviglia, V., (1992). Caldera formation on Santorini and the physiography of the islands in the late Bronze Age. Bull. Volcanol. 54, 484–493

Druitt, T.H., Edwards, L., Mellors, R.M., Pyle, D.M., Sparks, R.S.J., Lanphere, M., Davis, M., Barriero, B., (1999). Santorini Volcano. Geological Society Memoir No. 19, 165

Druitt, T.H., Mercier, M., Florentin, L., Deloule, E., Cluzel, N., Flaherty, T., Médard, E., Cadoux, A., (2016). Magma storage and extraction associated with Plinian and interplinian activity at Santorini caldera (Greece). J Petrol 57, 461–494

Fabbro, G.N., Druitt, T.H., Scaillet, S., (2013). Evolution of the crustal magma plumbing system during the build-up to the 22-ka caldera-forming eruption of Santorini (Greece), Bull. Volcanol., 75, 1– 22.

Fabbro, G.N., (2014). The timescales of magmatic processes prior to a caldera-forming eruption. Doctoral thesis, Université Blaise Pascal, Clermont-Ferrand.

Fabbro, G.N., Druitt, T.H., Costa, F., (2017). Storage and Eruption of Silicic Magma across the Transition from Dominantly Effusive to Caldera-forming States at an Arc Volcano (Santorini, Greece), Journal of Petrology, 58, 2429–2464.

Feuillet, N., (2013). The 2011–2012 unrest at Santorini rift: Stress interaction between active faulting and volcanism, Geophys. Res. Lett., 40, 3532–3537

Flaherty, T., Druitt, T.H., Tuffen, H., Higgins, M.D., Costa, F., Cadoux, A., (2018). Multiple timescale constraints for high-flux magma chamber assembly prior to the Late Bronze Age eruption of Santorini (Greece), Contributions to Mineralogy and Petrology, 173,75

Gudmundsson, A., (1987). Formation and mechanics of magma reservoirs in Iceland. Geophysical Journal of the Royal Astronomical Society, 91, 27-41.

Gudmundsson, A., (1999). Fluid overpressure and stress drop in fault zones. Geophys. Res. Lett. 26, 115–118

Gudmundsson, A., (2003). Surface stresses associated with arrested dykes in rift zones Bull. Volcanol., 65, 606-619

Gudmundsson, A., (2006). How local stresses control magma-chamber ruptures, dyke injections, and eruptions in composite volcanoes Earth Sci. Rev., 79, 1-31

Gudmundsson, A., (2012). Magma chambers: formation, local stresses, excess pressures, and compartments. Journal of Volcanology and Geothermal Research, 237-238, 19–41

Gudmundsson, A., (2011). Rock fractures in geological processes. Cambridge University Press, Cambridge.

Gudmundsson, A., Philipp, S. L., (2006). How local stress fields prevent volcanic eruptions. J. Volcanol. Geotherm. Res. 158, 257–268

Hooft, E.E., Nomikou, P., Toomey, D.R., Lampridou, D., Getz, C., Christopoulou, M., O'Hara, D., Arnoux, G.M., Bodmer, M., Gray, M., Heath, B.A., Vander Beek, B.P., (2017). Backarc tectonism, volcanism, and mass wasting shape seafloor morphology in the Santorini-Christiana-Amorgos region of the Hellenic Volcanic Arc, Tectonophysics, 712-713, 396-414

Huijsmans, J.P.P., (1985). Calc-Alkaline Lavas from the Volcanic Complex of Santorini, Aegean Sea, Greece: A Petrological, Geochemical and Stratigraphic Study, Utrecht Univ., Utrecht, Netherlands.

Jolivet L., Faccenna C., Huet, B., Labrousse L., Le Pourhiet L., Lacombe O., Lecomte E., Burov E., Denèle Y., Brun J.-P., Philippon M., Paul A., Salaün G., Karabulut H., Piromallo C., Monié P., Gueydan F., Okay A. I., Oberhänsli R., Pourteau A., Augier R., Gadenne L., Driussi O., (2013). Aegean tectonics: strain localisation, slab tearing and trench retreat. Tectonophysics 597–598, 1–33.

Le Pichon, X., Angelier, J., (1979). The Hellenic arc and trench system: A key to the neotectonic evolution of the eastern Mediterranean area. Tectonophysics, 60, 1-42

Lipman, P. W., Bachmann, O., (2015). Ignimbrites to batholiths: Integrating perspectives from geological, geophysical, and geochronological data, Geosphere, 11, 705– 743.

Mann, A.C., (1983). Trace element geochemistry of high alumina basalt - andesite - dacite - rhyodacite lavas of the main volcanic series of Santorini Volcano, Greece. Contrib Mineral Petrol, 84, 43-57.

Marsh, B.D., (1996). Solidification fronts and magmatic evolution, Mineralogical magazine, 60, 5-4

Nicholls, I.A., (1971). Petrology of Santorini volcano, Cyclades, Greece. J Petrol 12, 67–119

Nomikou, P., Papanikolaou, D., Alexandri, M., Sakellariou, D., Rousakis, G., (2013). Submarine volcanoes along the Aegean volcanic arc, Tectonophysics, 597, 123–146.

Pe-Piper, G., Piper, D.J.W., (2005). The South Aegean active volcanic arc: Relationships between magmatism and tectonics, Dev. Volcanol., 7, 113– 133.

Petersen, A.D.J., (2004). A geological and petrological study of the dikes in the Megalo Vouno volcano complex, Santorini. M.Sc. thesis, Copenhagen University.

Piper, D.J.W., Perissoratis, C., (2003). Quaternary neotectonics of the South Aegean arc Mar. Geol., 198, 259-288

Putirka, K., (2017). Down the crater: where magmas are stored and why they erupt. Elements, 13, 11-16.

Rubin, A. M., (1995). Propagation of magma-filled cracks. Annu. Rev. Earth Planet. Sci. 23, 287–336

Satow, C., Tomlinson, E. L., Grant, K. M., Albert, P. G., Smith, V. C., Manning, C. J., Ottolini, L., Wulf, S., Rohling, E. J., Lowe, J. J., Blockley, S. P. E, and Menzies, M. A., (2015). A new contribution to the Late Quaternary tephrostratigraphy of the Mediterranean: Aegean Sea core LC21, Quaternary Sci. Rev., 117, 96–112

Sinton, J. M., Detrick, R. S., (1992). Mid-ocean ridge magma chambers. J. Geophys. Res., 97, 197-216.

Sparks, S., Annen, C. J., Blundy, J., Cashman, K., Rust, A., & Jackson, M.D., (2019). Formation and dynamics of magma reservoirs. Philosophical Transactions of the Royal Society A: Mathematical, Physical and Engineering Sciences, 377, 2139

Tibaldi, A. (2015). Structure of volcano plumbing systems: a review of multi-parametric effects. J. Volcanol. Geotherm. Res. 298, 85–135

Yoder, H.S., (1976). Generation of basaltic magma, National Academy of Sciences.

Yoder, JR., H.S., Tilley., C.E., (1962). Origin of Basalt Magmas: An Experimental Study of Natural and Synthetic Rock Systems, Journal of Petrology, 3, 342–532

Williams, H., McBirney, A.R., (1979). Volcanology. San Francisco: Freeman, Cooper and Company

Zellmer, G., Turner, S. & Hawkesworth, C. (2000). Timescales of destructive plate margin magmatism: new insights from Santorini, Aegean volcanic arc. Earth and Planetary Science Letters, 174, 265-281.

Chapter 7

Manuscript in preparation for journal submission

Dyke propagation in a heterogeneous and anisotropic crust, the reconstruction of a volcanic plumbing system.

Statement of contribution:

Collection of primary field data and geological mapping done by KD with help from AR

All field photographs and figures designed by KD

Complete 1st draft of manuscript and figures by KD

Revisions and subsequent drafts made with all co-authors input

Interpretation of field and laboratory data along with final model conducted by KD with support from all co-authors

Dyke propagation in a heterogeneous and anisotropic crust, the reconstruction of a volcanic plumbing system.

Kyriaki Drymoni[*a], Alison Rust[b], Katharine Cashman[b], John Browning[c], Agust Gudmundsson[a]

[a] Department of Earth Sciences, Royal Holloway University of London, Egham, TW20 0EX, UK

[b] School of Earth Sciences, University of Bristol, Wills Memorial Building, Queens Road, Bristol BS8 1RJ, UK

[c] Department of Mining Engineering and Department of Structural and Geotechnical Engineering, Pontificia Universidad Católica de Chile, Santiago, Chile

* Corresponding author

E-mail address: Kyriaki.Drymoni.2015@live.rhul.ac.uk

Abstract

In subduction zone volcanism, magma travels through a considerable thickness of continental crust providing opportunities for a range of physical and chemical interactions with surrounding rocks. As volcanic successions (e.g. stratovolcanoes) often consist of sequences of intercalated effusive and pyroclastic deposits, sometimes with variations in primary chemistry or alteration (e.g. by hydrothermal fluids), a propagating dyke may encounter rocks of a wide variety of chemical,

physical (e.g. Young's modulus) properties along its path. To study how such heterogeneous successions, affect dyke paths, we have mapped sections of the northern caldera wall at Santorini volcano, Greece, which includes a dyke swarm dissecting a complex stratigraphy of lava flows, welded pyroclastics, non-welded scoria deposits, and sedimentary units. The dykes vary in thickness, orientation and colour, and there is clear evidence of incorporation and assimilation of pyroclasts, scoria and lava into dykes. By coupling the field and petrological data with geochemical analysis we provide insights into the crustal volcanic plumbing system and assess the degree of mechanical entrainment and chemical assimilation of wall rock materials.

KEYWORDS: heterogeneity, dyke propagation, assimilation, volcanic plumbing system

1. Introduction

A volcanic plumbing system is the framework that describes the production and movement of magma from deep reservoirs, to ephemeral or permanent magma chambers, at shallower crustal levels and ultimately to the surface to feed volcanic eruptions (Cashman et al., 2017). Plumbing systems have been well studied through time due to their importance for understanding the active magmatic systems on Earth and especially the ones that can potentially trigger large eruptions (e.g. Minoan, eruption, Krakatau etc.) in the near future (Newhall et al., 2018).

A volcanic plumbing system (VPS) constitutes of one or more magma chambers stored at various depths interconnected by a system of fractures that transports the magma vertically and laterally (Cashman and Giordano, 2014). The concept of a magma chamber as the system that allows

chemical and textural transitions to connect lava products (Becker, 1897) remained the central idea of volcanism for more than a century, debated by Daly (1911) who described it as a system of magmatic injections and abyssal fissures that penetrate to the surface without accumulating in the crust (Fig. 7.1A).

The plumbing systems in terms of the amount of energy and mass that they contain are categorized as 1) closed systems, where any T, P, X_{H2O} changes that take place reflect eruptive events or convective cycles in a magma chamber scale and 2) open systems, which represent compositional and textural changes that correspond to large scale events (Tepley et al., 1999). The open plumbing systems are usually associated with either magma recharge where primary, hot magma intrudes a magma chamber or magma contamination (Huppert and Sparks, 1985). The latter describes the assimilation or mixing process of a partial melt initially generated in a country rock, which becomes incorporated into the magma either from the magma chamber wall or during magma ascent through dyking (Walker et al., 1979).

Petrologists have studied volcanic plumbing systems in terms of investigating their volcanic timescales (Druitt et al., 2012), the processes occurred in a magma chamber before a volcanic eruption as defined by their textural analyses (Hildreth, 1981; Anderson, 1984; Tepley et al., 1999; Humphreys et al., 2006; Holness et al., 2007; Jerram and Martin, 2008; Viccaro et al., 2010; Renjith, 2013), their dynamics (effusive or explosive activity) (Di Genova et al., 2017; Cassidy et al., 2018) and physical properties (Carrichi et al., 2016). Experimental studies gave more insights into the depth, thermodynamic conditions and resident time of a stored magma before a volcanic eruption (Putirka, 1997; Druitt et al., 1999; Zellmer, 2000; Bachmann and Bergantz, 2004; Perugini

and Poli, 2004; Fabbro et al., 2013, 2014, Annen et al., 2015; Andujar et al., 2015; Neave et al., 2019).

Gudmundsson (1987, 1998, 2006, 2012) introduced the volcanotectonic concept of a double magma chamber, a shallow crustal chamber fed by a much larger magma reservoir located in the lower crust or upper mantle (Fig. 7.1B). This concept was introduced primarily to explain (1) the formation of major central volcanoes, stratovolcanoes and basaltic edifices, and (2) the different intrusion and eruption frequencies and composition (Gudmundsson, 1998) of the products between central volcanoes – as defined by Walker (1963, 1974) – and the volcanic systems/fields outside central volcanoes. The concept combined theories of fluid transport in porous and fractured media with theories of stresses in solids – particularly stress concentrations around cavities - and linked the presence of a deep reservoir with a shallow magma chamber through vertical dykes (fluid-flow fractures). Shallower in the crust, the chamber channels magma within a system of inclined (sheets) and vertical dykes that can either stall in the crust, form sills or ultimately feed volcanic eruptions (Gudmundsson, 2006, 2012). Special interest was given to the shape and size of the magma chambers (Gudmundsson, 2006, 2016) so as to understand how stress concentrating triggering dyke injections and the potential of the chamber to produce eruptions of different volumes.

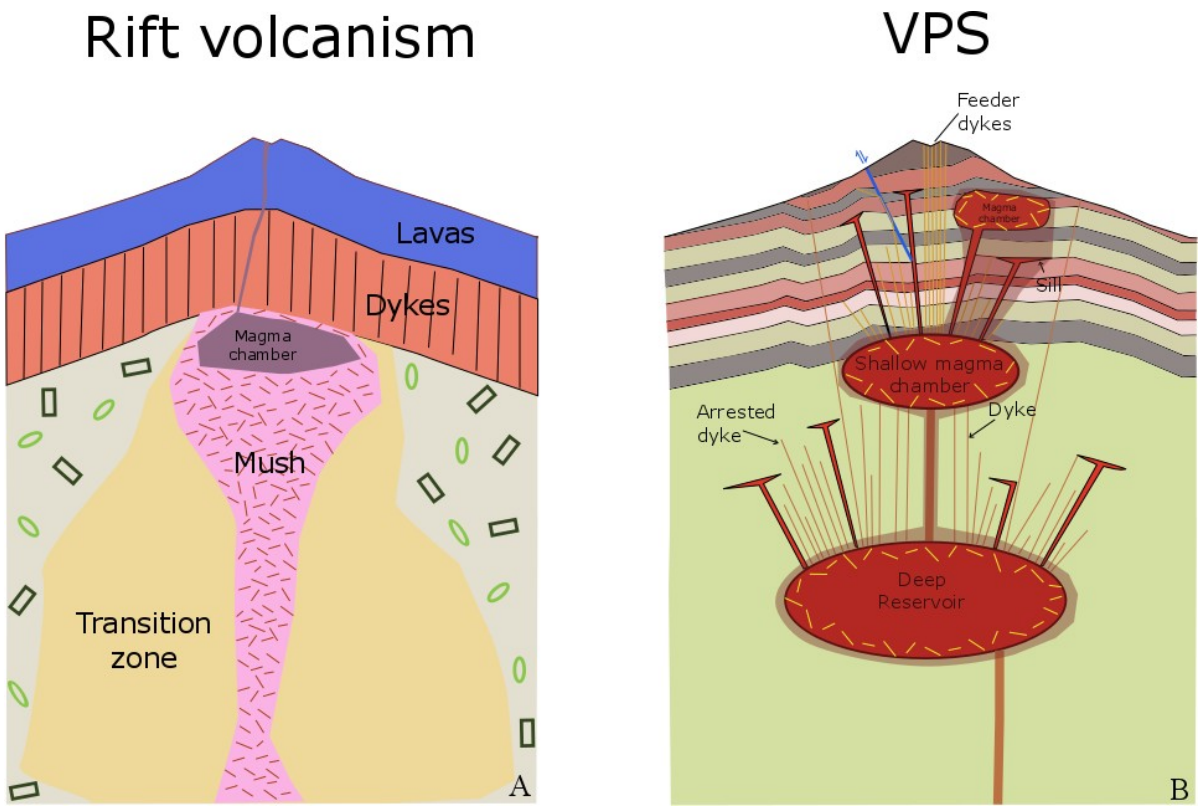

Fig. 7.1: (A) Classic, schematic view of a magmatic plumbing system in rift zones such as at mid-ocean ridges and ophiolites modified from Sinton and Detrick (1992), (B) Schematic illustration of a volcanic plumbing system in a stratovolcano. Not to scale.

From a petrological point of view a magma chamber may be regarded as the melt-dominated region of a magmatic system (Sparks et al., 2019). Mechanically, however, a magma chamber is the entire 'soft inclusion' whose elastic properties (particularly Young's modulus) differ significantly from those of the host rock and, therefore, concentrates stress (Gudmundsson, 2011). Many shallow chambers develop from sills, and some stay sill-like most of their lifetime (Gudmundsson, 2002). Magma chambers as mechanical entities were initially modelled by Anderson (1936), who used a

nucleus of strain – a point source (tiny spherical cavity) - to explain the formation of inclined sheets and ring-faults. This model was subsequently used by Mogi (1958) to model inflation and deflation during volcanic unrest periods, and is today a standard model, the 'Mogi model', for inferring the depth to a shallow magma chamber (e.g. Segall, 2013). Point sources do not provide any information on stress concentration around chambers, and therefore cannot be used to forecast magma-chamber rupture. Numerical studies (Gudmundsson, 2006, 2012) that model magma chambers as finite-size arbitrary oriented triaxial ellipsoidal cavities (a>b) make it possible to calculate actual stresses around the chambers, hence forecast magma-chamber rupture during unrest periods. Also, when layering is taken into account, these models allow use to forecast with reasonable reliability the likely dyke/sheet paths.

By adding the time dimension into a system, we can study its evolution and investigate how it matures (Zellmer and Annen, 2008) and what alters its dynamics (Gonnermann and Manga, 2013). The system likely initiates from a small size and ephemeral shallow chamber fed by permanent deep reservoirs to larger sizes and thicker shapes of more permanent and eruptible magma chambers that at the same time are concentrated to the upper parts of a large transcrustal magmatic system (TCMS) (Cashman et al., 2017). Accordingly, the magma filled fractures that emplaced in the crust and belong to individual eruption events are progressively forming regional dyke swarms that dissect the edifices of stratovolcanoes (Gudmundsson, 2003; Geshi et al., 2010; Tibaldi, 2015).

Although understanding the structure, processes and evolution of the magmatic plumbing systems are vital in volcanology, the systems are mostly observed and studied as aftermaths and not in real time during their actual progression. In active volcanoes they are mostly hidden, while some become partly exposed through erosion or caldera collapse events. Real-time data from unrest

episodes in well-monitored calderas report that the unrest results in an eruption in 54% of events at calderas with predominantly mafic magmas and in only 38% of calderas with predominantly silicic magmas (Newhall and Dzurisin, 1988). A more recent database that investigated similar unrest but in different types of volcanoes found that, again, around 47% of the unrest events result in a volcanic eruption (Phillipson et al., 2013). If these percentages reflect the percentage of dykes that become feeders for those eruptions, then it follows that the residual percentages belong, at least partly, to dykes that have become arrested or stalled in the crust. As a result, eruptive products only contribute to less than around 50% of the volcano's dynamic history, and hence the study of these products allows us to observe only a part of their magmatic evolution.

In this paper we study the volcanic plumbing system of the composite (central) volcano on Santorini (Greece), by combining volcanotectonic, petrological and geochemical studies both from their eruptive products (lava flows, pyroclastics) and the eroded dyke swarm. Santorini is an ideal case study as it is a long-lived Quaternary volcano that has experienced a sequence of explosive and effusive volcanic eruptions with a Plinian crescendo at 3.6 ka (Druitt et al., 1999) and remains active. On top of that, a local dyke swarm of 91 dyke segments is fossilized on the northern caldera wall and crosscuts the heterogeneous and anisotropic stratigraphic sequence allowing us to study it. We focus on both dyke-fed volcanism but also the arrested dykes that resulted in unsuccessful volcanic events. We use the observed dyke paths to identify the parts of the evolved plumbing system. The combination of their structural data, petrography and geochemical signatures shall give us answers on 1) the key parts and products that define the volcanic plumbing system, 2) the architecture of the Santorini plumbing system through time. All these will eventually help the community further on monitoring and forecasting volcanic eruptions.

2. Regional setting

The volcanism on Greece is mainly associated with the SW-NE subduction and slab rollback of the African oceanic plate beneath the Aegean Sea initiated on Pliocene (Mc Kenzie, 1972; Pe-Piper & Piper, 2005). The convergent processes initially produced an extensional regime in the northern Aegean microplate that accompanied by granitic intrusions during Miocene. Magmatism was gradually transferred to the southernmost part of the Aegean and formed a north eastward dipping Benioff zone (Makropoulos and Burton, 1984), the South Aegean Volcanic arc (Pe-Piper and Piper, 2002). However, the different motion rates of the connecting plates resulted to a fast-lithospheric extension (Tsapanos et al., 1994) and thinned out the back arc southern region generating tectonic structures associated with slab fragmentation and collision (Jolivet et al., 2013). As a result, eight aligned volcanic centres were formed (Aegina, Methana, Poros, Milos, Santorini (Thira), Kolumbo, Yali-Nisyros and Kos) following two tectonic E-W to NW-SE and NW-SE fracture zones (Pe-Piper et al., 2005).

Santorini volcano formed the southern volcanic activity of the South Aegean volcanic arc and is represented by a calk-alkaline (high-K) series in conjunction with a tholeiitic activity (Huijsmans, 1985; Druitt et al., 1999). The island is located geographically in between the islands of Crete, Ios and Anafi and is composed by five islands in total. The islands of Thira, Therasia and Aspronisi surround Nea and Palea Kameni, the most recent products of the Post Minoan (3.6ka) eruption and form a caldera in a shape of a circumferential ring fault. A reconstruction of the last Plinian eruption (Johnston et al., 2015) advocates that its effects (ash fallout, tsunamis, climatic effects) vanished the Mediterranean Bronze – Age civilisation (Druitt, 2014).

An integration of swath studies on the offshore perimeter areas (Nomikou et al., 2013; Hooft et al., 2017) revealed the tectonic structure and morphotectonic features of the region. The north-eastern part is characterised by an NE-SW Santorini Amorgos Tectonic Zone that separates the Attico-Cycladic basement from the Hellenic arc (Nomikou et al., 2016) which is defined by a series of grabens and basins as well as major marginal faults. The Quaternary normal and strike-slip faults follow an NE-SW orientation and overlie a series of ENE-WSW which terminate at N-S transfer faults (Piper et al., 2007). The zone is cut by NW-SE transverse (strike-slip) tectonic structures, which have cut the basin in blocks (Nomikou et al., 2016).

Two volcanotectonic lines that are hypothesized partly to control the magmatic and hydrothermal activity in the region (Druitt et al., 1999; Rizzo et al., 2016) as well as the Christiana-Santorini-Kolumbo (CSK) rift zone (Nomikou et al., 2013) which defines the three main volcanic centers of the region (Fig. 7.2) permeate the island.

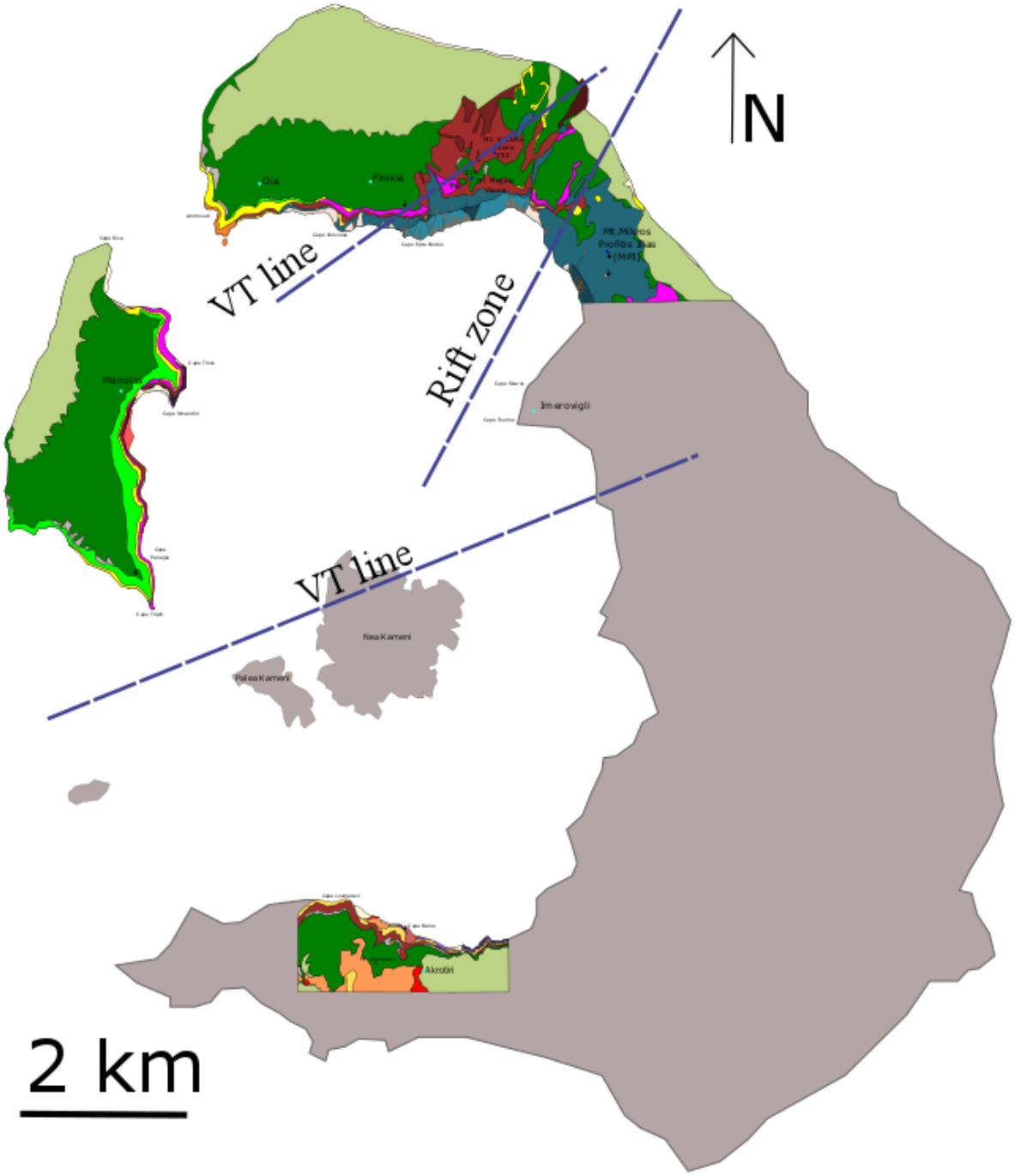

Fig. 7.2: Geological map of Santorini island with a focus on the studied areas and the observed dyke swarm along the northern caldera wall. The map shows also the two major volcanotectonic lines defined by Druitt et al. (1999) and rift zone by Nomikou et al. (2013).

3. Methods and materials

The study coupled field and petrological analysis. Specifically, we conducted several field campaigns on Santorini island to map and collect representative specimens from the dyke segments and the host rock. We completed a macroscopic description of all samples, reported their macroscopic textures, phenocrysts (if any), morphological lava fabrics (e.g. fingers, rafted rounded lavas, flow indicators, layering), structural features of flow-related textures, gas escape and oxidation, hydrothermal activity, vesicularity, xenoliths. We conducted a detailed petrographic analysis of seventy (70) thin sections of dykes (core and rims), chilled margins, and host rock samples. We focused on their mineralogical assemblage, size and morphology, microscopic textures, xenoliths, and crystal populations. The petrographic analyses were conducted with a polarised optical microscope, and the thin sections were analysed with an optic polarised microscope supplied with a digital camera (NIKON Microphot FX-35A with a NIKON DS-5M camera system).

We performed modal analysis measurements by using an electromechanical point-counting technique and the Java based Image J program (Delesse, 1848) to establish a quantitative analysis of the mineralogical assemblage of thirty-two (32) samples. For point counting we used a 1500 hitting point frequency and performed extra analysis for confining the error of the technique. The techniques and equipment mentioned before belonging to Royal Holloway University of London Optics Lab.

Based on the optical microscopic study, representative rock samples were selected for Scanning Electron Microscopy (SEM) analysis. The latter have been performed on a scanning electron

microscope (Hitachi S-3500N of variable pressure) equipped with a Thermo Noran energy dispersive spectrometer (energy dispersive X-Ray detector (EDS)) which belongs to the electronic microscopy laboratory at the School of Earth Sciences, University of Bristol. The method focused on 1) analysing the textures observed in the studied thin sections, 2) possible reactions between the crystals and the melt phase, 3) measuring the size of the microlites and the glass in the groundmass.

4. Origin and magma movement in a transcrustal VPS

A volcanic system develops during time as shown by its volcanic products (Zellmer and Annen, 2008). Many studies on the processes occurring in a magmatic system have focused on the textures and main components of their volcanic products. The latter are divided into 4 categories 1) phenocrysts; early formed larger crystals embedded in the groundmass, 2) antecrysts; crystals that formed in previous melt phases but incorporated into another melt in a later stage, 3) xenoliths; piece of materials that belong to the surrounding rocks (host rock or country wall) and not to the crystallised magma, and 4) enclaves; mafic components that originate from the magma chamber but are found crystallised in the rock. By studying the previous components, we can estimate their depth of origin as well as the part of the mush or the parts of the hanging wall that were detached during propagation and transferred to the shallow crust on their way to the surface.

We report observations from dykes that are the original transporters of the magma to the surface to explore the following questions: 1) What kinds of magmas and materials entrained by those magmas were propagating vertically in the VPS through the dykes and what can this tell us about the crystal-dominated zone (mush) and the melt-dominated zones in the magma chambers? 2) What

kinds of materials were being recycled in the magmas and how does this affect magma dynamics? 3) Which textural properties found in dyke segments can be associated with host rock entrainment and assimilation of the crust? Can those secondary processes change the physical properties of the magma or even the dyke composition towards the surface? These questions are answered below.

4.1 Magma propagation, mixing and recharge

During the lifetime of a magma chamber, various events and processes can change the lithostatic equilibrium between the chamber and the host rock, giving rise to changes in pressure which can be followed by a dyke injection. A triggering process (e.g., magma added to the chamber) can increase the pressure inside a magma chamber that can give rise to local stress concentrations that induces dyke injection under the following condition Eq. 1 (Gudmundsson, 2011):

$$P_l + P_e = \sigma_3 + T_o \quad (7.1)$$

where P_l is the lithostatic stress or overburden pressure at the top of the magma chamber, P_e is the excess magmatic pressure, σ_3 is the minimum principal compressive stress or tensile stress of the magma, T_o is the tensile strength of the host rock. The injected dykes move magma towards the surface, even if many of the dykes, as indicated above, become arrested and never erupt.

Several studies have estimated the processes that could potentially induce pressure changes inside a magma chamber. However, magma generation and pressure in Santorini chamber could also be partly controlled by specific processes according to their magmatic evolution and volcanotectonic history which are magma mixing and mingling (Nicholls, 1971; Fabbro et al., 2013), magma replenishment or recharge, and magma chamber subsidence (Nicholls, 1971; Huijsmans, 1985). All those processes can ideally trigger an injected dyke as follows:

- Magma mixing could cause superheating and heat convection (Sparks et al., 1977) enough to change the volume of the chamber and rise in the magmatic (excess) pressure (Pe). Resorbed cores, fine sieve textures and oscillatory zoning in phenocrysts are evidence for this process (Humphreys et al., 2006; Holness et al., 2007; Jerram and Martin, 2008; Viccaro et al., 2010; Renjith, 2013).

- Magma replenishment/recharge where the 'intruding' magma causes compression of the liquid phase in the chamber and expansion of the chamber walls. The latter generates enough overpressure which sometimes reaches the tensile strength of the host rock (Machado, 1974; Blake, 1981; Huppert et al., 1982; Gudmundsson, 1987; Tait, 1988).

- Magma chamber subsidence may occur when the tensile stress concentration around a magma chamber increases due to spreading. The chamber can increase its aspect (height/thickness) ratio which results in rising values of tensile stress in the top of the chamber and possible dyke injections (Gudmundsson, 1988).

Our macroscopic and microscopic study revealed the following components that record the aforementioned processes which can be shown in a cross section at Figure 7.3 and 7.4:

1.1a) amphibole antecrysts: Although Santorini's VPS in the early Akrotiri volcanism (Late Pliocene - 580ka) was discharged by a hornblende bearing magma (Druitt et al., 1999) comparable magmas have not erupted since the Peristeria eruptions (Druitt et al., 1999; Bailey et al., 2009). We found an amphibole crystal in a dyke that belonged to the Skaros shield subswarm (Fig. 7.3, A1). The crystal had a size of 0.3mm and was slightly pleochroic.

1.2) Phenocrysts populations of plagioclases, pyroxenes and olivine crystals. The plagioclase sizes and textures allowed us to observe different populations that could probably reflect a different magmatic origin. We generally observed large phenocrysts (up to 5mm) (1.2a) with coarse sieve textures, resorbed cores, oscillatory zoning and pyroxene inclusions which belonged to one population (Fig. 7.3, B1). The second had smaller crystals (up to 0.5mm) (1.2b), euhedral, twinned without observed textures, yellowish cores (sodic cores and calcic rims) and were swallow-tailed.

1.3) Xenoliths: We observed incorporated xenoliths of variable sizes (up to 25mm) and of variable compositions (plag+cpx in a trachytic groundmass, single plag laths in a fine groundmass, plag+opx+ol±cpx in a devitrified glassy groundmass, plag+cpx in a hollocrystallic groundmass).

1.4) Enclaves: We found a lava enclave in a dyke sample (up to 15 cm). It was studied under the microscope and we observed that it belongs to a crystallised cumulate magma that probably incorporated from the magma chamber.

We report the possible depth of origin from their textural characteristics (Humphreys et al., 2006; Holness et al., 2007; Jerram and Martin, 2008; Viccaro et al., 2010; Renjith, 2013) of the studied components in a vertical cross section of the Santorini VPS (Fig. 7.4).

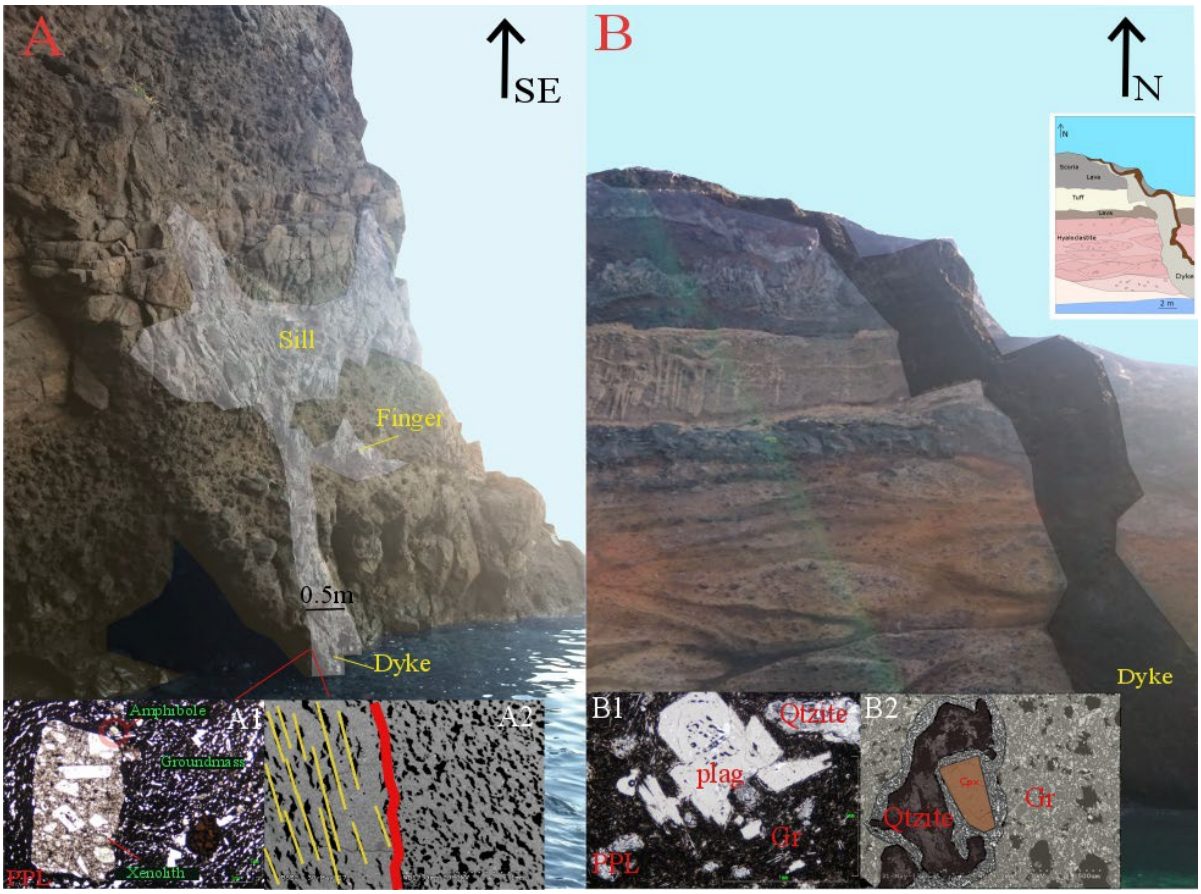

Fig. 7.3: (A) Dyke_6 as observed at Cape Eptapaides. The dyke turns into a sill and becomes arrested in the host rock which is highly heterogeneous and compliant (hyaloclastite), A1: PPL image of Dyke_6, the groundmass (Plag+pyroxene+ol+glass) includes angular or rounded xenoliths which are parts of possibly other magma batches. A2: SEM image of the anisotropic holohyaline groundmass (brown devitrified glass), (B) Dyke_4 as observed on the northern caldera wall (Cape Eptapaides). The dyke is found to intersect all the host rock stratigraphy. The host rock is composed by tuffs, scoria, lavas and hyaloclastites. Anastomosing textures on the latter horizon record macroscopically mixing processes. B1: PPL image of Dyke_4, the groundmass (Plag+pyroxene+ol+glass) has vesicles with crystallised Quartzite. We observe in the middle a

large plagioclase phenocryst (0.8 mm) with coarse sieve texture. B2: SEM image of the groundmass. A crystallised vesicle and a glassy groundmass rim surround a Cpx crystal.

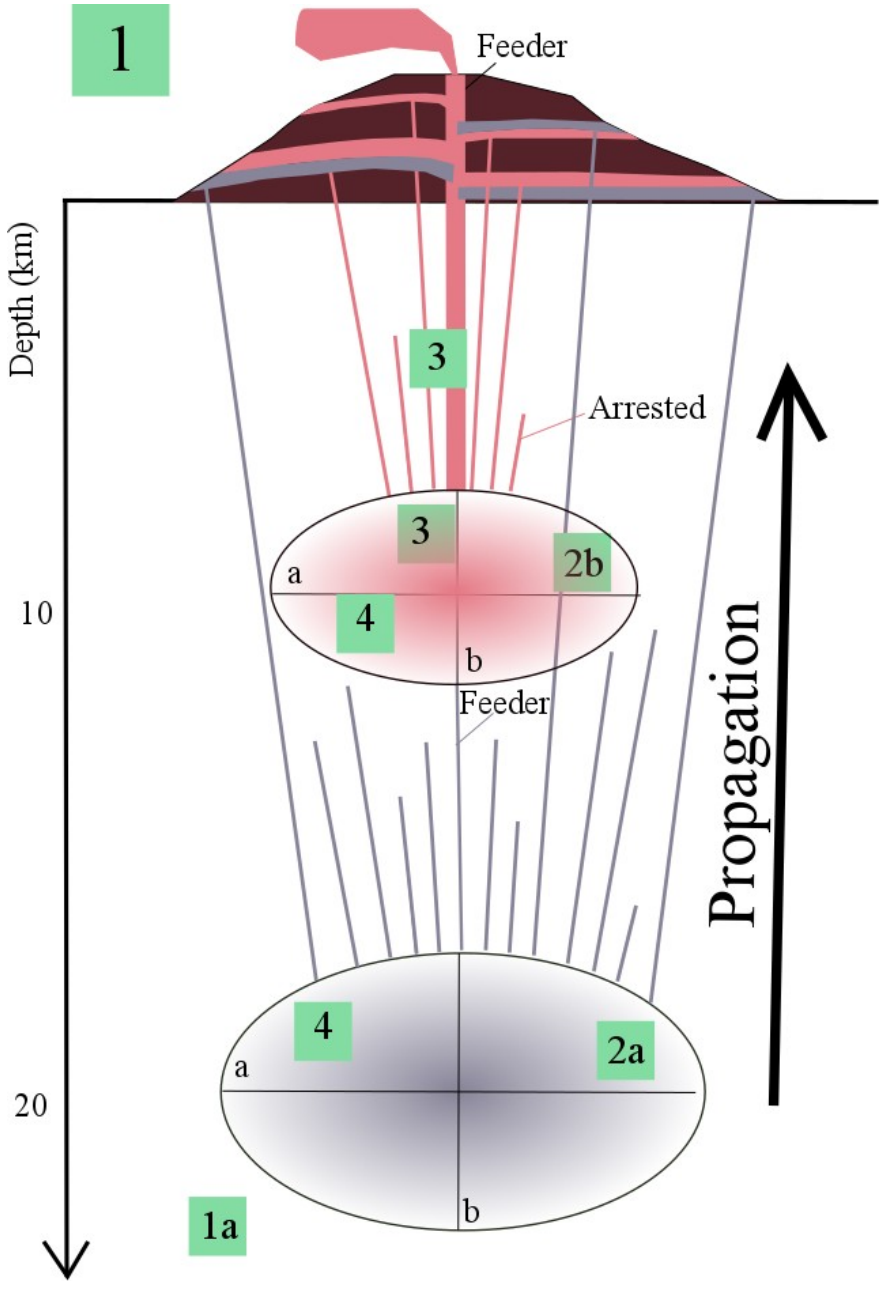

Fig. 7.4: Schematic vertical cross section of the transcrustal VPS of Santorini volcano. We propose the possible location of the observed components on the studied samples: 1a) antecrysts, 2)

phenocrysts (2a and b different populations), 3) xenoliths, 4) enclaves, (a and b are the ellipsoid geometrical terms with a>b). Not to scale.

4.2 Magma recycling and convection

Magma convection is a form of thermal recycling that is highly associated with magmatism (Marsh, 2009). While magma buoyantly rises it follows an adiabatic path. This adiabatic convection does not allow rocks to cool down so as a result they can propagate to the surface feeding the plumbing systems that lie atop. However, magma convection (mass fraction) is also associated with magma chamber processes. Forms of them are:

- Convective fractionation: Although fractional crystallisation is described as the separation of the melt from the crystal phase in dynamic systems (Bowen, 1928), a form of magma fractionation called convective fractionation is happening due to different magma diffusivities and heat (Sparks et al., 1984). Fractionation is recorded under the microscope by euhedral crystals, normal zoning, synneusis and glomerocrysts.
- Magma diffusion/advection: Heating could possibly remobilize the residual magma due to convection and potentially increase the magmatic pressure of the chamber (Murphy et al., 2000).

  Our macroscopic and microscopic study revealed the following components that record the aforementioned processes, which can be shown in a cross section at Figures 7.5 and 7.6:

2A) Synneusis: The mechanism of crystal aggregation formed by convection or advection in a magma chamber due to crystal growth (Cox et al., 1979). The magma is in near equilibrium

conditions and fractionates due to crystal settling. Synneusis is very often in Santorini dykes and host rock samples and the aggregates (glomerocrysts) range from 0.5-6mm. The glomerocrysts can be polymineralic, most commonly of plag+pyroxene+ol, or monomineralic (Fig. 7.5).

2B) Adcumulates: Monomineralic cumulates (xenoliths) were found in some dyke samples. They consist of plagioclase crystals and range from 0.5-1mm.

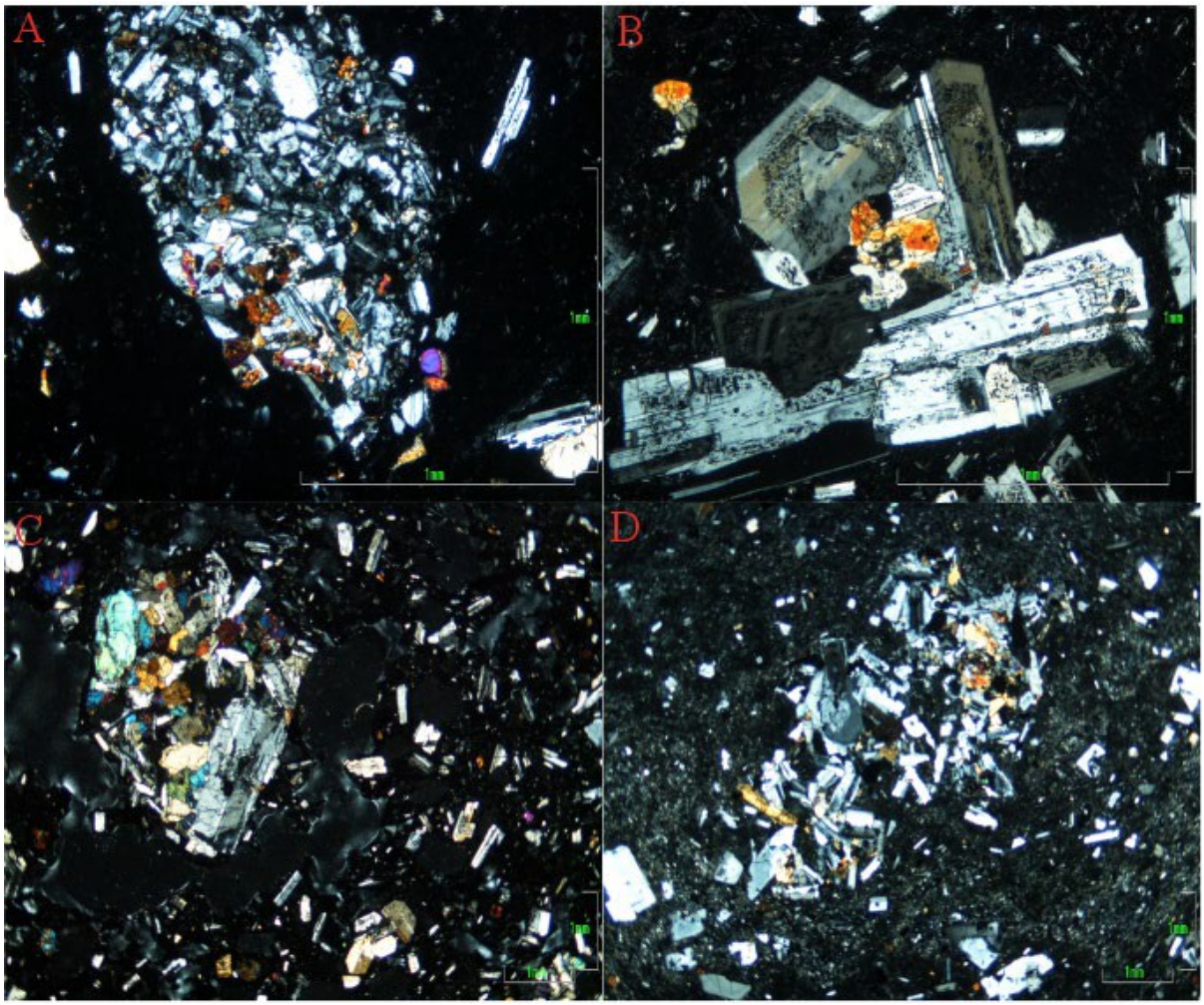

Fig. 7.5: XPL images of glomerocrysts in dykes and host rock samples from Santorini volcano. (A): A plag+ol+cpx glomerocrysts in Dyke_6, (B): plag+cpx aggregates in Dyke_1, (C): A

plag+cpx+ol+opx flomerocryst in a scoria sample, (D): plag+cpx glomerocryst in a Minoan ignimbrite sample.

We report the possible depth of origin of the magmas from the textural characteristics of the rocks (Humphreys et al., 2006; Holness et al., 2007; Jerram and Martin, 2008; Viccaro et al., 2010; Renjith, 2013) of the studied components in a vertical cross section of the Santorini VPS (Fig. 7.6).

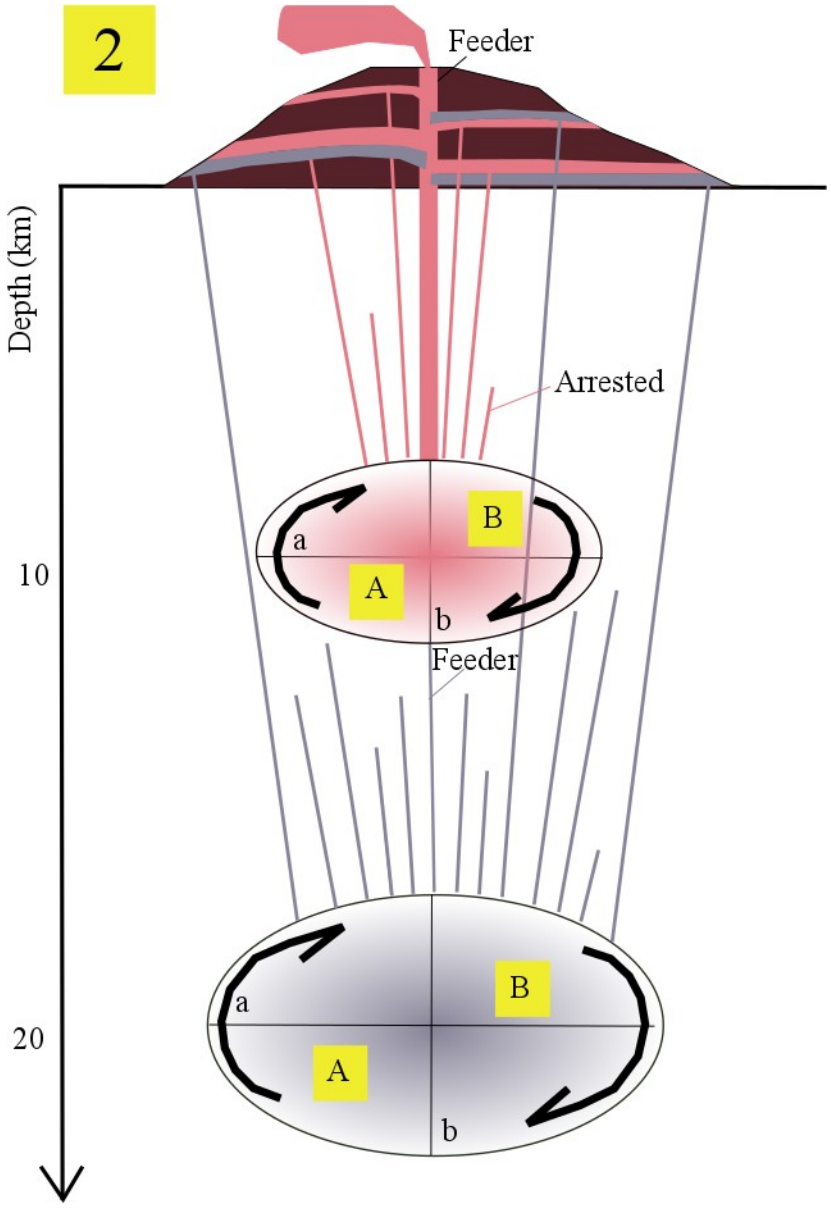

Fig. 7.6: Data of recycled material in the transcrustal VPS of Santorini volcano. (A) convection, (B) adcumulates in the magma chamber(s), (a and b are the semi-axes of the ellipsoidal chambers, with a>b). Not to scale.

4.3 Host-rock entrainment

The process that host rock is being incorporated in an advancing magma as xenoliths is called assimilation or host rock entrainment. If the assimilation is happening at the front of the propagating magma and crystallisation at the bottom is described as zone refining (Harris, 1957). Other ways that can produce assimilated magmas are hydrous fluids due to wall rock dehydration (Huppert and Sparks, 1985).

At Santorini, Druitt et al., (1999) and Bailey et al., (2009) showed that there is a positive correlation between the $^{87}Sr/^{86}Sr$ and SiO_2 content which demonstrates that AFC (assimilation and fractional crystallization) exists as the simple fractional crystallization processes could not always reproduce the exact products. The dykes have shown many signs of host rock assimilation which are reported below (Figs. 7.7 and 7.8):

I) Scoria entrainment: All the dykes that were sampled at Megalo Vouno mountain had accumulated scoria on their rims. During the propagation and cooling of the dyke margins, the scoria stuck on the dyke margins (Fig. 7.7A).

II) Xenoliths: A few dykes found to bear many xenoliths, parts of the intersected host rock such as scoria vesicles in a range of sizes.

III) Cumulates: a large cumulate of plag+cpx+opx+ol (8mm) was found only in one dyke sample.

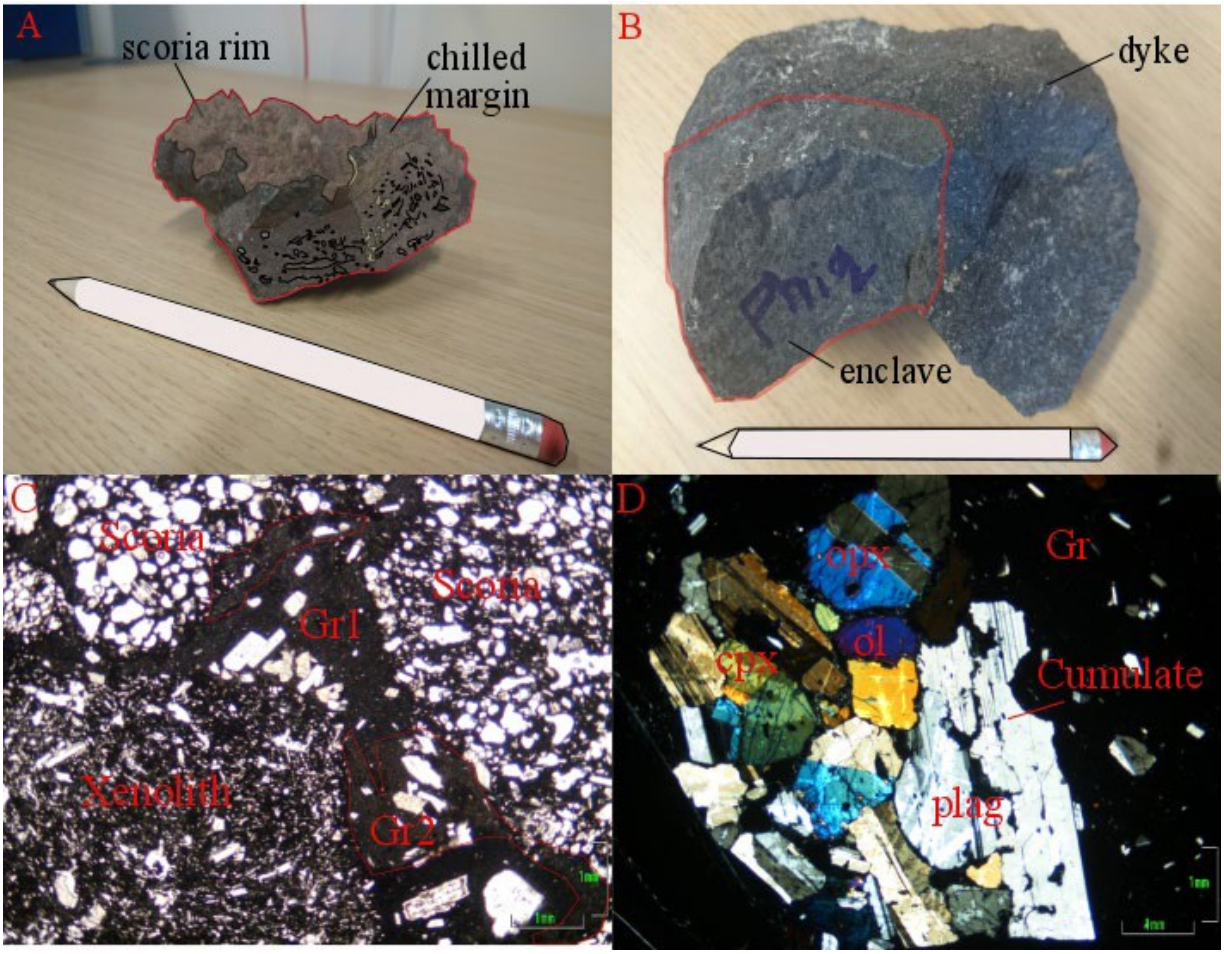

Fig. 7.7: Macroscopic samples of dyke rock. (A) A dyke sample (rim) where we observe a chilled margin, a highly viscous core and scoria material attached on the rims, (B) Dyke_77 sample (core) which includes an enclave cumulate, (C) PPL image of a dyke which consists of xenoliths, scoria and two types of groundmass a black and brown one, (D) A cumulate in a dyke sample.

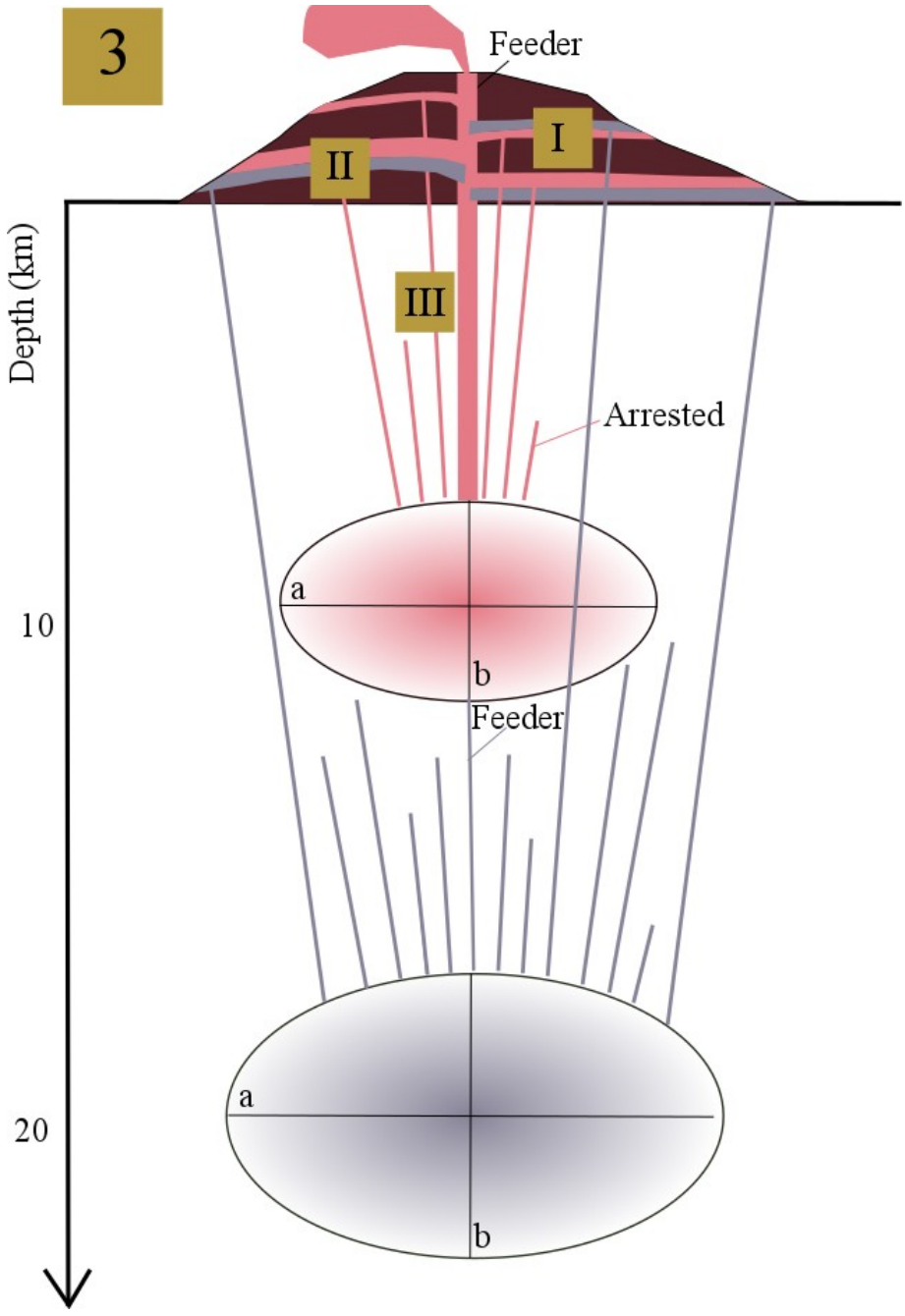

Fig. 7.8: Schematic illustration of the crustal components in the transcrustal VPS of Santorini volcano. (I) Scoria, (II) Xenoliths (III) Cumulates (a and b are the ellipsoid geometrical terms with a>b). Not to scale.

5. Discussion

Now we turn to a discussion of the results in terms of the amount and style of magmatic mixing and entrainment.

5.1 Magma mixing and recharge

The following interpretations are proposed for the following observed components:

1.1a) The antecryst found in the dykes reported parts of the crystal-dominated zones (mush) of the VPS of Santorini volcano. The amphibole crystal possibly belongs to the magmatic system that fed the earlier parts of the VPS, the Akrotiri lavas. Such an observation also reveals the deep origin of the amphibole-bearing dyke.

1.2) The phenocrysts' populations can give us insights on the magma chamber conditions of the VPS. We observed in all studied thin sections (n=70) two distinct plagioclase populations. The first one had large crystals with several textures (e.g. resorbed cores and sieve textures) that suggest mixing events, magma recharge and hybrid magmatism. In contrast the second plagioclase population consists of smaller euhedral crystals with normal zoning, which lack mixing textures. They implemented conditions of fractional crystallisation (crystal growth) and a magma chamber that is in equilibrium. The sizes of the crystals proposed that the large crystals formed firstly in a magma chamber that was near equilibrium. Then the magma intruded a second magma chamber, or a mixing event took place which is recorded in the textures of the first population (e.g. sieve texture, resorption). Later, magma differentiation occurred and a second population with smaller

crystals were formed while in the magma chamber. The dykes that include both populations probably visited the same magma chambers.

1.3) Several xenoliths were observed in the microscopic analysis. The plagioclase crystals in them either showed similarities with the first population or with the second. Such an observation could imply that the xenoliths are parts of other magmas which were in the magma chambers or incorporated from the hanging walls during fragmentation or were in the conduit and intruded the magma during ascent.

1.4) An enclave is material that originates from a magma chamber and gives insights into the variety of magmas of the VPS. The enclave found in the core of dyke_77 had a hypocrystalline groundmass, a seriate texture and included two different kind of xenoliths. The textural analysis proposed that the magma did not overlap with any studied host rock sample and probably belonged to an arrested magmatic event, or a not analysed subaerial deposit so far.

5.2 Magma recycling

Glomerocrysts are present in almost all studied dykes and host rock samples. We observed different type of combinations; many polymineralic aggregates such as plag+pyroxene+ol, plag+cpx+opx+ol, plag+cpx+ol, and monomineralic (adcumulates) plag+plag, ol+ol. Both record crystal growth and fractionation processes and could have been parts of different magma chambers during the evolution of the VPS.

5.3 Host rock entrainment

Host rock assimilation is a process that takes place particularly during dyke propagation in the crust or dyke emplacement. The dykes at the top of the caldera wall were emplaced in scoria, hence scoria entrainment was observed in all of them. Its crystals were often found in the vesicles. We calculated the amount of scoria xenoliths as function of distance from the dyke rim (wherever possible) and the results are shown in Figure 7.9. Scoria is incorporated into the magma up to 25cm from the wall-rock contact. The studied dyke has a thickness of 1.3m which means that it intruded approximately up to 40% from the dyke core.

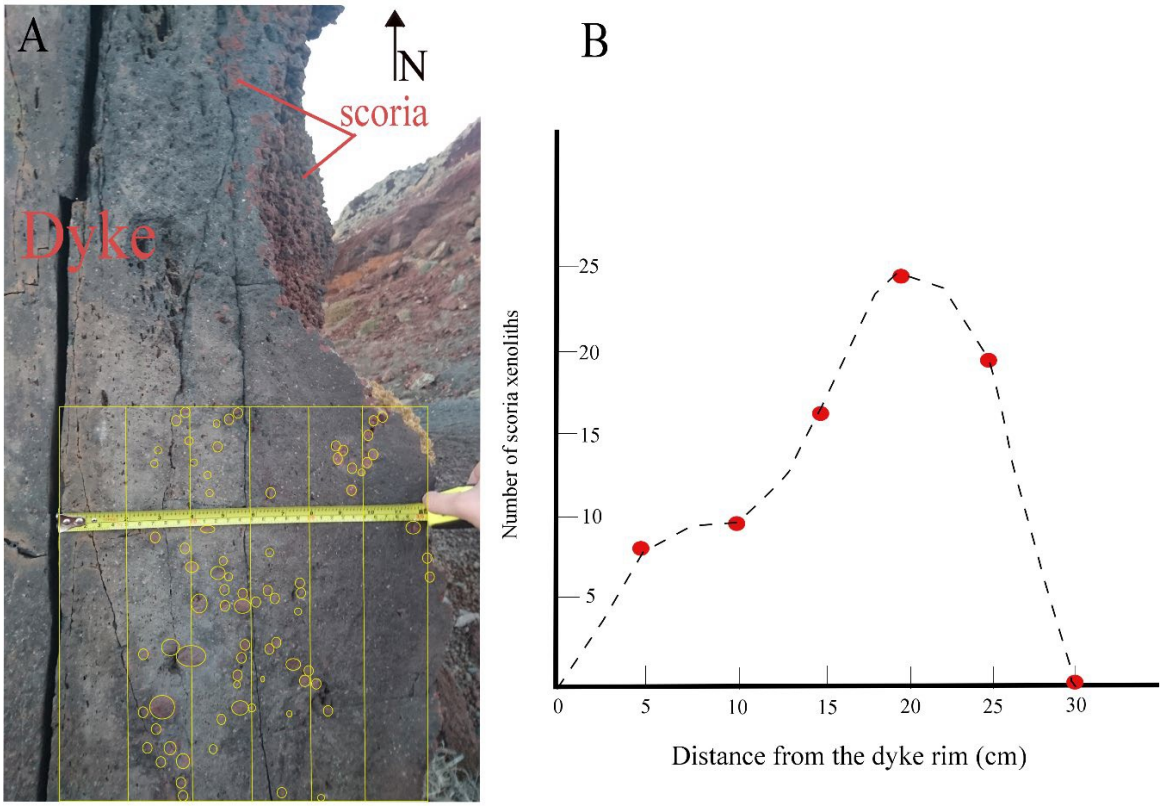

Fig. 7.9: Calculation of scoria entrainment into dyke_77. (A) We designed in situ a grid (30x30cm) and designed the number of the observed scoria xenoliths (red circular nodes) into the aphanitic groundmass. (B) Diagram reporting the frequency of the scoria xenoliths to the distance from the dyke rim (m).

We studied the spatial evolution of the host rock entrainment as recorded on the dykes sampled at the mountain level on Megalo Vouno. The dykes intruded the scoria cinder cones and has been emplaced after their formation and possibly belong to the Skaros local dyke swarm. The quantitative analysis of the scoria entrainment into the andesitic dyke (Fig. 7.9), the analysis of 9 petrographical thin section along the strike of the dyke as well across its rims and its core allowed us to map the location of the different components fossilised during the solidification of the magma in the dyke (Fig. 7.10).

In detail, we report that a magmatic enclave has been found in the core of the dyke indicating that magma mixing, or recharge has happened into either of the magma chambers that the specific dyke passed through during their lifespans and prior to dyke injection. However, that does not require that this was the absolute triggering dyke event. Glomerocrysts have also been found into the core but that could be expected as it is the result of magma convection/advection in a magma chamber.

In the dyke rims we found all kind of other components such as different populations of xenoliths, adcumulates, cumulates, and glomerocrysts. The components indicate i) magma flow into the magma chamber due to convection/advection, ii) host rock assimilation during magma ascent, and iii) host rock entrainment during emplacement.

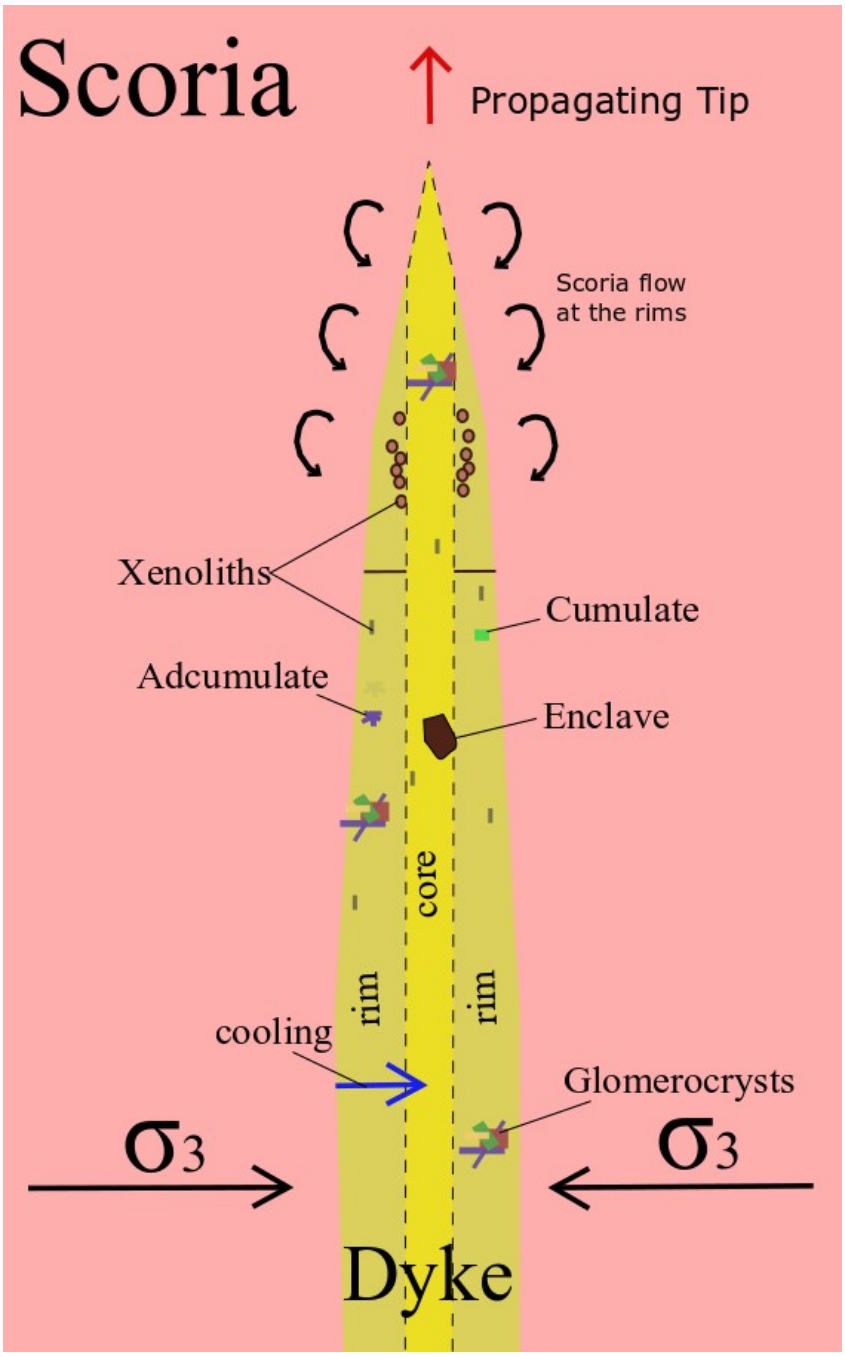

Fig. 7.10: Schematic illustration showing the flow and location of the studied components in a dyke. The red arrows show the displacement of the host-rock entrainment (scoria) during emplacement. The blue arrow shows the flow of the cooling (from the rim to the core). The black

arrows show the minimum principal compressive stress or tensile stress (σ_3). The red arrow shows the propagation of the dyke into the scoria. Not to scale.

5.4 Magma flow in the Santorini VPS

We studied in detail the different types of components found in the dykes and the host rock samples to define the possible origin, the direction of magma flow and to calculate the amount of host rock entrainment into the magma during emplacement.

In a transcrustal system (Fig. 7.11) magma moves vertically from the deep-seated reservoirs and shallow magma chambers to the surface to erupt. However, the material does not follow a single direction and hence a variety of processes act simultaneously to transport and even replace it inside the plumbing system. As such, the dykes, the interconnections of the permanent or ephemeral magma storages, bring parts of the deep system or shallow parts to the surface allowing us to observe their components, maturity and evolution.

This study revealed that phenocrysts of primary material and compositions (e.g. olivine, pyroxene), possibly antecrysts of amphibole are present in some of the dykes and could be interpreted as indications of magma upwelling from deep-seated reservoirs and deep fossilised parts of the magma mush. Enclaves, crystal synneusis and adcumulates found on dykes can be originated either by deep reservoirs or shallow ephemeral magma chambers. Materials that indicate a shallow magma chamber origin could be also phenocryst populations in general, monomineralic adcumulates but also xenoliths from the host rock. During the magma emplacement on the shallow

crust in heterogeneous segments (stiff/soft materials) the dykes can be found to assimilate magma cumulates from the conduit, xenoliths from the hanging walls, xenoliths and soft material (e.g. scoria in case of Santorini) (Fig. 7.11).

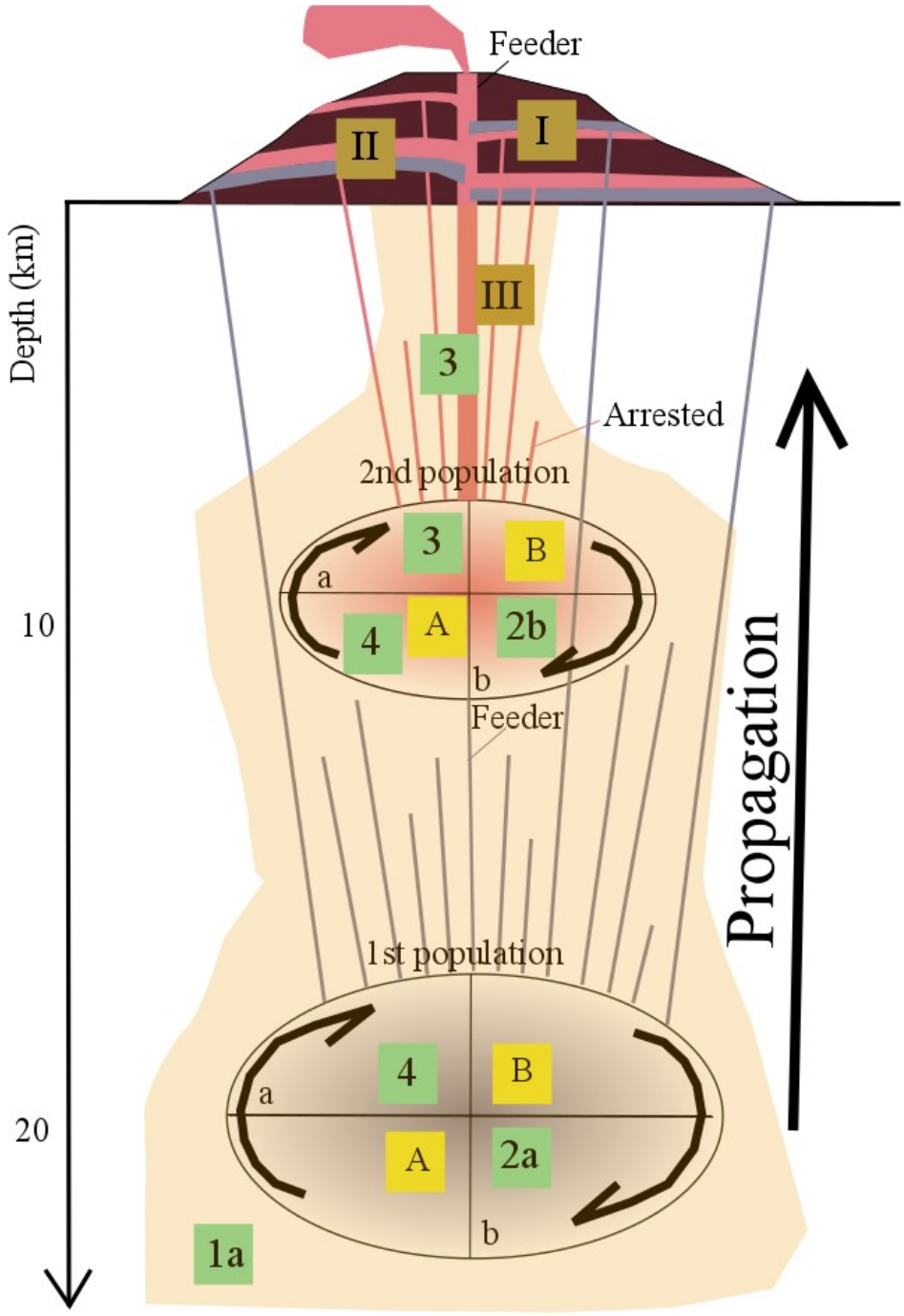

Fig. 7.11: Combined schematic illustration showing the vertical and lateral flow of the different studied components into the VPS on Santorini volcano after our coupled structural and petrological study. (A) crystal synneusis, (B) adcumulates in the magma chamber(s), 1a) antecrysts, 2) phenocrysts (2a and b different populations), 3) xenoliths, 4) enclaves, (I) Scoria, (II) Xenoliths (III) Cumulates (a and b are the ellipsoid geometrical terms with a>b). Not to scale.

6. Conclusions

The study revealed the following conclusions:

1) Dyke emplacement in heterogeneous crustal segments brings to the surface magmatic products assimilated with crustal materials from the stratigraphic horizons that it intersected. This is especially the case when the layers are very dissimilar (stiff-compliant such as lava-scoria). The magma in the dyke also exhibited evidence of magma replenishing from products of the underlying magma chamber such as xenocrysts, glomerocrysts, cumulates and even enclaves. In rare cases the magma in the dykes also contained adcumulates and antecrysts which are interpreted as deriving from the deeper parts of the magmatic mush.

2) Dyke emplacement in compliant materials can produce local material displacement of the host rock at the tips and the dyke margins allowing parts of the host rock to intrude into the magma and crystallise inside it. Observations in dyke segments with scoria entrainment shows that the host rock material can be found up to 30cm from the dyke margin with a concentration maximum at around 20cm (or in a general sense, at around 10% of the total dyke thickness).

3) Observed textures in the abundant minerals (e.g. plagioclase) show that convection or advection are the flow processes that rejuvenate magma chambers and could give information about the time that a new batch of magma resided in any one chamber as well as their physiochemical conditions.

4) The emplacement of a dyke in a heterogeneous crustal segment could change the final composition of the subaerial deposits and brought stratigraphic intersecting materials to the surface (Fig. 7.11). The main material that became entrained in the magma in the Santorini dykes is scoria which not only altered the composition at the rims but possibly the viscosity and mechanical properties of the magma. This scenario should be studied with more detail in the future.

The results are important for further understanding and considering the individual path that any dyke has taken to reach the surface. We hence recommend that future studies of dykes should take such information into account.

REFERENCES

Anderson, E.M., (1936). The dynamics of formation of cone sheets, ring dykes and cauldron subsidences. Proceedings of the Royal Society of Edinburgh, 56, 128-163.

Anderson, A.T., (1984). Probable relations between plagioclase zoning and magma dynamics, Fuego Volcano, Guatemala. American Mineralogist 69, 660–676.

Andújar, J., Scaillet, B., Pichavant, M., Druitt, T. H., (2015). Differentiation conditions of a basaltic magma from Santorini and its bearing on basalt–andesite to andesite magma production in arc settings. Journal of Petrology 56, 765–794.

Annen, C., Blundy, D.J., Leuthold, J., Sparks, R.S.J., (2015). Construction and evolution of igneous bodies: towards an integrated perspective of crustal magmatism. Lithos, 230, 206-221

Bachmann, O., Bergantz, G.W., (2004). On the origin of crystal-poor rhyolites: extracted from batholithic crystal mushes. J. Petrol. 45 (8), 1565–1582

Bailey, J.C., Jensen, E., Hansen, A., Kann, A., Kann, K., (2009). Formation of heterogeneous magmatic series beneath North Santorini, South Aegean island arc, Lithos, 110, 20–36.

Becker, G.F., (1897). Fractional crystallization of rocks. American Journal of Science 4, Series 4, 257-261

Blake, S., (1981). Volcanism and the dynamics of open magma chambers. Nature, 289, 783-785.

Bowen, N.L., (1928). The evolution of the igneous rocks: Princeton, New Jersey, Princeton University Press, New York

Cadoux, A., Scaillet, B., Druitt, T.H., Deloule, E., (2014). Magma storage conditions of large Plinian eruptions of Santorini. Journal of Petrology, 55, 1129–1171

Cashman, K.V., Sparks R.S.J., (2013). How volcanoes work: A 25-year perspective. Geological Society of America Bulletin 125, 664–690.

Cashman, K.V., Giordano, G., (2014). Calderas and magma reservoirs. J. Volcanol. Geotherm. Res. 288, 28–45

Cashman, K.V., Sparks, R.S.J., Blundy, J., (2017). Vertically extensive and unstable magmatic systems: A unified view of igneous processes, Science, Vol. 355, 30-55

Cassidy, M., Castro, J.C., Helo, C., Troll, V., Deegan, F., Muir, D. Neave, D.A., Meuller, S.P., (2018). Volatile dilution during magma injections and implications for volcano explosivity, Geology 12, 1027-1030

Caricchi, L., Simpson, G., Schaltegger, U., (2016). Estimates of volume and magma input in crustal magmatic systems from zircon geochronology: the effect of modelling assumptions and system variables: Frontiers in Earth Science, 48, 4

Cox, K.G., Bell, J.D., Pankhurst, R.J., (1979). The interpretation of igneous rocks. London: Allen and Unwin

Daly, R. A., (1911). The nature of volcanic action. Proc. Am. Acad. Arts Sci. 47, 48–119.

Delesse, A., (1848). Pour determiner la composition des Roches. Annales des Mines, Serie 4, 379-88.

Di Genova, D., Kolzenburg, S., Wiesmaier, S., Dallanave, E., Neuville, D.R, Hess, K.U., Dingwell, D.B., (2017). A compositional tipping point governing the mobilization and eruption style of rhyolitic magma. Nature volume 552, 235–238.

Druitt, T.H., Edwards, L., Mellors, R.M., Pyle, D.M., Sparks, R.S.J., Lanphere, M., Davis, M., Barriero, B., (1999). Santorini Volcano. Geological Society Memoir No. 19, 165.

Druitt, T. H. Costa, F., Deloule, E,. Dungan, M., Scaillet, B., (2012). Decadal to monthly timescales of magma transfer and reservoir growth at a caldera volcano. Nature 482, 77–80

Druitt, T. H., (2014). New insights into the initiation and venting of the Bronze-Age eruption of Santorini (Greece), from component analysis. Bulletin of Volcanology 76, 794

Fabbro, G.N., Druitt, T.H., Scaillet, S., (2013). Evolution of the crustal magma plumbing system during the build-up to the 22-ka caldera-forming eruption of Santorini (Greece), Bull. Volcanol., 75, 1– 22.

Fabbro, G.N., (2014). The timescales of magmatic processes prior to a caldera-forming eruption. Doctoral thesis, Université Blaise Pascal, Clermont-Ferrand.

Geshi, N., Kusumoto, S., Gudmundsson, A., (2010). Geometric difference between non-feeder and feeder dikes. Geology 38, 195-198

Gonnermann, H.M., Manga, M., (2013). Dynamics of magma ascent in the volcanic conduit in Modeling Volcanic Processes: The physics and mathematics of volcanism, (eds) Sarah A. Fagents, Tracy K. P. Gregg, Rosaly M. C. Lopes, 55-84.

Gudmundsson, A., (1987). Formation and mechanics of magma reservoirs in Iceland. Geophysical Journal of the Royal Astronomical Society, 91, 27-41.

Gudmundsson, A., (1988). Formation of collapse calderas. Geology, 16, 808-810.

Gudmundsson, (1998). Magma chambers modelled as cavities explain the formation of rift zone central volcanoes and their eruption and intrusion statistics J. Geophys. Res., 103, 7401-7412

Gudmundsson, A., (2002). Emplacement and arrest of sheets and dykes in central volcanoes. J. Volcanol. Geotherm. Res. 116, 279–298

Gudmundsson, A., (2003). Surface stresses associated with arrested dykes in rift zones Bull. Volcanol., 65, 606-619

Gudmundsson, A., (2006). How local stresses control magma-chamber ruptures, dyke injections, and eruptions in composite volcanoes Earth Sci. Rev., 79, 1-31

Gudmundsson, A., (2011). Rock fractures in geological processes. Cambridge University Press, Cambridge.

Gudmundsson, A., (2012). Magma chambers: formation, local stresses, excess pressures, and compartments. Journal of Volcanology and Geothermal Research, 237-238, 19–41

Gudmundsson, (2016). The mechanics of large eruptions. Earth Sci. Reviews. 163, 72-93

Harris, P.G., (1957). Zone refining and the origin of potassic basalts. Geochim. Cosmochim. Acta 12, 195-208.

Hildreth, W., (1981). Gradients in silicic magma chambers: implications for lithospheric magmatism J. Geophys. Res., 86, 10153-10192

Holness, M. B., Tegner, C., Nielsen, T. F., Stripp, G., Morse, S. A. (2007). A textural record of solidification and cooling in the Skaergaard intrusion, East Greenland. Journal of Petrology, 48, 2359–2377.

Hooft, E.E., P. Nomikou, D.R. Toomey, D. Lampridou, C. Getz, M. Christopoulou, D. O'Hara, G.M. Arnoux, M. Bodmer, M. Gray, B.A. Heath, and B.P. VanderBeek, (2017). Backarc tectonism, volcanism, and mass wasting shape seafloor morphology in the Santorini-Christiana-Amorgos region of the Hellenic Volcanic Arc, Tectonophysics, 712-713, 396-414

Huijsmans, J.P.P., (1985). Calc-Alkaline Lavas from the Volcanic Complex of Santorini, Aegean Sea, Greece: A Petrological, Geochemical and Stratigraphic Study, Utrecht Univ., Utrecht, Netherlands.

Humphreys, M.C.S., Blundy, J.D., Sparks, S.J., (2006). Magma evolution and open-system processes at shiveluch volcano: insights from phenocryst zoning Journal of Petrology, 47, 2303-2334

Huppert, H.E., (1982). The propagation of two-dimensional and axisymmetric viscous gravity currents over a rigid horizontal surface, J. Fluid Mech. (1982), 121, 43-58

Huppert, H.E., Sparks R.S.J., (1985). Cooling and contamination of mafic and ultramafic magmas during ascent through the continental crust. Earth Planet. Sci. Lett. 74, 371-86

Jerram, D.A., Martin, V.M., (2008). Understanding crystal populations and their significance through the magma plumbing system, in Dynamics of Crustal Magma Transfer, Storage and Differentiation, eds C. Annen and G. F. Zellmer (London: Geological Society), 133–148

Johnston, E.N., Sparks, R.S.J., Nomikou, P., Livanos, I., Carey, S., Phillips, J.C., Sigurdsson, H., (2015). 'Stratigraphic relations of Santorini's intracaldera fill and implications for the rate of post-caldera volcanism', Journal of the Geological Society, 172, 323-335

Jolivet, L., Faccenna, C., Huet, B., Labrousse, L., Le Pourhiet, L., Lacombe, O., Lecomte, E., Burov, E., Denèle, Y., Brun, J.-P., Philippon, M., Paul, A., Salaün, G., Karabulut, H., Piromallo, C., Monié, P., Gueydan, F., Okay, A. I., Oberhänsli, R., Pourteau, A., Augier, R., Gadenne, L., Driussi, O., (2013). Aegean tectonics: strain localisation, slab tearing and trench retreat. Tectonophysics, 597–598, 1–33.

Machado, F., (1974). The search for magmatic reservoirs L. Civetta, P. Gasparini, G. Luongo, A. Rapolla (Eds.), Physical Volcanology, Elsevier, Amsterdam, 255-273

McKenzie, D.P., (1972). Active tectonics of the Mediterranean Region Geophys. J.R. astr. Soc. 30 , 109.

Marsh, B.D., (2009). Magmatism, Magma and Magma chambers (ed.) Watts A. Crust and Lithosphere dynamics, Elsevier, 275-335.

Mogi, K., (1958). Relations between eruptions of various volcanoes and the deformations of the ground surfaces around them, Bull. Earthquake Res. Inst. Univ. Tokyo, 36, 99-134

Murphy, M.D., Sparks, R.S.J, Barclay, J., Carroll, M.R., Brewer, T.S., (2000). Remobilization of andesite magma by intrusion of mafic magma at the Soufrière Hills Volcano, Montserrat, West Indies, Journal of Petrology, 41, 21-42

Neave, D., Namur, O., Shorttle, O. & Holtz, F., (2019). Magmatic evolution biases basaltic records of mantle chemistry towards melts from recycled sources, In: Earth and Planetary Science Letters. DOI: 10.1016/j.epsl.2019.06.003

Newhall C.G. Dzurisin D., (1988). Historical unrest at large calderas of the world: U.S. Geological Survey Bulletin 1855, 1108

Newhall, C.G, Self, S., Robock, A., (2018). Anticipating future Volcanic Explosivity Index(VEI) 7 eruptions and their chilling impacts. Geosphere, 14, 572-603

Nomikou, P., Papanikolaou, D., Alexandri, M., Sakellariou, D., Rousakis, G., (2013). Submarine volcanoes along the Aegean volcanic arc, Tectonophysics, 597, 123–146.

Nomikou, P., Hübscher, C., Ruhnau, M., and Bejelou, K. (2016). Tectonophysics Tectono-stratigraphic evolution through successive extensional events of the Anydros Basin, hosting Kolumbo volcanic field at the Aegean. Tectonophysics 671, 202–217

Perugini, D. Poli, G. (2004). Analysis and numerical simulation of chaotic advection and chemical diffusion during magma mixing: petrological implications, Lithos, 78, 43-66

Phillipson, G., Sobradelo, R., Gottsmann, J., (2013). Global volcanic unrest in the 21st century: An analysis of the first decade. JVGR, 264, 183-196

Pe-Piper, G., Piper., D.J.W., (2002). The igneous rocks of Greece: anatomy of an orogen. Beitrage zur Regionalen Geologie der Erde. Berlin, Stuttgart: Gebruder Borntrager, 573

Pe-Piper, G., Piper, D.J.W., Perissoratis, C., (2005). Neotectonics and the Kos Plateau Tuff eruption of 161 ka, South Aegean arc Mar. Geol., 139, 315-338

Piper, D.J.W., Pe-Piper, G., Perissoratis, C., Anastasakis, G., (2007). Distribution and chronology of submarine volcanic rocks around Santorini and their relationship to faulting, 291, 99-111

Putirka, K., (1997). Magma transport at Hawaii: inferences based on igneous thermobarometry. Geology 25, 69–72

Renjith, M.L., (2013). Micro-textures in plagioclase from 1994–1995 eruption, Barren Island Volcano: Evidence of dynamic magma plumbing system in the Andaman subduction zone, Geoscience Frontiers, 5, 113-126

Segall, P., Llenos, A.L. Yun, S.H, Bradley, A.M., Syracus , E.M., (2013). Time-dependent dike propagation from joint inversion of seismicity and deformation data. J. Geophys. Res., 118

Sparks, R.S.J., Sigurdsson, H., Wilson, L., (1977). Magma mixing: A mechanism for triggering acid explosive eruptions: Nature

Sparks R. S. J., Huppert H. E., Turner J.S., (1984). The fluid-dynamics of evolving magma chambers. Philosophical Transactions of the Royal Society of London Series a – Mathematical Physical and Engineering Sciences 310, 511.

Sparks, S., Annen, C. J., Blundy, J., Cashman, K., Rust, A., & Jackson, M.D., (2019). Formation and dynamics of magma reservoirs. Philosophical Transactions of the Royal Society A: Mathematical, Physical and Engineering Sciences, 377, 2139

Tait S.R., (1988). Samples from the crystallizing boundary layer of a zoned magma chamber, Contributions to Mineralogy and Petrology, 100, 470-483

Tepley, F. J. III, Davidson, J.P., Clynne, M.A., (1999). Magmatic interactions as recorded in plagioclase phenocrysts of Chaos Crags, Lassen Volcanic Center, California. Journal of Petrology 40, 787–806.

Tibaldi, A., (1992). The role of transcurrent intra-arc tectonics in the configuration of a volcanic arc. Terra Nova, 4, 567–577.

Tibaldi, A., (2015). Structure of volcano plumbing systems: a review of multi-parametric effects. J. Volcanol. Geotherm. Res. 298, 85–135

Tsapanos, T.M., Galanopoulos, D., Burton, P.W., (1994). Seismicity in the Hellenic Volcanic Arc: relation between seismic parameters and the geophysical fields in the region. Geophysical Journal International, 117, 677–694

Viccaro, M., Giacomoni, P.P., Ferlito,C., Cristofolini, R., (2010). Dynamics of magma supply at Mt. Etna volcano (Southern Italy) as revealed by textural and compositional features of plagioclase phenocrysts, Lithos, 116, 77– 91.

Walker, (1974). The structure of eastern Iceland. In: L. Kristjansson (ed), Geodynamics of Iceland and the North Atlantic Area. Reidel, Dordrecth, 177-188.

Walker, G.P.L., (1979). A volcanic ash generated by explosions where ignimbrite entered the sea. Nature 281, 642-646

Zellmer, G., Turner, S. & Hawkesworth, C., (2000). Timescales of destructive plate margin magmatism: new insights from Santorini, Aegean volcanic arc. Earth and Planetary Science Letters, 174, 265-281.

Zellmer, G.F., and Annen, C., (2008). An introduction to magma dynamics. Geological Society, London, Special Publications, 304, 1-13

Chapter 8. Discussion, critical evaluation and future work

In this chapter, I bring together and discuss all the ideas that arose during this study and address answers to the main questions reported on the thesis aims and objectives.

This study focused mainly on the following topics:

1) Dyke propagation and arrest at Santorini volcano through a combination of field studies and finite element numerical modelling (chapter 4).

2) Interaction between dykes and faults at Santorini volcano through a combination of field observations and finite element numerical modelling (chapter 5).

3) The geological and volcanotectonic evolution of the Santorini dyke swarm and the reconstruction of magmatic emplacement processes through a combination of field studies, petrogenetic analysis (chapter 6)

4) The evolution of the crustal volcanic plumbing system of Santorini volcano to discern the relative amounts of magma assimilation and host rock entrainment associated with dyke propagation in heterogeneous volcanoes through a combination of field and petrogenetic studies (chapter 7)

5) Conceptualising and quantifying the likelihood of a dyke reaching the

surface to feed a volcanic eruption (chapter 3)

6) Reconstructing the Peristeria lava flows and the geological history of the studied area (chapter 3)

7) Creating a petrographic and geochemical database of the studied dyke segments and host rock specimens (chapter 3)

In this chapter, I describe the cutting-edge findings reported in this thesis in relation to the questions posed in Chapter 1:

Q1: Towards a reconstruction (geological history) of the early northern caldera wall. How were the structures in the northern part of the caldera formed?

The enormity of the Bronze Age eruption, which was associated with the most recent collapse caldera-forming event at Santorini, focused substantial scientific interest of both the volcanological and archaeological community (Marinatos, 1939; Heiken and McCoy, 1984; Druitt and Francaviglia, 1992; Druitt et al., 1999). The caldera collapse altered the geomorphology of the island to its present form, which left several steep cliffs exposed and ideal for in situ geological studies. A simplified stratigraphy of the northern caldera wall is presented in

Figure 8.1. We hypothesise that at least five caldera collapse events formed the current morphology of the Santorini islands, as is discussed in Chapters 3 and 6.

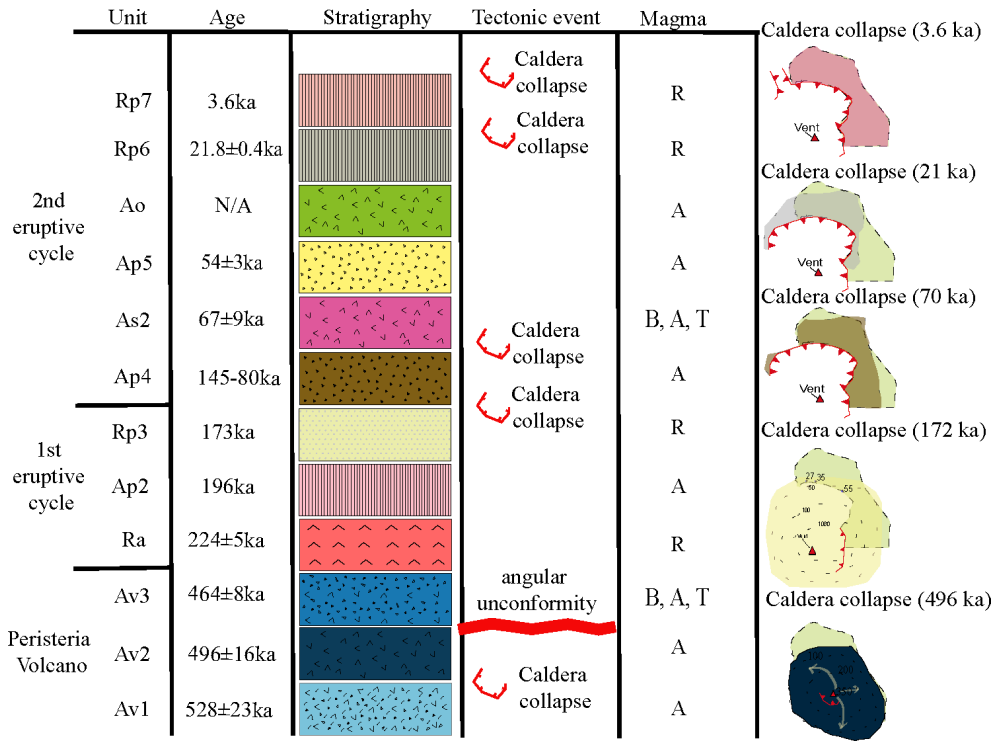

Fig. 8.1: The stratigraphy of the northern caldera wall, where magma type. A means andesite, B – basalt, D – dacite or combinations of all three. Ages are taken from Druitt et al. (1999); stratigraphic symbolism from the BGS d at ab as e (http:// bgs.ac.uk), faults (172-3.6ka) from Druitt et al. (1999).

In terms of the observed dyke swarm in the northern caldera wall, we propose, in Chapter 6, that at least five dyke clusters/groups (subswarms) were formed and overlapped in time. These swarms were associated with the construction of the main shields and stratocones that developed during the Peristeria volcano and the two explosive cycles (Ra – Rp3 and Ap4 – Rp7). Each dyke swarm produced

a set of distinct events that generated subsets of both inclined sheets and sub-vertical dykes of similar compositions.

Q2: Are Santorini dyke swarms locally or regionally controlled? And to what extent did the dykes interact with tectonic structures such as faults?

Previous studies (Mountrakis et al., 1996; Sakellariou et al., 2013; Nomikou et al., 2013) suggest that the dykes follow exclusively NE-SW pre-existing fractures (normal and strike-slip faults) that formed on the caldera wall because of the general extensional geodynamic setting of the central part of the Aegean. Other volcanological studies report that the dyke swarm (here dyke swarms) was associated with basement faults that also controlled the magma ascent and the location of the eruptive vents of the different volcanic eruptions (Druitt et al., 1999).

During this study, we suggest that the emplacement of the dyke swarms is driven predominantly by magmatic overpressure and the arrangement of source magma chambers. More specifically, we suggest that the dykes make their paths in the Earth's crust through magma-pressure driven fracturing (hydrofracturing) and only rarely use major pre-existing crustal weaknesses such as faults. More specifically, we suggest the dykes that constitute the swarms could have been

deflected into the faults only when the latter were active during their emplacement. The abundant field data – where dykes dissect numerous marker layers – shows that the vast majority of the dykes occupy pure extension fractures (mode I cracks) and thus do not follow faults (shear fractures). We made several numerical models of active and inactive dyke-fault interactions (chapter 5) which also show that dykes enter faults to use them as parts of their paths only under special mechanical conditions. Our results are in agreement with detailed field studies of dykes elsewhere, such as in Iceland and the Canary Islands, which show that dykes rarely deflect into crustal faults (Gudmundsson, 2011). In a smaller note, other volcanotectonic studies have reported the importance of gravity and the volcano's load in dyke propagation in areas with multiple caldera collapse events (Tibaldi, 1996, 2001). The effect of gravity forces have not been studied during this study as the data after the collapse events are restricted and do not allow us to calculate either the actual DRE of the erupted magma volume or the morphology of the island apart from speculations. Another reason is that the current analytical procedure takes gravity into account in the calculation of magmatic overpressure (Gudmundsson, 2011).

Chapters 4 and 5 focused on the parameters that produced stress barriers and other dyke traps in the host rock during dyke ascent and the interactions between dykes and/or inclined sheets and pre-existing fractures. Using realistic modelling conditions, the results show that the magmatic overpressure and the regional tectonics (extension or compression) may encourage dyke propagation to

shallow levels in the crust. In contrast, understandably, dyke traps tend to arrest the dykes.

More specifically, the study revealed that dyke arrest in the crust is affected by the thickness of the layers and to a lesser extent by the changes in the sequence of the layers and the thickness of the shallow crust. Similarly, dyke deflection is affected by the geometry (angle) of the dyke-fault interactions, the thickness of the fault zone, and, in particular, the stiffness of the fault core. As a result, the study has important implications on the magma movement in the crust and hence provided insights on this multi-parametric process (Fig. 8.2).

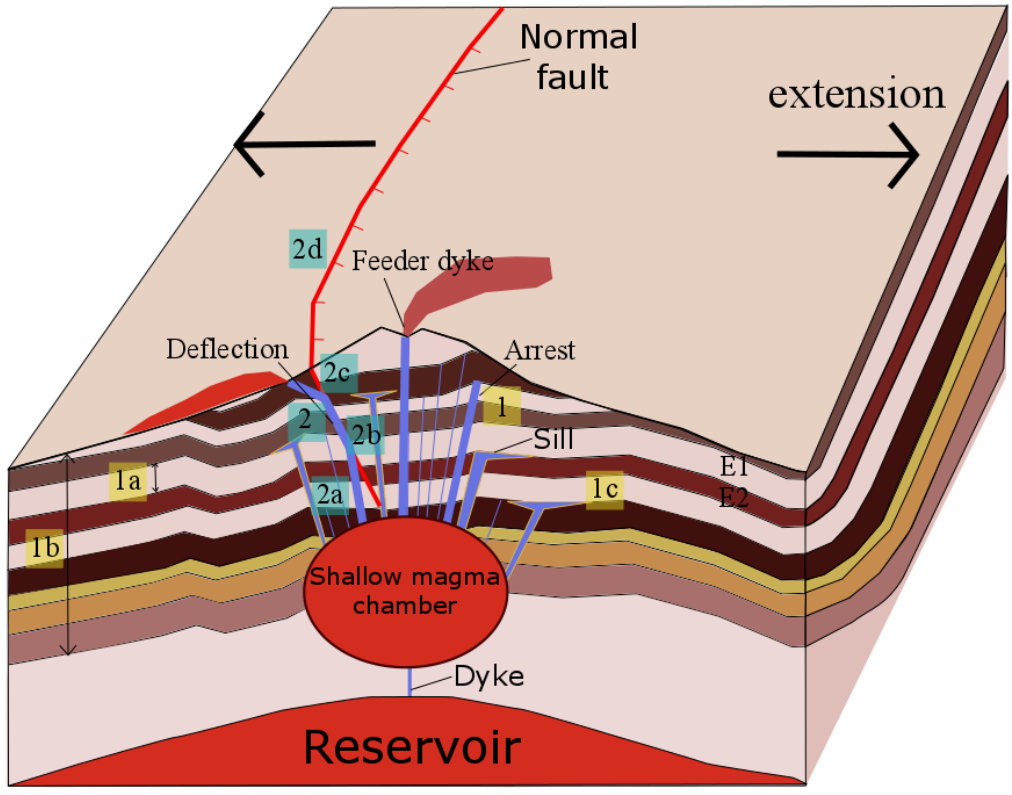

Fig. 8.2: Illustration showing a two-magma chamber plumbing system (a double

magma chamber with a cylindrical shallow one) which hosts a radial dyke swarm. The latter consists of dykes, which follow different paths often ending in (1) dyke arrest or (2) dyke deflection as studied in this thesis with finite element numerical modelling. The study shows that in addition to the stiffness of the layers and the regional tectonic setting other parameters can also control magma ascent in the crust such as the thickness of the layers (1a), the thickness of the crust (1b), the stratigraphic sequence (1c), the geometry of the dyke-fault interactions (2a), the thickness of the dyke and the fault (2b), the length of the fault (2c), the stiffness of the fault core (2d). Not to scale.

For Santorini volcano, our multidisciplinary study suggests that the dyke swarm is composed of at least five subgroups (subswarms) that have distinct compositions and either initiated from the same magma chamber location in different time periods or from different locations (compartments of the magma chamber) hence their variable composition but same range of magmatic overpressure (Fig. 8.3).

The study reveals that the Peristeria and Skaros dyke swarms are radial as shown by the dykes' attitude and location (Fig. 8.2). The Simandiri shield, however, was possibly fed by flank eruptions (Druitt et al., 1999) associated with a local dyke population controlled by a volcanotectonic lineament in the vicinity of the magma chamber. After the deposition of the Middle tuffs (at 80 ka) a pull-apart graben formed at the north-eastern part of the caldera wall. Four m-scale normal

faults dissected the previous stratigraphy and controlled the emplacement of a very low number of dykes (6 of the 91 dyke segments were observed to permeate the fault zones) that were formed as a part of the Skaros and the Therasia dome complex. We propose that the observed high frequency of NE-SW (N 20˚-40˚) striking dykes were not controlled by the regional faults but from the local stresses (σ_3 minimum principal stress) that controlled the extension in the Aegean and the plumbing system respectively.

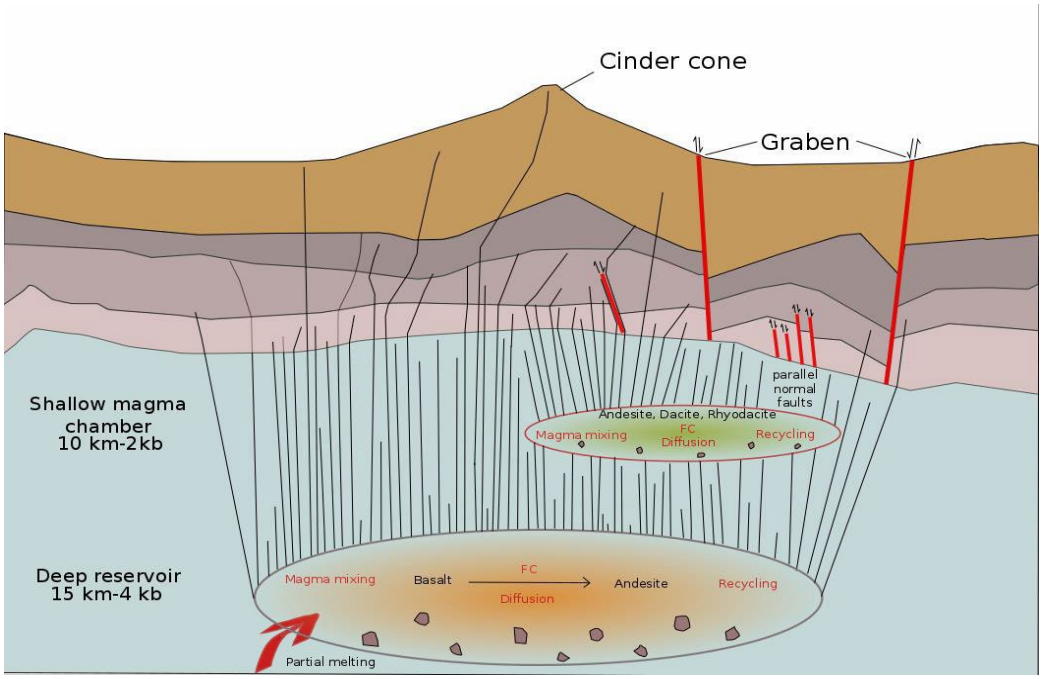

Fig. 8.3: Schematic illustration showing a cross section of the dyke swarm and the volcanotectonic evolution of the northern caldera wall. The depth data ofthe magma chambers and their composition are derived from Andujar et al. (2015) and Cadoux et al. (2014). Not to scale.

Q3: What is the probability that an injected dyke erupts at Santorini volcano?

The study of Santorini volcano, particularly the results in Chapter 3, suggest that many dykes became arrested. In contrast, others propagated through all the layers, and some of the latter may have made it to the surface to erupt. For the dykes that made it to the shallow depths as seen in the northern caldera wall, at least 30% became arrested. Some of the remaining 70% of the dykes appear to cut through all the exposed layers, but it is still unknown how many of these may have reached the surface to erupt. It is essential, however, to report the limitations of the statistical analysis of dykes in Santorini volcano:

1) Signs of dyke arrest are not very commonly observed in the field (tips that thin out, blunt tips or fingers).

2) On their way to the surface, the dykes usually propagated as segments, and it was not possible to follow many of the segments along strike into the caldera wall and determine their fates.

3) The host rock is highly heterogeneous and anisotropic so that dyke segments commonly change their attitude without necessarily being arrested – although perhaps appearing to be so from a distance.

The northern caldera wall dyke swarm consists of rather few dyke segments (n=91). For a more detailed statistical analysis using similar methodologies, a

swarm with many hundreds of dykes would be preferable.

Q4: What insights can multidisciplinary studies (i.e. petrography and structural geology) provide in the goal of understanding dyke arrest and deflection in the shallow crust?

Attempts to understand and ultimately forecast dyke propagation depend on the use of fracture mechanics, also using analogue, analytical, and numerical modelling. But active dyke injection is rarely observed in real-time. However, when such an event does occur, part of the process can be studied on the ground surface with the use of geodetic (LiDAR) techniques and, more generally, seismic methods. As yet we lack widely accepted forecasting tool that can link the application of fracture mechanics to predicative crustal fracture problems, such as dyke propagation.

The reason for this is partly because dyke propagation, or any hydraulically driven fracture propagation, is controlled by many parameters, the details of which are typically unknown for a given volcano. The number of possible paths for a propagating dyke is thus very high and difficult to predict the selected one for a particular dyke. A new methodology is needed to allow us to combine observation and experimentation on dyke propagation and investigate the

parameters that affect all the dominant processes and parameters. Unfortunately, crustal-scale field analyses in eroded stratovolcanoes that host calderas and dyke swarms have not been very common, partly due to the lack of adequate exposure.

Q5: Deciphering dyke fed volcanism in stratovolcanoes. Which methods are needed for reconstructing volcanic plumbing systems?

Understanding the dominant processes that occurred at depth and recording the in-situ evolution of a volcano is difficult. Data from unrest episodes in well-monitored calderas report that the unrest results in an eruption in 54% of events at calderas with predominantly mafic magmas and only 38% of calderas with predominantly silicic magmas (Newhall and Dzurisin, 1988). A more recent database that investigated similar unrest but in different types of volcanoes found that, again, around 47% of the unrest events result in a volcanic eruption (Phillipson et al., 2013). If these percentages reflect the percentage of dykes that become feeders for those eruptions, then it follows that the residual percentages belong, at least partly, to dykes that have become arrested or stalled in the crust.

Volcanological studies to date have mainly focused on collecting data from eruptive products, for example, lavas or pyroclastics, as these give invaluable insights into eruption dynamics, timescales of eruptions, and eruption

magnitudes etc. However, as discussed, eruptive products only contribute to less than around 50% of the volcano's dynamic history. Hence, the study of these products allows us to observe only a part of the magmatic evolution.

From these limitations, it follows that our reconstructions of the volcanic plumbing systems of volcanoes are with an amount of uncertainty, because of limited available data and the limitations of the applied methodologies. In Figs. 8.4-8.6, for example, we observe how different magma-chamber geometries, structures and magma-chamber processes can produce similar dyke-fed magmatism and structures. In Fig. 8.4, we observe the evolution of a magma chamber through time. Deep magma chambers/reservoirs need a long time to produce evolved, and fractionated magmas (e.g., 100ky for a basaltic magma chamber size of a 390km3 with a 100MW cooling rate) (Hawkesworth et al., 2000) but AFC processes in shallow chambers can take place in years or even weeks (Edwards and Russel, 1998). In Santorini, previous studies reported that the long-term cycles lasted about 170 ky divided by shorter cycles of 20-40 ky in between large silicic events or cones and shield formation (Druitt, 2015). In To, of Figure 8.4, we show an ellipsoidal, short-lived, mafic magma chamber that generates a dyke population that fed volcanic eruptions. With time (T_1) the magma chamber evolves to more felsic compositions with near-simultaneous changes in size and volume. A second dyke population, this time primarily felsic, may then be emplaced. In Fig. 8.5 we observe two different possible scenarios that could also be interpreted by the same stratigraphy. Figure 8.5 shows a new

batch of magma that intrudes the magma chamber that had previously triggered a mafic dyke population. A magma mixing event can produce a new hybrid magma composition or an entirely felsic composition which can locally alter the magmatic overpressure and trigger a new population of dykes.

Gudmundsson (2012) proposed compartments in magma chambers where regional faults can dissect shallow magma chambers – or, alternatively, other geometric constraints - resulting in isolated parts/compartments of a magma chamber which may evolve differently from other compartments in the chamber. As a result, different dyke populations with different compositions may derive from the same magma chamber. In Figure 8.6, a transcrustal volcanic plumbing system is shown, with a two-chamber model, a deeper mafic chamber and a shallow more evolved chamber. In this model, dykes can be triggered by both magma chambers simultaneously, depending on the triggering events.

In all previous examples, it is concluded that the host rock analysis could give us insights of the possible triggers, the origin, depth and processes that occurred but not the geometry, the structure and associated local stresses of the plumbing system which are the parameters that primarily control magma-chamber rupture and dyke injection and propagation. Hence, further multidisciplinary studies that combine petrogenetic modelling with volcanotectonic modelling are needed to understand this problem entirely.

Eroded dyke swarms with wide compositional ranges allow an examination of the evolution of the magmatic storage system through time. Explicitly, arrested dykes carry information about magmatic injections which never fed volcanic eruptions, and so they uniquely record data from unsuccessful magmatic triggering events – failed eruptions. Their study can ultimately provide insights on the evolution of volcanic plumbing systems and combined with the eruptive products can help decode the sequence of the processes (magma fractionation, differentiation, mixing) that occur in magma reservoirs and primarily diagnose under which conditions they lead to pressure increase (eruption triggers).

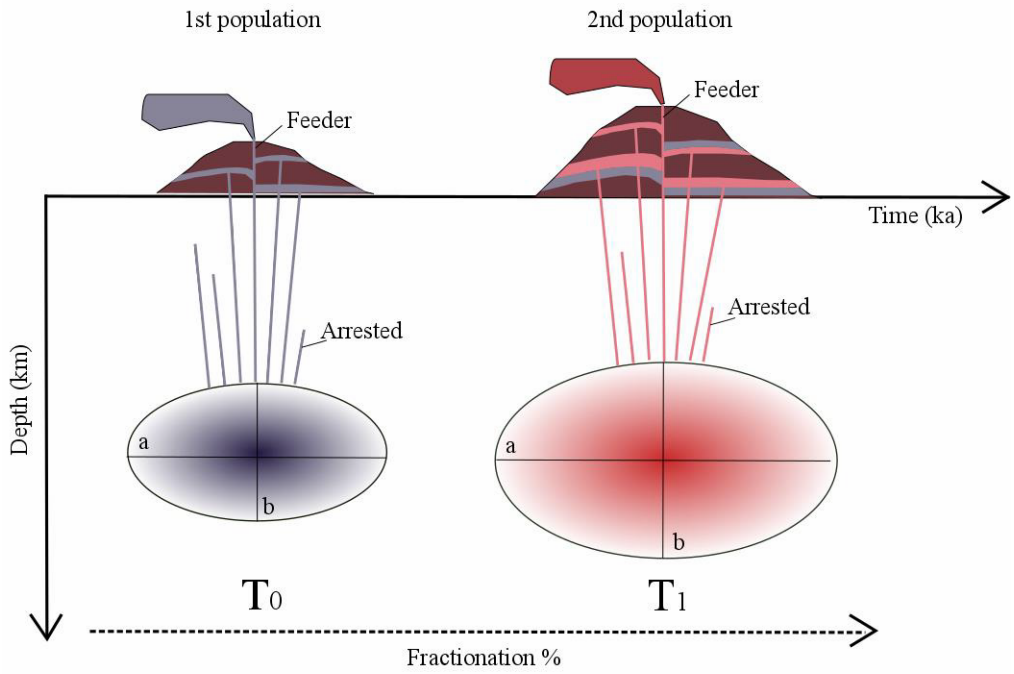

Fig. 8.4: Schematic illustration showing the evolution of a magma chamber through time. T_o stands for the initial magma chamber stages and T_1 for the evolved stage. The letters a and b denote the semi-axes of the ellipsoidal

chambers. Not to scale.

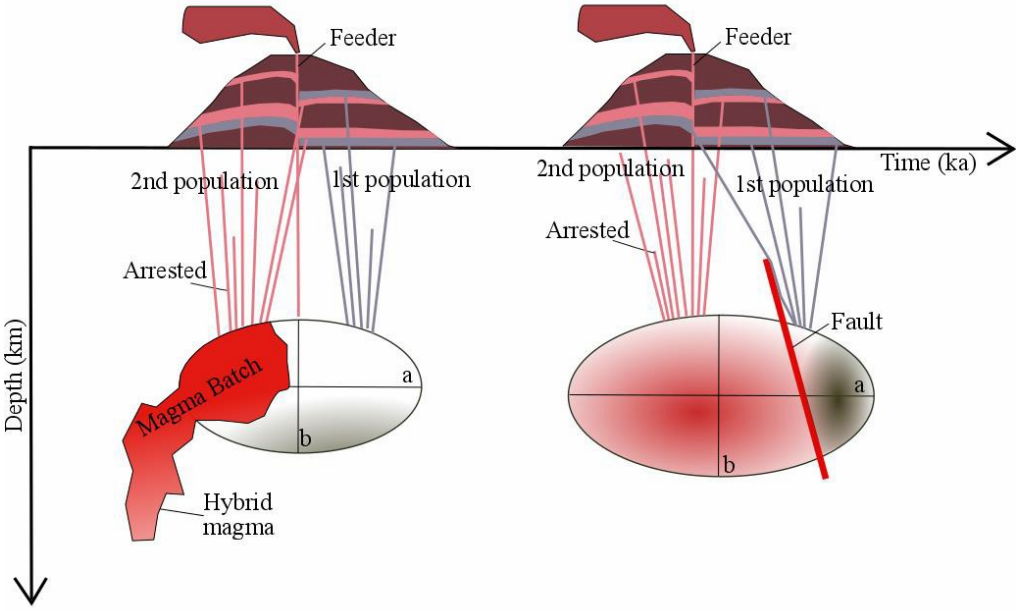

Fig. 8.5: Illustration showing different magmatic processes that can produce similar stratigraphic sequence in a volcanic edifice. Left: magma mixing. Right: Magma chamber compartments due to a transverse impermeable fault. The letters a and b denote the semi-axes of the ellipsoidal chamber.

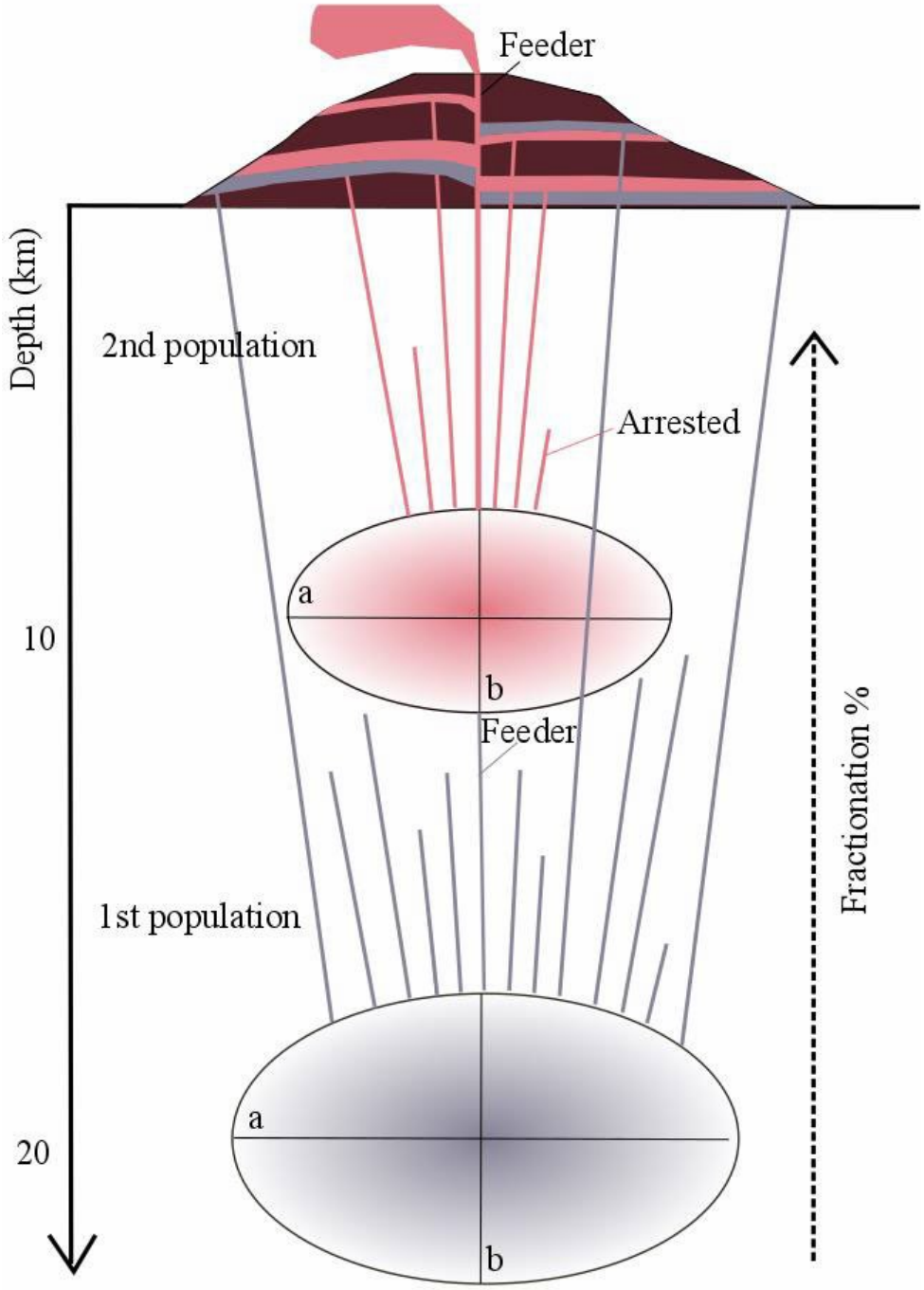

Fig. 8.6: Schematic illustration showing a transcrustal system. The latter consists of a deep mafic reservoir and a felsic shallow magma chamber. Both generate dyke populations but of different compositions. The letters a and b denote the semi-axes of the ellipsoidal chamber.

FUTURE WORK

Future work along the lines of that presented in this thesis could include:

1) Studying arrested dikes in different geotectonic regimes. This can give us insights into arrest mechanisms in different stress regimes.

2) Integrating numerical studies with physical-chemical processes to quantify the assimilation percentages of different material (components) during ascent in homogeneous and heterogeneous crustal segments.

Bibliography

Acocella, V., (2000). Space accommodation by roof lifting during pluton emplacement at Amiata (Italy). Terra Nova, 12, 149–155.

Akilas, B.I., (1925). Τα ηφαίστεια και η νήσος Θήρα. Αθήνα, Τύπος Ε & Ι Μπλαζουδάκη, Αθήνα, Ελλάδα.

Anderson, E. M., (1936). The dynamics of formation of cone sheets, ring-dykes, and cauldron subsidence. Proceedings of the Royal Society of Edinburgh 56, 128–163.

Anderson, E.M., (1951). Dynamics of faulting and dyke formation, 2nd edn. Olivier and Boyd, Edinburgh.

Anderson, A.T., Swihart, G.H., Artioli, G., Geiger, A., (1984). Segregation vesicles, gas filter-pressing, and igneous differentiation, Journal of Geology, 92, 55– 72.

Andújar, J., Scaillet, B., Pichavant, M., Druitt, T. H., (2015). Differentiation conditions of a basaltic magma from Santorini and its bearing on basalt–andesite to andesite magma production in arc settings. Journal of Petrology 56, 765–794.

Andújar, J., Scaillet, B., Pichavant, M., Druitt, T. H., (2016). Generation conditions of dacite and rhyodacite via the crystallization of an andesitic magma. Implications for the plumbing system at Santorini (Greece) and the origin of tholeiitic or calc-alkaline differentiation trends in arc magmas.

Journal of Petrology 57, 1887–1920.

Angelier, J., Lyberis, N., Le Pichon, X., Barrier, E., Huchon, P., (1982). The tectonic development of the Hellenic arc and the Sea of Crete: a synthesis. Tectonophysics, 86, 159-196.

Annen, C., Blundy, D.J., Leuthold, J., Sparks, R.S.J., (2015). Construction and evolution of igneous bodies: towards an integrated perspective of crustal magmatism. Lithos, 230, 206-221.

Armienti, P., Perinelli, C., Putirka, K.D., (2013). A new model to estimate deep level magma ascent rates, with applications to Mt. Etna (Sicily, Italy). Journal of Petrology, 54, 795–813.

Bailey, J.C., Jensen, E., Hansen, A., Kann, A., Kann, K., (2009). Formation of heterogeneous magmatic series beneath North Santorini, South Aegean island arc, Lithos, 110 (1), 20–36.

Bailey, E.H., Stevens, R.E., (1960). Amer. Min., 45, 1020-1025.

Balk, R., (1930). Structural Survey of the Adirondack Anorthosite, Journal of Geology 38, 289-302.

Bachmann, O., Bergantz, G.W., (2004). On the origin of crystal-poor rhyolites: extracted from batholithic crystal mushes. Journal of Petrology, 45, 1565–1582.

Bacon, C.R., Druitt, T.H., (1988). Compositional evolution of the zoned calcalkaline magma chamber of Mount Mazama, Crater Lake, Oregon.

Contributions to Mineralogy and Petrology, 98, 224–256.

Barnett, Z.A., Gudmundsson, A., (2014). Numerical modelling of dykes deflected into sills to form a magma chamber. Journal of Volcanology and Geothermal Research, 281, 1-11.

Beaumont, D., (2010). How the Earth's Geology Determined Human History, Sino-Platonic Papers, 203, 93.

Becerril, L., Galindo, I., Gudmundsson, A., Morales, J. M., (2013). Depth of origin of magma in eruptions. Sci. Rep. 3, 2762.

Behrensmeyer, A. K., (1982). The geological context of human evolution. Ann. Rev. Earth Planet. Sci., 10, 39-60.

Becker, G.F., (1897). Fractional crystallization of rocks. American Journal of Science, 4, 257-261.

Bell, F.G., (1983). Fundamentals of Engineering Geology, Butterworth-Heinemann, Elsevier.

Benoit, J.P., McNutt, S.R., (1996). Global Volcanic Earthquake Swarm Database 1979-1989, Open-File Report, 96-99, Geological Survey, U. S., 333

Best, M.G., (2003). Igneous and metamorphic petrology, Blackwell Science Ltd.

Blake, S., (1981). Volcanism and the dynamics of open magma chambers. Nature, 289, 783-785.

Blake, S., (1984). Volatile oversaturation during the evolution of silicic magma chambers as an eruption trigger. Journal of Geophysical Research, 89, 8237– 8244.

Blatt, H and Tracy, R., (1996). Petrology Igneous, sedimentary and metamorphic, 2nd edition., Freeman W.H. and Co Ltd.

Boone, T.J., Ingraffea, A.R., (1990). A numerical procedure for simulation of hydraulically driven fracture propagation in poroelastic media. Int. J. Numer. Anal. Meth. Geomech., 14, 27-47.

Bowen, N. L., (1928). The evolution of the igneous rocks: Princeton, New Jersey, Princeton University Press, New York, Dover.

Broek, D., (1982). Elementary engineering fracture mechanics. Martinus Nijhoff publishers, the Netherlands.

Brown, M., (1994). The generation, segregation, ascent and emplacement of granite magma: The migmatite-to-crustally-derived granite connection in thickened orogens, Earth Sci. Rev., 36, 83– 130.

Browning, J., (2016), 'Thermo-mechanical effects of magma chambers and caldera faults', Doctoral thesis, Royal Holloway, University of London.

Browning J., Gudmundsson A., (2015). Caldera faults capture and deflect inclined sheets: an alternative mechanism of ring dike formation Bull. Volcanol., 77, 1-13.

Browning, J., Drymoni K., Gudmundsson, A. (2015). Forecasting magma-

chamber rupture at Santorini volcano. Sci. Rep. Nature 5, 15785.

Cashman, K.V., Giordano, G., (2014). Calderas and magma reservoirs. J. Volcanol. Geotherm. Res. 288, 28–45.

Burnham, C.W., (1979). Magmas and hydrothermal fluids. In: Barnes HL (ed) Geochemistry of hydrothermal ore deposits, 2nd edition: Wiley Interscience, New York, 71–136.

Cadoux, A., Scaillet, B., Druitt, T. H., Deloule, E., (2014). Magma storage conditions of large Plinian eruptions of Santorini Volcano (Greece). Journal of Petrology 55, 1129–1171.

Caricchi, L., Simpson, G., Schaltegger, U., (2016). Estimates of volume and magma input in crustal magmatic systems from zircon geochronology: the effect of modelling assumptions and system variables: Frontiers in Earth Science, 4, 48.

Cashman K.V., Sparks R. S. J., (2013). How volcanoes work: A 25-year perspective. Geological Society of America Bulletin 125, 664–690.

Cashman, K.V., Sparks, R.S.J., Blundy, J., (2017). Vertically extensive and unstable magmatic systems: A unified view of igneous processes, Science, 355, 6331.

Cembrano, J., Lara, L., (2009). The link between volcanism and tectonics in the southern volcanic zone of the Chilean Andes: a review Tectonophysics, 471, 96-113.

Chamberlain, K.J., Wilson, C.J.N., Wooden, J.L., Charlier, B.L.A., Ireland, T.R., (2014). New perspectives on the bishop tuff from zircon textures, ages and trace elements. J. Petrol. 55, 395–426.

Chen, Z., Jin, Z-H., Johnson S.E., (2011). Transient dike propagation and arrest near the level of neutral buoyancy. Journal of Volc and Geothermal Research, 203, 81-86.

COMSOL (2012). COMSOL Multiphysics User's Guide, Version 4.3.

COMSOL (2017). Detailed explanation of the Finite Element Method (FEM) (www.comsol.com)

COMSOL Blog (2017). How to model Fluid-structure Interaction in a water balloon by Phillip Oberdorfer (www.comsol.com/blogs)

Coombs, M.L., Eichelberger, J.C., Rutherford, M.J., (2002). Experimental and textural constraints on mafic enclave formation in volcanic rocks, J. Volcanol. Geotherm. Res., 119, 125-144.

Couch, S., Sparks, R.S.J., Carroll, M.R., (2001). Mineral disequilibrium in lavas explained by convective self-mixing in open magma chambers, Nature, 411, 1037-1039.

Cottrell, E., Gardner, J.E., Rutherford, M.J., (1999). Petrologic and experimental evidence for the movement and heating of the pre-eruptive Minoan rhyodacite (Santorini, Greece), Contrib. Mineral. Petrol., 135, 315–331.

Cox, K.G., Bell, J.D., Pankhurst, R.J., (1979). The interpretation of igneous rocks. Allen and Unwin, London

Cruden, A.R., Weinberg, R.F., (2018). Mechanisms of Magma Transport and Storage in the Lower and Middle Crust-Magma Segregation, Ascent and Emplacement. In S. Burchardt (ed.), Volcanic and Igneous Plumbing Systems: Understanding Magma Transport, Storage, and Evolution in the Earth's Crust (pp. 13-53). Amsterdam: Elsevier

Crouch, S., Starfield, A., (1983). Boundary element methods in solid mechanics. George Allen and Unwin Ltd, London.

Dahm, T., (2000). Numerical simulations of the propagation path and the arrest of fluid-filled fractures in the Earth. Geophysical Journal International 141, 623–638.

Daly, R. A., (1911). The nature of volcanic action. Proc. Am. Acad. Arts Sci. 47, 48–119.

Daniels, K A., Kavanagh, J.L., Menand, T. and Sparks, S. J., (2012). The shapes of dikes: Evidence for the influence of cooling and inelastic deformation. GSA Bulletin, 124, 1102– 1112.

Davis, E.N. and Bastas, C., (1978). Petrology and geochemistry of the metamorphic system of Santorini. In Thera and the Aegean World. 1, 61 Delaney, P., Pollard, D., Ziony, J., McKee E., (1986). Field relations between dikes and joints: emplacement processes and paleostress analysis J. Geophys. Res., 91, 4920-4938.

Delesse, A., (1848). Pour determiner la composition des Roches. Annales des Mines, Serie 4,379-88.

Delcamp, A., Troll, V. R., van Wyk de Vries, B., Carracedo, J. C., Petronis, M. S., Pérez Torrado, F. J. and Deegan, F. M., (2012). Dykes and structures of the NE rift of Tenerife, Canary Islands: a record of stabilisation and destabilisation of ocean island rift zones Bulletin of Volcanology, 74, 963-980.

Dieterich, J., (1994). A constitutive law for rate of Earthquake production and its application to earthquake clustering, J. Geophys. Res. 99, 2601-2618.

Dimitriadis, I., Papazachos, C., Panagiotopoulos, D., Hatzidimitriou, P., Bohnhoff, M., Rische, M., Meier T., (2010). P and S velocity structures of the Santorini–Kolumbo volcanic system (Aegean Sea, Greece) obtained by non-linear inversion of travel times and its tectonic implications J. Volcanol. Geotherm. Res., 195, 13-30

Dobson, K.J., Coban, S.B., McDonald, S.A., Walsh, J., Atwood, R., Withers, P.J., (2016). 4D imaging of sub-second dynamics in pore-scale processes using real time synchrotron x-ray tomography. Solid Earth Discussions 1-27.

Druitt T. H. Costa F. Deloule E. Dungan M. Scaillet B. (2012). Decadal to monthly timescales of magma transfer and reservoir growth at a caldera volcano. Nature 482, 77–80.

Druitt, T. H., (2014). New insights into the initiation and venting of the Bronze-Age eruption of Santorini (Greece), from component analysis.

Bulletin of Volcanology 76, 794.

Druitt, T.H. (2015). Field guide to Santorini Volcano, MeMoVolc short course, Santorini.

Druitt, T. H., Francaviglia, V., (1992). Caldera formation on Santorini and the physiography of the islands in the late Bronze Age. Bull. Volcanol. 54, 484–493

Druitt, T.H., Edwards, L., Mellors, R.M., Pyle, D.M., Sparks, R.S.J., Lanphere, M., Davis, M., Barriero, B., (1999). Santorini Volcano. Geological Society Memoir No. 19, 165.

Druitt, T.H., Costa, F., Deloule, E., Dungan, M., Scaillet, B., (2012). Decadal to monthly timescales of magma transfer and reservoir growth at a caldera volcano. Nature, 482, 77–80.

Druitt, T.H., Mercier, M., Florentin, L., Deloule, E., Cluzel, N., Flaherty, T., Médard, E., Cadoux, A., (2016). Magma storage and extraction associated with Plinian and interplinian activity at Santorini caldera (Greece). J Petrol. 57, 461–494.

Dundurs, J. (1969) Journal of Applied Mechanics, 36, 650-652.

Duff, P. Mcl. D., (1993). Holmes' principles of physical geology, fourth edition, Chapman and Hall

Edwards, B. R. & Russell, J. K. (1998). Time scales of magmatic processes: new insights from dynamic models for magmatic assimilation. Geology, 26,

1103–1106.

Eggert, S., Walter, T.R., (2009). Volcanic activity before and after large tectonic earthquakes: Observations and statistical significance Tectonophysics, 471, 14-26.

Eleftheriadis, G., Christofides, G., Esson, G., Soldatos, T., Koroneos, A., (1996). Petrology and geochemistry ofthe volcanic dykes from the Santorini caldera walls. The European Laboratory Volcanoes -- Proceedings of the second workshop, Santorini, Greece, 137-155.

Encyclopaedia Britannica., (2018). Petrology, (www.britannica.com/science/petrology)

Fabbro, G.N., Druitt, T.H., Scaillet, S., (2013). Evolution of the crustal magma plumbing system during the build-up to the 22-ka caldera-forming eruption of Santorini (Greece), Bull. Volcanol., 75, 1– 22.

Fabbro, G.N., (2014). The timescales of magmatic processes prior to a caldera-forming eruption. Doctoral thesis, Université Blaise Pascal, Clermont-Ferrand.

Fabbro, G.N., Druitt, T.H., Costa, F., (2017). Storage and Eruption of Silicic Magma across the Transition from Dominantly Effusive to Caldera-forming States at an Arc Volcano (Santorini, Greece), Journal of Petrology, 58, 2429–2464.

Flaherty, T., Druitt, T.H., Tuffen, H., Higgins, M.D., Costa, F., Cadoux, A., (2018). Multiple timescale constraints for high-flux magma chamber

assembly prior to the Late Bronze Age eruption of Santorini (Greece), Contributions to Mineralogy and Petrology, 173, 75.

Forbes Inskip, N., (2019). The effects of heterogeneity and anisotropy on hydraulic fracture propagation, Doctoral thesis, Royal Holloway, University of London.

Francalanci, L., Vougioukalakis, G.E., Perini, G., Manetti, P., (2005). A west–east traverse along the magmatism of the south Aegean volcanic arc in the light of volcanological, chemical and isotope data. In: Fytikas M. Vougioukalakis G. E. (eds) The South Aegean Active Volcanic Arc: Present Knowledge and Future Perspectives. Developments in Volcanology, Amsterdam: Elsevier, 65–111.

Freund, L.B., Suresh, S., (2003). Thin Film Materials-Stress, Defect Formation and Surface Evolution, Cambridge University Press, Cambridge, U.K.

Galanopoulos, A.G. and Bacon, E., (1969). Atlantis: Truth behind the legend. London: Nelson.

Galland, O., S. Burchardt, E. Hallot, R. Mourgues, and C. Bulois (2014), Dynamics of dikes versus cone sheets in volcanic systems, J. Geophys. Res. Solid Earth, 118, 6178–6192.

Gertisser, R., Preece, K., Keller, J., (2009). The Plinian lower pumice 2 eruption, Santorini, Greece: Magma evolution and volatile behaviour, J. Volcanol. Geotherm. Res., 186, 387– 406.

Geshi, N., Shimano, T., Chiba, T., Nakada, S., (2002). Caldera collapse during the 2000 eruption of Miyakejima Volcano, Japan, Bull. Volcanol., 64, 55– 68.

Geshi, N., (2005). Structural development of dike swarms controlled by the change of magma supply rate: The cone sheets and parallel dike swarms of the Miocene Otoge igneous complex, central Japan, J. Volcanol. Geotherm. Res., 141, 267–281.

Geshi, N., Kusumoto, S., Gudmundsson, A., (2010). Geometric difference between non-feeder and feeder dikes. Geology 38, 195-198

Gonnermann, H., Taisne, B., (2015). Magma transport in dykes. In: Sigurdsson H., Houghton B., McNutt S., Rymer H., Stix J. (eds) The Encyclopedia of Volcanoes , 2nd edn. Academic Press, 215–224.

Green, T.H., (1980). Island arc and continent-building magmatism: a review of petrogenetic models based on experimental petrology and geochemistry. Tectonophysics 63, 367-85

Griffith, A.A., 1921. The phenomena of rupture and flow in solids. Phil.Trans. Roy. Soc. A., 221, 163-198.

Griffith, A.A., 1924. The theory of rupture. First international congress of Applied Mathematics, Delft, pp. 55-63.

Grosfils, E.B. (2007). Magma reservoir failure on the terrestrial planets: Assessing the importance of gravitational loading in simple elastic models. Journal of Volcanology and Geothermal Research, 166, 47-75.

Gudmundsson, A., (1983). Form and dimension of dykes in eastern Iceland, Tectonophysics, 95, 295-307.

Gudmundsson, A., (1984). Formation of dykes, feeder dykes, and the intrusion of dykes from magma chambers, Bulletin of Volcanology, 47, 537-550.

Gudmundsson, A., (1987). Formation and mechanics of magma reservoirs in Iceland. Geophysical Journal of the Royal Astronomical Society, 91, 27-41.

Gudmundsson, A., (1988). Formation of collapse calderas. Geology, 16, 808-810.

Gudmundsson, A., (1990). Emplacement of dikes, sills and crustal magma chambers at divergent plate boundaries Tectonophysics, 176, 257-275.

Gudmundsson, A. (1998). Formation and development of normal-fault calderas and the initiation of large explosive eruptions, Bull. Volcanol., 60, 160-170.

Gudmundsson, A. (1999). Fluid overpressure and stress drop in fault zones. Geophys. Res. Lett. 26, 115-118.

Gudmundsson, A., (2002). Emplacement and arrest of sheets and dykes in central volcanoes. J. Volcanol. Geotherm. Res. 116, 279-298.

Gudmundsson, A., (2003). Surface stresses associated with arrested dykes in rift zones Bull. Volcanol., 65, 606-619.

Gudmundsson, A., (2006). How local stresses control magma-chamber

ruptures, dyke injections, and eruptions in composite volcanoes Earth Sci. Rev., 79, 1-31.

Gudmundsson, A., (2008). Magma-chamber geometry, fluid transport, local stresses, and rock behaviour during collapse-caldera formation. In: Gottsmann, J., Marti, J. (eds.), Caldera Volcanism: Analysis, Modelling and Response. Developments in Volcanology 10. Elsevier, Amsterdam, 313-349.

Gudmundsson, A., (2011). Rock fractures in geological processes. Cambridge University Press, Cambridge.

Gudmundsson, A., (2012). Magma chambers: formation, local stresses, excess pressures, and compartments. Journal of Volcanology and Geothermal Research, 237-238, 19-41.

Gudmundsson, A., (2014). Energy release in great earthquakes and eruptions. Frontiers in Earth Science 2, 10.

Gudmundsson, (2016). The mechanics of large eruptions. Earth Sci. Reviews. 163, 72-93.

Gudmundsson, A., Brenner, S.L., (2001). How hydrofractures become arrested. Terra Nova, 13, 456-462.

Gudmundsson, A., Philipp, S. L., (2006). How local stress fields prevent volcanic eruptions. J. Volcanol. Geotherm. Res. 158, 257–268.

Gudmundsson, A., Lotveit, I.F., (2012). Sills as fractured hydrocarbon reservoirs: examples and models. Geological society, London, Special

publications, 374, 251-271.

Guzmán, S., Neri, M., Carniel, R., Martí, J., Grosse, P., et al. (2017). Remarkable variability of dyke features at the Vicuña Pampa Volcanic Complex, Southern Central Andes. Terra Nova, 29, 224-232.

Hansen, A., (1997). Megalo Vouno volcano in the northern part of Santorini. M.Sc. thesis, Copenhagen University, Denmark

Harris, P.G., (1957). Zone refining and the origin of potassic basalts. Geochim. Cosmochim. Acta 12, 195-208.

Hawkesworth, C.J., Blake, P., Evans, R., Hughes, R., Macdonald, L.E., Thomas, L.E., Turner, S.P., Zellmer, G., (2000). Time Scales of Crystal Fractionation in Magma Chambers-Integrating Physical, Isotopic and Geochemical Perspectives, Journal of Petrology, 41, 991–1006.

He, M.Y., Evans, A.G., Hutchinson, J.W., (1994). Crack deflection at an interface between dissimilar elastic materials. Int J Solids Struct, 25, 1053-1067.

He, M.Y., Hutchinson, J.W., (1989). Crack deflection at an interface between dissimilar elastic materials. Int J Solids Struct, 31, 3443–3455.

Heiken, G. and McCoy, F., (1984). Caldera Development During the Minoan Eruption, Thira, Cyclades, Greece. Journal of Geophysical Research, 89, 8441-8462.

Heimpel, M., Olson, P., (1994). Buoyancy-driven fracture and magma

transport through the lithosphere: models and experiments, in: Ryan, M. (ed.), 2933 Magmatic Systems. Academic Press, 223-240.

Heimisson, E.R., Hooper, A., Sigmundsson. F., (2015). Forecasting the path of a laterally propagating dike, J. Geophys. Res. Solid Earth, 120, 8774–8792.

Henry, C.D., Price, J.G., (1984). Variations in caldera development in the Tertiary volcanic field of trans-Pecos Texas. J Geophys Res, 89, 8765-8786.

Hess, P.C., (1989). Origins of Igneous rocks, President and Fellows of Harvard College, 276-285.

Hickey, J., and Gottsmann, J., (2014). Benchmarking and developing numerical Finite Element models of volcanic deformation. Journal of Volcanology and Geothermal Research, 280, 126-130.

Hildreth, W., (1979). The Bishop Tuff; Evidence for the origin of compositional zonation in silicic magma chambers, in Chapin, C.E. and Elston, W.E.(eds)., Ash-flow tuffs: Geological Society of America Special Paper 180, 43–75.

Hildreth, W., (1981). Gradients in silicic magma chambers: implications for lithospheric magmatism J. Geophys. Res., 86, 10153-10192

Holness M.B., Tegner C., Nielsen T.F., Stripp, G., Morse S. A., (2007). A textural record of solidification and cooling in the Skaergaard intrusion, East Greenland. Journal of Petrology, 48, 2359-2377.

Holohan, E. P., van Wyk de Vries, B., Troll, V. R. (2008). Analogue models of caldera collapse in strike-slip tectonic regimes. Bull. Volcanol. 70, 773–

796.

Holohan, E.P., Schöpfer, M.P.J., Walsh, J.J., (2015). Stress evolution during caldera collapse. Earth Planet. Sci. Lett. 421, 139–151.

Hooft, E.E.E., P. Nomikou, D.R. Toomey, D. Lampridou, C. Getz, M. Christopoulou, D. O'Hara, G.M. Arnoux, M. Bodmer, M. Gray, B.A. Heath, and B.P. Vander Beek, (2017). Backarc tectonism, volcanism, and mass wasting shape seafloor morphology in the Santorini-Christiana-Amorgos region of the Hellenic Volcanic Arc, Tectonophysics, 712-713, 396-414.

Hooft, E.E.E., Heath, B.A., Toomey, D.R., Paulatto, M., Papazachos, C.B., Nomikou, P., Morgan, J.V., Warner, M.R., (2019). Seismic imaging of Santorini: Subsurface constraints on caldera collapse and present-day magma recharge. Earth and Planetary Science Letters, 514, 48–61.

Hübscher, C., Ruhnau, M., Nomikou, P., (2015). Volcano-tectonic evolution of the polygenetic Kolumbo submarine volcano/Santorini (Aegean Sea), J. Volcanol. Geotherm. Res., 291, 101– 111.

Huijsmans, J.P.P., (1985). Calc-Alkaline Lavas from the Volcanic Complex of Santorini, Aegean Sea, Greece: A Petrological, Geochemical and Stratigraphic Study, Utrecht Univ., Utrecht, Netherlands.

Humphreys, M.C.S., Blundy, J.D., Sparks, R.S.J., (2006). Magma evolution and open-system processes at shiveluch volcano: insights from phenocryst zoning Journal of Petrology, 47, 2303-2334.

Hutchison, W., Fusillo, R., Pyle, D.M, Mather, T.M., Blundy, J.D, Biggs, J.,

Yirgu, G., Cohen, B.E., Brooker, R.A., Barfod, D.N., Calvert, A., (2016). A pulse of mid-Pleistocene rift volcanism in Ethiopia at the dawn of modern humans. Nat. Commun.7, 13192.

Hubbert, M.K., (1937). Theory of scale models as applied to the study of geologic structures. Bull of the Geological Society of America 48, 19549-1952.

Huppert, H.E., (1982). The propagation of two-dimensional and axisymmetric viscous gravity currents over a rigid horizontal surface, J. Fluid Mech. 121, 43-58.

Huppert, H.E., Sparks R.S.J., (1985). Cooling and contamination of mafic and ultramafic magmas during ascent through the continental crust. Earth Planet. Sci. Lett. 74, 371-86.

Huppert, H.E., Sparks, R.S.J. (1989). Chilled margins in igneous rocks, Earth Planet. Sci. Lett 92, 397-405.

Hutchinson, J.W., (1996). Stresses and failure modes in thin films and multilayers. Technical University of Denmark-Notes for a DCAMM course.

Inglis, C.E., (1913). Stresses in a Plate Due to the Presence of Cracks and Sharp Corners. SPIE Milestone Series, 137, 3-17.

Irvine, T.N., (1980). Magmatic infiltration metasomatism, double-diffusive fractional crystallisation, and adcumulus growth in the Muskox Intrusion and other layered intrusions. In: Hargraves, R.B. (ed.) Physics of Magmatic Processes. Princeton University Press, Princeton, New Jersey, USA, 325-383.

Jerram, D.A., and Martin, V.M. (2008). Understanding crystal populations and their significance through the magma plumbing system, in: Dynamics of Crustal Magma Transfer, Storage and Differentiation, (eds)., C. Annen and G. F. Zellmer (London: Geological Society), 133–148.

Jing, L., (2003). A review of techniques, advances and outstanding issues in numerical modelling for rock mechanics and rock engineering International Journal of Rock Mechanics and Mining Sciences, 40, 283.

Johnston, E.N., Sparks, R.S.J., Nomikou, P., Livanos, I., Carey, S., Phillips, J.C., Sigurdsson, H., (2015). 'Stratigraphic relations of Santorini's intracaldera fill and implications for the rate of post-caldera volcanism', Journal of the Geological Society, 172, 323-335.

Johanssen, A., (1931). A descriptive petrography of the igneous rocks. Chicago university press, Chicago.

Jolivet L., Faccenna C., Huet B., Labrousse L., Le Pourhiet L., Lacombe O., Lecomte E., Burov E., Denèle Y., Brun J.-P., Philippon M., Paul A., Salaün G., Karabulut H., Piromallo C., Monié P., Gueydan F., Okay A. I., Oberhänsli R., Pourteau A., Augier R., Gadenne L., Driussi O. (2013). Aegean tectonics: strain localisation, slab tearing and trench retreat. Tectonophysics, 597-598, 1-33.

Kalogeropoulos, S. Paritsis, S., (1990). Thera and the Aegean World, Vol. III, The Thera Foundation, 164-353.

Kann, K., (2004). Et petrologisk, geokemisk og vulkanologiske studie af

Thirassia vulkankomplekset, Santorini. M.Sc. thesis, Copenhagen University, Denmark.

Kavanagh, J.L., Menand, T., Sparks, R.S.J., (2006). An experimental investigation of sill formation and propagation in layered elastic media. Earth and Planetary Science Letters, 245, 799–813.

Kavanagh, J.L., Sparks, R.S.J., (2011). Insights of dyke emplacement mechanics from detailed 3D dyke thickness datasets. Journal of the Geological Society, London 168, 965–978.

Kavanagh, J.L., Rogers, B.D., Boutelier, D., Cruden, A.R., (2017). Controls on sill and dyke-sill hybrid geometry and propagation in the crust: The role of fracture toughness. Tectonophysics, 698, 109-120.

Kavanagh, J.L., Burns, A.J., Hazim, S.H., Wood, E.P., Martin, S.A., Hignett, S., Dennis, D.JC., (2018). Challenging dyke ascent models using novel laboratory experiments: Implications for reinterpreting evidence of magma ascent and volcanism, J. Volcanol. Geotherm. Res., 354, 87-101.

Keller, J., Kraml, M., Schwarz, M., (2000). Dating major volcanic paroxysms within the deep-sea record: the example of the Thera Formation, Santorini, Greece, Abstracts, IAVCEI General Assembly, Bali, Indonesia

Kennedy, B., Stix, J., Hon, K., Deering, C., Gelman, S., (2016). Magma storage, differentiation, and interaction at Lake City caldera, Colorado, USA. Geol. Soc. Am. Bull. 128, 764–776.

Kennedy, B.M., Holohan, E.P., Stix, J., Gravley, D.M., Davidson, J.R.J.,

Cole., J.W. (2018). Magma plumbing beneath collapse caldera volcanic systems, Earth-Science Reviews, 177, 404-424.

Kilias, S.P., Nomikou, P., Papanikolaou, D., Polymenakou, P.N., Godelitsas, A., Argyraki, A., Carey, S., Gamaletsos, P., Mertzimekis, T.J., Stathopoulou, E., (2013). New insights into hydrothermal vent processes in the unique shallow-submarine arc-volcano, Kolumbo (Santorini), Greece, Sci. Rep., 3, 2421.

Klaver, M., Carey, S., Nomikou, P., Smet, I., Godelitsas, A., Vroon, P., (2016). A distinct source and differentiation history for Kolumbo submarine volcano, Santorini volcanic field, Aegean arc. Geochem Geophys Geosyst 17, 3254–3273.

Kolmogorov, A.N., (1956). Foundations of the theory of probability. New York: Chelsea Publishing company.

Konstantinou, K.I., Kalogeras, I.S., Melis, N.S., Kourouzidis, M.C., Stavrakakis, G.N., 2006. The 8 January 2006 Earthquake (Mw 6.7) Offshore Kythira Island, Southern Greece: Seismological, Strong-motion, and Macroseismic Observations of an Intermediate-depth Event Seismological Research Letters Volume 77, Number 5 September/October 2006 pp 544-553

Konstantinou, K.I. (2010). Crustal rheology of the Santorini–Amorgos zone: implications for the nucleation depth and rupture extent of the 9 July 1956 Amorgos earthquake, southern Aegean. Journal of Geodynamics, 50, 400-409.

Kristjansson, L., (2005). George P.L. Walker and his geological research in Iceland, Society report, Institute of Earth Sciences, University of Iceland, Askja, Sturlugata 7, IS-101 Reykjavík, Iceland

Kusumoto, S., Geshi, N., Gudmundsson, A., (2013). Aspect ratios and magma overpressures of non-feeder dikes observed in the Miyakejima volcano (Japan), and fracture toughness of its upper part Geophys. Res. Lett., 40, 2013.

Lara, L.E., Lavenu, A., Cembrano, J., Rodríguez, C., (2006). Structural controls of volcanism in transversal chains: resheared faults and neotectonics in the Cordón Caulle-Puyehue area (40.5°S), Southern Andes Journal of Volcanology and Geothermal Research, 158, 70-86.

Le Bas, M.J., Le Maitre, R.W., Streckeisen, A., Zanettin, B., (1986). A chemical classification of volcanic rocks based on the total alkali-silica diagram. J Petrology 27, 745-750.

Le Corvec, N., Menand, T., Lindsay, J., (2013). Interaction of ascending magma with pre-existing crustal fractures in monogenetic basaltic volcanism: an experimental approach. J. Geophys. Res.-Solid Earth 118, 968-984.

Le Corvec, N., Muirhead, J.D., White, J.D.L., (2018). Shallow magma diversions during explosive diatreme-forming eruptions. Nature Communications, 9, 1459.

Le Pichon, X., Angelier, J., (1979). The Hellenic arc and trench system: A key to the neotectonic evolution of the eastern Mediterranean area.

Tectonophysics, 60, 1-42.

Lister, J. R. (1990). Buoyancy-driven fluid fracture: the effects of material toughness and of low-viscosity precursors J. Fluid Mech., 210, 263-280.

Lister, J. R., Kerr, R.C., (1991). Fluid-mechanical models of crack propagation and their application to magma transport in dykes. J. Geophys. Res. 96, 10049–10077.

Lipman, P.W., (1997). Subsidence of ash-flow calderas: relation to caldera size and magma-chamber geometry. Bulletin of Volcanology, 59, 198-218.

Livingood, P.C., and Cordell, A.S., (2008). Point/counter point: the accuracy and feasibility of digital image techniques in the analysis of the ceramic thin sections. Journal of Archaeological science, 36, 867-872.

Lucchi, F., Santo, A.P., Tranne, C.A., Peccerillo, A., Keller, J., (2013). Volcanism, magmatism, volcano-tectonics and sea-level fluctuations in the geological history of Filicudi (western Aeolian archipelago). In: Lucchi, F., Peccerillo, A., Keller, J., Tranne, C. A. & Rossi, P. L. (eds)., The Aeolian Islands Volcanoes. Geological Society, London, Memoirs, 37, 113-153.

Maccaferri, F., Bonafede, M., Rivalta, E., (2010). A numerical model of dyke propagation in layered elastic media. Geophys. J. Int. 180, 1107-1123.

Machado, F., (1974). The search for magmatic reservoirs L. Civetta, P. Gasparini, G. Luongo, A. Rapolla (eds.), Physical Volcanology, Elsevier, Amsterdam, 255-273.

Mann, A.C., (1983). Trace element geochemistry of high alumina basalt - andesite - dacite - rhyodacite lavas of the main volcanic series of Santorini Volcano, Greece. Contrib Mineral Petrol, 84, 43-57.

Marinatos, S., (1939). 'The Volcanic Destruction of Minoan Crete'. Antiquity.

Martin, V.M., Holness, M.B., Pyle, D.M., (2006). Textural analysis of magmatic enclaves from the Kameni Islands, Santorini, Greece, J. Volcanol. Geotherm. Res., 154, 89-102.

Marsh, B.D., (1982). On the mechanics of igneous diapirism, stoping, and zone-melting. American Journal of Science, 282, 808–855.

Marsh, B.D., (1989). Magma chambers. Ann Rev Earth Planet Sci., 17, 439-74.

Marsh, B.D., (1996). Solidification fronts and magmatic evolution, Mineralogical magazine, 60, 5-4.

Marsh, B.D., (2000). Magma chambers. In: Sigurdsson, H. (ed.), Encyclopedia of Volcanoes. Academic Press, New York, 191-206.

Marsh, B.D., (2009). Magmatism, Magma and Magma chambers (ed.) Watts A. Crust and Lithosphere dynamics, Elsevier, 275-335.

Mathieu, L., van Wyk de Vries, B., Pilato, M., Troll, V.R., (2011). The interaction between volcanoes and strike-slip, transtensional and transpressional fault zones: analogue models and natural examples. Journal of Structural Geology, 33, 898-906.

McKenzie, D.P., (1971). Convection in the earth's mantle, Tectonophysics, 12, 267-268.

McKenzie, D.P., (1972). Active tectonics of the Mediterranean Region Geophys. J.R. astr. Soc, 30, 109.

McBirney, A.R., Baker, B.H., Nilson, R.H., (1985). Liquid fractionation. Part I: Basic principles and experimental simulations, Journal of Volcanology and Geothermal Research, 24, 1-24.

McKenzie, D., (1984). The generation and compaction of partially molten rock. Journal of Petrology, 25, 713-765.

Mellors, R.A., Sparks, R.S.J., (1991). Spatter-rich pyroclastic flow deposits on Santorini, Greece. Bull. Volcanol., 53, 327-342.

Meriaux, C., Lister, J. R., (2002). Calculation of dike trajectories from volcanic centres. Journal of Geophysical Research, 107, 1-10.

Michaud, V., Clocchiatti, R., Sbrana, A., (2000). The Minoan and Post-Minoan eruptions, Santorini (Greece), in the light of melt inclusions: Chlorine and sulphur behavior. J Volcanol Geotherm Res, 99, 195-214.

Morgavi, D., Arienzo, I., Montagna, C., Perugini, D., Dingwell, D.B., (2017). Magma Mixing: History and Dynamics of an Eruption Trigger. In: Gottsmann J., Neuberg J., Scheu B. (eds) Volcanic Unrest. Advances in Volcanology. Springer

Mountrakis, D., Pavlides, S., Chatzipetros, A., Meletlidis, S., Tranos, M.,

Vougioukalakis, G., & Kilias, A., (1996). Active deformation of Santorini. In: Proceedings of the 2nd Workshop on European Laboratory Volcanoes, Santorini (Casale, R., Fytikas, M., Sigvaldasson, G., Vougioukalakis, G., eds), 13-22.

Muller, O.H., Pollard, D.D., (1977). The stress state near Spanish Peaks, Colorado, determined from a dike pattern. Pure Appl. Geophys. 115, 69–85.

Murphy, M.D., Sparks, R.S.J, Barclay, J., Carroll, M.R., Brewer, T.S., (2000). Remobilization of andesite magma by intrusion of mafic magma at the Soufrière Hills Volcano, Montserrat, West Indies, Journal of Petrology, 41, 21-42.

Nakashima, Y., (1993). Static Stability and Propagation of a Fluid-Filled Crack in Rock: Implication for Fluid Transport in Magmatism and Metamorphism. J. Phys. Earth 41, 189-202.

Newhall C.G. Dzurisin D., (1988). Historical unrest at large calderas of the world: U.S. Geological Survey Bulletin, 1855, 1108.

Nicholls, I.A., (1971). Petrology of Santorini volcano, Cyclades, Greece. J Petrol 12, 67-119.

Nomikou, P., S. Carey, D. Papanikolaou, K. Croff Bell, D. Sakellariou, M. Alexandri, and K. Bejelou (2012), Submarine volcanoes of the Kolumbo volcanic zone NE of Santorini Caldera, Greece, Global Planet. Change, 90-91, 135– 151

Nomikou, P., Papanikolaou, D., Alexandri, M., Sakellariou, D., and

Rousakis, G., (2013). Submarine volcanoes along the Aegean volcanic arc, Tectonophysics, 597, 123-146.

Nomikou, P., Druitt, T., Hübscher, C. et al. (2016). Post-eruptive flooding of Santorini caldera and implications for tsunami generation. Nat Commun 7, 13332.

Oldroyd, D.R (ed.) 2002. The earth inside and out: Some contributions to Geology in the twentieth century. Geological society, London, Special publications, 192, 1-16.

Papazachos, B.C., Comninakis, P.E., (1971). Geophysical and tectonic features of the Aegean arc. J. Geophys. Res. 76, 8517-8533.

Parks, M.M., Biggs, J., England, P., Mather, T.A., Nomikou, P., Palamartchouk, K., Papanikolaou, X., Paradissis, D., Parsons, B., Pyle D.M., (2012). Evolution of Santorini Volcano dominated by episodic and rapid fluxes of melt from depth, Nat. Geosci., 5, 749-754.

Paterson, S.R., Okaya, D., Memeti, V., Economos, R., Miller, R.B., (2011). Magma addition and flux calculations of incrementally constructed magma chambers in continental margin arcs: combined field, geochronologic, and thermal modeling studies. Geosphere, 7, 1439-1468.

Patchett, P.J., (1980). Thermal effects of basalt on continental crust and crustal contamination of magmas. Nature 283, 559-61.

Pe-Piper, G., Piper, D.J.W., (2005). The South Aegean active volcanic arc: Relationships between magmatism and tectonics, Dev. Volcanol., 7, 113–

133.

Pe-Piper, G., Piper, D.J.W., Perissoratis, C., (2005). Neotectonics and the Kos Plateau Tuff eruption of 161 ka, South Aegean arc Mar. Geol., 139, 315-338.

Pearce, J.A., (1983). The role of sub-continental lithosphere in magma genesis at destructive plate margins. In continental basalts and mantle xenoliths. C.J. Hawkesworth and M.J.Norry (eds), Nantwich: Shiva, 230-49.

Pearce, J.A., Peate, D.W., (1995). Tectonic implications of the composition of volcanic arc magmas. Annu Rev Earth Planet Sci, 23, 251-28.

Petersen, A.D.J., (2004). A geological and petrological study of the dikes in the Megalo Vouno volcano complex, Santorini. M.Sc. thesis, Copenhagen University, Denmark.

Perissoratis, C., (1995). The Santorini volcanic complex and its relation to the stratigraphy and structure of the Aegean arc, Greece Mar. Geol., 128, 37-58.

Phillipson, G., Sobradelo R., Gottsmann J., (2013). Global volcanic unrest in the 21st century: An analysis of the first decade. JVGR, 264, 183-196.

Piper, D.J.W., Pe-Piper, G., Perissoratis, C., Anastasakis, G., (2007). Distribution and chronology of submarine volcanic rocks around Santorini and their relationship to faulting, 291, Geological Society, London, 99-111.

Piper, D.J.W., Perissoratis, C., (2003). Quaternary neotectonics of the South

Aegean arc, Mar. Geol., 198, 259-288.

Pinel, V., Jaupart, C., (2004). Magma storage and horizontal dyke injection beneath a volcanic edifice. Earth and Planetary Science Letters 221, 262.

Pollard, D.D. (1987). Elementary fracture mechanics applied to the structural interpretation of dykes. In: Mafic dyke swarms (edited by Halls, H. C. & Fahrig, W. F.). Spec. Pap. geol. Ass. Canada

Pollard, D. D., Johnson, A. M., (1973). Mechanics of growth of some laccolithic intrusions in the Henry mountains, Utah, II. Bending and failure of overburden layers and sill formation. Tectonophysics, 18, 311-354.

Pollard, D. D., Muller, H., (1976). The effect of gradients in regional stress and magma pressure on the form of sheet intrusions in cross section, Solid Earth and Planets, 81, 975-984

Putirka, K., (1997). Magma transport at Hawaii: inferences based on igneous thermobarometry. Geology 25, 69-72.

Pyle, D.M., (2017). Visions of Volcanoes. 19: Interdisciplinary Studies in the Long Nineteenth Century, 25

Reddy, J. N. (2013). An Introduction to Continuum Mechanics, Cambridge Univ. Press, New York

Renjith, M.L., (2013). Micro-textures in plagioclase from 1994–1995 eruption, Barren Island Volcano: Evidence of dynamic magma plumbing system in the Andaman subduction zone, Geoscience Frontiers, 5, 113-126.

Rickwood P.C. (1990). The anatomy of a dyke and the determination of propagation and magma flow directions in: Parker A.J., Rickwood P.C., Tucker D.H. (Eds.), Mafic Dykes and Emplacement Mechanisms, Balkema, Rotterdam, 81-100.

Rivalta, E., Dahm, T., (2006). Acceleration of buoyancy-driven fractures and magmatic dikes beneath the free surface. Geophys. J. Int. 166, 1424-1439.

Rivalta, E., Taisne, B. Bunger, A. P. Katz., R. F. (2015). A review of mechanical models of dike propagation: Schools of thought, results and future directions, Tectonophysics, 638, 1-42.

Rizzo, A.L., Barberi, F., Carapezza, M.L., Di Piazza, A., Francalanci, L., Sortino, F., D'Alessandro, W., (2015). New mafic magma refilling a quiescent volcano: Evidence from He–Ne–Ar isotopes during the 2011–2012 unrest at Santorini, Greece. Geochemistry, Geophysics, Geosystems, 16, 798-814.

Rizzo, A.L., Caracausi, A., Chavagnac, V., Nomikou, P., Polymenakou, P., Mandalakis, M., Kotoulas, G., Magoulas, A., Castillo, A., Lampridou, D., (2016). Kolumbo submarine volcano (Greece): An active window into Aegean subduction system, Sci. Rep., 6, 1-9.

Robinson, P., (1991). The eye of the petrographer, the mind of the petrologist. Am. Mineral. 76, 1781-1810.

Roman, A. Jaupart, C., (2017). Post emplacement dynamics of basaltic intrusions in the continental crust, J. Geophys. Res.-Sol. Ea., 122, 966–987.

Rubin, A.M. (1993). Dykes vs. diapirs in viscoelastic rock Earth Planet. Sci. Lett., 119, 641-659.

Rubin, A. M., (1995). Propagation of magma-filled cracks. Annu. Rev. Earth Planet. Sci. 23, 287-336.

Rubin, A.M., Pollard, D.D., (1987). Origins of Blade-Like Dikes in Volcanic Rift Zones, in Volcanism in Hawaii, U.S. Geol. Surv. Prof. Pap., 1350, 1449-1470.

Rubin, A.M., (1998). Dike ascent in partially molten rock, J. geophys. Res. 103, 20901-20919.

Rubin, A., Gillard, D., (1998). Dike-induced earthquakes, Theoretical considerations. Journal of Geophysical Research 103, 10017-10030.

Rudnick, R., (1995). Making continental crust, Nature 378, 571–578.

Rudnick, R.L., Gao, S., (2003). The Composition of the Continental Crust. In: Holland, H.D. and Turekian, K.K., (eds)., Treatise on Geochemistry, The Crust, Elsevier- Pergamon, Oxford, 1-64.

Ryan, M.P., (1993). Neutral-buoyancy and the structure of midocean ridge magma reservoirs. Journal of Geophysical Research 98, 22321-22338.

Sackleton, N.J., (1987). Oxygen Isotopes, ice volume and sea level. Quaternary science reviews, 6, 183-190.

Sakellariou, D., Sigurdsson, H., Alexandri, M., Carey, S., Rousakis, G., Nomikou, P., Georgiou, P., & Ballas, D. (2010). Active tectonics in the

Hellenic volcanic arc: the Kolumbo submarine volcanic zone. Bulletin

of the Geological Society of Greece, 43, 1056-1063.

Sakellariou, D., Mascle, J., & Lykousis, V. (2013). Strike slip tectonics and transtensional deformation in the Aegean region and the Hellenic arc: Preliminary results. Bulletin of the Geological Society of Greece, 47, 647-656.

Sawi, T.M., Manga, M., (2018). Revisiting short-term earthquake triggered volcanism, Bulletin of Volcanology, 80, 7.

Schneider, C.A., Rasband, W.S., Eliceiri, K.W., (2012). NIH Image to Iamge J: 25 years of image analysis. Nat. Methods 9, 671-675.

Sielfeld, G., Ruz, J., Brogi, A., Cembrano, J., Stanton-Yonge, A., Pérez-Flores, P. and Iturrieta, P., (2019). Oblique-slip tectonics in an active volcanic chain: A case study from the Southern Andes. Tectonophysics, 770, 228221.

Sigurdsson, H., et al. (2006), Marine investigations of Greece's Santorini Volcanic Field, Eos Trans. AGU, 87, 337-342.

Simmons J.M., Cas R.A.F., Druitt T.H., Carey R.J. (2017). The initiation and development of a caldera forming Plinian eruption (172 ka Lower Pumice 2 eruption, Santorini, Greece). J. Volcanol. Geotherm. Res. 341, 332-350.

Skarpelis, N. and Liati, A., (1990). The prevolcanic basement of Thera at Athinios: metamorphism, plutonism and mineralization, Thera and the Aegean World III, 2, 172-82.

Smith, R.B., (1979). Ash-flow magmatism, Spec. Pap. Geol. Soc. Am., 180, 5-27.

Smith, E. I., Jacobs, Z., Johnsen, R., Ren, M., Fisher, E. C., Oestmo, S., Wilkins, J., Harris, J. A., Karkanas, P., Fitch, S., Ciravolo, A., Keenan, D., Cleghorn, N., Lane, C. S., Matthews, T., & Marean, C. (2018). Humans thrived in South Africa through the Toba eruption about 74,000 years ago. Nature, 555(7697), 511-515. https://doi.org/10.1038/nature25967

Sneddon, I.N., 1946. The distribution of stress in the neighbourhood of a crack in an elastic solid. Proceedings of the Royal society doi: 10.1098/rspa.1946.0077

Sparks, R.S.J., Sigurdsson, H., Wilson, L., (1977). Magma mixing: A mechanism for triggering acid explosive eruptions: Nature. 267, 315-218.

Sparks, R.S.J., Huppert H.E., Turner J.S., (1984). The fluid dynamics of evolving magma chambers. Phil Trans R. Soc. Lond. A310, 511-34.

Sparks, R.S.J., Cashman, K.V., (2017). Dynamic Magma Systems: Implications for Forecasting Volcanic Activity. Elements. 13, 35-40.

Sparks, S., Annen, C. J., Blundy, J., Cashman, K., Rust, A., & Jackson, M.D., (2019). Formation and dynamics of magma reservoirs. Philosophical Transactions of the Royal Society A: Mathematical, Physical and Engineering Sciences, 377, 2139.

Spakman, W., Wortel, M.J.R., Vlaar, N.J., (1988). The Hellenic subduction zone: a tomographic image and its geodynamic implications Geophys. Res. Lett. 15, 60-63.

Sun, S.S., (1980). Lead isotopic study of young volcanic rocks from mid-ocean ridges, ocean islands and island arcs. Phil. Trans. R. Soc. Lond. 297,409-445.

Sun, S., McDonough, W.F., (1989). Chemical and isotopic systematics of oceanic basalts: Implications for mantle composition and processes, Geol. Soc. Spec. Publ., 42, 313– 345.

Sun R.J., Jin, Z.H., (2012). Fracture Mechanics, Academic Press, Kilington, Oxford.

Tait S.R., (1988). Samples from the crystallizing boundary layer of a zoned magma chamber, Contributions to Mineralogy and Petrology, 100, 470-483.

Taisne, B., Jaupart, C., (2009). Dike propagation through layered rocks. Journal of Geophysical Research (Solid Earth) 114, 9203.

Takada, A., (1990). Experimental study on propagation of liquid-filled crack 3435 in gelatin: shape and velocity in hydrostatic stress conditions. J. Geophys. Res. 95, 8471–8481.

Tepley, F. J. III, Davidson, J. P. & Clynne, M. A. (1999). Magmatic interactions as recorded in plagioclase phenocrysts of Chaos Crags, Lassen Volcanic Center, California. Journal of Petrology 40, 787–806.

Tibaldi, A., (1992). The role of transcurrent intra-arc tectonics in the configuration of a volcanic arc. Terra Nova, 4, 567–577.

Tibaldi, A., (1995). Morphology of pyroclastic cones and tectonics. Journal

of Geophysical Research, 100, 24521-24535.

Tibaldi A (1996). Mutual influence of diking and collapses at Stromboli volcano, Aeolian Arc, Italy. Geol Soc Lond Spec Publ 110, 55–63.

Tibaldi A (2001). Multiple sector collapses at stromboli volcano, Italy: how they work, Bulletin of Volcanology 63, 112–125.

Tibaldi, A. (2015). Structure of volcano plumbing systems: a review of multi-parametric effects. J. Volcanol. Geotherm. Res. 298, 85–135.

Tibaldi, A., Pasquarè, F.A., Tormey, D., (2010). Volcanism in reverse and strike-slip fault settings. In: Cloetingh, S., Negendank, J. (eds.), New Frontiers in Integrated Solid Earth Sciences. Springer-Verlag, 315–348.

Tibaldi, A., Bonali, F.L., Corazzato, C., (2014). The diverging volcanic rift system. Tectonophysics 611, 94–113.

Thomson, R.N., Morrison, M.A., Hendry, G.L, Parry, S.J., (1984). An assessment of the relative roles of a crust and mantle in magma genesis: an elemental approach. Phil. Trans. R. Soc. Lond.A310, 549-590.

Thordarson, T., Self, S., (1993). The Laki (Skaftar Fires) and Grimsvötn eruptions in 1783–1785. Bull. Volcanol., 55, 233-263.

Townsend, M.R., Pollard, D.D., Smith, R.P., (2017). Mechanical models for dikes: A third school of thought, Tectonophysics, 703-704, 98-118.

Tyrell, G.W., (1926). The Principles of Petrology. Chapman & Hall

Ui, T., Kono, M., Hamano, Y., Monge, F., Aota, Y., (1984). Reconstruction

of a volcanic edifice using the dike swarm at Ocros, Peruvian Andes, Bull. Volcanol. Soc. Jpn, 29, 285- 296.

Vaggelli, G., Pellegrini, M., Vougioukalakis, G., Innocenti, S. & Francalanci, L., (2009). Highly Sr radiogenic tholeiitic magmas in the latest inter-Plinian activity of Santorini volcano, Greece. Journal of Geophysical Research, 114.

Van der Plas, L., Tobi, A.C., (1965). A chart for judging the reliability of point counting results. AM. J. Sci. 263, 87-90.

Van Wyk De Vries, B., Merle, O., (1998). Extension induced by volcanic loading in regional strike-slip zones. Geology, 26, 983-986.

Vervoort, L., (2016). No-Go Theorems face background-based theories for quantum Mechanics, Foundations of Physics 46, 458-472.

Vespa, M., Keller, J., Gertisser, R., (2006). Interplinian explosive activity of Santorini volcano (Greece) during the past 150,000 years, Journal of Volcanology and Geothermal Research, 153, 262-286.

Viccaro, M., Giacomoni, P.P., Ferlito, C., Cristofolini, R., (2010). Dynamics of magma supply at Mt. Etna volcano (Southern Italy) as revealed by textural and compositional features of plagioclase phenocrysts, Lithos, 116, 77– 91.

Von Mises, R., (1928). Probability, Statistics and Truth, 2nd revised English edition, Dover publications, New York

Wada, Y., (1994). On the relationship between dike width and magma viscosity. J. of Geophysical research. 99, 17.763-17.755.

Walker, G.P.L., (1963), The Breiddalur central volcano, eastern Iceland. Q.

J. Geol. Soc. London, 119, 29-63.

Walker, G.P.L., (1964). Geological investigations in eastern Iceland. Bull. Volcanol., 27, 351-363.

Walker, G.P.L., (1979). A volcanic ash generated by explosions where ignimbrite entered the sea. Nature, 281, 642-646.

Walker, G.P.L., (1980). The Taupo pumice: product of the most powerful known (ultraplinian) eruption? Journal of volcanology and geothermal research 8, 69-94.

Walker, G.P.L., (1984). Downsag calderas, ring faults, caldera sizes, and incremental caldera growth. J Geophys Res 89, 8407-8416.

Walker, G.P.L., (1986). Koolau dike complex, Oahu: Intensity and origin of a sheeted-dike complex high in a Hawaiian volcanic edifice. Geology 14, 310-313.

Walker, G.P.L., (1987). Pipe vesicles in Hawaiian basaltic lavas: their origin and potential as paleoslope indicators. Geology 15, 84–87

Walker, G.P.L., (1988). Three Hawaiian calderas: an origin through loading by shallow intrusions? J Geophys Res 93, 14773-14784.

Walker, G.P.L., (1992). Coherent intrusion complexes in large basaltic volcanoes- a new structural model. Journal of Volcan. And Geoth. Research 50, 41-54.

Weinberg, R.F., Regenauer-Lieb, K., (2010). Ductile fractures and magma migration from source. Geology, 38, 363-366.

Weertman, J., (1971). Theory of water-filled crevasses in glaciers applied to vertical magma transportbeneath oceanic ridges. J. Geophys. Res. 76, 1171–1183.

White, S. M., Crisp, J. A., Spera, F.J. (2006). Long-term volumetric eruption rates and magma budgets. Geochem. Geophy. Geosy. 7:Q03010.

White, R., McCausland, W., (2016). Volcano-tectonic earthquakes: a new tool for estimating intrusive volumes and forecasting eruptions. J. Volcanol. Geotherm. Res. 309, 139-155.

Wilkins, J., Harris, J.A., Karkanas, P., Fitch, S., Ciravolo, A., Keenan, D., Cleghorn, N., Lane, C.S., Matthews, T., & Marean, C.W., (2018). Humans thrived in South Africa through the Toba eruption about 74,000 years ago, Nature, 555, 511–515.

Wilson, M., (1989). Igneous Petrogenesis, Kluwer Academic Publishers, Dordrecht, the Netherlands

Wilson, M., (1993). Magmatic differentiation, Journal of the Geological Society, London, 150, 611-624.

Wilson, C.J.N., (2001). The 26.5ka Oruanui eruption, New Zealand: an introduction and overview. J. Volcanol. Geotherm. Res. 112, 133-174.

Woods, A., Pyle, D., (1997). The control of chamber geometry on triggering volcanic eruptions, Earth and Planetary Science Letters, 151, 155-166.

Wright, E., (1971). Chemistry of Kilauea and Mauna Loa lava in space and

time. U.S. Geol. Surv. Prof. Pap. 735.

Xu, R., Huang, Y.Y., Rosakis, A.J., (2003). Dynamic Crack Deflection and Penetration at Interfaces in Homogeneous Materials: Experimental Studies and Model Predictions Journal of the Mechanics and Physics of Solids 51, 461-486.

Zellmer, G., Turner, S. & Hawkesworth, C. (2000). Timescales of destructive plate margin magmatism: new insights from Santorini, Aegean volcanic arc. Earth and Planetary Science Letters, 174, 265-281